INFLAMMATORY SIGNALING IN CARDIOVASCULAR DISEASES: PATHOGENESIS AND ANTI-INFLAMMATION THERAPY

EDITED BY: Xiang Cheng, Guo-Ping Shi, Yimei Du and Hui-Hua Li
PUBLISHED IN: Frontiers in Cell and Developmental Biology

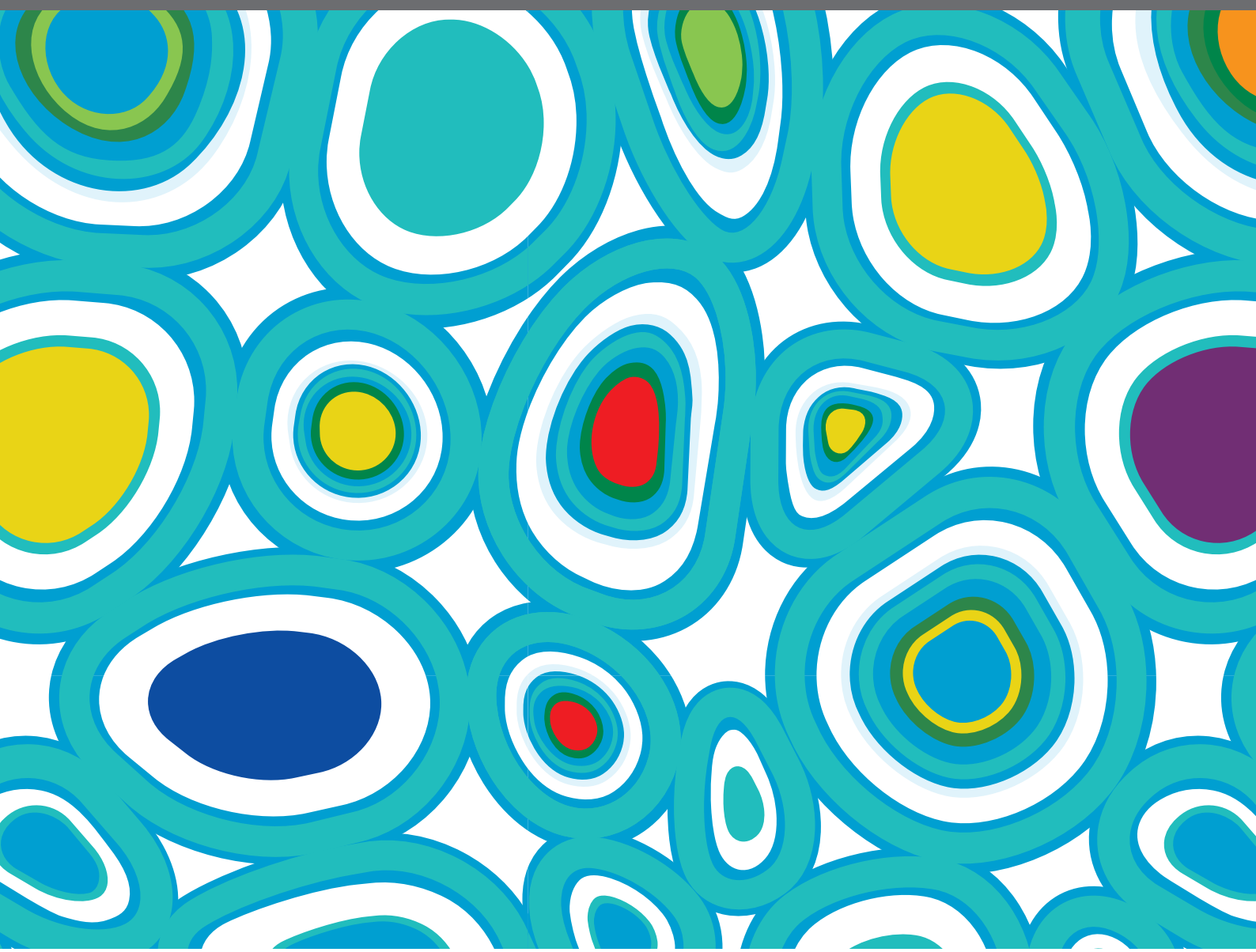

frontiers Research Topics

frontiers

ISSN 1664-8714
ISBN 978-2-88974-169-4
DOI 10.3389/978-2-88974-169-4

About Frontiers

Frontiers is more than just an open-access publisher of scholarly articles: it is a pioneering approach to the world of academia, radically improving the way scholarly research is managed. The grand vision of Frontiers is a world where all people have an equal opportunity to seek, share and generate knowledge. Frontiers provides immediate and permanent online open access to all its publications, but this alone is not enough to realize our grand goals.

Frontiers Journal Series

The Frontiers Journal Series is a multi-tier and interdisciplinary set of open-access, online journals, promising a paradigm shift from the current review, selection and dissemination processes in academic publishing. All Frontiers journals are driven by researchers for researchers; therefore, they constitute a service to the scholarly community. At the same time, the Frontiers Journal Series operates on a revolutionary invention, the tiered publishing system, initially addressing specific communities of scholars, and gradually climbing up to broader public understanding, thus serving the interests of the lay society, too.

Dedication to Quality

Each Frontiers article is a landmark of the highest quality, thanks to genuinely collaborative interactions between authors and review editors, who include some of the world's best academicians. Research must be certified by peers before entering a stream of knowledge that may eventually reach the public - and shape society; therefore, Frontiers only applies the most rigorous and unbiased reviews.
Frontiers revolutionizes research publishing by freely delivering the most outstanding research, evaluated with no bias from both the academic and social point of view. By applying the most advanced information technologies, Frontiers is catapulting scholarly publishing into a new generation.

What are Frontiers Research Topics?

Frontiers Research Topics are very popular trademarks of the Frontiers Journals Series: they are collections of at least ten articles, all centered on a particular subject. With their unique mix of varied contributions from Original Research to Review Articles, Frontiers Research Topics unify the most influential researchers, the latest key findings and historical advances in a hot research area! Find out more on how to host your own Frontiers Research Topic or contribute to one as an author by contacting the Frontiers Editorial Office: frontiersin.org/about/contact

INFLAMMATORY SIGNALING IN CARDIOVASCULAR DISEASES: PATHOGENESIS AND ANTI-INFLAMMATION THERAPY

Topic Editors:
Xiang Cheng, Huazhong University of Science and Technology, China
Guo-Ping Shi, Brigham and Women's Hospital, Harvard Medical School, United States
Yimei Du, Huazhong University of Science and Technology, China
Hui-Hua Li, Capital Medical University, China

Citation: Cheng, X., Shi, G.-P., Du, Y., Li, H.-H., eds. (2022). Inflammatory Signaling in Cardiovascular Diseases: Pathogenesis and Anti-inflammation Therapy. Lausanne: Frontiers Media SA. doi: 10.3389/978-2-88974-169-4

Table of Contents

frontiers in Cell and Developmental Biology

ORIGINAL RESEARCH
published: 23 October 2020
doi: 10.3389/fcell.2020.592048

Deficiency of LMP10 Attenuates Diet-Induced Atherosclerosis by Inhibiting Macrophage Polarization and Inflammation in Apolipoprotein E Deficient Mice

*Jiawei Liao[1], Xiangbo An[2], Xiaolei Yang[1], Qiu-Yue Lin[1], Shuang Liu[3], Yunpeng Xie[1], Jie Bai[3], Yun-Long Xia[1] and Hui-Hua Li[1,4]**

[1] Department of Cardiology, Institute of Cardiovascular Diseases, The First Affiliated Hospital of Dalian Medical University, Dalian, China, [2] Department of Interventional Therapy, The First Affiliated Hospital of Dalian Medical University, Dalian, China, [3] Department of Occupational and Environmental Health, School of Public Health, Dalian Medical University, Dalian, China, [4] Beijing Key Laboratory of Cardiopulmonary Cerebral Resuscitation, Department of Emergency Medicine, Beijing Chaoyang Hospital, Capital Medical University, Beijing, China

OPEN ACCESS

Edited by:
Narayanan Parameswaran, Michigan State University, United States

Reviewed by:
Sonika Patial, Louisiana State University, United States
Xuewei Zhu, Wake Forest School of Medicine, United States

***Correspondence:**
Hui-Hua Li
hhli1935@aliyun.com

Specialty section:
This article was submitted to Signaling, a section of the journal Frontiers in Cell and Developmental Biology

Received: 06 August 2020
Accepted: 05 October 2020
Published: 23 October 2020

Citation:
Liao J, An X, Yang X, Lin Q-Y, Liu S, Xie Y, Bai J, Xia Y-L and Li H-H (2020) Deficiency of LMP10 Attenuates Diet-Induced Atherosclerosis by Inhibiting Macrophage Polarization and Inflammation in Apolipoprotein E Deficient Mice. Front. Cell Dev. Biol. 8:592048. doi: 10.3389/fcell.2020.592048

Macrophage polarization and inflammation are key factors for the onset and progression of atherosclerosis. The immunoproteasome complex consists of three inducible catalytic subunits (LMP2, LMP10, and LMP7) that play a critical role in the regulation of these risk factors. We recently demonstrated that the LMP7 subunit promotes diet-induced atherosclerosis via inhibition of MERTK-mediated efferocytosis. Here, we explored the role of another subunit of LMP10 in the disease process, using ApoE knockout (ko) mice fed on an atherogenic diet (ATD) containing 0.5% cholesterol and 20% fat for 8 weeks as an *in vivo* atherosclerosis model. We observed that ATD significantly upregulated LMP10 expression in aortic lesions, which were primarily co-localized with plaque macrophages. Conversely, deletion of LMP10 markedly attenuated atherosclerotic lesion area, $CD68^+$ macrophage accumulation, and necrotic core expansion in the plaques, but did not change plasma metabolic parameters, lesional $SM22\alpha^+$ smooth muscle cells, or collagen content. Myeloid-specific deletion of LMP10 by bone marrow transplantation resulted in similar phenotypes. Furthermore, deletion of LMP10 remarkably reduced aortic macrophage infiltration and increased M2/M1 ratio, accompanied by decreased expression of pro-inflammatory M1 cytokines (MCP-1, IL-1, and IL-6) and increased expression of anti-inflammatory M2 cytokines (IL-4 and IL-10). In addition, we confirmed in cultured macrophages that LMP10 deletion blunted macrophage polarization and inflammation during ox-LDL-induced foam cell formation *in vitro*, which was associated with decreased IκBα degradation and NF-κB activation. Our results show that the immunoproteasome subunit LMP10 promoted diet-induced atherosclerosis in ApoE ko mice possibly through regulation of NF-κB-mediated macrophage polarization and inflammation. Targeting LMP10 may represent a new therapeutic approach for atherosclerosis.

Keywords: immunoproteasome, LMP10, diet, atherosclerosis, macrophage, inflammation, polarization

INTRODUCTION

Atherosclerosis is a chronic immune-inflammatory response within the artery, with lipid accumulation and oxidation in the intima being hallmarks of the disease (Ross, 1999). Once oxidized lipids accumulate in the intima, they attract circulating monocytes to enter the sub-endothelial space and differentiate into macrophages to scavenge these oxidized lipids (Moore et al., 2013). These lipid-laden macrophages (also known as foam cells) then secrete inflammatory cytokines, including chemokines and adhesion molecules, as well as pro- and anti-inflammatory cytokines, to recruit more monocytes, initiating inflammatory responses (Moore et al., 2013). Additionally, accumulation of oxidized lipids in foam cells activates the production of reactive oxygen species that cause cellular oxidative stress, leading to apoptotic and necrotic cell death, which plays a critical role in the formation of necrotic cores and plaque instability (Harrison et al., 2003).

The ubiquitin-proteasome system (UPS), which includes two sequential processes, namely ubiquitination and proteasome-mediated proteolysis, is the major non-lysosomal pathway for cellular proteolysis in eukaryotic cells (Hochstrasser, 1995; Ciechanover and Schwartz, 1998). The 26S proteasome complex is the proteolytic center of the UPS, which typically consists of three catalytic subunits, β1 (PSMB6), β2 (PSMB7), and β5 (PSMB5), that account for the caspase-like, trypsin-like, and chymotrypsin-like proteolytic activities, respectively (Hochstrasser, 1995; Ciechanover and Schwartz, 1998). In immune cells, and upon pro-inflammatory stimulation, these three subunits can be replaced by their inducible forms, namely β1i (PSMB9 and LMP2), β2i (PSMB10, LMP10, and Mecl-1), and β5i (PSMB8 and LMP7), to fill in a specialized type of proteasome called the immunoproteasome (Angeles et al., 2012; Basler et al., 2013). Compared to non-inducible constitutive proteasomes, immunoproteasomes elicit increased proteolytic capacity and greater efficiency in the presentation of major histocompatibility complex class I antigens to cytotoxic T lymphocytes (Angeles et al., 2012; Basler et al., 2013). Importantly, immunoproteasomes are also involved in other immune and non-immune activities, such as the activation of the nuclear factor kappa B (NF-κB) pathway and regulation of pro-inflammatory cytokine production, as well as management of oxidative stress and apoptosis (Angeles et al., 2012; Basler et al., 2013). Increased ubiquitin levels are observed in human systematic advanced plaques (Herrmann et al., 2002; Marfella et al., 2006; Versari et al., 2006), and pharmacological inhibition of ubiquitin activation attenuates experimental atherosclerosis (Liao et al., 2020b). Moreover, proteasome inhibition decreases early atherosclerosis (Feng et al., 2010; Wilck et al., 2012) but might promote advanced plaque instability (Van Herck et al., 2010; Wilck et al., 2017).

Recently, we uncovered a pro-atherogenic role of the immunoproteasome catalytic subunit LMP7 in apolipoprotein E (ApoE) knockout (ko) mice (Liao et al., 2020a). Here, we explored whether another subunit, LMP10, also contributes to diet-induced atherosclerosis.

Abbreviations: UPS, ubiquitin-proteasome system; ApoE, apolipoprotein E; ko, knockout; dko, double knockout; ATD, atherogenic diet; FPLC, fast protein liquid chromatography; BM, bone marrow; ox-LDL, oxidized low density lipoprotein; NF-κB, nuclear factor kappa B; IκB, inhibitor of NF-κB; Ang II, angiotensin II; SMC, smooth muscle cell; DOCA, deoxycorticosterone acetate.

MATERIALS AND METHODS

Animals

LMP10 ko mice (C57BL/6 background) were purchased from Jackson Laboratory as described previously (Li et al., 2018) and crossed with ApoE ko mice (C57BL/6 background, Beijing Vital River Laboratory) to generate LMP10/ApoE double ko (dko) mice. All mice were maintained in specific-pathogen-free conditions on a 12-h light/12-h dark cycle with free access to water and diet. At 8–12 weeks of age, mice were subjected to an atherogenic diet (containing 0.5% cholesterol and 20% fat, Biotech HD) as previously described for 8 weeks to induce atherosclerosis (Liao et al., 2017). Only males were included in the experiments. All the animal procedures were approved by the Animal Care and Use Committee of Dalian Medical University and conformed to the United States National Institutes of Health Guide for the Care and Use of Laboratory Animals.

Analysis of Plasma Lipids and Glucose

Blood samples were collected via retro-orbital puncture after a 4-h fasting. Plasma total cholesterol, triglycerides and glucose were measured with enzymatic kits (BioSino), according to the manufacturer's guidance. For lipoprotein profiles, plasma samples were pooled from 4 to 5 mice per group and fractioned by fast protein liquid chromatography (FPLC) as we previously described (Liao et al., 2018). For glucose tolerance tests, mice were fasted for 4 h and then received an i.p. glucose (2 g/kg body weight) injection. Blood samples were collected before (time 0) and at 15, 30, 60, and 120 min after the glucose injection. Plasma glucose was measured as described above.

Flow Cytometry

Flow cytometry analysis was performed as previously described (Liao et al., 2020b). Briefly, aorta samples were first cleaned of fatty tissues and digested with aorta dissociation enzyme stock solutions (125 U/ml collagenase type XI, 60 U/ml hyaluronidase type 1, 60 U/ml DNase I, and 450 U/ml collagenase type I, in 2.5 ml of PBS) to obtain single-cell suspensions. Then the single-cell suspensions were treated with Fc block and stained with CD45 PerCP-Cy5.5, CD11b FITC, F4/80 PE-Cy7, and CD206 APC. All the above antibodies were obtained from BD Biosciences. Events were acquired on a live gate on Fortessa flow cytometry (BD Biosciences).

Bone Marrow Transplantation

Bone marrow (BM) transplantation was performed as previously described (Wang et al., 2016). Briefly, APOE ko mice of 8 weeks' old were chosen as recipients and received lethal irradiation with 8.5 Gy dose from a cobalt source. BM was extracted by flushing the femurs and tibiae from donor mice (8 weeks of age) with RPMI-1640 (Gibco) supplemented with 2% fetal bovine

serum and heparin (5 U/mL). Each recipient mouse was injected with 5×10^6 BM cells by tail injection. Then the recipient mice were housed in clean, individually ventilated cages and fed with acidified, antibiotic water and sterilized food for 4 weeks to allow recovery.

Atherosclerosis Analysis

Mice were sacrificed and flushed with PBS through the left ventricle. Atherosclerosis in the aorta and the aortic root were visualized and calculated as we previously described (Zhang et al., 2018). Briefly, the entire aortas were cleaned of the fatty tissues and cut open longitudinally under a dissecting microscope. Atherosclerosis in the *en face* aorta was visualized by Oil-red O (Sigma) staining and calculated as Oil-red O positive area percent entire inner surface area. The hearts were embedded in OCT (Sakura Finetek), snap-frozen in liquid nitrogen and cross-sectioned serially at 7 μm thick at the aortic root level. Cytosections were mounted from the point where all the 3 aortic valve cusps were clearly visible and 5 sections, each separated by 70 μm of the tissue, were included into 1 slide. Atherosclerosis in the aortic root was calculated as mean Oil-red O positive area averaged from 5 sections. Plaque macrophages and smooth muscle cells were visualized by immunohistochemical staining with anti-CD68 antibody (MCA1957, diluted at 1:300; Bio-Rad) and anti-SM22α antibody (ab14106, diluted at 1:300; Abcam), while collagen content and necrotic areas were visualized by Picro-Sirius Red staining and H&E staining, respectively. Lesional LMP10 expression was visualized by immunofluorescent co-staining using anti-LMP10 antibody (ab183506, diluted at 1: 200; Abcam) and anti-CD68 antibody (MCA1957, diluted at 1:300; Bio-Rad) or anti-SM22α anti-body (ab14106, diluted at 1:300; Abcam). All quantifications were performed with Image J software.

Foam Cell Induction and Analysis

Murine peritoneal macrophages were induced by an intraperitoneal injection of 4% sterile thioglycollate media (Sigma) and harvested 72 h later. Collected macrophages were cultured in RPMI-1640 medium (Gibco) supplemented with 10% fetal bovine serum and 1% antibiotics (100 Units/ml penicillin and 100 μg/ml streptomycin) and maintained overnight in a humidified incubator at 37°C under 5% CO_2. Then macrophages were treated with oxidized low density lipoprotein (ox-LDL) (50 μg/ml, Unionbiol) to induce foam cell formation. After 24 h of ox-LDL treatment, macrophages were washed, fixed with 4% paraformaldehyde solution for Oil-red O staining. To quantify intracellular cholesterol content, washed foam cells were treated with 0.5 ml hexane: isopropanol (3:2) and dried in fume hood. Intracellular total cholesterol level was measured by an Amplex Red Cholesterol Assay Kit (#A12216, Invitrogen) according to the manufacture's protocol, normalized to the protein concentration determined by a bicinchoninic acid protein assay kit (Pierce Chemical).

Western Blot Analysis

Protein samples were extracted using radioimmunoprecipitation assay (RIPA). The protein concentration of each extract was determined using a bicinchoninic acid protein assay kit (Pierce Chemical). Western blot analyses were performed using anti-LMP10 antibody (ab183506, Abcam), anti-phospho–IκBα (Ser32/36) (5A5, #9246, CST) and anti-IκBα (#9242, CST) antibodies, anti-phospho–NF-κB p65 (Ser536) (93H1, #3033, CST) and anti-NF-κB p65 (C22B4, #4764, CST) antibodies, with anti-GAPDH antibody (60004-1-lg, Proteintech) as control. Quantifications were performed with Image J software.

Quantitative Real-Time PCR Analysis

RNA samples was extracted with Trizol (Invitrogen, United States). Complementary DNA was generated using a RT kit (MedChem Express). Quantitative real-time PCR was performed with SYBR Green qPCR reagents (MedChem Express), using primers listed in **Table 1**. All samples

TABLE 1 | Primer sequences used in the quantitative real-time PCR.

Name	Type	Sequence (5′–3′)
MCP-1	Forward	TAAAAACCTGGATCGGAACCAAA
	Reverse	GCATTAGCTTCAGATTTACGGGT
IL-1β	Forward	CTTCCCCAGGGCATGTTAAG
	Reverse	ACCCTGAGCGACCTGTCTTG
IL-4	Forward	GGTCTCAACCCCCAGCTAGT
	Reverse	GCCGATGATCTCTCTCAAGTGAT
IL-6	Forward	TTCCATCCAGTTGCCTTCTTG
	Reverse	TTGGGAGTGGTATCCTCTGTGA
IL-10	Forward	GCTCTTACTGACTGGCATGAG
	Reverse	CGCAGCTCTAGGAGCATGTG
TGF-β	Forward	CCACCTGCAAGACCATCGAC
	Reverse	CTGGCGAGCCTTAGTTTGGAC
CD36	Forward	CTCGGATGGCTAGCTGATTACT
	Reverse	AGCACTTGCTTCTTGCCAAC
SR-A	Forward	AGGGAGTGGATAAATCAGTGCT
	Reverse	TCCTCCTGTTGCTTTGCTGT
ABCA1	Forward	CGACCATGAAAGTGACACGC
	Reverse	GACAGCTGGCAGGACAATCT
ABCG1	Forward	GGTTGCGACATTTGTGGGTC
	Reverse	GAAGATGGTCCTCAGGTGGC
SR-BI	Forward	GCCTCTGTTTCTCTCCCACC
	Reverse	CTGTCCGCTGAGAGAGTCCT
CD80	Forward	ACCCCCAACATAACTGAGTCT
	Reverse	TTCCAACCAAGAGAAGCGAGG
CD40	Forward	TGTCATCTGTGAAAAGGTGGTC
	Reverse	ACTGGAGCAGCGGTGTTATG
SOX3	Forward	GCCGACTGGAAACTGCTGA
	Reverse	CGTAGCGGTGCATCTGAGG
CD163	Forward	ATGGGTGGACACAGAATGGTT
	Reverse	CAGGAGCGTTAGTGACAGCAG
CD206	Forward	CTCTGTTCAGCTATTGGACGC
	Reverse	CGGAATTTCTGGGATTCAGCTTC
Arg1	Forward	CTCCAAGCCAAAGTCCTTAGAG
	Reverse	AGGAGCTGTCATTAGGGACATC
GAPDH	Forward	TGATGACATCAAGAAGGTGGTGAAG
	Reverse	TCCTTGGAGGCCATGTAGGCCAT

were quantitated using the comparative CT method and normalized to GAPDH.

Statistical Analysis

Data were analyzed with Prism software and presented as mean ± SEM. Normally distributed data was evaluated by unpaired *t*-test, while non-parametric data by Mann–Whitney test. A *P*-value < 0.05 was regarded as statistically significant.

RESULTS

Upregulation of LMP10 in Lesional Macrophages in ApoE ko Mice

To investigate the role of the immunoproteasome subunit LMP10 in the development of atherosclerosis, we first examined the expression of LMP10 in the aorta of ApoE ko mice after 8 weeks of atherogenic diet (ATD) feeding. Immunoblotting analysis showed that protein expression of LMP10 was significantly upregulated in the aorta of mice fed on an ATD, as compared to mice without ATD feeding (**Figure 1A**). To further identify which cell types in atherosclerotic lesions predominantly expressed LMP10, we co-stained LMP10 with macrophage biomarker CD68 or smooth muscle cell (SMC) biomarker SM22α. Immunofluorescent staining revealed that LMP10 was highly co-localized with $CD68^+$ macrophages and hardly with $SM22\alpha^+$ SMCs (**Figure 1B**), indicating that increased LMP10 expression was mainly derived from lesional macrophages.

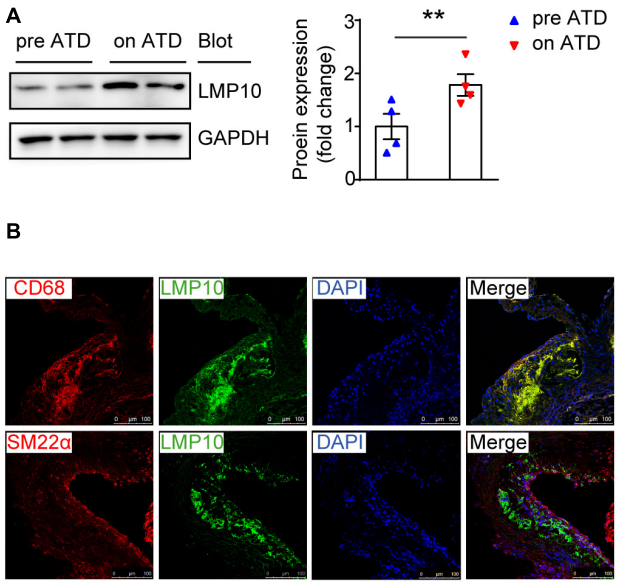

FIGURE 1 | LMP10 was abundantly expressed in lesional macrophages in diet-induced atherosclerosis in ApoE ko mice. **(A)** Western-blot analysis and quantitation of aortic LMP10 protein expression in ApoE ko mice before and after 8 weeks of ATD feeding. $n = 4$ per group, $^{**}p < 0.01$.
(B) Immunofluorescent co-staining of LMP10 with CD68 or SM22α in the aortic root of ApoE ko mice before and after 8 weeks of ATD feeding.

Ablation of LMP10 Had no Effect on Plasma Metabolic Parameters in ApoE ko Mice After ATD Feeding

To identify whether LMP10 contributed to diet-induced atherogenesis, we generated LMP10 and ApoE double knockout (LMP10/ApoE dko) mice in addition to ApoE ko controls, which were fed the ATD for 8 weeks to induce atherogenesis. We first compared plasma metabolic parameters in mice during ATD feeding and found that total plasma cholesterol, triglycerides, and glucose levels were similar between the LMP10/ApoE dko mice and the ApoE ko controls, both before and after the ATD feeding (**Figures 2A–C**). Furthermore, there was no significant difference in the plasma lipoprotein profiles and the glucose clearance rate, detected by FPLC and glucose tolerance test, respectively, between the LMP10/ApoE dko and ApoE ko mice (**Figures 2D–F**), suggesting that LMP10 is not involved in the regulation of circulating lipids and glucose.

Knockout of LMP10 Attenuated Diet-Induced Atherosclerosis in ApoE ko Mice

We then tested the effect of LMP10 on atherosclerotic plaques in the LMP10/ApoE dko and ApoE ko control mice after 8 weeks of ATD feeding. Oil-red O staining showed that atherosclerotic lesion areas on the entire inner aortic surface of LMP10/ApoE dko mice were markedly reduced, compared with that of the ApoE ko controls (**Figure 3A**). Reduction of lesion areas was further confirmed in the aortic root of LMP10/ApoE dko mice (**Figure 3B**).

Since macrophages play a key role in the onset and progression of atherosclerosis (Moore and Tabas, 2011; Tabas and Bornfeldt, 2016), we then examined the accumulation of macrophages in the aorta using anti-CD68 antibody. Immunochemical staining indicated that the infiltration of $CD68^+$ macrophages in aortic plaques of LMP10/ApoE dko mice was significantly reduced compared to levels observed in ApoE ko controls (**Figure 3C**). Moreover, plaques of LMP10/ApoE dko mice had less necrotic core formation (**Figure 3F**). However, immunochemical staining with anti-SM22α antibody and Sirius Red staining showed no significant change in $SM22\alpha^+$SMCs or collagen content between LMP10/ApoE dko mice and ApoE ko control mice (**Figures 3D,E**). Together, these data suggest that knockout of LMP10 attenuates diet-induced atherosclerosis possibly through inhibition of macrophage infiltration and death in ApoE ko mice.

Myeloid-Specific Knockout of LMP10 Inhibited Diet-Induced Atherosclerosis in ApoE ko Mice

Immunoproteasomes are known to be constitutively expressed in immune cells, particularly myeloid-derived monocytes and lymphocytes (Muchamuel et al., 2009). To directly explore whether myeloid-specific deletion of LMP10 affected diet-induced atherosclerosis, we created chimeric mice via bone marrow (BM) transplantation and treated them with ATD

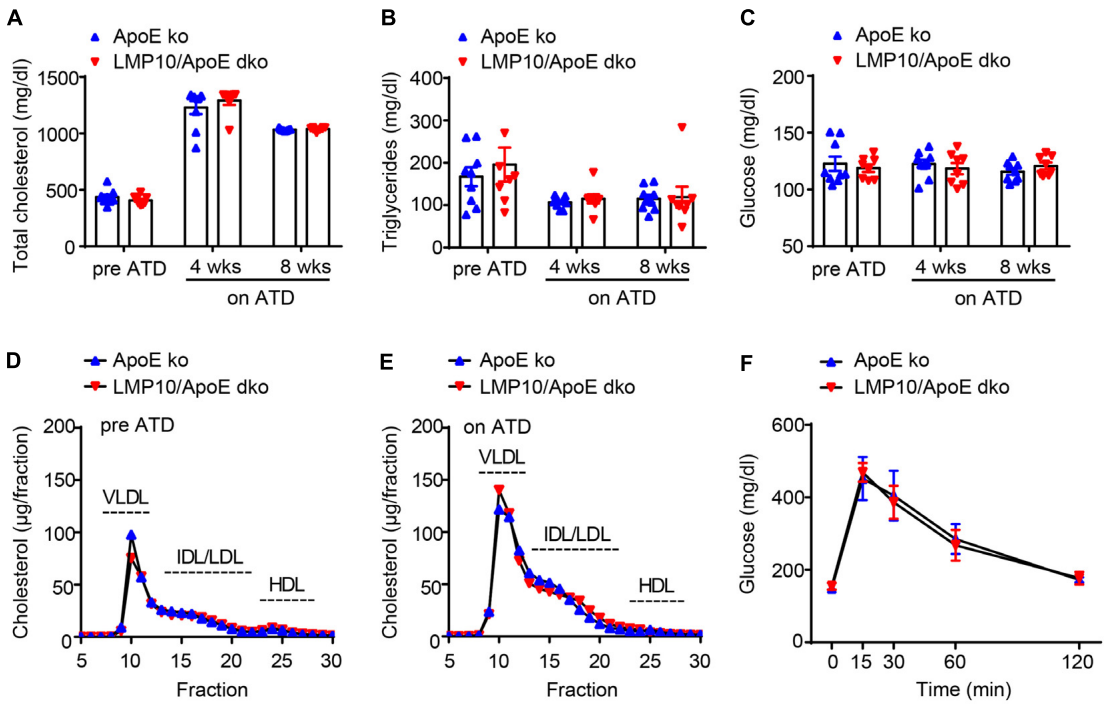

FIGURE 2 | LMP10 deletion did not change plasma metabolic parameters in ApoE ko mice during ATD feeding. **(A–C)** Analysis of plasma total cholesterol **(A)**, triglycerides **(B)**, and glucose **(C)** levels before and after ATD feeding. **(D,E)** Analysis of plasma lipoprotein profiles by FPLC before **(D)** and after 8 weeks **(E)** of ATD feeding. **(F)** Analysis of glucose clearance by glucose tolerance test after 8 weeks on ATD. For **(A–C,F)**, $n = 7$–9 per group; for **(D,E)**, samples were pooled from 4 to 5 mice per group.

feeding for 8 weeks, after 4 weeks' recovery from the transplantation. The procedure of chimeric mice construction was illustrated in **Figure 4A**, with LMP10/ApoE dko and ApoE ko mice as BM donors while ApoE ko mice as recipients. Our data showed that ApoE ko mice reconstituted with LMP10/ApoE dko BM cells exhibited a marked decrease in atherosclerotic lesion burdens in both the aorta and the aortic root (**Figures 4B,C**), as well as a marked decrease in macrophage infiltration, and necrotic core area in plaques (**Figures 4D,E**), as compared to ApoE ko mice reconstituted with ApoE ko BM cells. However, no significant change in plasma metabolic parameters was observed between the LMP10/ApoE dko and the ApoE ko control mice (data not shown). These results suggest that LMP10 in BM-derived inflammatory cells critically contributes to the formation of atherosclerosis in this model.

Deletion of LMP10 Reduced Diet-Induced Macrophage Infiltration and Polarization in ApoE ko Mice

Macrophage infiltration and polarization play a vital role in the immune-inflammatory response during atherosclerosis (Ross, 1999). We therefore examined aortic macrophage infiltration and polarization after 8 weeks of ATD via flow cytometry. As shown in **Figure 5A**, the numbers of aortic F4/80$^+$ macrophages were markedly lower in LMP10/ApoE dko mice when compared to ApoE ko controls. Consistent with this result, M1-type macrophages (marked as F4/80$^+$CD206$^-$ macrophages) and M2-type macrophages (marked as F4/80$^+$CD206$^+$ macrophages) were both decreased in LMP10/ApoE dko mice; however, the M2/M1 ratio was significantly increased, indicating a shift in polarization toward the M2 type (**Figure 5B**). Additionally, we analyzed changes in the expressions of M1 (such as MCP-1, IL-1β, and IL-6) and M2 (such as IL-4, IL-10, and TGF-β) signature genes in aortic lesions. Data from real-time PCR showed a roughly 50% decrease of M1-associated cytokine (MCP-1, IL-1β, and IL-6) expression and more than 1.5-fold increase of M2-associated cytokine (IL-4 and IL-10) expression in LMP10/ApoE dko mice compared with ApoE ko control mice (**Figure 5C**).

LMP10 Deletion Blunted Macrophage Polarization and Inflammation via Inhibiting NF-κB Activation in ox-LDL-Treated Macrophages

NF-κB signaling is a key transcriptional regulator for macrophage polarization and inflammation (Hoesel and Schmid, 2013; Lingappan, 2018). Therefore, we explored the NF-κB pathway in ox-LDL-treated macrophages isolated from the LMP10/ApoE dko mice and ApoE ko controls. Both Oil-red O staining and lipid extraction indicated that less cholesterol was accumulated in macrophages from LMP10/ApoE dko mice after ox-LDL stimulation (**Figures 6A,B**). Further, using real-time PCR analysis, we found in macrophages from LMP10/ApoE dko

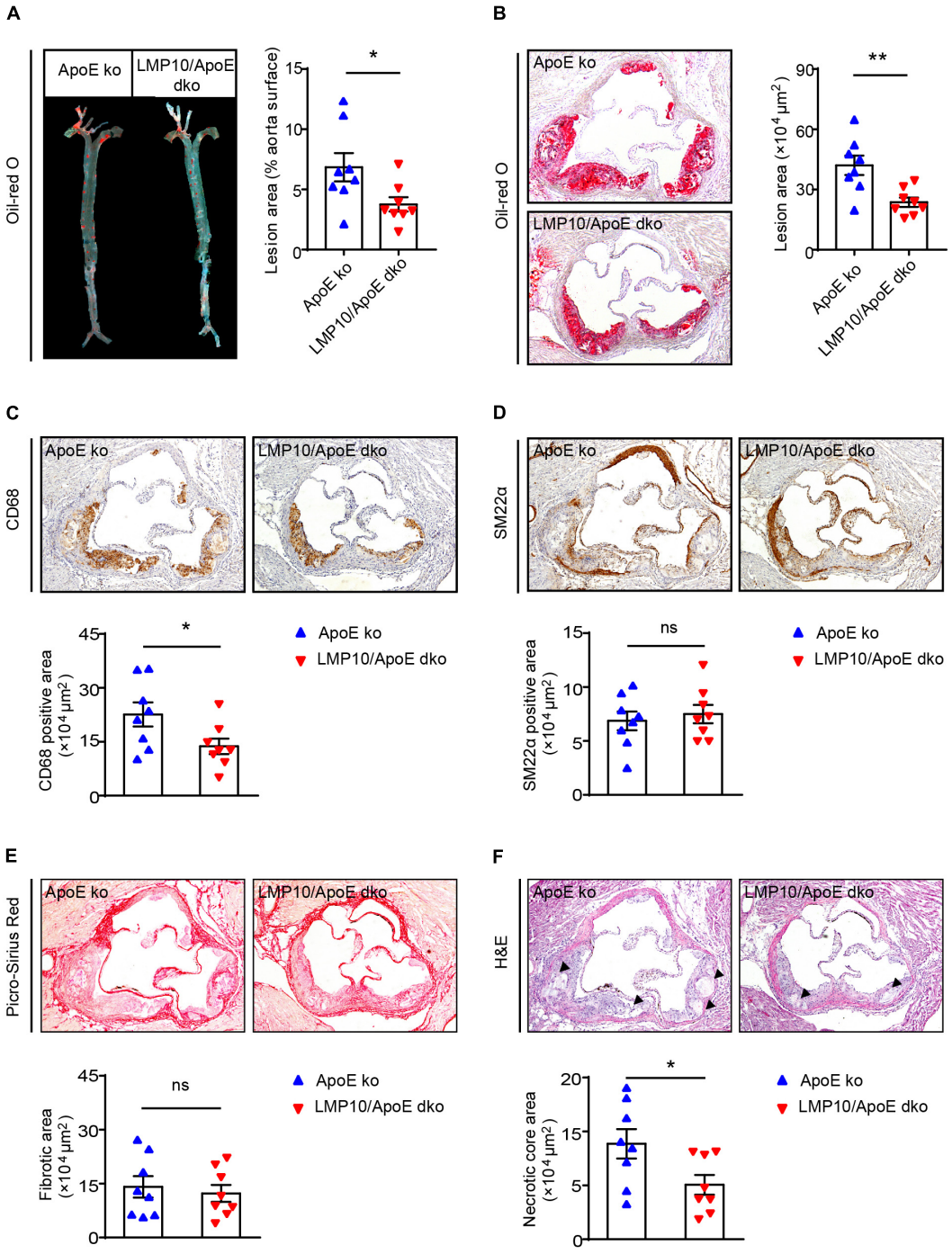

FIGURE 3 | LMP10 deletion attenuated diet-induced atherosclerosis in ApoE ko mice. **(A)** Oil-red O staining and quantification of the atherosclerotic lesions in *en face* aortas. **(B)** Oil-red O staining and quantification of atherosclerotic lesions in the aortic root. **(C)** CD68 immunohistochemical staining and quantification of $CD68^+$ macrophages in atherosclerotic lesions in the aortic root. **(D)** SM22α immunohistochemical staining and quantification of $SM22\alpha^+$ smooth muscle cells in atherosclerotic lesions in the aortic root. **(E)** Picro-Sirius Red staining and quantification of collagen in atherosclerotic lesions in the aortic root. **(F)** H&E staining and quantification of necrotic areas in atherosclerotic lesions in the aortic root. The triangle indicates the necrotic core. $n = 8$ per group, $^*p < 0.05$; $^{**}p < 0.01$; ns, not significant.

mice that genes associated with cholesterol uptake (CD36 and SR-A) were decreased, while those with cholesterol efflux (ABCA1) increased (**Figure 6C**); in addition, expressions of M1-associated cytokines (IL-1β and IL-6) and M1 signature genes (such as CD80, CD40 and SOX3, etc.) were both inhibited, while those of M2-associated cytokines (IL-4 and IL-10) and

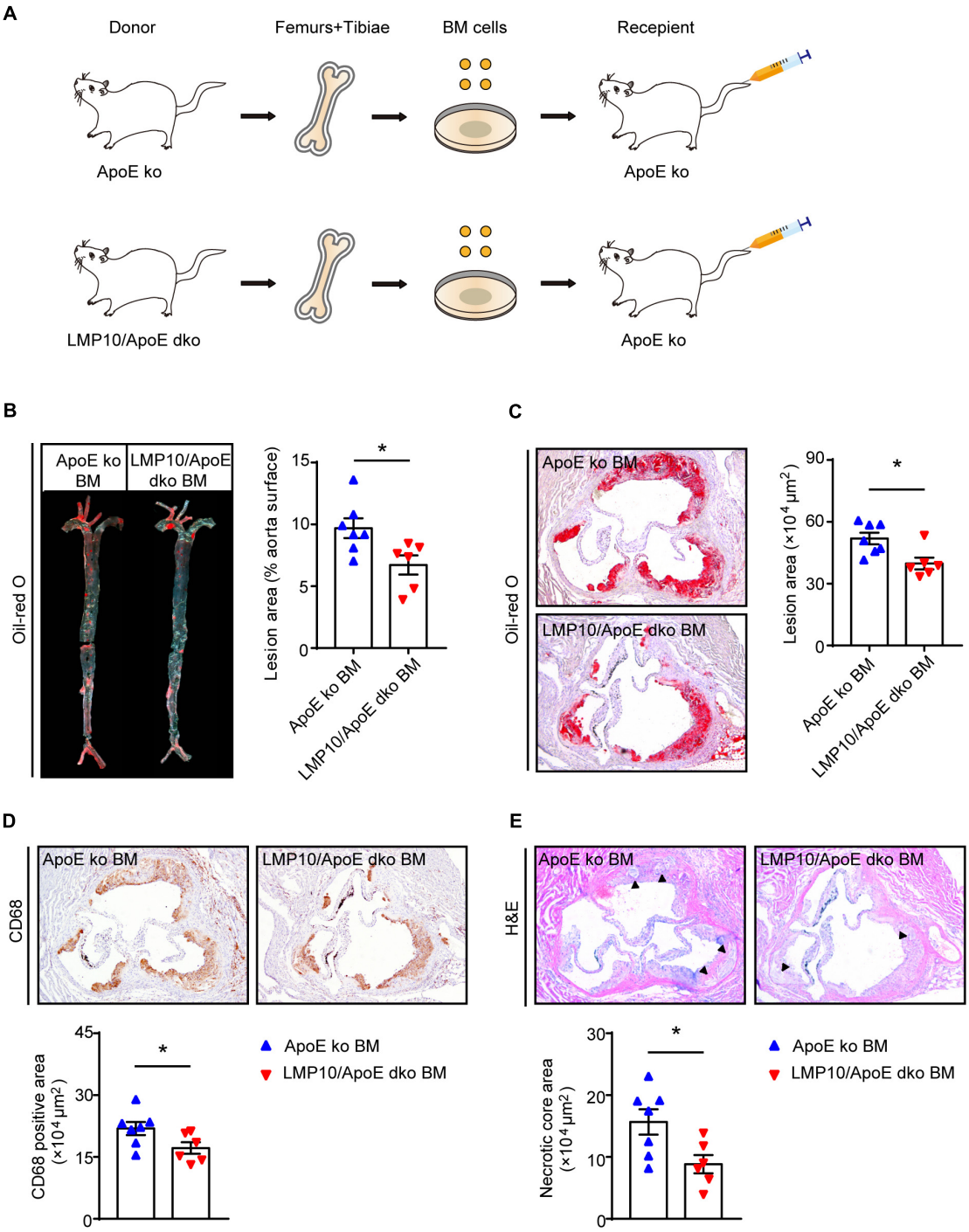

FIGURE 4 | Macrophage-specific LMP10 deletion attenuated diet-induced atherosclerosis in ApoE ko mice. **(A)** Graphic representation of bone-marrow chimeric mice construction. **(B)** Oil-red O staining and quantification of atherosclerotic lesions in *en face* aortas. **(C)** Oil-red O staining and quantification of atherosclerotic lesions in the aortic root. **(D)** CD68 immunohistochemical staining and quantification of $CD68^+$ cells in atherosclerotic lesions in the aortic root. **(E)** H&E staining and quantification of necrotic areas in atherosclerotic lesions in the aortic root. The triangle indicates the necrotic core. $n = 6–7$ per group, $^*p < 0.05$.

M2 signature genes (such as CD163, CD206, and Arg1, etc.) upregulated (**Figures 6D,E**). Finally, western blotting showed that the phosphorylation of IκBα, the inhibitor of NF-κB, and the phosphorylation/activation of NF-κB p65 were all reduced in macrophages from LMP10/ApoE dko mice challenged with ox-LDL, which might contribute to decreased polarization toward M1 and lower inflammation observed in LMP10 deleted conditions (**Figures 6F,G**).

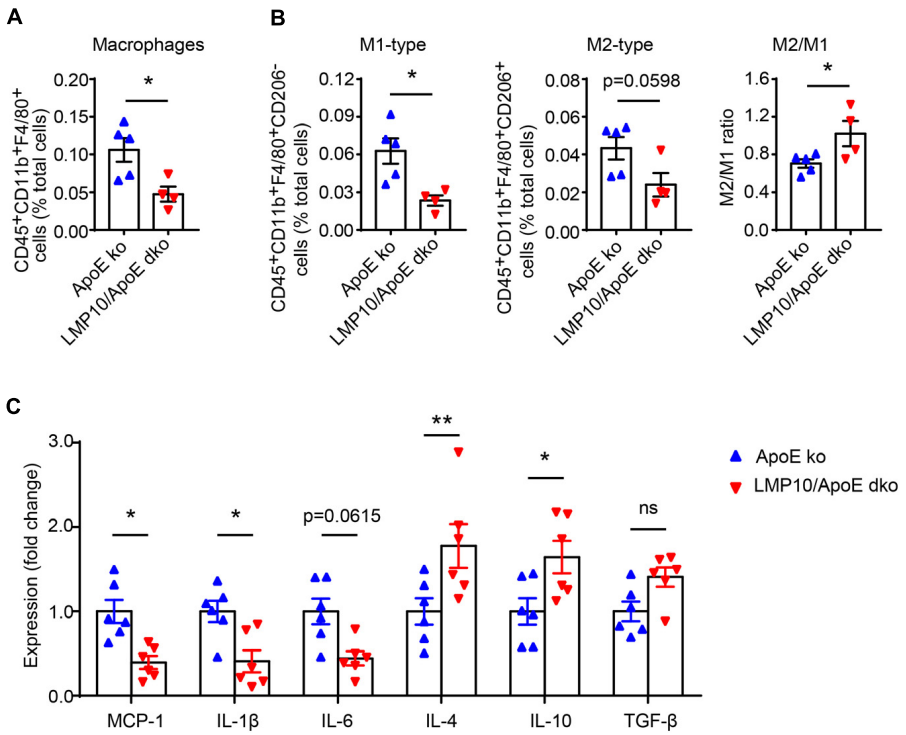

FIGURE 5 | LMP10 deletion inhibited diet-induced aortic macrophage infiltration and polarization in ApoE ko mice. **(A,B)** Flow cytometry analysis of aortic total macrophage infiltration **(A)** and M1/M2-type macrophage numbers **(B)** after 8 weeks of ATD. $n = 4$–5 per group. **(C)** Real-time PCR analysis of aortic M1- and M2-associated inflammatory cytokine expression after 8 weeks of ATD. $n = 6$ per group, $^{*}p < 0.05$; $^{**}p < 0.01$; ns, not significant.

DISCUSSION

Immunoproteasomes have been implicated in human atherosclerosis (Herrmann et al., 2012). Previous research has shown that LMP7 expression is increased in the shoulder areas of symptomatic carotid plaques and in correlation with inflammatory cell infiltration, but the causative roles and potential mechanisms of immunoproteasomes in atherosclerosis remain unclear (Herrmann et al., 2012). Recently, we demonstrated in ApoE ko mice that ATD feeding significantly induced LMP7 expression in plaque macrophages, and that genetic and pharmaceutical inhibition of LMP7 attenuated diet-induced atherosclerosis (Liao et al., 2020a). Furthermore, we identified in isolated macrophages that LMP7-mediated regulation of atherosclerosis was associated with efferocytosis of apoptotic cells during foam cell formation (Liao et al., 2020a). In the current study, we explored whether another immunoproteasome catalytic subunit LMP10 contributed to experimental atherosclerosis in ApoE ko mice. We demonstrated that (1) LMP10 is highly expressed in lesional macrophages in diet-induced atherosclerosis; (2) LMP10 deletion, especially myeloid-specific LMP10 deletion, attenuates diet-induced atherosclerosis; and (3) LMP10 deletion might inhibit NF-κB-mediated macrophage polarization and inflammation. The working model is illustrated in **Figure 7**. Interestingly, our current and previous studies all indicate that deletion of immunoproteasome subunit, either LMP10 or LMP7, do not elicit profound influence on plasma metabolic parameters in ApoE ko mice, suggesting that immunoproteasomes are possibly not involved in the regulation of global lipid/glucose metabolism during diet-induced atherosclerosis.

The roles of immunoproteasomes in cardiovascular health and disease have been extensively explored recently. In a mouse model of angiotensin II (Ang II)-induced cardiac remodeling, proteolytic activities and expression of the immunoproteasome subunits LMP2, LMP10, and LMP7 were found to be significantly up-regulated (Li et al., 2015). Genetic and pharmaceutical inactivation of LMP7 or LMP10 subunits is sufficient to elicit profound impacts on both ventricular hypertrophy and atrial fibrillation induced by Ang II infusion (Li et al., 2018, 2019; Xie et al., 2019, 2020). In addition to pressure overload, immunoproteasomes are also involved in other cardiac diseases, such as doxorubicin-induced cardiotoxicity (Zhao et al., 2015) and deoxycorticosterone acetate (DOCA)/Salt-induced heart failure (Yan et al., 2017). It was demonstrated that doxorubicin significantly decreases proteolysis activities and immunoproteasome (LMP2, LMP10, and LMP7) expression. Overexpression of immunoproteasome catalytic subunits (LMP2, LMP10, or LMP7) protected against doxorubicin-induced cardiomyocyte apoptosis, while inactivation promoted apoptosis (Zhao et al., 2015). In DOCA/salt-induced cardiac hypertrophy, LMP10 subunit expression was found to be significantly increased, while inactivation of LMP10 ameliorated DOCA/salt-induced cardiac fibrosis and inflammation

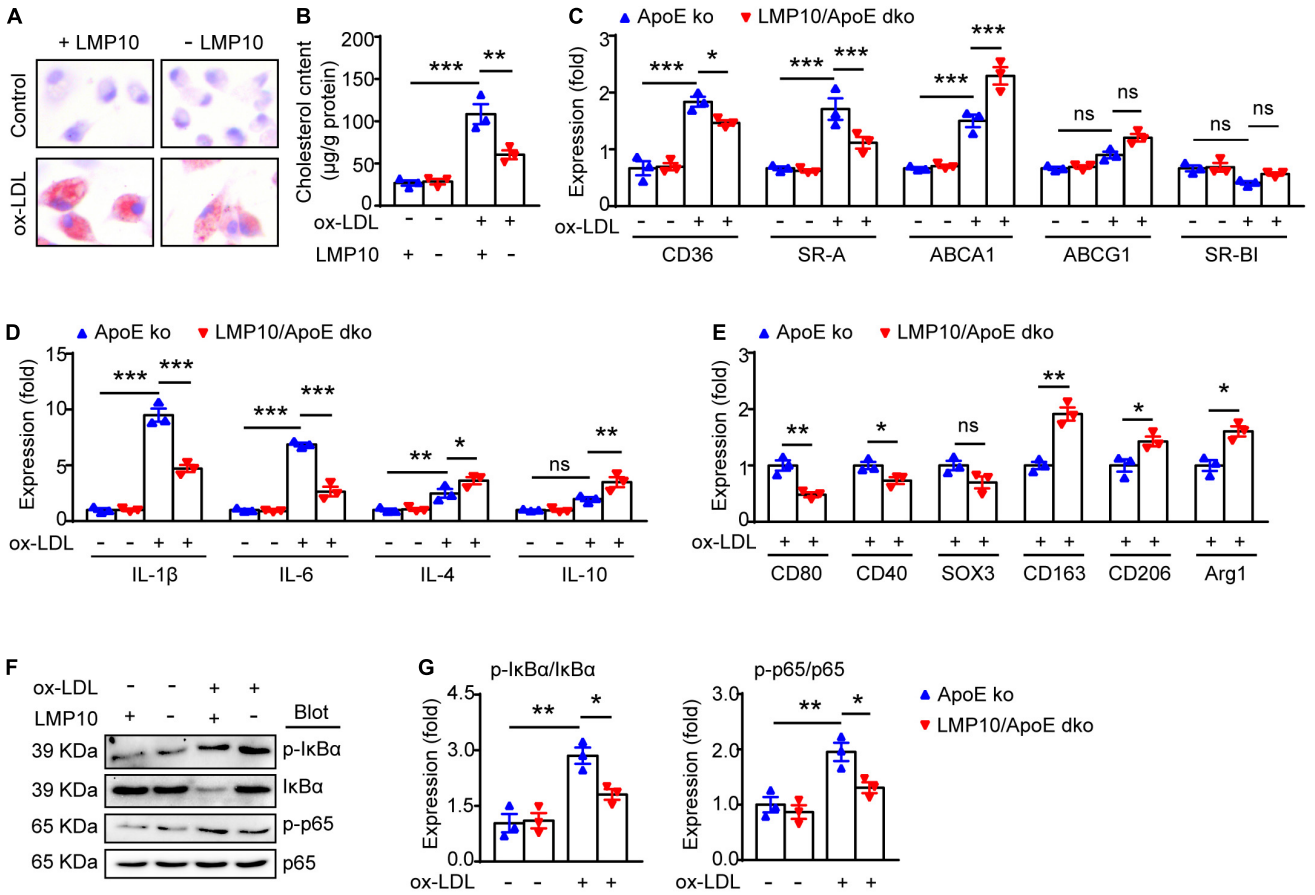

FIGURE 6 | LMP10 deletion blunted macrophage polarization and inflammation via inhibiting NF-κB activation in ox-LDL-treated macrophages. **(A)** Oil-red O staining of isolated peritoneal macrophages treated with or without ox-LDL. **(B)** Quantitation of intracellular cholesterol content in isolated peritoneal macrophages treated with or without ox-LDL. **(C)** Real-time PCR analysis of cholesterol uptake- and efflux-associated gene expression in isolated peritoneal macrophages treated with or without ox-LDL. **(D)** Real-time PCR analysis of M1- and M2-associated inflammatory cytokine expression in isolated peritoneal macrophages treated with or without ox-LDL. **(E)** Real-time PCR analysis of M1/M2 signature gene expression in isolated peritoneal macrophages treated with ox-LDL. **(F,G)** Western-blot analysis **(F)** and quantitation **(G)** of IκBα phosphorylation and NF-κB activation in isolated peritoneal macrophages treated with or without ox-LDL. $n = 3$ per group, $^{*}p < 0.05$; $^{**}p < 0.01$; $^{***}p < 0.001$.

(Yan et al., 2017). The present study and our previous LMP7 data in diet-induced atherosclerosis, together with the above described evidence, expand our knowledge about the role of immunoproteasomes in cardiovascular homeostasis and, most importantly, provide new therapeutic targets for human cardiovascular diseases.

Macrophages during inflammation are particularly dynamic, with diverse functional and phenotypic heterogeneity, depending on microenvironment and activated intracellular signaling pathways (Tabas and Bornfeldt, 2016). The M1/M2 nomenclature is well recognized, with M1-type macrophages tending to secrete pro-inflammatory cytokines (such as MCP-1, IL-1β, and IL-6) to augment the inflammatory cascade, while M2 cells tend to secrete anti-inflammatory cytokines (such as IL-4, IL-10, and TGF-β) helping to resolve inflammation. Previous studies have suggested a potential role of immunoproteasomes in macrophage polarization toward M1/M2 phenotypes. For example, in diet-induced obesity, LMP7 ablation promoted adipose macrophages to switch toward the anti-inflammatory M2 phenotype (Kimura et al., 2015b). Similarly, data from alveolar macrophages showed that LMP7 inactivation increased M2 polarization triggered by IL-4, but had no effect on LPS/IFN-γ-triggered M1 polarization (Chen et al., 2016). However, whether immunoproteasomes contribute to plaque macrophage polarization during atherosclerosis has not been elucidated. In the present study, we discussed the diet-induced M1/M2 polarization in atherosclerosis when LMP10 was inactivated. We observed an increased M2/M1 ratio in the vessels after ATD feeding in LMP10/ApoE dko mice, although the numbers of both M2- and M1-type macrophages were decreased, compared to ApoE ko controls (**Figure 5B**). Similarly, the expression of M1-associated cytokines was decreased, while the expression of M2-associated cytokines was increased in LMP10/ApoE dko mice (**Figure 5C**). These data suggested that LMP10 deletion reduced

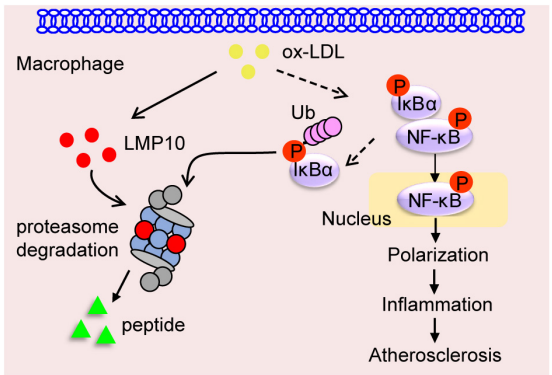

FIGURE 7 | Graphic representation of macrophage LMP10 in diet-induced atherosclerosis. The accumulation of lipids (such as ox-LDL) induces macrophage LMP10 expression, which facilitates the degradation of phosphorylated IκBα, followed by activation and translocation of phosphorylated NF-κB p65, finally promoting macrophage polarization and inflammation, therefore contributing to atherosclerosis.

macrophage polarization and inflammation, which was further confirmed in ox-LDL-induced foam cell models, using primary peritoneal macrophages collected from LMP10/ApoE dko mice and ApoE ko controls. Our data, for the first time, demonstrates that the immunoproteasome LMP10 subunit may be able to regulate macrophage polarization and inflammation, therefore contributing to diet-induced atherosclerosis.

Plaque macrophage polarization toward M1/M2 type is known to be regulated by several transcriptional signaling pathways. The key transcriptional factors for these signaling pathways include NF-κB, signal transducer and activator of transcription (STAT), peroxisome proliferator-activated receptor-γ (PPARγ), cAMP responsive element-binding protein (CREB), and interferon regulatory factors (IRFs) (De Paoli et al., 2014; Wang et al., 2014). Of these transcriptional pathways, NF-κB signaling has been suggested as one of the major regulatory mechanisms of immunoproteasomes in immune-inflammatory responses in cardiovascular diseases (Yang et al., 2009; Angeles et al., 2012; Kimura et al., 2015a). For example, in Ang II-induced cardiac hypertrophy, activation of immunoproteasomes was found to promote degradation of MKP-1 and IκBα and subsequent activation of STAT1 and NF-κB, thereby leading to Th1 cell differentiation and cardiac remodeling (Qin et al., 2018); while in DOCA/salt-induced cardiac hypertrophy, the immunoproteasome LMP10 subunit was shown to activate IκBα/ NF-κB and TGF-β1/Smad2/3 signaling to facilitate cardiac fibrosis and inflammation (Yan et al., 2017). The regulatory effects of LMP10 on IκBα/NF-κB activation and signaling has further been confirmed in hypertensive atrial fibrillation and retinopathy (Li et al., 2018; Wang et al., 2018). In these two models, LMP10 promoted PTEN degradation and subsequent AKT1 activation, which then stimulated IKKβ-mediated IκBα phosphorylation and degradation, ultimately facilitating activation of NF-κB pathway (Li et al., 2018; Wang et al., 2018). Importantly, blocking NF-κB activation by administration of IKKβ specific inhibitor IMD-0354 remarkably blunted inflammation and disease phenotypes (Li et al., 2018; Wang et al., 2018). These studies indicated that LMP10 targets NF-κB activation possibly through PTEN/AKT/IKK signaling. Interestingly, our recent study on experimental atherosclerosis also supports LMP7-mediated transcriptional regulation of efferocytosis through oxidized LDL-induced IκBα degradation and subsequent NF-κB activation (Liao et al., 2020a). In the current study, we observed that oxidized LDL-induced degradation of IκBα and activation of NF-κB pathway was also reduced in LMP10-deleted macrophages (**Figures 6F,G**), suggesting that LMP10 deletion inhibited NF-κB activation partially through blocking IκBα degradation.

CONCLUSION

Our data demonstrated for the first time that the immunoproteasome subunit LMP10 promoted diet-induced atherosclerosis in ApoE ko mice partially through regulation of NF-κB-mediated macrophage polarization and inflammation. Therefore, LMP10 might be exploited as a potential pharmaceutical target for atherosclerosis. Further studies might be needed to examine the involvement of other signaling pathways such as STAT, PPARγ, CREB, and IRFs in macrophage polarization and inflammation, as well as other mechanisms, such as oxidative stress and autophagy, in LMP10-mediated atherosclerosis in this model.

DATA AVAILABILITY STATEMENT

The original contributions presented in the study are included in the article/supplementary material, further inquiries can be directed to the corresponding author/s.

ETHICS STATEMENT

The animal study was reviewed and approved by the Animal Care and Use Committee of Dalian Medical University.

AUTHOR CONTRIBUTIONS

JL, Y-LX, and H-HL conceived the project and designed the experiments. JL, XA, XY, Q-YL, SL, YX, and JB performed the experiments and acquired the data. JL analyzed the data and wrote the original draft of the manuscript. Y-LX and H-HL reviewed and edited the manuscript. All authors have read and approved the final manuscript.

FUNDING

This study was supported by the Youth Science Fund Program of National Natural Science Foundation of China (81600335 to JL) and the National Natural Science Foundation of China (81630009 to H-HL).

REFERENCES

Angeles, A., Fung, G., and Luo, H. (2012). Immune and non-immune functions of the immunoproteasome. *Front. Biosci.* 17, 1904–1916. doi: 10.2741/4027

Basler, M., Kirk, C. J., and Groettrup, M. (2013). The immunoproteasome in antigen processing and other immunological functions. *Curr. Opin. Immunol.* 25, 74–80. doi: 10.1016/j.coi.2012.11.004

Chen, S., Kammerl, I. E., Vosyka, O., Baumann, T., Yu, Y., Wu, Y., et al. (2016). Immunoproteasome dysfunction augments alternative polarization of alveolar macrophages. *Cell. Death Differ.* 23, 1026–1037. doi: 10.1038/cdd.2016.3

Ciechanover, A., and Schwartz, A. L. (1998). The ubiquitin-proteasome pathway: the complexity and myriad functions of proteins death. *Proc. Natl. Acad. Sci. U S A.* 95, 2727–2730. doi: 10.1073/pnas.95.6.2727

De Paoli, F., Staels, B., and Chinetti-Gbaguidi, G. (2014). Macrophage phenotypes and their modulation in atherosclerosis. *Circ. J.* 78, 1775–1781. doi: 10.1253/circj.cj-14-0621

Feng, B., Zhang, Y., Mu, J., Ye, Z., Zeng, W., Qi, W., et al. (2010). Preventive effect of a proteasome inhibitor on the formation of accelerated atherosclerosis in rabbits with uremia. *J. Cardiovasc. Pharmacol.* 55, 129–138. doi: 10.1097/fjc.0b013e3181c87f8e

Harrison, D., Griendling, K. K., Landmesser, U., Hornig, B., and Drexler, H. (2003). Role of oxidative stress in atherosclerosis. *Am. J. Cardiol.* 91, 7A–11A. doi: 10.1016/s0002-9149(02)03144-2

Herrmann, J., Edwards, W. D., Holmes, D. R. Jr., Shogren, K. L., Lerman, L. O., Ciechanover, A., et al. (2002). Increased ubiquitin immunoreactivity in unstable atherosclerotic plaques associated with acute coronary syndromes. *J. Am. Coll. Cardiol.* 40, 1919–1927. doi: 10.1016/s0735-1097(02)02564-0

Herrmann, J., Willuweit, K., Loeffler, D., Peterson, K., Lerman, L., and Lerman, A. (2012). THE IMMUNOPROTEASOME – A NEW CHARACTERISTIC OF SYMPTOMATIC CAROTID ARTERY PLAQUES. *J. Am. Coll. Cardiol.* 59:E2054. doi: 10.1016/s0735-1097(12)62055-5

Hochstrasser, M. (1995). Ubiquitin, proteasomes, and the regulation of intracellular protein degradation. *Curr. Opin. Cell Biol.* 7, 215–223. doi: 10.1016/0955-0674(95)80031-x

Hoesel, B., and Schmid, J. A. (2013). The complexity of NF-κB signaling in inflammation and cancer. *Mole. Cancer* 12:86. doi: 10.1186/1476-4598-12-86

Kimura, H., Caturegli, P., Takahashi, M., and Suzuki, K. (2015a). New Insights into the Function of the Immunoproteasome in Immune and Nonimmune Cells. *J. Immun. Res.* 2015:541984.

Kimura, H., Usui, F., Karasawa, T., Kawashima, A., Shirasuna, K., Inoue, Y., et al. (2015b). Immunoproteasome subunit LMP7 Deficiency Improves Obesity and Metabolic Disorders. *Sci. Rep.* 5:15883.

Li, J., Wang, S., Bai, J., Yang, X. L., Zhang, Y. L., Che, Y. L., et al. (2018). Novel Role for the Immunoproteasome Subunit PSMB10 in Angiotensin II-Induced Atrial Fibrillation in Mice. *Hypertension* 71, 866–876. doi: 10.1161/hypertensionaha.117.10390

Li, J., Wang, S., Zhang, Y. L., Bai, J., Lin, Q. Y., Liu, R. S., et al. (2019). Immunoproteasome Subunit beta5i Promotes Ang II (Angiotensin II)-Induced Atrial Fibrillation by Targeting ATRAP (Ang II Type I Receptor-Associated Protein) Degradation in Mice. *Hypertension* 73, 92–101. doi: 10.1161/hypertensionaha.118.11813

Li, N., Wang, H. X., Han, Q. Y., Li, W. J., Zhang, Y. L., Du, J., et al. (2015). Activation of the cardiac proteasome promotes angiotension II-induced hypertrophy by down-regulation of ATRAP. *J. Mol. Cell Cardiol.* 79, 303–314. doi: 10.1016/j.yjmcc.2014.12.007

Liao, J., Guo, X., Wang, M., Dong, C., Gao, M., Wang, H., et al. (2017). Scavenger Receptor Class B Type 1 Deletion Led to Coronary Atherosclerosis and Ischemic Heart Disease in Low-density Lipoprotein Receptor Knockout Mice on Modified Western-type Diet. *J. Atheroscler. Thromb.* 24, 133–146. doi: 10.5551/jat.33019

Liao, J., Liu, X., Gao, M., Wang, M., Wang, Y., Wang, F., et al. (2018). Dyslipidemia, steatohepatitis and atherogenesis in lipodystrophic apoE deficient mice with Seipin deletion. *Gene* 648, 82–88. doi: 10.1016/j.gene.2018.01.062

Liao, J., Xie, Y., Lin, Q., Yang, X., An, X., Xia, Y., et al. (2020a). Immunoproteasome subunit beta5i regulates diet-induced atherosclerosis through altering MERTK-mediated efferocytosis in Apoe knockout mice. *J. Pathol.* 250, 275–287. doi: 10.1002/path.5368

Liao, J., Yang, X., Lin, Q., Liu, S., Xie, Y., Xia, Y., et al. (2020b). Inhibition of the Ubiquitin-Activating Enzyme UBA1 Suppresses Diet-Induced Atherosclerosis in Apolipoprotein E-Knockout Mice. *J. Immunol. Res.* 2020: 7812709.

Lingappan, K. N. F. - (2018). kappaB in Oxidative Stress. *Curr. Opin. Toxicol.* 7, 81–86.

Marfella, R., D'Amico, M., Di Filippo, C., Baldi, A., Siniscalchi, M., Sasso, F. C., et al. (2006). Increased activity of the ubiquitin-proteasome system in patients with symptomatic carotid disease is associated with enhanced inflammation and may destabilize the atherosclerotic plaque: effects of rosiglitazone treatment. *J. Am. Coll. Cardiol.* 47, 2444–2455. doi: 10.1016/j.jacc.2006.01.073

Moore, K. J., Sheedy, F. J., and Fisher, E. A. (2013). Macrophages in atherosclerosis: a dynamic balance. *Nat. Rev. Immunol.* 13, 709–721. doi: 10.1038/nri3520

Moore, K. J., and Tabas, I. (2011). Macrophages in the pathogenesis of atherosclerosis. *Cell* 145, 341–355. doi: 10.1016/j.cell.2011.04.005

Muchamuel, T., Basler, M., Aujay, M. A., Suzuki, E., Kalim, K. W., Lauer, C., et al. (2009). A selective inhibitor of the immunoproteasome subunit LMP7 blocks cytokine production and attenuates progression of experimental arthritis. *Nat. Med.* 15, 781–787. doi: 10.1038/nm.1978

Qin, X. Y., Zhang, Y. L., Chi, Y. F., Yan, B., Zeng, X. J., Li, H. H., et al. (2018). Angiotensin II Regulates Th1 T Cell Differentiation Through Angiotensin II Type 1 Receptor-PKA-Mediated Activation of Proteasome. *Cell Physiol. Biochem.* 45, 1366–1376. doi: 10.1159/000487562

Ross, R. (1999). Atherosclerosis–an inflammatory disease. *N. Engl. J. Med.* 340, 115–126.

Tabas, I., and Bornfeldt, K. E. (2016). Macrophage Phenotype and Function in Different Stages of Atherosclerosis. *Circ. Res.* 118, 653–667. doi: 10.1161/CIRCRESAHA.115.306256

Van Herck, J. L., De Meyer, G. R., Martinet, W., Bult, H., Vrints, C. J., and Herman, A. G. (2010). Proteasome inhibitor bortezomib promotes a rupture-prone plaque phenotype in ApoE-deficient mice. *Basic Res. Cardiol.* 105, 39–50. doi: 10.1007/s00395-009-0054-y

Versari, D., Herrmann, J., Gossl, M., Mannheim, D., Sattler, K., Meyer, F. B., et al. (2006). Dysregulation of the ubiquitin-proteasome system in human carotid atherosclerosis. *Arterioscler. Thromb. Vasc. Biol.* 26, 2132–2139. doi: 10.1161/01.atv.0000232501.08576.73

Wang, L., Zhao, X. C., Cui, W., Ma, Y. Q., Ren, H. L., Zhou, X., et al. (2016). Genetic and Pharmacologic Inhibition of the Chemokine Receptor CXCR2 Prevents Experimental Hypertension and Vascular Dysfunction. *Circulation* 134, 1353–1368. doi: 10.1161/circulationaha.115.020754

Wang, N., Liang, H., and Zen, K. (2014). Molecular mechanisms that influence the macrophage m1-m2 polarization balance. *Front. Immunol.* 5:614. doi: 10.3389/fimmu.2014.00614

Wang, S., Li, J., Bai, J., Li, J. M., Che, Y. L., Lin, Q. Y., et al. (2018). The immunoproteasome subunit LMP10 mediates angiotensin II-induced retinopathy in mice. *Redox. Biol.* 16, 129–138. doi: 10.1016/j.redox.2018.02.022

Wilck, N., Fechner, M., Dan, C., Stangl, V., Stangl, K., and Ludwig, A. (2017). The Effect of Low-Dose Proteasome Inhibition on Pre-Existing Atherosclerosis in LDL Receptor-Deficient Mice. *Int. J. Mol. Sci.* 18:781. doi: 10.3390/ijms18040781

Wilck, N., Fechner, M., Dreger, H., Hewing, B., Arias, A., Meiners, S., et al. (2012). Attenuation of early atherogenesis in low-density lipoprotein receptor-deficient mice by proteasome inhibition. *Arterioscler. Thromb. Vasc. Biol.* 32, 1418–1426. doi: 10.1161/atvbaha.112.249342

Xie, X., Bi, H. L., Lai, S., Zhang, Y. L., Li, N., Cao, H. J., et al. (2019). The immunoproteasome catalytic beta5i subunit regulates cardiac hypertrophy by targeting the autophagy protein ATG5 for degradation. *Sci. Adv.* 5:eaau0495.

Xie, X., Wang, H. X., Li, N., Deng, Y. W., Bi, H. L., Zhang, Y. L., et al. (2020). Selective Inhibition of the Immunoproteasome beta5i Prevents PTEN Degradation and Attenuates Cardiac Hypertrophy. *Front. Pharmacol.* 11:885. doi: 10.3389/fphar.2020.00885

Yan, W., Bi, H. L., Liu, L. X., Li, N. N., Liu, Y., Du, J., et al. (2017). Knockout of immunoproteasome subunit beta2i ameliorates cardiac fibrosis

and inflammation in DOCA/Salt hypertensive mice. *Biochem. Biophys. Res. Commun.* 490, 84–90. doi: 10.1016/j.bbrc.2017.05.011

Yang, Z., Gagarin, D., St Laurent, G. III, Hammell, N., Toma, I., Hu, C. A., et al. (2009). Cardiovascular inflammation and lesion cell apoptosis: a novel connection via the interferon-inducible immunoproteasome. *Arterioscler. Thromb. Vasc. Biol.* 29, 1213–1219. doi: 10.1161/atvbaha.109.189407

Zhang, Y., An, X., Lin, Q., Bai, J., Wang, F., and Liao, J. (2018). Splenectomy had no significant impact on lipid metabolism and atherogenesis in Apoe deficient mice fed on a severe atherogenic diet. *Cardiovasc. Pathol.* 36, 35–41. doi: 10.1016/j.carpath.2018.06.002

Zhao, W. J., Wei, S. N., Zeng, X. J., Xia, Y. L., Du, J., and Li, H. H. (2015). Gene expression profiling identifies the novel role of immunoproteasome in doxorubicin-induced cardiotoxicity. *Toxicology* 333, 76–88. doi: 10.1016/j.tox.2015.04.009

Conflict of Interest: The authors declare that the research was conducted in the absence of any commercial or financial relationships that could be construed as a potential conflict of interest.

frontiers in Cell and Developmental Biology

ORIGINAL RESEARCH
published: 30 October 2020
doi: 10.3389/fcell.2020.594683

Gallic Acid Ameliorates Angiotensin II-Induced Atrial Fibrillation by Inhibiting Immunoproteasome-Mediated PTEN Degradation in Mice

Dan Han[1†], Qi-Yu Zhang[1†], Yun-Long Zhang[2], Xiao Han[2], Shu-Bin Guo[2], Fei Teng[2], Xiao Yan[2] and Hui-Hua Li[1,2*]*

[1] *Department of Cardiology, Institute of Cardiovascular Diseases, First Affiliated Hospital of Dalian Medical University, Dalian, China,* [2] *Emergency Medicine Clinical Research Center, Beijing Chao-Yang Hospital, Beijing Key Laboratory of Cardiopulmonary Cerebral Resuscitation, Capital Medical University, Beijing, China*

OPEN ACCESS

Edited by:
Jiri Novotny,
Charles University, Czechia

Reviewed by:
Uwe Lendeckel,
University of Greifswald, Germany
Qiulun Lu,
Nanjing Medical University, China

***Correspondence:**
Xiao Yan
yanxiao0421@163.com
Hui-Hua Li
hhli1935@aliyun.com

† These authors have contributed equally to this work

Specialty section:
This article was submitted to Signaling, a section of the journal Frontiers in Cell and Developmental Biology

Received: *14 August 2020*
Accepted: *13 October 2020*
Published: *30 October 2020*

Citation:
Han D, Zhang Q-Y, Zhang Y-L, Han X, Guo S-B, Teng F, Yan X and Li H-H (2020) Gallic Acid Ameliorates Angiotensin II-Induced Atrial Fibrillation by Inhibiting Immunoproteasome- Mediated PTEN Degradation in Mice. Front. Cell Dev. Biol. 8:594683. doi: 10.3389/fcell.2020.594683

Atrial fibrillation (AF) is the most prevalent cardiac arrhythmia and is a major cause of stroke and heart failure. We and others have found that gallic acid (GA) plays a beneficial role in cardiac hypertrophic remodeling and hypertension. However, the effect of GA on angiotensin II (Ang II)-induced AF and atrial remodeling as well as the underlying mechanisms remain unknown. AF was induced in mice by Ang II infusion (2000 ng/kg/min) for 3 weeks. Blood pressure was measured using the tail-cuff method. Atrial volume was evaluated by echocardiography. Atrial remodeling was studied using hematoxylin and eosin, Masson's trichrome, and immunohistochemical staining. Atrial oxidative stress was assessed by dihydroethidium staining. The gene expression of fibrotic and inflammatory markers and protein levels of signaling mediators were measured by quantitative real-time PCR and western blot analysis. In mice, GA administration significantly attenuated Ang II-induced elevation of blood pressure, AF incidence and duration, atrial dilation, fibrosis, inflammation, and oxidative stress compared with the vehicle control. Furthermore, GA downregulated Ang II-induced activity and expression of immunoproteasome subunits (β2i and β5i), which reduced PTEN degradation and led to the inactivation of AKT1 and downstream signaling mediators. Importantly, blocking PTEN activity by VO-Ohpic markedly reversed the GA-mediated protective effects on Ang II-induced AF and atrial remodeling. Therefore, our results provide novel evidence that GA exerts a cardioprotective role by inhibiting immunoproteasome activity, which attenuates PTEN degradation and activation of downstream signaling, and may represent a promising candidate for treating hypertensive AF.

Keywords: gallic acid, atrial fibrillation, atrial structural remodeling, immunoproteasome, PTEN/AKT1

INTRODUCTION

Atrial fibrillation (AF) is the most prevalent cardiac arrhythmia and is associated with an increased risk of stroke, heart failure, and all-cause mortality (Staerk et al., 2017). AF is typically preceded by conduction abnormalities and structural remodeling, which is characterized by increased atrial fibrosis and dilation (Andrade et al., 2014). The renin–angiotensin system (RAS) plays an important role in the development of AF. As the main effector of the RAS, Ang II activates AKT1-mTOR, TGF-β1-Smad2/3, NF-κB, and NADPH oxidase through Ang II type 1 receptor (AT1R), which in turn promotes fibrosis, inflammation, production of reactive oxygen species, and an abnormal ion channel function in the atrium, thereby leading to the occurrence of AF (Gao and Dudley, 2009; Hu et al., 2015). Therefore, AT1R is the central mediator of atrial remodeling and AF, and thus represents a key target for early treatment of AF. Recent studies have demonstrated that phosphatase PTEN (a phosphatase and TENsin homolog deleted from chromosome 10) exhibits negative regulation of AT1R-induced signaling pathways and AF (Li et al., 2018, 2019). Importantly, we and others have revealed that the activity of PTEN is restored by natural compounds such as resveratrol and indole-3-carbinol (Chen et al., 2019; Lee et al., 2019; Zou et al., 2019). Thus, regulation of PTEN represents a promising strategy for treating cardiovascular disease.

Gallic acid (GA) is a natural phenolic acid that is abundant in several plants. Accumulating evidence has demonstrated that GA plays a beneficial role in apoptosis, hypertension, cardiac hypertrophy, and fibrosis (Ryu et al., 2016; Jin et al., 2017, 2018a,b). GA improved isoproterenol-induced cardiomyocyte hypertrophy and fibrosis by inhibiting the JNK2-Smad3 signaling pathway (Ryu et al., 2016). Moreover, GA also reduced cardiac oxidative stress and hypertension by regulating GATA4-NOX signaling in spontaneously hypertensive rats (Jin et al., 2017). Recently, we found that administration of GA attenuated pressure overload-induced cardiac hypertrophic remodeling and heart failure, which are associated with the autophagy-dependent degradation of hypertrophic mediators (EGFR, gp130, and calcineurin A) and the suppression of downstream signaling cascades (Yan et al., 2019). Moreover, GA ameliorated hypertension and vascular remodeling in Ang II-treated mice by suppressing the immunoproteasome-dependent degradation of endothelial nitric oxide synthase (Yan et al., 2020). However, the cardioprotective effect of GA against Ang II-induced AF and the underlying mechanism remain unknown.

In this study, we revealed that GA significantly reduced AF incidence and duration as well as atrial structural remodeling in Ang II-treated mice. Mechanistically, the protective effect is associated with suppression of the activity and expression of the immunoproteasome subunits β2i and β5i, which inhibit PTEN degradation and AKT1 activation, resulting in the downregulation of the TGF-β1-Smad2/3 and NF-κB signaling pathways. Collectively, our results suggest that GA is a novel regulator of the immunoproteasome and PTEN stabilization, and may provide a potential treatment option for hypertensive AF.

MATERIALS AND METHODS

Animal Models and Experimental Protocols

C57BL/6 mice (male, 8–10 weeks of age, n = 200) were used to establish the model of AF by subcutaneous infusion of Ang II (2000 ng/kg/min; Sigma-Aldrich, St. Louis, MO, United States) or saline for 3 weeks as described previously (Li et al., 2018, 2019; Zhang et al., 2020). The tail-cuff system (Softron BP98A; Softron Tokyo, Japan) was used to assess the systolic blood pressure (SBP) as previously described (Wang et al., 2016, 2018; Zhang et al., 2020). All animal studies were approved by the Animal Care and Use Committee of Dalian Medical University (No. LCKY2016-31) and conformed to the Guide for the Care and Use of Laboratory Animals published by the United States National Institutes of Health (NIH Publication No. 85-23, revised 1996).

Dosage Information

Animals were orally gavaged with vehicle or GA (5 or 20 mg/kg BW/day, Sigma-Aldrich, United Kingdom) 1 day before Ang II infusion. The specific PTEN inhibitor VO-OHpic (Selleck, Houston, TX, United States) was intraperitoneally administered (10 mg/kg/day per mouse) in mice beginning 1 day before Ang II infusion (Chen et al., 2019).

AF Induction

Mice were anesthetized with 2.5% tribromoethanol (0.02 mL/g; Sigma-Aldrich, United Kingdom) by intraperitoneal injection. A Millar 1.1 F octapolar EP catheter (Scisense, NY, United States) was guided into the right atrium and ventricle. AF Inducibility was gauged by applying a 5-s burst using the automated stimulator as described previously (Li et al., 2018, 2019; Zhang et al., 2020). The 1-lead body surface ECG and ≤4 intracardiac bipolar electrograms were recorded by the 15 A computer-based data acquisition system (GY6328B; HeNan HuaNan Medical Science and Technology, Co., Ltd.). A series of bursts was repeated three times after 5-min stabilization.

Echocardiography

Two-dimensional M-mode echocardiography was performed on mice using a 30 MHz probe (Vevo 1100 system; VisualSonics, Toronto, ON, Canada) as described previously (Wang et al., 2018; Chen et al., 2019; Yan et al., 2019; Zhang et al., 2020). The left atrium (LA) chamber dimensions were measured.

Histological Analysis

Atrial samples were fixed in 4% paraformaldehyde, embedded in paraffin, and then sectioned (5 μm). The staining of Hematoxylin and eosin (H&E) and Masson's Trichrome were performed on the atrial sections in accordance with the standard procedure (Li et al., 2018, 2019; Zhang et al., 2020). The immunohistochemistry staining was performed with anti-α-smooth muscle actin (α-SMA) (1:200, Abcam, MA, United States) and anti-Mac-2 (1:200, Abcam) as described (Wang et al., 2018). Cryosections were stained with the dihydroethidine (DHE, 1 μM in PBS) for 30 min at 37°C.

Fluorescence was detected using Nikon Labophot 2 microscope (Nikon, Tokyo, Japan).

Proteasome Activity Assay

The activity of proteasome in the atria was gauged by specific luminogenic peptide substrates, including Z-nLPnLD-aminoluciferin, Z-LRR-aminoluciferin, and Suc-LLVY-aminoluciferin for the caspase-like, trypsin-like, and chymotrypsin-like activities according to the manufacturer's instructions (Li et al., 2018, 2019; Chen et al., 2019).

Quantitative Real-Time PCR Analysis

The quantitative real-time PCR (qPCR) was gauged by an iCycler IQ system (Bio-Rad, CA, United States). Total RNA from atrium tissues were isolated with TRIzol and reverse transcribed as described (Wang et al., 2016). The cDNA was used for PCR amplification with gene-specific primers (Sangon Biotech, Shanghai, China), including α-SMA, collagen I, collagen III, IL-1β, IL-6, TNF-α, MCP-1, NOX2, NOX4, β1, β2, β5, β1i, β2i, and β5i (**Supplementary Table 1**). The transcript quantities were normalized to the amount of endogenous control (GAPDH).

Western Blot Analysis

Total proteins were extracted from snap-frozen atrium samples using RIPA buffer plus protease inhibitors (Solarbio Science Technology Co., China). The protein lysates were separated by electrophoresis in 8–12% SDS-PAGE gels, transferred to polyvinylidene difluoride (PVDF) membranes. The membranes were incubated with appropriate primary antibodies and then with horseradish peroxidase-conjugated secondary antibodies. The signal intensities of immunoblots were detected by the ECL Plus chemiluminescent system (Bio-Rad, CA, United States) and were analyzed with a Gel-pro 4.5 Analyzer (Media Cybernetics, United States) (Chen et al., 2019).

Statistical Analysis

The normality test (Shapiro–Wilk) was utilized to verify whether the data were normally distributed. The student *t*-test was performed to evaluate the significant difference between two groups in normal distribution. For the data that were not normally distributed, the Mann–Whitney test was used. For the other comparisons, the significance of the difference between means of the groups was determined by one-way ANOVA following Newman–Keuls multiple comparison test from GraphPad Prism 5 (GraphPad Prism Software). The values of $P < 0.05$ were considered statistically significant.

RESULTS

GA Inhibits Ang II-Induced AF in Mice

We first tested whether administration of GA could reduce AF. GA treatment significantly improved the elevation of SBP in Ang II-treated mice in a dose-dependent manner (**Figure 1A**). Moreover, the incidence and duration of Ang II-induced AF were significantly reduced in GA-treated mice compared with the vehicle-treated mice (**Figures 1B–D**). Furthermore, Ang II infusion resulted in a marked increase in LA dilation in mice, which was attenuated after GA treatment (**Figure 1E**). There was no significant difference in SBP, AF inducibility and duration, or LA dilation between the two groups after saline infusion (**Figures 1A–E**). Thus, these data suggest that GA administration attenuates Ang II-induced AF.

GA Suppresses Ang II-Induced Atrial Fibrosis

We next examined whether GA attenuates the formation of atrial fibrosis. After 3 weeks of Ang II infusion, the atrial fibrotic area, percentage of α-SMA$^+$ myofibroblasts, and mRNA expression of α-SMA, collagen I, and collagen III were increased in mice, and these effects were significantly abrogated by GA administration (**Figures 2A–C**). Moreover, Ang II infusion markedly upregulated the key signaling mediators of atrial fibrosis, including TGF-β1 and p-Smad2/3, while this effect was diminished in GA-treated mice (**Figure 2D**). Accordingly, these results indicate that GA treatment effectively improves adverse atrial structural remodeling after Ang II infusion.

GA Attenuates Ang II-Induced Atrial Inflammation and Oxidative Stress

The administration of GA dose-dependently inhibited Ang II-induced infiltration of inflammatory cells (as indicated by Mac-2-positive macrophages) and the mRNA expression levels of IL-1β, IL-6, TNF-α, and MCP-1 compared with the vehicle (**Figures 3A,C**). Furthermore, Ang II infusion increased atrial superoxide formation (demonstrated by DHE staining) and the gene expression of NOX2 and NOX4 (**Figures 3B,D**). These effects were reduced in GA-treated mice (**Figures 3B,D**). We next determined the effect of GA on NF-κB signaling and gap junction gene expression. In agreement with our recent studies (Li et al., 2018, 2019; Zhang et al., 2020), the protein expression levels of p-p65 and connexin 43 (Cx43) were upregulated in Ang II-treated atria, and this upregulation was reversed after GA treatment (**Figure 3E**).

GA Inhibits Immunoproteasome Activity and PTEN Degradation

Recent studies have demonstrated that PTEN and its downstream signaling are involved in Ang II-induced AF (Li et al., 2018, 2019), therefore next we investigated the effect of GA on proteasome-mediated PTEN degradation in the atria. The administration of GA significantly and dose-dependently suppressed Ang II-induced trypsin-like and chymotrypsin-like activities (**Figure 4A**). Because constitutively expressed β-subunits (β1, β2, and β5) and immunosubunits (β1i, β2i, and β5i) have proteasome activity, RT-PCR and western blotting analysis were utilized to evaluate subunit expression. Ang II infusion increased the mRNA expression levels of β2i and β5i compared with saline control (**Figure 4B**). Furthermore, GA treatment dose-dependently reduced the gene expression of the immunosubunits β2i and β5i but not β1i and constitutively expressed β-subunits (β1, β2, and β5) in the atria after Ang II

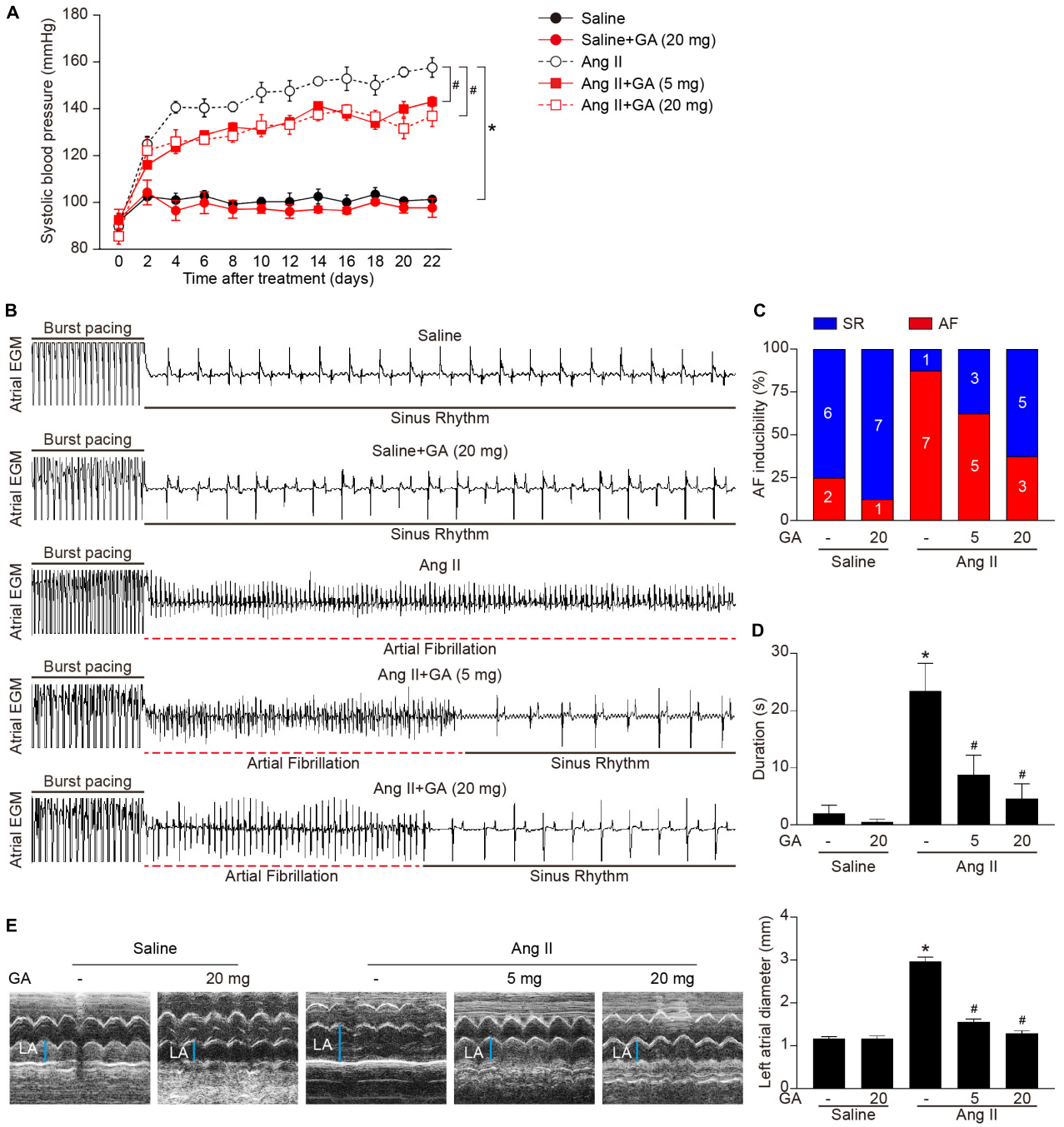

FIGURE 1 | Administration of GA attenuates Ang II-induced AF and atrial dilation. Mice were infused with Ang II (2000 ng kg^{-1} min^{-1}) for 21 days. **(A)** Systolic blood pressure (SBP) was measured by the non-invasive tail-cuff method in vehicle or GA-treated mice before and after Ang II infusion. **(B)** Representative atrial electrogram recordings. Burst pacing is highlighted by solid underlines, while dashed underlines indicate AF. **(C)** Percentage of mice in which AF was successfully achieved in each group (n = 8). **(D)** AF duration in mice with AF induction. **(E)** M-mode echocardiography of left atrium (LA) chamber (left), and quantification of LA diameter (right, n = 8). $^{*}P < 0.05$ versus saline, $^{\#}P < 0.05$ versus Ang II.

infusion (**Figure 4B**). In addition, the Ang II-induced increase in protein expression levels of β2i and β5i was also downregulated in GA-treated atria tissues (**Figure 4C**). In line with our previous findings (Li et al., 2018, 2019), Ang II infusion for 3 weeks increased PTEN degradation and p-AKT1 protein expression, and these effects were dose-dependently reversed by the administration of GA (**Figure 4C**). Taken together, these results demonstrate that GA treatment reduces PTEN degradation likely via suppressing the expression and activity of immunoproteasome subunits in Ang II-treated atria.

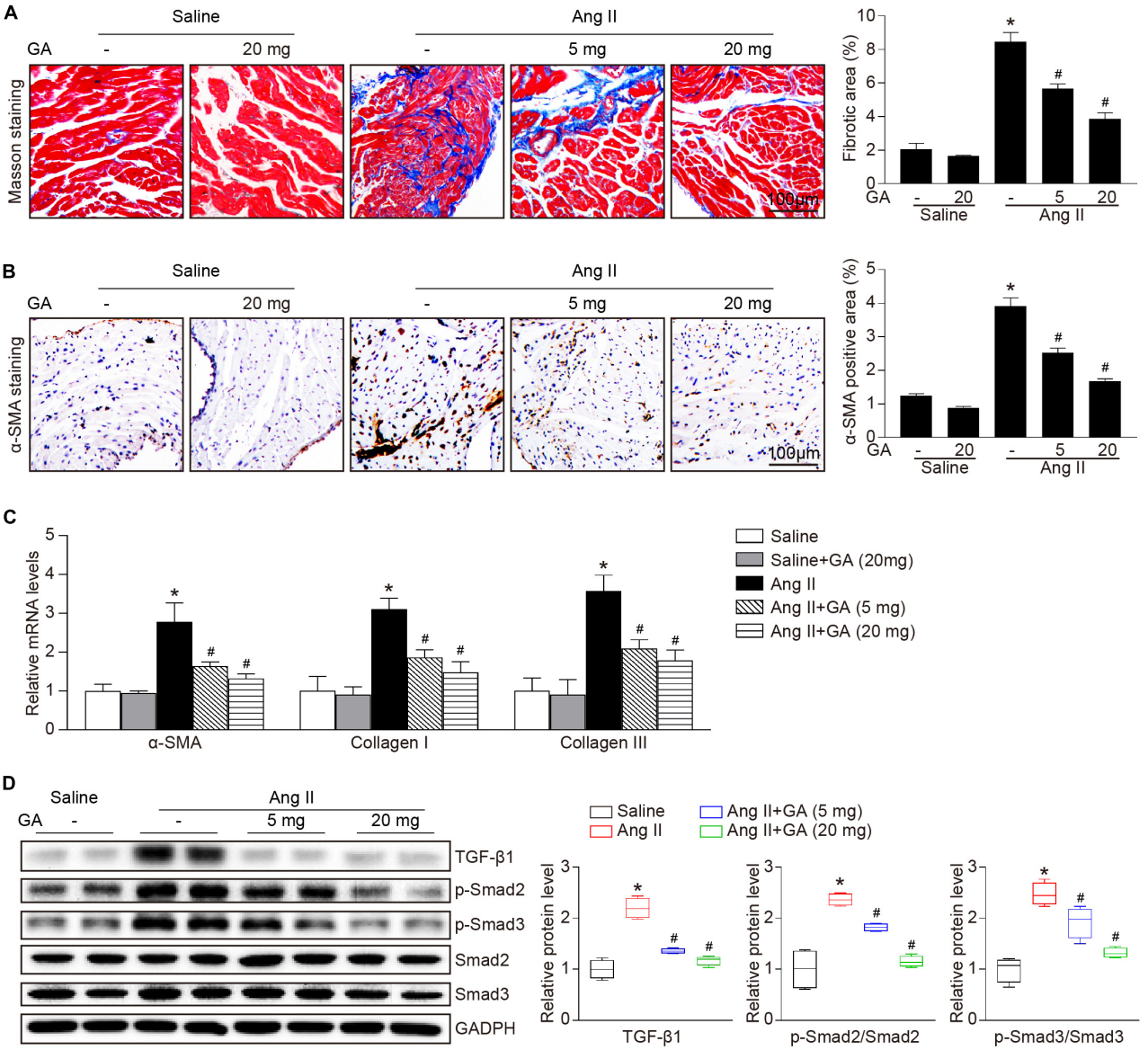

FIGURE 2 | GA inhibits Ang II-induced atrial remodeling. **(A)** Representative images of Masson trichrome staining for atrial fibrosis (left). Quantification of fibrotic area (right, $n = 6$). Scale bar: 100 μm. **(B)** Representative images of immunohistochemical staining of LA sections to detect myofibroblast activation (left). Quantification of α-SMA$^+$ areas (right, $n = 6$). Scale bar: 100 μm. **(C)** qPCR analyses of the mRNA expression levels of α-SMA, collagen I, and collagen III ($n = 6$). **(D)** Immunoblotting analysis of the protein levels of TGF-β1, p-Smad2/3, and Smad2/3 in the atria (left), and quantification of each protein band (right, $n = 4$). GAPDH as an internal control. $^*P < 0.05$ versus saline, $^{\#}P < 0.05$ versus Ang II.

Blockage of PTEN Activity Reduces the GA-Mediated Protective Effect on Ang II-Induced AF

To identify the role of PTEN in Ang II-induced atrial remodeling and AF after GA treatment, mice were treated with the PTEN specific inhibitor VO-OHpic with or without administration of GA. Three weeks after Ang II infusion, mice treated with GA exhibited a significant reduction of SBP, AF inducibility and duration, and LA dilation compared with the vehicle-treated mice (**Figures 5A–E**); these effects were abolished by VO-OHpic treatment (**Figures 5A–E**). Furthermore, the GA-mediated decrease in atrial fibrotic area, number of α-SMA-positive myofibroblasts, Mac-2$^+$ macrophage infiltration, superoxide production, and mRNA expression levels of α-SMA, collagen I, and collagen III were reversed by VO-OHpic in GA-treated mice (**Figures 6A–D** and **Supplementary Figure 1**). Accordingly, GA-induced reduction of PTEN degradation and protein expression of p-AKT1, TGF-β1, and p-p65 in Ang II-treated mice were blocked after VO-OHpic treatment (**Figure 6E**). Collectively, these results suggest that GA inhibits Ang II-induced atrial remodeling and AF via reducing PTEN degradation.

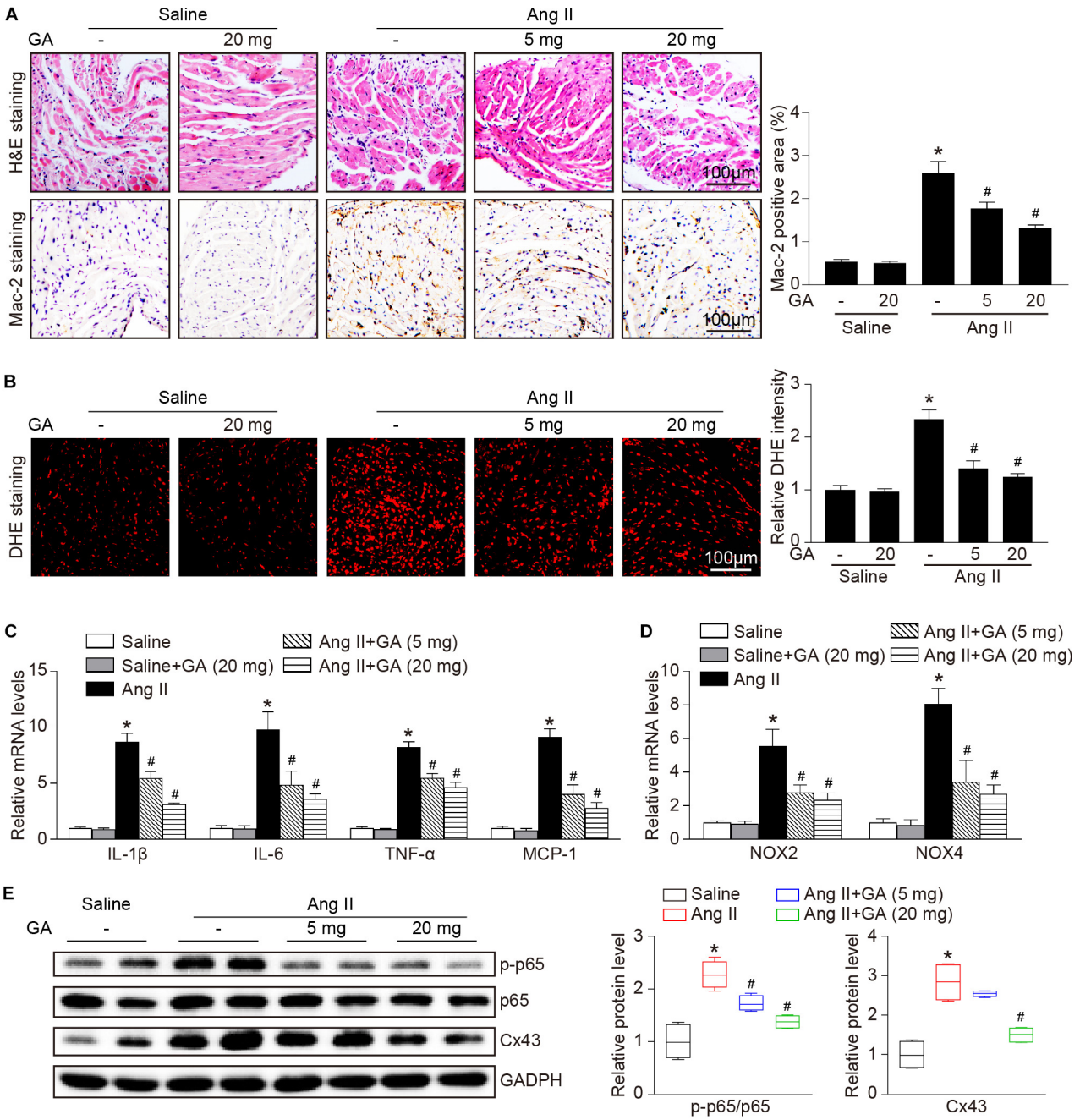

FIGURE 3 | GA reduces atrial inflammation and oxidative stress in mice after Ang II infusion. **(A)** Representative H&E staining (top) and Mac-2 immunohistochemistry (bottom) in the atria. Quantification of Mac-2–positive cells (right, $n = 6$). Scale bar: 100 μm. **(B)** DHE staining of atrial superoxide production (left), and quantification of DHE intensity (right, $n = 6$). Scale bar: 100 μm. **(C)** qPCR analyses of the mRNA expression levels of IL-1β, IL-6, TNF-α, and MCP-1 ($n = 6$). **(D)** qPCR analyses of the mRNA expression of NOX2 and NOX4. **(E)** Immunoblotting analysis of the protein expression levels of p-p65, p65, and Cx43 in the atria (left), and quantification of each protein band (right, $n = 4$). GAPDH as an internal control. $^{*}P < 0.05$ versus saline, $^{\#}P < 0.05$ versus Ang II.

DISCUSSION

Here, we revealed for the first time that the administration of GA inhibits Ang II-induced AF incidence and atrial dilation. Specifically, GA blocks the activity and expression of the immunoproteasome catalytic subunit β2i and β5i, which reduces PTEN degradation and AKT activation. This leads to the suppression of downstream signaling mediators (TGF-β1-Smad2/3, NF-κB, and Cx43), which improves atrial fibrosis, inflammation, and oxidative stress (**Figure 7**). Therefore, our results provide new evidence that GA serves as an effective inhibitor of the immunoproteasome

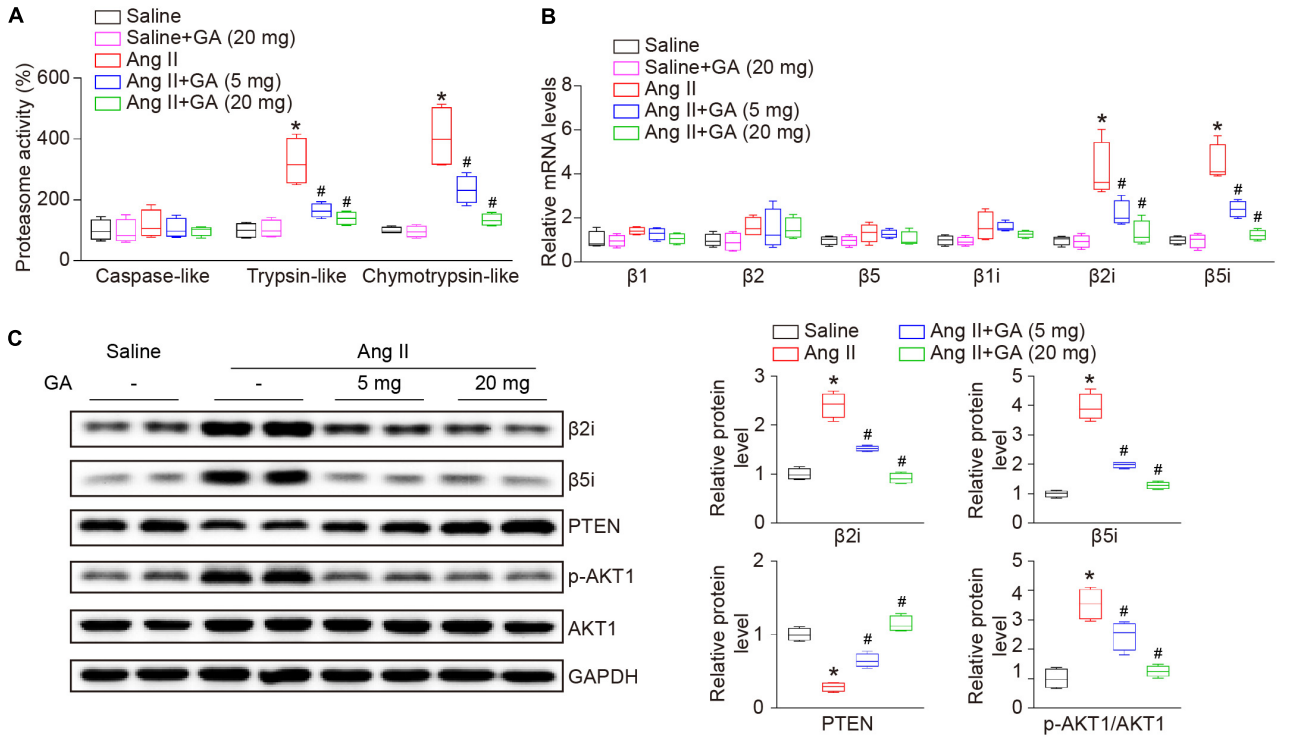

FIGURE 4 | GA reduces the activity and expression of immunoproteasome subunits β2i and β5i and PTEN degradation in the atria after Ang II infusion. **(A)** The proteasome activities in the atria after Ang II infusion in the presence or absence of GA treatment ($n = 4$). **(B)** qPCR analyses of the mRNA expression levels of β1, β2, β5, β1i, β2i, and β5i ($n = 4$). **(C)** Representative immunoblotting analyses of the protein expression levels of β2i, β5i, PTEN, p-AKT1, and AKT1 (left), and quantification of the relative protein levels (right, $n = 4$). GAPDH as an internal control. $^{*}P < 0.05$ versus saline, $^{\#}P < 0.05$ versus Ang II.

and is a promising agent for treating AF and atrial structural remodeling.

Atrial structural remodeling is the hallmark of the development and progression of AF, which subsequently causes LA enlargement and conduction abnormalities (Andrade et al., 2014). This process consists of several mechanisms, including atrial fibrosis, inflammation, and oxidative stress (Dzeshka et al., 2015). Ang II has been demonstrated to significantly increase SBP, left ventricular hypertrophy, and dysfunction, which are established clinical risk factors for AF (Purohit et al., 2013; Jansen et al., 2018). Current therapeutic agents for AF, which include oral anticoagulation, angiotensin-converting enzyme inhibitors, and antiarrhythmic drugs, focus on the common symptoms and complications. However, adverse events with these agents may increase mortality (Kirchhof, 2017). Therefore, new options targeting atrial structural remodeling, atrial dilation, and AF are urgently needed. GA is a natural polyphenol compound that exerts a key role in protecting against cardiac hypertrophy, hypertension, and fibrosis in several animal models (Jin et al., 2017, 2018b). Recently, we demonstrated that GA administration improved pressure overload-induced myocardial hypertrophic remodeling (including hypertrophy, fibrosis, inflammation, and oxidative stress) (Yan et al., 2019) and Ang II-induced hypertension and vascular dysfunction (Yan et al., 2020), suggesting that GA may exert a protective effect on AF. In agreement with this, we demonstrated that GA not only markedly reduced the elevation blood pressure but also attenuated atrial fibrosis, inflammation, and ROS production in Ang II-treated mice (**Figures 2**, **3**), which are involved in the pathogenesis of AF. Thus, our results indicate that GA markedly reduced AF development at least in part through blocking Ang II/hypertension-induced atrial remodeling.

Proteasomal degradation is the vital pathway for intracellular protein turnover in most mammalian cells and organs, including the heart (Lyon et al., 2013). After stimulation by inflammatory cytokines, H_2O_2, and heat shock, the immunoproteasome is induced and exhibits immune and non-immune functions, such as antigen presentation, inflammation, oxidative stress, and cell signaling (Angeles et al., 2012). Increasing evidence demonstrates that adverse stimuli including pressure overload, isoproterenol, deoxycortone acetate/salt, and Ang II increase the catalytic activity and expression of the immunoproteasome, leading to cardiac hypertrophy and AF (Depre et al., 2006; Drews et al., 2010; Li et al., 2015; Yan et al., 2017). In contrast, the proteasome inhibitor bortezomib effectively ameliorates Ang II-induced myocardial hypertrophy and contractile function (Li et al., 2015). Moreover, we recently found that the activity and expression of β2i and β5i are upregulated in the atria of Ang II-treated mice and the serum of patients with AF (Li et al., 2018, 2019). Knockout of β2i or β5i attenuates Ang II-induced atrial remodeling and development of AF (Li et al., 2018, 2019). Interestingly, several natural products, including quercetin and resveratrol, have

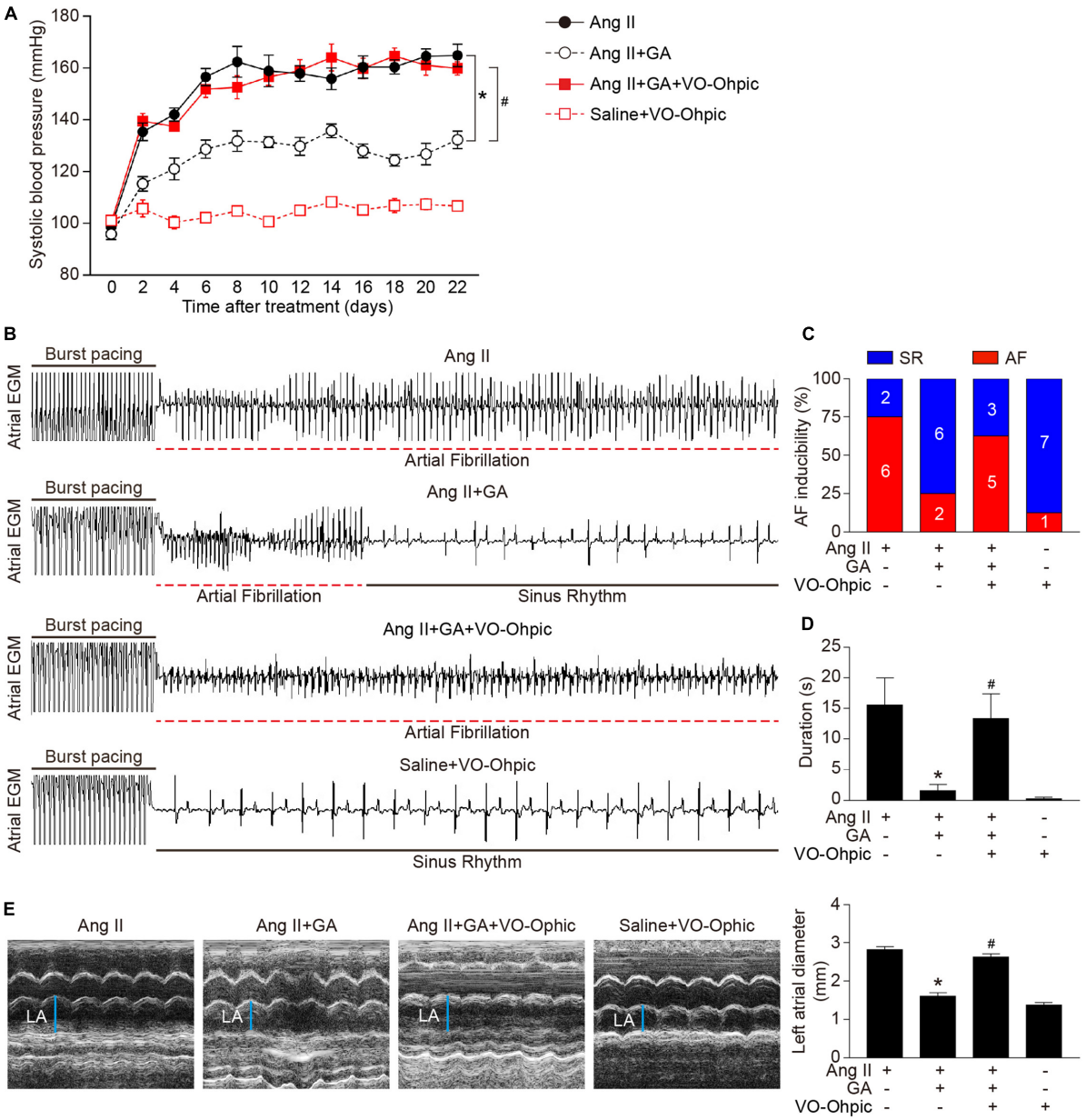

FIGURE 5 | Blocking of PTEN activity suppresses the GA-mediated beneficial effect on Ang II-induced AF. **(A)** SBP was measured by the non-invasive tail-cuff method in the vehicle or GA-treated mice before and after Ang II infusion with or without VO-OHpic treatment. **(B)** Representative atrial electrogram recordings. Burst pacing is highlighted by solid underlines, while dashed underlines indicate AF. **(C)** Percentage of mice in which AF was successfully achieved in each group ($n = 8$). **(D)** AF duration in mice with AF induction. **(E)** M-mode echocardiography of LA chamber (left), and quantification of LA diameter (right, $n = 8$). $^{*}P < 0.05$ versus Ang II, $^{\#}P < 0.05$ versus Ang II + GA.

been shown to inhibit proteasome activity, thereby ameliorating atherosclerosis and cardiac hypertrophy (Pashevin et al., 2011; Chen et al., 2019). In the present study, we have provided novel evidence that GA administration significantly suppresses the activity and expression of the immunoproteasome catalytic subunits β2i and β5i in the atria of Ang II-treated mice.

Accumulating evidence suggests that PTEN plays a critical role in cardiovascular disease by inhibiting AKT-dependent pathways (GSK3, FOXO, and mTOR) and PINK1-AMPK signaling cascades (Crackower et al., 2002; Song et al., 2012; Xu et al., 2014; Roe et al., 2015). The cardiomyocyte-specific dysfunction of PTEN in mice results in myocardial hypertrophy and contractility defects, which are accompanied by inhibition of autophagy (Crackower et al., 2002; Xu et al., 2014; Roe et al., 2015). However, these effects could be reversed by rapamycin-induced suppression of mTOR and metformin-dependent activation of AMPK (Xu et al., 2014; Roe et al., 2015). Of note, our recent studies have demonstrated that

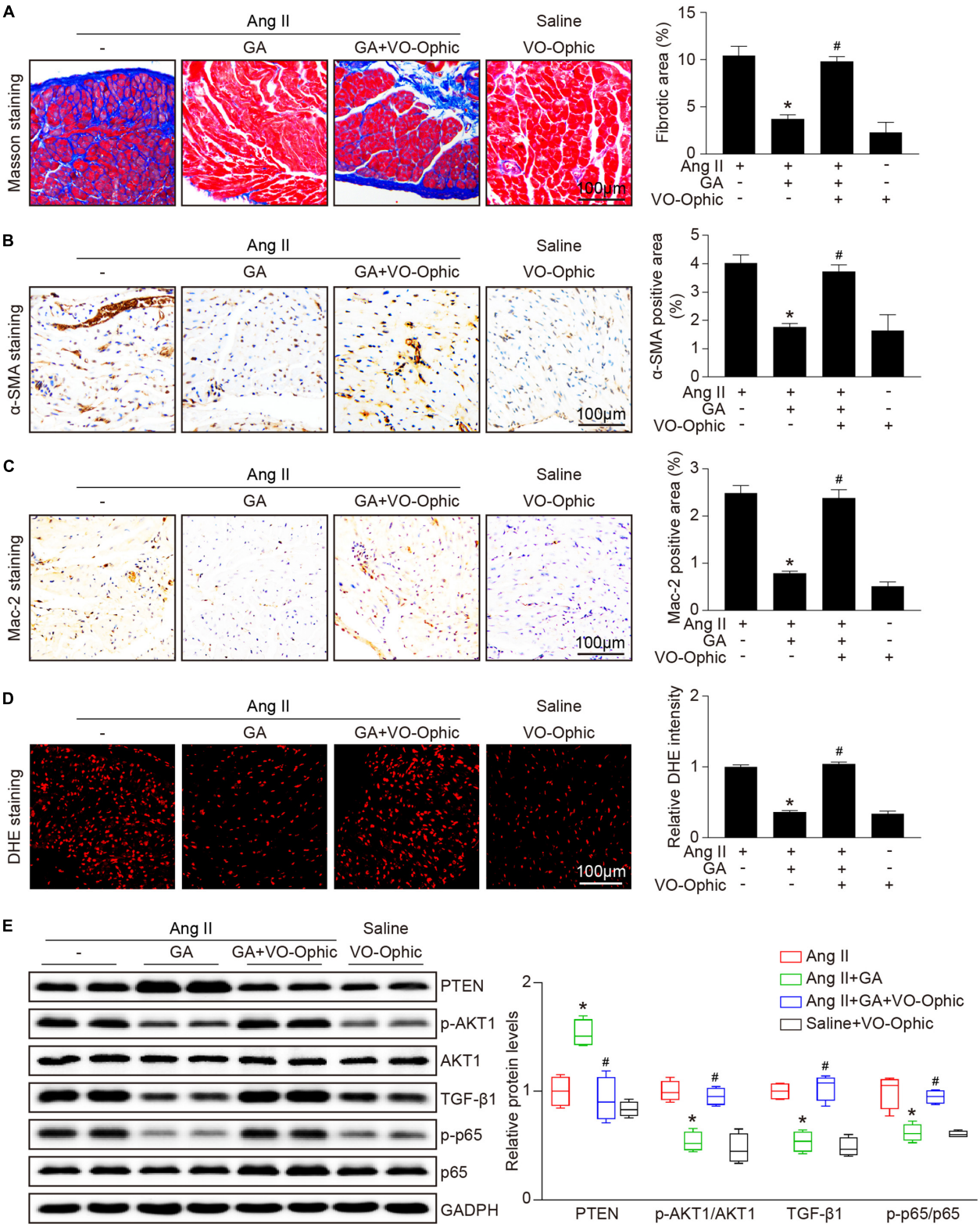

FIGURE 6 | PTEN inhibition blocks the GA-mediated protective effect on atrial remodeling and downstream signaling pathways. **(A)** Representative images of Masson trichrome staining for atrial fibrosis (left). Quantification of fibrotic area (right, $n = 6$). Scale bar: 100 μm. **(B)** Representative images of immunohistochemical staining of LA sections to detect myofibroblast activation (left). Quantification of α-SMA$^+$ areas (right, $n = 6$). Scale bar: 100 μm. **(C)** Representative Mac-2

(Continued)

FIGURE 6 | Continued

immunohistochemistry (left) in the atria. Scale bar: 100 μm. Quantification of Mac-2–positive cells (right, $n = 6$). **(D)** DHE staining of atrial superoxide production (left), and quantification of DHE intensity (right, $n = 6$). Scale bar: 100 μm. **(E)** Representative immunoblotting analyses of the protein expression levels of PTEN, p-AKT1, AKT1, TGF-β1, p-p65, and p65 (left), and quantification of the relative protein levels (right, $n = 4$). GAPDH as an internal control. $^{*}P < 0.05$ versus Ang II, $^{\#}P < 0.05$ versus Ang II + GA.

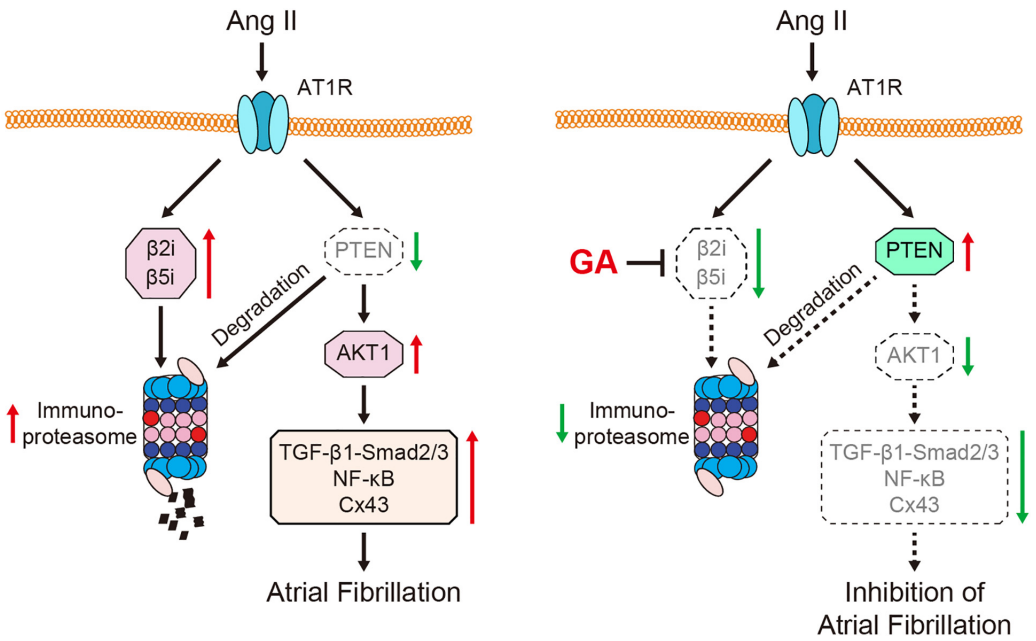

FIGURE 7 | A schematic model of the GA-mediated cardioprotection in Ang II-induced AF. GA inactivates immunoproteasome-dependent degradation of PTEN, leading to the downregulation of AKT1, TGF-β1-Smad2/3, NF-κB p65, and Cx43 signaling mediators. Therefore, GA ameliorates atrial remodeling and AF induced by Ang II infusion.

PTEN plays a role in Ang II-induced AF and atrial structural remodeling by ameliorating AKT1 and downstream signaling mediators (TGF-β1-Smad2/3, NF-κB, and Cx43) (Li et al., 2018, 2019). Thus, the regulation of PTEN activity and/or protein expression is considered as a promising therapeutic strategy for heart disease. PTEN activity is indeed modulated by post-translational modifications, especially ubiquitination-mediated proteasomal degradation (Lee et al., 2018). We and others demonstrated that proteasomal dysfunction induced by knockout of the immunoproteasome subunits β1i, β2i, or β5i in mice attenuated PTEN degradation, leading to the downregulation of AKT-associated signaling pathways in ischemic hearts and AF (Cai et al., 2008; Li et al., 2018, 2019). Interestingly, several natural compounds have been identified as potent inhibitors of PTEN degradation. Indole-3-carbinol, derived from cruciferous vegetables, directly blocks E3 ubiquitin ligase WWP1 and subsequently suppresses the K27-linked ubiquitination of PTEN (Lee et al., 2019). Moreover, we recently showed that resveratrol represents a novel inhibitor of the immunoproteasome and restores PTEN stability in pressure overload-induced cardiac hypertrophy and fibrosis (Chen et al., 2019; Zou et al., 2019). In the present study, we extended our previous findings and demonstrated that administration of GA markedly decreased PTEN degradation and activation of AKT1, leading to inhibition of AF and atrial remodeling in Ang II-treated mice. These effects were reversed by the specific PTEN inhibitor VO-OHpic. Collectively, our novel findings suggest that PTEN plays a role in the GA-mediated cardioprotective effects on Ang II-treated atria.

Several studies have explored the bioavailability of GA in humans (Manach et al., 2005). After the oral administration of pure tablets or black tea (each containing 50 mg GA), GA was rapidly absorbed and the plasma concentrations of GA reached 1.83 μmol/L (Shahrzad et al., 2001). Interestingly, our recent study revealed that the dosage of GA used in mice (5 or 20 mg/kg BW) was equivalent to 0.41 or 1.63 mg kg/BW in humans (Yan et al., 2019), which is consistent with the results of others. Moreover, we found that primary cardiomyocytes treated with GA (1–200 μmol) showed no significant toxic effect (Yan et al., 2019). Thus, GA may serve as a safe and effective natural product for the prevention and treatment of cardiovascular diseases. Further investigations are needed to verify the bioavailability of different forms of GA in foods.

CONCLUSION

In summary, in this study we demonstrated for the first time that GA administration significantly attenuated Ang

II-induced AF and atrial structural remodeling in mice. Moreover, GA suppressed the activity and expression of the immunoproteasome subunits β2i and β5i, which ameliorated PTEN degradation leading to inactivation of AKT1 and downstream signaling pathways (TGF-β1-Smad2/3, NF-κB, and Cx43). Thus, these findings identify GA as a novel inhibitor of the immunoproteasome and suggest a potential approach to AF prevention and treatment.

DATA AVAILABILITY STATEMENT

The data that support the findings of this study are available from the corresponding author upon reasonable request.

ETHICS STATEMENT

The animal study was reviewed and approved by the Animal Care and Use Committee of Dalian Medical University (No. LCKY2016-31) and conformed to the US National Institutes of Health Guide for the Care and Use of Laboratory Animals.

AUTHOR CONTRIBUTIONS

DH, Q-YZ, Y-LZ, and XH conducted the experiments. DH, FT, and XY analyzed the data. S-BG, XY, and H-HL designed the study. XY and H-HL drafted the manuscript, provided the funding for the study, and had primary responsibility for the final content. All authors contributed to the article and approved the submitted version.

FUNDING

This work was supported by grants from the China Postdoctoral Science Foundation (2020M670384 to XY) and the National Natural Science Foundation of China (81703217 to XY, 81630009 to H-HL).

SUPPLEMENTARY MATERIAL

The Supplementary Material for this article can be found online at: https://www.frontiersin.org/articles/10.3389/fcell.2020.594683/full#supplementary-material

REFERENCES

Andrade, J., Khairy, P., Dobrev, D., and Nattel, S. (2014). The clinical profile and pathophysiology of atrial fibrillation: relationships among clinical features, epidemiology, and mechanisms. *Circ. Res.* 114, 1453–1468. doi: 10.1161/CIRCRESAHA.114.303211

Angeles, A., Fung, G., and Luo, H. (2012). Immune and non-immune functions of the immunoproteasome. *Front. Biosci. (Landmark Ed)* 17:4027. doi: 10.2741/4027

Cai, Z. P., Shen, Z., Van Kaer, L., and Becker, L. C. (2008). Ischemic preconditioning-induced cardioprotection is lost in mice with immunoproteasome subunit low molecular mass polypeptide-2 deficiency. *FASEB J.* 22, 4248–4257. doi: 10.1096/fj.08-105940

Chen, C., Zou, L. X., Lin, Q. Y., Yan, X., Bi, H. L., Xie, X., et al. (2019). Resveratrol as a new inhibitor of immunoproteasome prevents PTEN degradation and attenuates cardiac hypertrophy after pressure overload. *Redox Biol.* 20, 390–401. doi: 10.1016/j.redox.2018.10.021

Crackower, M. A., Oudit, G. Y., Kozieradzki, I., Sarao, R., Sun, H., Sasaki, T., et al. (2002). Regulation of myocardial contractility and cell size by distinct PI3K-PTEN signaling pathways. *Cell* 110, 737–749. doi: 10.1016/s0092-8674(02)00969-8

Depre, C., Wang, Q., Yan, L., Hedhli, N., Peter, P., Chen, L., et al. (2006). Activation of the cardiac proteasome during pressure overload promotes ventricular hypertrophy. *Circulation* 114, 1821–1828. doi: 10.1161/CIRCULATIONAHA.106.637827

Drews, O., Tsukamoto, O., Liem, D., Streicher, J., Wang, Y., and Ping, P. (2010). Differential regulation of proteasome function in isoproterenol-induced cardiac hypertrophy. *Circ. Res.* 107, 1094–1101. doi: 10.1161/CIRCRESAHA.110.222364

Dzeshka, M. S., Lip, G. Y., Snezhitskiy, V., and Shantsila, E. (2015). Cardiac fibrosis in patients with atrial fibrillation: mechanisms and clinical mmplications. *J. Am. Coll. Cardiol.* 66, 943–959. doi: 10.1016/j.jacc.2015.06.1313

Gao, G., and Dudley, S. C. Jr. (2009). Redox regulation, NF-kappaB, and atrial fibrillation. *Antioxid. Redox Signal.* 11, 2265–2277. doi: 10.1089/ARS.2009.2595

Hu, Y. F., Chen, Y. J., Lin, Y. J., and Chen, S. A. (2015). Inflammation and the pathogenesis of atrial fibrillation. *Nat. Rev. Cardiol.* 12, 230–243. doi: 10.1038/nrcardio.2015.2

Jansen, H. J., Mackasey, M., Moghtadaei, M., Belke, D. D., Egom, E. E., Tuomi, J. M., et al. (2018). Distinct patterns of atrial electrical and structural remodeling in angiotensin II mediated atrial fibrillation. *J. Mol. Cell. Cardiol.* 124, 12–25. doi: 10.1016/j.yjmcc.2018.09.011

Jin, L., Piao, Z. H., Liu, C. P., Sun, S., Liu, B., Kim, G. R., et al. (2018a). Gallic acid attenuates calcium calmodulin-dependent kinase II-induced apoptosis in spontaneously hypertensive rats. *J. Cell. Mol. Med.* 22, 1517–1526. doi: 10.1111/jcmm.13419

Jin, L., Piao, Z. H., Sun, S., Liu, B., Kim, G. R., Seok, Y. M., et al. (2017). Gallic acid reduces blood pressure and attenuates oxidative stress and cardiac hypertrophy in spontaneously hypertensive rats. *Sci. Rep.* 7:15607. doi: 10.1038/s41598-017-15925-1

Jin, L., Sun, S., Ryu, Y., Piao, Z. H., Liu, B., Choi, S. Y., et al. (2018b). Gallic acid improves cardiac dysfunction and fibrosis in pressure overload-induced heart failure. *Sci. Rep.* 8:9302. doi: 10.1038/s41598-018-27599-4

Kirchhof, P. (2017). The future of atrial fibrillation management: integrated care and stratified therapy. *Lancet* 390, 1873–1887. doi: 10.1016/S0140-6736(17)31072-3

Lee, Y. R., Chen, M., Lee, J. D., Zhang, J., Lin, S. Y., Fu, T. M., et al. (2019). Reactivation of PTEN tumor suppressor for cancer treatment through inhibition of a MYC-WWP1 inhibitory pathway. *Science* 364:eaau0159. doi: 10.1126/science.aau0159

Lee, Y. R., Chen, M., and Pandolfi, P. P. (2018). The functions and regulation of the PTEN tumour suppressor: new modes and prospects. *Nat. Rev. Mol. Cell Biol.* 19, 547–562. doi: 10.1038/s41580-018-0015-0

Li, J., Wang, S., Bai, J., Yang, X. L., Zhang, Y. L., Che, Y. L., et al. (2018). Novel role for the immunoproteasome subunit PSMB10 in angiotensin II-induced atrial fibrillation in mice. *Hypertension* 71, 866–876. doi: 10.1161/HYPERTENSIONAHA.117.10390

Li, J., Wang, S., Zhang, Y. L., Bai, J., Lin, Q. Y., Liu, R. S., et al. (2019). Immunoproteasome subunit beta5i promotes Ang II (Angiotensin II)-induced atrial fibrillation by targeting ATRAP (Ang II type I receptor-associated protein) degradation in mice. *Hypertension* 73, 92–101. doi: 10.1161/HYPERTENSIONAHA.118.11813

Li, N., Wang, H. X., Han, Q. Y., Li, W. J., Zhang, Y. L., Du, J., et al. (2015). Activation of the cardiac proteasome promotes angiotension II-induced hypertrophy by down-regulation of ATRAP. *J. Mol. Cell. Cardiol.* 79, 303–314. doi: 10.1016/j.yjmcc.2014.12.007

Lyon, R. C., Lange, S., and Sheikh, F. (2013). Breaking down protein degradation mechanisms in cardiac muscle. *Trends Mol. Med.* 19, 239–249. doi: 10.1016/j.molmed.2013.01.005

Manach, C., Williamson, G., Morand, C., Scalbert, A., and Remesy, C. (2005). Bioavailability and bioefficacy of polyphenols in humans. I. Review of 97 bioavailability studies. *Am. J. Clin. Nutr.* 81(Suppl. 1), 230S–242S. doi: 10.1093/ajcn/81.1.230S

Pashevin, D. A., Tumanovska, L. V., Dosenko, V. E., Nagibin, V. S., Gurianova, V. L., and Moibenko, A. A. (2011). Antiatherogenic effect of quercetin is mediated by proteasome inhibition in the aorta and circulating leukocytes. *Pharmacol. Rep.* 63, 1009–1018. doi: 10.1016/s1734-1140(11)70617-x

Purohit, A., Rokita, A. G., Guan, X., Chen, B., Koval, O. M., Voigt, N., et al. (2013). Oxidized Ca(2+)/calmodulin-dependent protein kinase II triggers atrial fibrillation. *Circulation* 128, 1748–1757. doi: 10.1161/CIRCULATIONAHA.113.003313

Roe, N. D., Xu, X., Kandadi, M. R., Hu, N., Pang, J., Weiser-Evans, M. C., et al. (2015). Targeted deletion of PTEN in cardiomyocytes renders cardiac contractile dysfunction through interruption of Pink1-AMPK signaling and autophagy. *Biochim. Biophys. Acta* 1852, 290–298. doi: 10.1016/j.bbadis.2014.09.002

Ryu, Y., Jin, L., Kee, H. J., Piao, Z. H., Cho, J. Y., Kim, G. R., et al. (2016). Gallic acid prevents isoproterenol-induced cardiac hypertrophy and fibrosis through regulation of JNK2 signaling and Smad3 binding activity. *Sci. Rep.* 6:34790. doi: 10.1038/srep34790

Shahrzad, S., Aoyagi, K., Winter, A., Koyama, A., and Bitsch, I. (2001). Pharmacokinetics of gallic acid and its relative bioavailability from tea in healthy humans. *J. Nutr.* 131, 1207–1210. doi: 10.1093/jn/131.4.1207

Song, M. S., Salmena, L., and Pandolfi, P. P. (2012). The functions and regulation of the PTEN tumour suppressor. *Nat. Rev. Mol. Cell Biol.* 13, 283–296. doi: 10.1038/nrm3330

Staerk, L., Sherer, J. A., Ko, D., Benjamin, E. J., and Helm, R. H. (2017). Atrial fibrillation: epidemiology. pathophysiology, and clinical outcomes. *Circ. Res.* 120, 1501–1517. doi: 10.1161/CIRCRESAHA.117.309732

Wang, L., Zhang, Y. L., Lin, Q. Y., Liu, Y., Guan, X. M., Ma, X. L., et al. (2018). CXCL1-CXCR2 axis mediates angiotensin II-induced cardiac hypertrophy and remodelling through regulation of monocyte infiltration. *Eur. Heart J.* 39, 1818–1831. doi: 10.1093/eurheartj/ehy085

Wang, L., Zhao, X. C., Cui, W., Ma, Y. Q., Ren, H. L., Zhou, X., et al. (2016). Genetic and pharmacologic inhibition of the chemokine receptor CXCR2 prevents experimental hypertension and vascular dysfunction. *Circulation* 134, 1353–1368. doi: 10.1161/CIRCULATIONAHA.115.020754

Xu, X., Roe, N. D., Weiser-Evans, M. C., and Ren, J. (2014). Inhibition of mammalian target of rapamycin with rapamycin reverses hypertrophic cardiomyopathy in mice with cardiomyocyte-specific knockout of PTEN. *Hypertension* 63, 729–739. doi: 10.1161/HYPERTENSIONAHA.113.02526

Yan, W., Bi, H. L., Liu, L. X., Li, N. N., Liu, Y., Du, J., et al. (2017). Knockout of immunoproteasome subunit beta2i ameliorates cardiac fibrosis and inflammation in DOCA/Salt hypertensive mice. *Biochem. Biophys. Res. Commun.* 490, 84–90. doi: 10.1016/j.bbrc.2017.05.011

Yan, X., Zhang, Q.-Y., Zhang, Y.-L., Han, X., Guo, S.-B., and Li, H.-H. (2020). Gallic acid attenuates angiotensin II-induced hypertension and vascular dysfunction by inhibiting the degradation of endothelial nitric oxide synthase. *Front. Pharmacol.* 11:1121. doi: 10.3389/fphar.2020.01121

Yan, X., Zhang, Y. L., Zhang, L., Zou, L. X., Chen, C., Liu, Y., et al. (2019). Gallic acid suppresses cardiac hypertrophic remodeling and heart failure. *Mol. Nutr. Food. Res.* 63:e1800807. doi: 10.1002/mnfr.201800807

Zhang, Y. L., Cao, H. J., Han, X., Teng, F., Chen, C., Yang, J., et al. (2020). Chemokine receptor CXCR-2 initiates atrial fibrillation by triggering monocyte mobilization in mice. *Hypertension* 76, 381–392. doi: 10.1161/HYPERTENSIONAHA.120.14698

Zou, L. X., Chen, C., Yan, X., Lin, Q. Y., Fang, J., Li, P. B., et al. (2019). Resveratrol attenuates pressure overload-induced cardiac fibrosis and diastolic dysfunction via PTEN/AKT/Smad2/3 and NF-kappaB signaling pathways. *Mol. Nutr. Food Res.* 63:e1900418. doi: 10.1002/mnfr.201900418

Conflict of Interest: The authors declare that the research was conducted in the absence of any commercial or financial relationships that could be construed as a potential conflict of interest.

frontiers in Cell and Developmental Biology

REVIEW
published: 05 November 2020
doi: 10.3389/fcell.2020.574706

Post-translational Modifications of IκBα: The State of the Art

Xiuli Wang[1†], Hanlin Peng[1†], Yaqian Huang[1], Wei Kong[2,3], Qinghua Cui[4], Junbao Du[1,3] and Hongfang Jin[1]*

[1] Department of Pediatrics, Peking University First Hospital, Beijing, China, [2] Department of Physiology and Pathophysiology, Peking University Health Science Center, Beijing, China, [3] Key Laboratory of Molecular Cardiovascular Sciences, Ministry of Education, Beijing, China, [4] Department of Biomedical Informatics, Centre for Noncoding RNA Medicine, School of Basic Medical Sciences, Peking University, Beijing, China

The nuclear factor-kappa B (NF-κB) signaling pathway regulates a variety of biological functions in the body, and its abnormal activation contributes to the pathogenesis of many diseases, such as cardiovascular and respiratory diseases and cancers. Therefore, to ensure physiological homeostasis of body systems, this pathway is strictly regulated by IκBα transcription, IκBα synthesis, and the IκBα-dependent nuclear transport of NF-κB. Particularly, the post-translational modifications of IκBα including phosphorylation, ubiquitination, SUMOylation, glutathionylation and hydroxylation are crucial in the abovementioned regulatory process. Because of the importance of the NF-κB pathway in maintaining body homeostasis, understanding the post-translational modifications of IκBα can not only provide deeper insights into the regulation of NF-κB pathway but also contribute to the development of new drug targets and biomarkers for the diseases.

Keywords: IκBα, NF-κB, post-translational modifications, phosphorylation, ubiquitination, SUMOylation

OPEN ACCESS

Edited by:
Hui-Hua Li,
Dalian Medical University, China

Reviewed by:
Matthias Stein,
Max Planck Institute for Dynamics of Complex Technical Systems, Max Planck Society (MPG), Germany
Cynthia L. Bristow,
Alpha-1 Biologics, United States
Lluis Espinosa,
Mar Institute of Medical Research (IMIM), Spain

****Correspondence:***
Hongfang Jin
jinhongfang51@126.com;
jinhongfang@bjmu.edu.cn

[†] These authors have contributed equally to this work

Specialty section:
This article was submitted to Signaling, a section of the journal Frontiers in Cell and Developmental Biology

Received: *21 June 2020*
Accepted: *19 October 2020*
Published: *05 November 2020*

Citation:
Wang X, Peng H, Huang Y, Kong W, Cui Q, Du J and Jin H (2020) Post-translational Modifications of IκBα: The State of the Art. Front. Cell Dev. Biol. 8:574706. doi: 10.3389/fcell.2020.574706

INTRODUCTION

The nuclear factor-kappa B (NF-κB) is a critical class of transcriptional regulators belonging to the NF-κB/Rel protein family and is found in almost all cell types. In mammals, the NF-κB family has five members, namely RelA (p65), c-Rel, RelB, NF-κB1 (p50) and NF-κB2 (p52), which form homodimers and heterodimers, and the heterodimer of p50 and p65 is the most common form (Giridharan and Srinivasan, 2018). NF-κB plays a pivotal part in the immune response, inflammatory reaction, cell proliferation and apoptosis (Wu et al., 1996; Elewaut et al., 1999; Ellis et al., 2000; Jo et al., 2000). The overactivation of the NF-κB pathway can result in the inflammatory diseases, cardiovascular diseases, autoimmune diseases and cancers; therefore, the NF-κB pathway

Abbreviations: β-TrCP, β-transducin repeat-containing protein; ABC, activated B-cell type; AR, ankyrin repeat; ARD, ankyrin repeat domain; CK2, casein kinase II; Cox III, cytochrome c oxidase III; CRM1, chromosome region maintenance 1; FBW7, F-box and WD repeat domain-containing protein 7; GSH, glutathione; GSSG, glutathione disulfide; HKII, hexokinase II; IκBα-SR, IκBα-super repressor; IκB, inhibitor of NF-κB; IKK, IκB kinase; LPS, lipopolysaccharide; MM, multiple myeloma; NES, nuclear export sequence; NF-κB, nuclear factor-kappa B; NLS, nuclear localization signal; NPC, nuclear pore complex; NTD, N-terminal domain; PEST, proline–glutamic–serine–threonine; PI3K, phosphoinositide 3-kinase; PKC-ζ, protein kinase C-zeta; PRC2, polycomb repressive complex 2; PS-IκBα, phosphorylation and SUMOylation of IκBα; RHD, Rel-homology domain; SAE, SUMO-1-activating enzyme; SCF, S phase kinase-associated protein 1 (SKP1)–cullin 1 (CUL1)–F-box protein; SENP, sentrin/SUMO-specific protease; SO_2, sulfur dioxide; SRD, signal-receiving domain; SUMO, small ubiquitin-like modifier; Ub, ubiquitin; Ubc9, ubiquitin-conjugating enzyme 9; UPP, ubiquitin-proteasome-pathway; WD, tryptophan-aspartic acid.

is tightly regulated to ensure the physiological homeostasis of body systems (Barnes and Karin, 1997; Wong et al., 1999; Kis et al., 2003; DiDonato et al., 2012). The inhibitors of NF-κB (IκBs), including classical IκB proteins (IκBα, IκBβ and IκBε), non-classical IκB proteins (Bcl-3, IκBζ, IκBNS, IκBη and IκBL) and precursor IκB proteins (p105 and p100), are important molecules that regulate its activation. Among these proteins, IκBα is the first in the IκB family to be cloned (Hinz et al., 2012; Annemann et al., 2016) and is one of the members widely studied (Hinz et al., 2012; Annemann et al., 2016). Following exposure to inflammatory cytokines or microbial products, the IκBα protein is degraded, resulting in a decreased inhibitory effect on NF-κB; NF-κB is then translocates from the cytoplasm to the nucleus, where it regulates the transcription of NF-κB target genes (Hoffmann et al., 2006). The regulation of IκBα mainly occurs at post-translational level, including phosphorylation, ubiquitination and SUMOylation (Perkins, 2006). This review focuses on the advances in the molecular structure, function, post-translational modifications and the regulatory mechanisms of IκBα.

CELLULAR LOCALIZATION AND MOLECULAR STRUCTURE OF THE IκBα PROTEIN

IκB is an important protein regulating the activity of NF-κB. It forms a trimer with a homologous or heterodimer of NF-κB and retains inactive NF-κB in the cytoplasm (Mothes et al., 2015). IκBα is the most common member of the IκB protein family and can shuttle between the cytoplasm and nucleus. Therefore, it is located in both the cytoplasm and nucleus, and its intracellular distribution is dynamic (Huang et al., 2000).

The molecular mechanism by which IκBα inhibits NF-κB activity is closely related to its protein structure. The human IκBα protein has 317 amino acids (aa) with a molecular weight of 36 kDa. It mainly consists of the N-terminal signal-receiving domain (SRD; 1–72 aa), the intermediate ankyrin repeat domain (ARD; 73–280 aa), the C-terminal proline-glutamic-serine-threonine domain (PEST domain; 281–317 aa) and two nuclear export sequences (NESs; 45–54 aa and 265–277 aa) (Lin et al., 1996; Arenzana-Seisdedos et al., 1997; Johnson et al., 1999; Truhlar et al., 2006; Yazdi et al., 2015).

The large amount of amide exchange and 8-anilino-1-napthalenesulphonic acid-binding suggest that free IκBα has molten globule structure (Croy et al., 2004). The details are as follows (**Figure 1**): (1) N-terminal SRD is critical for receiving phosphorylation, ubiquitination and SUMOylation signals as it contains the phosphorylation sites Ser32, Ser36, and Tyr42, ubiquitination sites Lys21 and Lys22, and SUMOylation sites Lys21 and Lys38 (Mabb and Miyamoto, 2007; Hendriks et al., 2017). Additionally, SRD is significant to the activation of NF-κB. Furthermore, it consists of three stable α-helices to lie between residues 8–15 aa, 22–30 aa and 44–50 aa, which complement the six ankyrin repeats (ARs) present in crystallized IκBα. This finding lays a foundation for further studies on the signal transduction of SRD in the IκBα degron (Yazdi et al., 2015). (2) The AR is the characteristic structure of IκB and one of the most common protein sequence motifs that mediates protein–protein interactions (Sedgwick and Smerdon, 1999; Li et al., 2006). Particularly, human IκBα contains six ARs, each consisting of approximately 33 aa. An AR is folded into a β-hairpin, followed by two antiparallel α-helices and a variable loop, which connects it to the next. The α-helical stacks that are thought to form the small hydrophobic cores, whereas the β-hairpin "fingers" form the main protein–protein interaction sites (Sedgwick and Smerdon, 1999; Hendriks et al., 2017). The thermal stability of the ankyrin folding has been suggested to be mainly due to the local interaction between adjacent structural units and needs to be repeated many times to form a stable folding ARD. Amide exchange experiments have revealed that AR3 is the most compact; AR2 and AR4 are less compact; and AR1 and AR6 were solvent-exposed (Croy et al., 2004). ARD contains glutathionylation modification site Cys186 and hydroxylation modification sites Asn210 and Asn244 (Cockman et al., 2006; Kil et al., 2008). (3) The C-terminal PEST domain is highly solvent accessible (Croy et al., 2004); it is not necessary for the binding of IκBα with NF-κB but plays a pivotal role in inhibiting the competitive binding of NF-κB and DNA (Ernst et al., 1995; Sue and Dyson, 2009). The PEST domain contains phosphorylation modification sites Ser283, Ser289, Ser293, Thr291 and Thr299 (McElhinny et al., 1996; Schwarz et al., 1996). (4) Lastly, the two NES suquences are located in the N-terminal SRD domain (45–54 aa) and the C-terminal (265–277 aa). The N-terminal NES is necessary for the shuttling of IκBα between the nucleus and cytoplasm (Huang and Miyamoto, 2001; Lee and Hannink, 2001). Similarly, the C-terminal NES is involved in IκBα-mediated nuclear export of the retroviral oncoprotein v-Rel, which has structural homology with the NF-κB protein family members. However, the substitution of alanine in the C-terminal NES of IκBα did not affect the cytoplasmic relocalization of the mutant IκBα and c-Rel induced by the leptomycin B (Lee and Hannink, 2001). The abovementioned detailed protein structure can be found in references (Croy et al., 2004; Sue and Dyson, 2009; Truhlar et al., 2006; Yazdi et al., 2015).

IκBα and NF-κB form a broad non-continuous binding surface, and all six repeat sequences are involved in the formation of the non-continuous contact surface (Croy et al., 2004). NF-κB family members, such as p65, contain three main domains: the N-terminal domain (NTD), dimerization domain, and transactivation domain (Komives, 2012). AR1–3 contacts the nuclear localization signal (NLS) polypeptide in the N-terminal Rel-homology domain (RHD) of p65, whereas AR4–6 contacts the dimerization domain of p50. Meanwhile, the inner helices of AR5 and AR6 contact the dimerization domain of p65, and the PEST region interacts with the NTD of p65 (Croy et al., 2004). Compared with IκBα in the IκBα–NF-κB complex, free IκBα has higher flexibility (Yazdi et al., 2015). The abovementioned detailed protein structure can be found in references (Croy et al., 2004; Komives, 2012; Yazdi et al., 2015).

A series of conformational changes occur when IκBα binds to NF-κB. First, the ARD of IκBα is slightly twisted, and the distance between residues 166 and 262 increases (Trelle et al., 2016). Thereafter, its AR5 and AR6, whose β-hairpins are highly

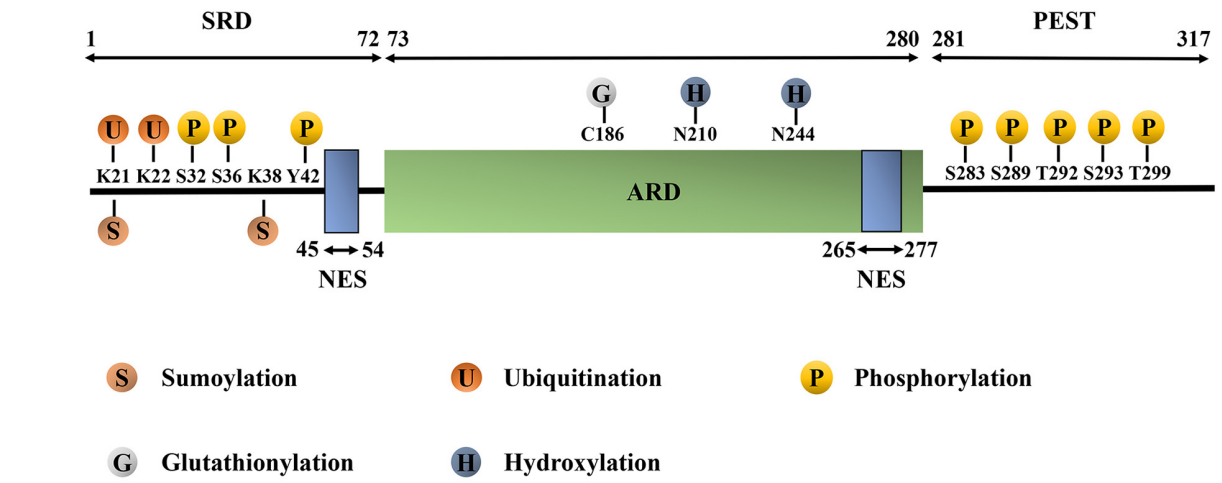

FIGURE 1 | Structure and post-translational modification sites of the human IκBα protein. IκBα, nuclear factor-kappa B inhibitor alpha; SRD, signal-receiving domain; ARD, ankyrin repeat domain; PEST domain, proline–glutamic–serine–threonine domain; NES, nuclear export sequence; K, Lys, lysine; S, Ser, serine; Y, Tyr, tyrosine; C, Cys, cysteine; N, Asn, asparagine; T, Thr, threonine.

dynamic in free IκBα, are folded. Amide hydrogen/deuterium (H/D) exchange is useful to identify protein regions that fold upon binding (Truhlar et al., 2006; Trelle et al., 2016). The amide H/D exchange experiments show that the β-hairpins of AR2 and AR3 are significantly resistant to the exchange, whereas those of AR5 and AR6 are completely exchanged in free IκBα within the first minute. When bound with NF-κB, this exchange is significantly reduced. The difference in amide H/D exchange between free and NF-κB-bound IκBα suggests that the β-hairpins in AR5 and AR6 undergo a folding transition upon binding (Truhlar et al., 2006). This folding involves multiple aspects of NF-κB regulation, such as regulating IκBα degradation, mediating its binding to different NF-κB dimers, and possibly promoting the dissociation of NF-κB from DNA (Truhlar et al., 2006). Notably, the AR5 and AR6 of IκBα in the free state are neither random coils nor completely unfolded. In fact, even if the amides in these two repeats are completely exchanged within one minute, when IκBα binds to NF-κB, no new secondary structure is formed (Ferreiro and Komives, 2010). Therefore, the AR5–6 area must be partially folded and may exhibit the molten globular structure in the free state (Sue and Dyson, 2009). Third, the NLS polypeptide of p65 is folded. NMR data revealed that free-form NSL is in a disordered, highly dynamic configuration. After binding to IκBα, its helices 3 and 4 can be folded, with helix 4 being essential for the interaction, particularly the single residue Phe309 of helix 4. The Phe309 ring acts as a "button" fixing the helix 4 to the "buttonhole" formed by Phe77 and Leu80 on the top surface of the ARD of IκBα. This highly specific interaction effectively covers the ARD, resulting in a significant beneficial binding energy (Cervantes et al., 2011). Lastly, the orientation of the p65 NTD is changed. Based on the structure, IκBα uses the bottom of AR6 and C-terminal PEST regions to interact with the p65 NTD. The main interaction occurs between the highly acidic patch of the PEST sequence (i.e., Glu282, Glu284, Asp285, Glu286 and Glu287) and the basic region of the NTD of p65 (Lys28, Arg30, Lys79, Arg158 and His181). Other residues (Trp258, Gln278, Met279 and Pro281) can also stabilize the interface through polar and van der Waals contact. These interactions are suggested to promote the allosteric regulation of DNA binding by NF-κB, i.e., the binding of IκBα changes the direction of the NTD of p65 and locks the NTD into a closed conformation, thereby interfering with the DNA binding of NF-κB (Sue and Dyson, 2009). The abovementioned detailed structure can be found in references (Truhlar et al., 2006; Sue and Dyson, 2009; Ferreiro and Komives, 2010; Cervantes et al., 2011; Trelle et al., 2016).

MOLECULAR MECHANISM OF IκBα REGULATION OF THE NF-κB PATHWAY ACTIVITY

The ARD of IκBα in unstimulated cells binds to the RHD region of the NF-κB dimer, forming a trimer complex in the cytoplasm. When the cells are stimulated, IκBα undergoes post-translational modifications, such as phosphorylation and ubiquitination, and then is degraded by the proteasomes. The NLS in the RHD region of NF-κB is subsequently exposed and recognized by the nuclear transport receptor importin α/β on the cytoplasm. Their binding forms a nuclear complex that is transferred to the nucleus through the nuclear pore complex (NPC) in an energy-dependent manner, thereby initiating the transcription of the target gene (Turpin et al., 1999; Lee and Hannink, 2002) (**Figure 2**). Because IκBα is also a target gene of NF-κB, IκBα is rapidly replenished when the NF-κB pathway is activated. The newly synthesized IκBα enters the nucleus and translocates

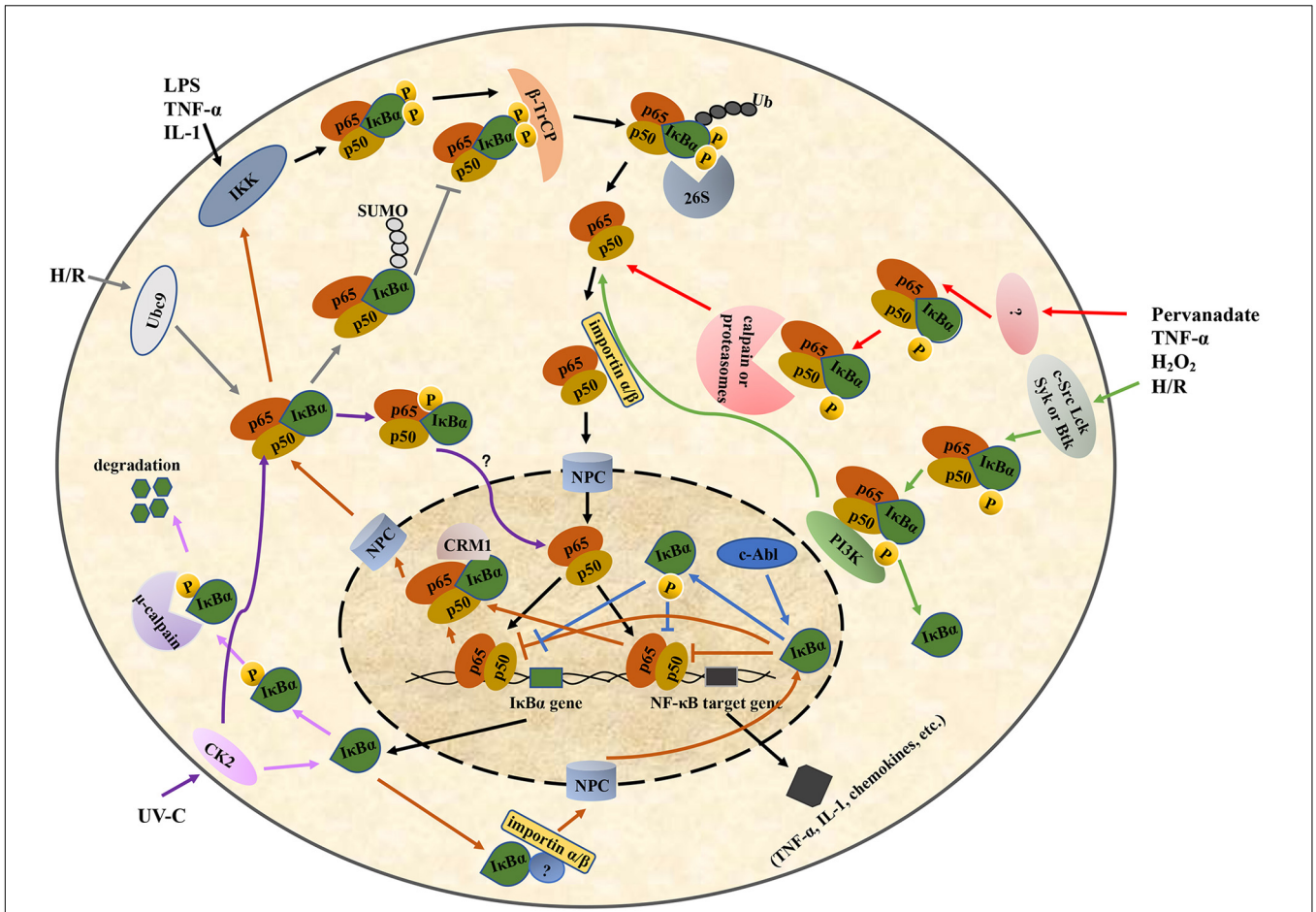

FIGURE 2 | Regulation of the IκBα/NF-κB pathway. IκBα, nuclear factor-kappa B inhibitor alpha; NF-κB, nuclear factor-kappa B. LPS, lipopolysaccharide; TNF-α, tumor necrosis factor-α; IL-1, interleukin-1; H/R, hypoxia/reoxygenation; UV-C, ultraviolet-C; IKK, IκB kinase; CK2, casein kinase II; 26S, 26S proteasome; PI3K, phosphoinositide 3-kinase; Ubc9, ubiquitin-conjugating enzyme 9; β-TrCP, β-transducin repeat-containing protein; NPC, nuclear pore complex; CRM1, chromosome region maintenance 1.

NF-κB dimer to the cytoplasm (Turpin et al., 1999; Chen and Greene, 2004) (**Figure 2**).

IκBα lacks a classical basic NLS, which is a basic amino acid sequence required for nuclear translocation and is originally found in nucleoplasmin and SV40 T antigen. Thus, it cannot enter the nucleus in a classical pathway similar to NF-κB (Turpin et al., 1999). Sachdev et al. found that the AR2 deletion or the mutation in its hydrophobic residues markedly relocalizes IκBα to the cytoplasm (Sachdev et al., 1998). Additional experiments demonstrated that there was a functional discrete NLS in the AR2 region of IκBα, consisting of an N-terminal β-hairpin, an N-terminal α-helix, a C-terminal α-helix, and an adjacent C-terminal β-hairpin (Sachdev et al., 1998). In addition to ARs, some studies have suggested that the nuclear translocation of IκBα requires some unidentified proteins containing a basic NLS and can interact with the ARs of IκBα (Turpin et al., 1999). The nuclear-transport receptor importin α/β heterodimer in the cytoplasm subsequently recognizes the NLS and transports the nascent IκBα into the nucleus (Turpin et al., 1999) (**Figure 2**).

In the export NF-κB dimer to the cytoplasm, the C-terminal PEST domain and NES of IκBα play an important role. Negatively charged residues in the PEST domain of nuclear IκBα can interact with positively charged residues in the NTD of NF-κB p50, resulting in a conformational change in the NF-κB–DNA complex and facilitating the dissociation of DNA from NF-κB. Thereafter, the PEST domain of IκBα occupies the DNA-binding cavity of NF-κB, with the Glu287 residue interacting with a positively charged residue (typically Arg246) in the p65 NTD, thereby further hindering the binding between DNA and NF-κB (Potoyan et al., 2016). The NF-κB–IκBα complex is specifically recognized by the nuclear export receptor chromosome region maintenance (CRM1)/exportin-1 under the mediation of the NES at the N-terminus of IκBα. It is then transferred to the cytoplasm in the inactive NF-κB–IκBα form via the NPC, thus forming a spontaneous negative-feedback inhibition loop (Sachdev et al., 2000; **Figure 2**).

Furthermore, studies investigating the regulation of IκBα in the nucleus–cytoplasm shuttle have shown that the masking of

the p50 NLS by IκBα in the cytoplasm is transient or incomplete. This leads to the partial exposure of the p50 NLS and causes the NF-κB–IκBα complex to enter the nucleus under the mediation of the NLS. An NES is specifically identified by the nuclear export receptor CRM1, thereby transporting the complex out of the nucleus. Therefore, the subcellular localization of the inactive NF-κB–IκBα complex is not static because of its dynamic shuttling between the nucleus and cytoplasm (Huang et al., 2000).

REGULATION OF THE PHOSPHORYLATION/ DEPHOSPHORYLATION OF IκBα

Protein phosphorylation refers to the process of transferring the γ-phosphate group of ATP or GTP to the amino acid residues of serine, threonine or tyrosine of the substrate protein and is catalyzed by protein kinases. "p-" designates that the protein is phosphorylated. A negatively charged phosphate group is added to the amino acid side chain of the protein, resulting in esterification. Esterification changes the protein configuration, activity and its ability to interact with other molecules, thereby greatly affecting cell signal transduction (Hunter, 2000; Kim et al., 2004). Meanwhile, protein dephosphorylation is the reverse process of protein phosphorylation, and is catalyzed by phosphatases (Domingo-Sananes et al., 2011). Therefore, the phosphorylation level of IκBα is regulated by both protein kinase-catalyzed phosphorylation and phosphatase-catalyzed dephosphorylation. Previous studies have shown that three main kinases promote IκBα protein phosphorylation, namely IκB kinase (IKK), casein kinase II (CK2) and tyrosine kinase (Perkins, 2006). The phosphatases that regulate IκBα dephosphorylation include calcineurin and protein tyrosine phosphatase L1 (Pons and Torres-Aleman, 2000; Wang et al., 2018).

IKK-Dependent Phosphorylation

The IKK complex can be activated by lipopolysaccharides (LPSs), viral proteins, oxygen free radicals, cytokines and other stimuli; it then phosphorylates the Ser36 and Ser32 residues in the SRD region of the N-terminus of IκBα (Traenckner et al., 1995; Hayden and Ghosh, 2004; Kato et al., 2012; Ko et al., 2017; Liu et al., 2018; Safi et al., 2018), leading to ubiquitination and the subsequent degradation of the IκBα in proteasome (**Figure 2**). IKK-dependent IκBα phosphorylation at the serine residues occurring in the cytosol is a key step in the release of active NF-κB and its nuclear translocation (Yazdi et al., 2017). A molecular dynamics simulation experiment showed that IKK first phosphorylates IκBα at Ser36, changing the local conformation of the N-terminal region and increasing the relative solvent-accessible surface area of Ser32. This enables Ser32 to interact with IKK via phosphorylation (Yazdi et al., 2017).

The subsequent changes in Ser32/Ser36 double-phosphorylated IκBα are as follows. (1) Conformational changes. First, the curved region between p-Ser32 and p-Ser36 is elongated, and the distance between them is increased. Then, the Met1 and Gln3 residues in the N-terminal move away from p-Ser32 to p-Ser36. Finally, the amides in the main chain of Met1 interact with the phosphate group of p-Ser36, whereas those in the main and side chains of Gln3 combine with the backbone carbonyl group of p-Ser36 to form hydrogen bonds (Yazdi et al., 2017). These changes result in the stabilization of the N-terminal tail. (2) Exposure of binding sites. The conformational change caused by double phosphorylation leads to the exposure of Leu34 and Lys21. Leu34 can interact with the β-transducin repeat-containing protein (β-TrCP), the main component of the IκBα-specific E3 ligase, whereas Lys21 is the ubiquitination site of IκBα. (3) Electrostatic interactions. In the non-phosphorylated state, strongly acidic residues (i.e., Asp27, Asp28, and Asp31 upstream of Ser32; and Asp39, Glu40, Glu41, and Glu43 downstream of Ser36) promote the formation of negatively charged regions on or near the protein surface around Ser32/Ser36. In contrast, the negative charge of the phosphate introduced during the double phosphorylation further changes the distribution of the surface charge and forms a more negatively charged protein surface, which is essential for the recognition of IκBα by the β-TrCP–S phase kinase-associated protein 1 (SKP1)–cullin 1 (CUL1)–F-box protein (SCF) complex and the ubiquitination of IκBα (Yazdi et al., 2017). More details can be found in reference (Yazdi et al., 2017).

Moreover, IKK-dependent IκBα phosphorylation might occur in the nucleus and play a transcriptional suppressive effect, together with transcriptional corepressors (Aguilera et al., 2004; Espinosa et al., 2011). Aguilera et al. have found that the nuclear IκBα bound to the promoter of the Notch target gene *hes1* to facilitate the recruitment of histone acetyltransferases and deacetylases, correlating with transcriptional repression in unstimulated cells. In addition, IKK-α and -β were recruited to the *hes1* promoter following TNF-α treatment, correlating with the IκBα phosphorylation, the release of chromatin-associated IκBα and gene transcriptional activation (Aguilera et al., 2004).

Heterozygous gain-of-function mutations associated with Ser32/Ser36 in IκBα can cause autosomal dominant form of anhidrotic ectodermal dysplasia with immunodeficiency. The mutations reported to date include missense mutations of Ser32, Ser36, or adjacent residues and nonsense mutations of upstream residues from Ser32, related to the reinitiation of truncated IκBα translation (Boisson et al., 2017). These mutations inhibit the phosphorylation of both Ser32 and Ser36, as well as the degradation of IκBα, thus enhancing the inhibitory activity of IκBα (Boisson et al., 2017). Fibroblasts, monocytes, and B and T cells of patients with these heterozygous mutations showed abnormal NF-κB regulatory responses to various surface receptor stimuli (Boisson et al., 2017). In addition, all patients suffered from severe B-cell deficiency, whereas some showed specific immunological characteristics, including increased lymphocytes and lack of peripheral lymph nodes. Often, purulent, mycobacterial, fungal and viral infections were also observed (Boisson et al., 2017). In patients with activated B-cell type (ABC) subgroup of diffuse large B-cell lymphoma, p-IκBα level in tissue microarrays of those with poor five-year survival rate was higher than those with good five-year survival

rate, suggesting that p-IκBα is an independent prognostic marker of poor survival in ABC patients (Hussain et al., 2013).

CK2-Dependent Phosphorylation

CK2 is a ubiquitous serine/threonine kinase, and it can phosphorylate multiple serine and threonine residues in the PEST domain of the IκBα protein, including Ser283, Ser289, Ser293, Thr291 and Thr299, among which Ser293 is the most important (McElhinny et al., 1996; Schwarz et al., 1996). When CK2 binds to atypical protein kinase C-zeta (PKC-ζ), Ser293 will be preferentially phosphorylated (Bren et al., 2000).

When IκBα binds to NF-κB, its PEST domain is masked by NF-κB. Therefore, the CK2-dependent phosphorylation of the PEST domain mainly occurs in free IκBα protein, which are degraded directly by the proteasomes in a non-ubiquitin-dependent manner (Mathes et al., 2008). The PEST domain can bind to the μ-calmodulin-like domain of the large subunit of μ-calpain to trigger the degradation of IκBα associated with μ-calpain. The CK2-dependent phosphorylation of the serine/threonine residues in the PEST domain enhances IκBα degradation by μ-calpain (Shumway et al., 1999; **Figure 2**). CK2 phosphorylation of the free IκBα protein does not depend on stimulation but mainly regulates the basic turnover rate of IκBα in resting cells (Shumway et al., 1999; Mathes et al., 2008). However, some studies have shown that IκBα bound to NF-κB could also undergo CK2-dependent phosphorylation. Particularly, when epithelial HeLa cells are stimulated using short-wavelength ultraviolet radiation, CK2 is phosphorylated and activated by p38 MAP kinase through a phosphorylation-dependent allosteric mechanism, and the activated CK2 then phosphorylates the PEST domain of IκBα, leading to IκBα degradation and NF-κB activation, thus protecting cells from ultraviolet-induced cell death (Sayed et al., 2000; Kato et al., 2003) (**Figure 2**).

Tyrosine Kinase-Dependent Phosphorylation

In addition to IKK and CK2, many types of tyrosine kinases are involved in the regulation of IκBα phosphorylation. Here, the modification sites of IκBα depend on the type of tyrosine kinases, stimulation factors and cell types, resulting in similar or opposite effects. The detailed regulation of tyrosine kinase-dependent phosphorylation is as follows.

In the pervanadate-stimulated human myeloid U937 cell, IκBα phosphorylation is induced at the Tyr42 residue, and IκBα is subsequently polyubiquitinated and degraded by the proteasome (**Figure 2**). This releases the NF-κB and translocates it to the nucleus, activating specific gene expression, including gene expression of IκBα (Mulero et al., 2013a). IκBα degradation and NF-κB activation are observed. However, the detailed regulation of tyrosine kinases in this process is unclear (Mukhopadhyay et al., 2000). U937 is a human leukemic monocyte-lymphoma cell line that is not homogeneous. In HIV-1 permissive clone 10 (plus), NF-κB p65 was constitutively phosphorylated, whereas in non-permissive clone 17 (minus), NF-κB p65 was not constitutively phosphorylated. In addition, both the α1 proteinase inhibitor and LPS induced the phosphorylation of NF-κB p65 Ser536 in the two clones; however, only the dephosphorylation of Ser529 was observed in the plus clone. These results indicated that the phosphorylation/dephosphorylation of NF-κB differs depending on the clone used, suggesting that the IκBα activity is also different (Bristow et al., 2008).

Second, the promotion of IκBα dissociation from the NF-κB complex occurs without its degradation (**Figure 2**). The tyrosine kinases c-Src, Lck, Syk or Btk are activated by many stimuli, such as TNF-α, pervanadate, hypoxia/reoxygenation, and H_2O_2, and phosphorylate IκBα at Tyr42, Tyr289 or Tyr305 residues. For example, when mouse bone marrow macrophages are stimulated by TNF-α, c-Src kinase is activated, and it then phosphorylates IκBα at Tyr42, resulting in the constant c-Src–IκBα association without IκBα degradation. This might be related to the release of the active RelA–p50 from IκBα–RelA–p50 complex and the subsequent of RelA–p50 nuclear translocation because the IκBα/RelA complex remains in the cytosol of c-Src$^{-/-}$ cell treated with TNF-α (Abu-Amer et al., 1998). Meanwhile, when epithelial HeLa cells were stimulated by pervanadate or hypoxia/reoxygenation, c-Src kinase promoted the transcriptional activity of NF-κB by phosphorylating IκBα at Tyr42 (Fan et al., 2003). Pervanadate and hypoxia/reoxygenation can also cause the phosphorylation of IκBα at Tyr42 in Jurkat cells, and this may be mediated by Lck. This activates NF-κB and is associated with the dissociation of IκBα–NF–κB complex (Imbert et al., 1996). Furthermore, H_2O_2 can induce the IκBα phosphorylation at tyrosine residues through Syk in human myeloid KBM-5 cells. This promoted the dissociation of the IκBα–NF–κB complex and the phosphorylation and nuclear translocation of p65 but did not affect IκBα degradation (Takada et al., 2003). Similarly, in anti-IgM-stimulated B cell, Btk is rapidly activated; thereafter, it then phosphorylates IκBα at Tyr305 and Tyr289 residues in the cytosol and associates with phosphorylated IκBα, which correlates with the nuclear translocation of p65 and mediated the early transcriptional activation of NF-κB-responsive genes activated via B cell receptor triggering (Pontoriero et al., 2019). Btk and NF-κB are upregulated in acute and chronic lymphocytic leukemia (Pal Singh et al., 2018). In addition, an inactivated mutation in Btk can lead to B-cell immunodeficiency, such as X-linked agammaglobulinemia, in humans (Pal Singh et al., 2018).

Regarding the mechanism by which IκBα phosphorylation at certain residues, such as Tyr42, activates the NF-κB pathway without accompanying IκBα degradation, the dissociation of IκBα from the NF-κB complex is speculated to be induced by other interacting proteins. Béraud et al. found that phosphoinositide 3-kinase (PI3K) is involved in NF-κB activation induced by IκBα phosphorylation at Tyr42, which is located in a consensus sequence of IκBα that binds to the SH2 domain of the PI3K p85 regulatory subunit. When Jurkat T cells were stimulated by pervanadate, the SH2 domain of PI3K p85 regulatory subunit could specifically bind to the phosphorylated Tyr42 of IκBα,

causing the dissociation of IκBα from NF-κB/IκBα complex (Béraud et al., 1999).

Lastly, in human embryonic kidney 293T cells and human osteosarcoma U2OS cells, the nuclear non-receptor tyrosine kinase c-Abl can enhance the stability of nuclear IκBα through Tyr305 phosphorylation, allowing IκBα to accumulate in the nucleus and thereby inhibiting NF-κB activation caused by TNF-α stimulation (Kawai et al., 2002).

IκBα phosphorylation at serine and tyrosine residues plays distinct roles in different pathophysiological processes. For instance, in cardiomyopathic mice with cardiac-specific expression of TNF-α (TNF-1.6 mice), NF-κB activation was completely blocked after crossing them with IκBα $^{(S32A,S36A,Y42F)}$ transgenic mice; however, it only partially blocked after crossing with IκBα $^{(S32A,S36A)}$ transgenic mice. In addition, NF-κB activation following acute injury, including TNF-α and ischemia/reperfusion was completely blocked in both IκBα $^{(S32A,S36A,Y42F)}$ and IκBα $^{(S32A,S36A)}$ transgenic mice. These findings suggested that IκBα phosphorylation at tyrosine serves as the second signal for NF-κB activation in the pathogenesis of certain disease, although IκBα phosphorylation at Ser32 and Ser36 is dominant in the regulation of NF-κB activation, thus providing guidance for exploring the multiple targets of IκBα phosphorylation inhibitors in drug design and discovery (Brown et al., 2005).

Regulation of Dephosphorylation

As described in the abovementioned studies, almost all of IκBα phosphorylation modifications promote NF-κB activation. Similarly, the dephosphorylation of IκBα is critical for inhibiting the activation of NF-κB. Studies have revealed that calcineurin in astrocytes can be activated by insulin-like growth factor-I, which leads to site-specific dephosphorylation of p-Ser32, inhibition of IκBα degradation, and subsequent nuclear translocation of NF-κB p65 stimulated by TNF-α (Pons and Torres-Aleman, 2000). In addition, the protein tyrosine phosphatase L1 inhibits the development of high-grade serous ovarian cancer through dephosphorylating p-Tyr42 to stabilize IκBα and attenuate the nuclear translocation of NF-κB (Wang et al., 2018). Thyme quinone (a natural compound isolated from *Nigella sativa*) can induce the release of superoxide anion and hydrogen peroxide in ABC cells which promoted IκBα dephosphorylation, arrested NF-κB p65 nuclear translocation, and finally inhibited the NF-κB pathway-mediated ABC cell survival pathway (Hussain et al., 2013).

REGULATION OF THE UBIQUITINATION/DEUBIQUITINATION OF IκBα

Ubiquitination is a cascade reaction involving the ubiquitin-proteasome-pathway (UPP), which is important for protein degradation in eukaryotes and is related to many biological processes including the cell cycle, apoptosis and inflammation. IκBα ubiquitination occurs following IκBα phosphorylation at Ser32/Ser36 and is recognized by the proteasome complex. The ubiquitinated IκBα is degraded in the proteasome, accompanied by the release of active NF-κB and the activation of the NF-κB pathway (Kanarek and Ben-Neriah, 2012).

The ubiquitination of IκBα is regulated by E1 ubiquitin-activating enzyme, E2 ubiquitin-conjugating enzyme, and E3 ubiquitin ligase (Kanarek and Ben-Neriah, 2012; Skaar et al., 2013). First, E1 ubiquitin-activating enzyme catalyzes the formation of a thioester bond between the C-terminal glycine residue of ubiquitin and the cysteine residue of E1. This activates ubiquitin in an ATP dependent manner and initiates ubiquitination modification. Thereafter, E1-ubiquitin intermediates transfer ubiquitin to E2, forming an E2-ubiquitin intermediate (Olsen et al., 2010; Singh et al., 2017). Finally, IκBα ubiquitination requires a specific E3 ubiquitin ligase, $SCF^{\beta\text{-TrCP}}$, comprising four subunits: Skp1, Cullin1, Rbx1 and β-TrCP. The crystal structure of $SCF^{\beta-TrCP}$ shows that Cullin1, as a scaffold protein, can bind to the N-terminus of Skp1 and the C-terminus of cyclin Rbx1. Rbx1 can bind to E2 and promote the switch of ubiquitin from E2 to the substrate (Kanarek et al., 2010) (**Figure 3**). Meanwhile, the β-TrCP protein consists of two characteristic domains, the N-terminal F-box domain (190–228 aa) and the C-terminal tryptophan-aspartic acid (WD) repeat domain (301–590 aa) (Bai et al., 1996; Deshaies, 1999). The F-box domain was defined because it was first found in cyclin F. Particularly, the F-box domain of β-TrCP is mainly responsible for binding to Skp1, in which Ile143 and Leu152 residues play an important role in maintaining the hydrophobic surface of the β-TrCP–Skp1 interaction (Herter and Fuchs, 2002). The WD repeat domain is critical for substrate recognition (Hu et al., 2017) (**Figure 3**) and is a typical seven-blade propeller domain with an overall doughnut shaped. Each blade in WD repeat domain contains a conserved WD motif comprising approximately 40 residues and folded into four anti-parallel β chains. The central hole of the WD repeat domain usually mediates interactions with other proteins (Hu et al., 2017). In human IκBα, a degradation sequence, DSGLDS (31–36 aa), has been identified. Upon treatment with stimulating factors (such as TNFα), its Ser32 and Ser36 residues were phosphorylated to induce a conformational change in IκBα that is recognized by the WD repeat domain of the β-TrCP protein (Yaron et al., 1997).

The following changes occur when IκBα combines with β-TrCP: 1) Conformational changes. The 24-residue phosphorylated peptide (24p-IκBα, 21–44 aa) in the free state exhibits a curvature around the ^{31}DpSGLDpS^{36} residue. Upon binding with β-TrCP, in addition to the curve corresponding to the ^{31}DpSGLDpS^{36} motif, the peptide has two bending regions (Lys22–Asp31 and Met37–Glu43) on both sides (Pons et al., 2007). NMR and crystal structure indicated that the interaction between IκBα and β-TrCP is due to the center curvature. The central bending of the DpSGLDpS motif region is responsible for high-affinity binding, and the N-terminal (^{25}LLDDRH^{30}) and C-terminal (^{35}DpSMKDE^{40}) turning regions can enhance the interaction between IκBα and the β-TrCP protein (Pons et al., 2007). 2) Interaction based on charge. In the DDR^{29}HDpS^{32}GLDpS^{36}MKDE^{40}E fragment, except for Gly33, Leu34 and Met37, all chain residues form a charged surface, which provides a reasonable binding area

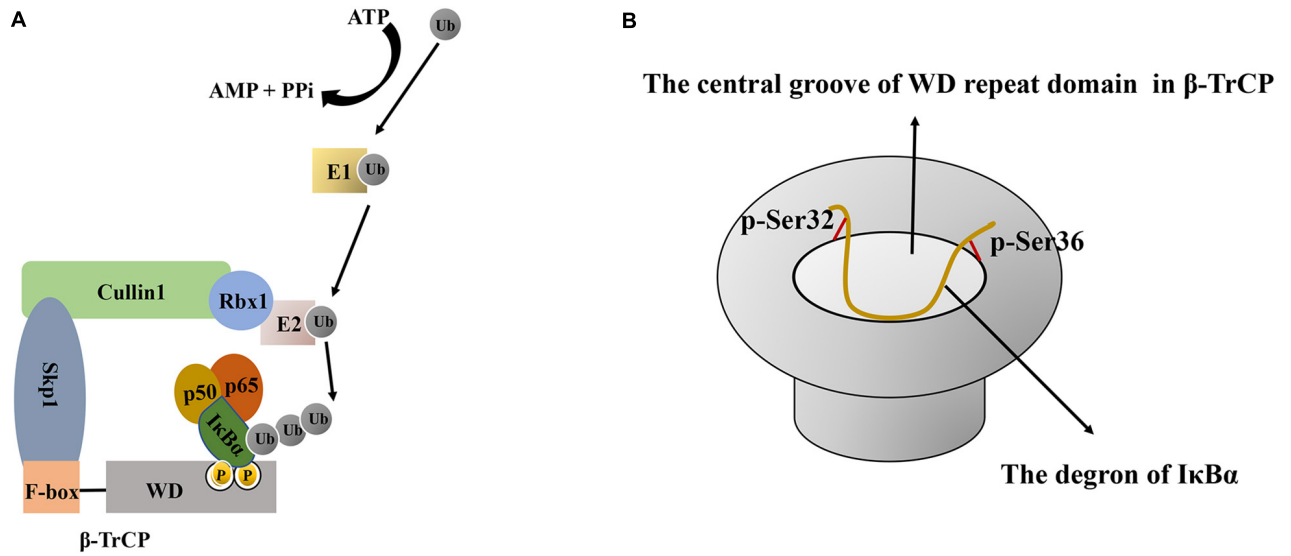

FIGURE 3 | The schematic diagram of IκBα ubiquitination and the interaction between β-TrCP and IκBα. **(A)** Schematic diagram of IκBα ubiquitination. First, E1-activating enzyme activates ubiquitin in an ATP-dependent manner, and then, the E1-ubiquitin intermediate transfers ubiquitin to E2 to form an E2-ubiquitin intermediate. Finally, IκBα ubiquitination requires a specific E3 ubiquitin ligase comprising Skp1, Cullin1, Rbx1, and β-TrCP. As a scaffold protein, Cullin1 can bind to the N-terminus of Skp1 and the C-terminus of Rbx1. Rbx1 binds to E2 and promotes the conversion of ubiquitin from E2 to IκBα, whereas the β-TrCP protein has two characteristic domains, namely the N-terminal F-box domain and the C-terminal WD repeat domain. The F-box domain of β-TrCP is mainly responsible for binding to Skp1, whereas the WD repeat domain is essential for IκBα recognition. **(B)** Schematic diagram of the interaction between the central groove of the WD repeat domain in β-TrCP and the degron of IκBα. All six residues in the IκBα degron are in contact with β-TrCP, and the phosphate groups of p-Ser32 and p-Ser36 bind at the edge of the groove. Ub, Ubiquitin; ATP, adenosine triphosphate; AMP, adenosine monophosphate; PPi, pyrophosphoric acid; IκBα, nuclear factor-kappa B inhibitor alpha; E1, E1 ubiquitin-activating enzyme; E2, E2 ubiquitin-conjugating enzyme; Skp1, S phase kinase-associated protein 1; β-TrCP, β–transducin repeat–containing protein; WD, tryptophan-aspartic acid.

with the surface of the charged protein β-TrCP (Pons et al., 2007). 3) Interaction between WD40 and the degradation sequence of IκBα. The central groove through the middle of the WD propeller structure can accommodate the degradation sequence of IκBα. All six residues in the IκBα degradation sequence are in contact with β-TrCP. Particularly, the aspartic acid side chain, the skeleton of the hydrophobic residue glycine and a spacer residue are inserted into the farthest recess, enabling intermolecular contact in mostly buried environments. Meanwhile, the phosphate groups of p-Ser32 and p-Ser36 bind at the edge of the groove and, along with aspartic acid, form the maximum number of contacts through hydrogen bonding and electrostatic interactions with the β-TrCP residues around the groove (Kanarek et al., 2010) (**Figure 3**). All seven WD repeats of β-TrCP facilitate contact with the substrate, and p-Ser32 may be the major site of interaction with β-TrCP (Yazdi et al., 2017). The abovementioned detailed protein structural information can be found in references (Pons et al., 2007; Kanarek et al., 2010). The recognition of IκBα by β-TrCP prompts the transfer of ubiquitin from the thioester intermediate formed with E2 to Lys21 and Lys22 of IκBα. When the first ubiquitin molecule is attached to the target protein, the other ubiquitin molecules are successively linked to the Lys48 residue of the ubiquitin molecule linked to the substrate in the presence of $SCF^{\beta\text{-}TrCP}$ E3, thereby forming a polyubiquitin chain, which is a target signal for the recognition and degradation of IκBα by the proteasome (**Figure 2**). Ubiquitinated IκBα enters the 26S proteasome and is degraded in the 20S catalytic center. Ubiquitins can be hydrolyzed from IκBα by deubiquitinating enzymes, such as ubiquitin-specific protease for reutilization, which is the deubiquitination of IκBα (Rape et al., 2006). In summary, the affinity of $SCF^{\beta\text{-}TrCP}$ and the activity of deubiquitinating enzymes co-regulate IκBα ubiquitination.

In addition to β-TrCP, the muscular atrophy F-box protein has been shown to ubiquitinate IκBα in cardiomyocytes (Usui et al., 2011). Additionally, a novel E3 ligase, F-box and WD repeat domain-containing protein 7 (FBW7), targeting IκBα has been identified; its upregulation promotes the ubiquitin-dependent IκBα degradation, NF-κB activation, and the subsequent intestinal inflammation caused by intestinal epithelial cells, whereas its inhibition has the opposite effects (Meng et al., 2020).

SUMOYLATION OF IκBα

Small ubiquitin-related modifier (SUMO) is a class of peptides comprising 98 aa and has low sequence identity with ubiquitin but forms a 3D structure similar to that of ubiquitin. To date, four members of the SUMO family (SUMO1–4) have been identified in mammalian cells (Carbia-Nagashima et al., 2007). SUMO proteins are expressed in a precursor or inactive form with a short C-terminus. Sentrin/SUMO-specific proteases (SENPs) possess hydrolase activity and cleave the inactive precursor of SUMO at the C-terminus to generate the active or mature SUMO. The

human SENP family is composed of SENP1, SENP2, SENP3, SENP5, SENP6, SENP7, and SENP8. However, SENP8 had no effect on SUMO, and only SENP1, SENP2 and SENP5 can proteolyze the precursor SUMO proteins (Yeh, 2009; Kumar and Zhang, 2015; Kunz et al., 2018). SUMOylation is the process of protein coupling with SUMO through three enzymatic steps similar to the ubiquitin-binding cascade reaction.

The SUMOylation of IκBα can be activated by hypoxia/reoxygenation, adenosine receptor agonists (Liu et al., 2009). Particularly, in mammalian cells, the SUMO-specific E1-activating enzyme is the heterodimer SAE1/SAE2, and the E2-binding enzyme is the ubiquitin-conjugating enzyme 9 (Ubc9). In the presence of ATP, the IκBα SUMOylation *in vitro* only requires SAE1/SAE2 and Ubc9 and not E3 protein ligase. However, whether the E3 protein ligase is necessary for the SUMOylation of IκBα *in vivo* remains unclear (Desterro et al., 1999).

IκBα SUMOylation based on *in vitro* experiments is described as follows (**Figure 4**). First, the active site Cys173 in SAE2 forms a thioester bond with the glycine residue at the C-terminus of SUMO in an ATP-dependent mannerr. This transfers SUMO to the catalytic cysteine residue Cys93 of Ubc9 (Olsen et al., 2010). Thereafter, Ubc9 directly interacts with IκBα by recognizing the consensus sequence ψKxE (ψ represents a hydrophobic amino acid residue, whereas x represents any amino acid residue) and transfers SUMO to IκBα. The glycine residue in the C-terminus of SUMO forms a covalent isopeptide bond with the side chain of Lys21 in IκBα (Rodriguez et al., 2001). In addition, the results of high-throughput screening for SUMOylated proteins recently identified Lys38 as another SUMOylation site of IκBα (Hendriks et al., 2017).

Complex interactions between the SUMOylated IκBα and other IκBα modifications, such as ubiquitination and phosphorylation, affect the functional effect of IκBα SUMOylation (Scherer et al., 1995; Desterro et al., 1998; Hay et al., 1999; Liu et al., 2009; Aillet et al., 2012; Mulero et al., 2013b; Marruecos et al., 2020). The effects of the complex interactions is described as follows. (1) The SUMO1 modification of IκBα inhibits the ubiquitination of Lys21 and Lys22 in IκBα and blocks IκBα degradation (**Figure 2**). Studies have shown that the SUMO1 overexpression blocks the ubiquitination and degradation of IκBα caused by TNF-α and IL-1 in African green monkey kidney fibroblast cell line COS7 (Desterro et al., 1998). The following mechanisms may be involved in the inhibition of IκBα ubiquitination by SUMO1 modification. First, because Lys21 is the site of both SUMO and ubiquitin modifications, SUMO1 can competitively bind to it. Many SUMO1 modifications can stabilize IκBα and protect it from degradation by the proteasome system, thus inhibiting NF-κB activation (Desterro et al., 1998). Moreover, the NTD of IκBα is flexible, and the SUMOylation of Lys21 may cause the conformational change of IκBα to prevent it from being recognized by the SCF complex. Second, ubiquitination can occur solely at Lys22 to promote the proteasome-mediated degradation of IκBα without modification at Lys21. However, the SUMOylation of Lys21 having a spherical structure may prevent Lys22 ubiquitination by the β-TrCP SCF complex (Scherer et al., 1995; Mabb and Miyamoto, 2007). (2) The SUMO2/3 modification of IκBα can promote the ubiquitin-dependent degradation of IκBα (Aillet et al., 2012). Studies have shown that the SUMO2/3 modification of IκBα can be detected under physiological conditions. Upon TNF-α stimulation, the heterologous chains of SUMO2/3 and ubiquitin can promote IκBα degradation by 26S proteasome more effectively than SUMO2/3 or ubiquitin alone (Aillet et al., 2012). (3) The SUMOylation of IκBα is blocked by its phosphorylation. Phosphorylated IκBα at Ser32/Ser36 cannot undergo SUMOylation, suggesting that the SUMO modification is only effective before IKK phosphorylates IκBα (Hay et al., 1999). (4) The phosphorylation and SUMOylation of IκBα (PS-IκBα) coexist and exert a NF-κB independent transcription repressive effect (Mulero et al., 2013b; Marruecos et al.,

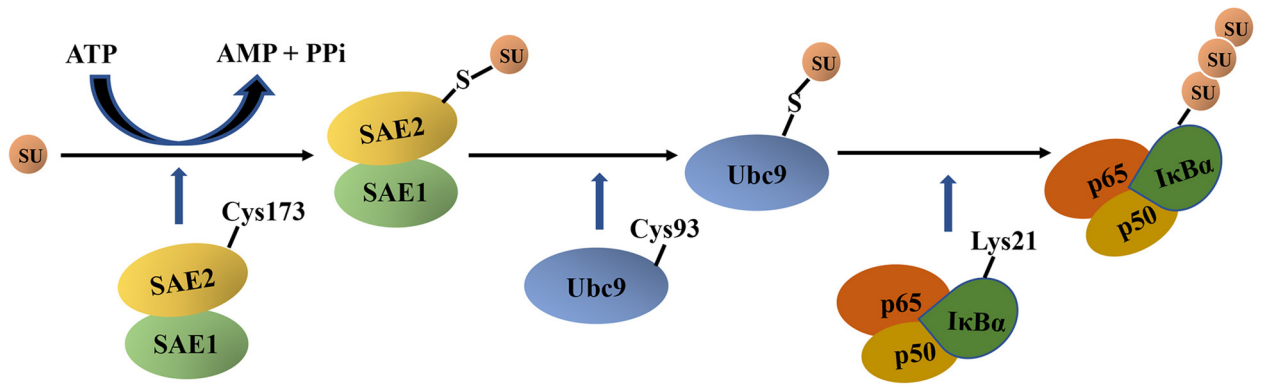

FIGURE 4 | The schematic diagram of IκBα SUMOylation. First, a C-terminal glycine residue of mature SUMO forms a thioester bond with the active site Cys173 in SAE2 in an ATP-dependent manner. Thereafter, SUMO is transferred to the catalytic cysteine residue Cys93 of Ubc9, and Ubc9 directly interacts with IκBα and transfers SUMO to IκBα. Next, the glycine residue at the C terminal of mature SUMO forms a covalent isopeptide bond with the Lys21 side chain in IκBα. IκBα, nuclear factor-kappa B inhibitor alpha; SU, SUMO, small ubiquitin-like modifier; SAE, SUMO-1–activating enzyme; Ubc9, ubiquitin-conjugating enzyme 9; ATP, adenosine triphosphate; AMP, adenosine monophosphate; PPi, pyrophosphoric acid.

2020). In unstimulated basal keratinocytes, IκBα undergoes IKK-independent phosphorylation modification and is then modified by SUMO2/3 to form PS-IκBα, which is retained in the nucleus. Nuclear PS-IκBα binds to the chromatin of the regulatory regions of target genes, such as *HOX* and *IRX*, and inhibits their transcription by recruiting the polycomb repressive complex 2 (PRC2), which is involved in the regulation of skin homeostasis and development. When keratinocytes are exposed to inflammatory stimuli or differentiation inducer, PS-IκBα dissociates from the chromatin, resulting in the inability to recruit PRC2 to the promoters of the target genes and subsequently upregulating gene expression. This ultimately establishes a link between inflammatory signals and skin homeostasis (Mulero et al., 2013b). Similarly, in intestinal crypt cells, phosphorylated and SUMOylated nuclear IκBα bind the PRC2 subunit SUZ12 and suppress the expression of fetal intestinal stem cell genes, which participated in the regulation of intestinal stem cell homeostasis and the intestinal response to inflammation, damage and repair (Marruecos et al., 2020). The abovementioned mechanism underlying nuclear PS-IκBα deepens the understanding of the IκBα function (Mulero et al., 2013b; Marruecos et al., 2020).

In addition to acting as a hydrolase to promote SUMO maturation, SENP possesses isopeptidase activity and cleaves the isopeptide bond between the glycine at the C-terminal of SUMO and lysine of the substrate protein. This leads to the release of the SUMO protein from its substrate, thereby arresting SUMOylation (Kumar and Zhang, 2015). SENP1, SENP2, SENP3, SENP5, SENP6, and SENP7 have been revealed to possess isopeptidase activities. SENP1 and SENP2 have broad specificity for SUMO-1/2/3, whereas the other SENPs preferentially dissociate SUMO-2/3 from its substrate (Kumar and Zhang, 2015).

GLUTATHIONYLATION OF IκBα

Glutathione is a tripeptide composed of glutamic acid, cysteine and glycine. It exists in an oxidized (GSSG) form and a reduced (GSH) form, which can protect cells from damage by reactive oxygen species and heavy metals (Lv et al., 2019). Glutathionylation is a reversible post-translational modification involving formation of a disulfide bond between glutathione and protein cysteine thiol and can be reversed by glutathionase (thiol transferase) in a process called for de-glutathionylation.

In IκBα, Cys186 is the target of glutathionylation (Kil et al., 2008). The stimulation of HeLα cells with an oxidant (such as diamide) that induces GSH oxidation can activate IκBα glutathionylation (Kil et al., 2008). Compared with the native protein, glutathionylated IκBα displayed increased quantum yield of the emission spectra and a red shift of the maximum emission wavelength at 337 nm. Moreover, the accessibility of the hydrophobic regions in glutathionylated IκBα is higher than that in the native protein (Kil et al., 2008). Regarding the functional effect of glutathionylated IκBα, Kil et al. found that the glutathionylation of IκBα suppressed IKK- and CK2-dependment IκBα phosphorylation and IκBα ubiquitination *in vitro*. The mechanism may be related to the conformational change of IκBα induced by glutathionylation (Kil et al., 2008). In addition, Seidel et al. found that IκBα glutathionylation inhibited IκBα degradation, NF-κB p65 nuclear entry, and NF-κB/DNA binding, therefore downregulating the expression of NF-κB target genes in airway smooth muscle cells (Seidel et al., 2011).

HYDROXYLATION OF IκBα

Both *in vitro* and *in vivo* experiments have demonstrated that human hypoxia-inducible factor hydroxylase can effectively hydroxylate Asn244 and Asn210 in IκBα, with Asn244 being more effectively hydroxylated than Asn210. Both these residues are located in the hairpin loops that connect the ARs (Cockman et al., 2006). However, the regulatory effect of IκBα hydroxylation modification on the NF-κB signaling pathway remains unclear. Considering that the hydroxylation of collagen prolyl and lysyl residues can promote the stability of the extracellular matrix structure, asparagine hydroxylation in IκBα is speculated to play a similar role in stabilizing the protein structure (Myllyharju and Kivirikko, 2004).

THERAPEUTIC OPPORTUNITIES BASED ON IκBα MODULATION

Abnormal NF-κB activation is related to various diseases, such as cardiovascular, neurodegenerative and autoimmune diseases and cancer. For example, the increase in p-IκBα and the activation of NF-κB p65 were detected in monocrotaline-induced pulmonary hypertensive rats, mice with Alzheimer's disease, rats with autoimmune myocarditis, and gastric cancer caused by *Helicobacter pylori* (Nozaki et al., 2005; Feng et al., 2017; Zhang et al., 2017; Fang et al., 2019). As a key regulator of the NF-κB signaling pathway, IκBα has attracted increasing research attention and its post-translational modification provides new therapeutic opportunities for diseases related to abnormal NF-κB activation (Vrábel et al., 2019).

For instance, proteasome inhibitors have been clinically used in the treatment of multiple myeloma (MM) (Tundo et al., 2020). Previous studies have demonstrated that the dysregulation of NF-κB pathway contribute to the development and clinical manifestations of MM via NF-κB target genes, including the growth factor interleukin-6 and insulin-like growth factor-1, cell cycle regulators cyclin D and c-Myc, and pro-angiogensis factors vascular endothelial growth factor-C and placental growth factor (Vrábel et al., 2019). Because the ubiquitination and subsequent degradation of IκBα in the proteasome are predominant mechanisms of the NF-κB pathway activation (Feng et al., 2017; Tundo et al., 2020), bortezomib, a reversible proteasome inhibitor, was used in the treatment of MM. Bortezomib binds directly to the β5-subunit of the proteasome and inhibits the enzymatic activity of the proteasome complex. As reported by many clinical trials, bortezomib alone or in combination with other drugs has dramatically improved the outcomes for patients with relapsed MM (Richardson et al., 2003; Lonial et al., 2011), which was in accordance with experimental results showing that

bortezomib inhibited NF-κB activation in MM cells by blocking IκBα degradation in the proteasome (Hideshima et al., 2002). In addition, carfilzomib, a second-generation proteasome inhibitor, has been shown to significantly reduce mortality compared with bortezomib. Carfilzomib is the first drug to increase the overall survival rate of MM patients (Dimopoulos et al., 2017). Thereafter, the first oral proteasome inhibitor, ixazomib, was developed for the treatment of relapsed or refractory MM (Narayanan et al., 2020). Compared with bortezomib, ixazomib inhibited tumor proteasome activity for a longer duration and exhibited greater antitumor effect in OCI-Ly10 and PHTX22L lymphoma mouse models (Narayanan et al., 2020). In addition to carfilzomib and ixazomib, second-generation proteasome inhibitors include oprzomib, dilanzomib and malizomib, and their clinical trials are underway (Tundo et al., 2020).

It should be emphasized that in addition to the NF-κB pathway, proteasome inhibitors regulate many other important cellular pathways that depend on proteasome function and affect these signal transduction pathways in both normal and cancer cells, resulting in some limitations to their clinical use, including dose-limiting side effects and the rapid onset of secondary drug resistance (Begalli et al., 2017). For example, bortezomib usually causes peripheral neuropathy, whereas carfilzomib can cause cardiotoxicity, acute renal failure, pulmonary toxicity and other adverse reactions (Narayanan et al., 2020). Therefore, it seems reasonable that the inhibition of IκBα ubiquitination may represent a safer alternative to proteasomal inhibition for blocking NF-κB activation.

Furthermore, because of their central role in regulating IκBα ubiquitination, β-TrCP and its interaction with IκBα are attractive targets (Kanarek and Ben-Neriah, 2012). Studies have found that brain-specific TRIpartite motif protein 9, A49, and GS143 can inhibit IκBα ubiquitination and NF-κB activation by binding to β-TrCP (Nakajima et al., 2008; Mansur et al., 2013; Shi et al., 2014). The IκBα-super repressor (IκBα-SR), a mutant form of IκBα, which can neither be phosphorylated nor ubiquitinated, is found to inhibit NF-κB activation. Furthermore, the intraperitoneal injection of purified IκBα-SR-loaded exosomes attenuates mortality and systemic inflammation in septic mouse models (Choi et al., 2020). IκBα-SR can also increase the sensitivity of pancreatic cancer and pancreatic ductal adenocarcinoma to chemotherapeutics and inhibit tumor development in hepatitis-related cancer murine models (Sato et al., 2003; Pikarsky et al., 2004; Waters et al., 2015). Moreover, the microinjection of IκBα phosphopeptides into TNF-α-stimulated cells blocked NF-κB activation by competing with endogenous IκBα for binding to β-TrCP (Yaron et al., 1997). Cyclic IκBα phosphopeptides, the backbone of which was cyclized to improve stability and selectivity, were designed to effectively block IκBα ubiquitination (Qvit et al., 2009). However, because the E3 ubiquitin ligase $SCF^{\beta\text{-}TrCP}$ has many substrates other than IκBα, potential adverse effects of β-TrCP inhibitors due to the accumulation of $SCF^{\beta\text{-}TrCP}$ may occur, thus partly limiting their clinical usage. Therefore, further in-depth studies are required to develop clinical drugs targeting IκBα post-translational modification.

Moreover, a new method, fragment-based virtual E-pharmacophore screening, has been developed to promote the development of drug design targeting on the NF-κB/IκBα complex (Kanan et al., 2019). An excellent study conducted by Kanan et al. investigated the structure of the binding pocket of NF-κB p65/p50 heterodimer complex with IκBα in detail, and therefore constructed the e-pharmacophore models to discover potential ligands with strong binding affinity as candidate NF-κB/IκBα inhibitors. Furthermore, the screening small molecules and known inhibitors were deeply analyzed on the MetaCore/MetaDrug platform and their therapeutic activity, pharmacokinetic and toxicity profile were predicted. The abovementioned computational biological study might provide a novel approach for exploring the potent and low toxicity NF-κB/IκBα inhibitors and give a new perspective of clinical treatment of diseases with abnormal NF-κB activation.

CONCLUSION AND PERSPECTIVES

In this review, we summarized the recent literature on post-translational modification of IκBα, including the associated structural changes and regulatory processes and their functional effect on NF-κB activation. These studies provide a theoretical basis for therapeutic interventions targeting IκBα post-translational modification for NF-κB-related disease. Many clinical trials on drugs targeting the IκBα post-translational modification achieved significant clinical benefit, thus confirming the therapeutic significance of these post-translational modifications.

However, there are many notable issues in the drug development based on the post-translational modification of IκBα to be addressed for their future clinical usage. First, considering the unavoidable adverse effects of the IκBα-related NF-κB inhibitors (Pancheri et al., 2020), the pathophysiological mechanisms and the significance of the IκBα–NF-κB pathway in the development of diseases should be further clarified to provide the best ratio of benefit to risk. Second, the drug release controllability to ensure the controllable release rate under certain specific pathophysiological conditions should be taken into account because of the vast regulatory role of NF-κB pathway (Chen and Stark, 2019). For example, endogenous sulfur dioxide (SO_2) is found to play extensive regulatory roles in the cardiovascular system as a novel gasotransmitter (Huang et al., 2016). Along with the increasing studies on the pathophysiological significance of endogenous SO_2 in the cardiovascular diseases, SO_2 donors and prodrugs with different triggering mechanisms, such as thiol-activated SO_2 prodrugs, thermally activated SO_2 prodrugs and hydrolysis-based SO_2 prodrugs, were designed in recent years (Day et al., 2016; Wang and Wang, 2018). The abovementioned studies might provide useful evidence for the drug design targeting the inhibition of NF-κB pathway. Third, novel post-translational modifications, such as persulfidation/sulfhydration (Mustafa et al., 2009; Fu et al., 2019), are being discovered. As reported in the previous studies, persulfidation of target protein characterized by a chemical modification of protein cysteinyl thiols to persulfides could

change the protein function (Du et al., 2014). Therefore, whether this new kind of post-translational modification occurs in the IκBα protein should be investigated. Fourth, the interaction among different post-translational modifications of IκBα is important and should be stressed. For example, the discovery of PS-IκBα in the nucleus provides a new target for the treatment of intestinal inflammatory diseases and skin cancers such as squamous cell carcinoma (Mulero et al., 2013b; Colomer et al., 2017; Marruecos et al., 2020).

Finally, the localization of NF-κB and IκBα in the mitochondrion and their regulation of mitochondrial DNA activities should be investigated. NF-κB p65 and IκBα have been detected in the mitochondrial (Bottero et al., 2001; Zamora et al., 2004; Pazarentzos et al., 2014). In addition, TNF-α stimulation induces mitochondrial IκBα phosphorylation and proteasome-independent IκBα degradation and promotes the accumulation of mitochondrial NF-κB p65, thus leading to decreased expression of mitochondrial DNA cytochrome c oxidase III and cytochrome b in U937 cells (Cogswell et al., 2003). Further, in the retina of dark-adapted rats exposed to bright light, the mitochondrial translocation of NF-κB p65 was associated with decreased cytochrome c oxidase III expression (Tomita et al., 2016). Studies on the mitochondrial IκBα–NF-κB may provide an alternative mechanism by which IκBα–NF-κB pathway regulates mitochondrial homeostasis, thus serving as a novel target for the treatment of mitochondria-related diseases.

AUTHOR CONTRIBUTIONS

XW sorted out, reviewed, and analyzed the literatures, drew the diagrams, and wrote the manuscript. HJ devised the concept. HP sorted out, reviewed, and analyzed the literatures and revised the manuscript. HJ, WK, QC, JD, and YH supervised the writing. All the authors revised and approved the final version of the manuscript.

FUNDING

This research was funded by the National Natural Science Foundation of China (81970424 and 81921001), Beijing Natural Science Foundation (7171010, 7191012, and 7182168), Peking University Clinical Medicine Plus X – Young Scholars Project (PKU2019LCXQ011) and the Fundamental Research Funds for the Central Universities.

REFERENCES

Abu-Amer, Y., Ross, F. P., McHugh, K. P., Livolsi, A., Peyron, J. F., and Teitelbaum, S. L. (1998). Tumor necrosis factor-alpha activation of nuclear transcription factor-kappaB in marrow macrophages is mediated by c-Src tyrosine phosphorylation of Ikappa Balpha. *J. Biol. Chem.* 273, 29417–29423. doi: 10.1074/jbc.273.45.29417

Aguilera, C., Hoya-Arias, R., Haegeman, G., Espinosa, L., and Bigas, A. (2004). Recruitment of IkappaBalpha to the hes1 promoter is associated with transcriptional repression. *Proc. Natl. Acad. Sci. U.S.A.* 101, 16537–16542. doi: 10.1073/pnas.0404429101

Aillet, F., Lopitz-Otsoa, F., Egaña, I., Hjerpe, R., Fraser, P., Hay, R. T., et al. (2012). Heterologous SUMO-2/3-ubiquitin chains optimize IκBα degradation and NF-κB activity. *PLoS One* 7:e51672. doi: 10.1371/journal.pone.0051672

Annemann, M., Plaza-Sirvent, C., Schuster, M., Katsoulis-Dimitriou, K., Kliche, S., Schraven, B., et al. (2016). Atypical IκB proteins in immune cell differentiation and function. *Immunol. Lett.* 171, 26–35. doi: 10.1016/j.imlet.2016.01.006

Arenzana-Seisdedos, F., Turpin, P., Rodriguez, M., Thomas, D., Hay, R. T., Virelizier, J. L., et al. (1997). Nuclear localization of I kappa B alpha promotes active transport of NF-kappa B from the nucleus to the cytoplasm. *J. Cell Sci.* 110(Pt 3), 369–378.

Bai, C., Sen, P., Hofmann, K., Ma, L., Goebl, M., Harper, J. W., et al. (1996). SKP1 connects cell cycle regulators to the ubiquitin proteolysis machinery through a novel motif, the F-box. *Cell* 86, 263–274. doi: 10.1016/s0092-8674(00)80098-7

Barnes, P. J., and Karin, M. (1997). Nuclear factor-kappaB: a pivotal transcription factor in chronic inflammatory diseases. *N. Engl. J. Med.* 336, 1066–1071. doi: 10.1056/NEJM199704103361506

Begalli, F., Bennett, J., Capece, D., Verzella, D., D'Andrea, D., Tornatore, L., et al. (2017). Unlocking the NF-κB conundrum: embracing complexity to achieve specificity. *Biomedicines* 5:50. doi: 10.3390/biomedicines5030050

Béraud, C., Henzel, W. J., and Baeuerle, P. A. (1999). Involvement of regulatory and catalytic subunits of phosphoinositide 3-kinase in NF-kappaB activation. *Proc. Natl. Acad. Sci. U.S.A.* 96, 429–434. doi: 10.1073/pnas.96.2.429

Boisson, B., Puel, A., Picard, C., and Casanova, J. (2017). Human IκBα gain of function: a severe and syndromic immunodeficiency. *J. Clin. Immunol.* 37, 397–412. doi: 10.1007/s10875-017-0400-z

Bottero, V., Rossi, F., Samson, M., Mari, M., Hofman, P., and Peyron, J. F. (2001). Ikappa b-alpha, the NF-kappa B inhibitory subunit, interacts with ANT, the mitochondrial ATP/ADP translocator. *J. Biol. Chem.* 276, 21317–21324. doi: 10.1074/jbc.M005850200

Bren, G. D., Pennington, K. N., and Paya, C. V. (2000). PKC-zeta-associated CK2 participates in the turnover of free IkappaBalpha. *J. Mol. Biol.* 297, 1245–1258. doi: 10.1006/jmbi.2000.3630

Bristow, C. L., Wolkowicz, R., Trucy, M., Franklin, A., Di, M. F., Kozlowski, M. T., et al. (2008). NF-kappaB signaling, elastase localization, and phagocytosis differ in HIV-1 permissive and nonpermissive U937 clones. *J. Immunol.* 180, 492–499. doi: 10.4049/jimmunol.180.1.492

Brown, M., McGuinness, M., Wright, T., Ren, X., Wang, Y., Boivin, G. P., et al. (2005). Cardiac-specific blockade of NF-kappaB in cardiac pathophysiology: differences between acute and chronic stimuli in vivo. *Am. J. Physiol. Heart Circ. Physiol.* 289, H466–H476. doi: 10.1152/ajpheart.00170.2004

Carbia-Nagashima, A., Gerez, J., Perez-Castro, C., Paez-Pereda, M., Silberstein, S., Stalla, G. K., et al. (2007). RSUME, a small RWD-containing protein, enhances SUMO conjugation and stabilizes HIF-1alpha during hypoxia. *Cell* 131, 309–323. doi: 10.1016/j.cell.2007.07.044

Cervantes, C. F., Bergqvist, S., Kjaergaard, M., Kroon, G., Sue, S.-C., Dyson, H. J., et al. (2011). The RelA nuclear localization signal folds upon binding to IκBα. *J. Mol. Biol.* 405, 754–764. doi: 10.1016/j.jmb.2010.10.055

Chen, J., and Stark, L. A. (2019). Insights into the relationship between nucleolar stress and the NF-κB pathway. *Trends Genet.* 35, 768–780. doi: 10.1016/j.tig.2019.07.009

Chen, L. F., and Greene, W. C. (2004). Shaping the nuclear action of NF-kappaB. *Nat. Rev. Mol. Cell Biol.* 5, 392–401. doi: 10.1038/nrm1368

Choi, H., Kim, Y., Mirzaaghasi, A., Heo, J., Kim, Y. N., Shin, J. H., et al. (2020). Exosome-based delivery of super-repressor IκBα relieves sepsis-associated organ damage and mortality. *Sci. Adv.* 6:eaaz6980. doi: 10.1126/sciadv.aaz6980

Cockman, M. E., Lancaster, D. E., Stolze, I. P., Hewitson, K. S., McDonough, M. A., Coleman, M. L., et al. (2006). Posttranslational hydroxylation of ankyrin repeats in IkappaB proteins by the hypoxia-inducible factor (HIF) asparaginyl hydroxylase, factor inhibiting HIF (FIH). *Proc. Natl. Acad. Sci. U.S.A.* 103, 14767–14772. doi: 10.1073/pnas.0606877103

Cogswell, P. C., Kashatus, D. F., Keifer, J. A., Guttridge, D. C., Reuther, J. Y., Bristow, C., et al. (2003). NF-kappa B and I kappa B alpha are found in the mitochondria. Evidence for regulation of mitochondrial gene expression by NF-kappa B. *J. Biol. Chem.* 278, 2963–2968. doi: 10.1074/jbc.M209995200

Colomer, C., Marruecos, L., Vert, A., Bigas, A., and Espinosa, L. (2017). NF-κB members left home: NF-κB-independent roles in cancer. *Biomedicines* 5:26. doi: 10.3390/biomedicines5020026

Croy, C. H., Bergqvist, S., Huxford, T., Ghosh, G., and Komives, E. A. (2004). Biophysical characterization of the free IkappaBalpha ankyrin repeat domain in solution. *Protein Sci.* 13, 1767–1777. doi: 10.1110/ps.04731004

Day, J. J., Yang, Z., Chen, W., Pacheco, A., and Xian, M. (2016). Benzothiazole sulfinate: a water-soluble and slow-releasing sulfur dioxide donor. *ACS Chem. Biol.* 11, 1647–1651. doi: 10.1021/acschembio.6b00106

Deshaies, R. J. (1999). SCF and cullin/ring H2-based ubiquitin ligases. *Annu. Rev. Cell Dev. Biol.* 15, 435–467. doi: 10.1146/annurev.cellbio.15.1.435

Desterro, J. M., Rodriguez, M. S., and Hay, R. T. (1998). SUMO-1 modification of IkappaBalpha inhibits NF-kappaB activation. *Mol. Cell* 2, 233–239. doi: 10.1016/s1097-2765(00)80133-1

Desterro, J. M., Rodriguez, M. S., Kemp, G. D., and Hay, R. T. (1999). Identification of the enzyme required for activation of the small ubiquitin-like protein SUMO-1. *J. Biol. Chem.* 274, 10618–10624. doi: 10.1074/jbc.274.15.10618

DiDonato, J. A., Mercurio, F., and Karin, M. (2012). NF-κB and the link between inflammation and cancer. *Immunol. Rev.* 246, 379–400. doi: 10.1111/j.1600-065X.2012.01099.x

Dimopoulos, M. A., Goldschmidt, H., Niesvizky, R., Joshua, D., Chng, W., Oriol, A., et al. (2017). Carfilzomib or bortezomib in relapsed or refractory multiple myeloma (ENDEAVOR): an interim overall survival analysis of an open-label, randomised, phase 3 trial. *Lancet Oncol.* 18, 1327–1337. doi: 10.1016/S1470-2045(17)30578-8

Domingo-Sananes, M. R., Kapuy, O., Hunt, T., and Novak, B. (2011). Switches and latches: a biochemical tug-of-war between the kinases and phosphatases that control mitosis. *Philos. Trans. R. Soc. Lond. B Biol. Sci.* 366, 3584–3594. doi: 10.1098/rstb.2011.0087

Du, J., Huang, Y., Yan, H., Zhang, Q., Zhao, M., Zhu, M., et al. (2014). Hydrogen sulfide suppresses oxidized low-density lipoprotein (ox-LDL)-stimulated monocyte chemoattractant protein 1 generation from macrophages via the nuclear factor κB (NF-κB) pathway. *J. Biol. Chem.* 289, 9741–9753. doi: 10.1074/jbc.M113.517995

Elewaut, D., DiDonato, J. A., Kim, J. M., Truong, F., Eckmann, L., and Kagnoff, M. F. (1999). NF-kappa B is a central regulator of the intestinal epithelial cell innate immune response induced by infection with enteroinvasive bacteria. *J. Immunol.* 163, 1457–1466.

Ellis, L., Gilston, V., Soo, C. C., Morris, C. J., Kidd, B. L., and Winyard, P. G. (2000). Activation of the transcription factor NF-kappaB in the rat air pouch model of inflammation. *Ann. Rheum. Dis.* 59, 303–307. doi: 10.1136/ard.59.4.303

Ernst, M. K., Dunn, L. L., and Rice, N. R. (1995). The PEST-like sequence of I kappa B alpha is responsible for inhibition of DNA binding but not for cytoplasmic retention of c-Rel or RelA homodimers. *Mol. Cell. Biol.* 15, 872–882. doi: 10.1128/mcb.15.2.872

Espinosa, L., Bigas, A., and Mulero, M. C. (2011). Alternative nuclear functions for NF-κB family members. *Am. J. Cancer Res.* 1, 446–459.

Fan, C., Li, Q., Ross, D., and Engelhardt, J. F. (2003). Tyrosine phosphorylation of I kappa B alpha activates NF kappa B through a redox-regulated and c-Src-dependent mechanism following hypoxia/reoxygenation. *J. Biol. Chem.* 278, 2072–2080. doi: 10.1074/jbc.M206718200

Fang, W., Liao, W., Zheng, Y., Huang, X., Weng, X., Fan, S., et al. (2019). Neurotropin reduces memory impairment and neuroinflammation via BDNF/NF-κB in a transgenic mouse model of Alzheimer's disease. *Am. J. Transl. Res.* 11, 1541–1554.

Feng, S., Chen, S., Yu, W., Zhang, D., Zhang, C., Tang, C., et al. (2017). HS inhibits pulmonary arterial endothelial cell inflammation in rats with monocrotaline-induced pulmonary hypertension. *Lab. Invest.* 97, 268–278. doi: 10.1038/labinvest.2016.129

Ferreiro, D. U., and Komives, E. A. (2010). Molecular mechanisms of system control of NF-kappaB signaling by IkappaBalpha. *Biochemistry* 49, 1560–1567. doi: 10.1021/bi901948j

Fu, L., Liu, K., He, J., Tian, C., Yu, X., and Yang, J. (2019). Direct proteomic mapping of cysteine persulfidation. *Antioxid. Redox Signal.* doi: 10.1089/ars.2019.7777 [Epub ahead of print].

Giridharan, S., and Srinivasan, M. (2018). Mechanisms of NF-κB p65 and. strategies for therapeutic manipulation. *J. Inflamm. Res.* 11, 407–419. doi: 10.2147/JIR.S140188

Hay, R. T., Vuillard, L., Desterro, J. M., and Rodriguez, M. S. (1999). Control of NF-kappa B transcriptional activation by signal induced proteolysis of I kappa B alpha. *Philos. Trans. R. Soc. Lond. B Biol. Sci.* 354, 1601–1609. doi: 10.1098/rstb.1999.0504

Hayden, M. S., and Ghosh, S. (2004). Signaling to NF-kappaB. *Genes Dev.* 18, 2195–2224. doi: 10.1101/gad.1228704

Hendriks, I. A., Lyon, D., Young, C., Jensen, L. J., Vertegaal, A. C. O., and Nielsen, M. L. (2017). Site-specific mapping of the human SUMO proteome reveals co-modification with phosphorylation. *Nat. Struct. Mol. Biol.* 24, 325–336. doi: 10.1038/nsmb.3366

Herter, J. R., and Fuchs, S. Y. (2002). Recognition of substrate and Skp1 by the homologue of Slimb (HOS) ubiquitin ligase receptor D role of the F-box. *Med. Sci. Monit.* 8, BR283–BR288.

Hideshima, T., Chauhan, D., Richardson, P., Mitsiades, C., Mitsiades, N., Hayashi, T., et al. (2002). NF-kappa B as a therapeutic target in multiple myeloma. *J. Biol. Chem.* 277, 16639–16647. doi: 10.1074/jbc.M200360200

Hinz, M., Arslan, S. Ç., and Scheidereit, C. (2012). It takes two to tango: IκBs, the multifunctional partners of NF-κB. *Immunol. Rev.* 246, 59–76. doi: 10.1111/j.1600-065X.2012.01102.x

Hoffmann, A., Natoli, G., and Ghosh, G. (2006). Transcriptional regulation via the NF-kappaB signaling module. *Oncogene* 25, 6706–6716. doi: 10.1038/sj.onc.1209933

Hu, X., Li, T., Wang, Y., Xiong, Y., Wu, X., Zhang, D., et al. (2017). Prokaryotic and highly-repetitive WD40 proteins: a systematic study. *Sci. Rep.* 7:10585. doi: 10.1038/s41598-017-11115-1

Huang, T. T., Kudo, N., Yoshida, M., and Miyamoto, S. (2000). A nuclear export signal in the N-terminal regulatory domain of IkappaBalpha controls cytoplasmic localization of inactive NF-kappaB/IkappaBalpha complexes. *Proc. Natl. Acad. Sci. U.S.A.* 97, 1014–1019. doi: 10.1073/pnas.97.3.1014

Huang, T. T., and Miyamoto, S. (2001). Postrepression activation of NF-kappaB requires the amino-terminal nuclear export signal specific to IkappaBalpha. *Mol. Cell. Biol.* 21, 4737–4747. doi: 10.1128/MCB.21.14.4737-4747.2001

Huang, Y., Tang, C., Du, J., and Jin, H. (2016). Endogenous sulfur dioxide: a new member of gasotransmitter family in the cardiovascular system. *Oxid. Med. Cell. Longev.* 2016:8961951. doi: 10.1155/2016/8961951

Hunter, T. (2000). Signaling–2000 and beyond. *Cell* 100, 113–127. doi: 10.1016/s0092-8674(00)81688-8

Hussain, A. R., Uddin, S., Ahmed, M., Al-Dayel, F., Bavi, P. P., and Al-Kuraya, K. S. (2013). Phosphorylated IκBα predicts poor prognosis in activated B-cell lymphoma and its inhibition with thymoquinone induces apoptosis via ROS release. *PLoS One* 8:e60540. doi: 10.1371/journal.pone.0060540

Imbert, V., Rupec, R. A., Livolsi, A., Pahl, H. L., Traenckner, E. B., Mueller-Dieckmann, C., et al. (1996). Tyrosine phosphorylation of I kappa B-alpha activates NF-kappa B without proteolytic degradation of I kappa B-alpha. *Cell* 86, 787–798. doi: 10.1016/s0092-8674(00)80153-1

Jo, H., Zhang, R., Zhang, H., McKinsey, T. A., Shao, J., Beauchamp, R. D., et al. (2000). NF-kappa B is required for H-ras oncogene induced abnormal cell proliferation and tumorigenesis. *Oncogene* 19, 841–849. doi: 10.1038/sj.onc.1203392

Johnson, C., Van Antwerp, D., and Hope, T. J. (1999). An N-terminal nuclear export signal is required for the nucleocytoplasmic shuttling of IkappaBalpha. *EMBO J.* 18, 6682–6693. doi: 10.1093/emboj/18.23.6682

Kanan, T., Kanan, D., Erol, I., Yazdi, S., Stein, M., and Durdagi, S. (2019). Targeting the NF-κB/IκBα complex via fragment-based E-pharmacophore virtual screening and binary QSAR models. *J. Mol. Graph. Model.* 86, 264–277. doi: 10.1016/j.jmgm.2018.09.014

Kanarek, N., and Ben-Neriah, Y. (2012). Regulation of NF-κB by ubiquitination and degradation of the IκBs. *Immunol. Rev.* 246, 77–94. doi: 10.1111/j.1600-065X.2012.01098.x

Kanarek, N., London, N., Schueler-Furman, O., and Ben-Neriah, Y. (2010). Ubiquitination and degradation of the inhibitors of NF-kappaB. *Cold Spring Harb. Perspect. Biol.* 2:a000166. doi: 10.1101/cshperspect.a000166

Kato, K., Tokuda, H., Matsushima-Nishiwaki, R., Natsume, H., Kondo, A., Ito, Y., et al. (2012). AMPK limits IL-1-stimulated IL-6 synthesis in osteoblasts: involvement of IκB/NF-κB pathway. *Cell. Signal.* 24, 1706–1712. doi: 10.1016/j.cellsig.2012.04.012

Kato, T., Delhase, M., Hoffmann, A., and Karin, M. (2003). CK2 is a C-terminal. IkappaB kinase responsible for NF-kappaB activation during the UV response. *Mol. Cell* 12, 829–839. doi: 10.1016/s1097-2765(03)00358-7

Kawai, H., Nie, L., and Yuan, Z. (2002). Inactivation of NF-kappaB-dependent cell survival, a novel mechanism for the proapoptotic function of c-Abl. *Mol. Cell. Biol.* 22, 6079–6088. doi: 10.1128/mcb.22.17.6079-6088.2002

Kil, I. S., Kim, S. Y., and Park, J. (2008). Glutathionylation regulates IkappaB. *Biochem. Biophys. Res. Commun.* 373, 169–173. doi: 10.1016/j.bbrc.2008.06.007

Kim, J. H., Lee, J., Oh, B., Kimm, K., and Koh, I. (2004). Prediction of phosphorylation sites using SVMs. *Bioinformatics* 20, 3179–3184. doi: 10.1093/bioinformatics/bth382

Kis, A., Yellon, D. M., and Baxter, G. F. (2003). Role of nuclear factor-kappa B activation in acute ischaemia-reperfusion injury in myocardium. *Br. J. Pharmacol.* 138, 894–900. doi: 10.1038/sj.bjp.0705108

Ko, E., Cho, S., Kwon, S., Eom, C., Jeong, M., Lee, W., et al. (2017). The roles of NF-κB and ROS in regulation of pro-inflammatory mediators of inflammation induction in LPS-stimulated zebrafish embryos. *Fish Shellfish Immunol.* 68, 525–529. doi: 10.1016/j.fsi.2017.07.041

Komives, E. A. (2012). Consequences of fuzziness in the NFκB/IκBα interaction. *Adv. Exp. Med. Biol.* 725, 74–85. doi: 10.1007/978-1-4614-0659-4_5

Kumar, A., and Zhang, K. Y. J. (2015). Advances in the development of SUMO specific protease (SENP) inhibitors. *Comput. Struct. Biotechnol. J.* 13, 204–211. doi: 10.1016/j.csbj.2015.03.001

Kunz, K., Piller, T., and Müller, S. (2018). SUMO-specific proteases and isopeptidases of the SENP family at a glance. *J. Cell Sci.* 131:jcs211904. doi: 10.1242/jcs.211904

Lee, S., and Hannink, M. (2002). Characterization of the nuclear import and export functions of Ikappa B(epsilon). *J. Biol. Chem.* 277, 23358–23366. doi: 10.1074/jbc.M111559200

Lee, S. H., and Hannink, M. (2001). The N-terminal nuclear export sequence of IkappaBalpha is required for RanGTP-dependent binding to CRM1. *J. Biol. Chem.* 276, 23599–23606. doi: 10.1074/jbc.M011197200

Li, J., Mahajan, A., and Tsai, M. (2006). Ankyrin repeat: a unique motif mediating protein-protein interactions. *Biochemistry* 45, 15168–15178. doi: 10.1021/bi062188q

Lin, R., Beauparlant, P., Makris, C., Meloche, S., and Hiscott, J. (1996). Phosphorylation of IkappaBalpha in the C-terminal PEST domain by casein kinase II affects intrinsic protein stability. *Mol. Cell. Biol.* 16, 1401–1409. doi: 10.1128/mcb.16.4.1401

Liu, J., Yuan, Y., Xu, J., Xiao, K., Xu, Y., Guo, T., et al. (2018). β-TrCP restricts lipopolysaccharide (LPS)-induced activation of TRAF6-IKK pathway upstream of IκBα signaling. *Front. Immunol.* 9:2930. doi: 10.3389/fimmu.2018.02930

Liu, Q., Li, J., Khoury, J., Colgan, S. P., and Ibla, J. C. (2009). Adenosine signaling mediates SUMO-1 modification of IkappaBalpha during hypoxia and reoxygenation. *J. Biol. Chem.* 284, 13686–13695. doi: 10.1074/jbc.M809275200

Lonial, S., Mitsiades, C. S., and Richardson, P. G. (2011). Treatment options for relapsed and refractory multiple myeloma. *Clin. Cancer Res.* 17, 1264–1277. doi: 10.1158/1078-0432.CCR-10-1805

Lv, H., Zhen, C., Liu, J., Yang, P., Hu, L., and Shang, P. (2019). Unraveling the potential role of glutathione in multiple forms of cell death in cancer therapy. *Oxid. Med. Cell. Longev.* 2019:3150145. doi: 10.1155/2019/3150145

Mabb, A. M., and Miyamoto, S. (2007). SUMO and NF-kappaB ties. *Cell. Mol. Life Sci.* 64, 1979–1996. doi: 10.1007/s00018-007-7005-2

Mansur, D. S., Maluquer de Motes, C., Unterholzner, L., Sumner, R. P., Ferguson, B. J., Ren, H., et al. (2013). Poxvirus targeting of E3 ligase β-TrCP by molecular mimicry: a mechanism to inhibit NF-κB activation and promote immune evasion and virulence. *PLoS Pathog.* 9:e1003183. doi: 10.1371/journal.ppat.1003183

Marruecos, L., Bertran, J., Guillén, Y., González, J., Batlle, R., López-Arribillaga, E., et al. (2020). IκBα deficiency imposes a fetal phenotype to intestinal stem cells. *EMBO Rep.* 21:e49708. doi: 10.15252/embr.201949708

Mathes, E., O'Dea, E. L., Hoffmann, A., and Ghosh, G. (2008). NF-kappaB dictates the degradation pathway of IkappaBalpha. *EMBO J.* 27, 1357–1367. doi: 10.1038/emboj.2008.73

McElhinny, J. A., Trushin, S. A., Bren, G. D., Chester, N., and Paya, C. V. (1996). Casein kinase II phosphorylates I kappa B alpha at S-283, S-289, S-293, and T-291 and is required for its degradation. *Mol. Cell. Biol.* 16, 899–906. doi: 10.1128/mcb.16.3.899

Meng, Q., Wu, W., Pei, T., Xue, J., Xiao, P., Sun, L., et al. (2020). miRNA-129/FBW7/NF-κB, a novel regulatory pathway in inflammatory bowel disease. *Mol. Ther. Nucleic Acids* 19, 731–740. doi: 10.1016/j.omtn.2019.10.048

Mothes, J., Busse, D., Kofahl, B., and Wolf, J. (2015). Sources of dynamic variability in NF-κB signal transduction: a mechanistic model. *Bioessays* 37, 452–462. doi: 10.1002/bies.201400113

Mukhopadhyay, A., Manna, S. K., and Aggarwal, B. B. (2000). Pervanadate-induced nuclear factor-kappaB activation requires tyrosine phosphorylation and degradation of IkappaBalpha. Comparison with tumor necrosis factor-alpha. *J. Biol. Chem.* 275, 8549–8555. doi: 10.1074/jbc.275.12.8549

Mulero, M. C., Bigas, A., and Espinosa, L. (2013a). IκBα beyond the NF-kB dogma. *Oncotarget* 4, 1550–1551. doi: 10.18632/oncotarget.1325

Mulero, M. C., Ferres-Marco, D., Islam, A., Margalef, P., Pecoraro, M., Toll, A., et al. (2013b). Chromatin-bound IκBα regulates a subset of polycomb target genes in differentiation and cancer. *Cancer Cell* 24, 151–166. doi: 10.1016/j.ccr.2013.06.003

Mustafa, A. K., Gadalla, M. M., Sen, N., Kim, S., Mu, W., Gazi, S. K., et al. (2009). H2S signals through protein S-sulfhydration. *Sci. Signal.* 2:ra72. doi: 10.1126/scisignal.2000464

Myllyharju, J., and Kivirikko, K. I. (2004). Collagens, modifying enzymes and their mutations in humans, flies and worms. *Trends Genet.* 20, 33–43. doi: 10.1016/j.tig.2003.11.004

Nakajima, H., Fujiwara, H., Furuichi, Y., Tanaka, K., and Shimbara, N. (2008). A novel small-molecule inhibitor of NF-kappaB signaling. *Biochem. Biophys. Res. Commun.* 368, 1007–1013. doi: 10.1016/j.bbrc.2008.01.166

Narayanan, S., Cai, C., Assaraf, Y. G., Guo, H., Cui, Q., Wei, L., et al. (2020). Targeting the ubiquitin-proteasome pathway to overcome anti-cancer drug resistance. *Drug Resist. Updat.* 48:100663. doi: 10.1016/j.drup.2019.100663

Nozaki, K., Tanaka, H., Ikehara, Y., Cao, X., Nakanishi, H., Azuma, T., et al. (2005). *Helicobacter pylori*-dependent NF-kappa B activation in newly established Mongolian gerbil gastric cancer cell lines. *Cancer Sci.* 96, 170–175. doi: 10.1111/j.1349-7006.2005.00030.x

Olsen, S. K., Capili, A. D., Lu, X., Tan, D. S., and Lima, C. D. (2010). Active site remodelling accompanies thioester bond formation in the SUMO E1. *Nature* 463, 906–912. doi: 10.1038/nature08765

Pal Singh, S., Dammeijer, F., and Hendriks, R. W. (2018). Role of Bruton's tyrosine kinase in B cells and malignancies. *Mol. Cancer* 17:57. doi: 10.1186/s12943-018-0779-z

Pancheri, E., Guglielmi, V., Wilczynski, G. M., Malatesta, M., Tonin, P., Tomelleri, G., et al. (2020). Non-hematologic toxicity of bortezomib in multiple myeloma: the neuromuscular and cardiovascular adverse effects. *Cancers* 12:E2540. doi: 10.3390/cancers12092540

Pazarentzos, E., Mahul-Mellier, A., Datler, C., Chaisaklert, W., Hwang, M., Kroon, J., et al. (2014). IκBα inhibits apoptosis at the outer mitochondrial membrane independently of NF-κB retention. *EMBO J.* 33, 2814–2828. doi: 10.15252/embj.201488183

Perkins, N. D. (2006). Post-translational modifications regulating the activity and. function of the nuclear factor kappa B pathway. *Oncogene* 25, 6717–6730. doi: 10.1038/sj.onc.1209937

Pikarsky, E., Porat, R. M., Stein, I., Abramovitch, R., Amit, S., Kasem, S., et al. (2004). NF-kappaB functions as a tumour promoter in inflammation-associated cancer. *Nature* 431, 461–466. doi: 10.1038/nature02924

Pons, J., Evrard-Todeschi, N., Bertho, G., Gharbi-Benarous, J., Sonois, V., Benarous, R., et al. (2007). Structural studies on 24P-IkappaBalpha peptide derived from a human IkappaB-alpha protein related to the inhibition of the activity of the transcription factor NF-kappaB. *Biochemistry* 46, 2958–2972. doi: 10.1021/bi061401f

Pons, S., and Torres-Aleman, I. (2000). Insulin-like growth factor-I stimulates dephosphorylation of ikappa B through the serine phosphatase calcineurin (protein phosphatase 2B). *J. Biol. Chem.* 275, 38620–38625. doi: 10.1074/jbc.M004531200

Pontoriero, M., Fiume, G., Vecchio, E., de Laurentiis, A., Albano, F., Iaccino, E., et al. (2019). Activation of NF-κB in B cell receptor signaling through Bruton's tyrosine kinase-dependent phosphorylation of IκB-α. *J. Mol. Med.* 97, 675–690. doi: 10.1007/s00109-019-01777-x

Potoyan, D. A., Zheng, W., Ferreiro, D. U., Wolynes, P. G., and Komives, E. A. (2016). PEST control of molecular stripping of NFκB from DNA transcription sites. *J. Phys. Chem. B* 120, 8532–8538. doi: 10.1021/acs.jpcb.6b02359

Qvit, N., Hatzubai, A., Shalev, D. E., Ben-Neriah, Y., and Gilon, C. (2009). Design and synthesis of backbone cyclic phosphopeptides: the IkappaB model. *Biopolymers* 91, 157–168. doi: 10.1002/bip.21098

Rape, M., Reddy, S. K., and Kirschner, M. W. (2006). The processivity of multiubiquitination by the APC determines the order of substrate degradation. *Cell* 124, 89–103. doi: 10.1016/j.cell.2005.10.032

Richardson, P. G., Barlogie, B., Berenson, J., Singhal, S., Jagannath, S., Irwin, D., et al. (2003). A phase 2 study of bortezomib in relapsed, refractory myeloma. *N. Engl. J. Med.* 348, 2609–2617. doi: 10.1056/NEJMoa030288

Rodriguez, M. S., Dargemont, C., and Hay, R. T. (2001). SUMO-1 conjugation in vivo requires both a consensus modification motif and nuclear targeting. *J. Biol. Chem.* 276, 12654–12659. doi: 10.1074/jbc.M009476200

Sachdev, S., Bagchi, S., Zhang, D. D., Mings, A. C., and Hannink, M. (2000). Nuclear import of IkappaBalpha is accomplished by a ran-independent transport pathway. *Mol. Cell. Biol.* 20, 1571–1582. doi: 10.1128/mcb.20.5.1571-1582.2000

Sachdev, S., Hoffmann, A., and Hannink, M. (1998). Nuclear localization of IkappaB alpha is mediated by the second ankyrin repeat: the IkappaB alpha ankyrin repeats define a novel class of cis-acting nuclear import sequences. *Mol. Cell. Biol.* 18, 2524–2534. doi: 10.1128/mcb.18.5.2524

Safi, S. Z., Shah, H., Qvist, R., Bindal, P., Mansor, M., Yan, G. O. S., et al. (2018). Beta adrenergic receptors stimulation attenuates phosphorylation of NF-κB and IκBα in hyperglycemic endothelial cells. *Cell. Physiol. Biochem.* 51, 1429–1436. doi: 10.1159/000495591

Sato, T., Odagiri, H., Ikenaga, S., Maruyama, M., and Sasaki, M. (2003). Chemosensitivity of human pancreatic carcinoma cells is enhanced by IkappaBalpha super-repressor. *Cancer Sci.* 94, 467–472. doi: 10.1111/j.1349-7006.2003.tb01466.x

Sayed, M., Kim, S. O., Salh, B. S., Issinger, O. G., and Pelech, S. L. (2000). Stress-induced activation of protein kinase CK2 by direct interaction with p38 mitogen-activated protein kinase. *J. Biol. Chem.* 275, 16569–16573. doi: 10.1074/jbc.M000312200

Scherer, D. C., Brockman, J. A., Chen, Z., Maniatis, T., and Ballard, D. W. (1995). Signal-induced degradation of I kappa B alpha requires site-specific ubiquitination. *Proc. Natl. Acad. Sci. U.S.A.* 92, 11259–11263. doi: 10.1073/pnas.92.24.11259

Schwarz, E. M., Van Antwerp, D., and Verma, I. M. (1996). Constitutive phosphorylation of IkappaBalpha by casein kinase II occurs preferentially at serine 293: requirement for degradation of free IkappaBalpha. *Mol. Cell. Biol.* 16, 3554–3559. doi: 10.1128/mcb.16.7.3554

Sedgwick, S. G., and Smerdon, S. J. (1999). The ankyrin repeat: a diversity of interactions on a common structural framework. *Trends Biochem. Sci.* 24, 311–316. doi: 10.1016/s0968-0004(99)01426-7

Seidel, P., Roth, M., Ge, Q., Merfort, I., S'ng, C. T., and Ammit, A. J. (2011). IκBα glutathionylation and reduced histone H3 phosphorylation inhibit eotaxin and RANTES. *Eur. Respir. J.* 38, 1444–1452. doi: 10.1183/09031936.00129610

Shi, M., Cho, H., Inn, K., Yang, A., Zhao, Z., Liang, Q., et al. (2014). Negative regulation of NF-κB activity by brain-specific TRIpartite motif protein 9. *Nat. Commun.* 5:4820. doi: 10.1038/ncomms5820

Shumway, S. D., Maki, M., and Miyamoto, S. (1999). The PEST domain of IkappaBalpha is necessary and sufficient for in vitro degradation by mu-calpain. *J. Biol. Chem.* 274, 30874–30881. doi: 10.1074/jbc.274.43.30874

Singh, R. K., Kazansky, Y., Wathieu, D., and Fushman, D. (2017). Hydrophobic patch of ubiquitin is important for its optimal activation by ubiquitin activating enzyme E1. *Anal. Chem.* 89, 7852–7860. doi: 10.1021/acs.analchem.6b04194

Skaar, J. R., Pagan, J. K., and Pagano, M. (2013). Mechanisms and function of substrate recruitment by F-box proteins. *Nat. Rev. Mol. Cell Biol.* 14, 369–381. doi: 10.1038/nrm3582

Sue, S.-C., and Dyson, H. J. (2009). Interaction of the IkappaBalpha C-terminal PEST sequence with NF-kappaB: insights into the inhibition of NF-kappaB DNA binding by IkappaBalpha. *J. Mol. Biol.* 388, 824–838. doi: 10.1016/j.jmb.2009.03.048

Takada, Y., Mukhopadhyay, A., Kundu, G. C., Mahabeleshwar, G. H., Singh, S., and Aggarwal, B. B. (2003). Hydrogen peroxide activates NF-kappa B through tyrosine phosphorylation of I kappa B alpha and serine phosphorylation of p65: evidence for the involvement of I kappa B alpha kinase and Syk protein-tyrosine kinase. *J. Biol. Chem.* 278, 24233–24241. doi: 10.1074/jbc.M212389200

Tomita, H., Tabata, K., Takahashi, M., Nishiyama, F., and Sugano, E. (2016). Light induces translocation of NF-κB p65 to the mitochondria and suppresses expression of cytochrome c oxidase subunit III (COX III) in the rat retina. *Biochem. Biophys. Res. Commun.* 473, 1013–1018. doi: 10.1016/j.bbrc.2016.04.008

Traenckner, E. B., Pahl, H. L., Henkel, T., Schmidt, K. N., Wilk, S., and Baeuerle, P. A. (1995). Phosphorylation of human I kappa B-alpha on serines 32 and 36 controls I kappa B-alpha proteolysis and NF-kappa B activation in response to diverse stimuli. *EMBO J.* 14, 2876–2883. doi: 10.1002/j.1460-2075.1995.tb07287.x

Trelle, M. B., Ramsey, K. M., Lee, T. C., Zheng, W., Lamboy, J., Wolynes, P. G., et al. (2016). Binding of NFκB appears to twist the ankyrin repeat domain of IκBα. *Biophys. J.* 110, 887–895. doi: 10.1016/j.bpj.2016.01.001

Truhlar, S. M. E., Torpey, J. W., and Komives, E. A. (2006). Regions of IkappaBalpha that are critical for its inhibition of NF-kappaB.DNA interaction fold upon binding to NF-kappaB. *Proc. Natl. Acad. Sci. U.S.A.* 103, 18951–18956. doi: 10.1073/pnas.0605794103

Tundo, G. R., Sbardella, D., Santoro, A. M., Coletta, A., Oddone, F., Grasso, G., et al. (2020). The proteasome as a druggable target with multiple therapeutic potentialities: cutting and non-cutting edges. *Pharmacol. Ther.* 213:107579. doi: 10.1016/j.pharmthera.2020.107579

Turpin, P., Hay, R. T., and Dargemont, C. (1999). Characterization of IkappaBalpha nuclear import pathway. *J. Biol. Chem.* 274, 6804–6812. doi: 10.1074/jbc.274.10.6804

Usui, S., Maejima, Y., Pain, J., Hong, C., Cho, J., Park, J. Y., et al. (2011). Endogenous muscle atrophy F-box mediates pressure overload-induced cardiac hypertrophy through regulation of nuclear factor-kappaB. *Circ. Res.* 109, 161–171. doi: 10.1161/CIRCRESAHA.110.238717

Vrábel, D., Pour, L., and Ševèíková, S. (2019). The impact of NF-κB signaling on pathogenesis and current treatment strategies in multiple myeloma. *Blood Rev.* 34, 56–66. doi: 10.1016/j.blre.2018.11.003

Wang, W. Y., and Wang, B. H. (2018). SO2 donors and prodrugs, and their possible applications: a review. *Front. Chem.* 6:559. doi: 10.3389/fchem.2018.00559

Wang, Y., Li, M., Huang, T., and Li, J. (2018). Protein tyrosine phosphatase L1 inhibits high-grade serous ovarian carcinoma progression by targeting IκBα. *Onco Targets Ther.* 11, 7603–7612. doi: 10.2147/OTT.S167106

Waters, J. A., Matos, J., Yip-Schneider, M., Aguilar-Saavedra, J. R., Crean, C. D., Beane, J. D., et al. (2015). Targeted nuclear factor-kappaB suppression enhances gemcitabine response in human pancreatic tumor cell line murine xenografts. *Surgery* 158, 881–888; discussion 888–889. doi: 10.1016/j.surg.2015.04.043

Wong, H. K., Kammer, G. M., Dennis, G., and Tsokos, G. C. (1999). Abnormal NF-kappa B activity in T lymphocytes from patients with systemic lupus erythematosus is associated with decreased p65-RelA protein expression. *J. Immunol.* 163, 1682–1689.

Wu, M., Lee, H., Bellas, R. E., Schauer, S. L., Arsura, M., Katz, D., et al. (1996). Inhibition of NF-kappaB/Rel induces apoptosis of murine B cells. *EMBO J.* 15, 4682–4690. doi: 10.1002/j.1460-2075.1996.tb00845.x

Yaron, A., Gonen, H., Alkalay, I., Hatzubai, A., Jung, S., Beyth, S., et al. (1997). Inhibition of NF-kappa-B cellular function via specific targeting of the I-kappa-B-ubiquitin ligase. *EMBO J.* 16, 6486–6494. doi: 10.1093/emboj/16.21.6486

Yazdi, S., Durdagi, S., Naumann, M., and Stein, M. (2015). Structural modeling of the N-terminal signal-receiving domain of IκBα. *Front. Mol. Biosci.* 2:32. doi: 10.3389/fmolb.2015.00032

Yazdi, S., Naumann, M., and Stein, M. (2017). Double phosphorylation-induced structural changes in the signal-receiving domain of IκBα in complex with NF-κB. *Proteins* 85, 17–29. doi: 10.1002/prot.25181

Yeh, E. T. H. (2009). SUMOylation and De-SUMOylation: wrestling with life's processes. *J. Biol. Chem.* 284, 8223–8227. doi: 10.1074/jbc.R800050200

Zamora, M., Meroño, C., Viñas, O., and Mampel, T. (2004). Recruitment of NF-kappaB into mitochondria is involved in adenine nucleotide translocase 1 (ANT1)-induced apoptosis. *J. Biol. Chem.* 279, 38415–38423. doi: 10.1074/jbc.M404928200

Zhang, J., Yang, Z., Fang, K., Shi, Z., Ren, D., and Sun, J. (2017). Oleuropein prevents the development of experimental autoimmune myocarditis in rats. *Int. Immunopharmacol.* 48, 187–195. doi: 10.1016/j.intimp.2017.05.013

Conflict of Interest: The authors declare that the research was conducted in the absence of any commercial or financial relationships that could be construed as a potential conflict of interest.

frontiers in Cell and Developmental Biology

ORIGINAL RESEARCH
published: 26 January 2021
doi: 10.3389/fcell.2021.629932

SOCS3 Negatively Regulates Cardiac Hypertrophy via Targeting GRP78-Mediated ER Stress During Pressure Overload

Shuang Liu[1], Wen-Chang Sun[2], Yun-Long Zhang[3], Qiu-Yue Lin[4], Jia-Wei Liao[4], Gui-Rong Song[5], Xiao-Lei Ma[4], Hui-Hua Li[3,4] and Bo Zhang[4]**

[1] College of Basic Medical Sciences, Dalian Medical University, Dalian, China, [2] Department of Microbiology, College of Basic Medical Sciences, Dalian Medical University, Dalian, China, [3] Beijing Key Laboratory of Cardiopulmonary Cerebral Resuscitation, Department of Emergency Medicine, Beijing Chaoyang Hospital, Capital Medical University, Beijing, China, [4] Department of Cardiology, Institute of Cardiovascular Diseases, First Affiliated Hospital of Dalian Medical University, Dalian, China, [5] Department of Health Statistics, School of Public Health, Dalian Medical University, Dalian, China

OPEN ACCESS

Edited by:
Juan Jose Sanz-Ezquerro, Consejo Superior de Investigaciones Científicas (CSIC), Spain

Reviewed by:
Jun Ren, University of Washington, United States
Tim Palmer, University of York, United Kingdom

***Correspondence:**
Hui-Hua Li
hhli1935@aliyun.com
Bo Zhang
dalianzhangbo@yahoo.com

Specialty section:
This article was submitted to Signaling, a section of the journal Frontiers in Cell and Developmental Biology

Received: 16 November 2020
Accepted: 06 January 2021
Published: 26 January 2021

Citation:
Liu S, Sun W-C, Zhang Y-L, Lin Q-Y, Liao J-W, Song G-R, Ma X-L, Li H-H and Zhang B (2021) SOCS3 Negatively Regulates Cardiac Hypertrophy via Targeting GRP78-Mediated ER Stress During Pressure Overload. Front. Cell Dev. Biol. 9:629932. doi: 10.3389/fcell.2021.629932

Pressure overload-induced hypertrophic remodeling is a critical pathological process leading to heart failure (HF). Suppressor of cytokine signaling-3 (SOCS3) has been demonstrated to protect against cardiac hypertrophy and dysfunction, but its mechanisms are largely unknown. Using primary cardiomyocytes and cardiac-specific SOCS3 knockout (SOCS3cko) or overexpression mice, we demonstrated that modulation of SOCS3 level influenced cardiomyocyte hypertrophy, apoptosis and cardiac dysfunction induced by hypertrophic stimuli. We found that glucose regulatory protein 78 (GRP78) was a direct target of SOCS3, and that overexpression of SOCS3 inhibited cardiomyocyte hypertrophy and apoptosis through promoting proteasomal degradation of GRP78, thereby inhibiting activation of endoplasmic reticulum (ER) stress and mitophagy in the heart. Thus, our results uncover SOCS3-GRP78-mediated ER stress as a novel mechanism in the transition from cardiac hypertrophy to HF induced by sustained pressure overload, and suggest that modulating this pathway may provide a new therapeutic approach for hypertrophic heart diseases.

Keywords: cardiac hypertrophy, heart failure, socs3, glucose regulatory protein 78, endoplasmic reticulum stress

INTRODUCTION

Pathological cardiac hypertrophy is typically characterized by increased cardiac myocyte cell size, interstitial fibrosis, myocyte apoptosis, and contractile dysfunction (Heineke and Molkentin, 2006; Nakamura and Sadoshima, 2018). Various forms of stress or injury, such as hypertension, valve disease, and ischemic heart disease, induce cardiac hypertrophy and heart failure (HF) through multiple mechanisms, including abnormal signal transduction, disrupted intracellular calcium handling, imbalance between protein synthesis and degradation, endoplasmic reticulum (ER) stress, and mitochondrial dysfunction. The ER is a critical organelle involved in intracellular protein synthesis, folding, and translocation, as well as calcium homoeostasis (Gotoh et al., 2011; Rashid et al., 2015). Recent evidence revealed that ER stress is associated with various heart diseases, such as ischemic heart diseases, cardiac hypertrophy, and HF (Yamaguchi et al., 2003; Fu et al., 2010; Minamino and Kitakaze, 2010; Yao et al., 2017).

Thus, improved understanding of the regulatory mechanisms of ER stress in heart disease will facilitate identification of potential targets for intervention.

The suppressor of cytokine signaling (SOCS) family of proteins includes eight intracellular proteins, SOCS1–7 and cytokine-inducible SH2 protein (CIS) (Yasukawa et al., 2012), which are structurally characterized by a variable N-terminal region, a central SH2 domain, and a C-terminal SOCS box motif (Masuhara et al., 1997; Hilton et al., 1998). Among them, CIS and SOCS1–3 proteins directly interact with gp130 and/or Janus kinases (JAKs), thereby inactivating downstream mediators. Gp130, a common β-receptor component of the IL-6 family of cytokines, regulates three downstream signaling pathways in cardiomyocytes, JAK/STAT, mitogen-activated protein kinase, and phosphoinositide 3 kinase (PI3K/AKT), which play a pathological role in the development of cardiac hypertrophy and HF after various stimuli, such as leukemia inhibitory factor (LIF) and pressure overload (Hirota et al., 1995; Kunisada et al., 1998; Uozumi et al., 2001; Yasukawa et al., 2001, 2012; Fischer and Hilfiker-Kleiner, 2007). Notably, SOCS3-knockout mice are embryonic-lethal as a result of placental deficiency and marked erythrocytosis (Marine et al., 1999; Roberts et al., 2001). Moreover, SOCS3 is a mechanical stress-inducible gene that is markedly upregulated in hypertrophic hearts after 2 weeks of transverse aortic constriction (TAC) (Yasukawa et al., 2001). However, clinical studies have shown reduced SOCS3 expression in failing human myocardium, where it plays a critical role as a negative feedback regulator of JAK-mediated gp130 signaling (Podewski et al., 2003; Margulies et al., 2005; Mann et al., 2010). Indeed, cardiac-specific knockout of SOCS3 (SOCS3cko) results in cardiac hypertrophy, chamber dilatation, and dysfunction accompanied by activation of gp130 signaling and abnormal myofilament $Ca2^{+}$ sensitivity after pressure overload (Yajima et al., 2011). Conversely, adenovirus-mediated overexpression of SOCS3 in cardiomyocytes markedly inhibits the LIF and CT-1-induced hypertrophic response, as well as activation of gp130 downstream signals (Yasukawa et al., 2001), suggesting that SOCS3 may be a new potential therapeutic target for treatment of cardiac hypertrophy and HF. Although the role of SOCS3 regulation on cardiac gp130 signaling in pressure overload has been relatively well-evaluated, little is known about whether other regulatory mechanisms are involved in the action of SOCS3 in cardiac function.

In this study, using primary cardiomyocytes, cardiac-specific knockout of SOCS3 (SOCS3cko) or overexpression mice infected with rAAV9-SOCS3, we found that SOCS3-GRP78-ER stress signaling was essential for the transition from cardiac hypertrophy to HF during pressure overload, we found that SOCS3 acts as a negative regulator of cardiac hypertrophy and dysfunction induced by pressure overload by targeting GRP78 for ubiquitination and degradation by the proteasome. Thus, we demonstrated that SOCS3-GRP78-ER stress signaling was essential for the transition from cardiac hypertrophy to HF during pressure overload, and suggest that SOCS3 may represent a potential therapeutic target for treating hypertrophic heart diseases.

MATERIALS AND METHODS

Animal Models and Treatment

Wild-type (WT) and SOCS3-flox (SOCS3f/f) mice were obtained from Jackson Laboratories (Bar Harbor, ME). Cardiac-specific knockout of SOCS3 (SOCS3cko) mice were generated by mating SOCS3f/f mice with mice expressing Cre recombinase under the α-myosin heavy chain (α-MHC) promoter as described previously (Oba et al., 2012). All animals were C57BL/6J background. To induce Cre-dependent recombination, tamoxifen (20 mg/kg body weight, Sigma-Aldrich) was injected intraperitoneally for 5 days over a 3-week duration before experiments. SOCS3f/f mice were used as a control for SOCS3cko mice. Male mice (aged 8–10 weeks) were maintained in a pathogen-free facility at the Laboratory Animal Center at Dalian Medical University. All procedures were performed in accordance with protocols outlined in the Guide for the Care and Use of Laboratory Animals published by the US National Institutes of Health (NIH publication No. 85-23, revised 1996) and approved by the Committee on the Ethics of Animal Experiments of Dalian Medical University, as described in our previous study (Xie et al., 2018).

Male SOCS3f/f and SOCS3cko mice were anesthetized with isoflurane and subjected to pressure overload induced by transverse aortic constriction (TAC) for 4 weeks, as previously described (Li et al., 2007; Xie et al., 2019). Sham-treated mice underwent the same operation without aortic constriction. After recovering from surgery, mice were injected intraperitoneally with 4-PBA (20 mg/kg/day) or vehicle (dimethyl sulfoxide, DMSO) daily for 4 weeks. 4-PBA was first dissolved in DMSO, then diluted in 0.9% NaCl (Metz et al., 1977).

Histopathological Analysis

Heart samples were quickly dissected out and rinsed with cool sterile saline, and then fixed in 10% paraformaldehyde, embedded in paraffin, and cut into 5-μm-thick sections for histological analysis. Heart sections were stained with hematoxylin and eosin (H&E), wheat germ agglutinin (WGA) and Masson's trichrome as previously described (Wang L. et al., 2018; Xie et al., 2018). All digital images were taken at ×100 or ×200 magnification of 15–20 random fields from each heart sample. Analysis of myocyte cross-sectional area was calculated by measuring 150 to 200 cells per slide. The areas of myocardial fibrosis were evaluated by Image Pro Plus 3.0 (Nikon, Japan).

Proteomic Analysis

Primary experimental procedures for proteomic analysis included protein extraction, trypsin digestion, high-performance liquid chromatography fractionation, liquid chromatography with tandem mass spectrometry, and data analysis supported by Jingjie PTM BioLabs (Hangzhou, China).

Statistical Analysis

All data are expressed as mean ± SEM. All statistical analyses were performed with SPSS 16.0 software (IBM, Armonk, NY). For two-group comparisons, we performed Student's *t*-test. For comparison of multiple groups, significance was determined

using 1-way or 2-way ANOVA with Tukey's *post-hoc* test. $P < 0.05$ was considered statistically significant.

RESULTS

SOCS3 Overexpression Inhibited Cardiomyocyte Hypertrophy and Activation of Gp130 Signaling *in vitro*

To identify which SOCS family members are essential for cardiac hypertrophy and dysfunction, we first evaluated expression of endogenous SOCS members after stimulation with hypertrophic agonists. Quantitative real-time PCR analysis showed that among the eight SOCS family members, only SOCS3 was significantly upregulated at week 2 (the hypertrophic stage) and decreased at week 4 (the HF stage) after TAC (**Figure 1A**). This change in SOCS3 protein level was further validated by immunoblotting (IB) of the same hearts at different time points (**Figure 1B**). SOCS3 expression was also appreciably increased in neonatal rat cardiomyocytes (NRCMs) in response to phenylephrine (PE, 100 μmol/L) stimulation for 12–48 h, but was decreased at 72 h (**Figure 1C**). However, SOCS3 expression was not altered in neonatal rat cardiac fibroblasts after PE stimulation at different time points (**Supplementary Figure 1A**).

We next investigated the role of SOCS3 in cardiac hypertrophy *in vitro*. NRCMs were infected with an adenovirus overexpressing SOCS3 (Ad-SOCS3) or empty vector with green fluorescent protein (GFP, Ad-GFP), and treated with PE (100 μM) for 72 h. SOCS3 overexpression (increased by ∼2-fold, **Supplementary Figure 1B**) significantly inhibited PE-induced increases of cardiomyocyte size and expression of the hypertrophic markers atrial natriuretic factor (ANF) and brain natriuretic peptide (BNP) (**Figures 1D,E**). Conversely, SOCS3 knockdown by siRNAs (decreased by ∼50%, **Supplementary Figure 1C**) enhanced PE-induced hypertrophic responses compared with siRNA-control (**Figures 1F,G**). Accordingly, SOCS3 overexpression remarkably inhibited activation of the downstream targets gp130, p-JAK2, and p-STAT3 compared with the Ad-GFP control in NRCMs after PE treatment (**Figure 1H**). Overall, these results indicated that SOCS3 exerts an antihypertrophic role *in vitro*.

SOCS3 Overexpression in Cardiomyocytes Prevented Cardiac Hypertrophy and Dysfunction Induced by Pressure Overload

To examine the *in vivo* pathophysiological role of SOCS3 in the heart, we increased SOCS3 expression in WT hearts by injecting a rAAV9 expressing SOCS3 (rAAV9-SOCS3) or ZsGreen (rAAV9-ZsGreen, a negative control). Transfection efficiency and expression of SOCS3 were confirmed in hearts by fluorescence microscopy of ZsGreen (**Supplementary Figure 2A**), and immunoblotting analysis indicated a 2.3-fold increase of SOCS3 expression compared with control (**Supplementary Figure 2B**). Four weeks after TAC operation, echocardiographic assessment revealed that TAC significantly impaired contractile function, as reflected by decreased ejection fraction (EF%) and fractional shortening (FS%) in rAAV9-ZsGreen-injected mice compared with Sham groups, whereas rAAV9-SOCS3-injected mice recovered cardiac dysfunction similar to or better than Sham mice (**Figure 2A**). Furthermore, TAC-induced decompensation of hypertrophy, as indicated by increases in heart size, ratios of heart weight/body weight (HW/BW) and heart weight/tibia length (HW/TL), cross-sectional area of myocytes, and fibrotic area in rAAV9-ZsGreen-injected mice, were also significantly abrogated in rAAV9-SOCS3-injected mice (**Figures 2B–D**). Accordingly, mRNA expressions of ANF, BNP, and β-myosin heavy chain (β-MHC), collagen I, and collagen III were markedly reduced in rAAV9-SOCS3-infected mice compared with rAAV9-ZsGreen-infected animals after TAC (**Supplementary Figures 2C,D**). Moreover, SOCS3 overexpression markedly reduced TAC-induced cardiomyocyte apoptosis, as indicated by the number of TUNEL-positive nuclei in WT hearts compared with rAAV9-ZsGreen-infected hearts (**Figure 2E**). In addition, gp130, p-JAK2, and p-STAT3 protein levels were consistently downregulated in rAAV9-SOCS3-injected mice compared with rAAV9-ZsGreen-injected mice (**Figures 2F,G**). These results suggested that cardiac overexpression of SOCS3 enabled improvement of TAC-induced cardiac hypertrophy and dysfunction.

Cardiac-Specific Ablation of SOCS3 Accelerated Pressure Overload-Induced Cardiac Hypertrophy and Dysfunction

To precisely ascertain whether loss of SOCS3 in cardiomyocytes predisposes mice to HF, SOCS3f/f mice were bred with α-MHC-Cre mice to generate cardiomyocyte-specific SOCS3-knockout mice (SOCS3cko). Specific deletion of SOCS3 in cardiomyocytes was confirmed by immunoblotting analysis, as previously described (Yajima et al., 2011). Wild-type (SOCS3f/f) and SOCS3cko mice were subjected to Sham or TAC operation for 4 weeks. SOCS3f/f mice exhibited characteristics of HF, as indicated by significant reductions in EF% and FS% compared with Sham groups, and this effect was aggravated in SOCS3cko mice (**Figure 3A**). Moreover, SOCS3cko mice developed severe cardiac hypertrophy and fibrosis, as indicated by increased heart size, HW/TL and LW/TL ratios, cross-sectional area of myocytes, and interstitial collagen deposition compared with SOCS3f/f mice following TAC (**Figures 3B–D**). Similarly, the mRNA levels of ANF, BNP, β-MHC, collagen I, and collagen III were markedly upregulated in SOCS3cko mice compared with SOCS3f/f animals after TAC (**Figures 3E,F**). Loss of SOCS3 also induced cardiomyocyte apoptosis (increased number of TUNEL-positive nuclei) in SOCS3cko hearts compared with SOCS3f/f hearts after TAC (**Figure 3G**). Finally, the protein levels of gp130, p-JAK2, and p-STAT3 were significantly upregulated in SOCS3cko mice compared with SOCS3f/f mice after TAC (**Figure 3H**). There was no difference in these pathological parameters between the two groups after Sham operation (**Figures 3A–H**). These results demonstrated that SOCS3cko mice were more susceptible to TAC-induced hypertrophic remodeling and dysfunction.

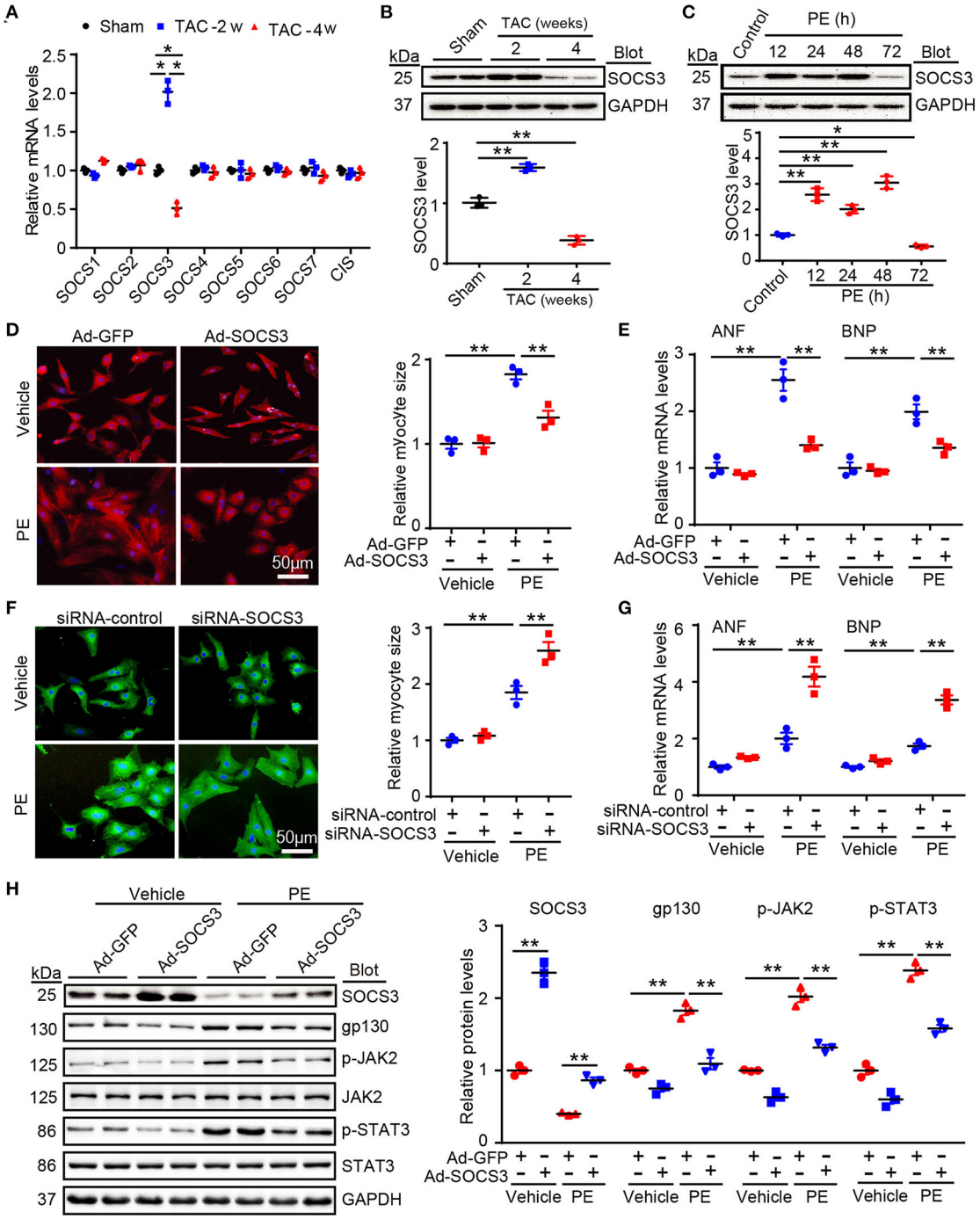

FIGURE 1 | SOCS3 regulated cardiomyocyte hypertrophy and gp130 signaling *in vitro*. **(A)** qPCR analyses of mRNA levels of eight SOCS family members, including SOCS1–7 and CIS, in hearts of Sham and TAC-treated mice at 2 and 4 weeks ($n = 3$ per group). **(B)** Immunoblotting analysis of SOCS3 protein levels in hearts of Sham and TAC-treated mice at 2 and 4 weeks (upper), and quantification (lower, $n = 3$ per group). **(C)** Immunoblotting analysis of SOCS3 protein levels in neonatal rat cardiomyocytes (NRCMs) exposed to PE (100 μmol/L) for different durations (upper), and quantification (lower, $n = 3$). **(D)** Images of double immunostaining (red indicates α-actinin, blue indicates DAPI-stained nuclei) of NRCMs infected with Ad-GFP control or SOCS3 after 72 h of PE treatment (left). Quantification of cell surface area (right, 150 cells counted per experiment, $n = 3$). Scale bar = 50 μm. **(E)** qPCR analyses of atrial natriuretic factor (ANF) and brain natriuretic peptide (BNP) mRNA expression in each group (right, $n = 3$). **(F)** Images of double immunostaining (green indicates α-actinin, blue indicates DAPI) of NRCMs infected with siRNA-control or siRNA-SOCS3 after 72 h of PE treatment (left). Quantification of cell surface area (right, 150 cells counted per experiment, $n = 3$). Scale bar = 50 μm. **(G)** qPCR analyses of ANF and BNP mRNA expression (right, $n = 3$). **(H)** Immunoblotting analysis of SOCS3, gp130, p-JAK2, JAK, p-STAT3, STAT3, and GAPDH protein levels in NRCMs infected with Ad-GFP control or SOCS3 after 72 h of PE treatment (left), and quantification (right, $n = 3$). Data are presented as mean ± SEM, and n represents number of samples per group. $^*P < 0.05$, $^{**}P < 0.01$.

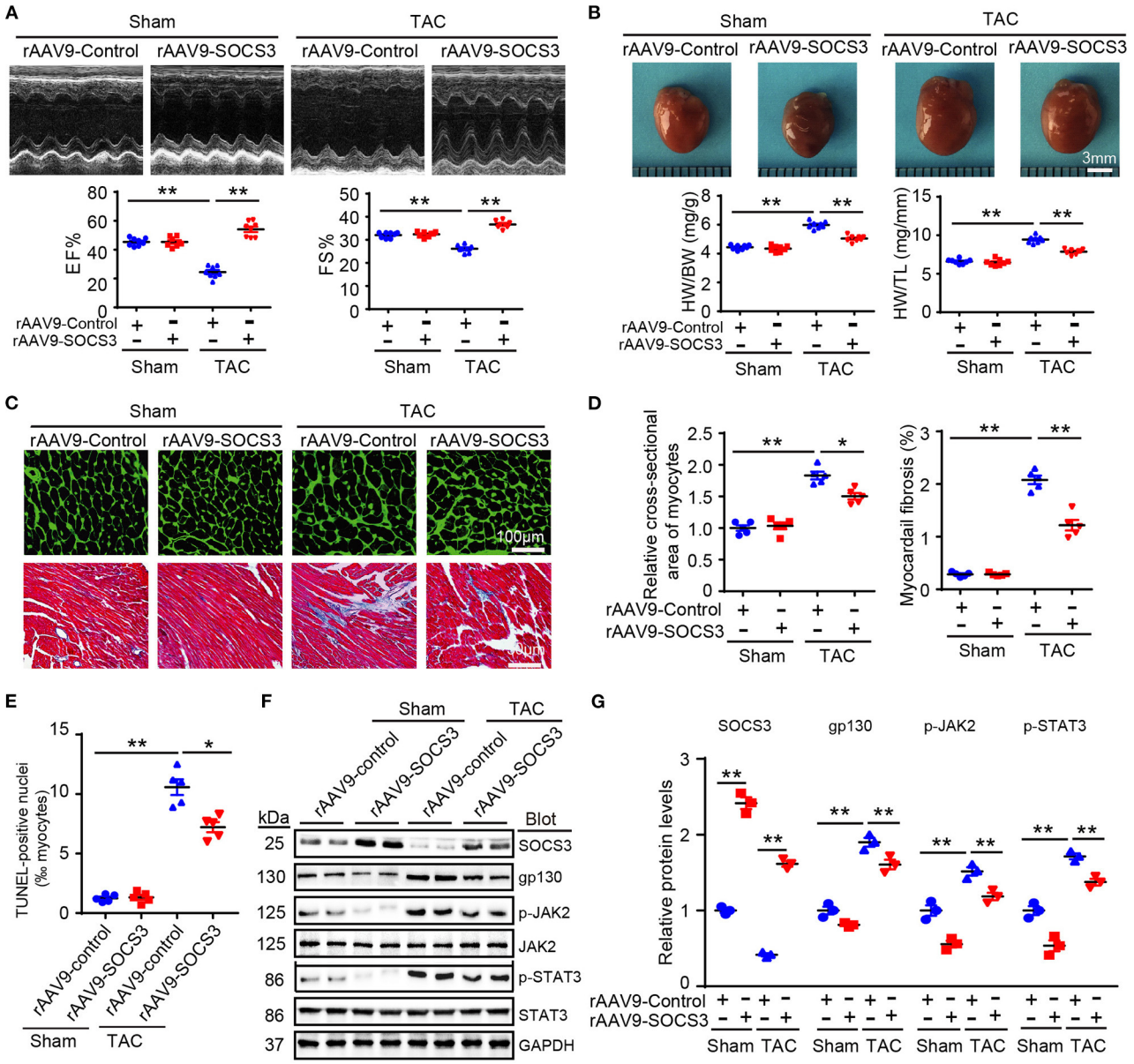

FIGURE 2 | SOCS3 overexpression in cardiomyocytes attenuated TAC-induced cardiac hypertrophy in mice. Wild-type (WT) mice were injected with rAAV9-SOCS3 or rAAV9-Control for 3 weeks, and then subjected to Sham or TAC operation for 4 weeks. **(A)** M-mode echocardiography of the left ventricle (top). Measurement of ejection fraction (EF%) and fractional shortening (FS%) (bottom, $n = 8$). **(B)** Images of hearts for size measurement, as photographed with a stereomicroscope (top), as well as heart weight/body weight (HW/BW) and HW/tibial length (TL) ratios (bottom, $n = 8$). **(C)** Cardiac sections were stained by FITC-labeled wheat germ agglutinin (WGA), and myocardial fibrosis was detected by Masson's trichrome staining. Scale bar = 100 μm. **(D)** Quantification of relative myocyte cross-sectional area (200 cells counted per heart) and fibrotic area ($n = 5$). **(E)** Quantification of percentages of TUNEL-positive nuclei ($n = 5$). **(F)** Immunoblotting analysis of SOCS3, gp130, p-JAK2, JAK, p-STAT3, STAT3, and GAPDH levels in hearts. **(G)** Quantification of relative protein levels ($n = 3$). Data are presented as mean ± SEM, and n represents number of samples per group. $^*P < 0.05$, $^{**}P < 0.01$.

Loss of SOCS3 Caused Activation of ER Stress and Autophagy Leading to Mitochondrial Dysfunction

Although ablation of SOCS3 in cardiomyocytes resulted in activation of gp130/JAK/STAT3 signaling leading to hypertrophic remodeling after long-term TAC (Yasukawa et al., 2001; Yajima et al., 2011), the underlying regulatory mechanism remains largely unknown. To identify novel targets or pathways involved in hypertrophic remodeling in SOCS3cko mice subjected to TAC, we performed proteomic analysis using an iTRAQ-based strategy (data are available via ProteomeXchange with identifier PXD014946). A total of 4,482 proteins were

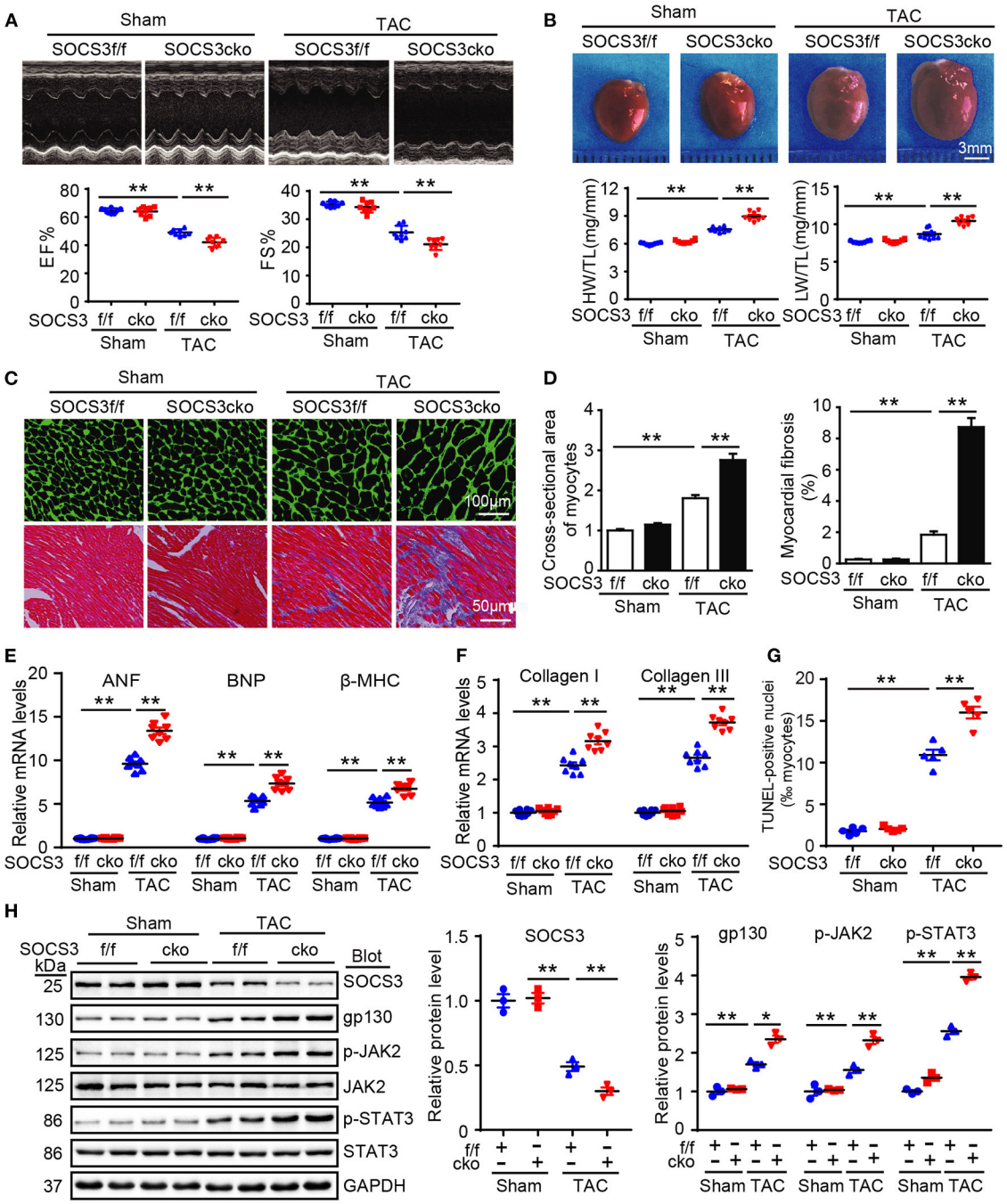

FIGURE 3 | Ablation of SOCS3 in cardiomyocytes aggravated cardiac hypertrophy in mice after pressure overload. WT (SOCS3f/f) and cardiomyocyte-specific SOCS3 knockout mice (SOCS3cko) were subjected to Sham or TAC operation for 4 weeks. **(A)** M-mode echocardiography of the left ventricle (top). Assessment of EF% and FS% (bottom, $n = 8$). **(B)** Images of hearts for size measurement (top). HW/BW and HW/TL ratios (bottom, $n = 8$). **(C)** Cardiac myocyte size and fibrosis were examined by FITC-labeled WGA staining and Masson's trichrome staining, respectively. Scale bar = 100 μm. **(D)** Quantification of relative myocyte cross-sectional area (200 cells counted per heart) and fibrotic area ($n = 5$). **(E)** qPCR analyses of ANF, BNP, and β-myosin heavy chain (β-MHC) mRNA levels ($n = 8$). **(F)** qPCR analyses of collagen I and collagen III mRNA levels ($n = 8$). **(G)** Quantification of percentages of TUNEL-positive nuclei ($n = 5$). **(H)** Immunoblotting analysis of SOCS3, gp130, p-JAK2, JAK, p-STAT3, STAT3, and GAPDH protein levels in hearts, and quantification ($n = 3$). GAPDH was used as an internal control. Data are presented as mean ± SEM, and *n* represents the number of animals per group. $^*P < 0.05$, $^{**}P < 0.01$.

identified from these pairs of heart tissues, among which 3,622 proteins had quantitative changes (**Figure 4A**). Differentially expressed proteins were selected by filtering with an average cut-off of 1.5-fold change in expression and p-value $\leq$ 0.05 when comparing TAC-treated heart samples with their corresponding Sham tissues (**Figure 4A**). A total of 534

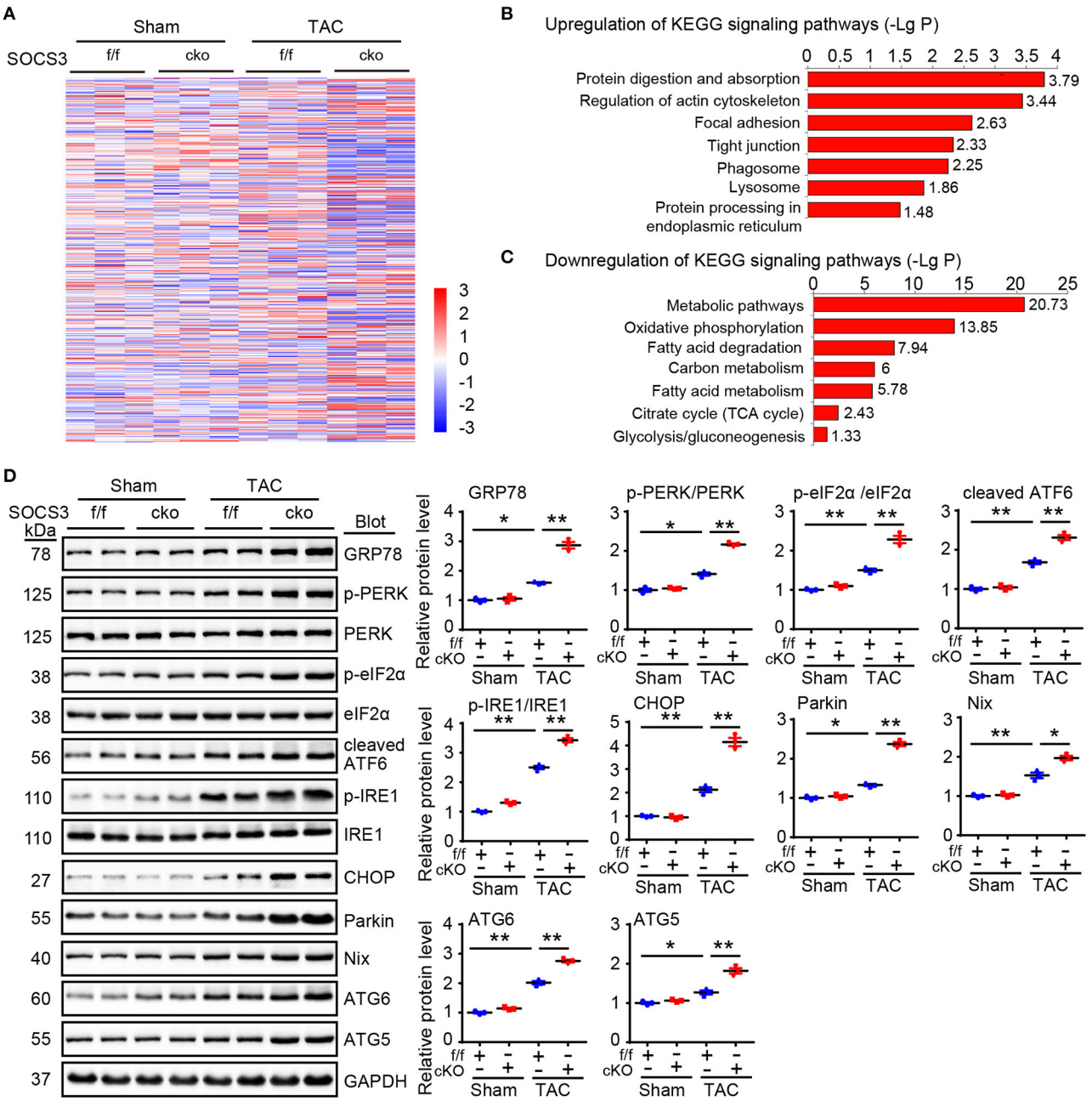

FIGURE 4 | Proteomic analysis of heart tissues. **(A)** WT (SOCS3f/f) and cardiomyocyte-specific SOCS3 knockout mice (SOCS3cko) were subjected to Sham or TAC operation for 4 weeks. Proteomic analysis was performed using an iTRAQ-based strategy. The heat map of the protein expression differences from the proteomics between SOCS3f/f and SOCS3cko mice. The red color indicates upregulation and blue is for downregulation. **(B,C)** Analysis of Kyoto Encyclopedia of Genes and Genomes pathway enrichment for differentially expressed proteins in heart tissues. LgP represents the logarithm of *P*-value. **(D)** Immunoblotting analysis of GRP78, p-PERK, PERK, p-eIF2α, eIF2α, cleaved ATF6, p-IRE1, IRE1, CHOP, Parkin, Nix, ATG6, and ATG5 protein levels in hearts, and quantification ($n = 3$). GAPDH was used as an internal control. Data are presented as mean ± SEM, and *n* represents the number of animals per group. $^{*}P < 0.05$, $^{**}P < 0.01$.

proteins qualified as differentially expressed between SOCS3f/f and SOCS3cko mice, including 297 upregulated and 237 downregulated proteins. Analysis of Kyoto Encyclopedia of Genes and Genomes (KEGG) pathway enrichment revealed that upregulated proteins in SOCS3cko mice were enriched for protein digestion and absorption, phagosomes and lysosomes, and protein processing in the endoplasmic reticulum (ER) (**Figure 4B**). Surprisingly, differentially expressed proteins that were downregulated were mostly localized to metabolic pathways and mitochondria. Indeed, 68 of 69 mitochondrial-related

proteins were downregulated in SOCS3cko mice after TAC, including proteins linked to mitochondria-related functions such as oxidative phosphorylation, the citrate cycle, carbon metabolism, fatty acid elongation and degradation, pyruvate metabolism, biosynthesis of unsaturated fatty acids, glycolysis, and gluconeogenesis (**Figure 4C**). These results suggested that increased activation of ER stress and autophagy, and decreased mitochondrial function may play a critical role in cardiac dysfunction of SOCS3cko mice.

We next focused how SOCS3 deletion stimulated activation of ER stress and autophagy in cardiomyocytes in response to TAC stress. We detected several markers of ER stress and mitochondrial autophagy (also known as mitophagy) in hearts of SOCS3f/f and SOCS3cko mice after TAC. Immunoblotting analysis showed that protein levels of GRP78 (also known as BiP and HSPA5), phosphorylated dsRNA-activated protein kinase-like ER kinase (p-PERK, Thr-982), p-elF2α, cleaved ATF6 (p50 fragment), phosphorylated inositol-requiring kinase 1 (p-IRE1, Ser724), CHOP, Parkin, Nix, ATG6 (Beclin 1), and ATG5 proteins were significantly increased in SOCS3cko mice compared with SOCS3f/f animals after TAC (**Figure 4D**), indicating that SOCS3 is involved in controlling GRP78-mediated ER stress-mitophagy pathway in the heart after TAC.

To further confirm the effect of SOCS3 deletion on mitophagy *in vitro*, NRCMs were transfected with small interfering RNA (siRNA) against SOCS3 (siRNA-SOCS3) or scrambled control (siRNA-control), and then stained with Mtphagy Dye and Lyso Dye after 24 h of PE or vehicle treatment. Consistent with immunoblotting results, PE stimulation significantly increased induction of mitophagy (red) and mitochondrial autophagosomes (green) in siRNA-control-treated cells, but was further enhanced by siRNA-SOCS3 (**Supplementary Figure 3A**). Moreover, PE-induced increase of mitochondrial superoxide [as indicated by MitoSOX (red) and MitoTracker Green (green)] and reduction of mitochondrial membrane potential ($\Delta\Psi$m; stained by MitoProbe JC-1) in cardiomyocytes transfected with siRNA-control was accelerated by transfection of siRNA-SOCS3 (**Supplementary Figures 3B,C**). Collectively, these results suggested that SOCS3 ablation in cardiomyocytes resulted in marked activation of ER stress and mitophagy leading to mitochondrial dysfunction, which may contribute to progression of cardiomyocyte apoptosis, hypertrophy, and HF.

SOCS3 Regulated GRP78 Ubiquitination and Degradation by the Proteasome

GRP78 protein is a marker of ER stress and major ER chaperone that controls the activation of transmembrane ER stress sensors. Prompted by our results showing that GRP78 protein (**Figure 4D**), but not mRNA (**Supplementary Figure 2E**), was markedly upregulated in SOCS3cko mice compared with SOCS3f/f controls after TAC, we first examined whether SOCS3 associated with GRP78 protein in NRCMs. Co-immunoprecipitation (Co-IP) assays showed that endogenous SOCS3 protein was precipitated by an anti-GRP78 antibody, but not by a non-specific IgG control (**Figure 5A**). The interaction between SOCS3 and GRP78 was confirmed by an *in vitro* glutathione-S-transferase (GST) pull-down assay (**Figure 5B**). Furthermore, an immunoprecipitation (IP) assay was performed in human embryonic kidney (HEK) 293T cells transfected with Myc-SOCS3 and Flag-GRP78. We detected Myc-SOCS3 in the Flag-GRP78 immune complex, whereas no Myc-SOCS3 was found in controls (**Figure 5C**), indicating that SOCS3 interacted directly with GRP78.

To examine whether SOCS3 regulates GRP78 ubiquitination as an E3 ligase, we con-transfected HEK293T cells with plasmids encoding Myc-ubiquitin, Flag-GRP78, and either GFP-tagged wild-type (WT) SOCS3 or a catalytically inactive mutant (ΔSB: deletion of SB domain). SOCS3 overexpression (WT) significantly enhanced GRP78 ubiquitination, especially Lys48-linked polyubiquitination, whereas this effect was markedly abrogated in cells transfected with SOCS3 (ΔSB) plasmid (**Figure 5D**). Moreover, upon examining the effect of endogenous SOCS3 on GRP78 ubiquitination in mice, we found that TAC markedly increased GRP78 ubiquitination in SOCS3f/f mice compared with Sham groups, but this effect was remarkably attenuated in SOCS3cko hearts (**Figure 5E**). Conversely, the TAC-induced response was further enhanced in rAAV9-SOCS3-injected mice compared with rAAV9-ZsGreen control after TAC operation (**Figure 5F**).

Next, we examined the involvement of the proteasome in SOCS3-mediated degradation of GRP78, a pulse-chase assay was performed in NRCMs using cycloheximide (CHX, a eukaryote protein synthesis inhibitor) with or without MG-132 (a proteasome inhibitor). We discovered that knockdown of SOCS3 by siRNA markedly prolonged the half-life of GRP78 protein compared with the siRNA-control (**Figure 5G**). Conversely, SOCS3 overexpression with Ad-SOCS3 yielded GRP78 protein with a short half-life compared with Ad-GFP control, but this reduction was completely reversed by MG-132 treatment (**Figure 5H**), suggesting that SOCS3 promotes GRP78 degradation via the proteasome.

GRP78 Knockdown Abrogated Pressure Overload-Induced Cardiac Hypertrophy in SOCS3cko Mice

To assess whether GRP78 mediates cardiac hypertrophy in SOCS3cko mice after TAC, we injected SOCS3f/f and SOCS3cko mice with rAAV9-siRNA to knock down endogenous GRP78 expression. After 3 weeks of injection, all mice were then subjected to TAC for 4 additional weeks. Injection of AAV9-siGRP78 significantly downregulated GRP78 protein levels in the heart by about 45–50% compared with rAAV9-siControl (**Figure 6D**). Moreover, consistent with results described above (**Figure 3**), after 4 weeks of TAC, SOCS3cko mice showed marked cardiac dysfunction (reduced EF% and FS%), hypertrophy (increased heart size, ratios of HW/BW and HW/TL and cross-sectional areas of myocytes), and interstitial fibrosis, as well as upregulation of ANF, BNP, collagen I, and collagen III mRNA expression compared with SOCS3f/f mice after injection of rAAV9-siControl (**Figures 6A–C**; **Supplementary Figures 4A,B**, lane 3 vs. 1). Conversely, these deleterious effects were markedly reversed in SOCS3cko mice injected with rAAV9-siGRP78

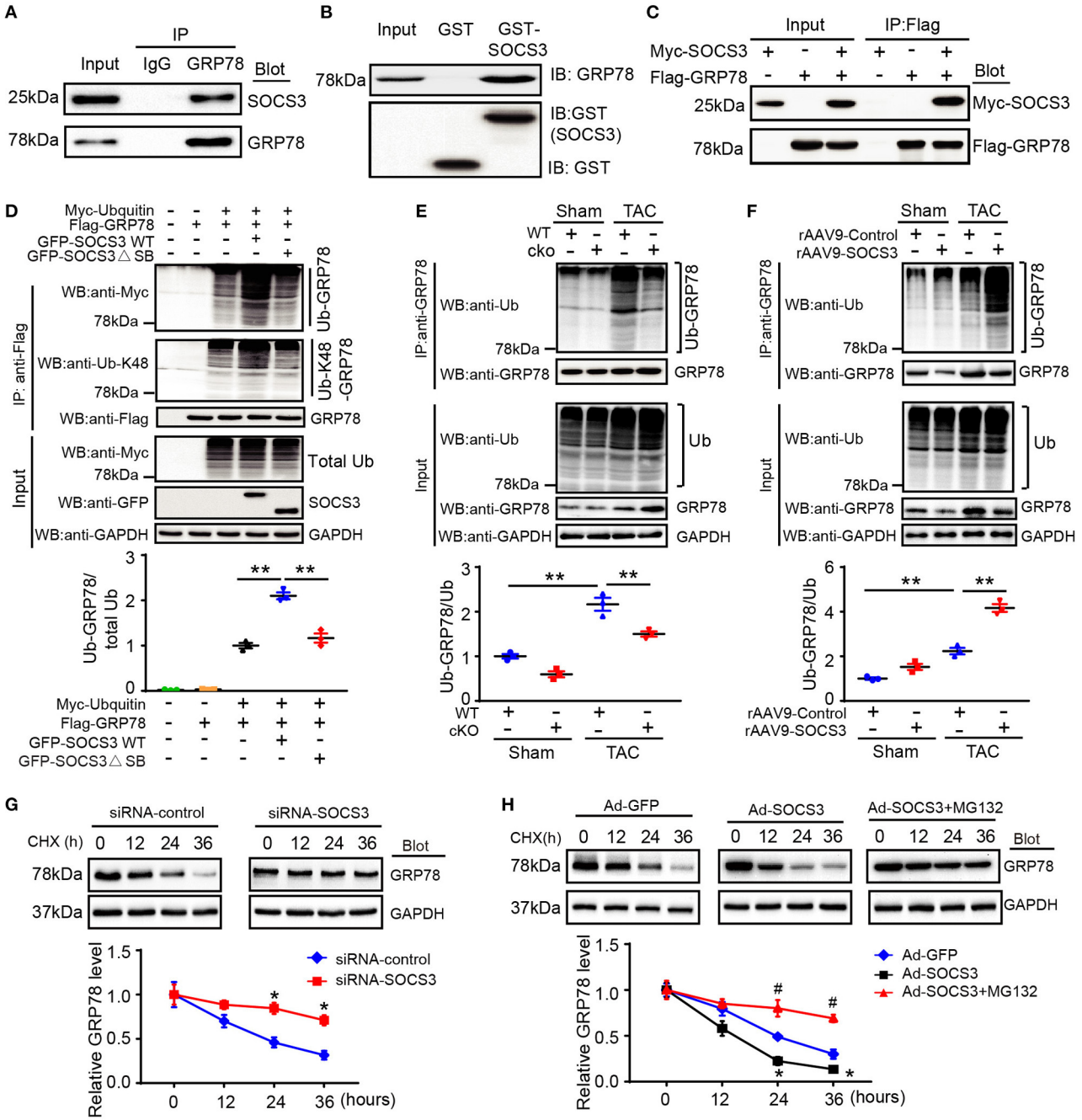

FIGURE 5 | SOCS3 associated with GRP78 to promote its ubiquitination and degradation. **(A)** Endogenous SOCS3 and GRP78 protein interactions in primary cardiomyocyte lysates were evaluated by immunoprecipitation with IgG control or anti-GRP78 antibody, and then analyzed by immunoblotting (IB) with antibodies against SOCS3 and GRP78. **(B)** Protein interactions of SOCS3 with GRP78 in GST pull-down assay *in vitro*. The ability of GRP78 (top) expressed in HEK293 cells to be retained by GST or a GST-SOCS3 fusion protein was analyzed by IB after binding reactions. **(C)** HEK293 cells were transfected with the indicated plasmids. Equal amounts of protein lysates were immunoprecipitated with anti-Flag antibody and analyzed by IB with an anti-Flag (GRP78) or anti-Myc (SOCS3) antibody. **(D)** HEK293 cells were transfected with plasmids encoding Myc-tagged ubiquitin (Ub), Flag-tagged GRP78, GFP-tagged SOCS3 (WT) or its mutant (ΔSB, inactive form of SOCS3) with different combination. Equal amounts of protein lysates were immunoprecipitated with an anti-Flag antibody and analyzed by IB with anti-Myc (Ub), anti-Ub-K48 (Lys48-linked polyubiquitin) or anti-Flag (GRP78) antibodies (top). Input showed the expression of corresponding proteins in whole cell lysates (middle). Quantification of ubiquitinated GRP78 (bottom, $n = 3$). **(E)** Lysates were extracted from heart tissues of WT (SOCS3f/f) or cko (SOCS3cko) mice after Sham or TAC, and then immunoprecipitated with an anti-GRP78 antibody. IB analysis of GRP78 ubiquitination with anti-Ub or GRP78 antibody (top). Input showed IB analysis of each protein with its corresponding antibody (middle). Quantification of relative ubiquitinated GRP78 level (bottom, $n = 3$). **(F)** Lysates were isolated from heart tissues of rAAV9-Control or rAAV9-SOCS3-injected mice after Sham or TAC, and then immunoprecipitated with an anti-GRP78 antibody. IB analysis of GRP78 ubiquitination

(Continued)

FIGURE 5 | with anti-Ub or GRP78 antibody (top). Input showed IB analysis of each protein with its corresponding antibody (middle). Quantification of the relative ubiquitinated GRP78 level (bottom, $n = 3$). **(G,H)** NRCMs were infected with siRNA-control, siRNA-SOCS3, Ad-GFP, or Ad-SOCS3, and then treated with cycloheximide (CHX; 10 μM) for the indicated durations. Representative IB analysis of GRP78 and SOCS3 protein levels for each group (top), and quantification of GRP78 protein level (bottom, $n = 3$). Data are presented as mean ± SEM, and *n* represents the number of animals per group. $^{*}P < 0.05$, $^{**}P < 0.01$, $^{\#}P < 0.05$ compared with Ad-SOCS3 + MG132.

(**Figures 6A–C**; **Supplementary Figures 4A,B**, lane 4 vs. 3). Similarly, rAAV9-siGRP78 injection of SOCS3f/f mice also improved TAC-induced cardiac dysfunction and hypertrophic responses compared with rAAV9-siControls (**Figures 6A–C**; **Supplementary Figures 4A,B**, lane 2 vs. 1). Correspondingly, GRP78 knockdown in SOCS3cko or SOCS3f/f mice reduced protein levels of p-PERK, cleaved ATF6, CHOP, and Parkin compared with rAAV9-siControl mice after TAC (**Figure 6D**). Together, these *in vivo* findings suggested that SOCS3 ablation aggravated cardiac hypertrophy and dysfunction by enhancing GRP78 and its downstream effectors.

Inhibition of ER Stress With 4-PBA Blunted Cardiac Hypertrophy in SOCS3cko Mice Induced by Pressure Overload

To further verify the involvement of GRP78-mediated activation of ER stress in TAC-induced cardiac hypertrophy in SOCS3cko mice, SOCS3f/f and SOCS3cko mice were administered 4-PBA, a reported inhibitor of ER stress that can attenuate pressure overload-induced hypertrophy (Luo et al., 2015). As expected, 4-PBA treatment reduced GRP78 expression in both SOCS3f/f and SOCS3cko mice after TAC (**Supplementary Figures 5E,F**). Consistent with observations from siRNA-GRP78 knockout experiments (**Figure 6**), TAC-induced increases in cardiac dysfunction (reduced EF% and FS%), hypertrophy (increased heart size, ratios of HW/BW and HW/TL and cross-sectional areas of myocytes), and interstitial fibrosis were enhanced in SOCS3cko mice compared with SOCS3f/f mice (**Supplementary Figures 5A–D**, lane 2 vs. 1), but were significantly reduced in SOCS3cko mice treated with 4-PBA compared with vehicle (**Supplementary Figures 5A–D**, lane 4 vs. 2). Furthermore, 4-PBA administration in SOCS3f/f mice also showed marked cardioprotection compared with vehicle control after TAC (**Supplementary Figures 5A–D**, lane 3 vs. 1). The preventive effect of 4-PBA treatment on activation of ER stress and autophagy markers (p-PERK, cleaved ATF6, CHOP, and Parkin) was further confirmed in SOCS3cko and SOCS3f/f mice (**Supplementary Figures 5E,F**). Thus, these *in vivo* observations confirmed that the prohypertrophic effect of SOCS3 ablation resulted from activation of ER stress.

DISCUSSION

In this study using primary cardiomyocytes, SOCS3cko mice, and rAAV9-injected wild-type mice, we identified a novel mechanism for SOCS3 to regulate cardiac hypertrophy and dysfunction through targeting of GRP78-mediated ER stress and mitophagy in a TAC-induced model. Prolonged pressure overload significantly downregulated SOCS3 expression and reduced GRP78 ubiquitination and degradation, which resulted in activation of ER stress and mitophagy, thereby leading to cardiac hypertrophy, apoptosis and dysfunction. This effect was aggravated in SOCS3cko mice, but attenuated in SOCS3-overexpression mice. Moreover, knockdown of GRP78 or inhibition of ER-stress with 4-PBA significantly attenuated ER stress and mitophagy, and restored cardiac hypertrophy and dysfunction in SOCS3cko mice (**Figure 7**). Thus, our novel evidence suggests that SOCS3 may be an important therapeutic target for antihypertrophic treatments.

Cardiac hypertrophy develops as an adaptive response to injury or increased workloads to maintain cardiac function. However, sustained hypertrophic remodeling contributes to progressive cardiac dysfunction and HF, although its mechanisms remain largely unknown. The ubiquitin-proteasome system is an important cellular protein degradation mechanism. Three enzymes (E1, E2, and E3) are involved in protein ubiquitination. Among them, E1 and E2 enzymes prepare the ubiquitin chain formation that is subsequently attached to the protein substrate, which is catalyzed by the E3 enzyme. During recent years, several E3 enzymes, such as F-box protein atrogin-1, muscle ring finger-1, TRAF6, and CDC20 have been reported to play roles in the development of cardiac hypertrophy through different mechanisms (Arya et al., 2004; Li et al., 2004, 2007; Ji et al., 2016; Xie et al., 2018). As an E3 ubiquitin ligase, SOCS3 targets inflammatory cytokine receptor components for proteasomal degradation. Moreover, SOCS3 is upregulated in TAC-induced hypertrophic heart (Yasukawa et al., 2001), but is reduced in failing human heart (Podewski et al., 2003; Margulies et al., 2005; Mann et al., 2010). Consistent with these data, our results also confirmed that SOCS3 expression was upregulated in hypertrophic hearts (2 weeks of TAC), but markedly downregulated in failing hearts (4 weeks of TAC, **Figures 1A,B**). These results suggest that SOCS3 may contribute to the transition from the adaptive cardiac hypertrophy to heart failure following pressure overload. Indeed, SOCS3 regulates cardiac hypertrophy and dysfunction partially through gp130/JAK signaling after hypertrophic stimulation (Yasukawa et al., 2001; Yajima et al., 2011). Until now, gp130 signals and myofilament $Ca2^{+}$ sensitivity have been considered as the main pathways for SOCS3 to regulate hypertrophic response (Yasukawa et al., 2001; Yajima et al., 2011); Moreover, the present study also confirmed that SOCS3 was a critical regulator for TAC-induced cardiomyocyte hypertrophy and dysfunction *in vivo* and *in vitro* (**Figures 1–3**). However, whether other mechanisms, especially ER stress-mediated autophagy, participate in the cardioprotection elicited by SOCS3 was unknown.

The ER plays a crucial role in the folding of secretory and membrane proteins, as well as lipid biosynthesis and calcium homeostasis. Various types of stress such as hypoxia, ischemia, and oxidative stress, can impair ER function, leading

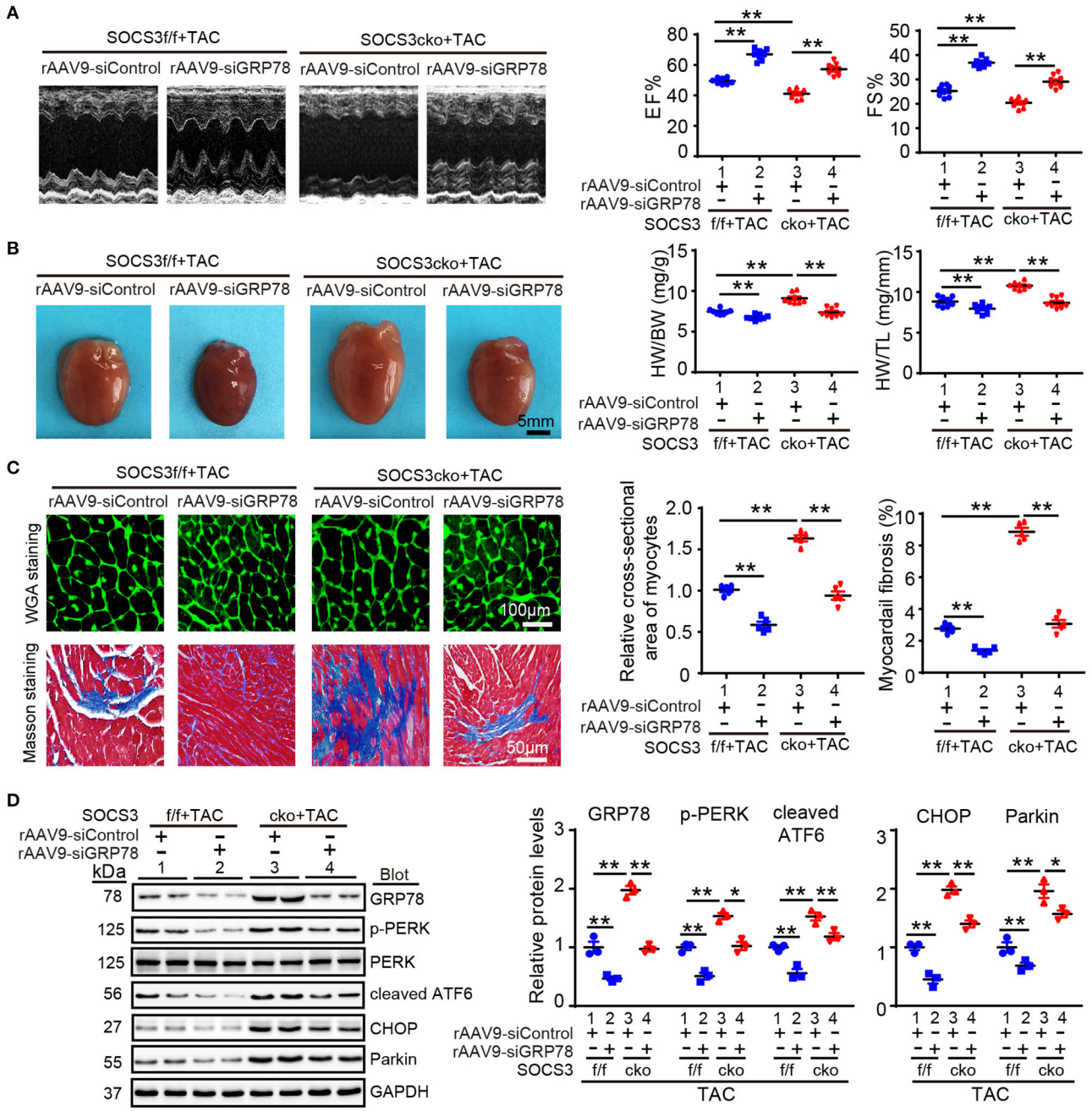

FIGURE 6 | Knockdown of GRP78 by AAV9-siRNAs abolished TAC-induced cardiac hypertrophy and dysfunction in SOCS3cko mice. SOCS3f/f and SOCS3cko mice were injected with rAAV9-siControl or rAAV9-SOCS3 for 3 weeks, and then subjected to TAC surgery for an additional 4 weeks. **(A)** M-mode echocardiography of the left ventricle (left). Assessment of EF% and FS% (right, $n = 8$). **(B)** Images of hearts for size measurement (left). Quantification of HW/BW and HW/TL ratios (right, $n = 8$). Scale bar = 5mm. **(C)** FITC-labeled WGA staining of cardiac myocytes and Masson's trichrome staining of myocardial fibrosis (left). Scale bar = 100 μm. Quantification of the relative cross-sectional area of myocytes (200 cells counted per heart) and fibrotic area (right, $n = 5$). **(D)** Immunoblotting analysis of GRP78, p-PERK, PERK, cleaved ATF6, CHOP, and Parkin protein levels in heart tissues, and quantification ($n = 3$). GAPDH was used as an internal control. Data are presented as mean ± SEM, and n represents number of animals per group. $^*P < 0.05$, $^{**}P < 0.01$.

to accumulation of misfolded and unfolded proteins – a process known as ER stress (Gotoh et al., 2011). ER stress can trigger the unfolded protein response (UPR) to induce autophagy through a number of signaling pathways (Hoyer-Hansen and Jaattela, 2007; B'Chir et al., 2013; Rashid et al., 2015). Moreover, Prolonged or severe ER stress leads to cell apoptosis, cardiac hypertrophy, and dysfunction (Yamaguchi et al., 2003; Fu et al., 2010; Minamino and Kitakaze, 2010; Yao et al., 2017). For example,

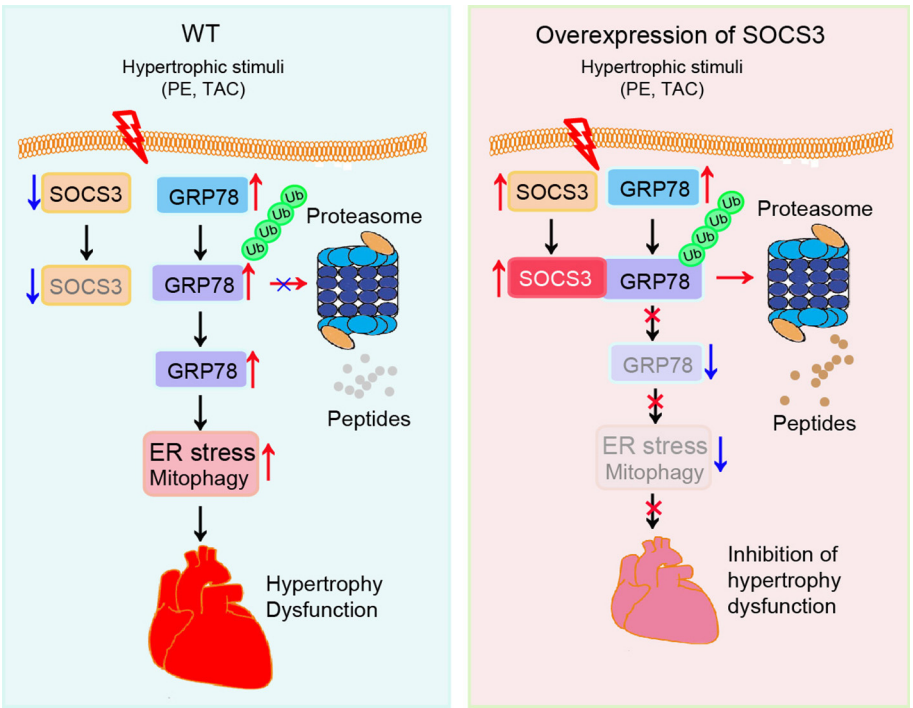

FIGURE 7 | A working model of SOCS3-mediated cardioprotection in pressure overloaded mice. Pressure overload induces reduction of SOCS3 in cardiomyocytes, which in turn reduces GRP78 degradation by the proteasome and causes activation of ER stress and mitophagy, thereby leading to cardiac hypertrophy and dysfunction. Conversely, these effects are attenuated by overexpression of SOCS3.

tunicamycin-induced ER stress results in cardiac dysfunction, oxidative stress, apoptosis through excessive autophagy, which can be attenuated by protein tyrosine phosphatase 1B (PTP1B) ablation (Wang S. et al., 2017). Further, mitochondrial aldehyde dehydrogenase (ALDH2) protects against LPS-induced cardiac contractile dysfunction via inhibition of ER stress and autophagy via CAMKKβ/AMPK/mTOR signaling pathways (Pang et al., 2019). It is reported that autophagy induced by ER stress mainly includes the ER stress-mediated autophagy and ER-phagy. The former is characterized by the generation of autophagosomes that include protein aggregates and damaged organelles. While the ER-phagy selectively degradates ER fragments. Both of them not only have differences, but also have close connections (Rashid et al., 2015; Grumati et al., 2018). Mitophagy is an autophagic pathway that exclusively removes damaged mitochondria. Several effectors, such as Parkin and Nix, have been implicated in mitophagy activation (Yussman et al., 2002; Diwan et al., 2008; Narendra et al., 2012; Han et al., 2017). Importantly, the UPR-autophagy pathway plays crucial roles in the development of cardiovascular diseases, such as HF, hypertrophy, and ischemic heart diseases (Yussman et al., 2002; Diwan et al., 2008; Minamino et al., 2010; Narendra et al., 2012; Han et al., 2017; Zhang et al., 2018). These findings prompted us to further investigate whether ER stress-mediated autophagy or ER-phagy is involved in the cardioprotective mechanism of SOCS3 against pressure overload. Here, quantitative proteomic analysis and KEGG signaling pathway enrichment revealed that SOCS3 ablation predominantly stimulated activation of ER stress, autophagy and reduced mitochondrial function but not ER-phagy in the heart (**Figures 4B,C**). These effects were further confirmed by upregulation of p-PERK, p-eIF2α, cleaved ATF6, p-IRE1, CHOP, Nix, Parkin, ATG6, and ATG5 proteins in SOCS3cko mice compared with SOCS3f/f animals detected by immunoblotting analysis (**Figure 4D**), as well as the increased mitophagy, mitochondrial superoxide production and reduced mitochondrial membrane potential in siRNA-SOCS3-transfected cardiomyocytes examined by immunostaining (**Supplementary Figures 3A–C**). Overall, this study provides novel evidence that SOCS3 ablation accelerates cardiac hypertrophy and dysfunction after pressure overload, possibly through activation of ER stress and mitophagy pathways. However, whether ER-phagy is involved in the development of pathological hypertrophy remains to be explored in the future.

There are at least three main ER stress sensors (PERK/eIF2α, ATF6/CHOP, and IRE1) on the ER membrane, which activate respective transcriptional cascades (ATF4, cleaved ATF6, and sXBP1, respectively) with a concomitant effect on protein translation and cell survival or death programs (Minamino et al., 2010; Gotoh et al., 2011; Senft and Ronai, 2015). GRP78 is a major ER chaperone that acts as the master regulator of the UPR through binding with inactive forms of ER-stress sensors. Increased GRP78 expression also serves as an indicator of ER stress (Gotoh et al., 2011; Wang S. et al., 2018). GRP78 is found not only in the ER lumen, but also in the cytosol, nucleus, mitochondria, and plasma membrane. Notably, intracellular GRP78 is involved in

regulating ER stress-induced UPR signaling and apoptosis (Ni et al., 2011). Selective inhibition of intracellular GRP78 in the lung endothelium attenuated lipopolysaccharide-induced lung inflammatory responses (Leonard et al., 2019). Moreover, GRP78 can increase p53 nuclear localization, which in turn induces autophagy (Wang Y. et al., 2017). Interestingly, GRP78 was first reported to be increased in failing human hearts in 2004 (Okada et al., 2004). Subsequent studies confirmed upregulation of GRP78 protein levels in hearts from isoproterenol- or TAC-treated mice, as well as human dilated cardiomyopathy patients (Fu et al., 2010; Yao et al., 2017). A recent study demonstrates that ischemia/reperfusion (I/R) induces GRP78 expression in cardiomyocytes, which stimulates Akt signaling and inhibits oxidative stress leading to protection from I/R injury (Bi et al., 2018). However, the role of GRP78 in TAC-induced cardiac hypertrophy remains unknown. Here, we found that knockdown of GRP78 by siRNA significantly attenuated TAC-induced cardiac hypertrophy and dysfunction compared with siRNA control (**Figure 6**), indicating that GRP78 promotes cardiac hypertrophic remodeling and HF.

It has been reported that post-translational modifications such as oxidation, acetylation and ubiquitination regulate GRP78 stability and activation in different cell types (Chang et al., 2016; Kim et al., 2018; Ning et al., 2019). The E3 ubiquitin ligase GP78 (also known as AMFR and RNF45) can promote GRP78 ubiquitylation for proteasomal degradation (Chang et al., 2016). Conversely, OTUD3 interacts with and deubiquitylates GRP78, leading to its stability in cancer cells (Du et al., 2019). However, significant changes in GP78 and OTUD3 mRNA were not observed in Ang II-infused mouse hearts by microarray, suggesting that they were not involved in regulation of GRP78 in cardiomyocytes. Here, we confirmed that TAC-induced upregulation of GRP78 protein was enhanced in SOCS3cko mice (**Figure 4D**). Moreover, SOCS3 was found to directly associate with GRP78 (**Figures 5A–C**). SOCS3 overexpression increased GRP78 ubiquitination in cells and mice (**Figures 5D,F**), In contrast, SOCS3 inactivation (ΔSB) or knockout reduced GRP78 ubiquitination (**Figures 5D,E**). Further, SOCS3 knockdown enhanced GRP78 protein levels (**Figure 5G**). Conversely, SOCS3 overexpression reduced GRP78 protein levels, but this decrease was completely reversed by the proteasome inhibitor MG-132 (**Figure 5H**), indicating that SOCS3 directly interacts with and promotes GRP78 ubiquitination and degradation by the proteasome. Importantly, GRP78 knockdown or inhibition of ER stress with 4-PBA not only effectively improved TAC-induced cardiac contractile dysfunction, hypertrophy, and fibrosis, but also suppressed ER stress and mitophagy in SOCS3f/f and SOCS3cko hearts (**Figures 6**, **7**), suggesting that GRP78-mediated ER stress plays an important role in the development of cardiac hypertrophy-related dysfunction. Overall, these results indicate that SOCS3 modulates cardiac hypertrophy and function, likely by targeting GRP78-mediated ER stress and mitophagy.

In conclusion, we discovered a novel mechanism for SOCS3 in cardioprotection, as it attenuated pressure overload-induced hypertrophic remodeling. SOCS3 most likely targets GRP78 ubiquitination for proteasomal degradation, which blocks activation of ER stress and mitophagy pathways to inhibit hypertrophic remodeling and dysfunction. Our data highlight that SOCS3 is a potential therapeutic target for treatment of hypertrophic diseases. Further studies are needed to identify activators for SOCS3, and to determine whether activation or upregulation of SOCS3 may be a therapeutic strategy for hypertrophic diseases in humans.

DATA AVAILABILITY STATEMENT

The datasets presented in this study can be found in online repositories. The names of the repository/repositories and accession number(s) can be found in the article/**Supplementary Material**.

ETHICS STATEMENT

The animal study was reviewed and approved by Committee on the Ethics of Animal Experiments of Dalian Medical University.

AUTHOR CONTRIBUTIONS

BZ and H-HL conceived the project. SL, W-CS, Y-LZ, Q-YL, J-WL, G-RS, and X-LM performed *in vivo* and *in vitro* experiments, and analyzed the results. SL and H-HL performed and analyzed biochemical and biophysical experiments. BZ and H-HL wrote the manuscript with input from all authors. All authors contributed to the article and approved the submitted version.

FUNDING

This work was supported by grants from the National Natural Science Foundation of China (81330003, 81630009, and 31571170, H-HL).

SUPPLEMENTARY MATERIAL

The Supplementary Material for this article can be found online at: https://www.frontiersin.org/articles/10.3389/fcell.2021.629932/full#supplementary-material

REFERENCES

Arya, R., Kedar, V., Hwang, J. R., McDonough, H., Li, H. H., Taylor, J., et al. (2004). Muscle ring finger protein-1 inhibits PKC{epsilon} activation and prevents cardiomyocyte hypertrophy. *J. Cell Biol.* 167, 1147–1159. doi: 10.1083/jcb.200402033

B'Chir, W., Maurin, A. C., Carraro, V., Averous, J., Jousse, C., Muranishi, Y., et al. (2013). The eIF2alpha/ATF4 pathway is essential for stress-induced autophagy gene expression. *Nucleic Acids Res.* 41, 7683–7699. doi: 10.1093/nar/gkt563

Bi, X., Zhang, G., Wang, X., Nguyen, C., May, H. I., Li, X., et al. (2018). Endoplasmic reticulum chaperone GRP78 protects heart from

ischemia/reperfusion injury through Akt activation. *Circ. Res.* 122, 1545–1554. doi: 10.1161/CIRCRESAHA.117.312641

Chang, Y. W., Tseng, C. F., Wang, M. Y., Chang, W. C., Lee, C. C., Chen, L. T., et al. (2016). Deacetylation of HSPA5 by HDAC6 leads to GP78-mediated HSPA5 ubiquitination at K447 and suppresses metastasis of breast cancer. *Oncogene* 35, 1517–1528. doi: 10.1038/onc.2015.214

Diwan, A., Wansapura, J., Syed, F. M., Matkovich, S. J., Lorenz, J. N., and Dorn, G. W. II. (2008). Nix-mediated apoptosis links myocardial fibrosis, cardiac remodeling, and hypertrophy decompensation. *Circulation* 117, 396–404. doi: 10.1161/CIRCULATIONAHA.107.727073

Du, T., Li, H., Fan, Y., Yuan, L., Guo, X., Zhu, Q., et al. (2019). The deubiquitylase OTUD3 stabilizes GRP78 and promotes lung tumorigenesis. *Nat. Commun.* 10:2914. doi: 10.1038/s41467-019-10824-7

Fischer, P., and Hilfiker-Kleiner, D. (2007). Survival pathways in hypertrophy and heart failure: the gp130-STAT3 axis. *Basic Res. Cardiol.* 102, 279–297. doi: 10.1007/s00395-007-0658-z

Fu, H. Y., Okada, K., Liao, Y., Tsukamoto, O., Isomura, T., Asai, M., et al. (2010). Ablation of C/EBP homologous protein attenuates endoplasmic reticulum-mediated apoptosis and cardiac dysfunction induced by pressure overload. *Circulation* 122, 361–369. doi: 10.1161/CIRCULATIONAHA.109.917914

Gotoh, T., Endo, M., and Oike, Y. (2011). Endoplasmic reticulum stress-related inflammation and cardiovascular diseases. *Int. J. Inflam.* 2011:259462. doi: 10.4061/2011/259462

Grumati, P., Dikic, I., and Stolz, A. (2018). ER-phagy at a glance. *J. Cell Sci.* 131:jcs217364. doi: 10.1242/jcs.217364

Han, K., Hassanzadeh, S., Singh, K., Menazza, S., Nguyen, T. T., Stevens, M. V., et al. (2017). Parkin regulation of CHOP modulates susceptibility to cardiac endoplasmic reticulum stress. *Sci. Rep.* 7:2093. doi: 10.1038/s41598-017-02339-2

Heineke, J., and Molkentin, J. D. (2006). Regulation of cardiac hypertrophy by intracellular signalling pathways. *Nat. Rev. Mol. Cell Biol.* 7, 589–600. doi: 10.1038/nrm1983

Hilton, D. J., Richardson, R. T., Alexander, W. S., Viney, E. M., Willson, T. A., Sprigg, N. S., et al. (1998). Twenty proteins containing a C-terminal SOCS box form five structural classes. *Proc. Natl. Acad. Sci. U. S. A.* 95, 114–119. doi: 10.1073/pnas.95.1.114

Hirota, H., Yoshida, K., Kishimoto, T., and Taga, T. (1995). Continuous activation of gp130, a signal-transducing receptor component for interleukin 6-related cytokines, causes myocardial hypertrophy in mice. *Proc. Natl. Acad. Sci. U. S. A.* 92, 4862–4866. doi: 10.1073/pnas.92.11.4862

Hoyer-Hansen, M., and Jaattela, M. (2007). Connecting endoplasmic reticulum stress to autophagy by unfolded protein response and calcium. *Cell Death Differ.* 14, 1576–1582. doi: 10.1038/sj.cdd.4402200

Ji, Y. X., Zhang, P., Zhang, X. J., Zhao, Y. C., Deng, K. Q., Jiang, X., et al. (2016). The ubiquitin E3 ligase TRAF6 exacerbates pathological cardiac hypertrophy via TAK1-dependent signalling. *Nat. Commun.* 7:11267. doi: 10.1038/ncomms11267

Kim, S. Y., Kim, H. J., Kim, D. H., Han, J. H., Byeon, H. K., Lee, K., et al. (2018). HSPA5 negatively regulates lysosomal activity through ubiquitination of MUL1 in head and neck cancer. *Autophagy* 14, 385–403. doi: 10.1080/15548627.2017.1414126

Kunisada, K., Tone, E., Fujio, Y., Matsui, H., Yamauchi-Takihara, K., and Kishimoto, T. (1998). Activation of gp130 transduces hypertrophic signals via STAT3 in cardiac myocytes. *Circulation* 98, 346–352. doi: 10.1161/01.CIR.98.4.346

Leonard, A., Grose, V., Paton, A. W., Paton, J. C., Yule, D. I., Rahman, A., et al. (2019). Selective inactivation of intracellular BiP/GRP78 attenuates endothelial inflammation and permeability in acute lung injury. *Sci. Rep.* 9:2096. doi: 10.1038/s41598-018-38312-w

Li, H. H., Kedar, V., Zhang, C., McDonough, H., Arya, R., Wang, D. Z., et al. (2004). Atrogin-1/muscle atrophy F-box inhibits calcineurin-dependent cardiac hypertrophy by participating in an SCF ubiquitin ligase complex. *J. Clin. Invest.* 114, 1058–1071. doi: 10.1172/JCI200422220

Li, H. H., Willis, M. S., Lockyer, P., Miller, N., McDonough, H., Glass, D. J., et al. (2007). Atrogin-1 inhibits Akt-dependent cardiac hypertrophy in mice via ubiquitin-dependent coactivation of Forkhead proteins. *J. Clin. Invest.* 117, 3211–3223. doi: 10.1172/JCI31757

Luo, T., Chen, B., and Wang, X. (2015). 4-PBA prevents pressure overload-induced myocardial hypertrophy and interstitial fibrosis by attenuating endoplasmic reticulum stress. *Chem. Biol. Interact.* 242, 99–106. doi: 10.1016/j.cbi.2015.09.025

Mann, D. L., Topkara, V. K., Evans, S., and Barger, P. M. (2010). Innate immunity in the adult mammalian heart: for whom the cell tolls. *Trans. Am. Clin. Climatol. Assoc.* 121, 34-50; discussion 50–31.

Margulies, K. B., Matiwala, S., Cornejo, C., Olsen, H., Craven, W. A., and Bednarik, D. (2005). Mixed messages: transcription patterns in failing and recovering human myocardium. *Circ. Res.* 96, 592–599. doi: 10.1161/01.RES.0000159390.03503.c3

Marine, J. C., McKay, C., Wang, D., Topham, D. J., Parganas, E., Nakajima, H., et al. (1999). SOCS3 is essential in the regulation of fetal liver erythropoiesis. *Cell* 98, 617–627. doi: 10.1016/S0092-8674(00)80049-5

Masuhara, M., Sakamoto, H., Matsumoto, A., Suzuki, R., Yasukawa, H., Mitsui, K., et al. (1997). Cloning and characterization of novel CIS family genes. *Biochem. Biophys. Res. Commun.* 239, 439–446. doi: 10.1006/bbrc.1997.7484

Metz, O., Stoll, W., and Plenert, W. (1977). "Prophylactic" intrathecal radiogold (198au) in leukaemia in children (author's transl). *Dtsch. Med. Wochenschr.* 102, 43–46. doi: 10.1055/s-0028-1104839

Minamino, T., and Kitakaze, M. (2010). ER stress in cardiovascular disease. *J. Mol. Cell. Cardiol.* 48, 1105–1110. doi: 10.1016/j.yjmcc.2009.10.026

Minamino, T., Komuro, I., and Kitakaze, M. (2010). Endoplasmic reticulum stress as a therapeutic target in cardiovascular disease. *Circ. Res.* 107, 1071–1082. doi: 10.1161/CIRCRESAHA.110.227819

Nakamura, M., and Sadoshima, J. (2018). Mechanisms of physiological and pathological cardiac hypertrophy. *Nat. Rev. Cardiol.* 15, 387–407. doi: 10.1038/s41569-018-0007-y

Narendra, D., Walker, J. E., and Youle, R. (2012). Mitochondrial quality control mediated by PINK1 and Parkin: links to parkinsonism. *Cold Spring Harb. Perspect. Biol.* 4:a011338. doi: 10.1101/cshperspect.a011338

Ni, M., Zhang, Y., and Lee, A. S. (2011). Beyond the endoplasmic reticulum: atypical GRP78 in cell viability, signalling and therapeutic targeting. *Biochem. J.* 434, 181–188. doi: 10.1042/BJ20101569

Ning, J., Lin, Z., Zhao, X., Zhao, B., and Miao, J. (2019). Inhibiting lysine 353 oxidation of GRP78 by a hypochlorous probe targeting endoplasmic reticulum promotes autophagy in cancer cells. *Cell Death Dis.* 10:858. doi: 10.1038/s41419-019-2095-y

Oba, T., Yasukawa, H., Hoshijima, M., Sasaki, K., Futamata, N., Fukui, D., et al. (2012). Cardiac-specific deletion of SOCS-3 prevents development of left ventricular remodeling after acute myocardial infarction. *J. Am. Coll. Cardiol.* 59, 838–852. doi: 10.1016/j.jacc.2011.10.887

Okada, K., Minamino, T., Tsukamoto, Y., Liao, Y., Tsukamoto, O., Takashima, S., et al. (2004). Prolonged endoplasmic reticulum stress in hypertrophic and failing heart after aortic constriction: possible contribution of endoplasmic reticulum stress to cardiac myocyte apoptosis. *Circulation* 110, 705–712. doi: 10.1161/01.CIR.0000137836.95625.D4

Pang, J., Peng, H., Wang, S., Xu, X., Xu, F., Wang, Q., et al. (2019). Mitochondrial ALDH2 protects against lipopolysaccharide-induced myocardial contractile dysfunction by suppression of ER stress and autophagy. *Biochim. Biophys. Acta Mol. Basis Dis.* 1865, 1627–1641. doi: 10.1016/j.bbadis.2019.03.015

Podewski, E. K., Hilfiker-Kleiner, D., Hilfiker, A., Morawietz, H., Lichtenberg, A., Wollert, K. C., et al. (2003). Alterations in Janus kinase (JAK)-signal transducers and activators of transcription (STAT) signaling in patients with end-stage dilated cardiomyopathy. *Circulation* 107, 798–802. doi: 10.1161/01.CIR.0000057545.82749.FF

Rashid, H. O., Yadav, R. K., Kim, H. R., and Chae, H. J. (2015). ER stress: autophagy induction, inhibition and selection. *Autophagy* 11, 1956–1977. doi: 10.1080/15548627.2015.1091141

Roberts, A. W., Robb, L., Rakar, S., Hartley, L., Cluse, L., Nicola, N. A., et al. (2001). Placental defects and embryonic lethality in mice lacking suppressor of cytokine signaling 3. *Proc. Natl. Acad. Sci. U. S. A.* 98, 9324–9329. doi: 10.1073/pnas.161271798

Senft, D., and Ronai, Z. A. (2015). UPR, autophagy, and mitochondria crosstalk underlies the ER stress response. *Trends Biochem. Sci.* 40, 141–148. doi: 10.1016/j.tibs.2015.01.002

Uozumi, H., Hiroi, Y., Zou, Y., Takimoto, E., Toko, H., Niu, P., et al. (2001). gp130 plays a critical role in pressure overload-induced cardiac hypertrophy. *J. Biol. Chem.* 276, 23115–23119. doi: 10.1074/jbc.M100814200

Wang, L., Zhang, Y. L., Lin, Q. Y., Liu, Y., Guan, X. M., Ma, X. L., et al. (2018). CXCL1-CXCR2 axis mediates angiotensin II-induced cardiac hypertrophy and remodelling through regulation of monocyte infiltration. *Eur. Heart J.* 39, 1818–1831. doi: 10.1093/eurheartj/ehy085

Wang, S., Binder, P., Fang, Q., Wang, Z., Xiao, W., Liu, W., et al. (2018). Endoplasmic reticulum stress in the heart: insights into mechanisms and drug targets. *Br. J. Pharmacol.* 175, 1293–1304. doi: 10.1111/bph.13888

Wang, S., Chen, X., Nair, S., Sun, D., Wang, X., and Ren, J. (2017). Deletion of protein tyrosine phosphatase 1B obliterates endoplasmic reticulum stress-induced myocardial dysfunction through regulation of autophagy. *Biochim. Biophys. Acta Mol. Basis Dis.* 1863, 3060–3074. doi: 10.1016/j.bbadis.2017.09.015

Wang, Y., Wu, H., Li, Z., and Yang, P. (2017). A positive feedback loop between GRP78 and VPS34 is critical for GRP78-mediated autophagy in cancer cells. *Exp. Cell Res.* 351, 24–35. doi: 10.1016/j.yexcr.2016.12.017

Xie, X., Bi, H. L., Lai, S., Zhang, Y. L., Li, N., Cao, H. J., et al. (2019). The immunoproteasome catalytic beta5i subunit regulates cardiac hypertrophy by targeting the autophagy protein ATG5 for degradation. *Sci. Adv.* 5:eaau0495. doi: 10.1126/sciadv.aau0495

Xie, Y. P., Lai, S., Lin, Q. Y., Xie, X., Liao, J. W., Wang, H. X., et al. (2018). CDC20 regulates cardiac hypertrophy via targeting LC3-dependent autophagy. *Theranostics* 8, 5995–6007. doi: 10.7150/thno.27706

Yajima, T., Murofushi, Y., Zhou, H., Park, S., Housman, J., Zhong, Z. H., et al. (2011). Absence of SOCS3 in the cardiomyocyte increases mortality in a gp130-dependent manner accompanied by contractile dysfunction and ventricular arrhythmias. *Circulation* 124, 2690–2701. doi: 10.1161/CIRCULATIONAHA.111.028498

Yamaguchi, O., Higuchi, Y., Hirotani, S., Kashiwase, K., Nakayama, H., Hikoso, S., et al. (2003). Targeted deletion of apoptosis signal-regulating kinase 1 attenuates left ventricular remodeling. *Proc. Natl. Acad. Sci. U. S. A.* 100, 15883–15888. doi: 10.1073/pnas.2136717100

Yao, Y., Lu, Q., Hu, Z., Yu, Y., Chen, Q., and Wang, Q. K. (2017). A non-canonical pathway regulates ER stress signaling and blocks ER stress-induced apoptosis and heart failure. *Nat. Commun.* 8:133. doi: 10.1038/s41467-017-00171-w

Yasukawa, H., Hoshijima, M., Gu, Y., Nakamura, T., Pradervand, S., Hanada, T., et al. (2001). Suppressor of cytokine signaling-3 is a biomechanical stress-inducible gene that suppresses gp130-mediated cardiac myocyte hypertrophy and survival pathways. *J. Clin. Invest.* 108, 1459–1467. doi: 10.1172/JCI13939

Yasukawa, H., Nagata, T., Oba, T., and Imaizumi, T. (2012). SOCS3: a novel therapeutic target for cardioprotection. *JAKSTAT* 1, 234–240. doi: 10.4161/jkst.22435

Yussman, M. G., Toyokawa, T., Odley, A., Lynch, R. A., Wu, G., Colbert, M. C., et al. (2002). Mitochondrial death protein Nix is induced in cardiac hypertrophy and triggers apoptotic cardiomyopathy. *Nat. Med.* 8, 725–730. doi: 10.1038/nm719

Zhang, Y., Whaley-Connell, A. T., Sowers, J. R., and Ren, J. (2018). Autophagy as an emerging target in cardiorenal metabolic disease: from pathophysiology to management. *Pharmacol. Ther.* 191, 1–22. doi: 10.1016/j.pharmthera.2018.06.004

Conflict of Interest: The authors declare that the research was conducted in the absence of any commercial or financial relationships that could be construed as a potential conflict of interest.

frontiers in Cell and Developmental Biology

ORIGINAL RESEARCH
published: 01 April 2021
doi: 10.3389/fcell.2021.644954

Krüppel-Like Factor 15 Modulates *CXCL1/CXCR2* Signaling-Mediated Inflammatory Response Contributing to Angiotensin II-Induced Cardiac Remodeling

Shun He[1,2], Yuanyuan Lu[1,2], Yuetong Guo[1,2], Shijin Li[1,2], Xiao Lu[1,2], Shuai Shao[1,2], Handan Zhou[1,2], Ruiqi Wang[1,2], Jiguang Wang[1,2], Pingjin Gao[1,2] and Xiaodong Li[1,2]**

[1] Department of Cardiovascular Medicine, Ruijin Hospital and State Key Laboratory of Medical Genomics, Shanghai Key Laboratory of Hypertension, Shanghai Institute of Hypertension, Shanghai Jiao Tong University School of Medicine, Shanghai, China, [2] Department of Hypertension, Ruijin Hospital and State Key Laboratory of Medical Genomics, Shanghai Key Laboratory of Hypertension, Shanghai Institute of Hypertension, Shanghai Jiao Tong University School of Medicine, Shanghai, China

OPEN ACCESS

Edited by:
Hui-Hua Li,
Capital Medical University, China

Reviewed by:
Qiulun Lu,
Nanjing Medical University, China
Shijun Hu,
Soochow University, China

***Correspondence:**
Yuanyuan Lu
luyuanyuanzj@126.com
Xiaodong Li
flylxd@163.com

Specialty section:
This article was submitted to Signaling, a section of the journal Frontiers in Cell and Developmental Biology

Received: 22 December 2020
Accepted: 18 February 2021
Published: 01 April 2021

Citation:
He S, Lu Y, Guo Y, Li S, Lu X, Shao S, Zhou H, Wang R, Wang J, Gao P and Li X (2021) Krüppel-Like Factor 15 Modulates CXCL1/CXCR2 Signaling-Mediated Inflammatory Response Contributing to Angiotensin II-Induced Cardiac Remodeling. Front. Cell Dev. Biol. 9:644954. doi: 10.3389/fcell.2021.644954

Inflammation is involved in cardiac remodeling. In response to pathological stimuli, activated cardiac fibroblasts (CFs) secreting inflammatory cytokines and chemokines play an important role in monocyte/macrophage recruitment. However, the precise mechanism of CF-mediated inflammatory response in hypertension-induced cardiac remodeling remains unclear. In the present study, we investigated the role of transcription factor Krüppel-like factor 15 (KLF15) in this process. We found that KLF15 expression decreased while chemokine *CXCL1* and its receptor *CXCR2* expression increased in the hearts of angiotensin II (Ang II)-infused mice. Compared to the wild-type mice, KLF15 knockout (KO) mice aggravated Ang II-induced cardiac hypertrophy and fibrosis. Deficiency of KLF15 promoted macrophage accumulation, increase of *CXCL1* and *CXCR2* expression, and mTOR, ERK1/2, NF-κB-p65 signaling activation in the hearts. Mechanistically, Ang II dose- dependently decreased KLF15 expression and increased *CXCL1* secretion from cardiac fibroblasts but not cardiac myoblasts. Loss- or gain-of-function studies have shown that KLF15 negatively regulated *CXCL1* expression through its transactivation domain (TAD). Intriguingly, the adenovirus-mediated full length of KLF15—but not KLF15 with TAD deletion overexpression—markedly prevented pathological change in Ang II-infused mice. Notably, the administration of *CXCR2* inhibitor SB265610 reversed KLF15 knockout-mediated aggravation of cardiac dysfunction, remodeling, and inflammation induced by Ang II. In conclusion, our study identifies that KLF15 in cardiac fibroblasts negatively regulates *CXCL1/CXCR2* axis-mediated inflammatory response and subsequent cardiac remodeling in hypertension.

Keywords: hypertension, renin-angiotensin system, transcription factor, cardiac remodeling, inflammation

INTRODUCTION

Hypertensive heart failure is a terrible disease with high morbidity and mortality characterized by cardiac remodeling including left ventricular hypertrophy and interstitial fibrosis (Katz and Rolett, 2016). The renin-angiotensin system (RAS) plays a pivotal role in hypertension, and the sustained RAS activation contributes to the development and progression of heart failure (Te Riet et al., 2015). Clinical and experimental studies reported that deregulated Ang II, the major effector in the renin-angiotensin system, plays an important role in the pathogenesis of cardiac remodeling (Kurdi and Booz, 2011). Besides the role of cardiomyocytes and cardiac fibroblasts, other cells that reside in or infiltrate into the heart in response to Ang II also significantly participate in this process. For example, Ang II promotes endothelial cells to secrete TGF-beta, which accelerates pathological cardiac fibrosis and hypertrophy (Liu et al., 2019). Ang II also induces the infiltration of inflammatory cells, especially monocytes/macrophages in the heart and then promotes the development of heart failure (McMaster et al., 2015; Wang et al., 2018). These studies suggest that a multifaceted crosstalk between cardiac cells and non-cardiac cells contributes to cardiac remodeling. Therefore, investigation of the critical molecule that promotes these cells' interaction in the heart after hypertensive stress may provide new therapeutic strategies for cardiac remodeling.

Krüppel-like factors (KLFs) are zinc finger-containing transcription factors involved in a broad range of functions in regulating proliferation, differentiation, development, and programmed cell death (McConnell and Yang, 2010). As a member of the KLF family, KLF15 mainly functions as a transcription repressor, the alteration of whose expression is associated with numerous diseases, including cardiovascular disease, metabolic disorders, and cancer (Yoda et al., 2015; Zhao et al., 2019). Moreover, it is reported that KLF15 is highly expressed in cardiac fibroblasts and cardiomyocytes and is essential for cardiac remodeling by controlling downstream gene expression (Noack et al., 2019). Our previous study found that Ang II induced phenotypic transformation of fibroblasts into inflammatory myofibroblasts through down-regulating KLF15 expression (Lu et al., 2019), suggesting the critical role of KLF15 in regulation of inflammatory gene expression. However, it's important to identify the mechanism of the KLF15-mediated inflammatory response and its effects on cardiac cellular crosstalk in hypertension-induced cardiac remodeling.

Cardiac macrophages have been shown to be involved in the regulation of cardiac injury in myocardial infarction, ischemia reperfusion, and hypertension (Shirakawa et al., 2018; Wang et al., 2018; Petz et al., 2019). Chemokines and their receptors play critical roles in promoting the recruitment of monocytes/macrophages into the injured heart (Wang et al., 2018). Recently, we have found that KLF15 is necessary for repressing adventitial fibroblast-derived CCL2 excretion, which mediated macrophage infiltration into injury arteries (Lu et al., 2019). However, little is known about the function of KLF15 in cardiac fibroblasts, which regulates inflammation response-mediated cardiac remodeling in hypertension. In this study, we sought to determine whether KLF15 negatively regulates chemokine-mediated macrophage recruitment, which exacerbates cardiac hypertrophy and fibrosis in Ang II-induced hypertension.

MATERIALS AND METHODS

Animals

All animal welfare and procedures were adhered to according to the Guide for the Care and Use of Laboratory Animals established by Shanghai Jiao Tong University School of Medicine. $KLF15^{flox/flox}$ (C57BL/6J background) was generated by Cyagen Biosciences Inc., by introducing loxP sites flanking the coding exon 2 of the Klf15 gene. $KLF15^{flox/flox}$ mice were crossed with CAG-Cre mice to generate global KLF15 knockout (KO) mice. The mice were maintained under the specific pathogen-free (SPF) environment with 12 h of light/dark cycles and free access to food and water. Male, 8-week-old KLF15 KO mice and WT littermates were infused by angiotensin II (1,000 ng/kg/min, Sigma, United States) for 14 days using subcutaneously implanted minipumps (Alzet, 1002) to study cardiac remodeling as previously described (Zuo et al., 2018).

Rat KLF15 (Accession no. AAH89782.1) and deletion of TAD at amino acids 132–152 (KLF15-DTAD; VSRPFQPTLEEIEEFLEENME) cloned into an adenovirus vector (padenoMCMVEGFP-P2A-3FLAG) were constructed by Obio Technology (Shanghai, China). Adenoviruses of AdCTL, AdKLF15, or AdKLF15-ΔTAD were injected through the tail vein at a dose of 1×10^9 PFU per mouse 1 day before Ang II infusion. For the SB265610 treatment group, after implantation of mini-pumps infused with Ang II or saline, SB265610 (2 mg/kg/day) was intraperitoneally injected once per day for 2 weeks.

After 14 days, mice were weighed and sacrificed by intraperitoneal administration of an overdose of pentobarbitone. Then, they were perfused with cold 0.9% PBS, and the hearts were weighed, harvested, fixed, or frozen for histologic and molecular analyses.

Blood Pressure Measurement

Systolic blood pressure was taken by the non-invasive tail-cuff method using BP-2000 Blood Pressure Analysis System (VisitechSystems, Apex, NC, United States). Systolic blood pressure was measured at least three times for each mouse.

Cardiac Function Assessment by Echocardiography

A non-invasive transthoracic echocardiographic examination was performed using Vevo 2,100 (Visualsonics, Canada), equipped with a 30 MHz transducer. The mice were anesthetized with continuous flow of 1–2% isoflurane. Two-dimensional guide M-mode tracings were recorded, ejection fraction (EF), and fractional shortening (FS) were measured and further calculated.

Histology and Immunohistochemistry

Histological analyses were performed essentially as described (Li et al., 2020). Paraffin sections were stained with hematoxylin and eosin (HE, Servicebio, China), or Masson's trichrome (Servicebio, China) according to standard procedures. Immunofluorescence staining was performed with indicated primary antibodies overnight at 4°C and secondary antibodies conjugated with FITC or Texas Red (Thermo Fisher Scientific, United States) for 30 min at room temperature. Wheat germ agglutinin staining (WGA) was applied following the manufacturer's instructions (Invitrogen, W11261, CA, United States). Pictures were taken using a fluorescence microscope (Axio Imager M2; Carl Zeiss, Oberkochen, Germany). Quantifications were performed with ImageJ software. Primary antibodies used in Immunohistochemistry include KLF15 (Santa Cruz Biotechnology, sc-271675, United States), ACTA2 (Abcam, ab7817, United States), F4/80 (Servicebio, GB11027, China), and *CXCR2* (Abclonal, A3301, China).

Cell Culture, Infection, Transfection, Reporter Assay, and Elisa

CFs were isolated according to manufacturer's instruction (MACS, 130-098-373, Germany). H9c2 cells and HEK293T cells were purchased from ATCC (CRL-1466, CRL-3216). CFs and H9c2 cells were cultured in a complete medium containing DMEM supplemented with 10% fetal bovine serum (FBS; Thermo Fisher Scientific, United States), 100 U/ml penicillin, and streptomycin. Bone marrow-derived macrophages (BMDM) were isolated by flushing mice femur and tibia with a syringe and a 26-gauge needle with RPMI1640 supplemented with 100 U/ml penicillin, 100 μg/ml streptomycin and 0.2% fetal bone serum (FBS). After centrifugation, the pellet was resuspended with RPMI1640 with 10%FBS. Cells were stimulated by 50ng/ml M-CSF for 7 days to obtain BMDM. Cells were cultured at 37°C in a humidified atmosphere containing 5% CO_2. Transient transfections were performed with jetPRIME® (Polyplus Transfection, United States) according to the manufacturer's instructions. AdCTL, AdKLF15, or AdKLF15-ΔTAD was infected as previous described (Lu et al., 2019). Small interfering RNAs were constructed by Genepharma Co. (Shanghai, China). Cells were harvested after stimulation by vehicle or Ang II with the indicated concentration and time after 48 h of transfection. The human *CXCL1* promoter covering a region from −2,000 to +1 was ligated into a pGL4.10 luciferase reporter vector and transfected into HEK293T cells by Lipofectamine 3,000. Reporter activity was measured using a luciferase reporter assay system (Promega, E1910/E1960, United States) as previously described (Lu et al., 2019). Cell supernatant was collected for a *CXCL1* Elisa assay according to the manufacturer's instructions (Raybiotech, ELM-KC-1, United States).

Protein Extraction and Western Blot

Proteins were extracted from heart tissue or cells using RIPA lysis buffer (Millipore, HY-K0010) with a proteinase inhibitor cocktail (Millipore, HY-K0010). The protein was separated by 10% SDS-PAGE gel and then transferred onto PVDF membranes (Millipore, IPFL00005, United States). Membranes were blocked with 5% non-fat milk in TBST at room temperature for 60 min and incubated overnight with indicated primary antibodies at 4°C, followed incubation with HRP-linked secondary antibodies at room temperature for 60 min, and the specific proteins were detected by an ECL Detection System (Pierce, Rockford, IL, United States). The primary antibodies used in Western Blot include KLF15 (Proteintech, 66185, China), P-mTOR (CST, 5536, United States), mTOR (CST, 2983, United States), P-NF-κB p65 (CST, 3039, United States), NF-κB p65 (CST, 8242, United States), P-ERK1/2 (CST, 4370, United States), ERK1/2 (CST, 4695, United States), *CXCL1* (ABclonal, A5802, China),*CXCR2* (ABclonal, A3301, China), GAPDH (CST, 8884, United States), Flag (Sigma, F1804, United States), and anti-rabbit or anti-mouse secondary antibodies (CST, 7074 or 7076, United States).

RNA Isolation and Real-Time PCR

Total mRNA was extracted from heart tissue or cells by the commercial RNA purification kit (EZBioscience, B0009, United States) following the manufacturer's instruction. And 1,000 ng of total mRNA was reverse-transcribed into cDNA using HiScript III RT SuperMix (Vazyme, R323, China). Realtime PCR reactions were performed using a commercial SYBR Green kit (Vazyme, Q311-02, China) on an ABI Prism StepOne Plus system (ABI, United States). Sequences of the primers were listed in **Supplementary Table S1**.

Statistical Analysis

A *t*-test for two groups and one-way ANOVA or two-way ANOVA with Tukey's *post hoc* test for multiple groups were performed by Prism 6 (GraphPad, La Jolla, CA, United States). *P*-values less than 0.05 were considered statistically significant.

RESULTS

Ang II Induced Decrease of KLF15 Expression Associated With Increase of *CXCL1/CXCR2* Expression

Our previous study found that Ang II induced decrease of KLF15 in adventitial fibroblasts (Lu et al., 2019). In this study, the expression of cardiac KLF15 was measured in WT mice infused with Ang II. Ang II decreased cardiac KLF15 mRNA and protein expression in a time-dependent manner (**Figures 1A,B**). The decrease of KLF15 was also validated by immunofluorescence (**Figure 1C**). It is reported that *CXCL1/CXCR2* axis mediates Ang II-induced cardiac hypertrophy and remodeling (Wang et al., 2018). In addition, inspired by the RNA-seq results that identified several KLF15-regulated chemokines expression in smooth muscle cells (Sasse et al., 2017), we found that Ang II increased cardiac *CXCL1* expression (**Figure 1D**), which showed an opposite trend compared with cardiac KLF15 expression. Moreover, *CXCR2*, the receptor of *CXCL1,* was also significantly increased after Ang II infusion (**Figure 1E**). These findings

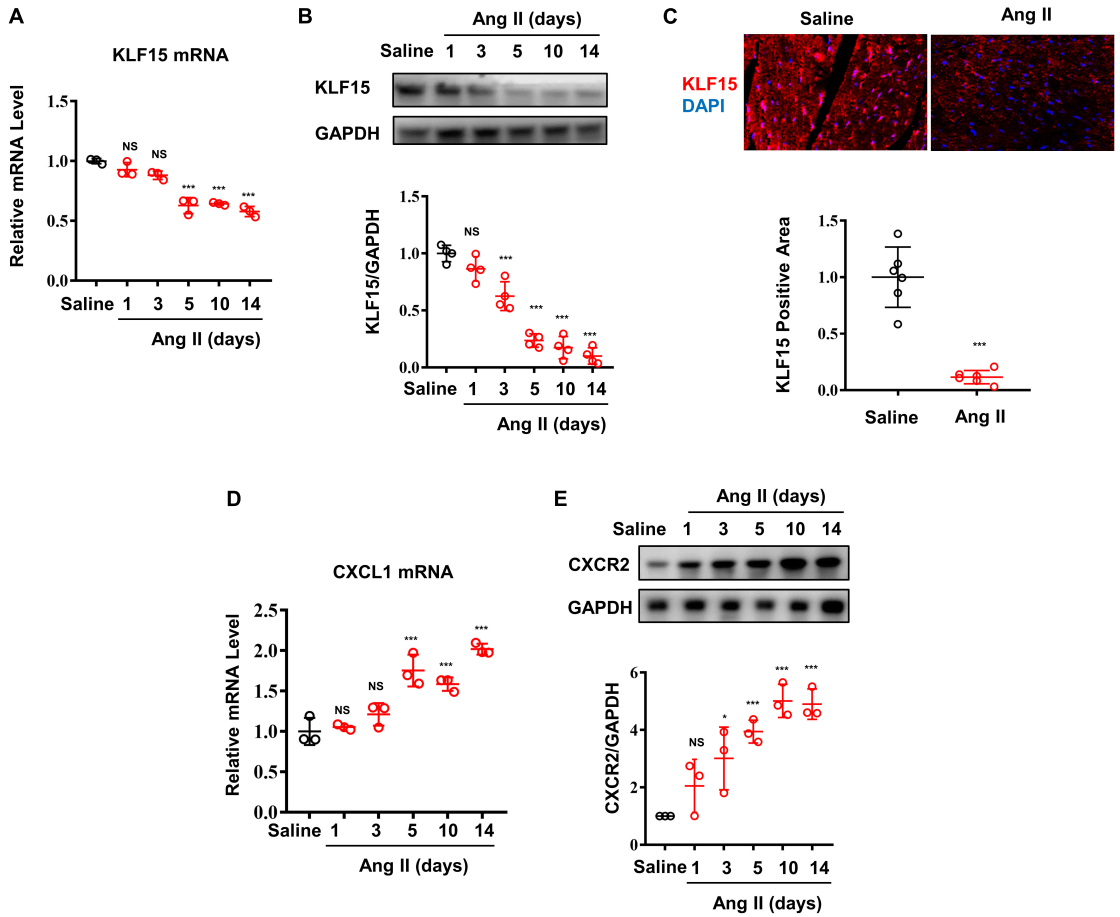

FIGURE 1 | Ang II induced decrease of KLF15 expression associating with increase of *CXCL1/CXCR2* expression. Mice were infused with saline or Ang II (1,000 ng/kg/min) for the indicated time. **(A)** Cardiac KLF15 mRNA was detected and analyzed by qPCR. **(B)** KLF15 protein expression was detected and analyzed by Western Blot. **(C)** Representative immunofluorescence image of KLF15 in mice heart section (upper) and quantification analysis (lower). **(D)** *CXCL1* mRNA was measured and analyzed by qPCR. **(E)** *CXCR2* protein was detected and analyzed by Western Blot. $^{*}P < 0.05$ and $^{***}P < 0.001$.

suggested that Ang II may induce *CXCL1/CXCR2*-associated inflammatory response via suppressing KLF15 expression.

Deficiency of KLF15 Aggravated Ang II-Induced Cardiac Hypertrophy and Fibrosis

Next, WT and KLF15 KO mice were used to investigate the effect of KLF15 on Ang II-induced cardiac remodeling. After 2 weeks of Ang II treatment, the cardiomyocyte hypertrophy was markedly aggravated in the KLF15 KO mice, which was revealed by histological analysis with HE and WGA, heart weight, and body weight (**Figures 2A–C**). In addition, KLF15 KO aggravated Ang II-induced cardiac fibrosis revealed by Masson stain (**Figures 2A,D**). Accordingly, myofibroblasts showed more activated in KLF15 KO mice tested by immunofluorescence of α-SMA positive cells (**Figures 2A,E**). However, the blood pressure levels between KLF15 KO and WT mice were indistinguishable (**Figure 2F**). Moreover, mRNA levels of ANP and BNP were higher in KLF15 KO mice compared with the WT mice (**Figure 2G**), which indicated deteriorated cardiac hypertrophy. Collagen 1a1 mRNA level was also higher in KLF15 KO mice which revealed aggravated fibrosis (**Figure 2H**). Most importantly, *CXCL1* mRNA level showed significantly increase in KLF15 KO heart (**Figure 2I**).

Deficiency of KLF15 Promoted Inflammatory Cell Infiltration and Multiple Signaling Activation

CXCL1/CXCR2 axis mediates inflammatory cell infiltration and subsequent multiple cardiac pathological signal activation (Wang et al., 2018). We found that the number of F4/80 positive and *CXCR2* positive cells were increased in the heart of KLF15 KO mice compared with WT mice (**Figures 3A–C**). Moreover, *CXCR2* protein level showed an increasing trend in heart of KLF15 KO mice (**Figures 3D,E**). To elucidate the molecular mechanism that underlying aggravated cardiac remodeling and dysfunction in KLF15 KO mice, we examined multiple signaling pathways that mediate cardiac pathological

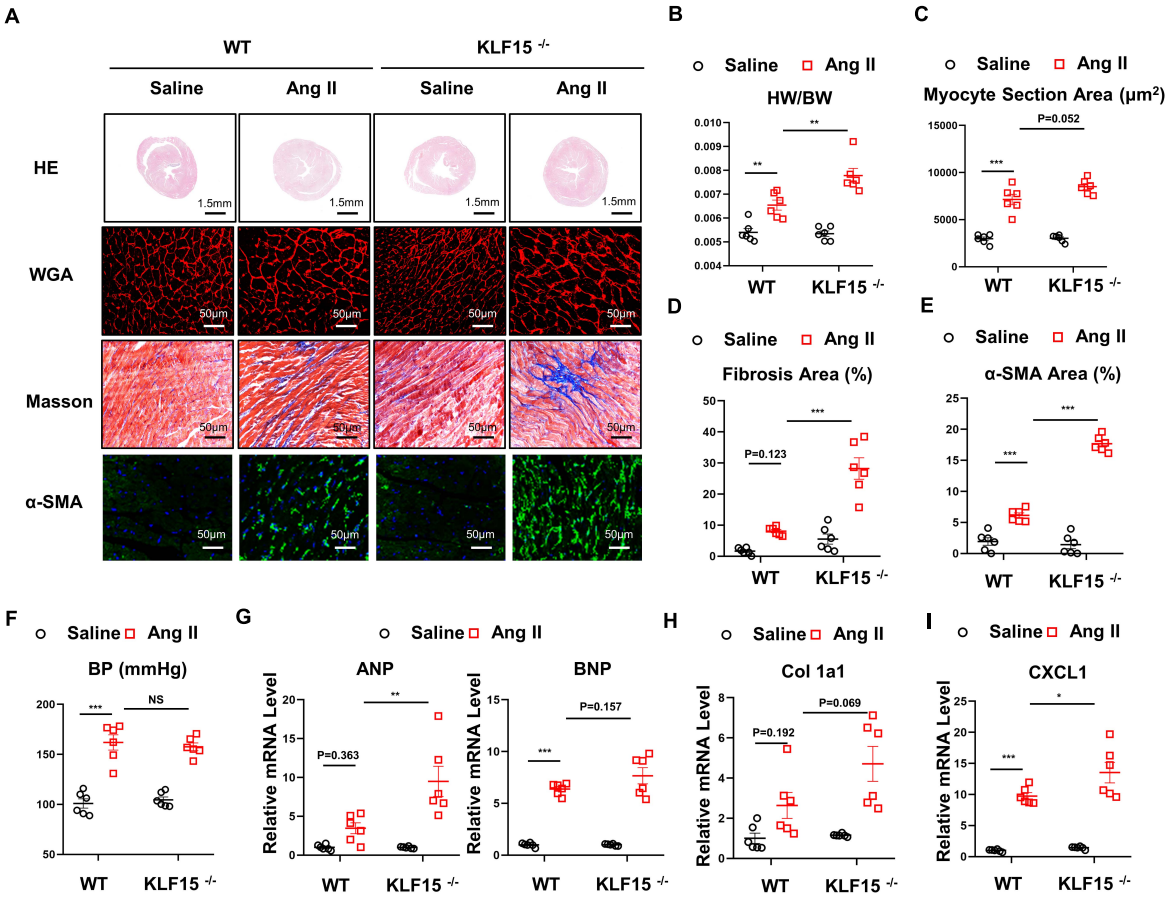

FIGURE 2 | Deficiency of KLF15 aggravated Ang II-induced cardiac remodeling. Wild-type (WT) mice and KLF15 knockout (KO) mice were infused with saline or Ang II for 14 days. **(A)** Representative heart size, WGA stain, Masson stain, and α-SMA immunofluorescence image. **(B)** Statistical analysis of heart weight/body weight ratio. **(C)** Quantification analysis of myocyte section area. **(D)** Quantification analysis of fibrotic area measured by Masson stain. **(E)** Quantification analysis of α-SMA positive area measured by immunofluorescence. **(F)** Statistical analysis of blood pressure. **(G–I)** qPCR analysis of mRNA levels of ANP, BNP, Collagen 1a1, and *CXCL1*. $^{*}P < 0.05$, $^{**}P < 0.01$, and $^{***}P < 0.001$.

changes (Wang et al., 2018). We found that Ang II-induced increase of P-mTOR, P-ERK1/2, P-p65 protein levels, which were all remarkedly aggravated in the hearts of KLF15 KO mice compared with WT mice (**Figures 3F–J**).

KLF15 Negatively Regulated *CXCL1* Transcription Through TAD in Cardiac Fibroblasts

To determine which cell type in the heart contributes to the secretion of *CXCL1*, cardiac fibroblasts (CF) and cardiomyocytes (H9c2) were treated with different doses of Ang II. Dose-dependent decrease of KLF15 was observed both in CFs and H9c2 after Ang II stimulation (**Figures 4A,B**). Next, *CXCL1* expression in the supernatant of Ang II-treated CF and H9c2 cells was analyzed by ELISA assay. The results showed that Ang II induced-*CXCL1* secretion mainly derived from CF (**Figures 4C,D**). Western Blot was used to measure the expression of *CXCL1* and *CXCR2*. The results also showed that *CXCL1* was especially up-regulated in CFs but not H9c2 cells. Furthermore, Ang II has no effect on the expression of *CXCR2* in CFs and H9c2 cells (**Supplementary Figures S1A,B**). To further investigate whether KLF15 regulates *CXCL1* transcription, KLF15 expression was successful knockdown by KLF15 siRNA1 and confirmed by Western Blot (**Figure 4E**). SiKLF15-transfected CFs showed higher *CXCL1* expression than siCon-transfected CFs in response to Ang II (**Figure 4F**). Previous study has shown that KLF15 regulates inflammatory factor expression through TAD (Lu et al., 2019). We infected CFs with AdKLF15 and AdKLF15-ΔTAD to determine whether TAD is involved in KLF15-dependent *CXCL1* transcription (**Figure 4G**). Interestingly, luciferase and qPCR assay revealed that KLF15-overexpressed CF, but not KLF15-ΔTAD-overexpressed CF, showed a lower *CXCL1* promoter activity and *CXCL1* mRNA level (**Figures 4H,I**). These results indicated that KLF15 regulates *CXCL1* transcription through TAD. Furthermore, to exclude the function of macrophage, BMDM was cultured and stimulated by Ang II. We found that Ang II increased *CXCR2* expression but had no effect on the regulation of KLF15 and *CXCL1* expression in BMDM

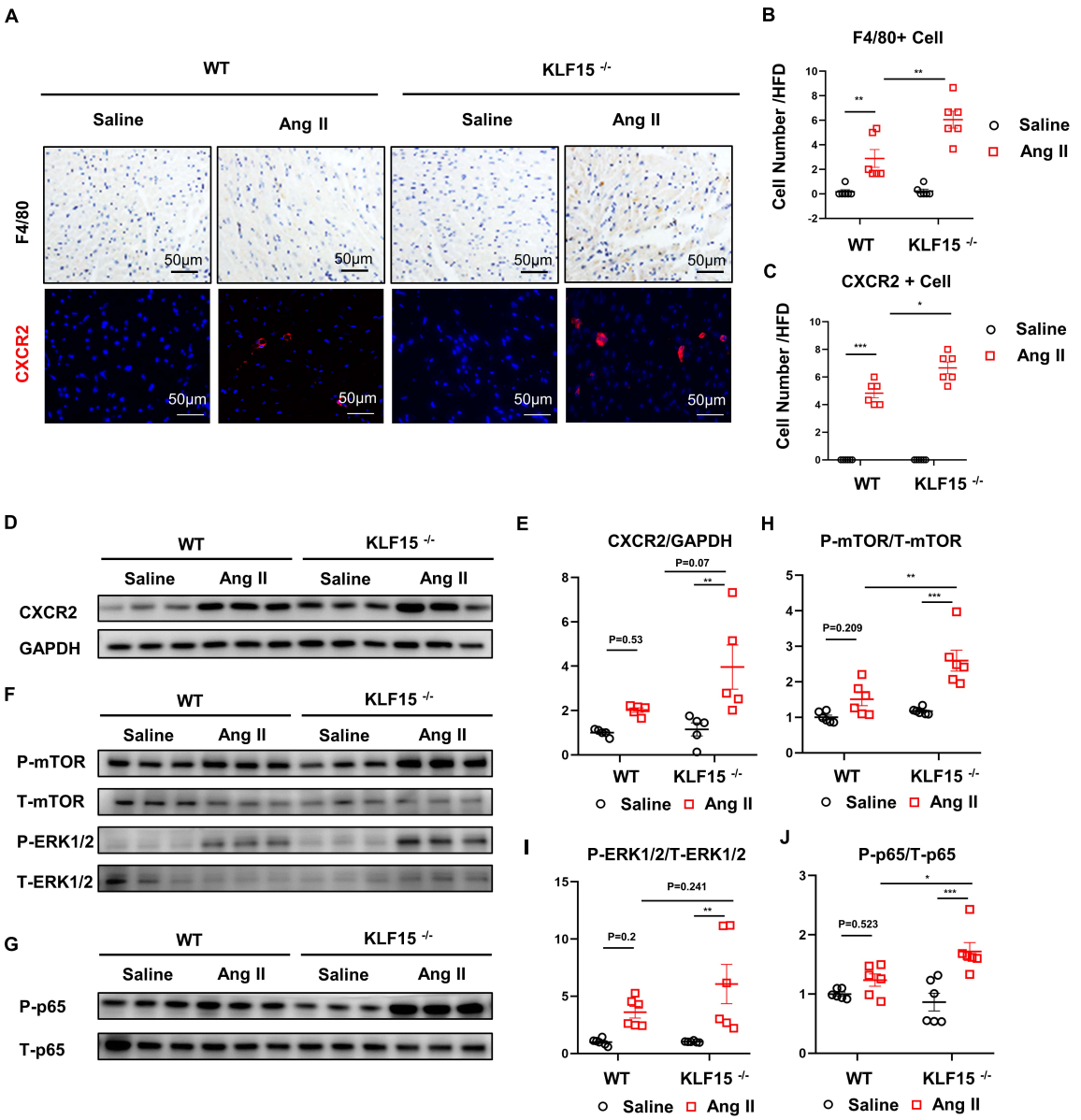

FIGURE 3 | KLF15 regulated *CXCR2*-mediated inflammatory cell infiltration and downstream signal. WT and KO mice were infused with saline or Ang II for 14 days. **(A)** Representative immunohistology and immunofluorescence image of F4/80, *CXCR2* positive cell in heart. **(B,C)** Quantification analysis of F4/80, *CXCR2* positive cell infiltration in mice heart. **(D,E)** Western Blot and quantification analysis of *CXCR2*/GAPDH. **(F–J)** Western Blot and quantification analysis of P-mTOR/T-mTOR, P-ERK1/2/T-ERK1/2 and P-p65/T-p65 of mice heart. $^{*}P < 0.05$, $^{**}P < 0.01$, and $^{***}P < 0.001$.

(**Supplementary Figure S1C**). Overexpression of KLF15 or KLF15-ΔTAD showed no effect on *CXCR2* expression in BMDM (**Supplementary Figure S1D**).

KLF15 Alleviated Ang II-Induced Cardiac Hypertrophy and Fibrosis Through TAD

Next, we tested whether overexpression of KLF15 or KLF15-ΔTAD can reverse Ang II-induced cardiac hypertrophy and fibrosis. WT mice were injected with KLF15 and KLF15-ΔTAD adenovirus 1 day before Ang II infusion. After 2 weeks of Ang II infusion, AdKLF15-infected mice displayed improved cardiac hypertrophy (heart/body weight ratio, heart size, myocyte area, and mRNA level of ANP, BNP) as compared to the AdCTL-infected mice (**Figures 5A–C,G**). Moreover, less myocardial fibrosis, α-SMA-positive myofibroblasts, and the expression of collagen 1a1 mRNA were observed in AdKLF15 mice heart (**Figures 5A,D,E,H**). Interestingly, contrary to AdKLF15, AdKLF15-ΔTAD showed no effect on cardiac hypertrophy (heart/body weight ratio, heart size, myocyte area and mRNA level of ANP, BNP) compared with the AdCTL-infected mice (**Figures 5A–C,G**). Myocardial fibrosis, α-SMA-positive

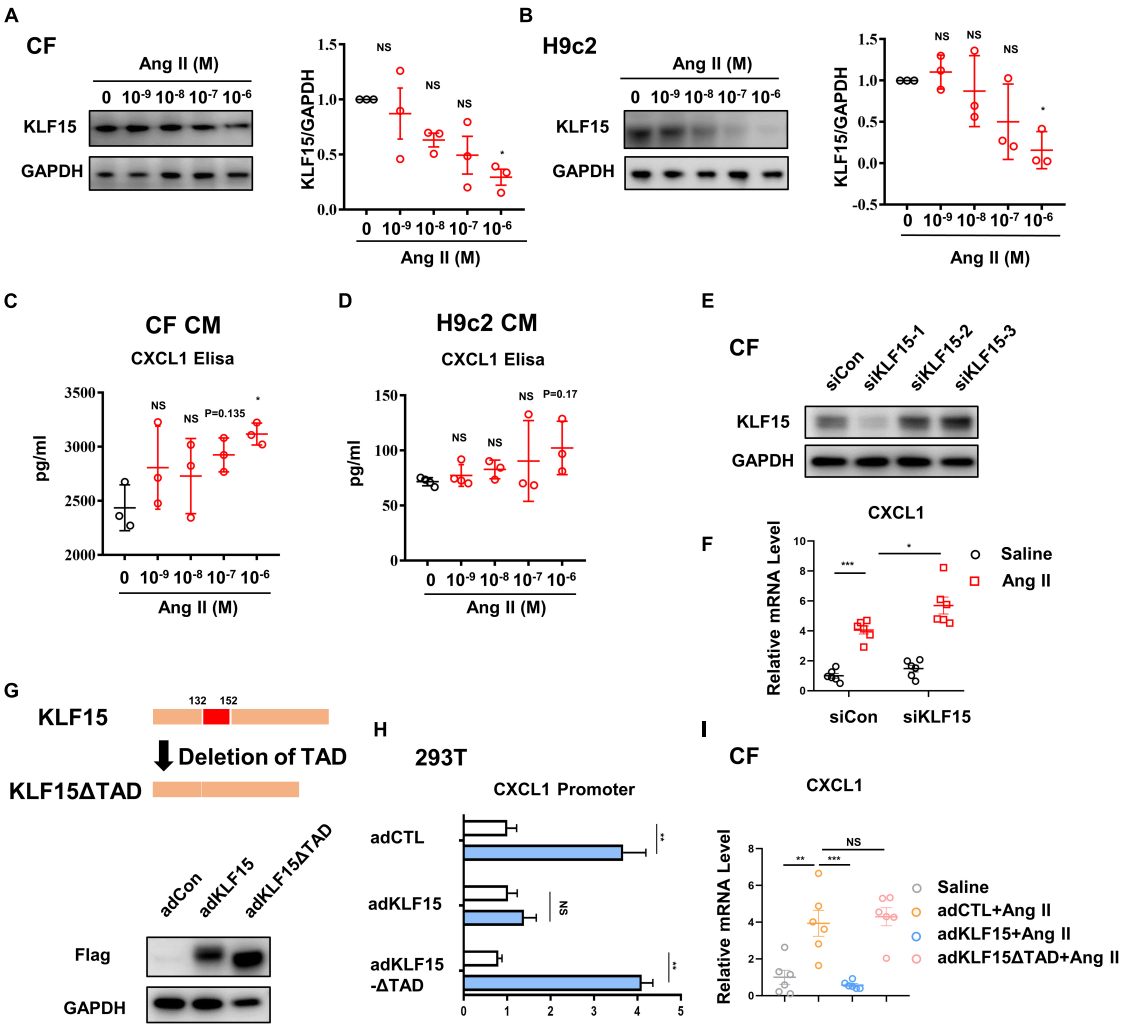

FIGURE 4 | KLF15-TAD negatively regulated *CXCL1* transcription in CF. CF and H9c2 cells were stimulated by different doses of Ang II for 24 h. **(A,B)** KLF15 level was measured and quantified by Western Blot analysis. **(C,D)** The *CXCL1* protein in cell supernatant of Ang II treated CF and H9c2 cells was detected by an Elisa assay. **(E)** CF cells were transfected with con-siRNA and KLF15-siRNA. Successful knockout of KLF15 by KLF15-siRNA was confirmed by Western Blot. **(F)** *CXCL1* mRNA levels of Ang II-treated WT CF and KLF15 knockdown CF were measured by qPCR. **(G)** Adenovirus-mediated overexpression of KLF15 and deletion of transactivation domain (TAD) of KFL15 were verified by Western Blot. **(H)** Luciferase assay was used to detect *CXCL1* promoter activity in AdCTL, AdKLF15, and AdKLF15-ΔTAD-infected CFs. **(I)** *CXCL1* mRNA levels of AdCTL, AdKLF15, and AdKLF15-ΔTAD infected CFs were measured and analyzed by qPCR. $^{*}P < 0.05$, $^{**}P < 0.01$, and $^{***}P < 0.001$.

myofibroblasts, and the mRNA expression of collagen 1a1 also showed no difference between AdKLF15-ΔTAD and AdCTL-infected mice (**Figures 5A,D,E,H**). The improved blood pressure was observed in AdKLF15 group but not AdKLF15-ΔTAD group (**Figure 5F**). Consistent with the results *in vitro*, mRNA expression of *CXCL1* in heart was regulated by KLF15-TAD *in vivo* (**Figure 5I**). These results showed that the protective role of KLF15 in cardiac remodeling depends on its TAD.

Inhibition of *CXCR2* Rescued KLF15 KO Aggravated Cardiac Remodeling

To confirm the effect of KLF15 on *CXCL1/CXCR2* axis *in vivo*, KLF15 KO mice was treated with a *CXCR2*-specific antagonist SB265610 (2 mg/kg, once a day) and infused with Ang II for 2 weeks. Compared with the KLF15 KO mice, both contractile dysfunction (EF and FS) and cardiac hypertrophy (heart/body weight ratio, heart size, myocyte area and mRNA level of ANP, BNP) were improved in SB265610-treated KLF15 mice (**Figures 6A–E,J**). Furthermore, myocardial fibrosis, α-SMA-positive myofibroblasts, and the mRNA expression of collagen 1a1 in KLF15 KO mice hearts were blunted by SB265610 treatment (**Figures 6C,F,G,I**). However, SB265610 showed no effect on the blood pressure (**Figure 6H**). The expression of *CXCR2* protein showed no significant difference between two groups, but there is a certain downward trend (**Figures 6K,L**). The increase of P-mTOR, P-ERK1/2, and P-p65 expression was also rescued by inhibition of *CXCR2* (**Figures 6M–P**).

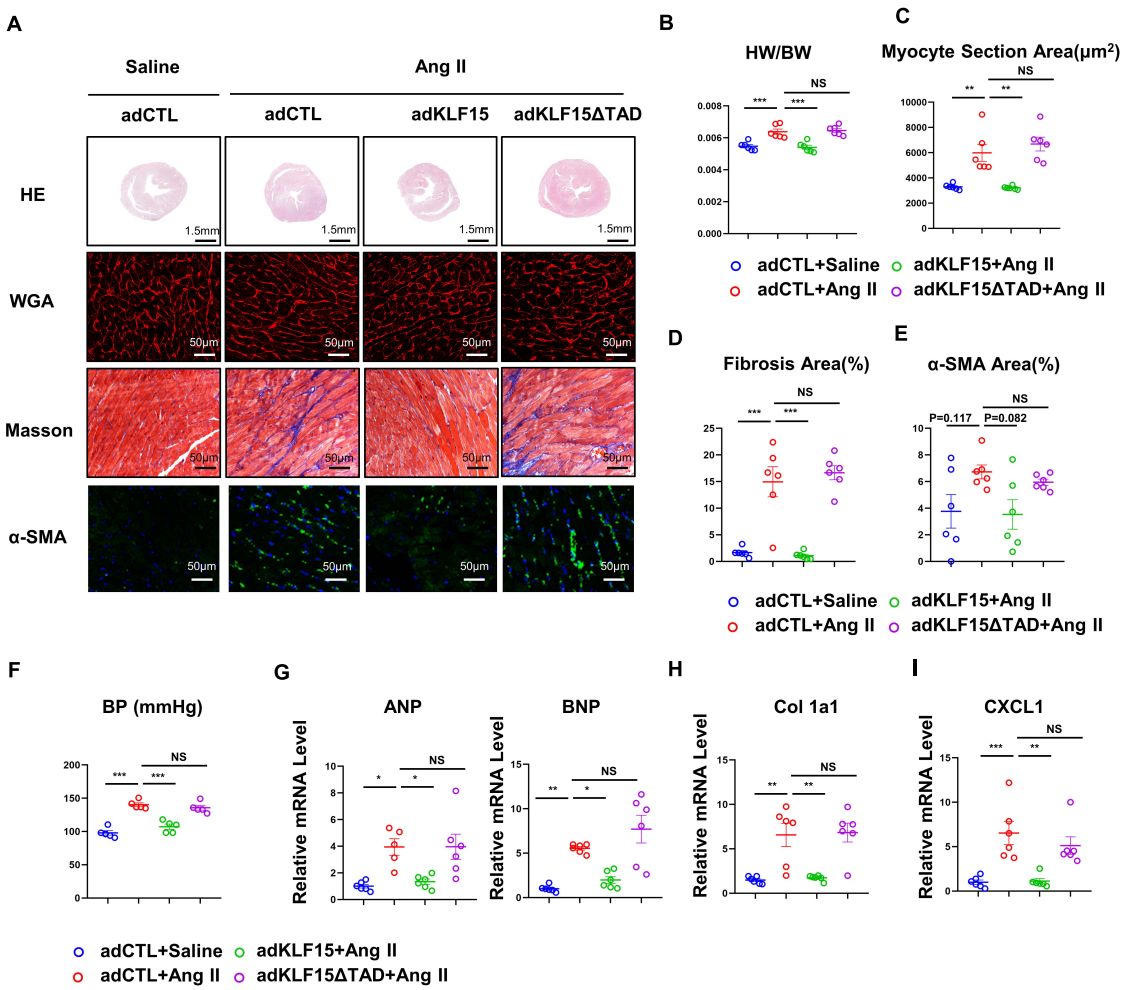

FIGURE 5 | KLF15 improved Ang II-induced cardiac remodeling through TAD. AdCTL, AdKLF15 and Ad KLF15-ΔTAD-infected mice were infused with saline or Ang II for 14 days. **(A)** Representative heart size, WGA stain, Masson stain and α-SMA immunofluorescence image. **(B)** Statistical analysis of heart weight/body weight ratio. **(C)** Quantification analysis of myocyte section area. **(D)** Quantification analysis of fibrotic area measured by Masson stain. **(E)** Quantification analysis of α-SMA positive area measured by immunofluorescence. **(F)** Statistical analysis of blood pressure. **(G–I)** qPCR analysis of mRNA levels of ANP, BNP, Collagen 1a1 and *CXCL1*. $^{*}P < 0.05$, $^{**}P < 0.01$, and $^{***}P < 0.001$.

DISCUSSION

Crosstalk between cardiac cells and inflammatory cells significantly contributes to cardiac remodeling (Frangogiannis, 2018). In this study, we have demonstrated that KLF15 controls cardiac inflammatory response by regulating *CXCL1* expression in the cardiac fibroblasts, which promoted *CXCR2* positive inflammatory cells infiltration and aggravated cardiac dysfunction, hypertrophy, and fibrosis. Importantly, we found that KLF15 but not KLF15-ΔTAD attenuated inflammation-associated cardiac pathological change. KLF15 negatively regulated *CXCL1* expression through TAD to mediate macrophage infiltration into injured heart. Blockade of *CXCL1/CXCR2* signaling attenuated KLF15 deficiency-induced accelerated cardiac remodeling, which provides a new KLF15/*CXCL1* axis in regulation of hypertension-associated cardiac remodeling (**Figure 6Q**).

A major finding is that KLF15 negatively regulates Ang II-induced cardiac remodeling through transactivation domain. Experimental evidence suggested that KLF15 functions as a transcription repressor of cardiac hypertrophy and fibrosis (Zhao et al., 2019). The KLF15 protein domain map shows highly conserved regions including the transactivation domain (Otteson et al., 2004). Functional analysis demonstrated that the KLF15 transactivation domain participates in transcription regulation of mRNA expression (Mas et al., 2011). It is reported that KLF15 TAD peptide competed with full-length KLF15 for binding to P300, and deletion of TAD also showed no effect on downstream gene expression, suggesting the functional role of KLF15 TAD in diseases (Lu et al., 2013). By using adenovirus producing full-length KLF15 or KLF15 with deletion of the transactivation domain, we found that overexpression of KLF15, but not KLF15-ΔTAD, attenuated Ang II-induced cardiac dysfunction, hypertrophy, and fibrosis. These data

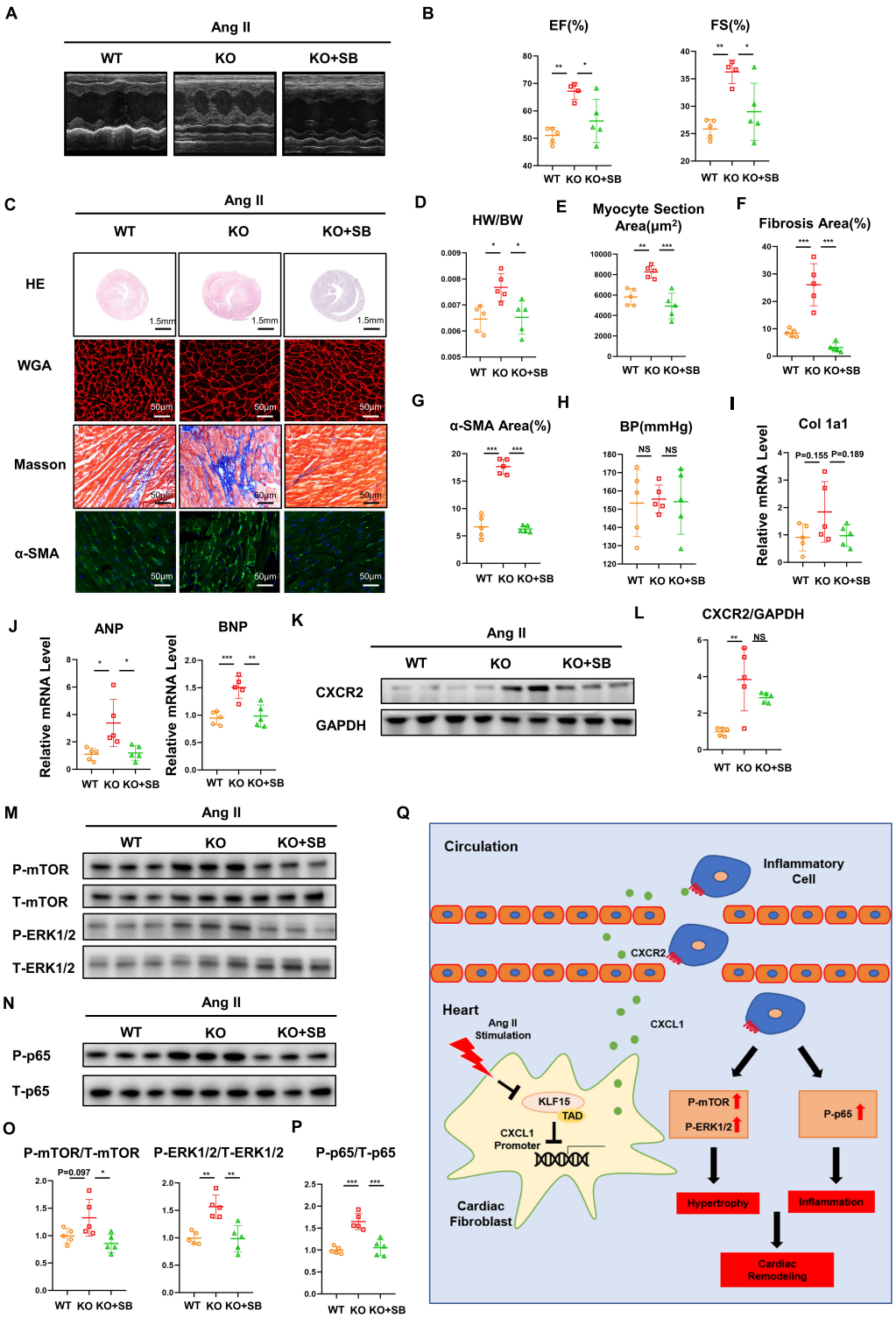

FIGURE 6 | Inhibition of CXCR2 rescued KLF15 KO-aggravated cardiac remodeling. KLF15 KO mice was i.p. injected with SB265610 (2 mg/kg/day) and infused with Ang II for 14 days. WT and KLF15 KO mice only infused with Ang II were used as control. **(A)** M-mode echocardiography of left ventricular chamber. **(B)** Measurement of ejection fraction (EF%) and fractional shortening (FS%). **(C)** Representative heart size, WGA stain, Masson stain and α-SMA immunofluorescence image. **(D)** Heart weight/body weight ratio. **(E)** Quantification of myocyte section area. **(F)** Quantification of fibrotic area revealed by Masson staining. **(G)** Quantification of α-SMA positive area. **(H)** Statistical analysis of blood pressure. **(I,J)** qPCR analysis of mRNA levels of Collagen 1a1, ANP and BNP. **(K,L)** Western Blot and quantification analysis of *CXCR2*/GAPDH. **(M–P)** Western Blot and quantification analysis of P-mTOR/T-mTOR, P-ERK1/2/T-ERK1/2 and P-p65/T-p65 of mice hearts. $^{*}P < 0.05$, $^{**}P < 0.01$, and $^{***}P < 0.001$. **(Q)** A working model describing that KLF15 in cardiac fibroblasts negatively regulates *CXCL1/CXCR2* axis-mediated inflammatory response and subsequent cardiac remodeling in hypertension.

suggest the important role of the conservative transactivation domain in KLF15.

Chemokines play an important role in the pathogenesis of remodeling following cardiac injury by recruiting and activating inflammatory cells, which in turn exert direct effects on resident cardiac cells (Dobaczewski and Frangogiannis, 2009). Recently, we found that KLF15 negatively regulates chemokine CCL2 expression, which recruits macrophages into injured arteries in hypertension (Lu et al., 2019). In this study, we found that KLF15 negatively regulates Ang II-induced *CXCL1* expression in cardiac fibroblasts through transactivation domain. Cardiac fibroblasts traditionally recognized for their structural role in synthesizing and remodeling the ECM in tissues. Growing evidence suggests that activated cardiac fibroblasts are able to secrete different cytokines, chemokines, and growth factors to communicate with inflammatory cells (Van Linthout et al., 2014). Although KLF15 is highly expressed both in cardiac fibroblasts and cardiomyocyte (Chin, 2008), we found that Ang II induced decrease of KLF15 especially in cardiac fibroblasts. Indeed, KLF15 negatively regulates *CXCL1* expression through TAD. Knockout of KLF15 increased Ang II-induced *CXCL1* expression, while overexpression of KLF15 attenuated *CXCL1* expression. Interestingly, we further found that deletion of TAD in KLF15 failed to attenuate Ang II-induced inflammation and cardiac remodeling (Lu et al., 2019). Therefore, the protective role of KLF15 in cardiac remodeling is possible due to the decrease of *CXCL1* expression-mediated inflammatory response.

Recruitment and activation of monocytes and macrophages exert important effects on experimental model of cardiac remodeling (Burchfield et al., 2013). Recently, it has been reported that the *CXCL1/CXCR2* axis is essential for recruitment of monocytes and macrophages into hearts and arteries in hypertension (Wang et al., 2016, 2018). In keeping with those data, we found that the decrease of KLF15 expression was associated with an increase of *CXCL1* and *CXCR2* expression in heart of Ang II infused wild-type mice. Deficiency of KLF15 increased *CXCL1* expression associated with more cardiac $CXCR2^{+}$ positive cells and thereby aggravated cardiac dysfunction and remodeling in response to Ang II. Furthermore, *CXCR2* inhibitors have emerged as a promising therapeutic method for the treatment of inflammatory cardiovascular disease in animal models, including ischemia/reperfusion injury, vascular injury, and cardiac remodeling (Tarzami et al., 2003; Wang et al., 2016; Wang et al., 2018). Therefore, we found that *CXCR2* inhibitors significantly attenuated KLF15 deficiency-induced exacerbation of pathological changes but not blood pressure in response to Ang II. However, a previous study found that *CXCR2* inhibitors reverse Ang II-induced elevated blood pressure (Wang et al., 2016). The inconsistence may be due to the changes of downstream factors regulated by KLF15 that counteract the antihypertensive effect of *CXCR2* inhibitors. In general, these data suggest that KLF15 in cardiac fibroblasts modulates *CXCL1/CXCR2* signaling mediated-inflammatory responses contributing to angiotensin II-induced cardiac remodeling.

Studies have shown that cardiac fibrosis and hypertrophy is involved in several activating signaling pathway including ERK1/2, mTOR, and NFκB (Zhao et al., 2015; Liu et al., 2016). A previous study showed that KLF15 suppressed isoproterenol-induced cardiac hypertrophy and fibrosis by inhibiting mTOR signaling (Gao et al., 2017). Besides, KLF15 was demonstrated to have a protective effect on atherosclerosis via inhibition of NF-κB signaling (Lu et al., 2013). Consistently with these, we found that deficiency of KLF15 promoted activation of mTOR, ERK, and NFκB signaling in hearts, thereby worsening cardiac remodeling and dysfunction. Blockade of the *CXCL1/CXCR2* axis suppressed KLF15 deficiency-mediated aggravated mTOR, ERK, and NFκB signaling pathway activation in response to Ang II, suggesting that inflammatory cells may also participate in this signaling activation.

In summary, by using both KLF15 loss- and gain-of-function mice, our results demonstrate that KLF15 through its transactivation domain modulates *CXCL1* expression-mediated pathological cardiac remodeling processes including inflammatory response, cardiac dysfunction, fibrosis and hypertrophy. Therefore, therapeutic targeting of the KLF15 or *CXCL1/CXCR2* axis may serve as an innovative approach for the treatment of hypertension-associated cardiovascular disease.

DATA AVAILABILITY STATEMENT

The raw data supporting the conclusions of this article will be made available by the authors, without undue reservation.

ETHICS STATEMENT

The animal study was reviewed and approved by the Ethics Review Board of Ruijin Hospital, Shanghai, China.

AUTHOR CONTRIBUTIONS

XDL, YL, JW, and PG designed the research. SH and YL analyzed the data. SH, YL, YG, SL, XL, SS, HZ, and RW performed the research. SH, YL, XDL, and PG wrote the manuscript. All authors contributed to the article and approved the submitted version.

FUNDING

This study was supported by grants from the National Natural Science Foundation of China (82030006, 81770415, 82070245, and 82000255), Natural Science Foundation of Shanghai (20ZR1447500), Laboratory Animals Research Field of Shanghai (201409005700).

SUPPLEMENTARY MATERIAL

The Supplementary Material for this article can be found online at: https://www.frontiersin.org/articles/10.3389/fcell.2021.644954/full#supplementary-material

REFERENCES

Burchfield, J. S., Xie, M., and Hill, J. A. (2013). Pathological ventricular remodeling: mechanisms: part 1 of 2. *Circulation* 128, 388–400. doi: 10.1161/circulationaha.113.001878

Chin, M. T. (2008). KLF15 and cardiac fibrosis: the heart thickens. *J. Mol. Cell. Cardiol.* 45, 165–167. doi: 10.1016/j.yjmcc.2008.05.022

Dobaczewski, M., and Frangogiannis, N. G. (2009). Chemokines and cardiac fibrosis. *Front. Biosci.* 1, 391–405. doi: 10.2741/s33

Frangogiannis, N. G. (2018). Cardiac fibrosis: Cell biological mechanisms, molecular pathways and therapeutic opportunities. *Mol. Aspects Med.* 65, 70–99. doi: 10.1016/j.mam.2018.07.001

Gao, L., Guo, Y., Liu, X., Shang, D., and Du, Y. (2017). KLF15 protects against isoproterenol-induced cardiac hypertrophy via regulation of cell death and inhibition of Akt/mTOR signaling. *Biochem. Biophys. Res. Commun.* 487, 22–27. doi: 10.1016/j.bbrc.2017.03.087

Katz, A. M., and Rolett, E. L. (2016). Heart failure: when form fails to follow function. *Eur. Heart J.* 37, 449–454. doi: 10.1093/eurheartj/ehv548

Kurdi, M., and Booz, G. W. (2011). New take on the role of angiotensin II in cardiac hypertrophy and fibrosis. *Hypertension* 57, 1034–1038. doi: 10.1161/HYPERTENSIONAHA.111.172700

Li, X. D., Hong, M. N., Chen, J., Lu, Y. Y., Ye, M. Q., Ma, Y., et al. (2020). Adventitial fibroblast-derived vascular endothelial growth factor promotes vasa vasorum-associated neointima formation and macrophage recruitment. *Cardiovasc. Res.* 116, 708–720. doi: 10.1093/cvr/cvz159

Liu, J., Zhuang, T., Pi, J., Chen, X., Zhang, Q., Li, Y., et al. (2019). Endothelial Foxp1 regulates pathological cardiac remodeling through TGF-beta1-endothelin-1 signal pathway. *Circulation* 140, 665–680. doi: 10.1161/CIRCULATIONAHA.119.039767

Liu, R., van Berlo, J. H., York, A. J., Vagnozzi, R. J., Maillet, M., and Molkentin, J. D. (2016). DUSP8 regulates cardiac ventricular remodeling by altering ERK1/2 signaling. *Circ. Res.* 119, 249–260. doi: 10.1161/CIRCRESAHA.115.308238

Lu, Y., Zhang, L., Liao, X., Sangwung, P., Prosdocimo, D. A., Zhou, G., et al. (2013). Kruppel-like factor 15 is critical for vascular inflammation. *J. Clin. Invest.* 123, 4232–4241. doi: 10.1172/jci68552

Lu, Y. Y., Li, X. D., Zhou, H. D., Shao, S., He, S., Hong, M. N., et al. (2019). Transactivation domain of Kruppel-like factor 15 negatively regulates angiotensin II-induced adventitial inflammation and fibrosis. *FASEB J.* 33, 6254–6268. doi: 10.1096/fj.201801809R

Mas, C., Lussier-Price, M., Soni, S., Morse, T., Arseneault, G., Di Lello, P., et al. (2011). Structural and functional characterization of an atypical activation domain in erythroid Kruppel-like factor (EKLF). *Proc. Natl. Acad. Sci. U.S.A.* 108, 10484–10489. doi: 10.1073/pnas.1017029108

McConnell, B. B., and Yang, V. W. (2010). Mammalian Kruppel-like factors in health and diseases. *Physiol. Rev.* 90, 1337–1381. doi: 10.1152/physrev.00058.2009

McMaster, W. G., Kirabo, A., Madhur, M. S., and Harrison, D. G. (2015). Inflammation, immunity, and hypertensive end-organ damage. *Circ. Res.* 116, 1022–1033. doi: 10.1161/CIRCRESAHA.116.303697

Noack, C., Iyer, L. M., Liaw, N. Y., Schoger, E., Khadjeh, S., Wagner, E., et al. (2019). KLF15-Wnt-dependent cardiac reprogramming up-regulates SHISA3 in the mammalian heart. *J. Am. Coll. Cardiol.* 74, 1804–1819. doi: 10.1016/j.jacc.2019.07.076

Otteson, D. C., Liu, Y., Lai, H., Wang, C., Gray, S., Jain, M. K., et al. (2004). Kruppel-like factor 15, a zinc-finger transcriptional regulator, represses the rhodopsin and interphotoreceptor retinoid-binding protein promoters. *Invest. Ophthalmol. Vis. Sci.* 45, 2522–2530. doi: 10.1167/iovs.04-0072

Petz, A., Grandoch, M., Gorski, D. J., Abrams, M., Piroth, M., Schneckmann, R., et al. (2019). Cardiac hyaluronan synthesis is critically involved in the cardiac macrophage response and promotes healing after ischemia reperfusion injury. *Circ. Res.* 124, 1433–1447. doi: 10.1161/CIRCRESAHA.118.313285

Sasse, S. K., Kadiyala, V., Danhorn, T., Panettieri, R. A. Jr., Phang, T. L., and Gerber, A. N. (2017). Glucocorticoid receptor ChIP-Seq identifies PLCD1 as a KLF15 target that represses airway smooth muscle hypertrophy. *Am. J. Respir. Cell Mol. Biol.* 57, 226–237. doi: 10.1165/rcmb.2016-0357OC

Shirakawa, K., Endo, J., Kataoka, M., Katsumata, Y., Yoshida, N., Yamamoto, T., et al. (2018). IL-10-STAT3-galectin-3 axis is essential for osteopontin-producing reparative macrophage polarization after myocardial infarction. *Circulation* 138, 2021–2035. doi: 10.1161/CIRCULATIONAHA.118.035047

Tarzami, S. T., Miao, W., Mani, K., Lopez, L., Factor, S. M., Berman, J. W., et al. (2003). Opposing effects mediated by the chemokine receptor *CXCR2* on myocardial ischemia-reperfusion injury: recruitment of potentially damaging neutrophils and direct myocardial protection. *Circulation* 108, 2387–2392. doi: 10.1161/01.CIR.0000093192.72099.9A

Te Riet, L., van Esch, J. H., Roks, A. J., van den Meiracker, A. H., and Danser, A. H. (2015). Hypertension: renin-angiotensin-aldosterone system alterations. *Circ. Res.* 116, 960–975. doi: 10.1161/CIRCRESAHA.116.303587

Van Linthout, S., Miteva, K., and Tschope, C. (2014). Crosstalk between fibroblasts and inflammatory cells. *Cardiovasc. Res.* 102, 258–269. doi: 10.1093/cvr/cvu062

Wang, L., Zhang, Y. L., Lin, Q. Y., Liu, Y., Guan, X. M., Ma, X. L., et al. (2018). CXCL1-*CXCR2* axis mediates angiotensin II-induced cardiac hypertrophy and remodelling through regulation of monocyte infiltration. *Eur. Heart J.* 39, 1818–1831. doi: 10.1093/eurheartj/ehy085

Wang, L., Zhao, X. C., Cui, W., Ma, Y. Q., Ren, H. L., Zhou, X., et al. (2016). Genetic and pharmacologic inhibition of the chemokine receptor *CXCR2* prevents experimental hypertension and vascular dysfunction. *Circulation* 134, 1353–1368. doi: 10.1161/CIRCULATIONAHA.115.020754

Yoda, T., McNamara, K. M., Miki, Y., Onodera, Y., Takagi, K., Nakamura, Y., et al. (2015). KLF15 in breast cancer: a novel tumor suppressor? *Cell. Oncol.* 38, 227–235. doi: 10.1007/s13402-015-0226-8

Zhao, Q. D., Viswanadhapalli, S., Williams, P., Shi, Q., Tan, C., Yi, X., et al. (2015). NADPH oxidase 4 induces cardiac fibrosis and hypertrophy through activating Akt/mTOR and NFkappaB signaling pathways. *Circulation* 131, 643–655. doi: 10.1161/CIRCULATIONAHA.114.011079

Zhao, Y., Song, W., Wang, L., Rane, M. J., Han, F., and Cai, L. (2019). Multiple roles of KLF15 in the heart: underlying mechanisms and therapeutic implications. *J. Mol. Cell. Cardiol.* 129, 193–196. doi: 10.1016/j.yjmcc.2019.01.024

Zuo, C., Li, X., Huang, J., Chen, D., Ji, K., Yang, Y., et al. (2018). Osteoglycin attenuates cardiac fibrosis by suppressing cardiac myofibroblast proliferation and migration through antagonizing LPA3/MMP2/EGFR signaling. *Cardiovasc. Res.* 114, 703–712. doi: 10.1093/cvr/cvy035

Conflict of Interest: The authors declare that the research was conducted in the absence of any commercial or financial relationships that could be construed as a potential conflict of interest.

frontiers in Cell and Developmental Biology

ORIGINAL RESEARCH
published: 09 April 2021
doi: 10.3389/fcell.2021.583492

Myeloid MKL1 Disseminates Cues to Promote Cardiac Hypertrophy in Mice

Li Liu[1,2†], Qianwen Zhao[2†], Lin Lin[1†], Guang Yang[3†], Liming Yu[2], Lili Zhuo[4], Yuyu Yang[1,5]* and Yong Xu[2,5]*

[1] Jiangsu Key Laboratory for Molecular and Medical Biotechnology, College of Life Sciences, Nanjing Normal University, Nanjing, China, [2] Key Laboratory of Targeted Intervention of Cardiovascular Disease and Collaborative Innovation Center for Cardiovascular Translational Medicine, Department of Pathophysiology, Nanjing Medical University, Nanjing, China, [3] Department of Pathology, Suzhou Municipal Hospital Affiliated with Nanjing Medical University, Suzhou, China, [4] Department of Geriatrics, The Second Affiliated Hospital of Nanjing Medical University, Nanjing, China, [5] Institute of Biomedical Research, Liaocheng University, Liaocheng, China

OPEN ACCESS

Edited by:
Hui-Hua Li,
Dalian Medical University, China

Reviewed by:
Aijun Sun,
Fudan University, China
Sonika Patial,
Louisiana State University, United States

***Correspondence:**
Yuyu Yang
yuyujq0818@163.com
Lili Zhuo
zhuolili@njmu.edu.cn

† These authors have contributed equally to this work

Specialty section:
This article was submitted to Signaling, a section of the journal Frontiers in Cell and Developmental Biology

Received: 16 July 2020
Accepted: 04 January 2021
Published: 09 April 2021

Citation:
Liu L, Zhao Q, Lin L, Yang G, Yu L, Zhuo L, Yang Y and Xu Y (2021) Myeloid MKL1 Disseminates Cues to Promote Cardiac Hypertrophy in Mice. Front. Cell Dev. Biol. 9:583492. doi: 10.3389/fcell.2021.583492

Cardiac hypertrophy is a key pathophysiological process in the heart in response to stress cues. Although taking place in cardiomyocytes, the hypertrophic response is influenced by other cell types, both within the heart and derived from circulation. In the present study we investigated the myeloid-specific role of megakaryocytic leukemia 1 (MKL1) in cardiac hypertrophy. Following transverse aortic constriction (TAC), myeloid MKL1 conditional knockout (MFCKO) mice exhibit an attenuated phenotype of cardiac hypertrophy compared to the WT mice. In accordance, the MFCKO mice were protected from excessive cardiac inflammation and fibrosis as opposed to the WT mice. Conditioned media collected from macrophages enhanced the pro-hypertrophic response in cardiomyocytes exposed to endothelin in an MKL1-dependent manner. Of interest, expression levels of macrophage derived miR-155, known to promote cardiac hypertrophy, were down-regulated in the MFCKO mice compared to the WT mice. MKL1 depletion or inhibition repressed miR-155 expression in macrophages. Mechanistically, MKL1 interacted with NF-κB to activate miR-155 transcription in macrophages. In conclusion, our data suggest that MKL1 may contribute to pathological hypertrophy via regulating macrophage-derived miR-155 transcription.

Keywords: transcriptional regulation, cardiac hypertrophy, macrophage, miRNA, NF-κB

INTRODUCTION

Heart failure is defined as irreversible or permanent loss of rhythmic contraction and relaxation of the myocardium rendering insufficient supply of blood and oxygen to peripheral organs and tissues (Gaetani et al., 2020). Heart failure is one of the leading causes of non-accidental deaths worldwide (Udelson and Stevenson, 2016). A host of pathologies, including hypertension, infection, diabetes, and congenital structural heart disease, can cause heart failure. Regardless of the etiologies, heart failure is almost invariably preceded by cardiac hypertrophy, a process morphologically seen as an expansion in cross-sectional area of cardiomyocyte (Liu and Molkentin, 2016; Zhao et al., 2020). At the transcriptional level, cardiac hypertrophy is characterized by the re-activation of fetal genes (e.g., β-MHC). Generally perceived as a compensatory response attempting to preserve heart

function under stress/injurious conditions, persistent hypertrophic response leads to maladaptation and eventually heart failure (Heineke and Molkentin, 2006).

Although the hypertrophic response takes place in the myocardium, it is hardly a cardiomyocyte-autonomous behavior. Instead, different cell types, including cardiac fibroblasts, endothelial cells, and circulating immune cells, contribute to the pathogenesis of pathological hypertrophy by forming cell-cell crosstalk with cardiomyocytes (Zhang et al., 2012; Frieler and Mortensen, 2015; Gogiraju et al., 2019). In addition, numerous humoral factors, originating from both intra-cardiac and extra-cardiac sources, act on the cardiomyocytes to regulate pathological hypertrophy (Ranjan et al., 2019). MicroRNAs or miRNAs, a group of ∼22 nt non-coding small RNAs, represent one of such factors (Patil et al., 2019; Dexheimer and Cochella, 2020). Transported via exosomes, miRNAs can transmit regulatory signals to cardiomyocytes from non-cardiomyocytes to regulate the hypertrophic response (Fan C. et al., 2020). Cardiac fibroblast derived miR-21-3p, for instance, promotes cardiomyocyte hypertrophy via targeting sorbin and SH3 domain-containing protein 2 (SORBS2) and PDZ and LIM domain 5 (PDLIM5) (Bang et al., 2014). Similarly, fibroblast derived miR-27a, miR-28-3p, and miR-34a promote oxidative stress, adverse cardiac remodeling, and heart failure in mice by targeting the antioxidant Nrf2 (Tian et al., 2018). On the contrary, a series of mesenchymal stem cell (MSC) derived miRNAs exert protective effects on cardiomyocytes to avert heart failure (Barile et al., 2014; Feng et al., 2014; Wang et al., 2015).

Megakaryocytic leukemia 1 (MKL1) is a transcriptional regulator with ubiquitous expression patterns (Wang et al., 2002). Developmentally redundant, MKL1 appears to play essential roles in a wide range of postnatal pathophysiological processes. MKL1 has been long considered as a key mechanosensor in various pathophysiological processes (Olson and Nordheim, 2010). Kuwahara et al. (2010) have reported that germline deletion of MKL1 in mice reduced the susceptibility to pressure overload induced cardiac hypertrophy. Further analysis revealed that MKL1 directly bound to the promoters of hypertrophic genes (e.g., atrial natriuretic peptide/ANP) in cultured cardiomyocytes in response to mechanical stretch and that MKL1 deficiency suppressed the expression of hypertrophic genes. Therefore, it was concluded that MKL1 might play a key role in the pathogenesis of pathological hypertrophy. However, whether the ability of MKL1 to regulate cardiac hypertrophy is cardiomyocyte-autonomous remains undetermined. In the present study, we report that MKL1 can contribute to the pathogenesis of cardiac hypertrophy by regulating myeloid-derived pro-hypertrophic cues.

MATERIALS AND METHODS

Animals

All the animal experiments were reviewed and approved by the intramural Ethics Committee on Humane Treatment of Experimental Animals. Myeloid-specific deletion of MKL1 was achieved by crossing the *Mkl1*$^{f/f}$ strain (Liu et al., 2018) with the *LyzM*-Cre strain, respectively (Yu et al., 2018). The offspring were designated based on genotyping: those with the *Mkl1*$^{f/f}$; *LyzM*-Cre genotype (Cre positive) were called MFCKO and those with the *Mkl1*$^{f/f}$ genotype (Cre negative) were called WT. Pathological cardiac hypertrophy was induced in mice by the transverse aortic constriction (TAC) procedure as previously described (Yu et al., 2015). Cardiac functions were evaluated by echocardiography (GE Vivid 7 equipped with a 14-MHz phase array linear transducer, S12, allowing a 150 maximal sweep rate). Mice were anesthetized using 1.5% isoflurane. The body temperature was maintained at 37°C using a heating pad.

Cell Culture, Plasmids, Transient Transfection, and Reporter Assay

Murine macrophages RAW264.7 (ATCC) were maintained in DMEM supplemented with 10% FBS. Murine bone marrow-derived macrophages (BMDM) were isolated and cultured as described before (Yu et al., 2014). Neonatal rat ventricular myocytes (NRVM) were isolated and maintained as previously described (Yang et al., 2017). Endothelin (ET-1) was purchased from Peprotech. CCG-1423 (Chen et al., 2020a; Wu et al., 2020) and PDTC (Xu et al., 2017) were purchased from Selleck. MKL1 expression constructs and miR-155 promoter-luciferase constructs have been described previously (Basso et al., 2012; Thompson et al., 2013; Li et al., 2019c). Small interfering RNAs were purchased from Dharmacon. Transient transfection was performed with Lipofectamine 2,000. Cells were harvested 48 h after transfection and reporter activity was measured using a luciferase reporter assay system (Promega) as previously described (Yang et al., 2019a,b; Chen et al., 2020b,c; Li et al., 2020a).

RNA Extraction and Real-Time PCR

RNA was extracted using an RNeasy RNA isolation kit (Qiagen) as previously described (Fan Z. et al., 2020). Reverse transcriptase reactions were performed using a SuperScript First-strand synthesis system (Invitrogen) as previously described (Li et al., 2020c; Lv et al., 2020; Mao et al., 2020; Yang et al., 2020). Real-time PCR reactions were performed on an ABI STEPONE Plus (Life Tech) with primers and Taqman probes purchased from Applied Biosystems. Ct values of target genes were normalized to the Ct values of housekeekping control gene (18s, 5′-CGCGGTTCTATTTTGTTGGT-3′ and 5′-TCGTCTTCGAAACTCCGACT-3′ for both human and mouse genes) using the ΔΔCt method and expressed as relative mRNA expression levels compared to the control group which is arbitrarily set as 1.

Histology

Histological analysis was performed as previously described (Zhao et al., 2019; Dong et al., 2020; Li et al., 2020b). For immunofluorescence staining, antigen retrieval was performed by boiling the slides in sodium citrate (pH 6.0) for 1 min. The slides were washed 2 × 5 min in TBS plus 0.025% Triton X-100 with gentle agitation, blocked with 5% BSA,

and incubated with anti-CD45 (Abcam, 1:200) overnight. After several washes with PBS, the slides were incubated with FITC-labeled secondary antibodies (Jackson, 1:200) for 30 min. DAPI (Sigma) was added and incubated with cells for 5 min prior to observation. Immunofluorescence was visualized on a confocal microscope (LSM 710, Zeiss). For quantification, stain-positive cells were counted on each slide and normalized to the control group which is arbitrarily set as 1. Images were quantified with ∼10 fields counted per mouse.

Chromatin Immunoprecipitation

Chromatin Immunoprecipitation (ChIP) assays were performed essentially as described before (Fan Z. et al., 2019; Kong et al., 2019a,b; Li et al., 2019a,b,c,d,e; Liu et al., 2019; Lu et al., 2019; Shao et al., 2019; Weng et al., 2019; Sun et al., 2020). Briefly, chromatin was cross-linked with 1% formaldehyde. DNA was fragmented into ∼500 bp pieces using a Branson 250 sonicator. Aliquots of lysates containing 200 μg of protein were used for each immunoprecipitation reaction with anti-MKL1 (Santa Cruz, sc-32909), anti-acetyl H3 (Millipore, 06-599), anti-trimethyl H3K4 (Millipore, 07-473), anti-NF-κB/RelA (Santa, Cruz, sc-372), and anti-BRG1 (Santa Cruz, sc-10768). Precipitated genomic DNA was amplified by real-time PCR. A total of 10% of the starting material is also included as the input. Data are then normalized to the input and expressed as% of recovery.

Statistical Analysis

One-way ANOVA with *post hoc* Scheffe analyses were performed using an SPSS package. Unless otherwise specified, *P*-values smaller than 0.05 were considered statistically significant.

RESULTS

MKL1 Deletion in Myeloid Cells Attenuates Pathological Cardiac Hypertrophy in Mice

Macrophages play key roles in the pathogenesis of cardiac hypertrophy (Schiattarella and Hill, 2015). To evaluate whether MKL1 deficiency in macrphages would impact pathological hypertrophy, the TAC procedure was performed in myeloid conditional MKL1 knockout (MFCKO) mice and wild type (WT) littermates. The deletion of MKL1 in myeloid cells was verified by Western blotting (**Supplementary Figure 1**). Measurements of heart weight/body weight ratios (**Figure 1A**), heart weight/tibia bone length ratios (**Figure 1B**), left ventricular systolic diameter (LVSd) values (**Figure 1C**), left ventricular posterior wall diameter (LVPWd) values (**Figure 1D**), qPCR examination of atrial natriuretic peptide (ANP, **Figure 1E**), brain natriuretic peptide (BNP, **Figure 1F**), and myosin heavy chain beta isoform (β-MHC, **Figure 1G**) in the heart, and wheat germ agglutinin (WGA, which detects cell membrane components such as N-acetylglucosamine and N-acetylneuraminic acid) staining of cardiomyocyte cross-sectional areas (**Figure 1H**) all indicated that pressure overload induced cardiac hypertrophy was attenuated in MFCKO mice compared to WT mice. At 4 week after the surgical procedure, heart functions, as indicated by left ventricular ejection fraction (EF) values and fractional shortening (FS) values, were preserved better in MFCKO mice than in WT mice (**Figures 1I,J**).

MKL1 Deletion in Myeloid Cells Ameliorates Pressure Overload Induced Cardiac Inflammation and Fibrosis in Mice

Next, we analyzed the effects of myeloid-specific MKL1 deletion on cardiac inflammation and cardiac fibrosis during the pathogenesis of cardiac hypertrophy in mice. Quantitative PCR showed that expression levels of pro-inflammatory cytokines, including IL-1β (**Figure 2A**), IL-6 (**Figure 2B**), and TNF-α (**Figure 2C**), were lower in the MFCKO mice than in the WT mice. Suppression of cardiac inflammation as a result of MKL1 loss in myeloid cells was confirmed by immunofluorescence staining of $CD45^+$ cells showing that there were much fewer immune infiltrates in the MFCKO hearts than the WT hearts (**Figure 2D**). On the other hand, qPCR analysis demonstrated that cardiac expression of pro-fibrogenic genes, including α-SMA (**Figure 2E**), collagen type I (**Figure 2F**), and collagen type III (**Figure 2G**), was down-regulated in the MFCKO mice compared to the WT mice. Picrosirius red staining (**Figure 2H**) and Masson's trichrome staining (**Figure 2I**) both confirmed that cardiac fibrosis was mitigated by myeloid-specific deletion of MKL1 in mice. Taken together, these data suggest that the pro-hypertrophic ability of MKL1 may originate from macrophages.

MKL1 Regulates a Pro-Hypertrophic Cue From Macrophages

Having determined that macrophage MKL1 plays an essential role in the development of pressure overload induced pathological hypertrophy in mice, we hypothesized that an MKL1-dependent pro-hypertrophic cue may be transmitted from macrophages to cardiomyocytes. To this send, conditioned media (CM) were collected from cultured macrophages (RAW) and applied to freshly isolated neonatal rat left ventricular myocytes (NRVM) in the presence of ET-1, a potent pro-hypertrophic factor. The addition of macrophage CM enhanced the pro-hypertrophic effects of ET-1 as judged by the expression levels of ANP (**Figure 3B**), BNP (**Figure 3C**), and β-MHC (**Figure 3D**). MKL1 depletion (**Figure 3A** for knockdown efficiency) in macrophages, however, severely compromised the potency of the CM to potentiate ET-1 induced hypertrophy of NRVM. Similarly, pre-treatment of macrophages with CCG-1423, a small-molecule MKL1 inhibitor, significantly dampened the production of the pro-hypertrophic signal (**Figures 3E–G**). Finally, it was observed that CM collected from WT bone marrow

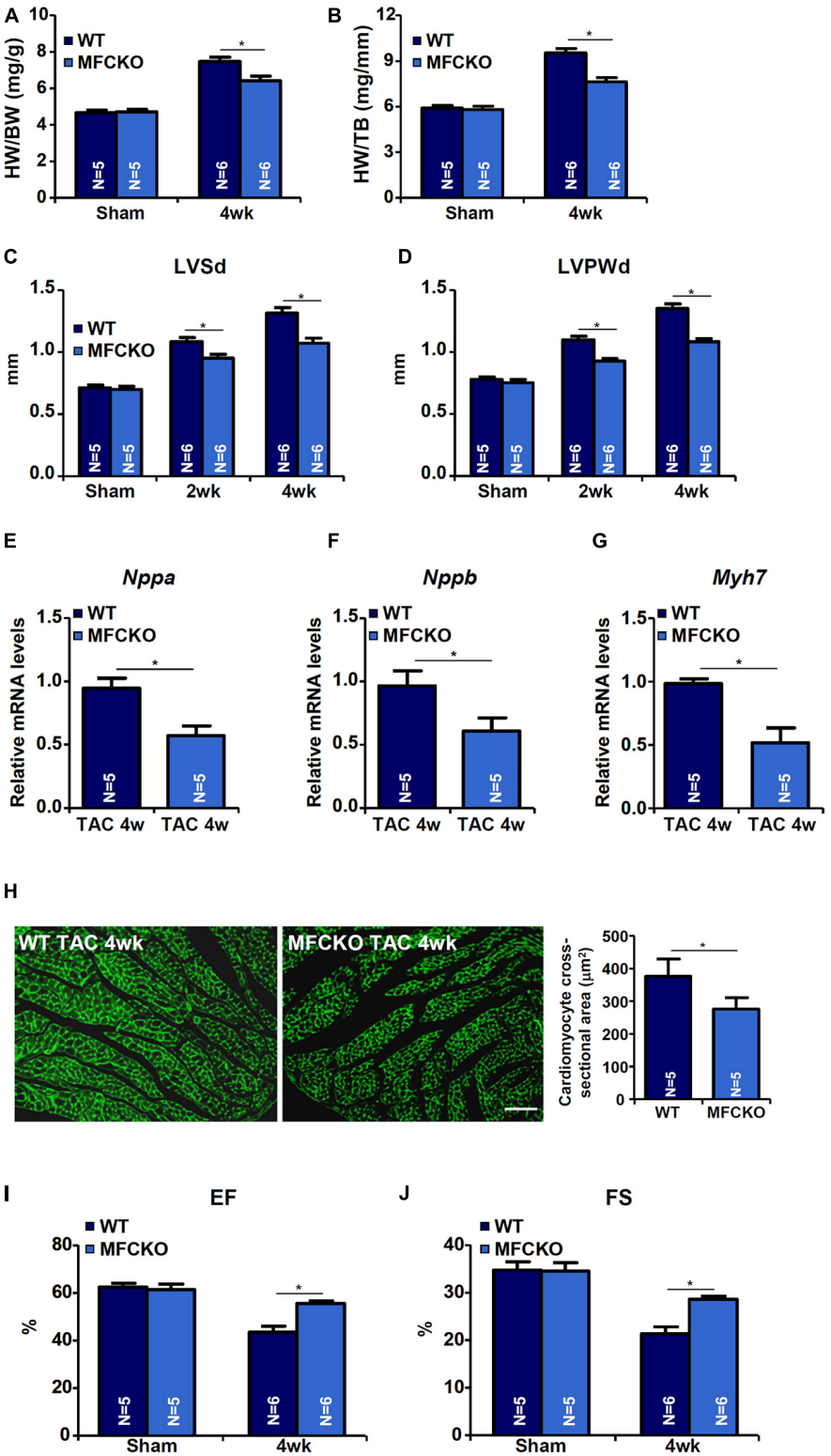

FIGURE 1 | MKL1 deletion in macrophages attenuates pathological cardiac hypertrophy in mice. Myeloid-specific MKL1 knockout mice (MFCKO) and wild type (WT) littermates were subjected to the TAC procedure or the sham procedure. **(A)** Heart weight versus body weight. **(B)** Heart weight versus tibia bone length. **(C)** Left ventricular systolic diameter (LVSd) values. **(D)** Left ventricular posterior wall diameter (LVPWd) values. **(E–G)** Hypertrophic genes were measured by qPCR. **(H)** Cardiomyocyte cross-section areas were measured by wheat germ agglutinin (WGA) staining and quantified by Image J. **(I)** Ejection fraction (EF) values. **(J)** Fractional shortening (FS) values. N = 5∼6 mice. Data represent mean ±SD. $^*p < 0.05$, two-tailed t-test.

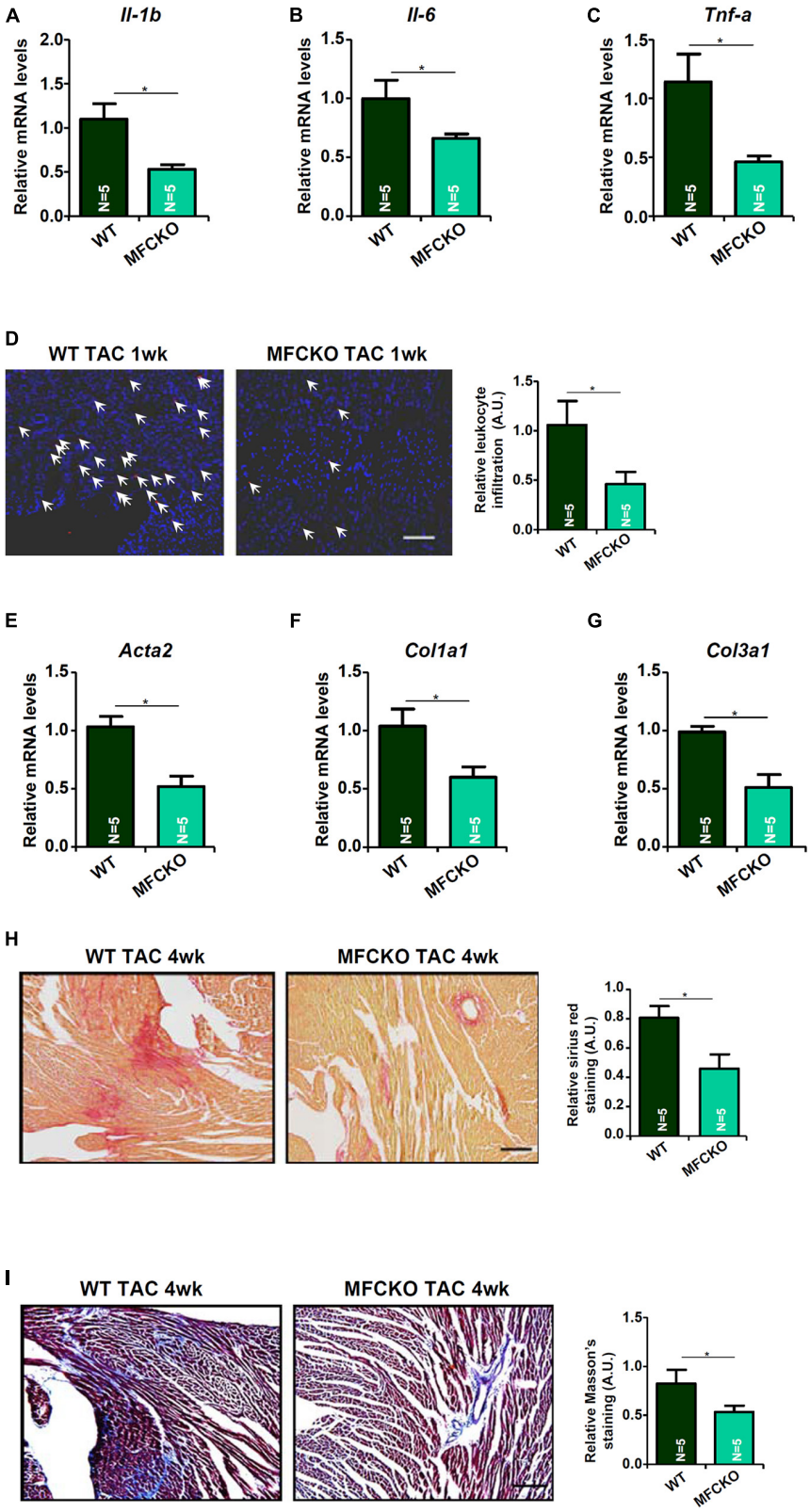

FIGURE 2 | MKL1 deletion in macrophages ameliorates pressure overload induced cardiac inflammation and fibrosis in mice. MFCKO mice and WT mice were subjected to the TAC procedure. **(A–C)** Pro-inflammatory genes were measured by qPCR. **(D)** CD45 staining. **(E–G)** Pro-fibrogenic genes were measured by qPCR. **(H)** Picrosirius red staining. **(I)** Masson's trichrome staining. $N = 5$ mice for each group. Data represent mean ± SD. $^*p < 0.05$, two-tailed t-test.

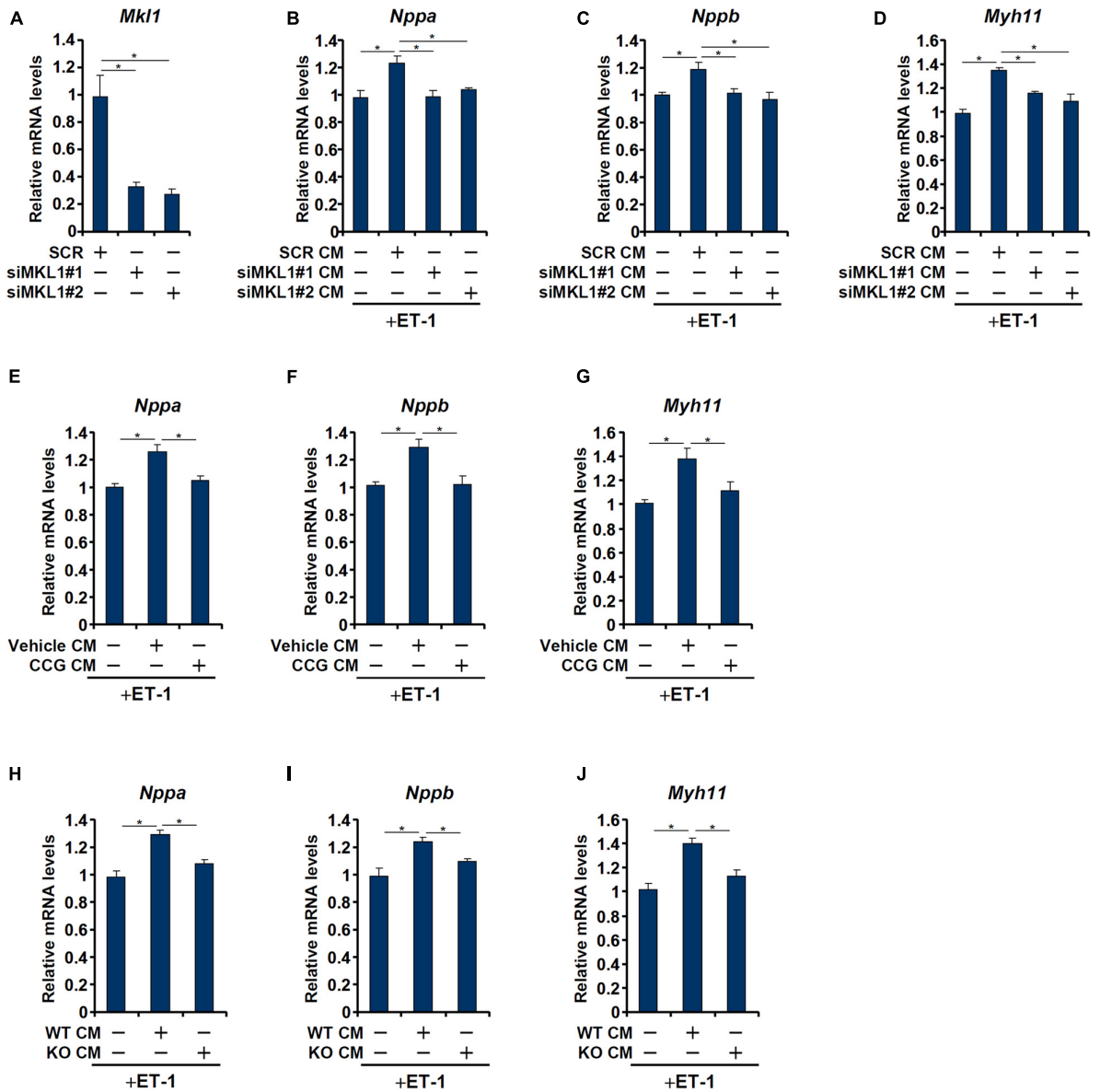

FIGURE 3 | MKL1 regulates a pro-hypertrophic cue from macrophages. **(A–D)** RAW cells were transfected with siRNA targeting MKL1 or scrambled siRNA (SCR). Conditioned media were collected 48 h after transfection and applied to primary neonatal rat ventricular myocytes along with endothelin. Knockdown efficiencies were verified by qPCR and Western **(A)**. ANP **(B)**, BNP **(C)**, and β-MHC **(D)** levels were examined by qPCR. **(E–G)** RAW cells were treated with or without CCG-1423 (10 μM) for 24 h. Conditioned media were collected 48 h after transfection and applied to primary neonatal rat ventricular myocytes along with endothelin. ANP **(E)**, BNP **(F)**, and β-MHC **(G)** levels were examined by qPCR. **(H–J)** Conditioned media were collected from WT and MFCKO bone marrow derived macrophages and applied to primary neonatal rat ventricular myocytes along with endothelin. ANP **(E)**, BNP **(F)**, and β-MHC **(G)** levels were examined by qPCR. Data represent mean ± SD. *$p < 0.05$, One-way ANOVA with *post hoc* Scheffe test.

derived macrophages (BMDMs) had a much stronger pro-hypertrophic effect than those from MKL1 KO BMDMs (**Figures 3H–J**).

MKL1 Regulates miR-155 Expression in Macrophages

Heymans et al. (2013) have reported that macrophage-derived miR-155 is essential for the development of pressure overload induced pathological hypertrophy in mice. We therefore postulated that MKL1 might regulate miR-155 expression in macrophages. Indeed, miR-155 levels were decreased in the MFCKO hearts compared to the WT hearts (**Figure 4A**). Overexpression of MKL1 potentiated the induction of miR-155 expression by ET-1 treatment in RAW cells (**Figure 4B**). Next, endogenous MKL1 was silenced in RAW cells; MKL1 knockdown dampened the induction of miR-155 by ET-1 (**Figure 4C**). Likewise, inhibition of MKL1 activity by CCG-1423 suppressed

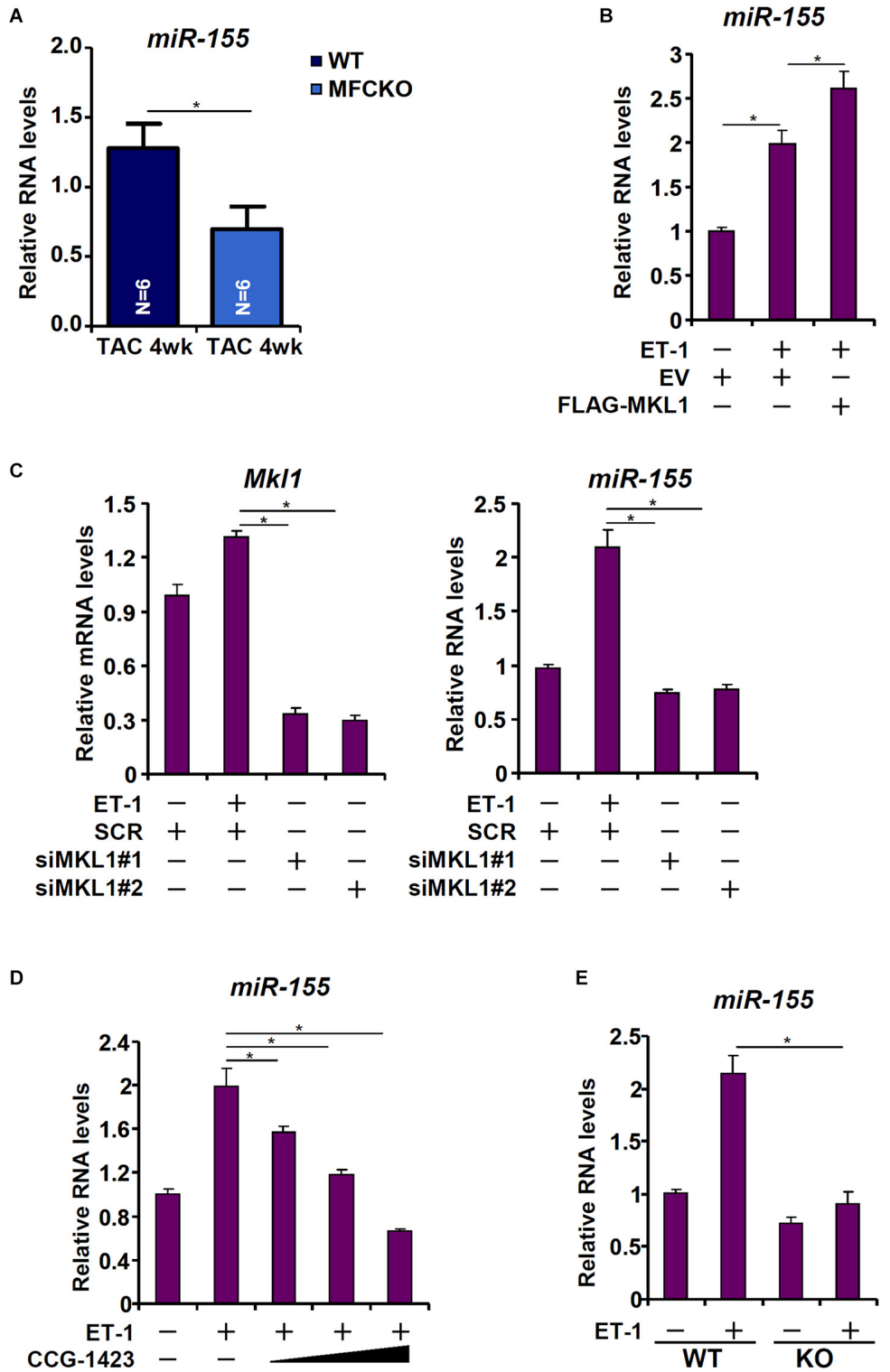

FIGURE 4 | MKL1 regulates miR-155 expression in macrophages. **(A)** MFCKO mice and WT mice were subjected to the TAC procedure. miR-155 levels were examined by qPCR. $N = 5$ mice for each group. Data represent mean ± SD. $^*p < 0.05$, two-tailed *t*-test. **(B)** RAW cells were transfected with MKL1 expression construct or an empty vector (EV) followed by treatment with endothelin. miR-155 levels were examined by qPCR. **(C)** RAW cells were transfected with siRNA targeting MKL1 or SCR followed by treatment with endothelin. miR-155 levels were examined by qPCR. **(D)** RAW cells were treated with endothelin and CCG-1423. miR-155 levels were examined by qPCR. **(E)** BMDMs isolated from WT and MFCKO were treated with endothelin. miR-155 levels were examined by qPCR. Data represent mean ± SD. $^*p < 0.05$, One-way ANOVA with *post hoc* Scheffe test.

the induction of miR-155 by ET-1 (**Figure 4D**). Comparison of miR-155 expression levels in WT BMDMs and MKL1 KO BMDMs confirmed that MKL1 played an essential role in regulating miR-155 expression in macrophages (**Figure 4E**).

MKL1 Interacts With NF-κB to Activate miR-155 Transcription in Macrophages

To investigate whether the regulation of miR-155 expression by MKL1 occurred at the transcriptional level, a miR-155 promoter-luciferase construct (-350/-1) was transfected into HEK293 cells. MKL1 over-expression dose-dependently activated the miR-155 promoter (**Figure 5A**), indicating that MKL1 may indeed directly regulate miR-155 transcription. Next, a series of truncated miR-155 promoter-luciferase constructs were transfected into HEK293 cells with or without MKL1 to determine the region where MKL1 may potentially bind. As shown in **Figure 5B**, MKL1 was able to activate the miR-155 promoter only in the presence of an intact NF-κB site. When the NF-κB site was mutated, MKL1 lost the ability to activate the miR-155 promoter (**Figure 5C**). ChIP assay demonstrated that there was significant MKL1 binding within the proximal miR-155 promoter surrounding the NF-κB site, which was further augmented by ET-1 treatment; in contrast, no appreciable MKL1 binding was detected on the distal miR-155 promoter (**Figure 5D**). Re-ChIP assay confirmed that a RelA-MKL1 complex was detectable on the proximal, but not the distal, miR-155 promoter (**Figure 5E**). Either RelA knockdown (**Figures 5F,G**) or RelA inhibition (**Figure 5H**) by a small-molecule compound (PDTC) abrogated the binding of MKL1, suggesting that MKL1 may rely on NF-κB/RelA to be recruited to the miR-155 promoter. Of interest, MKL1 knockdown weakened the binding of RelA to the miR-155 promoter (**Figure 5I**). This was likely due to an altered chromatin structure because MKL1 deficiency reduced the levels of acetyl H3 (**Figure 5J**) and trimethyl H3K4 (**Figure 5K**) and abolished the recruitment of chromatin remodeling protein BRG1 (**Figure 5L**) on the miR-155 promoter. We thus conclude that interplay between MKL1 and NF-κB/RelA contributes to miR-155 transcription in macrophages.

DISCUSSION

Cell–cell crosstalk represents an important mechanism that guards the physiological and functional integrity of the heart but at the same time underlies the pathogenesis of cardiovascular diseases including pathological hypertrophy and heart failure (Tirziu et al., 2010). Traditionally, cardiac macrophages are thought to contribute to disturbances of cardiomyocyte function by producing/releasing inflammatory cytokines and reactive oxygen species. However, recent studies have found that macrophages may influence cardiomyocyte conductance and regeneration (Gomez et al., 2018). Here we report that MKL1 may indirectly regulate cardiomyocyte hypertrophy by controlling the production of a pro-hypertrophic cue (miR-155) in macrophages (**Figure 6**).

Kuwahara et al. (2010) have shown that mice with germ line deletion of MKL1 are resistant to pressure overload induced cardiac hypertrophy; it was not determined whether the ability of MKL1 to modulate the hypertrophic response is cardiomyocyte autonomous. A recent report showed that TAC-induced cardiac hypertrophy is equivalent in mice with a systemic deletion of MKL1 and a simultaneous cardiomyocyte conditional deletion of its closest sibling MKL2 (also known as MRTF-B) and in WT mice (Trembley et al., 2018). Unlike MKL2, MKL1 is dispensable for embryonic development (Oh et al., 2005; Sun et al., 2006). Although both MKL1 and MKL2 exhibit similar tissue/cell distribution, MKL1 has been reported to function as a much stronger transcriptional activator than MKL2 in cultured cells (Fang et al., 2011; Yang et al., 2013, 2014; Yu et al., 2014, 2017). It is not clear at this point how the loss of MKL1/MKL2 is tolerated during cardiac hypertrophy. One possibility is that myocardin, the founding member of the MRTF family, becomes hyper-activated and mediates pressure overload induced pathological hypertrophy (Xing et al., 2006).

Our data suggest that myeloid conditional MKL1 knockout (MFCKO) mice were more resistant to the development of cardiac hypertrophy than WT mice (**Figure 1**). This is consistent with our recent finding that myeloid MKL1, but not cardiomyocyte MKL1, contributes to cardiac ischemia-reperfusion injury in mice (Yu et al., 2018). This also strongly argues for the indispensable role of MKL1 in regulating macrophage phenotype and function to promote disease pathogenesis when combined with previous reports indicating that MKL1 contributes to colitis (Yu et al., 2014), atherosclerosis (Minami et al., 2012), and sepsis (Yu et al., 2017). We further demonstrate that MKL1 activated the transcription of miR-155, a macrophage-derived pro-hypertrophic cue (Heymans et al., 2013), by interacting with NF-κB/RelA. Again, this piece of evidence echoes previous findings, based on analysis of single gene expression (Fang et al., 2011; Yang et al., 2014; Chen et al., 2015) and genomewide expression (Xie, 2014; Yu et al., 2017), that transcription regulation by MKL1 in macrophage is often considered an extension of its interaction with NF-κB/RelA. Congruently, several reports suggest that NF-κB inhibition suppresses cardiac hypertrophy although a direct role of macrophage RelA has yet to be established *in vivo* (Andersen et al., 2012; Gaspar-Pereira et al., 2012). It should be pointed out that we do not propose miR-155 as the sole macrophage-derived, MKL1-dependent pro-hypertrophic cue. We have previously shown that MKL1 is a transcriptional activator of matrix metalloproteinase 9 (MMP9) in lung cancer cells (Cheng et al., 2015). Coincidently, macrophage-specific over-expression of MMP9 significantly exacerbates cardiac hypertrophy in mice (Toba et al., 2017). In addition, other transcriptional targets of MKL1 including inflammatory cytokines, chemokines, and oxidants may contribute to cardiac hypertrophy.

There are a few lingering issues that deserve further attention. First, although we propose that miR-155 derived from macrophages is directly regulated by MKL1 and may contribute to the pro-hypertrophic response in cardiomyocytes. An alternative scenario taking place in cardiomyocytes could equally contribute to cardiac hypertrophy because miR-155 is expressed and can be up-regulated by pro-hypertrophic stimuli in cardiomyocytes (Seok et al., 2014). It has also been

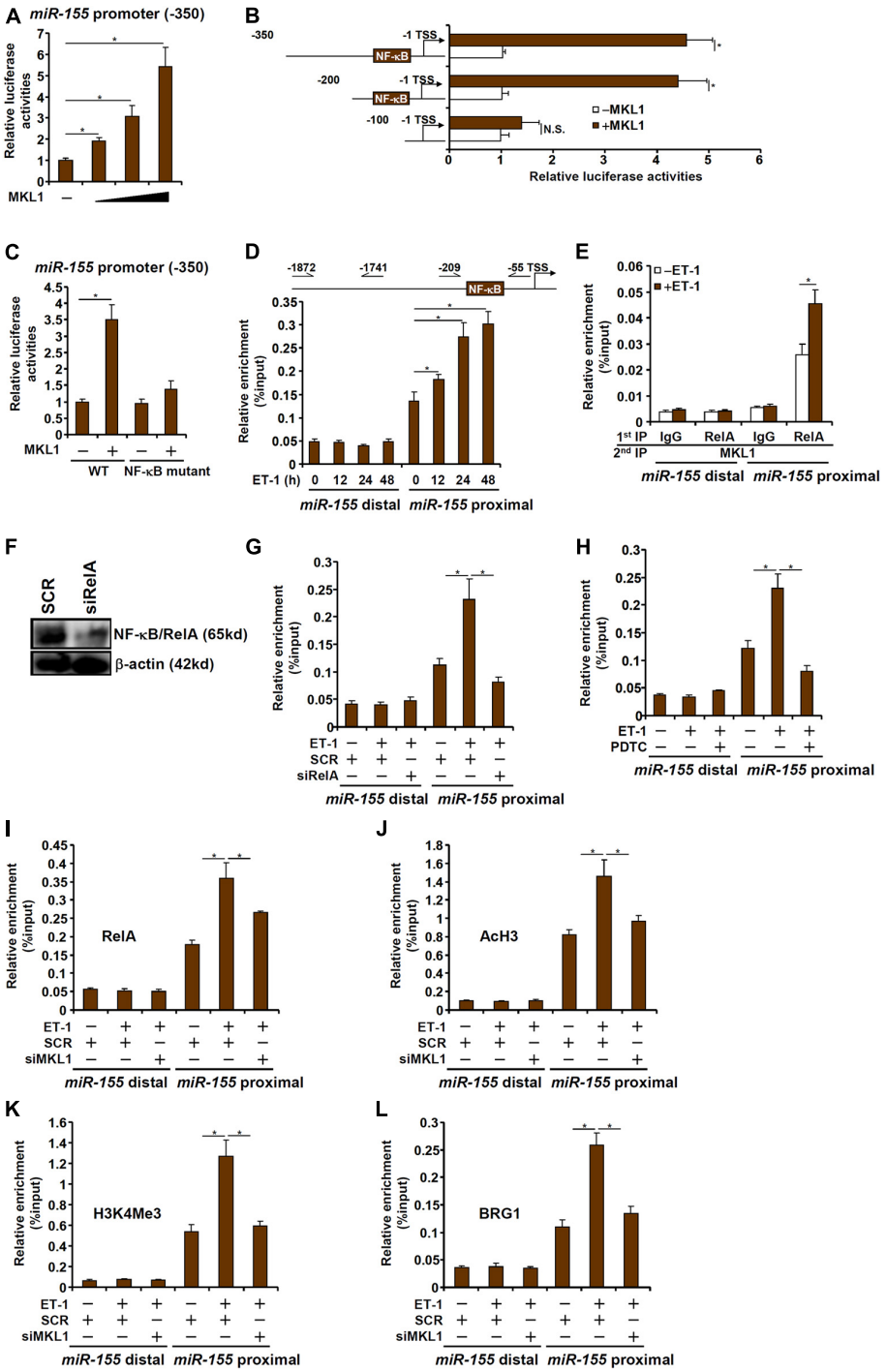

FIGURE 5 | MKL1 interacts with NF-κB to activate miR-155 transcription in macrophages. **(A)** A miR-155 promoter-luciferase construct was transfected into HEK293 cells with or without MKL1. Luciferase activities were normalized by both protein concentration and GFP fluorescence. **(B)** miR-155 promoter-luciferase constructs of various lengths were transfected into HEK293 cells with or without MKL1. Luciferase activities were normalized by both protein concentration and GFP fluorescence. **(C)** Wild type or NF-κB site mutant miR-155 promoter-luciferase construct was transfected into HEK293 cells with or without MKL1. Luciferase activities were normalized by both protein concentration and GFP fluorescence. **(D)** RAW cells were treated with endothelin and harvested at indicated time points. ChIP assays were performed with anti-MKL1. **(E)** RAW cells were treated with or without endothelin for 24h. Re-ChIP assays were performed with indicated antibodies. **(F,G)** RAW cells were transfected with siRNA targeting NF-κB or SCR followed by treatment with endothelin. Knockdown efficiencies and were verified by Western. ChIP assays were performed with anti-MKL1. **(H)** RAW cells were treated with endothelin and/or PDTC. ChIP assays were performed with anti-MKL1. **(I–L)** RAW cells were transfected with siRNA targeting MKL1 or SCR followed by treatment with endothelin. ChIP assays were performed with anti-RelA **(I)**, anti-acetyl H3 **(J)**, anti-H3K4Me3 **(K)**, and anti-BRG1 **(L)**. Data represent mean ± SD. *$p < 0.05$, One-way ANOVA with *post hoc* Scheffe test.

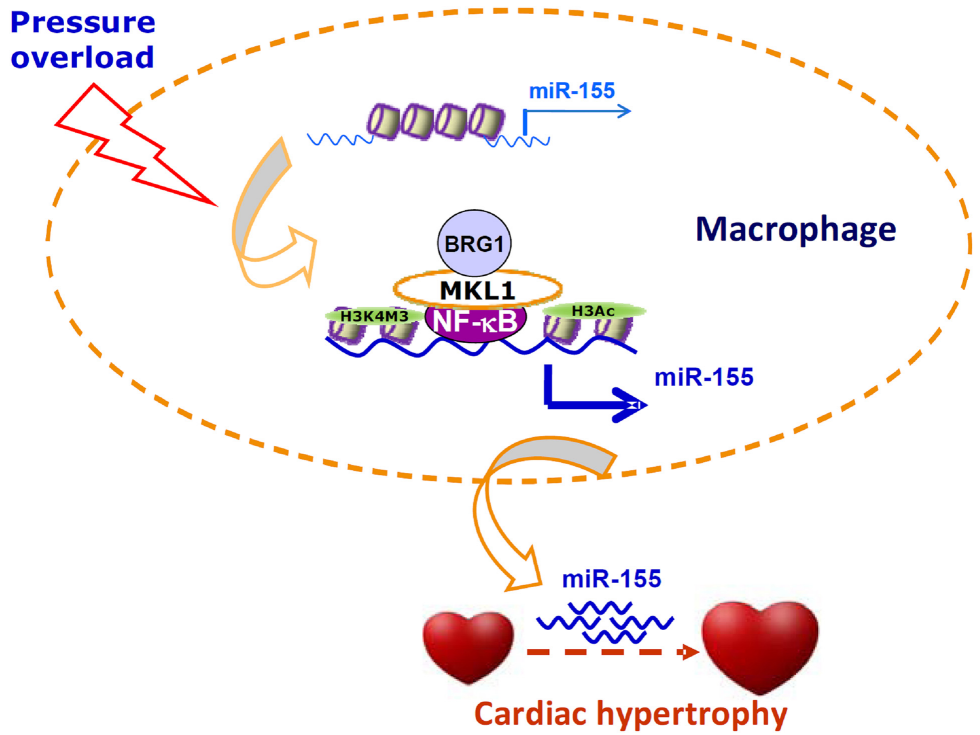

FIGURE 6 | A schematic model. In response to pressure overload, MKL1 is recruited to the miR-155 promoter by interacting with NF-κB in macrophages. MKL1 recruitment leads to altered histone modifications and active chromatin remodeling stabilizing NF-κB binding and activating miR-155 transcription. miR-155, likely transmitted via exosomes, acts on the cardiomyocytes to promote hypertrophy.

shown that ablation of miR-155 in cardiomyocytes appears to be sufficient to blunt the hypertrophic response induced by phenoephrine (PE) (Seok et al., 2014). This alternative model wherein MKL1 activates miR-155 transcription in cardiomyocytes to promote cardiac hypertrophy is certainly tempting in light of our recent report that cardiomyocyte-specific MKL1 deletion attenuates angiotensin II induced cardiac hypertrophy in mice (Wu et al., 2020). Second, the finding that MKL1 relies on NF-κB to regulate miR-155 transcription reinforces the notion that MKL1 and NF-κB are functionally interconnected given previous investigations linking these two factors in the pathogenesis of atherosclerosis (Fang et al., 2011), colitis (Yu et al., 2014), and septic shock (Yu et al., 2017), However, the precise role of NF-κB in the pathogenesis of cardiac hypertrophy has not been conclusively demonstrated especially in animal models likely due to the isoform-specific effects of NF-κB (Gordon et al., 2011). In addition, no direct evidence exists to demonstrate the influence of myeloid-specific NF-κB manipulation on cardiac hypertrophy. Therefore, our observation that MKL1 interacts with NF-κB to activate miR-155 transcription in macrophages cannot be construed as proof of myeloid NF-κB regulating cardiac hypertrophy. Instead, further investigations are needed to disentangle the functional overlap of NF-κB and MKL1 in regulating macrophage behavior and its implication *in vivo*.

In summary, we present evidence to show that myeloid MKL1 plays an essential role in the pathogenesis of cardiac hypertrophy. Previously, we have shown that endothelial MKL1 contributes to cardiac hypertrophy by activating ET-1 transcription (Weng et al., 2015a,b). These data collectively suggest that MKL1 regulates cardiac hypertrophy, at least in part, in a non-autonomous manner.

DATA AVAILABILITY STATEMENT

The original contributions presented in the study are included in the article/**Supplementary Material**, further inquiries can be directed to the corresponding author/s.

ETHICS STATEMENT

The animal study was reviewed and approved by the Nanjing Normal University Ethics Committee on Humane Treatment of Experimental Animals.

AUTHOR CONTRIBUTIONS

YY and LZ conceived the project. LLu, QZ, LLn, GY, and LY designed and performed experiments and collected and analyzed the data. YX wrote the manuscript. YY

and LZ secured funding and provided supervision. All authors contributed to the article and approved the submitted version.

FUNDING

This work was supported by grants from the National Natural Science Foundation of China (81870326 and 81700211), Natural Science Foundation of the Jiangsu Higher Education Institutions of China (20KJB310017), the Key Laboratory of Emergency and Trauma of Ministry of Education (Hainan Medical University) Ministry of Education (KLET-201914), the Priority Academic Program Development of Jiangsu Higher Education Institutions (PAPD), and Six Talent Peaks Project in Jiangsu Province.

SUPPLEMENTARY MATERIAL

The Supplementary Material for this article can be found online at: https://www.frontiersin.org/articles/10.3389/fcell.2021.583492/full#supplementary-material

REFERENCES

Andersen, N. M., Tang, R., Li, L., Javan, H., Zhang, X. Q., and Selzman, C. H. (2012). Inhibitory kappa-B kinase-beta inhibition prevents adaptive left ventricular hypertrophy. *J. Surg. Res.* 178, 105–109. doi: 10.1016/j.jss.2012.03.003

Bang, C., Batkai, S., Dangwal, S., Gupta, S. K., Foinquinos, A., Holzmann, A., et al. (2014). Cardiac fibroblast-derived microRNA passenger strand-enriched exosomes mediate cardiomyocyte hypertrophy. *J. Clin. Invest.* 124, 2136–2146. doi: 10.1172/JCI70577

Barile, L., Lionetti, V., Cervio, E., Matteucci, M., Gherghiceanu, M., Popescu, L. M., et al. (2014). Extracellular vesicles from human cardiac progenitor cells inhibit cardiomyocyte apoptosis and improve cardiac function after myocardial infarction. *Cardiovasc. Res.* 103, 530–541. doi: 10.1093/cvr/cvu167

Basso, K., Schneider, C., Shen, Q., Holmes, A. B., Setty, M., Leslie, C., et al. (2012). BCL6 positively regulates AID and germinal center gene expression via repression of miR-155. *J. Exp. Med.* 209, 2455–2465. doi: 10.1084/jem.20121387

Chen, B., Fan, Z., Sun, L., Chen, J., Feng, Y., Fan, X., et al. (2020a). Epigenetic activation of the small GTPase TCL contributes to colorectal cancer cell migration and invasion. *Oncogenesis* 9:86. doi: 10.1038/s41389-020-00269-9

Chen, B., Yuan, Y., Sun, L., Chen, J., Yang, M., Yin, Y., et al. (2020b). MKL1 mediates TGF-β Induced RhoJ transcription to promote breast cancer cell migration and invasion. *Front. Cell Dev. Biol.* 8:832. doi: 10.3389/fcell.2020.00832

Chen, B., Zhao, Q., Xu, T., Yu, L., Zhuo, L., Yang, Y., et al. (2020c). BRG1 activates PR65A transcription to regulate NO bioavailability in vascular endothelial cell. *Front. Cell Dev. Biol.* 8:774. doi: 10.3389/fcell.2020.00774

Chen, D., Yang, Y., Cheng, X., Fang, F., Xu, G., Yuan, Z., et al. (2015). Megakaryocytic leukemia 1 directs a histone H3 lysine 4 methyltransferase complex to regulate hypoxic pulmonary hypertension. *Hypertension* 65, 821–833. doi: 10.1161/HYPERTENSIONAHA.114.04585

Cheng, X., Yang, Y., Fan, Z., Yu, L., Bai, H., Zhou, B., et al. (2015). MKL1 potentiates lung cancer cell migration and invasion by epigenetically activating MMP9 transcription. *Oncogene* 34, 5570–5581. doi: 10.1038/onc.2015.14

Dexheimer, P. J., and Cochella, L. (2020). MicroRNAs: from mechanism to organism. *Front. Cell Dev. Biol.* 8:409. doi: 10.3389/fcell.2020.00409

Dong, W., Kong, M., Zhu, Y., Shao, Y., Wu, D., Lu, J., et al. (2020). Activation of TWIST transcription by chromatin remodeling protein brg1 contributes to liver fibrosis in mice. *Front. Cell Dev. Biol.* 8:340. doi: 10.3389/fcell.2020.00340

Fan, C., Zhang, E., Joshi, J., Yang, J., Zhang, J., and Zhu, W. (2020). Utilization of human induced pluripotent stem cells for cardiac repair. *Front. Cell Dev. Biol.* 8:36. doi: 10.3389/fcell.2020.00036

Fan, Z., Kong, M., Li, M., Hong, W., Fan, X., and Xu, Y. (2020). Brahma related gene 1 (Brg1) regulates cellular cholesterol synthesis by acting as a Co-factor for SREBP2. *Front. Cell Dev. Biol.* 8:259. doi: 10.3389/fcell.2020.00259

Fan, Z., Li, N., Xu, Z., Wu, J., Fan, X., and Xu, Y. (2019). An interaction between MKL1, BRG1, and C/EBPbeta mediates palmitate induced CRP transcription in hepatocytes. *Biochim. Biophys. Acta Gene Regul. Mech.* 1862:194412. doi: 10.1016/j.bbagrm.2019.194412

Fang, F., Yang, Y., Yuan, Z., Gao, Y., Zhou, J., Chen, Q., et al. (2011). Myocardin-related transcription factor A mediates OxLDL-induced endothelial injury. *Circ. Res.* 108, 797–807. doi: 10.1161/CIRCRESAHA.111.240655

Feng, Y., Huang, W., Wani, M., Yu, X., and Ashraf, M. (2014). Ischemic preconditioning potentiates the protective effect of stem cells through secretion of exosomes by targeting Mecp2 via miR-22. *PLoS One* 9:e88685. doi: 10.1371/journal.pone.0088685

Frieler, R. A., and Mortensen, R. M. (2015). Immune cell and other noncardiomyocyte regulation of cardiac hypertrophy and remodeling. *Circulation* 131, 1019–1030. doi: 10.1161/CIRCULATIONAHA.114.008788

Gaetani, R., Zizzi, E. A., Deriu, M. A., Morbiducci, U., Pesce, M., and Messina, E. (2020). When stiffness matters: mechanosensing in heart development and disease. *Front. Cell Dev. Biol.* 8:334. doi: 10.3389/fcell.2020.00334

Gaspar-Pereira, S., Fullard, N., Townsend, P. A., Banks, P. S., Ellis, E. L., Fox, C., et al. (2012). The NF-kappaB subunit c-Rel stimulates cardiac hypertrophy and fibrosis. *Am. J. Pathol.* 180, 929–939. doi: 10.1016/j.ajpath.2011.11.007

Gogiraju, R., Bochenek, M. L., and Schafer, K. (2019). Angiogenic endothelial cell signaling in cardiac hypertrophy and heart failure. *Front. Cardiovasc. Med.* 6:20. doi: 10.3389/fcvm.2019.00020

Gomez, I., Duval, V., and Silvestre, J. S. (2018). Cardiomyocytes and macrophages discourse on the method to govern cardiac repair. *Front. Cardiovasc. Med.* 5:134. doi: 10.3389/fcvm.2018.00134

Gordon, J. W., Shaw, J. A., and Kirshenbaum, L. A. (2011). Multiple facets of NF-kappaB in the heart: to be or not to NF-kappaB. *Circ. Res.* 108, 1122–1132. doi: 10.1161/CIRCRESAHA.110.226928

Heineke, J., and Molkentin, J. D. (2006). Regulation of cardiac hypertrophy by intracellular signalling pathways. *Nat. Rev. Mol. Cell Biol.* 7, 589–600. doi: 10.1038/nrm1983

Heymans, S., Corsten, M. F., Verhesen, W., Carai, P., van Leeuwen, R. E., Custers, K., et al. (2013). Macrophage microRNA-155 promotes cardiac hypertrophy and failure. *Circulation* 128, 1420–1432. doi: 10.1161/CIRCULATIONAHA.112.001357

Kong, M., Chen, X., Lv, F., Ren, H., Fan, Z., Qin, H., et al. (2019a). Serum response factor (SRF) promotes ROS generation and hepatic stellate cell activation by epigenetically stimulating NCF1/2 transcription. *Redox Biol.* 26:101302. doi: 10.1016/j.redox.2019.101302

Kong, M., Hong, W., Shao, Y., Lv, F., Fan, Z., Li, P., et al. (2019b). Ablation of serum response factor in hepatic stellate cells attenuates liver fibrosis. *J. Mol. Med.* 97, 1521–1533. doi: 10.1007/s00109-019-01831-8

Kuwahara, K., Kinoshita, H., Kuwabara, Y., Nakagawa, Y., Usami, S., Minami, T., et al. (2010). Myocardin-related transcription factor A is a common mediator of mechanical stress- and neurohumoral stimulation-induced cardiac hypertrophic signaling leading to activation of brain natriuretic peptide gene expression. *Mol. Cell Biol.* 30, 4134–4148. doi: 10.1128/MCB.00154-10

Li, N., Liu, S., Zhang, Y., Yu, L., Hu, Y., Wu, T., et al. (2020a). Transcriptional activation of matricellular protein Spondin2 (SPON2) by BRG1 in vascular endothelial cells promotes macrophage chemotaxis. *Front. Cell Dev. Biol.* 8:794. doi: 10.3389/fcell.2020.00794

Li, Z., Kong, X., Zhang, Y., Yu, L., Guo, J., and Xu, Y. (2020b). Dual roles of chromatin remodeling protein BRG1 in angiotensin II-induced endothelial-mesenchymal transition. *Cell Death Dis.* 11:549. doi: 10.1038/s41419-020-02744-y

Li, Z., Zhang, Y., Yu, L., Xiao, B., Li, T., Kong, X., et al. (2020c). BRG1 stimulates endothelial derived alarmin MRP8 to promote macrophage infiltration in an animal model of cardiac Hypertrophy. *Front. Cell Dev. Biol.* 8:569. doi: 10.3389/fcell.2020.00569

Li, Z., Chen, B., Dong, W., Kong, M., Fan, Z., Yu, L., et al. (2019a). MKL1 promotes endothelial-to-mesenchymal transition and liver fibrosis by activating TWIST1 transcription. *Cell Death Dis.* 10:899. doi: 10.1038/s41419-019-2101-4

Li, Z., Chen, B., Dong, W., Kong, M., Shao, Y., Fan, Z., et al. (2019b). The chromatin remodeler Brg1 integrates ROS production and endothelial-mesenchymal transition to promote liver fibrosis in mice. *Front. Dev. Cell Biol.* 7:245. doi: 10.3389/fcell.2019.00245

Li, Z., Li, P., Lu, Y., Sun, D., Zhang, X., and Xu, Y. (2019c). A non-autonomous role of MKL1 in the activation of hepatic stellate cells. *Biochim. Biophys. Acta Gene Regul. Mech.* 1862, 609–618. doi: 10.1016/j.bbagrm.2019.03.001

Li, Z., Lv, F., Dai, C., Wang, Q., JIang, C., Fang, M., et al. (2019d). Activation of galectin-3 (LGALS3) transcription by injurious stimuli in the liver is commonly mediated by BRG1. *Front. Cell Dev. Biol.* 7:310. doi: 10.3389/fcell.2019.00310

Li, Z., Xia, J., Fang, M., and Xu, Y. (2019e). Epigenetic regulation of lung cancer cell proliferation and migration by the chromatin remodeling protein BRG1. *Oncogenesis* 8:66. doi: 10.1038/s41389-019-0174-7

Liu, L., Mao, L., Wu, X., Wu, T., Liu, W., Yang, Y., et al. (2019). BRG1 regulates endothelial-derived IL-33 to promote ischemia-reperfusion induced renal injury and fibrosis in mice. *Biochim. Biophys. Acta Mol. Basis Dis.* 1865, 2551–2561. doi: 10.1016/j.bbadis.2019.06.015

Liu, L., Wu, X., Xu, H., Yu, L., Zhang, X., Li, L., et al. (2018). Myocardin-related transcription factor A (MRTF-A) contributes to acute kidney injury by regulating macrophage ROS production. *Biochim. Biophys. Acta Mol. Basis Dis.* 1864, 3109–3121. doi: 10.1016/j.bbadis.2018.05.026

Liu, R., and Molkentin, J. D. (2016). Regulation of cardiac hypertrophy and remodeling through the dual-specificity MAPK phosphatases (DUSPs). *J. Mol. Cell Cardiol.* 101, 44–49. doi: 10.1016/j.yjmcc.2016.08.018

Lu, Y., Lv, F., Kong, M., Chen, X., Duan, Y., Sun, D., et al. (2019). A cAbl-MRTF-A feedback loop contributes to hepatic stellate cell activation. *Front. Cell Dev. Biol.* 7:243. doi: 10.3389/fcell.2019.00243

Lv, F., Li, N., Kong, M., Wu, J., Fan, Z., Miao, D., et al. (2020). CDKN2a/p16 antagonizes hepatic stellate cell activation and liver fibrosis by modulating ROS levels. *Front. Cell Dev. Biol.* 8:176. doi: 10.3389/fcell.2020.00176

Mao, L., Liu, L., Zhang, T., Qin, H., Wu, X., and Xu, Y. (2020). Histone deacetylase 11 contributes to renal fibrosis by repressing KLF15 transcription. *Front. Cell Dev. Biol.* 8:235. doi: 10.3389/fcell.2020.00235

Minami, T., Kuwahara, K., Nakagawa, Y., Takaoka, M., Kinoshita, H., Nakao, K., et al. (2012). Reciprocal expression of MRTF-A and myocardin is crucial for pathological vascular remodelling in mice. *EMBO J.* 31, 4428–4440. doi: 10.1038/emboj.2012.296

Oh, J., Richardson, J. A., and Olson, E. N. (2005). Requirement of myocardin-related transcription factor-B for remodeling of branchial arch arteries and smooth muscle differentiation. *Proc. Natl. Acad. Sci. U.S.A.* 102, 15122–15127. doi: 10.1073/pnas.0507346102

Olson, E. N., and Nordheim, A. (2010). Linking actin dynamics and gene transcription to drive cellular motile functions. *Nat. Rev. Mol. Cell Biol.* 11, 353–365. doi: 10.1038/nrm2890

Patil, M., Henderson, J., Luong, H., Annamalai, D., Sreejit, G., and Krishnamurthy, P. (2019). The art of intercellular wireless communications: exosomes in heart disease and therapy. *Front. Cell Dev. Biol.* 7:315. doi: 10.3389/fcell.2019.00315

Ranjan, P., Kumari, R., and Verma, S. K. (2019). Cardiac fibroblasts and cardiac fibrosis: precise role of exosomes. *Front. Cell Dev. Biol.* 7:318. doi: 10.3389/fcell.2019.00318

Schiattarella, G. G., and Hill, J. A. (2015). Inhibition of hypertrophy is a good therapeutic strategy in ventricular pressure overload. *Circulation* 131, 1435–1447. doi: 10.1161/CIRCULATIONAHA.115.013894

Seok, H. Y., Chen, J., Kataoka, M., Huang, Z. P., Ding, J., Yan, J., et al. (2014). Loss of MicroRNA-155 protects the heart from pathological cardiac hypertrophy. *Circ. Res.* 114, 1585–1595. doi: 10.1161/CIRCRESAHA.114.303784

Shao, J., Weng, X., Zhuo, L., Yu, L., Li, Z., Shen, K., et al. (2019). Angiotensin II induced CSF1 transcription is mediated by a crosstalk between different epigenetic factors in vascular endothelial cells. *Biochim. Biophys. Acta Gene Regul. Mech.* 1862, 1–11. doi: 10.1016/j.bbagrm.2018.10.001

Sun, L., Chen, B., Wu, J., Jiang, C., Fan, Z., Feng, Y., et al. (2020). Epigenetic regulation of a disintegrin and metalloproteinase (ADAM) promotes colorectal cancer cell migration and invasion. *Front. Cell Dev. Biol.* 8:581692. doi: 10.3389/fcell.2020.581692

Sun, Y., Boyd, K., Xu, W., Ma, J., Jackson, C. W., Fu, A., et al. (2006). Acute myeloid leukemia-associated Mkl1 (Mrtf-a) is a key regulator of mammary gland function. *Mol. Cell Biol.* 26, 5809–5826. doi: 10.1128/MCB.00024-06

Thompson, R. C., Vardinogiannis, I., and Gilmore, T. D. (2013). Identification of an NF-kappaB p50/p65-responsive site in the human MIR155HG promoter. *BMC Mol. Biol.* 14:24. doi: 10.1186/1471-2199-14-24

Tian, C., Gao, L., Zimmerman, M. C., and Zucker, I. H. (2018). Myocardial infarction-induced microRNA-enriched exosomes contribute to cardiac Nrf2 dysregulation in chronic heart failure. *Am. J. Physiol. Heart Circ. Physiol.* 314, H928–H939. doi: 10.1152/ajpheart.00602.2017

Tirziu, D., Giordano, F. J., and Simons, M. (2010). Cell communications in the heart. *Circulation* 122, 928–937. doi: 10.1161/CIRCULATIONAHA.108.847731

Toba, H., Cannon, P. L., Yabluchanskiy, A., Iyer, R. P., D'Armiento, J., and Lindsey, M. L. (2017). Transgenic overexpression of macrophage matrix metalloproteinase-9 exacerbates age-related cardiac hypertrophy, vessel rarefaction, inflammation, and fibrosis. *Am. J. Physiol. Heart Circ. Physiol.* 312, H375–H383. doi: 10.1152/ajpheart.00633.2016

Trembley, M. A., Quijada, P., Agullo-Pascual, E., Tylock, K. M., Colpan, M., Dirkx, R. A. Jr., et al. (2018). Mechanosensitive gene regulation by myocardin-related transcription factors is required for cardiomyocyte integrity in load-induced ventricular hypertrophy. *Circulation* 138, 1864–1878. doi: 10.1161/CIRCULATIONAHA.117.031788

Udelson, J. E., and Stevenson, L. W. (2016). The future of heart failure diagnosis. Therapy, and Management. *Circulation* 133, 2671–2686. doi: 10.1161/CIRCULATIONAHA.116.023518

Wang, D. Z., Li, S., Hockemeyer, D., Sutherland, L., Wang, Z., Schratt, G., et al. (2002). Potentiation of serum response factor activity by a family of myocardin-related transcription factors. *Proc. Natl. Acad. Sci. U.S.A.* 99, 14855–14860. doi: 10.1073/pnas.222561499

Wang, Y., Zhang, L., Li, Y., Chen, L., Wang, X., Guo, W., et al. (2015). Exosomes/microvesicles from induced pluripotent stem cells deliver cardioprotective miRNAs and prevent cardiomyocyte apoptosis in the ischemic myocardium. *Int. J. Cardiol.* 192, 61–69. doi: 10.1016/j.ijcard.2015.05.020

Weng, X., Yu, L., Liang, P., Chen, D., Cheng, X., Yang, Y., et al. (2015a). Endothelial MRTF-A mediates angiotensin II induced cardiac hypertrophy. *J. Mol. Cell Cardiol.* 80, 23–33. doi: 10.1016/j.yjmcc.2014.11.009

Weng, X., Yu, L., Liang, P., Li, L., Dai, X., Zhou, B., et al. (2015b). A crosstalk between chromatin remodeling and histone H3K4 methyltransferase complexes in endothelial cells regulates angiotensin II-induced cardiac hypertrophy. *J. Mol. Cell Cardiol.* 82, 48–58. doi: 10.1016/j.yjmcc.2015.02.010

Weng, X., Zhang, Y., Li, Z., Yu, L., Xu, F., Fang, M., et al. (2019). Class II transactivator (CIITA) mediates IFN-gamma induced eNOS repression by enlisting SUV39H1. *Biochim. Biophys. Acta Gene Regul. Mech.* 1862, 163–172. doi: 10.1016/j.bbagrm.2019.01.005

Wu, T., Wang, H., Xin, X., Yang, J., Hou, Y., Fang, M., et al. (2020). An MRTF-A-Sp1-PDE5 axis mediates angiotensin-ii-induced cardiomyocyte hypertrophy. *Front. Cell Dev. Biol.* 8:839. doi: 10.3389/fcell.2020.00839

Xie, L. (2014). MKL1/2 and ELK4 co-regulate distinct serum response factor (SRF) transcription programs in macrophages. *BMC Genomics* 15:301. doi: 10.1186/1471-2164-15-301

Xing, W., Zhang, T. C., Cao, D., Wang, Z., Antos, C. L., Li, S., et al. (2006). Myocardin induces cardiomyocyte hypertrophy. *Circ. Res.* 98, 1089–1097. doi: 10.1161/01.RES.0000218781.23144.3e

Xu, W., Xu, H., Fang, M., Wu, X., and Xu, Y. (2017). MKL1 links epigenetic activation of MMP2 to ovarian cancer cell migration and invasion. *Biochem. Biophys. Res. Commun.* 487, 500–508. doi: 10.1016/j.bbrc.2017.04.006

Yang, G., Weng, X., Zhao, Y., Zhang, X., Hu, Y., Dai, X., et al. (2017). The histone H3K9 methyltransferase SUV39H links SIRT1 repression to myocardial infarction. *Nat. Commun.* 8:14941. doi: 10.1038/ncomms14941

Yang, Y., Chen, D., Yuan, Z., Fang, F., Cheng, X., Xia, J., et al. (2013). Megakaryocytic leukemia 1 (MKL1) ties the epigenetic machinery to hypoxia-induced transactivation of endothelin-1. *Nucleic Acids Res.* 41, 6005–6017. doi: 10.1093/nar/gkt311

Yang, Y., Cheng, X., Tian, W., Zhou, B., Wu, X., Xu, H., et al. (2014). MRTF-A steers an epigenetic complex to activate endothelin-induced pro-inflammatory transcription in vascular smooth muscle cells. *Nucleic Acids Res.* 42, 10460–10472. doi: 10.1093/nar/gku776

Yang, Y., Li, Z., Guo, J., and Xu, Y. (2020). Deacetylation of MRTF-A by SIRT1 defies senescence induced down-regulation of collagen type I in fibroblast cells. *Biochim. Biophys. Acta Mol. Basis Dis.* 1866:165723. doi: 10.1016/j.bbadis.2020.165723

Yang, Y., Liu, L., Fang, M., Bai, H., and Xu, Y. (2019a). The chromatin remodeling protein BRM regulates the transcription of tight junction proteins: Implication in breast cancer metastasis. *Biochim. Biophys. Acta Gene Regul. Mech.* 1862, 547–556. doi: 10.1016/j.bbagrm.2019.03.002

Yang, Y., Liu, L., Li, M., Cheng, X., Fang, M., Zeng, Q., et al. (2019b). The chromatin remodeling protein BRG1 links ELOVL3 trans-activation to prostate cancer metastasis. *Biochim. Biophys. Acta Gene Regul. Mech.* 1862, 834–845. doi: 10.1016/j.bbagrm.2019.05.005

Yu, L., Fang, F., Dai, X., Xu, H., Qi, X., Fang, M., et al. (2017). MKL1 defines the H3K4Me3 landscape for NF-kappaB dependent inflammatory response. *Sci. Rep.* 7:191. doi: 10.1038/s41598-017-00301-w

Yu, L., Weng, X., Liang, P., Dai, X., Wu, X., Xu, H., et al. (2014). MRTF-A mediates LPS-induced pro-inflammatory transcription by interacting with the COMPASS complex. *J. Cell Sci.* 127, 4645–4657. doi: 10.1242/jcs.152314

Yu, L., Yang, G., Weng, X., Liang, P., Li, L., Li, J., et al. (2015). Histone methyltransferase SET1 mediates angiotensin ii-induced endothelin-1 transcription and cardiac hypertrophy in mice. *Arterioscler Thromb. Vasc. Biol.* 35, 1207–1217. doi: 10.1161/ATVBAHA.115.305230

Yu, L., Yang, G., Zhang, X., Wang, P., Weng, X., Yang, Y., et al. (2018). Megakaryocytic Leukemia 1 (MKL1) bridges epigenetic activation of NADPH oxidase in macrophages to cardiac ischemia-reperfusion injury. *Circulation* 138, 2820–2836. doi: 10.1161/CIRCULATIONAHA.118.035377

Zhang, P., Su, J., and Mende, U. (2012). Cross talk between cardiac myocytes and fibroblasts: from multiscale investigative approaches to mechanisms and functional consequences. *Am. J. Physiol. Heart Circ. Physiol.* 303, H1385–H1396. doi: 10.1152/ajpheart.01167.2011

Zhao, M. T., Ye, S., Su, J., and Garg, V. (2020). Cardiomyocyte proliferation and maturation: two sides of the same coin for heart regeneration. *Front. Cell Dev. Biol.* 8:594226. doi: 10.3389/fcell.2020.594226

Zhao, Q., Yang, J., Chen, H., Li, J., Que, L., Zhu, G., et al. (2019). Peli1 induction impairs cardiac microvascular endothelium through Hsp90 dissociation from IRE1alpha. *Biochim. Biophys. Acta Mol. Basis Dis.* 1865, 2606–2617. doi: 10.1016/j.bbadis.2019.06.017

Conflict of Interest: The authors declare that the research was conducted in the absence of any commercial or financial relationships that could be construed as a potential conflict of interest.

frontiers in Cell and Developmental Biology

ORIGINAL RESEARCH
published: 13 April 2021
doi: 10.3389/fcell.2021.654051

LCZ696 Attenuated Doxorubicin-Induced Chronic Cardiomyopathy Through the TLR2-MyD88 Complex Formation

Shiju Ye[1,2,3†], Lan Su[1,2†], Peiren Shan[1,2], Bozhi Ye[1,2], Shengjie Wu[1,2], Guang Liang[1,3] and Weijian Huang[1,2*]*

[1] Department of Cardiology, The First Affiliated Hospital of Wenzhou Medical University, Wenzhou, China, [2] The Key Laboratory of Cardiovascular Disease of Wenzhou, Wenzhou, China, [3] Chemical Biology Research Center, School of Pharmaceutical Sciences, Wenzhou Medical University, Wenzhou, China

OPEN ACCESS

Edited by:
Guo-Ping Shi, Brigham and Women's Hospital, Harvard Medical School, United States

Reviewed by:
Xufeng Tao, Dalian University of Technology, China
Tahir Ali, Peking University, China

***Correspondence:**
Guang Liang
wzmcliangguang@163.com
Weijian Huang
weijianhuang69@126.com

† These authors have contributed equally to this work

Specialty section:
This article was submitted to Signaling, a section of the journal Frontiers in Cell and Developmental Biology

Received: *15 January 2021*
Accepted: *24 March 2021*
Published: *13 April 2021*

Citation:
Ye S, Su L, Shan P, Ye B, Wu S, Liang G and Huang W (2021) LCZ696 Attenuated Doxorubicin-Induced Chronic Cardiomyopathy Through the TLR2-MyD88 Complex Formation. Front. Cell Dev. Biol. 9:654051. doi: 10.3389/fcell.2021.654051

Background and Purpose: The profibrotic and proinflammatory effects induced by doxorubicin (DOX) are key processes in the development of serious heart damage. Lack of effective drugs and the unclear mechanisms of its side effects limit the clinical treatment of DOX-induced cardiac injury. This study aimed to explore the protective role of LCZ696 and the potential mechanism of Toll-like receptor 2 (TLR2) in doxorubicin-induced cardiac failure.

Experimental Approach: DOX (5 mg/kg/week, three times) was used to establish a chronic cardiomyopathy mouse model. Heart function tests, pathology examinations and molecular biology analyses were used to explore the effects of LCZ696 and TLR2 deficiency *in vivo* and *in vitro*. Computational docking was applied to predict the key residues for protein-ligand interaction.

Key Results: The EF% declined, and the LVIDd, pro-fibrosis marker levels and NF-κB related inflammatory response increased in the chronic cardiomyopathy group induced by DOX. LCZ696 treatment and TLR2 deficiency reversed these heart damage *in vivo*. In H9C2 cells, pre-treatment with LCZ696 and TLR2 knockdown suppressed the DOX-induced high expression of profibrotic and proinflammatory markers. Moreover, DOX notably increased the TLR2-MyD88 interaction *in vivo* and *in vitro*, which was inhibited by LCZ696. Finally, we demonstrated the direct interaction between DOX and TLR2 via hydrogen bonds on Pro-681 and Glu-727 and Pro-681 and Ser-704 may be the key residues by which LCZ696 affects the interaction between DOX and TLR2.

Conclusion and Implications: LCZ696 prevents DOX-induced cardiac dilation failure, fibrosis and inflammation by reducing the formation of TLR2-MyD88 complexes. LZC696 may be a potential effective drug to treat DOX-induced heart failure.

Keywords: doxorubicin, LZC696, toll-like receptors, heart failure, molecular target

Abbreviations: COL-I, collagen I; DMSO, dimethyl sulfoxide; DOX, doxorubicin; GAPDH, glyceraldehyde 3-phosphate dehydrogenase; HF, heart failure; IL-6, interleukin 6; MCP-1, monocyte chemotactic protein 1; NC, negative control; NF-κB, nuclear factor-κB; TGF-β, transforming growth factor-β; TLR, toll-like receptor; TNF-α, tumor necrosis factor-α.

INTRODUCTION

Doxorubicin (DOX), a member of the family of anthracyclines and an antitumor antibiotic, has been widely used to treat breast cancer, bladder cancer, and so on (Tacar et al., 2013). However, it has been well documented that the most dangerous side effect of doxorubicin is cardiovascular toxicity, and the clinical manifestations are as follows, such as tachycardia, hypotension, arrhythmias, and dilated cardiomyopathy (DCM), which leads to congestive heart failure (HF) (Chatterjee et al., 2010; Wallace et al., 2020). Notably, this side effect is positively correlated with the cumulative dose of DOX. As previously reported, the incidence of DOX cardiomyopathy increases to 36% when the dose exceeds 600 mg/m^2 (Lefrak et al., 1973), and the incidence of congestive HF affects 26% of the patients receiving DOX when the cumulative dose exceeds 550 mg/m^2 (Swain et al., 2003).

Previous studies have suggested that doxorubicin causes cardiomyopathy related to oxidative stress, downregulation of contractile protein genes and p53-mediated apoptosis (Vejpongsa and Yeh, 2014). Recent studies have found that doxorubicin has a strong inflammatory effect, which mainly manifests as doxorubicin further promoting the expression of the following cardiac inflammatory factors: (1) DOX indirectly induces interleukin 6 (IL-6) and tumor necrosis factor-α (TNF-α) through autocrine and paracrine processes; (2) DOX promotes cardiac fibroblast proliferation and extracellular matrix protein synthesis; and (3) Toll-like receptor-4, PI3Kγ and other inflammatory mediators are activated, which leads to a vicious cycle of inflammatory reactions in cardiac cells (Riad et al., 2008; Li et al., 2018). Increasing attention should be paid to the inflammatory response to cardiomyopathy caused by doxorubicin.

LCZ696, also known as the sacubitril/valsartan, consists of the neprilysin inhibitor sacubitril and the angiotensin receptor blocker valsartan, is a combination drug for use in patients with HF and a reduced ejection fraction (Lillyblad, 2015; Hubers and Brown, 2016; Yancy et al., 2016). Recently, many studies have explored the anti-inflammatory effect of LCZ696 in basic research, with evidence that this drug can attenuate cardiac dysfunction after myocardial infarction (von Lueder et al., 2015), inhibit oxidative stress, inflammation, and fibrosis, improve renal function in CKD (Jing et al., 2017) and ameliorate NLRP3 after relieving the pressure overload in mice (Li X. et al., 2020). In addition, Xia et al. (2017) found that LCZ696 protects cardiac function from doxorubicin-induced DCM by alleviating Drp1-mediated mitochondrial dysfunction. However, the potential effect of LCZ696 on DOX-induced cardiac inflammation and cardiac dysfunction, especially the underlying mechanisms of its anti-inflammatory effects, remains to be elucidated.

Toll-like receptor 2 (TLR2) is one part of the family of Toll-like receptors (TLRs), which mainly mediate pathogen-induced inflammation in innate immunity (Henrick et al., 2016; Elshabrawy et al., 2017). Although there is no involvement of endotoxins such as viruses and bacteria, recent studies have demonstrated that TLR2 may play a potential role in the inflammatory response to the process of cardiac remodeling caused by DOX. Nozaki et al. (2004) found that TLR2 knockout mice exhibited preserved cardiac function and an increased survival rate compared to DOX-challenged mice through mediating cardiac inflammatory and apoptosis, and Liang et al. (2018) found that the levels of TLR2 were upregulated in doxorubicin-treated patients who developed heart dysfunction. Similarly, after analyzing a large amount of clinical data, Pop-Moldovan et al. (2017) found that the expression of TLR4 and TLR2 was higher in patients with diastolic dysfunction treated with doxorubicin. These findings indicated that TLR2 may play a role in the mediation of DOX-induced cardiomyopathy. However, how DOX activates TLR2-related inflammation and whether LCZ696 could attenuate DOX-induced cardiac failure in a TLR2-dependent manner remain unaddressed.

In this study, utilizing LCZ696 and TLR2 knockout mice, we investigated the effect of LCZ696 and TLR2 deficiency on DOX-induced mouse cardiomyopathy. Our results found that LCZ696 treatment and TLR2 deficiency reversed DOX-induced diastolic HF, cardiac fibrosis and inflammation. More interesting, we found that LCZ696 may directly inhibit the formation of the TLR2/MyD88 complex activated by DOX, which results in the attenuation of DOX-induced DCM.

MATERIALS AND METHODS

Cell Culture and Reagents

Cultured H9C2 cell lines (immortalized rat cardiomyocytes) were obtained from the Shanghai Institute of Biochemistry and Cell Biology (Shanghai, China). The cells were cultured in Dulbecco's modified Eagle 110 medium (DMEM) supplemented with 10% fetal bovine serum, 100 U/mL penicillin and 100 U/mL streptomycin at 37°C in a humidified 5% CO2 incubator.

Doxorubicin (D107159) was purchased from Aladdin (Los Angeles, CA, United States). LCZ696 (S7678) was obtained from Sellerk (Shanghai, China). Antibodies against IκBα (4812S), nuclear factor-κB (NF-κB) (p65) (8242S), and GADPH (5174) were purchased from Cell Signaling Technology (CST, United States), and antibodies against TLR2 (12276), TLR4 (ab22048), MyD88 (ab2064), COL-1 (ab34710), transforming growth factor (TGF-β) (ab92486), TNF-α (ab6671), and Lamin B (ab133741) were purchased from Abcam (Shanghai, China).

DOX-Induced Chronic Cardiac Injury in Mice

All animal care and experimental procedures were approved by the Animal Policy and Welfare Committee of Wenzhou Medical University (Approval Document No. wydw2016-0124), and all animals received humane care according to the National Institutes of Health (United States) guidelines. All studies followed the ARRIVE guidelines for reporting experiments involving animals (Lilley et al., 2020; Percie du Sert et al., 2020).

C57BL/6 male mice were obtained from the Animal Center of Wenzhou Medical University, and male TLR2KO mice (B6.129-TLR2tm1Kir/J) backcrossed to C57BL/6 were provided by the Jackson Laboratory of America (Bar Harbor, ME, United States). The mice were housed with a 12:12 h light–dark cycle at a constant room temperature and fed a standard rodent diet. The

mice were acclimatized to the laboratory for at least 2 weeks before initiating the studies. Detailed methods for the model are presented below. Sample sizes were defined by *a priori* power calculations with G-Power 3.1.9 software[1], considering a statistical power of 80% and $\alpha = 0.05$.

Eight-week-old C57BL/6 mice and TLR2KO mice were randomly divided into five groups: (I) untreated C57BL/6 mice receiving PBS (WT-Ctrl, $n = 7$); (II) DOX-injected C57BL/6 mice receiving PBS (WT-DOX; $n = 7$); (III) DOX-injected C57BL/6 mice treated orally with LCZ696 (60 mg/kg/day) (Suematsu et al., 2016) (WT-DOX + LCZ696; $n = 7$); (IV) uninjected TLR2 KO mice receiving PBS (TLR2KO-Ctrl; $n = 7$); and (V) DOX-injected TLR2 KO mice receiving PBS (TLR2KO-DOX; $n = 7$). DOX (5 mg/kg, once a week, total cumulative dose of 15 mg/kg) was administered three times via intraperitoneal injection as described previously (Pop-Moldovan et al., 2017). LCZ696 treatments were initiated 1 day after starting the DOX injections and continued throughout the 6-week follow-up. Six weeks after DOX treatment, cardiotoxicity was evaluated.

The animals were sacrificed using sodium pentobarbital anesthesia. Heart tissues were snap frozen in liquid nitrogen for gene and protein expression analyses or fixed with 4% paraformaldehyde for histological analysis.

Cardiac Function Evaluation

Cardiac function was determined non-invasively by transthoracic echocardiography in anesthetized mice 1 day before sacrifice as described previously (Kandalam et al., 2010). The mice were anesthetized using isoflurane, and echocardiography was performed with a SONOS 5500 ultrasound (Philips Electronics, Amsterdam, Netherland) with a 15-MHz linear array ultrasound transducer.

Real-Time PCR

RNA was isolated from cultured H9C2 cells and heart tissue by using TRIZOL (Thermo Fisher Scientific, United States). Reverse transcription and quantitative PCR were carried out using a two-step PrimeScript™ RT reagent kit (Perfect Real Time) (TAKARA), Eppendorf Mastercycler ep realplex detection system (Eppendorf, Hamburg, Germany) for reverse transcription and QuantStudio3 Real-Time PCR Systems (Applied Biosystems, Thermo Fisher Scientific, United States) for real-time PCR. Primers for the genes were synthesized and obtained from Thermo Fisher Scientific. The primer sequences are presented in **Supplementary Table 1**. mRNA levels of the target genes were normalized to *Actb* gene mRNA.

Western Blot Analysis

Fifty micrograms of total protein from cell or tissue lysates was separated by 10% SDS-PAGE and electrotransferred to PVDF membranes. Membranes were blocked in Tris-buffered saline containing 0.05% Tween 20 and 5% non-fat milk for 1.5 h. The PVDF membranes were then incubated with specific primary antibodies. Immunoreactive bands were detected by incubating the membranes with secondary antibodies conjugated to horseradish peroxidase and an enhanced chemiluminescence reagent (Bio-Rad). Densitometric quantification was performed using ImageJ analysis software version 1.38e and normalized to their respective controls (glyceraldehyde 3-phosphate dehydrogenase (GAPDH) for cytosolic proteins, Lamin B for nuclear fractions, and total protein for phosphorylated-form detection).

Heart Histology and Immunostaining

Hearts were fixed in 4% paraformaldehyde and embedded in paraffin. Five-micrometer-thick sections were stained with hematoxylin and eosin (H&E) (C0105, Beyotime Biotechnology) for histological analysis and Sirius Red and Masson's trichrome (G1340-7 × 100 ml, Solarbio Life Science) to evaluate cardiac fibrosis. The sections were observed under a light microscope (Nikon, Japan).

For immunohistochemical staining, the sections were deparaffinized and rehydrated. The sections were treated with 3% H2O2 for 30 min to block endogenous peroxidase activity and then with 1% BSA in PBS for 30 min. The slides were incubated overnight at 4°C with the primary antibody (TNF-α, 1:50; both from Santa Cruz). Peroxidase-conjugated secondary antibodies were used for detection (Santa Cruz; 1:100 dilution; 1 h incubation). The slides were counterstained with hematoxylin for 5 min, dehydrated, and mounted. Images were viewed by a bright field microscope (Nikon).

ELISA

The TNF-α (70-EK382/3-96) levels in heart tissue were measured using ELISA kits (eBioscience, San Diego, CA, United States). All experiments followed the manufacturer's instructions.

siRNA Transfection and Gene Silencing

Gene silencing in cells was achieved using specific siRNA sequences. TLR2 siRNAs were purchased from GenePharma Co., Ltd. (Shanghai, China). Custom siRNAs were synthesized for rat TLR2, TLR4, and MD2. The sequences are presented in **Supplementary Table 1**. The H9C2 cells were transfected with siRNA using LipofectAMINE™ 2000 (Thermo Fisher Scientific, Carlsbad, CA, United States).

Immunoprecipitation

Following treatments, cell lysates or heart tissues were prepared and incubated with an anti-TLR2 or MyD88 antibody overnight. Complexes were retrieved with protein G-Sepharose beads at 4°C for 4 h. The TLR2 and MyD88 levels were further detected by immunoblot using anti-TLR2 and MyD88 antibodies (IB), respectively.

Computational Docking and Molecular Simulation

The crystal structure of the TIR domain of human TLR2 (PDB code 1FYW) was derived from Protein Data Bank repository. Input files of ligand and receptor for docking were prepared using Graphical User Interface program AutoDock Tools 1.5.6 (The Scripps Research Institute, La Jolla, CA, United States)

[1] http://www.gpower.hhu.de/

(Morris et al., 2009). Molecular docking was performed by AutoDock Vina 1.0.2. Celastrol was docked into the TIR domain of TLR2 to generate 20 binding poses, respectively. The binding free energy between each docking pose and TLR2 was scored by the MM/GBSA method in AmberTools package after a structure minimization (Salomon-Ferrer et al., 2012). Finally, based on the per-residue decomposition energy calculations, the key residues for protein-ligand interaction were identified.

Statistical Analysis

The data presented in this study are representative of five independent experiments and are expressed as the mean ± SEM. The exact group size (n) for each experiment is provided, and "n" refers to independent values. Statistical analysis was performed with GraphPad Prism 8.0 software (San Diego, CA, United States). We used one-way ANOVA followed by Dunnett's *post hoc* test when comparing more than two groups of data and one-way ANOVA and non-parametric Kruskal–Wallis tests followed by Dunn's *post hoc* test when comparing multiple independent groups. A P value < 0.05 was considered to be statistically significant. Post-tests were run only if F achieved $P < 0.05$ and there was no significant variance in homogeneity.

RESULTS

LCZ696 Treatment and TLR2 Deficiency Attenuated Doxorubicin-Induced Cardiac Systolic Dysfunction

Firstly, our objective was to determine whether LCZ696 and TLR2 deficiency could inhibit the doxorubicin-induced cardiotoxicity in mice. As previously reported, doxorubicin was used to establish chronic cardiac injury in mice through intraperitoneal injection. Then, LCZ696 was administered orally to determine whether it could prevent heart injury, and the model of doxorubicin-induced cardiac injury was also established in TLR2KO mice to explore the potential role of TLR2.

Before sacrificed, the cardiac function of each group was evaluated by external echocardiography (**Figure 1A** and **Table 1**). As shown in **Figure 1A** and **Table 1**, DOX significantly impaired heart function by decreasing EF%, FS%, IVSD, and PWd and increasing LVIDd, which resulted in serious systolic dysfunction. Interestingly, these challenges were normalized with oral LCZ696 treatment and TLR2 deficiency, which indicated that LCZ696 and TLR2 deficiency attenuated DOX-induced cardiac systolic dysfunction in mice.

To deeply explore the alterations of the heart cavity, histological assessments of the whole heart were performed for all groups by H&E staining. As shown in **Figure 1B**, DOX induced thinning of the ventricular wall and enlargement of the heart cavity, which were obviously improved in the hearts of LCZ696-treated and TLR2-deficient mice. These above results show that treatment with LCZ696 and TLR2 deficiency prevented DOX-induced cardiac systolic dysfunction.

LCZ696 Treatment and TLR2 Deficiency Alleviated Doxorubicin-Induced Cardiac Fibrosis

Next, we assessed fibrosis in the heart tissues. Masson's trichrome and Sirius Red stains were chosen to evaluate connective tissue and collagen, respectively, and validated the anti-fibrotic effects of LCZ696 and TLR2 deficiency. As shown in **Figures 2A–C**, DOX promoted collagen deposition in myocardial tissue, and these histological changes were obviously improved in LCZ696-treated and TLR2-deficient mice.

In addition to the histological results, the hearts from DOX-challenged mice showed significantly increased mRNA levels of the profibrotic genes *Col1a* (**Figure 2D**) and *Tgfb* (**Figure 2E**), which were notably reduced by LCZ696 and TLR2 deficiency.

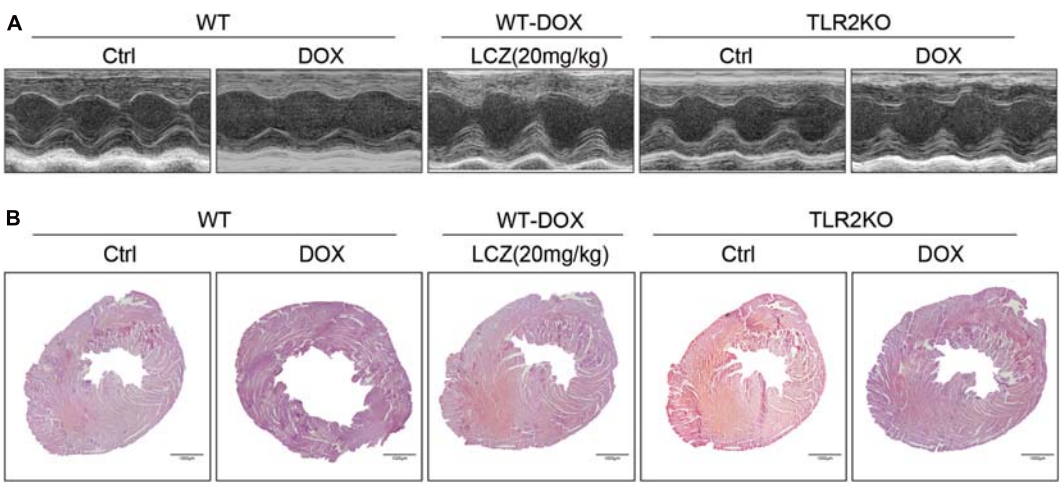

FIGURE 1 | LCZ696 treatment and TLR2 deficiency attenuated doxorubicin-challenged systolic dysfunction. **(A)** Representative echocardiogram images of each group. **(B)** Representative H&E staining of heart tissues showing the effect of LCZ696 and TLR2 deficiency on doxorubicin-induced dilated cardiomyopathy in mice [original magnification 1×].

TABLE 1 | Biometric and echocardiographic parameters of the experimental mice.

	WT			TLR2KO	
	Ctrl *N* = 7	**DOX *N* = 7**	**DOX + LCZ *N* = 7**	**Ctrl *N* = 7**	**DOX *N* = 7**
EF%	80.14 ± 1.05	75.74 ± 1.08***	78.25 ± 1.17###	81.08 ± 1.75	79.18 ± 2.01###
FS%	40.26 ± 2.49	35.11 ± 2.11***	38.36 ± 2.47###	39.27 ± 1.81	38.75 ± 1.41###
LVIDd, mm	2.11 ± 0.28	2.35 ± 0.56**	2.18 ± 0.14##	2.10 ± 0.58	2.15 ± 0.78##
IVSD, mm	0.98 ± 0.11	0.95 ± 0.14*	0.99 ± 0.22#	0.98 ± 0.07	0.99 ± 0.1#
PWd, mm	0.70 ± 0.03	0.67 ± 0.04**	0.71 ± 0.13#	0.71 ± 0.21	0.71 ± 0.35#
E wave, m/s	0.68 ± 0.05	0.70 ± 0.07**	0.69 ± 0.07#	0.67 ± 0.08	0.69 ± 0.11#
Tei Index	0.82 ± 0.04	0.80 ± 0.10**	0.82 ± 0.12#	0.81 ± 0.11	0.82 ± 0.25#
IRT, ms	15.33 ± 1.14	17.28 ± 1.58*	14.56 ± 1.97#	14.23 ± 1.46	14.28 ± 1.41#

*Transthoracic echocardiography was performed on mice at the end of the animal study. EF, ejection fraction%, FS, fractional shortening%; LVIDd, diastole left ventricle internal dimension; PWd, diastole posterior wall thickness; IVSd, diastole interventricular septal thickness; E wave; IRT, isovolumic relaxation time; Tei index; Data are presented as the mean ± SEM, n = 7. *P < 0.05 compared to ctrl; **P < 0.01 compared to ctrl; ***P < 0.001 compared to ctrl; #P < 0.05 compared to Ang II; ##P < 0.01 compared to Ang II; ###P < 0.001 compared to Ang II; ns = not significant.*

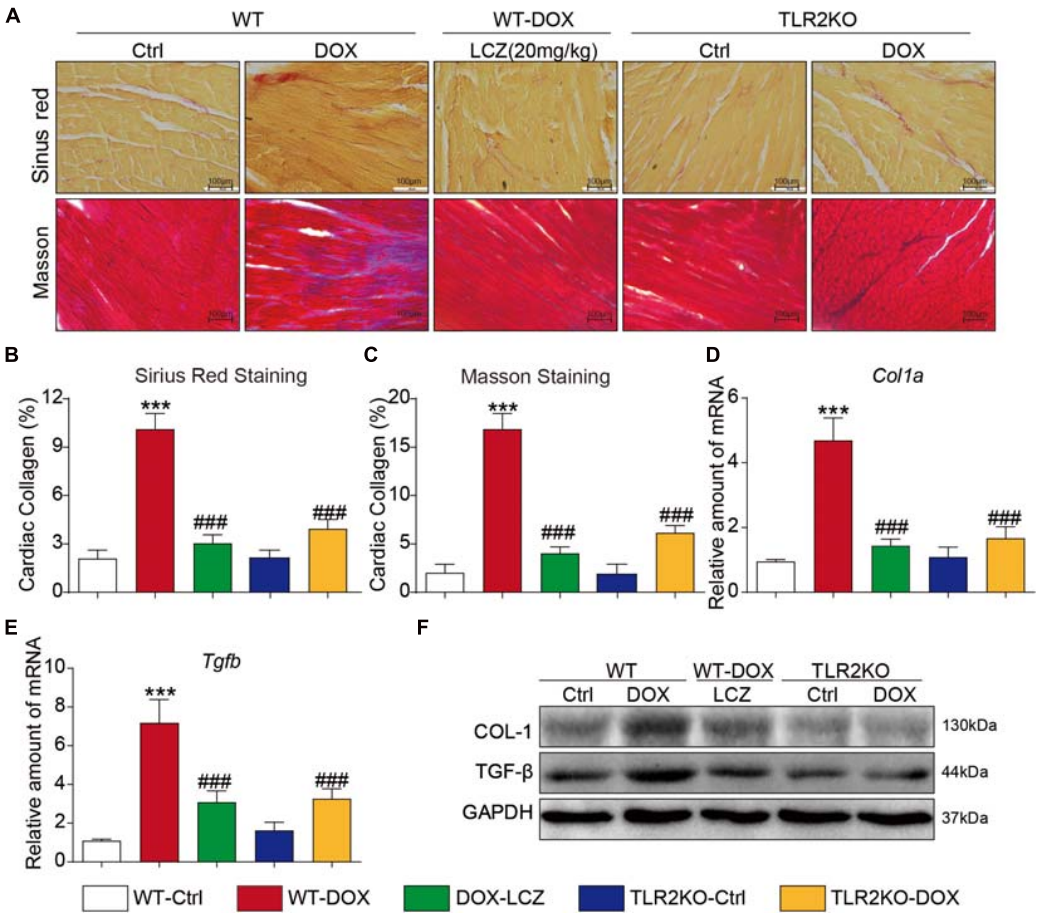

FIGURE 2 | LCZ696 treatment and TLR2 deficiency attenuated doxorubicin-induced cardiac fibrosis. **(A)** Representative images of Sirius Red and Masson trichrome staining of longitudinal sections of the hearts (200×). **(B,C)** Quantification of interstitial fibrotic areas (%) from Sirius Red-stained heart sections **(B)** and Masson's Trichome staining **(C)**. **(D,E)** The mRNA levels of *Col1a1* **(D)** and *Tgfb* **(E)** were detected by real-time PCR in the heart tissue from the above transplanted mice (data were normalized to *Actb*). **(F)** Heart tissue from each group of mice was homogenized for western blot analysis of collagen I, TGF-β, and GAPDH. (*n* = 7; *** *P* < 0.001 as indicated; ###*P* < 0.001 compared to Ang II; and ns is not significant).

These results paralleled the protein levels of collagen I (COL-I) and TGF-β in the hearts of each group (**Figure 2F** and **Supplementary Figures 1A,B**).

These results demonstrated that LCZ696 treatment and TLR2 deficiency reduced doxorubicin-induced cardiac fibrosis.

LCZ696 Treatment and TLR2 Knockdown Attenuated Doxorubicin-Induced Cardiac Inflammation in Mice

As previously reported, fibrosis and inflammation complement each other during diseases. Moreover, considering the potential effect of LCZ696 and the critical role of TLR2 in anti-inflammatory processes, we next assessed the inflammatory response in the hearts of each group.

Immunohistochemistry staining showed that TNF-α was significantly increased in the DOX treated mice compared to the control mice. As expected, LCZ696 treatment and TLR2 knockdown prevented the heart from developing high TNF-α expression (**Figure 3A** and **Supplementary Figure 2A**). Similar results were also observed in the ELISA results (**Figure 3B**). NF-κB-related proteins, as the well-established downstream signaling proteins in the TLR2 pathway, participate in acute and chronic inflammation. Then, we tested whether these alterations occurred in heart tissues. As shown in **Figures 3C,D**, LCZ696 treatment and TLR2 deficiency effectively prevented IκBα degradation (**Figure 3C**) and inhibited the nuclear translation of NF-κB (**Figure 3D**) in heart tissue compared with the DOX-induced mice. Moreover, the mRNA levels of the pro-inflammation-related genes *Tnf*α (**Figure 3E**), monocyte chemotactic protein 1 (*Mcp1*) (**Figure 3F**), and *Il6* (**Figure 3G**) were validated by RT-qPCR, which provided additional evidence to show the anti-inflammatory effects of LCZ696 treatment and TLR2 deficiency.

Thus, these results indicated that LCZ696 treatment and TLR2 deficiency significantly inhibited DOX-induced cardiac inflammation in heart tissues, which may be associated with the cardioprotective effect.

LCZ696 Treatment and TLR2 Knockdown Attenuated Doxorubicin-Induced H9C2 Cell Fibrosis *in vitro*

Next, H9C2 cells were cultured to further confirm the potential effect of LCZ696 treatment and TLR2 deficiency in cardiac injury induced by DOX, and we then determined the role of TLR2 in DOX treatment.

Toll-like receptor 2 siRNA was used to silence the expression of TLR2 in the H9C2 cell line (**Figures 4A,B**). As expected, DOX stimulated significantly high protein levels of COL-I and TGF-β protein as well as the mRNA levels, which were normalized to the control levels as the TLR2 was knocked down or pre-treated with LCZ696 in H9C2 cells (**Figures 4C–F**).

LCZ696 Treatment and TLR2 Knockdown Attenuated the Doxorubicin-Induced H9C2 Cell Inflammatory Response *in vitro*

Furthermore, we also assessed the inflammatory response induced by DOX *in vitro*. Similar to the above results, TLR2

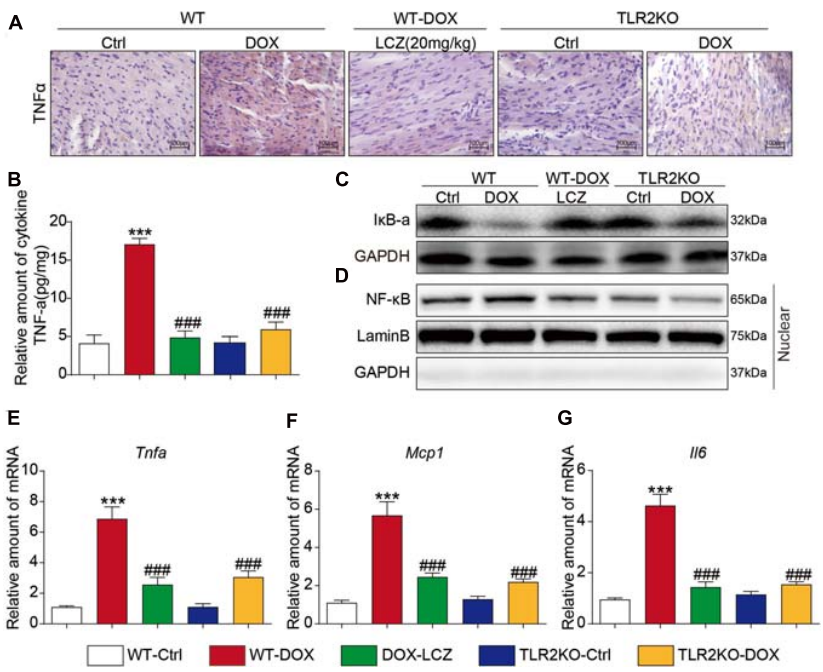

FIGURE 3 | LCZ696 treatment and TLR2 knockdown attenuated doxorubicin-induced cardiac inflammation in mice. **(A)** Representative images of anti-TNF-α staining in the hearts of each group (200×). **(B)** TNF-α levels in mouse heart tissue homogenates determined by ELISA. **(C)** Western blot analysis of IκBα levels in heart tissue. GAPDH was used as a loading control. **(D)** Nuclei were isolated from mouse heart tissue, and NF-κB in the nucleus was detected by western blot. Lamin B and GAPDH were used as controls. **(E–G)** Real-time PCR was used to determine the mRNA levels of *Tnfa* **(E)**, *Mcp1* **(F)**, and *Il-6* **(G)** in mouse heart tissue (data were normalized to *Actb*). ($n = 7$; *** $P < 0.001$ vs. WT control group; ### $P < 0.001$ vs. DOX group).

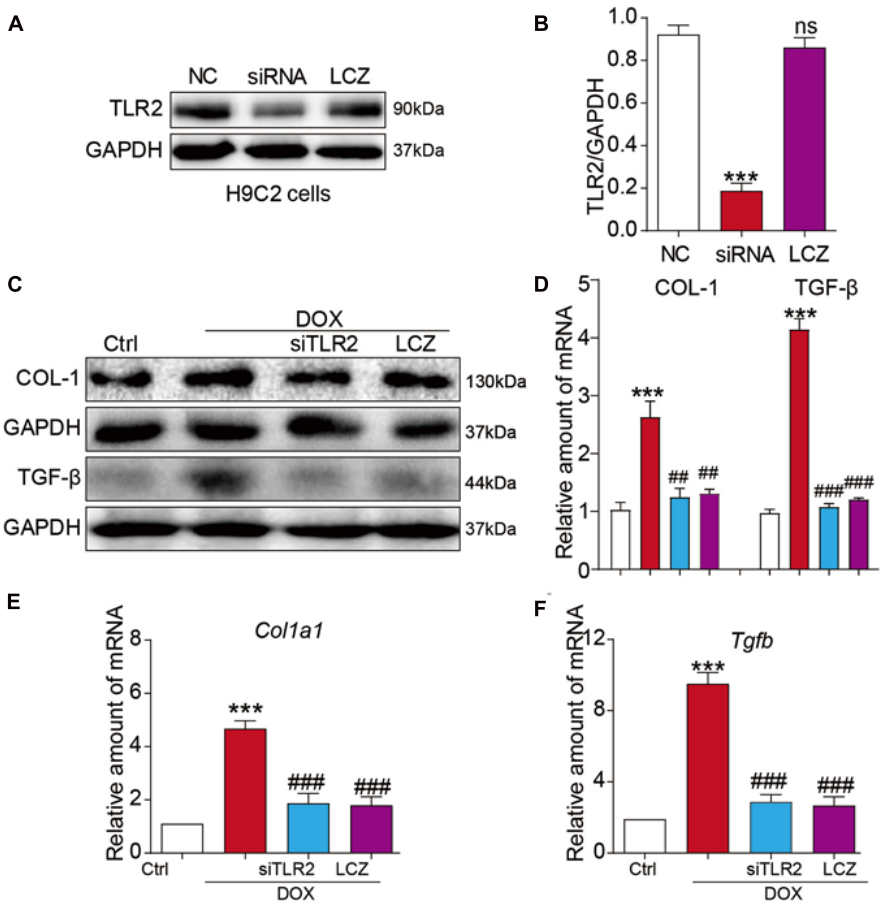

FIGURE 4 | LCZ696 treatment and TLR2 knockdown attenuated doxorubicin-induced H9C2 cell fibrosis *in vitro*. **(A)** H9C2 cells were transfected with control siRNA (NC) or TLR2 siRNA (siTLR2) and treated with LCZ696 (20 μmol/l) for 24 h. Western blot detected TLR2 and GAPDH protein levels. **(B)** Densitometric quantification of TLR2/GAPDH levels in the immunoblots presented in panel **(A)**. **(C)** H9C2 cells were transfected with control siRNA or TLR2 siRNA and pre-treated with LCZ696 (20 μmol/l) and then stimulated with DOX (1 μM) for 24 h. Western blot analysis of the protein levels of collagen I and TGF-β in whole cell lysates. **(D)** Densitometric quantification of collagen I/GAPDH and TGF-β/GAPDH levels in immunoblots presented in panel **(C)**. **(E,F)** The mRNA levels of *Col1a1* **(E)** and *Tgfb* **(F)** were detected by real-time PCR. ($n = 5$; *** $P < 0.001$ vs. Ctrl group; ##$P < 0.01$ compared to Ang II; ### $P < 0.001$ vs. DOX group).

silencing or pre-treated with LCZ696 significantly reversed DOX-induced IκB-a degradation and the nuclear translocation of NF-κB (**Figures 5A–D**). In addition, cardiac inflammation was ameliorated by TLR2 knockdown or LCZ696 treatment, as shown by the gene expression of *Tnfa*, *Mcp1*, and *Il-6* (**Figures 5E–G**).

These results provide evidence that LCZ696 treatment and TLR2 knockdown attenuated doxorubicin-induced cardiac cell fibrosis and inflammation *in vitro*.

Administration of LCZ696 Attenuated Doxorubicin-Induced Cardiac Injury by Inhibiting TLR2-MyD88 Complex Formation

To explore the underlying mechanism of the effect of LCZ696 and TLR2 deficiency in DOX-related cardiac injury, we analyzed the TLR2-MyD88 complex formation and the well-established TLR2 downstream pathway.

Firstly, H9C2 cells were treated with DOX in a time-dependent manner. The Co-IP assay results showed that DOX significantly increased the TLR2-MyD88 interaction in 15 min (**Figure 6A**), which indicated the potential mechanism of TLR2-mediated DOX-related cardiomyopathy. More interestingly, DOX-induced TLR2-MyD88 complex formation was attenuated by pre-treatment with LCZ696 (**Figure 6B**). Besides, we further tested the effect of LCZ696 on TLR2-MyD88 complex formation in mice heart tissues. As the data shown in **Figure 6C**, with no alteration in TLR2 and Myd88 protein level, DOX significantly promoted TLR2-MyD88 interaction in the mouse heart evidenced by Co-IP assay and treated with LCZ696 attenuated the formation of TLR2-MyD88 complex. These results indicated that the treatment effect of LCZ696 manifested by inhibiting the TLR2-MyD88 complex formation induced by DOX.

To understand the potential molecular mechanism of DOX interacting with TLR2 protein, we conducted a molecular docking and simulation study using the crystal structure of the TIR domain of human TLR2 (PDB code 1FYW). The TIR

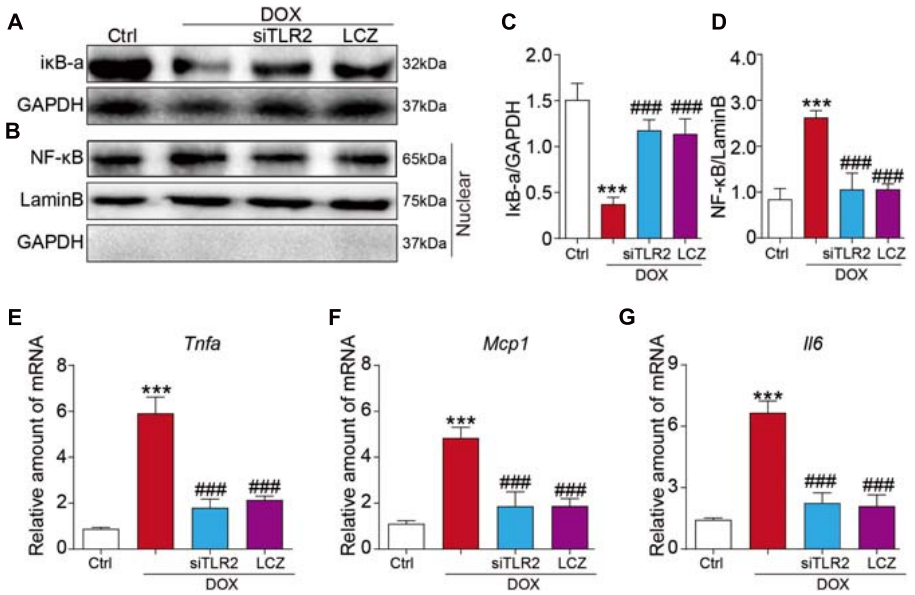

FIGURE 5 | LCZ696 treatment and TLR2 knockdown attenuated the doxorubicin-induced H9C2 cell inflammatory response *in vitro*. **(A,B)** H9C2 cells were transfected with control siRNA, TLR2 siRNA, and LCZ696 (20 μmol/l) and then stimulated with DOX (1 μM) for 8 h. Western blot detected IκBa and GAPDH protein levels in whole cell lysates **(A)** and detected NF-κB, Lamin B, and GAPDH protein levels in the nuclear extractions **(B)**. **(C)** Densitometric quantification of IκBa/GAPDH levels in the immunoblots presented in panel **(A)**. **(D)** Densitometric quantification of NF-κB/Lamin B levels in the immunoblots presented in panel **(B)**. **(E–G)** The mRNA levels of *Tnfa* **(E)**, *Mcp1* **(F)**, and *Il-6* **(G)** were measured by real-time PCR. ($n = 5$; *** $P < 0.001$ vs. Ctrl group; ### $P < 0.001$ vs. DOX group).

domain, as the most important structures of TLR2, is responsible for MyD88 interaction and the activation of downstream inflammation signaling pathway (O'Neill and Bowie, 2007).

The docking uses the QVina-W program to search in the global scope of the protein surface. As shown in the **Figure 6D**, a total of 20 binding conformations are generated, among which pose1 (marked in yellow) has the best conformation score for docking.

To predict the binding position of DOX on TIR domain, a per-residue decomposition energy calculation was performed for the 20 docking poses (**Supplementary Figure 4**).

Distributions of both docking scores and MM/GBSA scores show that DOX may bind the TIR domains of TLR2 (**Figure 6D**, right). Greater negative scores are obtained in DOX- TIR domain interaction, indicating that DOX has a higher binding affinity to TIR domain in pose17compared to the pose1. Five key residues in the TIR domain with the top-lowest average energy values are Glu-727, Ile-686, Arg-677, Trp-684, and Pro-681 (**Figure 6D** and **Supplementary Figure 4**). Among these, ARG-677 showed the lowest energy. Among these, based on the energy values, Pro-681 and Glu-727 appeared to be key residues which DOX combined with TLR2.

Similarly, we also conducted the molecular docking and simulation study of TLR2 and LCZ696. The pose in **Figure 6E** is the best conformation of 20 top-scoring docking conformations of LCZ696 and TLR2 (**Supplementary Figure 5**). As shown in **Figure 6E**, the key residues in the Sacubitril with the top-lowest average energy values are Pro-681, Gly-682, and Lys-683 (**Figure 6E**). And for the Valsartan, Ser-704 showed the lowest energy (**Figure 6E**). Among these, Pro-681 and Ser-704 appeared to be key residues based on the energy values, which predicts the potential mechanism by which LCZ696 affects the interaction between DOX and TLR2.

Furthermore, we found that the TLR2-MyD88 complex formation induced by DOX was independent with TLR4 and MD2, as it was not affected by TLR4 or MD2 knockdown (**Supplementary Figures 6A,B**).

In conclusion, our results found that the mechanism by which LCZ696 relieves DOX-induced cardiac injury lies in inhibiting the formation of TLR2-MyD88 complexes (**Figure 7**).

DISCUSSION

Dilated cardiomyopathy is one of the most serious side effects of doxorubicin treatment, significantly reducing its anticancer value and causing a large societal burden. However, the mechanisms of DCM are still unclear, and an effective therapy to prevent the progression of existing cardiac inflammation and fibrosis induced by DOX are urgently needed. Our study aimed to determine the potential effect of LCZ696 and the role of TLR2 in DOX-induced cardiac dysfunction, fibrosis and inflammation, which may help to find an effective drug to protect the heart and provide a potential signaling pathway for the treatment of DOX-induced DCM.

In our study, we showed that LCZ696 treatment and TLR2 deficiency attenuated DOX-related dilated HF by improving the decreased EF% and increased LVIDd. In addition, *in vivo* and *in vitro*, our results showed that DOX stimulated the expression of matrix proteins and inflammatory cytokines in the heart

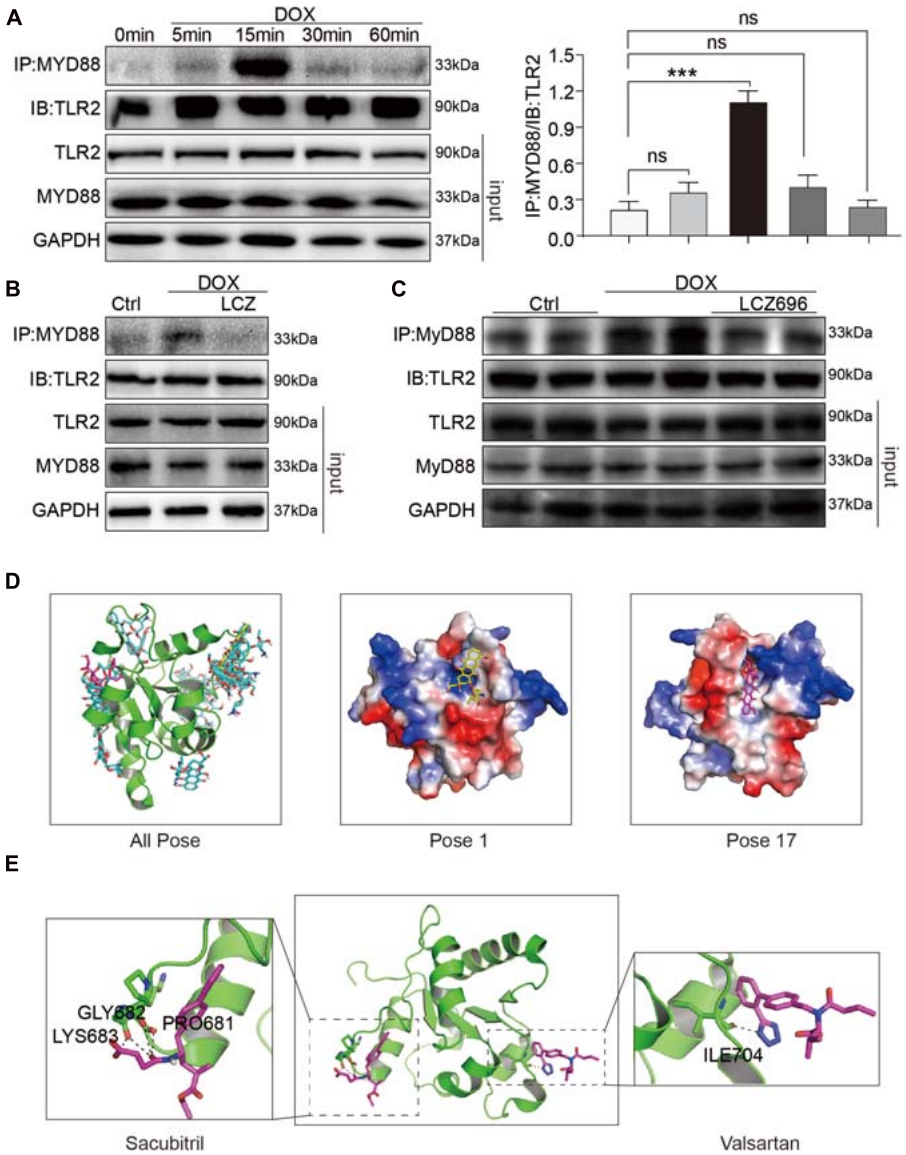

FIGURE 6 | LCZ696 treatment attenuated doxorubicin-induced cardiac injury by inhibiting TLR2-MyD88 complex formation. **(A)** Time course of the DOX-induced TLR2-MyD88 interaction in H9C2 cells. Cells were treated with 1 μM DOX for up to 1 h. Quantification is shown below. **(B)** H9C2 cells were pre-treated with LCZ696 (20 μmol/l) for 1 h and then stimulated with DOX (1 μM) for 30 min. The TLR2-MyD88 interaction was analyzed. **(C)** A co-immunoprecipitation assay determined the TLR2-MyD88 interaction in mice heart tissues. **(D)** The total of 20 binding conformations (right) are produced by the docking program QVina-W, of which pose 1 (marked yellow) has the best docking score. The details of the binding pose of DOX with the lowest binding energy for TLR2-TIR is shown in the middle, and the details of the binding pose of DOX with TLR2-TIR calculated by MM/GBSA method is shown in the right. **(E)** The details of the binding pose of LCZ696 (Sacubitril-right and Valsartan-left) with the lowest binding energy is shown for TLR2-TIR. Magenta is the optimal conformation for scoring (unit is kcal/mol). ***$P < 0.001$ compared to ctrl.

and that LCZ696 treatment and TLR2 knockdown ameliorated these alterations and ultimately improved cardiac function. Furthermore, the underlying mechanisms involved in DOX-induced cardiomyopathy were revealed that DOX stimulated the formation of the TLR2-MyD88 complex, which activated the NF-κB pathway, leading to cardiac cell inflammation and fibrosis. This TLR2-MyD88 interaction was TLR4 or MD2 independent and could be inhibited by LZC696, which explained the strong effect of this drug in preventing heart injury caused by DOX.

It is well established that LCZ696, as a novel angiotensin receptor-neprilysin inhibitor, significantly reduced mortality and hospitalization due to heart failure in HF patients with a reduced ejection fraction (HFrEF) (Mann et al., 2020). The results of the PARADIGM-HF trial (McMurray et al., 2014) suggested a second function of sacubitril/valsartan: degrading peptides that regulate the cardiovascular, nervous, inflammatory, and immune systems (Turner et al., 2001; D'Elia et al., 2017). Recent studies found that LCZ696 increased local BNP/CNP

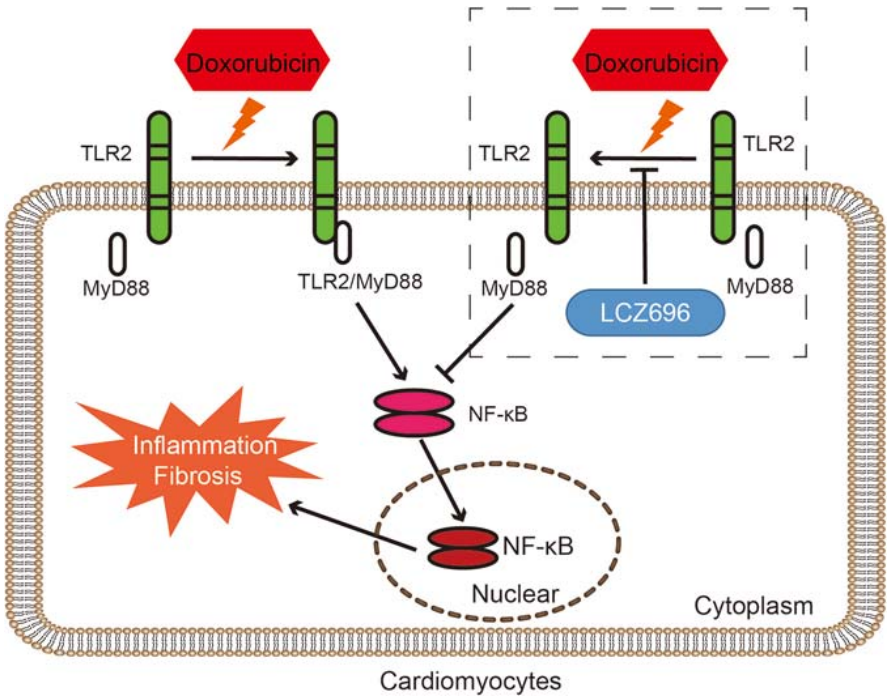

FIGURE 7 | LCZ696 attenuated doxorubicin-induced heart injury through the TLR2-MyD88 pathway. The mechanism by which LCZ696 relieves DOX-induced cardiac inflammation, fibrosis and heart failure lies in reducing the formation of TLR2-MyD88 complexes.

levels, interfered with angiotensin II-mediated signaling, and then reduced the magnitude of cardiac remodeling in animal models of hypertension and myocardial infarction (von Lueder et al., 2015; Oatmen et al., 2018). Regarding the cardiotoxicity induced by DOX, accumulating evidences have discovered the pathophysiological mechanisms, but the treatments to mitigate cardiac damage are still limited (Hu et al., 2020; Yang et al., 2020). Xia et al. (2017) found that Drp1 and its Ser-616 phosphorylation were significantly increased in DCM patients and demonstrated that the use of LCZ696 against DOX-induced cardiac dysfunction is associated with alleviated Drp1-mediated mitochondrial dysfunction. Similar to our results, we focused on the anti-inflammatory effect of LCZ696. Our data indicated that LCZ696 prevented IκBα degradation, inhibited the nuclear translation of NF-κB and reduced the expression of inflammatory cytokines *in vivo* and *in vitro*. More impressively, we found that pre-treatment with LCZ696 inhibited the increased formation of the TLR2/MyD88 complex induced by DOX. This finding partly explains the mechanism of the anti-inflammatory effect of LZC696.

Similar to other TLRs, TLR2 is the most characteristic member of pattern recognition receptors (PRRs), which play an important role in innate immune mechanisms (Jacquet and Robinson, 2020). TLRs play different roles in different stages of infection of atherosclerosis-related pathogens such as Chlamydia pneumoniae (Li B. et al., 2020). Since Nozaki et al. (2004) found that TLR2 may play a role in the regulation of inflammatory and apoptotic mediators in the heart after DOX administration in 2004, little research has explored the mechanism by which TLR2 mediates DOX-induced cardiotoxicity. Our current study indicated that DOX induced the increased formation of the TLR2/MyD88 complex, which leads to the activation of the NF-κB pathway and stimulates the expression of cardiac inflammation and fibrosis. This result partially compensates for the inflammatory mechanism of DOX-induced myocardial injury. Moreover, we found that this interaction of TLR2 and MyD88 induced by DOX is independent with TLR4 or MD2, but the clear role of TLR4 and MD2 in DOX-induced cardiac side effects still needs further research. Finally, we also performed the molecular docking and simulation study to find potential key residues where DOX combined with to stimulating the interaction of TLR2 and MyD88, and which prevented from by LCZ696. We were careful in our interpretation and reporting of the data and elected not to overstate that these residues are the specific positions of the cardiotoxicity of DOX and the cardioprotection of LCZ696 in DOX induced cardiac failure.

Taken together, our results demonstrated that the mechanism by which LCZ696 relieves DOX-induced cardiac inflammation fibrosis and HF lies in reducing the formation of TLR2-MyD88 complex. LCZ696 may be a potential drug to treat DOX-related HF, and TLR2-MyD88 could be a parallel target in the prevention and treatment of DOX-related heart injury.

DATA AVAILABILITY STATEMENT

The raw data supporting the conclusions of this article will be made available by the authors, without undue reservation.

ETHICS STATEMENT

The animal study was reviewed and approved by the Animal Policy and Welfare Committee of Wenzhou Medical University (Approval Document No. wydw2016-0124).

AUTHOR CONTRIBUTIONS

SY, LS, PS, BY, and GL: conception and design, collection, analysis, and interpretation of data, and manuscript writing. SY, LS, and SW: collection, interpretation, and analysis of data. GL and WH: conception and design, interpretation of data, and manuscript revision. All authors contributed to the article and approved the submitted version.

FUNDING

This study was supported by the Key Research and Development Program of Zhejiang (Grant Number 2019C03012); Major Project of the Science and Technology of Wenzhou (Grant Number ZS2017010); and National Natural Science Foundation of China (Grant Number 82000224).

SUPPLEMENTARY MATERIAL

The Supplementary Material for this article can be found online at: https://www.frontiersin.org/articles/10.3389/fcell.2021.654051/full#supplementary-material

REFERENCES

Chatterjee, K., Zhang, J., Honbo, N., and Karliner, J. S. (2010). Doxorubicin cardiomyopathy. *Cardiology* 115, 155–162.

D'Elia, E., Iacovoni, A., Vaduganathan, M., Lorini, F. L., Perlini, S., and Senni, M. (2017). Neprilysin inhibition in heart failure: mechanisms and substrates beyond modulating natriuretic peptides. *Eur. J. Heart Fail.* 19, 710–717. doi: 10.1002/ejhf.799

Elshabrawy, H. A., Essani, A. E., Szekanecz, Z., Fox, D. A., and Shahrara, S. (2017). TLRs, future potential therapeutic targets for RA. *Autoimmun. Rev.* 16, 103–113. doi: 10.1016/j.autrev.2016.12.003

Henrick, B. M., Yao, X. D., Taha, A. Y., German, J. B., and Rosenthal, K. L. (2016). Insights into soluble toll-like receptor 2 as a downregulator of virally induced inflammation. *Front. Immunol.* 7:291. doi: 10.3389/fimmu.2016.00291

Hu, C., Zhang, X., Zhang, N., Wei, W. Y., Li, L. L., Ma, Z. G., et al. (2020). Osteocrin attenuates inflammation, oxidative stress, apoptosis, and cardiac dysfunction in doxorubicin-induced cardiotoxicity. *Clin. Transl. Med.* 10:e124.

Hubers, S. A., and Brown, N. J. (2016). Combined angiotensin receptor antagonism and neprilysin inhibition. *Circulation* 133, 1115–1124. doi: 10.1161/circulationaha.115.018622

Jacquet, A., and Robinson, C. (2020). Proteolytic, lipidergic and polysaccharide molecular recognition shape innate responses to house dust mite allergens. *Allergy* 75, 33–53. doi: 10.1111/all.13940

Jing, W., Vaziri, N. D., Nunes, A., Suematsu, Y., Farzaneh, T., Khazaeli, M., et al. (2017). LCZ696 (Sacubitril/valsartan) ameliorates oxidative stress, inflammation, fibrosis and improves renal function beyond angiotensin receptor blockade in CKD. *Am. J. Transl. Res.* 9, 5473–5484.

Kandalam, V., Basu, R., Abraham, T., Wang, X., Soloway, P. D., Jaworski, D. M., et al. (2010). TIMP2 deficiency accelerates adverse post-myocardial infarction remodeling because of enhanced MT1-MMP activity despite lack of MMP2 activation. *Circ. Res.* 106, 796–808. doi: 10.1161/circresaha.109.209189

Lefrak, E. A., Pitha, J., Rosenheim, S., and Gottlieb, J. A. (1973). A clinicopathologic analysis of adriamycin cardiotoxicity. *Cancer* 32, 302–314. doi: 10.1002/1097-0142(197308)32:2<302::aid-cncr2820320205>3.0.co;2-2

Li, B., Xia, Y., and Hu, B. (2020). Infection and atherosclerosis: TLR-dependent pathways. *Cel. Mol. Life Sci.* 77, 2751–2769. doi: 10.1007/s00018-020-03453-7

Li, M., Sala, V., De Santis, M. C., Cimino, J., Cappello, P., Pianca, N., et al. (2018). Phosphoinositide 3-kinase gamma inhibition protects from anthracycline cardiotoxicity and reduces tumor growth. *Circulation* 138, 696–711. doi: 10.1161/circulationaha.117.030352

Li, X., Zhu, Q., Wang, Q., Zhang, Q., Zheng, Y., Wang, L., et al. (2020). Protection of Sacubitril/Valsartan against pathological cardiac remodeling by inhibiting the NLRP3 Inflammasome after relief of pressure overload in mice. *Cardiovasc. Drugs Ther.* 34, 629–640. doi: 10.1007/s10557-020-06995-x

Liang, S., Xinyong, C., Hongmin, Z., Jing, W., Lang, H., and Ping, Z. (2018). TLR2 and TLR3 expression as a biomarker for the risk of doxorubicin-induced heart failure. *Toxicol. Lett.* 295, 205–211. doi: 10.1016/j.toxlet.2018.06.1219

Lilley, E., Stanford, S. C., Kendall, D. E., Alexander, S. P. H., Cirino, G., Docherty, J. R., et al. (2020). ARRIVE 2.0 and the british journal of pharmacology: updated guidance for 2020. *Br. J. Pharmacol.* 177, 3611–3616. doi: 10.1111/bph.15178

Lillyblad, M. P. (2015). Dual angiotensin receptor and neprilysin inhibition with Sacubitril/Valsartan in chronic systolic heart failure: understanding the new PARADIGM. *Ann. Pharmacother.* 49, 1237–1251. doi: 10.1177/1060028015593093

Mann, D. L., Greene, S. J., Givertz, M. M., Vader, J. M., Starling, R. C., Ambrosy, A. P., et al. (2020). Sacubitril/Valsartan in advanced heart failure with reduced ejection fraction: rationale and design of the LIFE trial. *JACC. Heart Fail.* 8, 789–799.

McMurray, J. J., Packer, M., Desai, A. S., Gong, J., Lefkowitz, M. P., Rizkala, A. R., et al. (2014). Angiotensin-neprilysin inhibition versus enalapril in heart failure. *N. Engl. J. Med.* 371, 993–1004.

Morris, G. M., Huey, R., Lindstrom, W., Sanner, M. F., Belew, R. K., Goodsell, D. S., et al. (2009). AutoDock4 and AutoDockTools4: automated docking with selective receptor flexibility. *J. Comput. Chem.* 30, 2785–2791. doi: 10.1002/jcc.21256

Nozaki, N., Shishido, T., Takeishi, Y., and Kubota, I. (2004). Modulation of doxorubicin-induced cardiac dysfunction in toll-like receptor-2-knockout mice. *Circulation* 110, 2869–2874. doi: 10.1161/01.cir.0000146889.46519.27

Oatmen, K. E., Zile, M. R., Burnett, J. C. Jr., and Spinale, F. G. (2018). Bioactive signaling in next-generation pharmacotherapies for heart failure: a review. *JAMA Cardiol.* 3, 1232–1243. doi: 10.1001/jamacardio.2018.3789

O'Neill, L. A., and Bowie, A. G. (2007). The family of five: TIR-domain-containing adaptors in Toll-like receptor signalling. *Nat. Rev. Immunol.* 7, 353–364. doi: 10.1038/nri2079

Percie du Sert, N., Hurst, V., Ahluwalia, A., Alam, S., Avey, M. T., Baker, M., et al. (2020). The ARRIVE guidelines 2.0: updated guidelines for reporting animal research. *J. Physiol.* 597, 3793–3801. doi: 10.1113/JP280389

Pop-Moldovan, A. L., Trofenciuc, N. M., Darabantiu, D. A., Precup, C., Branea, H., Christodorescu, R., et al. (2017). Customized laboratory TLR4 and TLR2 detection method from peripheral human blood for early detection of doxorubicin-induced cardiotoxicity. *Cancer Gene Ther.* 24, 203–207. doi: 10.1038/cgt.2017.4

Riad, A., Bien, S., Gratz, M., Escher, F., Westermann, D., Heimesaat, M. M., et al. (2008). Toll-like receptor-4 deficiency attenuates doxorubicin-induced cardiomyopathy in mice. *Eur. J. Heart Fail.* 10, 233–243. doi: 10.1016/j.ejheart.2008.01.004

Salomon-Ferrer, R., Case, R. A., and Walker, R. C. (2012). An overview of the Amber biomolecular simulation package. *WIREs Comput. Mol. Sci.* 3, 198–210. doi: 10.1002/wcms.1121

Suematsu, Y., Miura, S., Goto, M., Matsuo, Y., Arimura, T., Kuwano, T., et al. (2016). LCZ696, an angiotensin receptor-neprilysin inhibitor, improves cardiac function with the attenuation of fibrosis in heart failure with reduced ejection fraction in streptozotocin-induced diabetic mice. *Eur. J. Heart Fail.* 18, 386–393. doi: 10.1002/ejhf.474

Swain, S. M., Whaley, F. S., and Ewer, M. S. (2003). Congestive heart failure in patients treated with doxorubicin: a retrospective analysis of three trials. *Cancer* 97, 2869–2879. doi: 10.1002/cncr.11407

Tacar, O., Sriamornsak, P., and Dass, C. R. (2013). Doxorubicin: an update on anticancer molecular action, toxicity and novel drug delivery systems. *J. Pharm. Pharmacol.* 65, 157–170. doi: 10.1111/j.2042-7158.2012.01567.x

Turner, A. J., Isaac, R. E., and Coates, D. (2001). The neprilysin (NEP) family of zinc metalloendopeptidases: genomics and function. *BioEssays* 23, 261–269. doi: 10.1002/1521-1878(200103)23:3<261::aid-bies1036>3.0.co;2-k

Vejpongsa, P., and Yeh, E. T. (2014). Prevention of anthracycline-induced cardiotoxicity: challenges and opportunities. *J. Am. Coll. Cardiol.* 64, 938–945.

von Lueder, T. G., Wang, B. H., Kompa, A. R., Huang, L., Webb, R., Jordaan, P., et al. (2015). Angiotensin receptor neprilysin inhibitor LCZ696 attenuates cardiac remodeling and dysfunction after myocardial infarction by reducing cardiac fibrosis and hypertrophy. *Circ. Heart Fail.* 8, 71–78. doi: 10.1161/circheartfailure.114.001785

Wallace, K. B., Sardão, V. A., and Oliveira, P. J. (2020). Mitochondrial determinants of doxorubicin-induced cardiomyopathy. *Circ. Res.* 126, 926–941. doi: 10.1161/circresaha.119.314681

Xia, Y., Chen, Z., Chen, A., Fu, M., Dong, Z., Hu, K., et al. (2017). LCZ696 improves cardiac function via alleviating Drp1-mediated mitochondrial dysfunction in mice with doxorubicin-induced dilated cardiomyopathy. *J. Mol. Cell. Cardiol.* 108, 138–148. doi: 10.1016/j.yjmcc.2017.06.003

Yancy, C. W., Jessup, M., Bozkurt, B., Butler, J., Casey, D. E. Jr., Colvin, M. M., et al. (2016). 2016 ACC/AHA/HFSA focused update on new pharmacological therapy for heart failure: an update of the 2013 ACCF/AHA guideline for the management of heart failure: a report of the American college of Cardiology/American Heart Association task force on clinical practice guidelines and the heart failure Society of America. *J. Am. Coll. Cardiol.* 68, 1476–1488. doi: 10.1016/j.jacc.2016.05.011

Yang, H. L., Hsieh, P. L., Hung, C. H., Cheng, H. C., Chou, W. C., Chu, P. M., et al. (2020). Early moderate intensity aerobic exercise intervention prevents doxorubicin-caused cardiac dysfunction through inhibition of cardiac fibrosis and inflammation. *Cancers* 12:1102. doi: 10.3390/cancers12051102

Conflict of Interest: The authors declare that the research was conducted in the absence of any commercial or financial relationships that could be construed as a potential conflict of interest.

frontiers in Cell and Developmental Biology

ORIGINAL RESEARCH
published: 17 June 2021
doi: 10.3389/fcell.2021.672335

Homocysteine Causes Endothelial Dysfunction via Inflammatory Factor-Mediated Activation of Epithelial Sodium Channel (ENaC)

Chen Liang†, Qiu-Shi Wang†, Xu Yang, Di Zhu, Yu Sun, Na Niu, Jie Yao, Bi-Han Dong, Shuai Jiang, Liang-Liang Tang, Jie Lou, Chang-Jiang Yu, Qun Shao, Ming-Ming Wu and Zhi-Ren Zhang**

Departments of Pharmacy and Cardiology, Harbin Medical University Cancer Hospital, Institute of Metabolic Disease, Heilongjiang Academy of Medical Science, Heilongjiang Key Laboratory for Metabolic Disorder and Cancer Related Cardiovascular Diseases, NHC Key Laboratory of Cell Transplantation, Harbin Medical University and Key Laboratories of Education Ministry for Myocardial Ischemia Mechanism and Treatment, Harbin, China

Background: Hyperhomocysteinemia (HHcy) causes cardiovascular diseases via regulating inflammatory responses. We investigated whether and how the epithelial sodium channel (ENaC), a recently identified ion channel in endothelial cells, plays a role in HHcy-induced endothelial dysfunction.

Methods: Cell-attached patch-clamp recording in acute split-open aortic endothelial cells, western blot, confocal imaging, and wire myograph combined with pharmacological approaches were used to determine whether HHcy-mediated inflammatory signaling leads to endothelial dysfunction via stimulating ENaC.

Results: The data showed that 4 weeks after L-methionine diet the levels of plasma Hcy were significantly increased and the ENaC was dramatically activated in mouse aortic endothelial cells. Administration of benzamil, a specific ENaC blocker, ameliorated L-methionine diet-induced impairment of endothelium-dependent relaxation (EDR) and reversed Hcy-induced increase in ENaC activity. Pharmacological inhibition of NADPH oxidase, reactive oxygen species (ROS), cyclooxygenase-2 (COX-2)/thromboxane B2 (TXB2), or serum/glucocorticoid regulated kinase 1 (SGK1) effectively attenuated both the Hcy-induced activation of endothelial ENaC and impairment of EDR. Our *in vitro* data showed that both NADPH oxidase inhibitor and an ROS scavenger reversed Hcy-induced increase in COX-2 expression in human umbilical vein endothelial cells (HUVECs). Moreover, Hcy-induced increase in expression levels of SGK-1, phosphorylated-SGK-1, and phosphorylated neural precursor cell-expressed developmentally downregulated protein 4-2 (p-Nedd4-2) in HUVECs were significantly blunted by a COX-2 inhibitor.

OPEN ACCESS

Edited by:
Hui-Hua Li,
Capital Medical University, China

Reviewed by:
Yong Xia,
The Ohio State University, United States
Tianxin Yang,
The University of Utah, United States
Yuchun Gu,
Aston University, United Kingdom

***Correspondence:**
Zhi-Ren Zhang
zhirenz@yahoo.com
Ming-Ming Wu
mingmingwu@hrbmu.edu.cn

†These authors have contributed equally to this work

Specialty section:
This article was submitted to Signaling, a section of the journal Frontiers in Cell and Developmental Biology

Received: *25 February 2021*
Accepted: *18 May 2021*
Published: *17 June 2021*

Citation:
Liang C, Wang Q-S, Yang X, Zhu D, Sun Y, Niu N, Yao J, Dong B-H, Jiang S, Tang L-L, Lou J, Yu C-J, Shao Q, Wu M-M and Zhang Z-R (2021) Homocysteine Causes Endothelial Dysfunction via Inflammatory Factor-Mediated Activation of Epithelial Sodium Channel (ENaC). Front. Cell Dev. Biol. 9:672335. doi: 10.3389/fcell.2021.672335

Conclusion: We show that Hcy activates endothelial ENaC and subsequently impairs EDR of mouse aorta, via ROS/COX-2-dependent activation of SGK-1/Nedd4-2 signaling. Our study provides a rational that blockade of the endothelial ENaC could be potential method to prevent and/or to treat Hcy-induced cardiovascular disease.

Keywords: hyperhomocysteinemia, endothelial epithelial sodium channel, inflammation and cyclooxygenase-2, reactive oxygen species, vascular dysfunction

INTRODUCTION

As an independent risk factor, hyperhomocysteinemia (HHcy) is closely associated with coronary heart disease, venous and arterial thrombosis, atherosclerosis, and hypertension (Rodrigo et al., 2003; Ganguly and Alam, 2015). However, the underlying molecular mechanisms of HHcy-induced endothelial dysfunction remain to be elucidated.

Previous studies showed that homocysteine (Hcy) led to vascular dysfunction by regulating a variety of ion channels, including big- (BK_{Ca}), intermediate- (IK_{Ca}), and small-conductance (SK_{Ca}) Ca^{2+}-activated K^+ channels. For instance, Hcy inhibited BK_{Ca} channels in a dose-dependent manner in human umbilical vein endothelial cells (Zhang et al., 2005). Moreover, Hcy induced porcine coronary endothelial dysfunction through ER stress-mediated inhibition of SK_{Ca} and IK_{Ca} channels (Wang et al., 2015). In addition, studies showed that Hcy significantly inhibited BK_{Ca} channels in isolated human and rat artery smooth muscle cells and that the effects of Hcy on BK_{Ca} channels were reversed by the DPI, an inhibitor of NADPH oxidase (Cai et al., 2007). Furthermore, Hcy also suppressed BK_{Ca} channel probably by activating NADPH oxidase in porcine coronary smooth muscle cells. However, whether Hcy regulates endothelial epithelial sodium channel (ENaC), a newly identified ion channel in endothelium, remains unclear.

Previous studies showed that the activation of endothelial ENaC causes vascular stiffness (Guo et al., 2016; Tarjus et al., 2017), which is the first indication of the regulatory role of ENaC in vascular function. The later functional studies showed that endothelial ENaC plays an important role in a variety of pathological stimuli including oxidized LDL-, high fat diet-, and high salt diet-induced endothelial dysfunction and impairment of endothelium-dependent relaxation (EDR) (Liang et al., 2018; Wang et al., 2018b; Yang et al., 2020; Niu et al., 2021). We recently showed that manipulating the expression levels of endothelial ENaC or pharmacological blockade of ENaC alleviates high fat diet-induced production and secretion of proinflammatory cytokines, including TNF-α, IL-1β, IL-6, thereby reduces the formation of atherosclerotic lesion in LDL receptor knockout ($LDLr^{-/-}$) mice (Niu et al., 2021). These results strongly suggest that activation of endothelial ENaC is tightly linked to inflammatory factor-mediated dysfunction of endothelial dysfunction and pathogenesis of atherosclerosis. These results led us to hypothesize that endothelial ENaC may involve in Hcy-induced vascular dysfunction via ROS accumulation and activation of inflammatory signaling.

It has been well documented that cyclooxygenase-2 (COX-2), a pro-inflammatory factor, is involved in inflammation-mediated endothelial dysfunction (Tian et al., 2012; Zhang et al., 2018). COX-2 converts arachidonic acid into prostanoids, including thromboxane, prostaglandin, and prostacyclins. The productions of pro-inflammatory prostanoids such as thromboxane A2 (TXA2) and prostaglandin E2 (PGE2) are the main pathways, where COX-2 elicits the onset of inflammation. Recent studies indicate that COX-2 is highly expressed in endothelial cells in response to different stimuli such as angiotensin II (Niazi et al., 2017), palmitate (Gao et al., 2014), and bone morphogenic protein 4 (Wong et al., 2010) in hypertensive and diabetic models. These results suggest that COX-2 plays a role in these stimuli-induced endothelial dysfunctions. In addition, it has been reported that Hcy-induced increase in COX-2 expression contributes to inflammatory processes in murine macrophages (Lee et al., 2013), chondrocytes (Ma et al., 2018), and hepatic cells (Wu et al., 2009). More importantly, studies showed that celecoxib, a selective COX-2 inhibitor, improves endothelial function and reduces the systemic inflammatory response in coronary artery disease (Chenevard et al., 2003). Consistently, our recent study provides a clue that high fat diet-induced activation of ENaC may regulate COX-2-dependent inflammatory signaling (Niu et al., 2021).

In this study, we investigated the role of endothelial ENaC and underlying mechanisms in HHcy-induced vascular dysfunction, using L-methionine administration-induced HHcy mouse model combined with a variety of experimental approaches. We show that Hcy leads to vascular dysfunction by stimulating ENaC via ROS/COX-2-mediated activation of SGK1/Nedd4-2 signaling.

MATERIALS AND METHODS

Animals

All animal care and experimental procedures were approved by the Animal Research Ethical Committee of Harbin Medical University. All studies involving animals are reported conformed to the ARRIVE guidelines for reporting experiments (Kilkenny et al., 2010; McGrath et al., 2010).

C57BL/6J mice were purchased from the animal center of the second affiliated hospital of Harbin Medical University (Harbin, China). Male C57BL/6J mice aged 8–10 weeks (18–20 g) were fed with standard laboratory chow and had free access to water

Abbreviations: COX-2, cyclooxygenase-2; CVDs, cardiovascular diseases; EDR, endothelium-dependent relaxation; ENaC, epithelial sodium channel; Hcy, homocysteine; HHcy, Hyperhomocysteinemia; HUVECs, human umbilical vein endothelial cells; Nedd4-2, neural precursor cell-expressed developmentally downregulated protein 4-2; P_O, open probability; SGK1, serum/glucocorticoid regulated kinase 1; TXB2, thromboxane B2.

under a 12-h light/dark cycle with the ambient humidity at 50–80% and the controlled temperature at 22–24°C. C57BL/6J mice were given 2% (wt/wt) L-methionine in a chow diet for 4 weeks to establish the HHcy mouse model and the plasma levels of Hcy were significantly elevated. We also treated the aortic arteries and HUVECs with 100 μM Hcy to mimic the HHcy in mice, as previously described (Zhang et al., 2012). Mice were intragastrical administrated with benzamil (1 mg/kg/day) for 4 weeks, as previously described (Niu et al., 2021). C57BL/6J mice were randomly divided into four groups as follows: control, standard chow; HHcy, 2% (wt/wt) L-methionine diet; HHcy plus benzamil; and benzamil alone. Four weeks later, all animals were anesthetized, blood was collected, and the aorta were isolated for performing the experiments described down below. Plasma concentrations of Hcy and TXB2 were measured by the ELISA kits (Nan Jing Jian Cheng Biotech Co., Ltd., China) according to the manufacturer's guidelines. The measurements were performed in multiple duplications. The produced color intensity was assessed at a wavelength of 450 nm using a multifunctional microplate reader (SpectraMax M5, Sunnyvale, MD, United States).

Cell Culture

Human umbilical vein endothelial cells were cultured in endothelial cell growth medium (Hyclone, United States) supplemented with 10% FBS (Hyclone, United States) and 1% penicillin/streptomycin (Invitrogen, United States), as described previously (Zheng et al., 2016). When HUVECs had grown to 80–90% confluency in six-well plates, they were incubated with indicated reagents and maintained at 37°C under 95% air and 5% CO_2. Cells were used within 7–9 passages.

COX-2 Gene Silencing

One day prior to infection, HUVECs were cultured in the six-well plates until the density of the cells was achieved to 20–30%. The HUVECs were, respectively, transfected with either COX-2-shRNA green fluorescent protein (GFP) lentivirus (COX-2 gene silencing group) or with a scrambled shRNA GFP lentivirus (control group), in the presence of HiTransG A in order to enhance the virus infection. Three days post transfection, the gene silencing efficiency was examined by quantitative real-time polymerase chain reaction (qRT-PCR) and Western blot assays. The sequences of COX-2-shRNA and control were as follows: 5′-GCAGATGAAATACCAGTCTTT-3′ and, 5′- TTCTCCGAACGTGTCACGT-3′. The lentiviruses were purchased from Shanghai GeneChem Co., Ltd. (Shanghai, China). The infected HUVECs were, respectively, treated with 100 μM Hcy for 6 h, followed by testing the expression levels of t-SGK1, p-SGK1, t-Nedd4-2, and p-Nedd4-2.

In situ Patch-Clamp Recording

As described previously (Liu et al., 2015; Liang et al., 2018), *in situ* patch-clamp recordings of ENaC single-channel currents were performed in intact vascular endothelia. Each dissected aortic pectoralis was placed in a Petri dish containing physiological salt solution (PSS). They were then placed on a 5 × 5 mm cover glass coated with L-polylysine and transferred into a recording chamber mounted on an inverted Nikon microscope (Tokyo, Japan), allowing direct access to the endothelial cell layer.

The single-channel ENaC currents were recorded in a cell-attached configuration with an Axon Multiclamp 200B amplifier (Axon Instruments; United States) connected to a PC running Clampex 10.2 software at room temperature (22–24°C). Patch pipettes were fabricated from borosilicate glass capillaries using a Sutter P-97 horizontal puller. The pipettes had the resistance of ranged from 6 to 10 MΩ when filled with the pipette solution containing (in mM) 135 NaCl, 4.5 KCl, 0.1 EGTA, 5 HEPES, and 5 Na-HEPES (pH 7.2; adjusted with NaOH). The bath solution, contained (in mM) 135 NaCl, 4.5 KCl, 1 $MgCl_2$, 1 $CaCl_2$, 5 HEPES, and 5 Na-HEPES (pH 7.2; adjusted with NaOH). Single-channel currents were recorded immediately after gigaseal formation for at least 15 min. The data were recorded by application of 0 mV to the patch pipettes at 5 kHz with a low-pass filter at 1 kHz. Prior to analyses, single-channel traces were further filtered at 30 Hz and single-channel events were listed and values of the ENaC open probability (P_O) were analyzed by using Clampfit 10.2 software.

qRT-PCR and Western Blot Analysis

For western blot analyses were performed in HUVECs in the absence or in the presence of 100 μM Hcy for 6 h. Cell lysates were centrifuged at 12,000 rpm at 4°C for 15 min to remove debris. Protein concentration was assayed by BCA Protein Assay Kit (APPLYGEN, China). Protein samples were electrophoresed through 10% SDS-polyacrylamide gels and then transferred to nitrocellulose membranes using a *Trans*-blot unit (Bio-Rad Laboratories) for 90 min at 300 mA. Membranes were incubated in 5% (wt/vol) non-fat milk dissolved in 1 × TBS-T for 1 h at room temperature (22–24°C) to block non-specific binding sites. Then, the membrane was probed with the primary antibodies against COX-1 (1:1,000, ab109025, Abcam, United Kingdom), COX-2 (1:1,000, ab52237, Abcam, United Kingdom), SGK1 (1:500, ab59337, Abcam, United Kingdom), p-SGK1 (1:500, ab55281, Abcam, United Kingdom), Nedd4-2 (1:10,000, ab131167, Abcam, United Kingdom), p-Nedd4-2 (1:1,000, ab168349, Abcam, United Kingdom), or GAPDH (1:10,000, ab8245, Abcam, United Kingdom) overnight at 4°C. The membranes were washed in TBS-T and subsequently incubated with goat anti-rabbit IRDye® 800 CW (1:10,000, P/N 926-32211, LI-COR) or goat anti-mouse IRDye® 800 CW (1:10,000, P/N 926-32210, LI-COR) at room temperature (22–24°C) for another 1 h. Membranes were finally washed again in TBS-T and the protein bands were detected by the Odyssey infrared imaging system (LI-COR) and Odyssey v3.0 software.

Total RNA was extracted from HUVECs using TRIzol reagent (Invitrogen, Carlsbad, CA, United States). Reverse transcription was performed with the RT system protocol in a 20 μL reaction mixture, similar to that described previously (Wu et al., 2014; Niu et al., 2021). Total RNA (1 μg) was used in the reaction, and a random primer was used for the initiation of cDNA synthesis. The reaction mixture was incubated at 25°C for 10 min, 37°C for 120 min and 85°C for 5 min. RT-PCR was performed by an ABI Prism 7500 sequence detection system

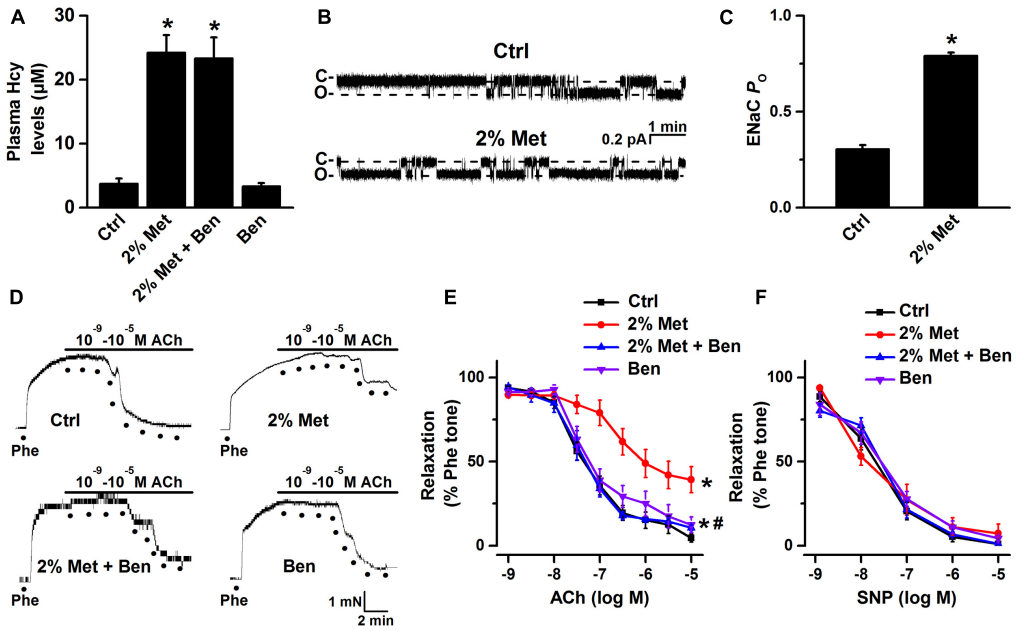

FIGURE 1 | L-methionine-induced HHcy activated aortic endothelial ENaC and impaired EDR was reversed by blockade of ENaC. **(A)** Mean plasma Hcy levels were measured in control and L-methionine (Met)-treated mice with or without benzamil (Ben) treatment. Data are means ± SEM of six mice. *$P < 0.05$ vs. ctrl. **(B)** Representative ENaC single-channel currents were recorded in endothelial cells of the split-open aorta isolated from control (Ctrl) and L-methionine-treated mice. **(C)** ENaC activity (P_O) summarized from the experiments as shown in **(B)**. Data are means ± SEM of six mice. *$P < 0.05$ vs. ctrl. **(D)** Representative traces obtained from wire myograph assays and **(E)** summarized data of acetylcholine (ACh)-induced relaxation of aorta pectoralis from control and L-methionine-treated mice with or without benzamil treatment. The first dot indicates the application of 10^{-9} M ACh to the 1 μM phenylephrine (Phe) precontracted arterial rings, whereas the following dots indicate ACh concentrations gradually increased from $10^{-8.5}$ to 10^{-5} M. Data are means ± SEM of six mice. *$P < 0.05$ vs. ctrl; #$P < 0.05$ vs. 2% Met groups. **(F)** Summary of artery relaxation induced by different doses of sodium nitroprusside (SNP) concentrations ranged from 10^{-9} to 10^{-5} M in control and L-methionine -treated mice with or without benzamil treatment.

using SYBR Green PCR core reagents (Bimake). PCR was performed by following the manufacturer's recommendations for a 25 μL reaction volume. Transcript quantities were compared by using the relative quantitation method, where the amount of detected mRNA was normalized to the amount of endogenous control (GAPDH) mRNA. The value relative to the control sample value is given by $2^{-\Delta\Delta CT}$. Expression levels of mRNA were determined using the following primers: COX-2-human-Forward (GCTCAGCCATACAGCAAATC), COX-2-human-Reverse (TGTGTTTGGAGTGGGTTTCA), GAPDH-human-Forward (CAACTTTGGTATCGTGAAGG), GAPDH-human -Reverse (AGAGGCAGGGATGATGTTCTG).

Isometric Force Measurement in a Wire Myograph

Myograph function analysis was performed as previously described (Wong et al., 2010; Liang et al., 2018; Niu et al., 2021). Male C57BL/6J mouse aortic pectoralis was gently isolated and then placed in oxygenated ice-cold Krebs solution (composition in mM: 119 NaCl, 4.7 KCl, 2.5 $CaCl_2$, 1 $MgCl_2$, 25 $NaHCO_3$, 1.2 KH_2PO_4, and 11 D-glucose, pH 7.2–7.4). Each aorta was stripped of surrounding connective tissues under a dissecting microscope and cut into 2 mm length ring segments. Rings were exposed to 100 μM Hcy with or without each of the following inhibitor for 6 h: benzamil (0.5 μM, ENaC blocker), TEMPOL (100 μM; ROS scavenger), apocynin (100 μM, NADPH oxidase inhibitor), sc560 (0.3 μM; COX-1 inhibitor), celecoxib (3 μM; COX-2 inhibitor), furegrelate (10 μM; thromboxane synthase inhibitor), and GSK650394 (10 μM; SGK1 inhibitor). The aortic pectoralis was mounted to a wire myograph system (Danish Myo Technology, Aarhus, Denmark) and bathed in oxygenated Krebs solution at 37°C. Each ring was stretched to 3 mN and then allowed to equilibrate for 1 h before the myograph experiment. After the stabilization period, KPSS (containing 60 mM K^+) was added to the chambers and washed out with Krebs solution until a reproducible maximal contraction was achieved. Endothelium-dependent relaxations were studied in phenylephrine (1 μM) pre-contracted endothelium-intact segments in response to cumulative addition of acetylcholine (ACh, in a range of concentration from 1 nM to 10 μM). Sodium nitroprusside (SNP, in a range of concentration from 1 nM to 10 μM), an exogenous NO donor, was used to examine endothelium-independent relaxation.

Confocal Laser Scanning Microscopy Analysis

Confocal microscopy (Olympus Fluoview 1200, Japan) studies were performed as previously described (Tian et al., 2012; Wang et al., 2018a). Aortic segments were fresh-frozen in optimal cutting temperature compound and sectioned at 5 μm

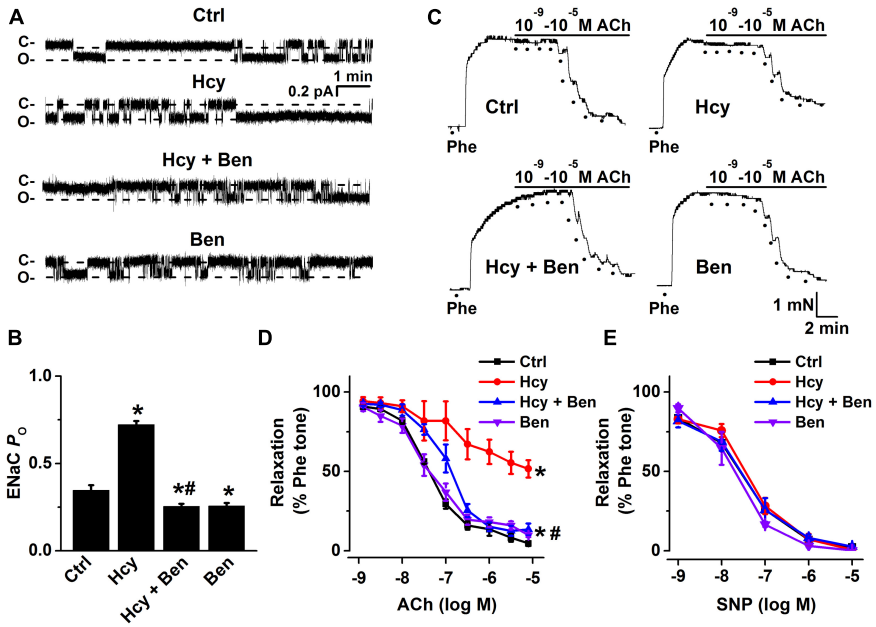

FIGURE 2 | Benzamil attenuates exogenous Hcy-induced increase in endothelial ENaC activity and impairment of EDR in mouse aorta. **(A)** Representative ENaC single-channel currents were recorded from endothelial cells from split-open aorta either under control conditions or, respectively, treated with 100 μM Hcy, 100 μM Hcy plus 0.5 μM benzamil (Ben), or 0.5 μM benzamil alone for 6 h. **(B)** ENaC activity (P_O) summarized from the recordings as shown as shown in **(A)**. Data are means ± SEM of six mice. *$P < 0.05$ vs. ctrl; #$P < 0.05$ vs. Hcy. **(C)** Representative traces obtained from wire myograph assays under each indicated condition (Ctrl, control; Hcy, the isolated aorta treated with Hcy; Hcy + Ben, the aorta incubated with Hcy plus benzamil; Ben, benzamil) and **(D)** summarized data of ACh-induced relaxation of aorta under each condition, as indicated in **(C)**. The first dot indicates the application of 10^{-9} M ACh to the 1 μM Phe precontracted arterial rings, whereas the following dots indicate ACh concentrations in a range of $10^{-8.5}$ to 10^{-5} M. Data are means ± SEM of six mice. *$P < 0.05$ vs. ctrl; #$P < 0.05$ vs. Hcy. **(E)** Summary of artery relaxation induced by different doses of SNP at the concentrations from 10^{-9} to 10^{-5} M in aorta from the four groups indicated above.

with a freezing microtome (CryoStar NX70, Thermo Fisher Scientific, Waltham, MA, United States). Cryosections were incubated in dihydroethidium (DHE) (Ex515/Em585 nm, 5 μM; Invitrogen, United States) in dark at 37 °C for 15 min. All slides were washed with PBS twice and imaged using a confocal microscope. The signal density was analyzed by ImageJ software (Java-based imaging processing program, National Institute of Health, United States).

5-(and-6)-carboxy-2′,7′-dichlorodihydrofluorescein diacetate (carboxy-H2DCFDA, Invitrogen, United States) was used as the membrane-permeable ROS-sensitive fluorescent indicator, that becomes fluorescent when oxidized. HUVECs grown on confocal dishes were loaded with 2.5 μM carboxy-H2DCFDA for 1 h. Before application of indicated reagents, HUVECs were treated with an iron chelator, 50 μM 2,2′-dipyridyl which suppresses the damaging Fenton reaction for 3 min (Shatalin et al., 2011). Next, labeled cells were washed twice in modified PBS before confocal microscopy analysis. Excitation at 488 nm and emission at 520 nm were used to evaluate the amount of intracellular ROS level in response to indicated reagents.

Chemicals and Reagents

Unless otherwise noted, all chemicals and reagents were purchased from Sigma-Aldrich. GSK650394 was purchased from Tocris and furegrelate was purchased from Cayman. Acetylcholine, phenylephrine, and TEMPOL were prepared in distilled water and the others in DMSO. TEMPOL and SNP were prevented from light during preparation and experiments.

Data Analysis

All data are presented as the mean values ± SEM. Statistical analysis was performed with GraphPad Prism 5 software (GraphPad; La Jolla, CA) for all statistical calculations. The student's *t*-test was used between two groups. Analysis of variance was used for multiple comparisons. In the cases, where ANOVA was used, a *post hoc* test (Bonferroni) was used. The results were considered significant at $P < 0.05$.

RESULTS

Blockade of ENaC by Benzamil Reverses Vascular Dysfunction in L-Methionine-Treated Mice

We have previously reported that blockade of ENaC has a protective effect on ox-LDL-induced vascular dysfunction in mice (Liang et al., 2018). Here, we investigated whether blockade of endothelial ENaC ameliorated HHcy-induced vascular dysfunction in mice. As shown in **Figure 1A**, the mean plasma level of Hcy was significantly elevated in L-methionine-treated mice as compared with control; whereas administration of benzamil, a selective ENaC blocker, had no effect on the elevated

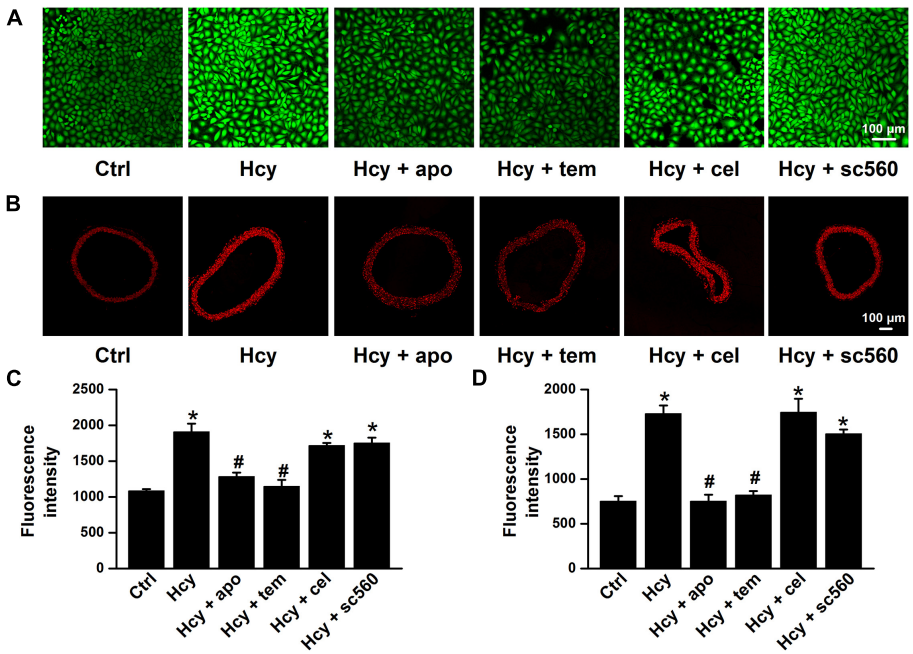

FIGURE 3 | NADPH oxidase inhibitor or TEMPOL reverses exogenous Hcy-induced ROS generation in both HUVECs and mouse aorta. **(A,B)** Representative confocal microscopy images, taken from HUVECs **(A)** or aorta **(B)**, under control condition (Ctrl) or treated with 100 μM Hcy in the absence or in the presence of 100 μM apocynin (apo), 100 μM TEMPOL (tem), 3 μM celecoxib (cel), and 0.3 μM sc560 for 6 h, respectively. **(C,D)** Summarized fluorescent intensities in HUVECs (DCF staining) or aorta (DHE staining), measured from the data shown in **(A,B)**, reflect the ROS levels in HUVECs or aorta. Data are means ± SEM of six individual experiments. *$P < 0.05$ vs. ctrl; #$P < 0.05$ vs. Hcy.

plasma level of Hcy in L-methionine-treated mice (**Figure 1A**). Importantly, our patch-clamp data showed that the ENaC activity was significantly increased in intact endothelial cells of the aorta from L-methionine-treated mice, compared with the control (**Figures 1B,C**). Since our previous data showed that elevation of ENaC activity impaired ACh-induced EDR in the salt-sensitive rats (Wang et al., 2018b), therefore, we hypothesize that blockade of ENaC may prevent Hcy-induced vascular dysfunction in L-methionine-treated mice. As expected, the ACh-induced EDR was dramatically impaired by L-methionine in mice, which was reversed by benzamil; while the ACh-induced EDR was not affected by benzamil (**Figures 1D,E**). Moreover, neither L-methionine nor benzamil affected SNP-induced endothelium-independent artery relaxation (**Figure 1F**).

To further confirm that L-methionine-induced activation of ENaC was brought about by HHcy, we treated isolated mouse aorta with 100 μM Hcy for 6 h and performed single-channel recordings intact endothelial cells. Consistent with the data obtained from *in vivo* experiments, our *ex vivo* data demonstrated that exogenous Hcy led to the significantly increased ENaC activity and that the exogenous Hcy-induced increase in ENaC activity was reversed by benzamil (**Figures 2A,B**). Moreover, exogenous Hcy treatment-induced impairment of EDR was dramatically alleviated by benzamil (benzamil did not affect EDR; **Figures 2C,D**); whereas exogenous Hcy or benzamil had no effect on SNP-induced endothelium-independent relaxation (**Figure 2E**). These data together suggest that HHcy stimulates endothelial ENaC and that blockade of endothelial ENaC by benzamil ameliorates HHcy-induced impairment of EDR in mice.

An NADPH Oxidase Inhibitor or a Superoxide Scavenger Reverses Hcy-Induced Activation of ENaC and Endothelial Dysfunction

It has been reported that Hcy induces activation of NADPH oxidase, a major source of ROS produced by endothelial cells, and leads to vascular dysfunction (Babior, 2000; Zeng et al., 2003; Liu et al., 2019), and our previous findings showed that the accumulation of intracellular ROS stimulates ENaC in both aortic endothelial cells and renal epithelial cells (Zhang et al., 2013; Liang et al., 2018; Wang et al., 2018a; Wu et al., 2019). Thus, we examined whether Hcy increased ENaC activity by promoting ROS generation in the intact endothelial cells of the mouse aorta. Indeed, our data showed that exogenous Hcy significantly elevated ROS production in both mouse aorta and HUVECs, as determined by DHE and DCF staining, respectively. In addition, apocynin, an NADPH oxidase inhibitor, and TEMPOL, a superoxide scavenger, significantly inhibited Hcy-induced ROS production in mouse aorta and in HUVECs. Whereas, celecoxib (a COX-2 inhibitor) and sc560 (a COX-1 inhibitor) had no effect on exogenous Hcy-induced oxidative stress (**Figures 3A–D**).

Moreover, both apocynin and TEMPOL significantly attenuated exogenous Hcy-induced increases in ENaC activity, without affecting the basal ENaC activity in aortic endothelial

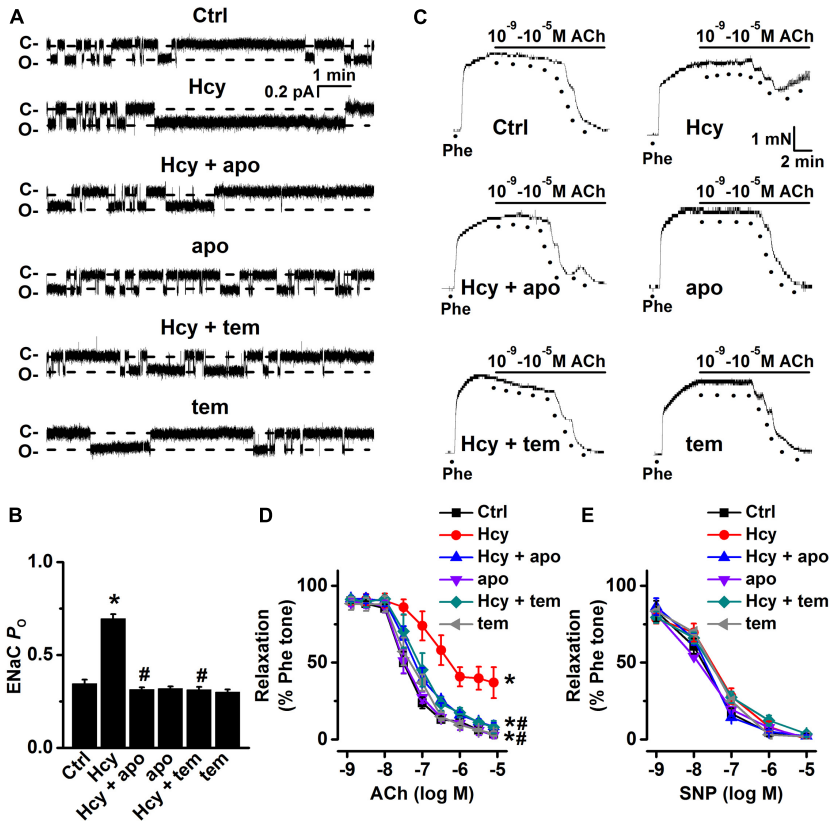

FIGURE 4 | Inhibition of ROS attenuates Hcy-induced increase in ENaC activity and impairment of EDR in mouse aorta. **(A)** Representative ENaC single-channel currents were recorded in endothelial cells from split-open aorta either under control conditions or treated with 100 μM Hcy, 100 μM Hcy plus 100 μM apocynin (apo), 100 μM apo alone, 100 μM Hcy plus 100 μM TEMPOL (tem), or 100 μM TEMPOL alone for 6 h, respectively. **(B)** Summarized ENaC P_O obtained from recordings as shown in **(A)**. Data are means ± SEM of six mice. *$P < 0.05$ vs. ctrl; #$P < 0.05$ vs. Hcy. **(C)** Representative traces obtained from wire myograph assays under each indicated condition and **(D)** summarized data of ACh-induced relaxation under each indicated condition. The first dot indicates the application of 10^{-9} M ACh to the 1 μM Phe precontracted arterial rings, whereas the following dots indicate ACh concentrations gradually increasing from $10^{-8.5}$ to 10^{-5} M. Data are means ± SEM of six mice. *$P < 0.05$ vs. ctrl; #$P < 0.05$ vs. Hcy. **(E)** Summary of artery relaxation induced by different doses of SNP increasing from 10^{-9} to 10^{-5} M in aorta from each indicated group.

cells (**Figures 4A,B**). Importantly, apocynin or TEMPOL ameliorated exogenous Hcy-induced impairment of aortic EDR (**Figures 4C,D**), while endothelial-independent relaxations in response to SNP were unaffected by all reagents (**Figure 4E**). These data suggest that exogenous Hcy increases ENaC activity, which leads to impairment of EDR via promoting the accumulation of intracellular ROS.

Hcy-Induced Endothelial Dysfunction Is Mediated by COX-2

Several lines of evidence showed that Hcy significantly increased COX-2 expression in human chondrocytes (Ma et al., 2018), and human monocytes (Chien et al., 2015). Consistently, we observed that the expression levels of COX-2, but not the expression levels of COX-1, were significantly increased by exogenous 100 μM Hcy for 6 h in HUVECs and this effect was completely prevented by pre-treatment of HUVECs with either apocynin or TEMPOL (**Figures 5A,B**). We then next examined whether COX-2 was involved in Hcy-induced increase in ENaC activity in the intact endothelial cells of aorta. Our data showed that pre-treatment of aorta with the celecoxib, the COX-2 inhibitor, but not sc560, the COX-1 inhibitor, attenuated Hcy-induced increase in ENaC activity in these cells and that each inhibitor alone had no effect on the basal ENaC activity (**Figures 5C,D**). Consistently, celecoxib, but not sc560, prevented exogenous Hcy-induced impairment of mouse aortic EDR (**Figures 5E,F**). However, endothelial-independent relaxations in response to SNP were unaffected by exogenous Hcy, celecoxib and sc560 (**Figure 5G**). These data together suggest that the ROS generation and an increased COX-2 expression contribute to Hcy-induced elevation of ENaC activity, which accounts for impaired EDR in Hcy-treated aorta.

Inhibition of TXB2 Synthesis Attenuated Hcy-Induced ENaC Activity and Impaired Endothelial Relaxation

Previous studies showed that elevation of COX-2 expression led to a dramatically increased production of TXB2

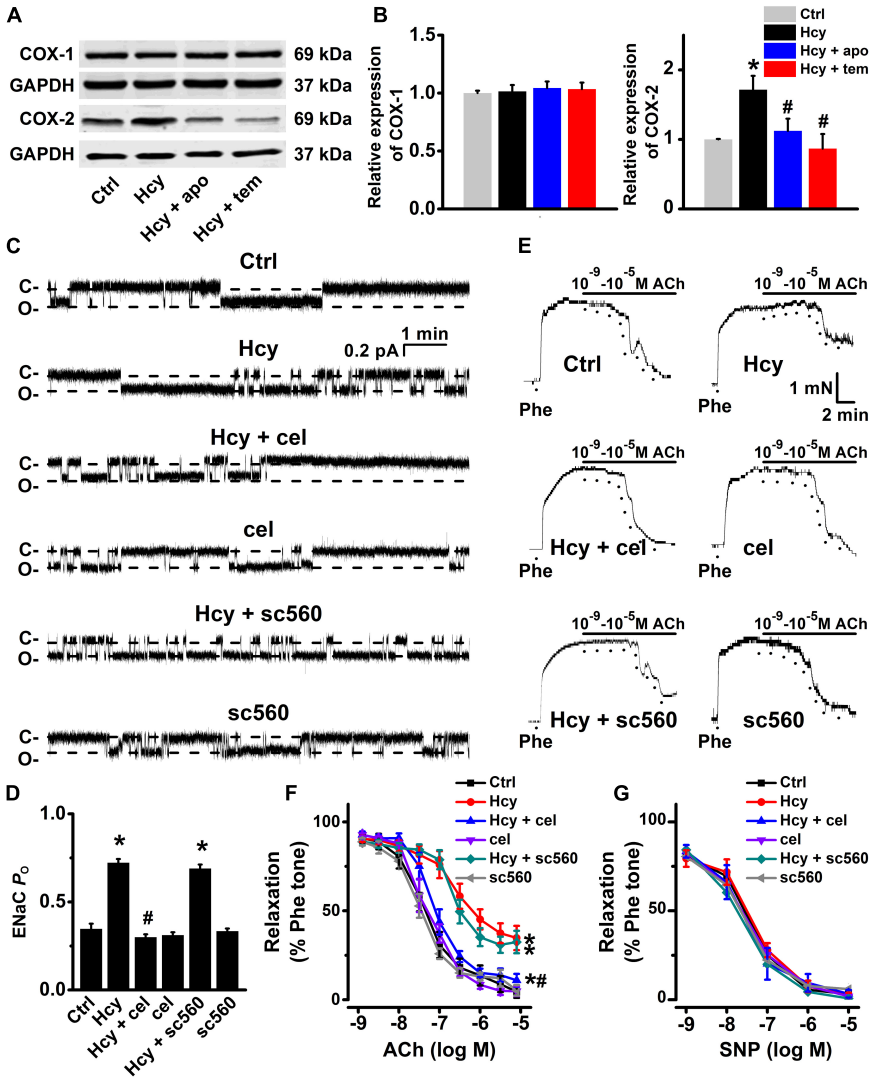

FIGURE 5 | Inhibition of COX-2 by celecoxib attenuates Hcy-induced increase in ENaC activity and impairment of EDR in mouse aorta. **(A)** Representative Western blots demonstrating COX-1 and COX-2 expression in HUVECs under control condition or treated with 100 μM Hcy, 100 μM Hcy plus 100 μM apocynin (apo), or 100 μM Hcy plus 100 μM TEMPOL (tem) for 6 h, respectively. **(B)** Summary plots of Western blots, showing the expression levels of COX-1 (left) and COX-2 (right) under each indicated condition. Data are means ± SEM of six experiments in each group. *P < 0.05 vs. ctrl; #P < 0.05 vs. Hcy. **(C)** Representative ENaC single-channel currents recorded in endothelial cells from split-open aorta under control conditions or, respectively, treated with 100 μM Hcy, 100 μM Hcy plus 3 μM celecoxib (cel), 3 μM celecoxib alone, 100 μM Hcy plus 0.3 μM sc560, or 0.3 μM sc560 alone for 6 h. **(D)** Summarized ENaC P_O, reflecting ENaC activity, from recordings as shown in **(C)**. Data are means ± SEM of six mice. *P < 0.05 vs. ctrl; #P < 0.05 vs. Hcy. **(E)** Representative traces obtained from wire myograph assays under each indicated condition and **(F)** summarized data of ACh-induced relaxation of aorta under each indicated condition. The first dot indicates the application of 10^{-9} M ACh to the 1 μM Phe precontracted arterial rings, whereas the following dots indicate ACh concentrations gradually increasing from $10^{-8.5}$ to 10^{-5} M. Data are means ± SEM of six mice. *P < 0.05 vs. ctrl; #P < 0.05 vs. Hcy. **(G)** Summary of artery relaxation induced by 10^{-9} to 10^{-5} M SNP in aorta from the six individual experiments under indicated conditions.

(Feletou et al., 2011). Indeed, our data showed that the mean plasma level of TXB2 was significantly increased by L-methionine in mice as compared with control (**Figure 6A**). Then, we further examined whether inhibition of TXB2 attenuated Hcy-induced increase in ENaC activity in the intact endothelial cells of mouse aorta. Our data showed that pre-treatment of mouse aorta with furegrelate, a thromboxane synthase inhibitor, significantly attenuated exogenous Hcy-induced activation of ENaC in aortic endothelial cells, whereas furegrelate alone had no effect on basal ENaC activity in the intact endothelial cells of mouse aorta (**Figures 6B,C**). Consistently, furegrelate significantly improved the Hcy-induced impairment of endothelial-dependent relaxations (aorta treated with 100 μM Hcy for 6 h), while furegrelate alone had no effect on ACh-induced relaxations in the control aorta (**Figures 6D,E**). In addition, endothelial-independent relaxations in response to SNP were unaffected by either Hcy or furegrelate (**Figure 6F**). These data suggest that COX-2-derived TXB2

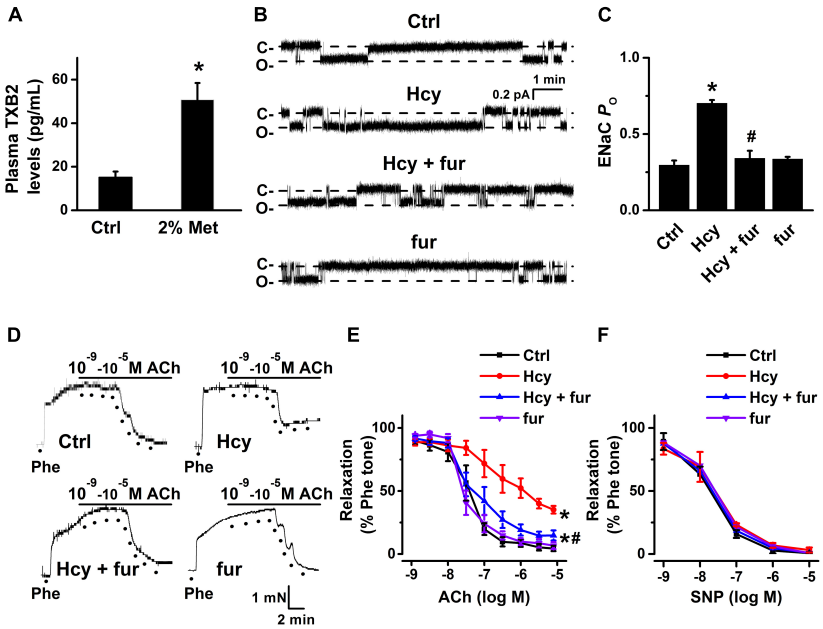

FIGURE 6 | Inhibition of TXB2 by furegrelate ameliorated Hcy-induced increase in ENaC activity and impairment of EDR in mouse aorta. **(A)** Mean plasma TXB2 levels, the stable metabolic product of TXA_2, were measured in control and L-methionine (Met)-treated mice. Data are means ± SEM of six mice. *$P < 0.05$ vs. ctrl. **(B)** Representative ENaC single-channel currents recorded in endothelial cells from split-open aorta either under control condition or, respectively, treated with 100 μM Hcy, 100 μM Hcy plus 10 μM furegrelate (fur), or 10 μM furegrelate alone for 6 h. **(C)** Summarized ENaC P_O under conditions as shown in **(B)**. Data are means ± SEM of six mice. *$P < 0.05$ vs. ctrl; #$P < 0.05$ vs. Hcy. **(D)** Representative traces obtained from wire myograph assays under each indicated condition and **(E)** summarized data of ACh-induced relaxation of aorta under each indicated condition. The first dot indicates the application of 10^{-9} M ACh to the 1 μM Phe precontracted arterial rings, whereas the following dots indicate ACh concentrations increasing from $10^{-8.5}$ to 10^{-5} M. Data are means ± SEM of six mice. *$P < 0.05$ vs. ctrl; #$P < 0.05$ vs. Hcy. **(F)** Summary of artery relaxation induced by 10^{-9} to 10^{-5} M SNP in aortas from the four individual experiments under indicated conditions.

mediates Hcy-induced increase in ENaC activity and impaired EDR in mouse aorta.

Activation of SGK1/Nedd4-2 Signaling Contributes to Hcy-Induced Impairment of EDR

A number of studies demonstrated that activation of SGK1/Nedd4-2 signaling stimulates ENaC activity (Kamynina and Staub, 2002; Wu et al., 2019; Yang et al., 2020). We then examined whether activation of SGK1/Nedd4-2 signaling may contribute to Hcy/COX-2 mediated impairment of EDR in mouse aorta. Our data showed that GSK650394, the SGK1 inhibitor, ameliorated Hcy-induced impairment of EDR in mouse aorta; while GSK650394 alone had no effect on EDR in control aorta (**Figures 7A,B**). Moreover, endothelial-independent relaxations in response to SNP were unaffected by Hcy or GSK650394 (**Figure 7C**). Moreover, Western blots data showed that the expression levels of phosphorylated Nedd4-2, phosphorylated SGK1, and total SGK1 expression, but not total Nedd4-2 were significantly increased by exogenous Hcy and that these effects were dramatically attenuated by celecoxib (**Figures 7D,E**).

To further confirm the role and mechanisms of COX-2 in mediating Hcy-induced ENaC activity, COX-2 gene-silencing experiments were performed in HUVECs. The data showed that the lentivirus shRNA agonist COX-2 (LV-COX-2), but not the scrambled shRNA (LV-NC), significantly reduced COX-2 expression at both the mRNA and protein levels (**Figures 8A–C**). We then examined the effect of COX-2 knockdown on Hcy-induced activation of SGK1/Nedd4-2 signaling in HUVECs. The results showed that the Hcy-induced increase in the expression levels of p-SGK1, t-SGK1, and p-Nedd4-2 were significantly attenuated by knockdown COX-2, but not by scramble shRNA; whereas Hcy did not affect t-Nedd4-2 expression (**Figures 8D,E**). These data suggest that COX-2 stimulated SGK1/Nedd4-2 signaling may account for Hcy-induced activation of ENaC, as well as impairment of EDR.

DISCUSSION

The major findings of the present project are as follows: HHcy led to impairment of EDR by stimulating ENaC, through promoting ROS generation and COX-2 expression mediated activation of SGK1/Nedd4-2 signaling. Our data suggest that blockade of endothelial ENaC could be a potential therapeutic strategy for HHcy-induced vascular dysfunction.

It has been reported that HHcy is an independent risk factor for cardiovascular diseases (Kalra, 2004; Mazza et al., 2004). Our previous studies showed that pathological stimuli, including high salt and oxidized LDL activated endothelial ENaC contributes to the development of vascular dysfunction

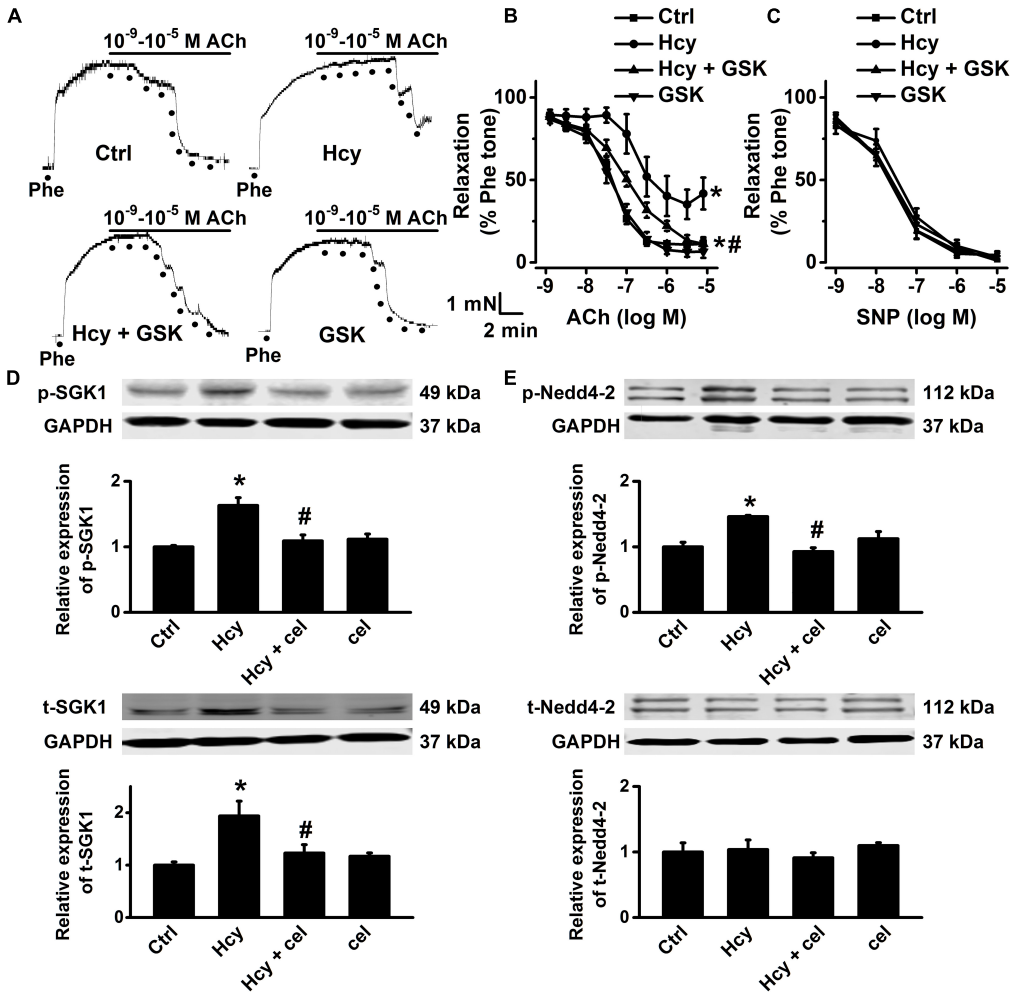

FIGURE 7 | Celecoxib ameliorated Hcy-induced impairment of EDR by inhibition of SGK1/Nedd4-2 signaling. **(A)** Representative traces obtained from wire myograph assays under each indicated condition and **(B)** summarized data of ACh-induced relaxation of aorta either under control condition or, respectively, treated with 100 μM Hcy, 100 μM Hcy plus 10 μM GSK650394 (GSK), or 10 μM GSK650394 alone for 6 h. The first dot indicates the application of 10^{-9} M ACh to the 1 μM Phe precontracted arterial rings, whereas the following dots indicate ACh concentrations ranged from $10^{-8.5}$ to 10^{-5} M. Data are means ± SEM of six mice. *$P < 0.05$ vs. ctrl; #$P < 0.05$ vs. Hcy. **(C)** Summary of artery relaxation induced by 10^{-9} to 10^{-5} M SNP in aorta from the four individual experiments. **(D,E)** Representative Western blots demonstrating the expression of total SGK1 (t-SGK1), phosphorylated SGK1 (p-SGK1), total Nedd4-2 (t-Nedd4-2) and phosphorylated Nedd4-2 (p-Nedd4-2) under control condition or, respectively, treated with 100 μM Hcy, 100 μM Hcy plus 3 μM celecoxib, or 3 μM celecoxib alone for 6 h. Summary plots of Western blots, showing the summarized expression levels of t-SGK1, p-SGK1, t-Nedd4-2, and p-Nedd4-2 under each indicated condition. Data are means ± SEM of six experiments in each group. *$P < 0.05$ vs. ctrl; #$P < 0.05$ vs. Hcy.

and/or hypertension (Liang et al., 2018; Wang et al., 2018b; Yang et al., 2020; Niu et al., 2021). One of the mechanisms of these pathological stimuli activate endothelial ENaC is associated with excessive accumulation of ROS. More recently, we demonstrated that benzamil, a potent ENaC blocker, effectively ameliorates high fat diet-induced impairment of aortic EDR and formation of the atherosclerotic lesion, via reducing expression of proinflammatory cytokines and production of adhesion molecules in $LDLr^{-/-}$ mice (Niu et al., 2021). These results suggest that ENaC is involved in stimulating hyperlipidemia mediated vascular inflammation. In addition, HHcy is known to regulate inflammatory responses by increasing COX-2 expression in a variety of cell types (Wu et al., 2009; Lee et al., 2013; Ma et al., 2018). Furthermore, celecoxib could greatly attenuate systemic inflammatory response in coronary artery disease (Chenevard et al., 2003). These results led us to hypothesize that HHcy leads to vascular dysfunction via activation of endothelial ENaC.

To this end, we established an experimental HHcy mouse model using dietary modification (Zhang et al., 2012), because dietary L-methionine-induced HHcy has been associated with vascular dysfunction and reduction of eNOS activity in mice (Jiang et al., 2005). Our data show that 4 weeks after L-methionine administration the levels of plasma Hcy increased significantly, which is an indication for establishing HHcy in mouse. More importantly, the aortic endothelial ENaC was greatly activated and EDR of aorta was impaired by

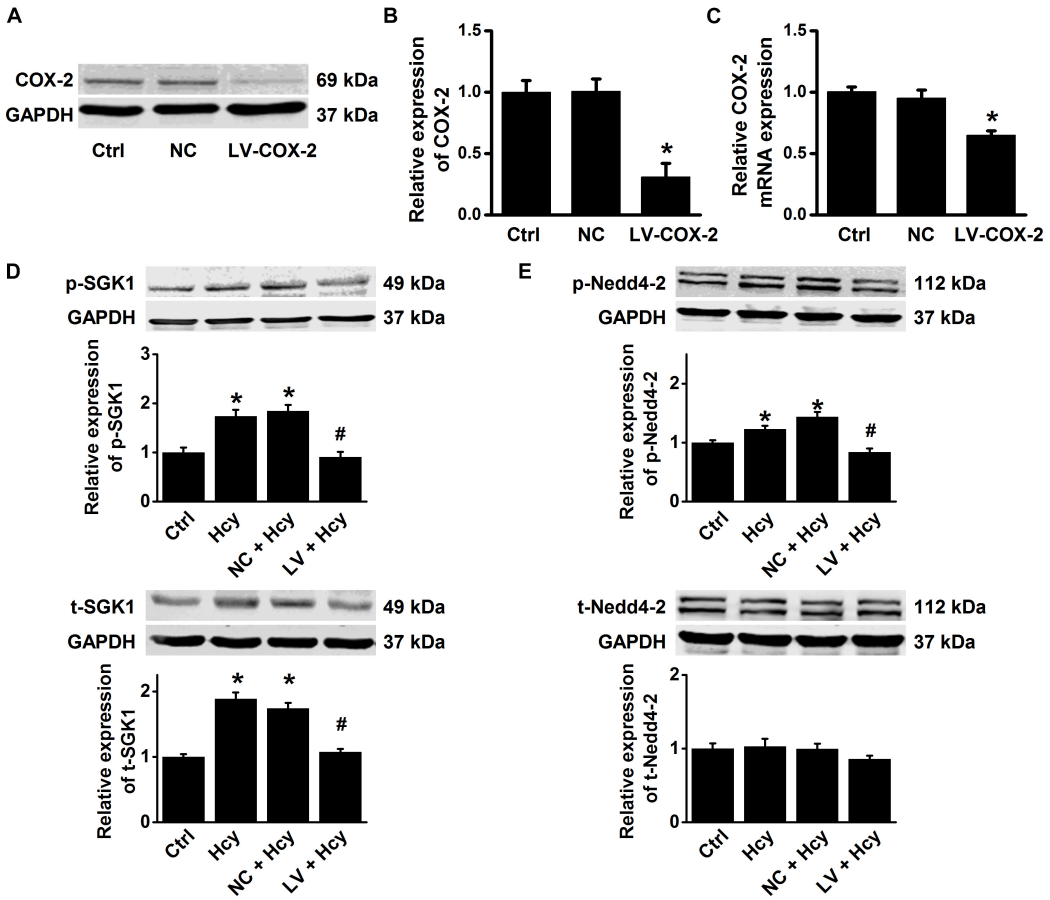

FIGURE 8 | COX-2 gene silencing attenuates Hcy-induced activation of SGK1/Nedd4-2 signaling in HUVECs. **(A)** Representative Western blots demonstrating COX-2 expression in HUVECs under the conditions of control, or transiently transfected with either COX-2 control LV or COX-2 shRNA LV (MOI = 10). **(B)** Summary plots of Western blots, showing the expression levels under each indicated condition. Data are means ± SEM of six experiments in each group. *$P < 0.05$ vs. ctrl. **(C)** Quantification of the results obtained from Real-time PCR analysis demonstrating the levels of COX-2 mRNA expression in HUVECs under each indicated condition. Data are means ± SEM of six experiments in each group. *$P < 0.05$ vs. ctrl. **(D)** Representative Western blots and summarized plots demonstrating the effects of Hcy (100 μM for 6 h) on the expression levels of p-SGK1 (upper panels) and t-SGK1 (lower panels) in control HUVECs, or in HUVECs transfected with either shRNA against COX-2 or scramble shRNA. **(E)** Representative Western blots and summarized plots demonstrating the effects of Hcy (100 μM for 6 h) on the expression levels of p-Nedd4-2 (upper panels) and t-Nedd4-2 (lower panels) in control HUVECs, or in HUVECs transfected with either shRNA against COX-2 or scramble shRNA. Data are means ± SEM of six experiments in each group. *$P < 0.05$ vs. ctrl; #$P < 0.05$ vs. Hcy.

L-methionine administration, suggesting HHcy may stimulate endothelial ENaC and subsequently induces impaired EDR in L-methionine administered mice. We then isolated and treated mouse aorta with exogenous Hcy to examine whether exogenous Hcy application could mimic the effects of L-methionine on ENaC and EDR. Consistently, exogenous application of Hcy to isolated aorta resulted in a significant increase in endothelial ENaC activity and led to an impairment of EDR, which were abolished by benzamil. These results strongly suggest that HHcy-induced activation of ENaC, in aortic endothelial cells, is tightly associated with the impairment of EDR.

Previous studies suggested that HHcy could cause endothelial injury and vascular dysfunction by accumulating intracellular ROS (Esse et al., 2019). Additionally, our recent studies showed that ROS-mediated strong activation of ENaC, in both the endothelial cells and the distal nephron principal cells, contributes to the development of hypertension (Wang et al., 2018a; Wu et al., 2019). Therefore, we reasoned that the increased intracellular ROS levels may participate in Hcy-induced increase in ENaC activity. Consistent with this notion, our data demonstrated that exogenous Hcy significantly induced accumulation of intracellular ROS in both mouse aorta and HUVECs, which were reversed by apocynin or TEMPOL, suggesting NADPH-mediated ROS accumulation plays role in Hcy-induced activation endothelial ENaC. This notion is strongly supported by the experiments, where apocynin or TEMPOL restored Hcy-induced activation of ENaC and impairment of EDR. Previous studies have shown that p-SGK1 mediated elevation of phosphorylated Nedd4-2 levels reduces the interaction between Nedd4-2 and ENaC and therefore increases the abundance of functional ENaC in the cell membrane (Debonneville et al., 2001). Moreover, we and others have

shown that an elevation of ROS significantly increases SGK1 expression in both renal cortical collecting ducts principal cells and peritoneal fibroblasts (Yamahara et al., 2009; Wu et al., 2019). Therefore, we suggest that the ROS-induced increase in ENaC activity contributes to Hcy-induced vascular dysfunction.

Previous study showed that COX-2 is an inducible enzyme involved in chronic inflammation (Subedi et al., 2019) and that excessive ROS increases the expression of COX-2 in the arteries of aging, diabetic, and hypertensive rats (Shi and Vanhoutte, 2008; Shi et al., 2008; Wong et al., 2010; Tian et al., 2012). Consistently, our data showed that the expression of COX-2, rather than COX-1, was significantly increased by exogenous Hcy in HUVECs, which was reversed by apocynin or TEMPOL. These results suggest that the increased COX-2 expression may involve in Hcy-mediated activation of ENaC. This notion is supported by the data that Hcy-induced activation of endothelial ENaC and dysfunction of vascular relaxation were reversed by celecoxib, but not by COX-1 inhibitor. These findings further imply that increased intracellular ROS stimulates COX-2 expression, which is responsible for Hcy-induced activation of endothelial ENaC and vascular dysfunction.

Our recent study demonstrated that endothelial ENaC plays an important role in high-fat diet-induced atherosclerosis in $LDLr^{-/-}$ mice, via stimulating COX-2 mediated inflammatory signaling (Niu et al., 2021). Interestingly, our data obtained from the current study further demonstrated that an increased ENaC activity is tightly linked with Hcy-induced elevation of by COX-2 expression. Furthermore, we show that Hcy-induced increase in the expression levels of p-SGK1/SGK1 and p-Nedd4-2 was dramatically inhibited by celecoxib, suggesting the involvement of COX-2 in Hcy-induced activation of ENaC through SGK1/Nedd4-2 signaling. Therefore, we argue that there is most likely a positive feedback between ENaC and COX-2 and that this positive feedback amplifies inflammatory responses under the condition of Hcy. Nevertheless, our findings also extend the pathophysiological role of COX-2 in Hcy-induced vascular dysfunction, where the endothelial ENaC plays a critical role.

TXA2 is a powerful vasoconstrictor and aggregating factor with proinflammatory properties in the cardiovascular system; its overproduction is closely associated with vascular dysfunction (de Sotomayor et al., 2005; Vessieres et al., 2010; Romacho et al., 2016). We found that the plasma levels of TXB2 were significantly increased by L-methionine in mice. This is not surprising, because it has been suggested that ROS triggers the release of TXA2 via COX-2 in high glucose-treated human aortic endothelial cells and hypertensive rat arteries (Cosentino et al., 2003; Tian et al., 2012). Our data further demonstrated that furegrelate, the thromboxane synthase inhibitor, significantly attenuated Hcy-induced ENaC activity and impairment of EDR in mouse aorta, suggesting that the release of TXA2 (as reflected by increase in its stable metabolite TXB2) plays a critical role in Hcy-induced activation of endothelial ENaC, as well as the impartment of EDR.

Recent studies suggest that high salt diet stimulates ENaC in dendritic cells, thereby leading to vascular dysfunction and hypertension (Barbaro et al., 2017; Van Beusecum et al., 2019). Therefore, we cannot completely rule out the possibility that activation of ENaC in dendritic cells may contribute to Hcy-induced vascular dysfunction. Nevertheless, our data showed that Hcy increased ROS-mediated COX-2 expression, which augments the release of TXA2; the latter elevated endothelial ENaC activity and expression via SGK1/Nedd4-2 signaling and thus impairs EDR. The present study demonstrated that inhibition of ENaC and COX-2 or ROS scavenger could be a potential therapeutic strategy to ameliorate HHcy related vascular diseases.

DATA AVAILABILITY STATEMENT

The original contributions presented in the study are included in the article/supplementary material, further inquiries can be directed to the corresponding author/s.

ETHICS STATEMENT

The animal study was reviewed and approved by the Animal Research Ethical Committee of Harbin Medical University.

AUTHOR CONTRIBUTIONS

Z-RZ and M-MW were responsible for the major conception and design of the study. CL, Q-SW, XY, DZ, YS, NN, JY, B-HD, SJ, L-LT, JL, C-JY, and QS carried out the experiments. CL analyzed the data and prepared the figures. CL, M-MW, and Z-RZ drafted and revised the manuscript. All authors approved the final version of the manuscript.

FUNDING

This work was generously supported by grants from the National Natural Science Foundation of China (Nos. 81930009, 91639202, and 81870370 to Z-RZ; 81800365 to CL; and 81800513 to C-JY) and Nn10 Program of Harbin Medical University Cancer Hospital, and Petrel Science Foundation (No. JJQN2018-01 to CL).

REFERENCES

Babior, B. M. (2000). The NADPH oxidase of endothelial cells. *IUBMB Life* 50, 267–269. doi: 10.1080/713803730

Barbaro, N. R., Foss, J. D., Kryshtal, D. O., Tsyba, N., Kumaresan, S., Xiao, L., et al. (2017). Dendritic cell amiloride-sensitive channels mediate sodium-induced inflammation and hypertension. *Cell Rep.* 21, 1009–1020. doi: 10.1016/j.celrep.2017.10.002

Cai, B., Gong, D., Pan, Z., Liu, Y., Qian, H., Zhang, Y., et al. (2007). Large-conductance Ca2+-activated K+ currents blocked and impaired by homocysteine in human and rat mesenteric artery smooth muscle cells. *Life Sci.* 80, 2060–2066. doi: 10.1016/j.lfs.2007.03.003

Chenevard, R., Hurlimann, D., Bechir, M., Enseleit, F., Spieker, L., Hermann, M., et al. (2003). Selective COX-2 inhibition improves endothelial function in coronary artery disease. *Circulation* 107, 405–409. doi: 10.1161/01.cir.0000051361.69808.3a

Chien, S. J., Chen, T. C., Kuo, H. C., Chen, C. N., and Chang, S. F. (2015). Fulvic acid attenuates homocysteine-induced cyclooxygenase-2 expression in human monocytes. *BMC Complement Altern. Med.* 15:61. doi: 10.1186/s12906-015-0583-x

Cosentino, F., Eto, M., De Paolis, P., Van Der Loo, B., Bachschmid, M., Ullrich, V., et al. (2003). High glucose causes upregulation of cyclooxygenase-2 and alters prostanoid profile in human endothelial cells: role of protein kinase C and reactive oxygen species. *Circulation* 107, 1017–1023. doi: 10.1161/01.cir.0000051367.92927.07

de Sotomayor, M. A., Perez-Guerrero, C., Herrrera, M. D., Jimenez, L., Marin, R., Marhuenda, E., et al. (2005). Improvement of age-related endothelial dysfunction by simvastatin: effect on NO and COX pathways. *Br. J. Pharmacol.* 146, 1130–1138. doi: 10.1038/sj.bjp.0706420

Debonneville, C., Flores, S. Y., Kamynina, E., Plant, P. J., Tauxe, C., Thomas, M. A., et al. (2001). Phosphorylation of Nedd4-2 by Sgk1 regulates epithelial Na(+) channel cell surface expression. *EMBO J.* 20, 7052–7059. doi: 10.1093/emboj/20.24.7052

Esse, R., Barroso, M., Tavares, De Almeida, I., and Castro, R. (2019). The contribution of homocysteine metabolism disruption to endothelial dysfunction: state-of-the-art. *Int. J. Mol. Sci.* 20:867. doi: 10.3390/ijms20040867

Feletou, M., Huang, Y., and Vanhoutte, P. M. (2011). Endothelium-mediated control of vascular tone: COX-1 and COX-2 products. *Br. J. Pharmacol.* 164, 894–912. doi: 10.1111/j.1476-5381.2011.01276.x

Ganguly, P., and Alam, S. F. (2015). Role of homocysteine in the development of cardiovascular disease. *Nutr. J.* 14:6.

Gao, Z., Zhang, H., Liu, J., Lau, C. W., Liu, P., Chen, Z. Y., et al. (2014). Cyclooxygenase-2-dependent oxidative stress mediates palmitate-induced impairment of endothelium-dependent relaxations in mouse arteries. *Biochem. Pharmacol.* 91, 474–482. doi: 10.1016/j.bcp.2014.08.009

Guo, D., Liang, S., Wang, S., Tang, C., Yao, B., Wan, W., et al. (2016). Role of epithelial Na+ channels in endothelial function. *J. Cell Sci.* 129, 290–297.

Jiang, X., Yang, F., Tan, H., Liao, D., Bryan, R. M. Jr., et al. (2005). Hyperhomocystinemia impairs endothelial function and eNOS activity via PKC activation. *Arterioscler. Thromb. Vasc. Biol.* 25, 2515–2521. doi: 10.1161/01.atv.0000189559.87328.e4

Kalra, D. K. (2004). Homocysteine and cardiovascular disease. *Curr. Atheroscler. Rep.* 6, 101–106.

Kamynina, E., and Staub, O. (2002). Concerted action of ENaC, Nedd4-2, and Sgk1 in transepithelial Na(+) transport. *Am. J. Physiol. Renal Physiol.* 283, F377–F387.

Kilkenny, C., Browne, W., Cuthill, I. C., Emerson, M., and Altman, D. G. (2010). Animal research: reporting in vivo experiments: the ARRIVE guidelines. *Br. J. Pharmacol.* 160, 1577–1579. doi: 10.1111/j.1476-5381.2010.00872.x

Lee, Y. S., Lee, S. J., Seo, K. W., Bae, J. U., Park, S. Y., and Kim, C. D. (2013). Homocysteine induces COX-2 expression in macrophages through ROS generated by NMDA receptor-calcium signaling pathways. *Free Radic. Res.* 47, 422–431. doi: 10.3109/10715762.2013.784965

Liang, C., Wang, Q. S., Yang, X., Niu, N., Hu, Q. Q., Zhang, B. L., et al. (2018). Oxidized low-density lipoprotein stimulates epithelial sodium channels in endothelial cells of mouse thoracic aorta. *Br. J. Pharmacol.* 175, 1318–1328. doi: 10.1111/bph.13853

Liu, H. B., Zhang, J., Sun, Y. Y., Li, X. Y., Jiang, S., Liu, M. Y., et al. (2015). Dietary salt regulates epithelial sodium channels in rat endothelial cells: adaptation of vasculature to salt. *Br. J. Pharmacol.* 172, 5634–5646. doi: 10.1111/bph.13185

Liu, X., Qin, Z., Liu, C., Song, M., Luo, X., Zhao, H., et al. (2019). Nox4 and soluble epoxide hydrolase synergistically mediate homocysteine-induced inflammation in vascular smooth muscle cells. *Vascul. Pharmacol.* 120:106544. doi: 10.1016/j.vph.2019.01.001

Ma, C. H., Chiua, Y. C., Wu, C. H., Jou, I. M., Tu, Y. K., Hung, C. H., et al. (2018). Homocysteine causes dysfunction of chondrocytes and oxidative stress through repression of SIRT1/AMPK pathway: a possible link between hyperhomocysteinemia and osteoarthritis. *Redox Biol.* 15, 504–512. doi: 10.1016/j.redox.2018.01.010

Mazza, A., Bossone, E., Mazza, F., and Distante, A. (2004). [Homocysteine and cardiovascular risk]. *Monaldi Arch. Chest Dis.* 62, 29–33.

McGrath, J. C., Drummond, G. B., Mclachlan, E. M., Kilkenny, C., and Wainwright, C. L. (2010). Guidelines for reporting experiments involving animals: the ARRIVE guidelines. *Br. J. Pharmacol.* 160, 1573–1576. doi: 10.1111/j.1476-5381.2010.00873.x

Niazi, Z. R., Silva, G. C., Ribeiro, T. P., Leon-Gonzalez, A. J., Kassem, M., Mirajkar, A., et al. (2017). EPA:DHA 6:1 prevents angiotensin II-induced hypertension and endothelial dysfunction in rats: role of NADPH oxidase- and COX-derived oxidative stress. *Hypertens Res.* 40, 966–975. doi: 10.1038/hr.2017.72

Niu, N., Yang, X., Zhang, B. L., Liang, C., Zhu, D., Wang, Q. S., et al. (2021). Endothelial epithelial sodium channel involves in high-fat diet-induced atherosclerosis in low-density lipoprotein receptor-deficient mice. *Biochim. Biophys. Acta Mol. Basis Dis.* 1867:165989. doi: 10.1016/j.bbadis.2020.165989

Rodrigo, R., Passalacqua, W., Araya, J., Orellana, M., and Rivera, G. (2003). Homocysteine and essential hypertension. *J. Clin. Pharmacol.* 43, 1299–1306. doi: 10.1177/0091270003258190

Romacho, T., Vallejo, S., Villalobos, L. A., Wronkowitz, N., Indrakusuma, I., Sell, H., et al. (2016). Soluble dipeptidyl peptidase-4 induces microvascular endothelial dysfunction through proteinase-activated receptor-2 and thromboxane A2 release. *J. Hypertens* 34, 869–876. doi: 10.1097/hjh.0000000000000886

Shatalin, K., Shatalina, E., Mironov, A., and Nudler, E. (2011). H2S: a universal defense against antibiotics in bacteria. *Science* 334, 986–990. doi: 10.1126/science.1209855

Shi, Y., Man, R. Y., and Vanhoutte, P. M. (2008). Two isoforms of cyclooxygenase contribute to augmented endothelium-dependent contractions in femoral arteries of 1-year-old rats. *Acta Pharmacol. Sin.* 29, 185–192. doi: 10.1111/j.1745-7254.2008.00749.x

Shi, Y., and Vanhoutte, P. M. (2008). Oxidative stress and COX cause hyperresponsiveness in vascular smooth muscle of the femoral artery from diabetic rats. *Br. J. Pharmacol.* 154, 639–651. doi: 10.1038/bjp.2008.110

Subedi, L., Lee, J. H., Yumnam, S., Ji, E., and Kim, S. Y. (2019). Anti-Inflammatory effect of sulforaphane on LPS-Activated microglia potentially through JNK/AP-1/NF-kappaB inhibition and Nrf2/HO-1 activation. *Cells* 8:194. doi: 10.3390/cells8020194

Tarjus, A., Maase, M., Jeggle, P., Martinez-Martinez, E., Fassot, C., Loufrani, L., et al. (2017). The endothelial alphaENaC contributes to vascular endothelial function in vivo. *PLoS One* 12:e0185319. doi: 10.1371/journal.pone.0185319

Tian, X. Y., Wong, W. T., Leung, F. P., Zhang, Y., Wang, Y. X., Lee, H. K., et al. (2012). Oxidative stress-dependent cyclooxygenase-2-derived prostaglandin f(2alpha) impairs endothelial function in renovascular hypertensive rats. *Antioxid. Redox. Signal.* 16, 363–373. doi: 10.1089/ars.2010.3874

Van Beusecum, J. P., Barbaro, N. R., Mcdowell, Z., Aden, L. A., Xiao, L., Pandey, A. K., et al. (2019). High salt activates CD11c(+) Antigen-Presenting cells via SGK (Serum Glucocorticoid Kinase) 1 to promote renal inflammation and salt-sensitive hypertension. *Hypertension* 74, 555–563. doi: 10.1161/hypertensionaha.119.12761

Vessieres, E., Belin, De Chantemele, E. J., Toutain, B., Guihot, A. L., Jardel, A., et al. (2010). Cyclooxygenase-2 inhibition restored endothelium-mediated relaxation in old obese zucker rat mesenteric arteries. *Front. Physiol.* 1:145. doi: 10.3389/fphys.2010.00145

Wang, Q. S., Liang, C., Niu, N., Yang, X., Chen, X., Song, B. L., et al. (2018a). Palmitate stimulates the epithelial sodium channel by elevating intracellular calcium, reactive oxygen species, and phosphoinositide 3-Kinase activity. *Oxid. Med. Cell Longev.* 2018:7560610.

Wang, Z. R., Liu, H. B., Sun, Y. Y., Hu, Q. Q., Li, Y. X., Zheng, W. W., et al. (2018b). Dietary salt blunts vasodilation by stimulating epithelial sodium channels in endothelial cells from salt-sensitive Dahl rats. *Br. J. Pharmacol.* 175, 1305–1317. doi: 10.1111/bph.13817

Wang, X. C., Sun, W. T., Yu, C. M., Pun, S. H., Underwood, M. J., He, G. W., et al. (2015). ER stress mediates homocysteine-induced endothelial dysfunction: modulation of IKCa and SKCa channels. *Atherosclerosis* 242, 191–198. doi: 10.1016/j.atherosclerosis.2015.07.021

Wong, W. T., Tian, X. Y., Chen, Y., Leung, F. P., Liu, L., Lee, H. K., et al. (2010). Bone morphogenic protein-4 impairs endothelial function through oxidative stress-dependent cyclooxygenase-2 upregulation: implications on hypertension. *Circ. Res.* 107, 984–991. doi: 10.1161/circresaha.110.222794

Wu, M. M., Liang, C., Yu, X. D., Song, B. L., Yue, Q., Zhai, Y. J., et al. (2019). Lovastatin attenuates hypertension induced by renal tubule-specific knockout of ATP-binding cassette transporter A1, by inhibiting epithelial sodium channels. *Br. J. Pharmacol.* 176, 3695–3711. doi: 10.1111/bph.14775

Wu, M. M., Lou, J., Song, B. L., Gong, Y. F., Li, Y. C., Yu, C. J., et al. (2014). Hypoxia augments the calcium-activated chloride current carried by anoctamin-1 in cardiac vascular endothelial cells of neonatal mice. *Br. J. Pharmacol.* 171, 3680–3692. doi: 10.1111/bph.12730

Wu, N., Siow, Y. L., and Karmin, O. (2009). Induction of hepatic cyclooxygenase-2 by hyperhomocysteinemia via nuclear factor-kappaB activation. *Am. J. Physiol. Regul. Integr. Comp. Physiol.* 297, R1086–R1094.

Yamahara, H., Kishimoto, N., Nakata, M., Okazaki, A., Kimura, T., Sonomura, K., et al. (2009). Direct aldosterone action as a profibrotic factor via ROS-mediated SGK1 in peritoneal fibroblasts. *Kidney Blood Press. Res.* 32, 185–193. doi: 10.1159/000225379

Yang, X., Niu, N., Liang, C., Wu, M. M., Tang, L. L., Wang, Q. S., et al. (2020). Stimulation of epithelial sodium channels in endothelial cells by bone morphogenetic protein-4 contributes to salt-sensitive hypertension in rats. *Oxid. Med. Cell Longev.* 2020:3921897.

Zeng, X., Dai, J., Remick, D. G., and Wang, X. (2003). Homocysteine mediated expression and secretion of monocyte chemoattractant protein-1 and interleukin-8 in human monocytes. *Circ. Res.* 93, 311–320. doi: 10.1161/01.res.0000087642.01082.e4

Zhang, D., Xie, X., Chen, Y., Hammock, B. D., Kong, W., and Zhu, Y. (2012). Homocysteine upregulates soluble epoxide hydrolase in vascular endothelium in vitro and in vivo. *Circ. Res.* 110, 808–817. doi: 10.1161/circresaha.111.259325

Zhang, H. S., Xiao, J. H., Cao, E. H., and Qin, J. F. (2005). Homocysteine inhibits store-mediated calcium entry in human endothelial cells: evidence for involvement of membrane potential and actin cytoskeleton. *Mol. Cell. Biochem.* 269, 37–47. doi: 10.1007/s11010-005-3168-z

Zhang, J., Chen, S., Liu, H., Zhang, B., Zhao, Y., Ma, K., et al. (2013). Hydrogen sulfide prevents hydrogen peroxide-induced activation of epithelial sodium channel through a PTEN/PI(3,4,5)P3 dependent pathway. *PLoS One* 8:e64304. doi: 10.1371/journal.pone.0064304

Zhang, M. Z., Wang, S., Wang, Y., Zhang, Y., Ming Hao, C., and Harris, R. C. (2018). Renal medullary interstitial COX-2 (Cyclooxygenase-2) is essential in preventing salt-sensitive hypertension and maintaining renal inner medulla/papilla structural integrity. *Hypertension* 72, 1172–1179. doi: 10.1161/hypertensionaha.118.11694

Zheng, W. W., Li, X. Y., Liu, H. B., Wang, Z. R., Hu, Q. Q., Li, Y. X., et al. (2016). AMP-Activated protein kinase attenuates high salt-induced activation of epithelial sodium channels (ENaC) in human umbilical vein endothelial cells. *Oxid. Med. Cell. Longev.* 2016:1531392.

Conflict of Interest: The authors declare that the research was conducted in the absence of any commercial or financial relationships that could be construed as a potential conflict of interest.

frontiers in Cell and Developmental Biology

ORIGINAL RESEARCH
published: 21 July 2021
doi: 10.3389/fcell.2021.687868

Statins Mitigate Stress-Related Vascular Aging and Atherosclerosis in *apoE*-Deficient Mice Fed High Fat-Diet: The Role of Glucagon-Like Peptide-1/Adiponectin Axis

Yanna Lei[1†], Qingsong Cui[1†], Guang Yang[2], Limei Piao[2], Aiko Inoue[3], Hongxian Wu[4], Xiang Li[1], Masafumi Kuzuya[3,5] and Xian Wu Cheng[1,3]**

[1] Department of Intensive Care Unit, Yanbian University Hospital, Yanjin, China, [2] Department of Cardiology and Hypertension, Yanbian University Hospital, Yanjin, China, [3] Institute of Innovation for Future Society, Nagoya University Graduate School of Medicine, Nagoya, Japan, [4] Department of Cardiology, Shanghai Institute of Cardiovascular Disease, Zhongshan Hospital, Fudan University, Shanghai, China, [5] Department of Community Healthcare & Geriatrics, Nagoya University Graduate School of Medicine, Nagoya, Japan

OPEN ACCESS

Edited by:
Xiang Cheng,
Huazhong University of Science and Technology, China

Reviewed by:
Shrivani Pirahas,
University of Calgary, Canada
Daiju Fukuda,
Tokushima University, Japan

***Correspondence:**
Xian Wu Cheng
chengxw0908@163.com
Xiang Li
zhongtian200330@163.com

† These authors have contributed equally to this work

Specialty section:
This article was submitted to Signaling, a section of the journal Frontiers in Cell and Developmental Biology

Received: 30 March 2021
Accepted: 04 June 2021
Published: 21 July 2021

Citation:
Lei Y, Cui Q, Yang G, Piao L, Inoue A, Wu H, Li X, Kuzuya M and Cheng XW (2021) Statins Mitigate Stress-Related Vascular Aging and Atherosclerosis in apoE-Deficient Mice Fed High Fat-Diet: The Role of Glucagon-Like Peptide-1/Adiponectin Axis. Front. Cell Dev. Biol. 9:687868. doi: 10.3389/fcell.2021.687868

Objectives: Exposure to chronic psychosocial stress is a risk factor for atherosclerotic cardiovascular diseases. Given that the 3-hydroxy-3-methylglutaryl-coenzyme reductase inhibitor statins prevent atherogenesis, we evaluated whether pitavastatin prevents chronic stress- and high fat diet-induced vascular senescence and atherogenesis in apolipoprotein *E*-deficient (*ApoE*$^{-/-}$) mice, with a special focus on glucagon-like peptide-1 (GLP-1)/adiponectin (APN) axis.

Methods and Results: 6-week-old *ApoE*$^{-/-}$ mice loaded a high-fat diet were randomly assigned into non-stress (n = 12) and stress (n = 13) groups for 12 weeks. Non-stress control mice were left undisturbed. Chronic stress accelerated high fat diet-induce arterial senescence and atherosclerotic plaque growth. The chronic stress lowered the levels of circulating GLP-1 as well as adipose and plasma APN. As compared with the stress alone mice, the pitavastatin-treated mice had reduced macrophage infiltration, elastin fragments, and increased plaque collagen volume, and lowered levels of osteopontin, toll-like receptor-2/-4, macrophage chemoattractant protein-1, C-X-C chemokine receptor-4, p47^{phox}, p47^{phox}, gp91^{phox}, cathepsins S, p16, and p21, mRNAs and/or proteins. Pitavastatin increased plasma GLP-1 and APN levels and suppressed matrix metalloproteinase-2/-9 gene expressions and activities in the aortas. Finally, the protective effect of pitavastatin was abrogated by APN blocking.

Conclusion: These findings suggested that the pitavastatin-mediated pleiotropic vasculoprotective effects are likely attributable, at least in part, to the elevation of GLP-1 and APN levels and the inhibition of diet-induced plaque inflammation, oxidative stress, and proteolysis in *ApoE*$^{-/-}$ mice received chronic stress conditions.

Keywords: chronic stress, statins, atherosclerosis, inflammation, adiponectin

INTRODUCTION

Accumulating evidence indicated that chronic stress is involved in metabolic and inflammatory cardiovascular disorders (Bernberg et al., 2012; Heidt et al., 2014). The mechanisms underlying chronic stress-related diseases have thus become a research focus. At present, most of the evidence suggests that the pathogenic effect of chronic stress is exerted mainly on the hypothalamic-pituitary-adrenal axis and/or the body's sympathetic nervous system, followed by the induction of disorders such as atherosclerosis (Barik et al., 2013; Cox et al., 2014; Heidt et al., 2014). Recently we demonstrated that chronic stress can prompt the formation of atherosclerosis by accelerating inflammation and oxidative stress (Lei et al., 2017; Yang et al., 2017). Despite the large number of studies that have been performed, the precise mechanisms are not yet clear, and effective strategies to cope with chronic stress-related diseases remain to be established.

Statins are traditional anti-atherosclerosis drugs, although they are normally used against low-density lipoprotein cholesterol (LDL-C); statins have also been shown to have an anti-atherosclerotic effect partly by inhibiting inflammation and oxidative stress (Lin et al., 2015). Statins have been widely adopted as a clinical atherosclerosis treatment, but the question of whether statins also have a beneficial effect on chronic stress-related atherosclerosis has not been resolved. We conducted the present study to explore the potential mechanisms involved in chronic stress-related atherosclerosis formation, focusing on inflammation and oxidative stress. We also investigated whether the traditional anti-atherosclerosis drug pitavastatin can ameliorate this stress-related atherosclerosis and its mechanisms, with a special focus on glucagon-like peptide-1 (GLP-1)/adiponectin (APN) axis.

MATERIALS AND METHODS

Animals

Four-week-old male *ApoE*$^{-/-}$ mice (21–24 g body weight; KOR/StmSlc-Apoe^{shl}, BALB/c background) were purchased from Chubu Science and Material Science Company (SLC, Hamamatsu, Japan). For their adaptation to the new environment, the mice were all fed a standard diet for 2 weeks and housed two per cage under standard conditions (50 ± 5% humidity, 23 ± 1°C). The animal experimental protocols were approved by the Institutional Animal Care and Use Committee of Nagoya University (Protocol No. 27304) and of Yanbian University (Protocol No. 2018-10) and performed according to the Guide for the Care and Use of Laboratory Animals published by the U.S. National Institutes of Health.

Mouse Immobilized Stress Protocol and Tissue Correction

The 6-week-old male *ApoE*$^{-/-}$ mice (n = 25) were randomly assigned into the following two groups for the first phase of the experiment: The control group (HF-C, n = 12) received a high-fat (HF) diet (21.00% fat and 0.15% cholesterol) only, and the stress group (HF-S, n = 13) received the same HF diet and were subjected to restraint stress (12 weeks) (Lei et al., 2017). For the second phase of the experiment, the *ApoE*$^{-/-}$ mice fed a HF diet were divided to another two groups: Stress 2 group (Stress): the mice subjected to restraint stress for 12 weeks as mentioned above, and the stress + pitavastatin group (S-Pis): Except for HF diet and restraint stress (12 weeks), the mice were treated with pitavastatin (1 mg/kg/d). The pitavastatin used in this experiment was provided by Kowa Pharmaceutical Co. Ltd. (Nagoya, Japan). For the APN deletion examinations, the mice (n = 10) fed with HF-diet were divided to one of two groups and gave pitavastatin + control rabbit IgG (Control, 450 μg/kg/d, ab27472, Cambridge, United Kingdom) or pitavastatin plus neutralizing rabbit APN antibody (S-NAPN, 450 μg/kg/d, ab3455) given by subcutaneous injection every week under chronic stress conditions for 8 weeks.

After euthanasia of the *ApoE*$^{-/-}$ mice by means of an overdose of pentobarbital (50 mg/kg; Dainippon Pharmaceutical, Osaka, Japan) at the end of stress/no stress treatment, blood samples were collected just before perfusion into syringes containing heparin. After perfusion with 0.01 M phosphate-buffered saline (PBS, pH 7.4), the aorta tissues were collected for biological analyses and histological characterization analyses.

Histological Analysis

The cross-sections of the aortas were examined as we described (Cheng et al., 2011). The heart was sliced in a plane between the lower tips of the left and right atria, and the upper portion of the heart was isolated. The hearts were kept in 4% formalin. Serial sections (3-μm thick at 15-μm intervals) were isolated on slides for morphological analysis and immunostaining.

Quantitative Real-Time PCR

Total RNA was extracted from the aortic tissues and preadipocytes with the use of the RNeasy Fibrous Tissue MiNi-Kit (Qiagen, Hilden, Germany) and was subjected to reverse transcription following the manufacturer's instructions. The cDNA was generated by the SuperScript III CellsDirect cDNA Synthesis kit (Invitrogen, Carlsbad, CA, United States). A polymerase chain reaction (PCR) was done by the ABI 7300 Real-time PCR System (Applied Biosystems, Foster City, CA, United States). The expression of glyceraldehyde 3-phosphate dehydrogenase (GAPDH) was used as an internal standard for each targeted gene levels. The primer sequences for the macrophage chemoattractant protein-1 (MCP-1), toll-like receptor-2/-4 (TLR-2/-4), p47^{phox}, p47^{phox}, gp91^{phox}, cathepsins S (Cat S), matrix metalloproteinase-2/-9, (MMP-2/-9), and C-X-C chemokine receptor-4 (CXCR-4) are listed in **Table 1**.

Immunohistochemistry

The 3-μm-thick paraffin sections of aortas were H&E stained as we described (Cheng et al., 2011). Corresponding slides were immunostained with mouse antibodies against macrophages (CD68; 1:100, Chemicon, Billerica, MA, United States), mouse antibodies against osteopontin (1:125, Sigma-Aldrich, St. Louis, MO, United States), rabbit antibodies against alpha-smooth muscle actin (α-SMA; 1:100, Neo Markers, Fremont, CA, United States). Elastin and collagen contents were quantified using the Elastica van Gieson (EVG)-stained and picrosirius

TABLE 1 | Primer sequences for mice used for quantitative real-time PCR.

Genes name	Forward primers	Reverse primers
MMP-2	CCCCATGAAGCCTTGTTTACC	TTGTAGGAGGTGCC CTGGAA
MMP-9	CCAGACGCTCTTCGA GAACC	GTTATAGAAGTGGC GGTTGT
Cat S	GTGGCCACTAAAGG GCCTG	ACCGCTTTTGTAGAAGAAGA AGGAG
gp 91	ACTTTCCATAAGATGGTAGC TTGG	GCATTCACACACCAC TCAACG
MCP-1	GCCCCACTCACCTGC TGCTACT	CCTGCTGCTGGTGATCC TCTTGT
TLR-2	AAGAAGCTGGCATTC CGAGGC	CGTCTGACTCCGAGGG GTTGA
TLR-4	AGTGGGTCAAGGAACA GAAGCA	CTTTACCAGCTCATTT CTCACC
CXCR- 4	CCACCCAGGACAGTGTGACTCT AA	GATGGGATTTCTGTAT GAGGATT
p47^{phox}	CTGAGGGTGAAGCCA TTGAGG	GCCGGTGATATC CCCTTTCC
p67^{phox}	AACTACCTGGAGCC AGTTGAG	AATTAGGAGGTGGTGGAAT ATCGG

red (PSR)-stained positive areas. Images of sections stained for macrophages, elastin, osteopontin, α-SMC, and collagen were quantified with ImagePro software (BZ9000 Analysis, Keyence, Japan). Six cross-sections of each aortas were calculated and averaged for each mouse. The results are expressed as the percentage of intima area that contained the lesion.

Oil Red O Staining and Senescence-Associated β-Galactosidase (β-Gal) Staining

The whole aortas from mice of each group were selected. We first removed the extra fatty and adventitia tissue from the vessels using forceps and scissors. The vessels were then incised longitudinally along the artery and fixed in formalin overnight for oil red O staining, as described in our previous study (Lei et al., 2017). Images of each vessel were obtained, and the extent of atherosclerosis was determined with the ImagePro software. β-Gal staining and quantitative analyses were made as described with our previous study (Lei et al., 2017).

ELISA and Biochemical Assays

According to manufacturers' instructions, the plasma GLP-1 and adiponectin (APN) levels were evaluated using the commercially available ELISA kits (GLP-1, Cat. EZGLP1T-36K; EMD Millipore, Billerica, MA, United States; APN, Cat. MRP300; R&D Systems, Minneapolis, MN, United States). The levels of the mouse plasma non-esterified fatty acid (NEFA), high-density lipoprotein cholesterol (HDL-C), low-density lipoprotein cholesterol (LDL-C), glucose, triglyceride (TG), creatinine, and blood urea nitrogen (BUN) were evaluated at a commercial laboratory (SRL, Tokyo).

Gelatin Zymography

For gelatin zymography, 20 μg of aortic protein extract was mixed with sodium dodecyl sulfate (SDS) sample buffer without reducing agent and loaded onto a 10% SDS-polyacrylamide gel containing gelatin (1 mg/mL) containing 1 mg/mL gelatin as described as described in Lei et al. (2017). Following staining and destaining with the related buffers, the areas of gelatinolytic activity were visualized under a light microscope and the digestion bands were measured by an image analyzer software program (NIH Image 1.62).

Western Blot Analysis

The total aortic protein was extracted with lysis buffer. The DC protein assay kit (Bio-Rad Laboratories, Hercules, CA, United States) was applied to measure the concentration of each sample. The protein abundance was detected with antibodies against Sirt-1 (cat. no. 2028, Cell Signaling Technology, Danvers, MA, United States), p16^{INK4A} (CDKN2A, cat. no. 10883-1-AP, Proteintech Group Inc., Rosemont, IL, United States), adiponectin receptor-1 (AdipR-1, ab70362), β-actin monoclonal antibody (1: 1000, AC-15, Sigma-Aldrich), and p21 (ab109199, both from Abcam, Cambridge, United Kingdom). The membranes then were incubated with the secondary antibodies. The protein contents calculated from western blots were normalized by loading β -actin.

Preadipocyte Isolation and Culture

Inguinal adipose tissues of the non-stress and stressed mice-derived immature adipocytes were prepared as described previously (Hao et al., 2014). The preadipocytes were cultured in Dulbecco's modified Eagle's medium (DMEM)/10% fetal bovine serum (FBS), antibiotics (penicillin/streptomycin), and 4.5 g/l glucose in a humidified atmosphere (95% air and 5% CO_2) at 37°C. Following culturing in serum-free medium for 12 h, the cells were applied to a biological assay.

Statistical Analysis

The data are expressed as the mean ± standard error of the mean (SEM). We used Student's *t*-test for comparisons of two groups, and we conducted a one-way analysis of variance (ANOVA) for comparisons of three or more groups followed by Tukey's *post hoc* test. Probability (p)-values < 0.05 were considered significant. All of the examinations were performed by two observers blinded to the treatment of the animals.

RESULTS

Effects of Chronic Stress on Body Weight, Plasma Lipid Profile, and Plasma GLP-1/APN Axis

The mice were weighed weekly and as expected, chronic stress significantly reduced the body weights of the stressed mice in a time-dependent manner compared to the non-stressed mice (**Figure 1A**) and also reduced the weight of subcutaneous and inguinal fat (**Figures 1C,D**). As shown in **Table 2**, except for

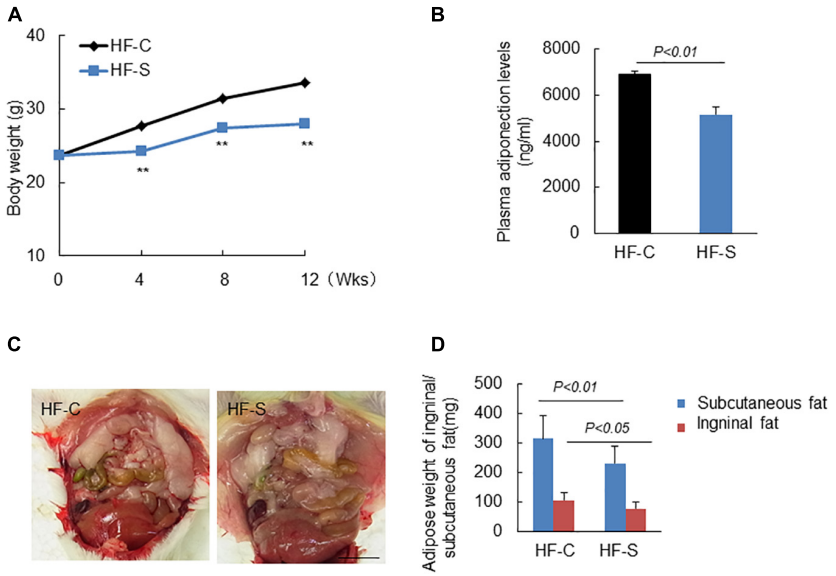

FIGURE 1 | Body weight (BW), adipose weight and adiponectin levels in the two experimental groups during the experimental period. **(A)** Chronic stress reduced BW in a time dependent manner. **(B)** Chronic stress decreased serum APN levels. **(C,D)** Representative images show the inguinal fat, and chronic stress reduced the weight of subcutaneous and inguinal fat. Data are presented as means ± SEM (n = 6–8). $P < 0.05$ was considered statistically significant by Student's un-paired t-test. Scale bars: 200 μm **(D).**

TABLE 2 | Levels of lipids, GLP-1 activity, and other biochemical parameters.

Parameter	HF-C	HF-S
TG (mg/dL)	188.0 ± 4.7	113.5 ± 11.6*
LDL (mg/dL)	224.0 ± 18.4	228.5 ± 20.4
HDL (mg/dL)	28.0 ± 5.6	26.5 ± 4.8
NEFA (μEQ/L)	882.5 ± 26.3	793.5 ± 21.3
Glucose (mg/dL)	172.0 ± 16.4	161.5 ± 14.7
BUN (mg/dL)	18.0 ± 2.7	18.0 ± 3.1
CREA (mg/dL)	0.5 ± 0.0	0.5 ± 0.0
GLP-1 (pM)	15.2 ± 0.9	11.7 ± 1.2**

*TG, triglyceride; LDL, high-density lipoprotein; HDL, high-density lipoprotein; BUN, blood urine nitrogen; CREA, creatinine; NEFA, non-esterified fatty acid; GLP-1, glucagon-like peptide-1. All results are presented as means ± SEM, *P < 0.05, **P < 0.01 vs. corresponding controls by Student's un-paired t-test.*

TG levels, chronic stress had no effect on other plasma lipid profile levels or the blood glucose and BUN, CREA levels. However, the plasma ANP and GLP-1 levels of the stressed mice were significantly decreased as compared to the non-stress mice (APN: 6904.4 ± 124.3 ng/ml vs. 5167.1 ± 301.7 ng/ml; GLP-1: 15.2 ± 0.9pM vs. 11.7 ± 1.2pM, respectively; $p < 0.01$, **Figure 1B** and **Table 2**).

Chronic Stress Accelerated the Diet-Induced Lipid Accumulation, Inflammatory Response and Oxidative Stress of Atherosclerotic Lesions

As we expected, the chronic stress significantly increased the atherosclerotic lesion area in the aortic root compared to the control values (atherosclerotic area: 521.3 ± 57.6 × 10^3 μm^2 vs. 285.1 ± 36.2% × 10^3 μm^2, $p < 0.01$, **Figures 2A,B**), indicating that the chronic stress promoted atherosclerotic plaque expansion. Lipid deposition is known to be an initial process of atherosclerosis formation and development. Herein, we used oil red O staining to evaluate the lipid content of the plaques, which represents the severity of atherosclerosis. As shown in **Figures 2A,C**, the lipid accumulation in the atherosclerotic plaques was more severe in the stress groups compared to the controls. Clinically, after the lipid accumulation, the inflammation response and oxidative stress started to play critical roles in the development of atherosclerotic lesions. As shown in **Figures 2A,D,E**, chronic stress significantly increased the accumulation of macrophages (CD68: 35.5 ± 2.1% vs. 24.7 ± 0.8%, $p < 0.01$) and the expression of osteopontin proteins (osteopontin: 31.1 ± 0.8% vs. 24.2 ± 0.7%, $p < 0.01$) in the atherosclerotic plaques. The results of the RT-PCR confirmed that the expressions of the oxidative stress (p67^{phox}, gp91^{phox}, and p47^{phox}), inflammation (MCP-1, TLR-2, TLR-4, and CXCR-4), and proteolysis (MMP-2, MMP-9, and Cat S)-related genes were markedly elevated in the aortas of the stressed mice compared to the control aortas (**Table 3**).

Chronic Stress Prompted Vascular Senescence

Endothelial dysfunction is a common pathological phenomenon for many cardiovascular diseases, and it often occurs before atherosclerosis. In this study, the senescence-associated β-gal staining showed that the positive staining area in the stressed mice was larger than that of the controls (**Figures 3A,B**), indicating that the chronic stress resulted in endothelial cell dysfunction.

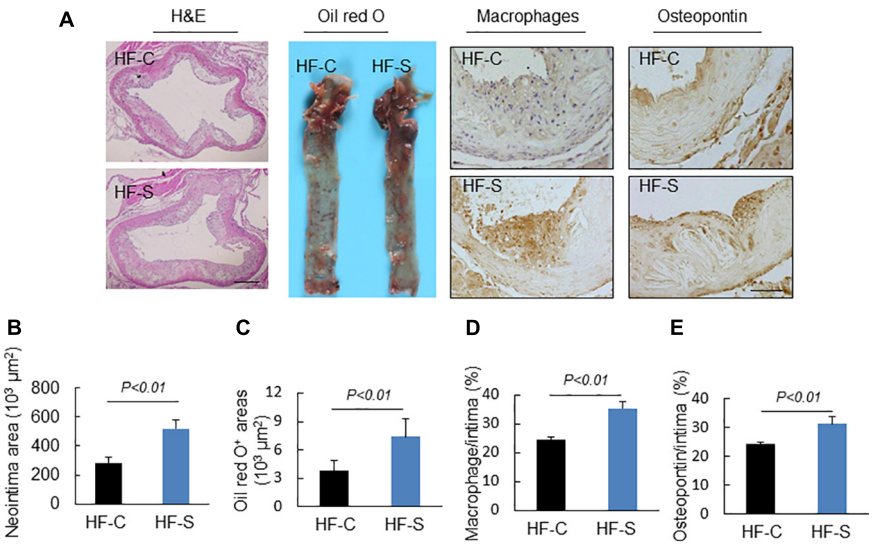

FIGURE 2 | Histological characterization of atherogenic plaques in aortic roots of two experimental groups (high-fat diet alone, HF-C; high-fat diet plus stress, HF-S). **(A)** Representative images applied to evaluate the neointimal hyperplasia, content of lipid-rich plaques, macrophages accumulation and osteopontin expression. **(B–E)** The areas for H&E, Oil red O^+ and positive areas in the neointimas for osteopontin and CD68 were quantified for each section. Results are presented as neointima area, the ratio of Oil red O-stained area to the total aortic root, the ratio of the positively stained area (CD68, osteopontin) to the neointimal area in the atherosclerotic lesions. Values are presented as means ± SEM (n = 6–7). $p < 0.01$ vs. HF-C by Student's t-test. Scale bars: 50 μm.

TABLE 3 | Real-time PCR analysis of the targeted genes in the aortic roots and APN in subcutaneous fat of both experimental group mice.

Parameter	HF-C	HF-S
TLR-2	34.2 ± 0.9	41.5 ± 1.3**
TLR-4	37.8 ± 1.9	49.7 ± 2.1**
CXCR-4	71.6 ± 3.6	96.0 ± 3.3**
MCP-1	9.8 ± 0.5	15.2 ± 0.9**
gp 91^{phox}	19.2 ± 0.8	26.3 ± 0.6**
$p47^{phox}$	29.9 ± 1.5	35.8 ± 4.4*
$P67^{phox}$	17.1 ± 0.5	22.7 ± 1.0**
Cat S	19.6 ± 1.5	29.3 ± 1.1**
MMP-2	26.7 ± 3.4	31.0 ± 3.5**
MMP-9	22.6 ± 3.1	46.0 ± 3.2**
APN	107.4 ± 22.8	69.2 ± 19.2**

*TLR-2, toll-like receptor 2; CXCR-4, C-X-C chemokine receptor-4; MMP-2, matrix metalloproteinase-2; Cat S, cathepsin S; MCP-1, monocyte chemotaxis protein-1; APN, adiponectin. All results are presented as means ± SEM, *P < 0.05, **P < 0.01 vs. corresponding controls by Student's un-paired t-test.*

Chronic Stress Changed the Atherosclerotic Plaque Stability

Extracellular matrix (ECM) remodeling is responsible for the stability of atherosclerotic plaques, including the synthesis and degradation of collagen, elastin, and other glycoproteins. In this study, chronic stress significantly reduced the atherosclerotic plaques' contents of collagen and α-SMC (the main source of collagen) compared to the control group (α-SMC: 26.6 ± 0.5% vs. 23.9 ± 0.6%, collagen: 31.6 ± 1.3% vs. 19.2 ± 1.9%, respectively; $p < 0.05$, $p < 0.01$; **Figures 3A,C,D**). The results of the EVG staining demonstrated that the chronic stress significantly destroyed the integrity of elastin in the media layer compared to the control group (number of breaks: 8.2 ± 0.3 vs. 5.7 ± 0.2, $p < 0.01$, **Figures 3A,E**).

Pitavastatin Mitigated the Chronic Stress-Related Lipid Accumulation, Inflammatory Response, Oxidative Stress, and Plasma GLP-1/APN Axis

At the second phase of the experiment, we evaluated the effects of a statin, i.e., pitavastatin, on stress-related atherosclerosis. Pitavastatin significantly reduced the levels of LDL-C without changing the levels of the other parameters (TG, HDL, NEFA, glucose, BUN, CREA, and body weight) (**Table 4**). More importantly, we observed that pitavastatin significantly improved plasma adiponectin (APN: 7904.4 ± 664.1 ng/ml vs. 4980.3 ± 363.7 ng/ml; $p < 0.01$) and GLP-1 (GLP-1: 18.8 ± 1.2Pm vs. 13.9 ± 1.4pM, $p < 0.01$) levels of the stressed mice as compared to control mice (**Table 4**).

Pitavastatin treatment also reduced atherosclerotic area compared to the stress alone group (atherosclerotic area: 496.9 ± 28.1 × 10^3μm^2 vs. 321.2 ± 41.9 × 10^3μm^2; $p < 0.01$; **Figures 4A,B**). Compared to the non-treated stress group, the group of stressed mice treated with pitavastatin exhibited significantly reduced lipid deposition, macrophage accumulation, and osteopontin expression in the stress-related atherosclerotic lesions (**Figures 4A,C–E**). The mRNA expressions of $p67^{phox}$, $p47^{phox}$, $gp91^{phox}$, CXCR4, MCP-1, TLR-4, and TLR-2 were inhibited (**Table 5**).

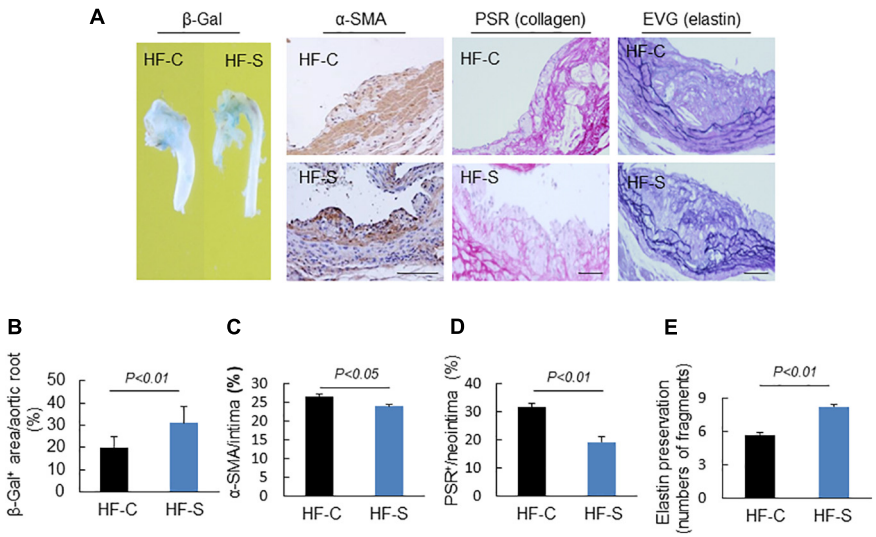

FIGURE 3 | Morphological characterization of the plaques in aortic roots of two experimental groups. **(A)** Representative images applied to evaluate vascular senescence, α-SMCs, collagen, and elastin disruption. **(B–E)** The areas for β-Gal$^+$, α-SMCs, PSR$^+$ staining, and the elastic disruption degree in atherosclerotic lesions were calculated for each section. Results are presented as the ratio of β-Gal$^+$ area to the total aortic root, the ratio of the positively stained area (α-SMCs, PSR$^+$) to the neointimal area in the atherosclerotic lesions, and the elastic broken numbers in the atherosclerotic lesions. Values are presented as means ± SEM (n = 6–7). $p < 0.01$ vs. HF-C by Student's t-test. Scale bars: 50 μm.

TABLE 4 | Levels of lipids activity and other biochemical parameters.

Parameter	Stress	Pitavastatin
TG (mg/dL)	111.0 ± 10.4	108.5 ± 11.2
LDL (mg/dL)	213.5 ± 19.6	123.5 ± 13.2*
HDL (mg/dL)	24.5 ± 3.9	26.4 ± 3.7
NEFA (μEQ/L)	773.5 ± 20.8	712.2 ± 18.4
Glucose (mg/dL)	159.5 ± 13.9	158.6 ± 15.6
BUN (mg/dL)	19.0 ± 3.8	21.5 ± 5.1
CREA (mg/dL)	0.5 ± 0.0	0.5 ± 0.0
GLP-1 (pM)	13.9 ± 1.4	18.8 ± 1.2**
APN(ng/ml)	4980.3 ± 363.7	7904.4 ± 664.1**

*Abbreviations are in **Table 2**. APN, adiponectin. Data are presented as means ± SEM, *P < 0.05, ** P < 0.01 vs. corresponding controls by Student's un-paired t-test.*

Pitavastatin Alleviated Vascular Aging and Atherosclerotic Plaque Instability

The vascular aging was clearly alleviated by the pitavastatin treatment, as shown in **Figures 5A,B**. In addition, the pitavastatin treatment increased the collagen and α-SMC contents of the atherosclerotic plaques and preserved the continuity of the elastic lamina (**Figures 5A,C–E**). To explore the cause of the destruction of the ECM, we determined the expressions and activities of ECM-degrading enzymes. The RT-PCR results revealed that the aortas of S-Pis mice had decreased levels of MMP-2, MMP-9, and Cat S mRNAs (**Table 5**). In addition, the gelatinolytic activity of MMP-9 and MMP-2 was also inhibited by pitavastatin treatment (**Figures 6A,B**).

It is known that APN is produced mainly by adipose tissue, and we therefore investigated the mRNA expression in the subcutaneous fat of the three groups of mice. As shown in **Tables 3**, **5**, the chronic stress significantly inhibited the APN expression of the subcutaneous fat of the mice, and the pitavastatin treatment ameliorated the expression of APN. We also observed that the pitavastatin treatment mitigated the alterations in the senescence-related proteins (p16, p21, Sirt-1, and AdipR-1) (**Figures 6C,D**). We used an APN neutralizing antibody to test the anti-atherosclerotic effect of pitavastatin in the stressed mice, and the results showed that this antibody abolished the protective effects of pitavastatin in stress-related atherogenesis (**Table 6**). *In vitro*, exenatide as a GPL-1 receptor agonist increased APN gene expression in cultured immature adipocytes in a dose-dependent manner (**Figure 6E**).

DISCUSSION

In addition to conventional cardiovascular risk factors such as high cholesterol, hypertension, and diabetes mellitus, chronic stress is now considered a risk factor for cardiovascular diseases. Explorations of the underlying mechanisms and the identification of pharmacotherapeutic targets for clinical use are thus of great significance. Our present study's findings may contribute to this field, as we observed the following: (a) Chronic stress significantly enhanced the inflammation action and oxidative stress process in *ApoE*$^{-/-}$ mice fed a high-fat diet, and it increased endothelial senescence, which promoted the development of atherosclerosis. (b) Chronic stress favored the formation of vulnerable plaques by changing the components of the ECM, and it decreased the plaques' α-SMC content. (c) As expected, the traditional anti-atherosclerosis drug pitavastatin alleviated the progression of atherosclerosis and promoted the

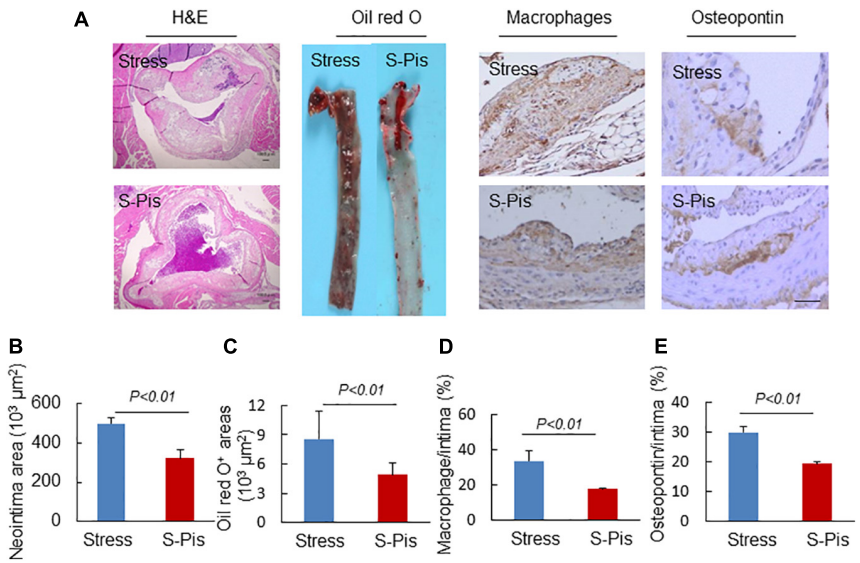

FIGURE 4 | Morphological characterization of atherosclerotic plaques in aortic roots of the stress-alone and stress plus pitavastatin (S-Pis) groups. **(A)** Representative images used to assess the neointimal hyperplasia, content of lipid-rich plaques, macrophages accumulation and osteopontin expression. **(B–E)** The areas for H&E, Oil red O^+, and positive areas in atherosclerotic neointimas for CD68 and osteopontin were calculated for each section. Results are expressed as neointima area, the ratio of Oil red O-stained area to the total aortic root, the ratio of the positively stained area (CD68, osteopontin) to the neointimal area in the atherosclerotic lesions. Values are presented as means ± SEM (n = 6–7). $p < 0.01$ vs. Stress group by Student's t-test. Scale bars: 50 μm.

TABLE 5 | Real-time PCR analysis of the targeted genes in the aortic roots and APN in subcutaneous fat of both experimental group mice.

Parameter	Stress	Pitavastatin
TLR-2	40.8 ± 2.6	22.3 ± 1.7**
TLR-4	46.7 ± 2.2	19.7 ± 0.9**
CXCR-4	87.0 ± 5.7	54.2 ± 4.0**
gp 91^{phox}	27.1 ± 1.8	16.8 ± 0.9**
p47^{phox}	32.7 ± 2.1	20.0 ± 1.1**
P67^{phox}	23.6 ± 1.3	15.2 ± 0.8**
Cat S	26.9 ± 2.3	11.3 ± 1.1**
MMP-2	27.9 ± 3.6	24.1 ± 6.5*
MMP-9	39.8 ± 3.3	21.4 ± 0.8**
APN	76.4 ± 11.3	125.3 ± 27.4**

*Abbreviations are in **Table 3**. Data are presented as means ± SEM, *P < 0.05, **P < 0.01 vs. corresponding controls by Student's un-paired t-test.*

stability of atherosclerotic plaques by ameliorating the vascular aging, inhibiting inflammation action and oxidative stress, and this effect may be exerted partly through the modulation of GLP-1/APN axis.

Atherosclerosis as an inflammatory disease and a great deal of evidence has confirmed the fundamental role of inflammation in the process of atherosclerosis (Zhu et al., 2018). The results of the present study demonstrated that chronic (12-week) stress significantly increased the accumulation of macrophages and the expression of osteopontin proteins of atherosclerotic plaques; the stress also increased the mRNA levels of TLR-2, TLR-4, MCP-1, and CXCR-4 in the mouse aorta. The inflammatory effects on atherosclerosis of these parameters have been fully proved by previous studies (Chiba et al., 2002; Cole et al., 2010; Cheng et al., 2011). Coincidentally, it was reported that statin treatment of $ApoE^{-/-}$ mice inhibited an acute stress-related inflammation of atherosclerotic plaques (Janssen et al., 2015). In agreement with several previous studies (Isingrini et al., 2011; Hayashi et al., 2014; Heidt et al., 2014), the present data indicate that chronic stress accelerated the process of atherosclerosis by enhancing inflammatory action.

The negative effects of oxidative stress in atherosclerosis have been described, including endothelial cell dysfunction, foam cell formation, plaque disruption and their interaction with inflammation, all of which contribute to atherosclerosis (Linton et al., 2000; Lankin and Tikhaze, 2017). Our present findings revealed that chronic stress significantly increased the mRNA expressions of gp91^{phox}, p47^{phox}, and p67^{phox} in the aorta tissue. p67^{phox}, p47^{phox}, and gp91^{phox} are the components of NAD(P)H oxidases, which are the main source of reactive oxygen species (ROS) (Cai et al., 2003). It has been demonstrated that gp91^{phox} and p47^{phox} play critical roles in the development of atherosclerosis (Barry-Lane et al., 2001; Sorescu et al., 2002). In our present investigation, β-gal galactosidase staining revealed that chronic stress promoted the senescence of endothelial cells. Based on our present data, we speculate that chronic stress affects atherosclerosis in part by increasing the production of oxidative stress.

Plaque rupture is the leading cause of acute cardiovascular events, and such ruptures are always due to the formation of vulnerable plaques. An excessive inflammatory response, oxidative stress, and degradation of the ECM are all responsible

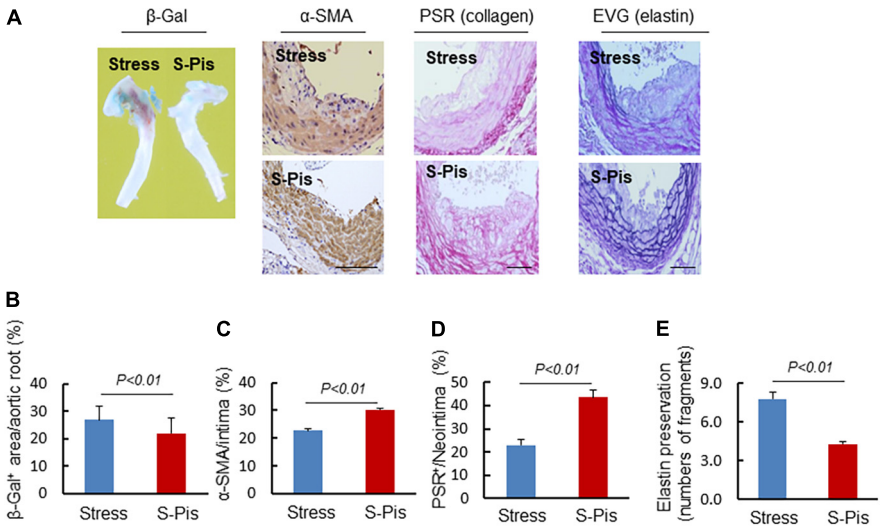

FIGURE 5 | Histological characterization of atherosclerotic plaques in aortic roots of the Stress and S-Pis groups. **(A)** Representative images were used to assess vascular senescence, α-SMCs, collagen and elastin disruption, and. **(B–E)** The areas for β-Gal$^+$, α-SMCs, PSR$^+$ staining and the elastic disruption degree in atherosclerotic lesions were quantified for each section. Results are expressed as the ratio of β-Gal$^+$ area to the total aortic root, the ratio of the positively stained area (α-SMCs, PSR$^+$) to the neointimal area in the atherosclerotic lesions, and the elastic broken numbers in the atherosclerotic lesions. Values are presented as means ± SEM (n = 6–7). $p < 0.01$ vs. Stress group by Student's t-test. Scale bars: 50 μm.

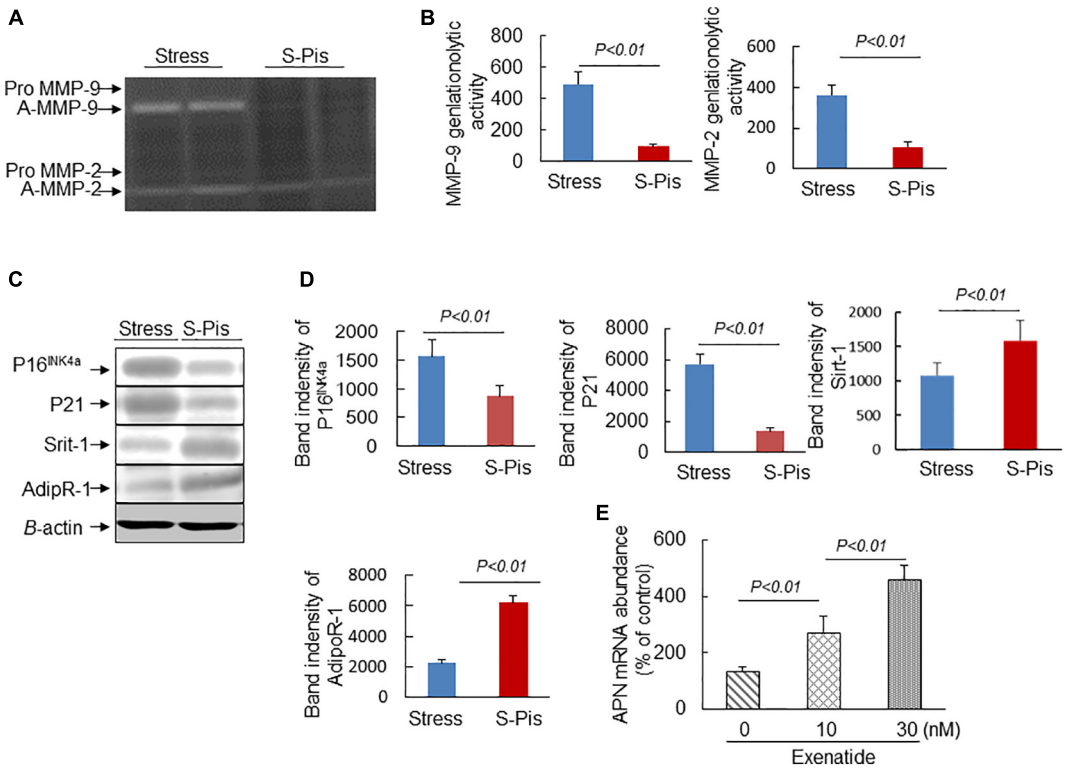

FIGURE 6 | Pitavastatin mitigated MMP-2/-9 expression/activity and targeted protein expressions in the aortic roots. **(A,B)** Representative gelatin zymography images and quantitative data for MMP-9 and MMP-2 activities. **(C,D)** Representative Western blot images and quantitative data show the protein expressions of P16^{INK4a}, P21, Sirt-1, and Adip R-1. **(E)** Exenatide elevated APN gene expression in the stressed mouse inguinal adipose tissue-derived immature adipocytes. Values are presented as means ± SEM (n = 3–6). $p < 0.05$, $p < 0.01$ vs. Stress group by Student's t-test and one-way ANOVA followed by Tukey *post hoc* tests.

TABLE 6 | Histological characterization of atherosclerotic lesions in the aortic roots of both experimental group mice.

Parameter (Aortic root, *n* = 6)	S-Pis-C	S-Pis-NAPN
Intima ($\times 10^3/\mu m^2$)	308.4 ± 19.3	335.1 ± 4.2*
Media ($\times 10^3/\mu m^2$)	201.2 ± 26.0	219.3 ± 17.1
Intima/media ratio	1.6 ± 0.4	1.8 ± 0.6*

*The ratio of intima to media was expressed as the ratio of intimal to media area in lesional cross-sections of heart aortic roots of HF-diet loaded stressed mice received pitavastatin (1mg/kg/d) plus rabbit IgG (Control, 450 μg/kg/d, S-Pis-C) or rabbit neutralizing APN antibody (450 μg/kg/d, S-Pis-NAPN). Data are presented as means ± SEM, *P < 0.05 was considered statistically significant.*

for the formation of vulnerable plaques (Quesada et al., 2015; Ruddy et al., 2016; Morariu et al., 2019). As mentioned before, chronic stress promoted the progression of atherosclerosis in a mouse model by enhancing inflammation and oxidative stress, and the enhanced inflammation and oxidative stress can also change the characteristics of atherosclerotic plaques and promote ruptures. We also observed that chronic stress markedly decreased the atherosclerotic plaques' collagen and α-SMC contents. The elastin integrity of the elastic laminae was destroyed under the condition of chronic stress, and it is known that the elastin, collagen and α-SMC contents are responsible for the stability of atherosclerotic plaques (Kumar et al., 2016; Yurdagul et al., 2016). Our results therefore indicate that the chronic stress changed the properties of the plaques, inducing the formation of vulnerable plaques.

Regarding the underlying mechanisms, we found that the chronic stress promoted the expressions of collagen-degrading enzymes (i.e., MMP-2, MMP-9, and Cat S) and also increased the activity of MMP-2 and MMP-9. The main function of members of the MMP (matrix metalloproteinase) family is to degrade and deposit structural proteins within the ECM, which would affect the plaque stability (Amin et al., 2016). Similarly to the MMP family, the cysteine proteases (which have collagenolytic and elastolytic activities) also involve in ECM degradation in the process of atherosclerosis—especially Cat K and Cat S (Sukhova et al., 2003; Lutgens et al., 2006). In the present study we noted that not only the expressions of MMPs and Cats but also the activities of MMP-2 and MMP-9 were significantly increased by chronic stress, suggesting that chronic stress changed the properties of atherosclerotic plaques via ECM-degrading enzymes.

The anti-atherosclerotic effects of statins have been well confirmed by basic research and in clinical practice. In addition to statins' ability to reduce LDL-C levels, it has been demonstrated that statins exert other anti-atherosclerotic effects, including anti-inflammation, improving endothelial function, and reducing the production of ROS (Jarvisalo et al., 1999; Ascer et al., 2004; Ekstrand et al., 2015). The present study is the first to investigate the anti-inflammation and anti-oxidative stress effects of statins in stress-related atherosclerosis. Pitavastatin reduced the LDL-C levels in stressed $ApoE^{-/-}$ mice and we also observed that: (a) Pitavastatin decreased the inflammatory response of the atherosclerosis by reducing the accumulation of macrophages and the expression of osteopontin proteins. The mRNA levels of CXCR4, MCP-1, and TLR-2/-4 of the atherosclerotic plaques were also decreased. (b) Pitavastatin decreased the mRNA expressions of $gp91^{phox}$, $p47^{phox}$, and $p67^{phox}$, all of which are related to oxidative stress. (c) Pitavastatin enhanced the stability of atherosclerotic plaques by increasing the collagen and α-SMC contents in the plaques, and it reduced the expressions and/or activities of ECM-degrading enzymes (MMP-2, MMP-9, and Cat S), preserving the integrity of the elastic laminae. All of these effects of pitavastatin contributed to the alleviation of stress-related atherosclerosis, beyond lowering the LDL-C level. (d) Pitavastatin rectified the alterations in the senescence-related protein levels (p61, p21, and Sirt-1).

We studied the potential mechanisms underlying the effects of the chronic stress on atherosclerosis, and it is noteworthy that the pro-atherosclerosis effect of chronic stress was accompanied by a change in the level of GLP-1 and APN. Adipose tissue has been recognized as an important endocrine organ, capable of secreting various endocrine factors that modulate a wide variety of physiological functions (Fang and Judd, 2018). APN is one of the adipokines that has exhibited anti-inflammatory properties and an endothelial cell-protective effect. Several studies confirmed that APN can activate AMP kinase and NFκB activity in human aortic endothelial cells under hyperglycemic conditions, and intervention with APN resulted in a marked reduction of the atherogenic plaque area on the abdominal aorta in a murine model (Wu et al., 2017). Together with our research, the above-described findings indicate that chronic stress induced a significant decrease in the APN level, resulting in the aggravation of atherosclerosis. We also observed that the expression of AdipR-1 in the aortic root was reversed by the pitavastatin treatment and APN neutralizing antibody abolished the protective effects of pitavastatin in stress-related atherogenesis. Moreover, in immature adipocytes, GLP-1 receptor activation by the exenatide stimulated APN expression in a dose-dependent manner. We therefore speculate that the protective effect of pitavastatin in chronic stress-related atherosclerosis may depend in part on the GLP-1/APN pathway.

One major potential limitation of the present study is that although current studies contains *in vivo* APN depletion experiments and GLP-1-mediated regulation of APN expression in immature adipocytes, we could not conduct used genetic GLP-1 and APN animals to provide a direct evidence for the link between vascular aging and atherosclerosis and GLP-1/APN axis. Furthermore, it was proposed that chronic stress accelerated the oxidative stress of atherosclerotic lesions. Our findings for the oxidative stress were only based on the quantitative RT-PCR data analysis of the components of NAD(P)H oxidases. Additional data including the actual readout for oxidative stress in the vascular lesions the rescuing lesions in the presence of antioxidants, and an alteration in mitochondrial oxidative stress levels will be more convincing for exploring

proposed mechanisms. Further study will be needed to investigate these issues.

CONCLUSION

We observed that chronic stress aggravated high fat diet-induced atherosclerosis in a mouse model by inhibiting the GLP-1-mediated APN/adipoR1 pathway, and it subsequently enhanced the inflammation and oxidative stress process and changed the properties of atherosclerotic plaques. As anticipated, treatment with pitavastatin ameliorated this stress-related atherosclerosis. A greater understanding of the precise effects of chronic stress is of great importance for combating stress-related disorders. Although there are limitations to our present findings in mice, they demonstrate the influence of chronic stress on atherosclerosis, including potential mechanisms. Moreover, the beneficial effects of statins on chronic stress-related atherosclerosis were confirmed for the first time, which is meaningful in clinical treatment.

DATA AVAILABILITY STATEMENT

The original contributions presented in the study are included in the article/supplementary material, further inquiries can be directed to the corresponding author/s.

ETHICS STATEMENT

The animal study was reviewed and approved by the Nagoya University Graduate School of Medicine.

AUTHOR CONTRIBUTIONS

YL: main contributor to the collection and assembly of data, manuscript drafting, biological and morphological analyses, data statistical analysis, and interpretation. LP, GY, AI, and XL: collection and assembly of samples and data. QC, HW, and MK: financial support and editing of the manuscript. XWC: main contributor to financial support, design, and editing of the manuscript. All authors approved the final version of submission.

FUNDING

This work was supported in part by grants from the National Natural Science Foundation of China (Nos. 81770485, 81560240, 81800380, and 82060052), a grant from the Young Investigation Foundation of Yanbian University (No. 2019-39) and Fudan University Hospital (No. 2018ZSQN03), "135" science and technology project of Jilin Provincial Department of Education (No. JJKH20200528KJ), and a grant from the Ministry of Education, Culture, Sports, Science, and Technology of Japan (No. 20H03574).

REFERENCES

Amin, M., Pushpakumar, S., Muradashvili, N., Kundu, S., Tyagi, S. C., Sen, U., et al. (2016). Regulation and involvement of matrix metalloproteinases in vascular diseases. *Front. Biosci.* 21, 89–118. doi: 10.2741/4378

Ascer, E., Bertolami, M. C., Venturinelli, M. L., Buccheri, V., Souza, J., Nicolau, J. C., et al. (2004). Atorvastatin reduces proinflammatory markers in hypercholesterolemic patients. *Atherosclerosis* 177, 161–166. doi: 10.1016/j.atherosclerosis.2004.07.003

Barik, J., Marti, F., Morel, C., Fernandez, S. P., Lanteri, C., Godeheu, G., et al. (2013). Chronic stress triggers social aversion via glucocorticoid receptor in dopaminoceptive neurons. *Science* 339, 332–335. doi: 10.1126/science.1226767

Barry-Lane, P. A., Patterson, C., van der Merwe, M., Hu, Z., Holland, S. M., Yeh, S. M. H., et al. (2001). p47phox is required for atherosclerotic lesion progression in ApoE(-/-) mice. *J. Clin. Invest.* 108, 1513–1522. doi: 10.1172/JCI11927

Bernberg, E., Ulleryd, M. A., Johansson, M. E., and Bergstrom, G. M. (2012). Social disruption stress increases IL-6 levels and accelerates atherosclerosis in ApoE-/- mice. *Atherosclerosis* 221, 359–365. doi: 10.1016/j.atherosclerosis.2011.11.041

Cai, H., Griendling, K. K., and Harrison, D. G. (2003). The vascular NAD(P)H oxidases as therapeutic targets in cardiovascular diseases. *Trends Pharmacol. Sci.* 24, 471–478. doi: 10.1016/S0165-6147(03)00233-5

Cheng, X. W., Song, H., Sasaki, T., Hu, L., Inoue, A., Bando, Y. K., et al. (2011). Angiotensin type 1 receptor blocker reduces intimal neovascularization and plaque growth in apolipoprotein E-deficient mice. *Hypertension* 57, 981–989. doi: 10.1161/HYPERTENSIONAHA.110.168385

Chiba, S., Okamoto, H., Kon, S., Kimura, C., Murakami, M., Inobe, M., et al. (2002). Development of atherosclerosis in osteopontin transgenic mice. *Heart Vessels* 16, 111–117. doi: 10.1007/s003800200005

Cole, J. E., Georgiou, E., and Monaco, C. (2010). The expression and functions of toll-like receptors in atherosclerosis. *Med. Inflamm.* 2010:393946. doi: 10.1155/2010/393946

Cox, S. S., Speaker, K. J., Beninson, L. A., Craig, W. C., Paton, M. M., Fleshner, M., et al. (2014). Adrenergic and glucocorticoid modulation of the sterile inflammatory response. *Brain Behav. Immun.* 36, 183–192. doi: 10.1016/j.bbi.2013.11.018

Ekstrand, M., Gustafsson Trajkovska, M., Perman-Sundelin, J., Fogelstrand, P., Adiels, M., Johansson, M., et al. (2015). Imaging of intracellular and extracellular ROS levels in atherosclerotic mouse aortas ex vivo: effects of lipid lowering by Diet or Atorvastatin. *PLoS One* 10:e0130898. doi: 10.1371/journal.pone.0130898

Fang, H., and Judd, R. L. (2018). Adiponectin regulation and function. *Compr. Physiol.* 8, 1031–1063. doi: 10.1002/cphy.c170046

Hao, C., Shintani, S., Shimizu, Y., Kondo, K., Ishii, M., Wu, H., et al. (2014). Therapeutic angiogenesis by autologous adipose-derived regenerative cells: comparison with bone marrow mononuclear cells. *Am. J. Physiol. Heart Circ. Physiol.* 307, H869–H879. doi: 10.1152/ajpheart.00310.2014

Hayashi, M., Takeshita, K., Uchida, Y., Yamamoto, K., Kikuchi, R., Nakayama, T., et al. (2014). Angiotensin II receptor blocker ameliorates stress-induced adipose tissue inflammation and insulin resistance. *PLoS One* 9:e116163. doi: 10.1371/journal.pone.0116163

Heidt, T., Sager, H. B., Courties, G., Dutta, P., Iwamoto, Y., Zaltsman, A., et al. (2014). Chronic variable stress activates hematopoietic stem cells. *Nat. Med.* 20, 754–758. doi: 10.1038/nm.3589

Isingrini, E., Belzung, C., d'Audiffret, A., and Camus, V. (2011). Early and late-onset effect of chronic stress on vascular function in mice: a possible model of the impact of depression on vascular disease in aging. *Am. J. Geriatr. Psychiatry* 19, 335–346. doi: 10.1097/JGP.0b013e318202bc42

Janssen, H., Wagner, C. S., Demmer, P., Callies, S., Solter, G., Loghmani-khouzani, H., et al. (2015). Acute perioperative- stress-induced increase of atherosclerotic plaque volume and vulnerability to rupture in apolipoprotein-E-deficient mice is amenable to statin treatment and IL-6 inhibition. *Dis. Model. Mech.* 8, 1071–1080. doi: 10.1242/dmm.018713

Jarvisalo, M. J., Toikka, J. O., Vasankari, T., Mikkola, J., Viikari, J. S., Hartiala, J. J., et al. (1999). HMG CoA reductase inhibitors are related to improved systemic endothelial function in coronary artery disease. *Atherosclerosis* 147, 237–242. doi: 10.1016/s0021-9150(99)00189-6

Kumar, S., Chen, M., Li, Y., Wong, F. H., Thiam, C. W., Hossain, M. Z., et al. (2016). Loss of ADAMTS4 reduces high fat diet-induced atherosclerosis and enhances plaque stability in ApoE(-/-) mice. *Sci. Rep.* 6:31130. doi: 10.1038/srep31130

Lankin, V. Z., and Tikhaze, A. K. (2017). Role of oxidative stress in the genesis of atherosclerosis and diabetes mellitus: a personal look back on 50 years of research. *Curr. Aging Sci.* 10, 18–25. doi: 10.2174/1874609809666160926142640

Lei, Y., Yang, G., Hu, L., Piao, L., Inoue, A., Jiang, H., et al. (2017). Increased dipeptidyl peptidase-4 accelerates diet-related vascular aging and atherosclerosis in ApoE-deficient mice under chronic stress. *Int. J. Cardiol.* 243, 413–420. doi: 10.1016/j.ijcard.2017.05.062

Lin, C. P., Huang, P. H., Lai, C. F., Chen, J. W., Lin, S. J., Chen, J.-S., et al. (2015). Simvastatin attenuates oxidative stress, NF-kappaB activation, and artery calcification in LDLR-/- Mice fed with high fat diet via down-regulation of tumor necrosis factor-alpha and TNF receptor 1. *PLoS One* 10:e0143686. doi: 10.1371/journal.pone.0143686

Linton, M. R. F., Yancey, P. G., Davies, S. S., Jerome, W. G., Linton, E. F., et al. (2000). "The role of lipids and lipoproteins in atherosclerosis," in *Endotext*, eds K. R. Feingold, B. Anawalt, A. Boyce, G. Chrousos, W. W. de Herder, K. Dungan, et al. (South Dartmouth, MA: MDText.com, Inc).

Lutgens, E., Lutgens, S. P., Faber, B. C., Heeneman, S., Gijbels, M. M., de Winther, M. P. J., et al. (2006). Disruption of the cathepsin K gene reduces atherosclerosis progression and induces plaque fibrosis but accelerates macrophage foam cell formation. *Circulation* 113, 98–107. doi: 10.1161/circulationaha.105.561449

Morariu, M., Hodas, R., Benedek, T., Benedek, I., Opincariu, D., Mester, A., et al. (2019). Impact of inflammation- mediated response on pan-coronary plaque vulnerability, myocardial viability and ventricular remodeling in the postinfarction period - the VIABILITY study: protocol for a non-randomized prospective clinical study. *Medicine* 98:e15194. doi: 10.1097/MD.0000000000015194

Quesada, I. M., Lucero, A., Amaya, C., Meijles, D. N., Cifuentes, M. E., Pagano, P. J., et al. (2015). Selective inactivation of NADPH oxidase 2 causes regression of vascularization and the size and stability of atherosclerotic plaques. *Atherosclerosis* 242, 469–475. doi: 10.1016/j.atherosclerosis.2015.08.011

Ruddy, J. M., Ikonomidis, J. S., and Jones, J. A. (2016). Multidimensional contribution of matrix metalloproteinases to atherosclerotic plaque vulnerability: multiple mechanisms of inhibition to promote stability. *J. Vasc. Res.* 53, 1–16. doi: 10.1159/000446703

Sorescu, D., Weiss, D., Lassegue, B., Clempus, R. E., Szocs, K., Sorescu, G. P., et al. (2002). Superoxide production and expression of nox family proteins in human atherosclerosis. *Circulation* 105, 1429–1435. doi: 10.1161/01.cir.0000012917.74432.66

Sukhova, G. K., Zhang, Y., Pan, J. H., Wada, Y., Yamamoto, T., Naito, M., et al. (2003). Deficiency of cathepsin S reduces atherosclerosis in LDL receptor-deficient mice. *J. Clin. Invest.* 111, 897–906. doi: 10.1172/JCI14915

Wu, W., Wang, H., Jiao, G., Yue, J., and Wang, G. (2017). Aerobic exercise suppresses atherosclerosis through adiponectin-nuclear transcription factor kappaB pathway in Apolipoprotein E-deficient mice. *Am. J. Med. Sci.* 353, 275–281. doi: 10.1016/j.amjms.2016.11.002

Yang, G., Lei, Y., Inoue, A., Piao, L., Hu, L., Jiang, H., et al. (2017). Exenatide mitigated diet-induced vascular aging and atherosclerotic plaque growth in ApoE-deficient mice under chronic stress. *Atherosclerosis* 264, 1–10. doi: 10.1016/j.atherosclerosis.2017.07.014

Yurdagul, A. Jr., Finney, A. C., Woolard, M. D., and Orr, A. W. (2016). The arterial microenvironment: the where and why of atherosclerosis. *Biochem. J.* 473, 1281–1295. doi: 10.1042/BJ20150844

Zhu, Y., Xian, X., Wang, Z., Bi, Y., Chen, Q., Han, X., et al. (2018). Research progress on the relationship between atherosclerosis and inflammation. *Biomolecules* 8:80. doi: 10.3390/biom8030080

Conflict of Interest: The authors declare that the research was conducted in the absence of any commercial or financial relationships that could be construed as a potential conflict of interest.

frontiers in Cell and Developmental Biology

REVIEW
published: 23 July 2021
doi: 10.3389/fcell.2021.659666

Innate Immune Cells in Pressure Overload-Induced Cardiac Hypertrophy and Remodeling

Xin Liu[1,2], *Guo-Ping Shi*[1]* *and Junli Guo*[1,3]*

[1] Department of Medicine, Brigham and Women's Hospital and Harvard Medical School, Boston, MA, United States, [2] Department of Cardiology, Renmin Hospital of Wuhan University, Cardiovascular Research Institute, Wuhan University, Hubei Key Laboratory of Cardiology, Wuhan, China, [3] Hainan Provincial Key Laboratory for Tropical Cardiovascular Diseases Research & Key Laboratory of Emergency and Trauma of Ministry of Education, Institute of Cardiovascular Research of the First Affiliated Hospital, Hainan Medical University, Haikou, China

Pressure overload and heart failure are among the leading causes of cardiovascular morbidity and mortality. Accumulating evidence suggests that inflammatory cell activation and release of inflammatory mediators are of vital importance during the pathogenesis of these cardiac diseases. Yet, the roles of innate immune cells and subsequent inflammatory events in these processes remain poorly understood. Here, we outline the possible underlying mechanisms of innate immune cell participation, including mast cells, macrophages, monocytes, neutrophils, dendritic cells, eosinophils, and natural killer T cells in these pathological processes. Although these cells accumulate in the atrium or ventricles at different time points after pressure overload, their cardioprotective or cardiodestructive activities differ from each other. Among them, mast cells, neutrophils, and dendritic cells exert detrimental function in experimental models, whereas eosinophils and natural killer T cells display cardioprotective activities. Depending on their subsets, macrophages and monocytes may exacerbate cardiodysfunction or negatively regulate cardiac hypertrophy and remodeling. Pressure overload stimulates the secretion of cytokines, chemokines, and growth factors from innate immune cells and even resident cardiomyocytes that together assist innate immune cell infiltration into injured heart. These infiltrates are involved in pro-hypertrophic events and cardiac fibroblast activation. Immune regulation of cardiac innate immune cells becomes a promising therapeutic approach in experimental cardiac disease treatment, highlighting the significance of their clinical evaluation in humans.

Keywords: pressure overload, hypertrophy, fibrosis, innate immune cell, cardiomyocyte, cardiac fibroblast

OPEN ACCESS

Edited by:
Sigmar Stricker,
Freie Universität Berlin, Germany

Reviewed by:
John Baugh,
University College Dublin, Ireland
Nikolaos G. Frangogiannis,
Albert Einstein College of Medicine, United States

***Correspondence:**
Guo-Ping Shi
gshi@bwh.harvard.edu
Junli Guo
guojl0511@126.com

Specialty section:
This article was submitted to Signaling, a section of the journal Frontiers in Cell and Developmental Biology

Received: *28 January 2021*
Accepted: *28 June 2021*
Published: *23 July 2021*

Citation:
Liu X, Shi G-P and Guo J (2021) Innate Immune Cells in Pressure Overload-Induced Cardiac Hypertrophy and Remodeling. Front. Cell Dev. Biol. 9:659666. doi: 10.3389/fcell.2021.659666

INTRODUCTION

Pressure overload refers to the left ventricular (LV) pressure overload caused by aortic stenosis, hypertension, and coarctation of the aorta, and right ventricular (RV) pressure overload triggered by pulmonary stenosis and pulmonary hypertension, leading to cardiac hypertrophy and fibrosis (Berk et al., 2007). Such remodeling exhibits extensive morphological changes, including cardiomyocyte mass increase, sarcomere rearrangement, and extracellular matrix (ECM) deposition in cardiac interstitial or perivascular regions (Schiattarella and Hill, 2015). At the

early stage, cardiac hypertrophy and ventricular dilatation are compensatory responses to pressure overload stimuli (Schiattarella and Hill, 2015). Yet, chronic pressure overload stimulation increases heart wall thickness, fibrotic protein deposition, and inflammatory cell infiltration, which give rise to myocardial compliance reduction and hemodynamic dysfunction. At the late stage, sustained pressure overload results in life-threatening heart failure (HF) accompanied by serious adverse events including respiratory failure and cardiac arrest (Shimizu and Minamino, 2016). Therefore, pressure overload-induced cardiac hypertrophy has been used as an experimental model to study human HF with preserved ejection fraction HFpEF (Mishra and Kass, 2021). One popular theory in HFpEF patients is the established pro-inflammatory state with elevated levels of $CD3^+$ T cells, $CD68^+$ macrophages and monocytes, or total $CD45^+$ leukocytes in myocardial biopsy specimens from these patients (Westermann et al., 2011; Hahn et al., 2020). Further evidence of inflammatory conditions in HFpEF patients came from elevated blood inflammatory biomarkers, including interleukin-1β (IL1β), IL6, IL10, immunoglobulin-like transcript 6, tumor necrosis factor-α (TNF-α), TNF-receptor, matrix metalloproteinases (MMP-7), MMP-9, and myeloperoxidase (Chirinos et al., 2020). Similarly, the activation of immune cells, especially innate immune cells, orchestrates pressure overload-induced cardiac hypertrophy and fibrosis. Activated immune cells produce high levels of cytokines that induce cardiomyocyte hypertrophy, such as TNF-α, IL1β, and IL6. Increased TNF-α expression was associated with cardiac hypertrophy (You et al., 2018). TNF-α deficiency blunted pressure overload-induced cardiac hypertrophy (Sun et al., 2007). Similarly, IL1β deficiency also protected mice from pressure-mediated hypertrophy (Honsho et al., 2009) and deficiency of IL6 suppressed angiotensin-II (Ang-II)-induced cardiomyocyte hypertrophy (Chen et al., 2017). In addition, inflammation is also critical in the initiation, propagation, and development of cardiac fibrosis. Immune signaling triggers the accumulation, proliferation, and activation of fibroblasts by producing proteases that participate in matrix metabolism, fibrogenic mediator, and ECM protein secretion that exert contact-dependent actions on fibroblast phenotype (Dostal et al., 2015). Herein, we summarize the current understanding of innate immune cells with a focus on pressure overload-induced cardiac hypertrophy. We highlight the cross talk between innate immune cells and cardiac remodeling to propose a therapeutic potential to target these cells in humans.

Pressure Overload-Induced Cardiac Hypertrophy and Fibrosis

Use of experimental models makes it possible to study the molecular and cellular mechanisms by which pressure overload induces heart hypertrophy. The murine transverse aortic constriction (TAC) model was first validated by Rockman et al. (1991), and has since been commonly used to mimic human clinical aortic stenosis with high LV afterload. Chronic subjection to Ang-II in mice imitates chronic systemic hypertension due to neurohumoral activation of the renin–angiotensin–aldosterone system (Paul et al., 2006). The murine model of pulmonary artery constriction (PAC) generates RV hypertrophy and fibrosis following pulmonary artery hypertension (Braun et al., 2003). Another model that mimics pressure overload is aldosterone analog deoxycorticosterone acetate (DOCA) accompanied by unilateral nephrectomy and high-salt diet. Chronic subjection of DOCA promotes hypertension and subsequent development of HF in mice (Silberman et al., 2010; Lovelock et al., 2012). Hypertension from the DOCA model could be divided into two phases: an initial peak in blood pressure at an early phase and sustained hypertension and cardiac remodeling at the late phase (Alex and Frangogiannis, 2018). Together, pressure overload-induced hypertrophy in experimental animals displayed enhanced systolic and diastolic blood pressures, increased cardiac mass, and eventually elevated cardiac fibrosis.

Innate Immune Cells

Innate immune cells are a group of cells that sense signals from pathogens and endogenous sources and can be triggered to give an immediate and non-specific response. Pathogenic bacteria, viruses, fungi, and parasites share small molecular motifs, known as pathogen-associated molecular patterns (PAMPs). These patterns could be identified by pattern recognition receptors (PRR) and toll-like receptors (TLRs) in resident immune cells or myocardial cells (Takeuchi and Akira, 2010). After cardiac injury, autoimmunity leads to cardiac cell apoptosis or necrotic cell death followed by productions of damage-associated molecular patterns (DAMPs) (Frangogiannis, 2014; Shinde and Frangogiannis, 2014). The main DAMPs include IL1α, galectin-3, high mobility box group1 protein (HMGB1), S100 protein, and heat shock protein (HSP) (Seong and Matzinger, 2004) that bind to IL1 receptor-1 (Di Paolo and Shayakhmetov, 2016), CD45 and CD71 (Stillman et al., 2006), TLR4 and receptor for advanced glycation end (RAGE) (Yang et al., 2020), RAGE (Leclerc et al., 2009), and G-protein cell receptors (Streicher, 2019), respectively, to exert their pathophysiological activities. A large body of evidence shows that innate immune cells play a considerable role in the development of cardiac hypertrophy and fibrosis (Frieler and Mortensen, 2015). Single-cell RNA sequencing from recent studies demonstrated that the majority innate immune cell subpopulations, including mast cells (MCs), monocytes and macrophages, neutrophils, dendritic cells (DCs), eosinophils (EOS), and invariant natural killer T (iNKT) cells underwent extensive activation in pressure overload-induced HF in mice (Martini et al., 2019). Different innate immune cells accumulate in hearts at different time points after pressure overload injury. On heart sections from mice with PAC-induced pressure overload, toluidine blue staining revealed increase of MCs in mouse RV myocardium. Cardiac MCs peaked at 21 days after the injury. MC degranulation was also increased rapidly and reached to about 80% within a week after cardiac injury (Luitel et al., 2017; **Figure 1A**, upper panel). In contrast, neutrophils are probably the first immune cells that come to the hearts in response to pressure overload injury. In TAC-treated mice, LV neutrophils peaked in 3 days after injury and remained high in 3 weeks or longer (Weisheit et al., 2014;

Figure 1A, bottom panel). DCs acted differently. In TAC-induced hypertrophy in mice, FACS analysis illustrated that $CD11c^{low}MHC\text{-}II^{+}B220^{+}$ plasmacytoid DCs (pDCs) peaked in 1 week after the injury. In contrast, $CD11c^{+}MHC\text{-}II^{+}B220^{-}$ conventional DCs (cDCs) accumulated in the heart tissue in a biphasic manner, with peaks at both early (1 week) and late (8 weeks) phases after TAC injury (Patel et al., 2017; **Figure 1A**, bottom panel). Macrophages and monocytes are probably the most studied cell types in hypertrophic hearts. In TAC-induced mouse hypertrophic hearts, FACS analysis showed that the $CD206^{+}$ or $CD206^{-}$ macrophages or $CD11b^{+}F4/80^{+}MHC\text{-}II^{+}$ macrophages peaked at 6–7 days after TAC injury in mice (Patel et al., 2017; **Figure 1B**, upper panel). A separate study showed slightly different results. $Ly6C^{low}$ macrophages in heart or LV tissues peaked at 7 days after TAC injury, but $Ly6C^{high}$ macrophages in LV tissues peaked at 3 days after TAC injury (Weisheit et al., 2014, 2021; **Figure 1B**, upper panel). Bromodeoxyuridine (BrdU) FACS analysis showed that the proliferation of cardiac resident macrophages peaked at 3 days after TAC injury, whereas the proliferation of total macrophages peaked at 7 days after TAC surgery (**Figure 1B**, bottom panel) (Liao et al., 2018). In blood, both $Ly6C^{high}$ and $Ly6C^{low}$ monocytes peaked at 7 days after TAC surgery and then went back to the baseline in 3 to 4 weeks (**Figure 1C**, upper and bottom panels) (Weisheit et al., 2014, 2021; Patel et al., 2017). Yet, limited information is available from many other innate immune cells regarding their cardiac infiltration. Time cause differences in cardiac infiltration of these innate immune cells suggest their differences in cardioprotective or cardiodestructive functions in pressure overload-induced hypertrophic heart.

MAST CELLS

Mast cells were first linked to cardiac fibrosis more than 50 years ago following the observation that these cells accumulated in the endocardial fibrotic region from an autopsy series of 672 cases (Fernex and Sternby, 1964). Since then, the bulk of evidence has shown that myocardial MCs increased after cardiac injury from multiple etiologies. MCs are considered non-circulating cells and developed only from bone-marrow-derived precursors. Driven by stem cell factor (SCF) and its receptor c-kit, MC progenitors are recruited through the blood stream and target the terminal tissues where MCs differentiate and mature. Cardiac MCs possess IgE receptor FcεRI, TNF-α receptor I, and C5a complement receptor (Ito et al., 1993; Fureder et al., 1995; Patella et al., 1995). After activation of these receptors, cardiac MCs are capable of degranulating and releasing preformed mediators from their granules, although MCs can also *de novo* synthesize and secrete their intracellular mediators without granule involvement (Kandere-Grzybowska et al., 2003; Zhang et al., 2012). MC granules contain excessive specific substances (e.g., histamine), proteases (e.g., tryptase and chymase), non-MC-specific proteases (cathepsin G), amines (serotonin and dopamine), cytokines (TNF-α, IL4, and IL5), and growth factors (SCF and fibroblast growth factor [bFGF]) (Wernersson and Pejler, 2014; **Figure 2**).

MC Function in Pressure Overload-Induced Cardiac Hypertrophy and Fibrosis

Several studies suggested MC involvement in pressure overload-induced cardiac hypertrophy and HF. In a study of 86 aortic valve stenosis patients who underwent valve replacement and 17 control subjects, cardiac expression of cathepsin G, a common MC protease, was associated with areas rich in MCs. Cathepsin G expression correlated with heart collagen I and III contents (Helske et al., 2006). In hypertrophic and failing human hearts, both MC contents and MC chymase expression were increased (Batlle et al., 2006). Animal studies also reported high MC density in the myocardium from different animal models of pressure overload-induced cardiac hypertrophy. MCs were found increased by more than threefold in rat RV myocardium following PAC injury, resulting in hemodynamic dysfunction, RV enlargement, and fibrosis (Olivetti et al., 1989). In a mouse model of PAC-induced pressure overload and RV hypertrophy, the number of MCs and their degranulation increased by two- to threefold in RV after PAC (Luitel et al., 2017; **Figure 1A**, upper panel). In TAC-induced hypertrophic mice, MCs were also increased by over twofold in the atrium (Liao et al., 2010). In 36-week-old spontaneously hypertensive rats with established LV hypertrophy, increase of LV MC number occurred together with increased interstitial and perivascular fibrosis and hydroxyproline concentration, an indication of increased collagen contents. Univariate regression test showed that MC number in LV correlated significantly with collagen volume fraction ($r = 0.87$, $p < 0.001$; Panizo et al., 1995).

Mast cell activation and mediator release have also been proven essential in experimental cardiac hypertrophy. After TAC treatment, all rats with or without ovariectomization developed cardiac hypertrophy and myocardium MC accumulation. Yet, ovariectomized rats showed increased myocardium collagen fraction, with much greater release of myocardial chymase and active transforming growth factor-β1 (TGF-β1), and even increased plasma chymase levels. Estrogen (17β-estradiol) replacement, chymase inhibition with chymostatin, or MC stabilization with nedocromil reduced pressure overload-induced ventricular hypertrophy in ovariectomized rats, along with reduced myocardial chymase, TGF-β1, and MC contents, and plasma chymase levels (Li et al., 2015). It seems that estrogen blocked MC function in this study (**Figure 2**). Yet, prior studies showed that female sex hormones, estradiol and progesterone, activate MCs (Zierau et al., 2012). Women at reproductive age or receiving sex hormone therapy showed increased risk of asthma (Zierau et al., 2012). Therefore, estrogen (17β-estradiol) replacement-mediated reduction of pressure overload-induced hypertrophy in ovariectomized rats may be independent of MC function. For example, estrogen induces β-adrenergic receptor expression

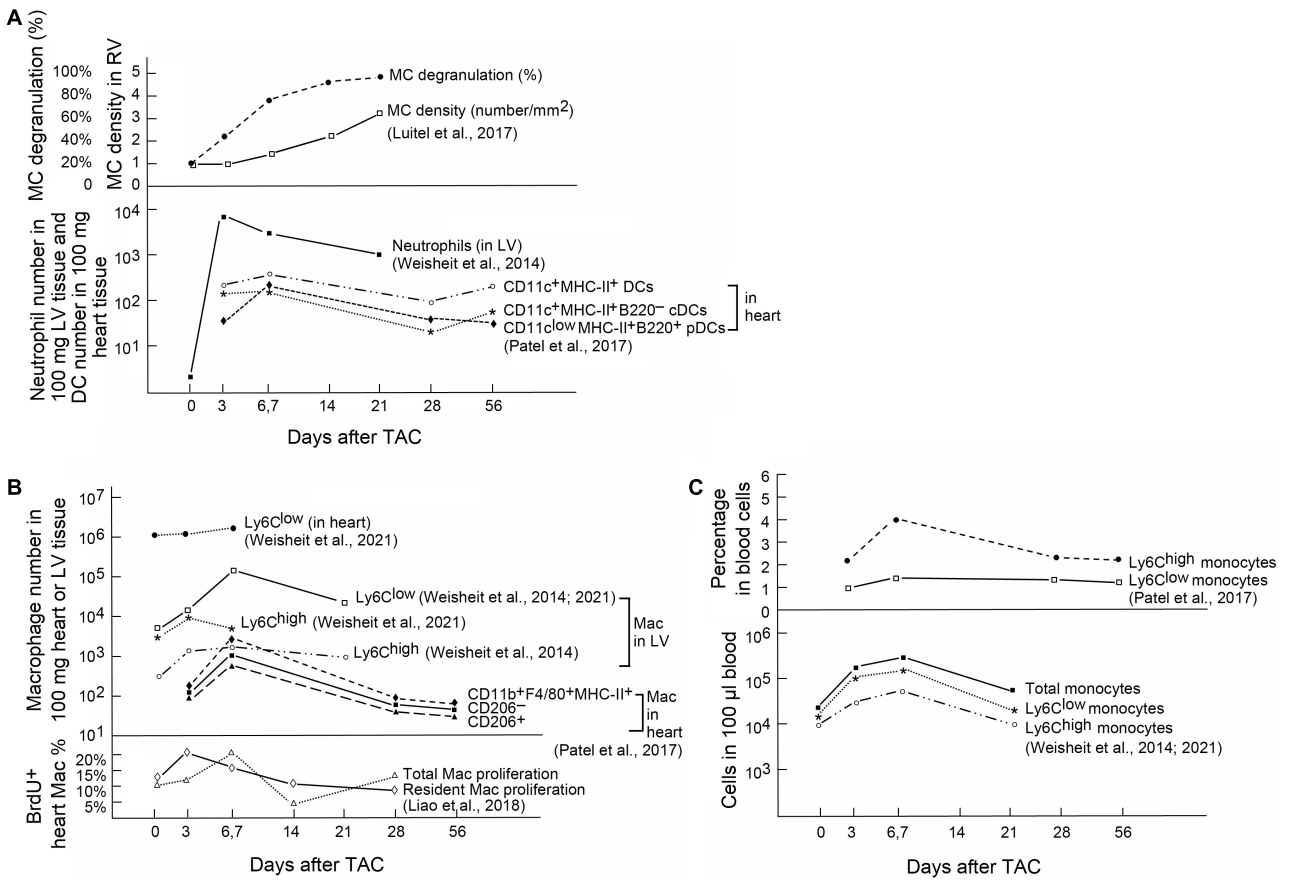

FIGURE 1 | Innate immune cells in heart and blood from mice after pressure overload-induced cardiac hypertrophy. **(A)** Upper: Toluidine blue staining detected MC density and percentage of degranulated MCs in RV from mice with PAC-induced pressure overload. Bottom: FACS determined the absolute number of neutrophils and different DCs in 100 mg heart or LV tissues from mice after TAC-induced pressure overload. **(B)** Upper: FACS analysis of different macrophage subsets in 100 mg heart or LV tissues from mice with TAC-induced pressure overload. Bottom: BrdU staining followed by FACS analysis to detect proliferation of heart-resident and total macrophages in TAC-treated mice. **(C)** Upper: Percentage of different monocyte subsets in total blood cells from TAC-treated mice. Bottom: Absolute numbers of different monocyte subsets in 100 µl of blood from TAC-treated mice. Graphs were generated by grouping the results from different studies. References are indicated.

(Wagner et al., 1979) and directly targets cardiomyocytes and cardiac fibroblasts that also express estrogen receptor (Grohe et al., 1997).

Mast cell-deficient W/Wv mice have been used widely to examine their roles in different hypertrophic models. From suprarenal abdominal aortic constriction (SAC)-induced pressure overload, wild-type (WT) mice showed worse LV performance with decompensated hypertrophy and pulmonary congestion at 4 weeks after constriction than W/Wv mice. In contrast, throughout 15 weeks after constriction, W/Wv mice still showed preserved LV performance, and neither their decompensation of cardiac function or pulmonary congestion was observed. In addition, perivascular fibrosis and MC chymase upregulation were less apparent in W/Wv mice (Li et al., 2008). In TAC-treated hypertrophic mice, programmed electrical stimulation to the right atrium under Langendorff perfusion induced atrial fibrillation (AF). In these mice, TAC induced MC infiltration and fibrosis in the atrium and enhanced AF susceptibility. MC stabilization with cromolyn or reconstitution of bone marrow from W/Wv mice did not change echocardiographic parameters of LV hypertrophy and systolic functions, but markedly reduced AF episode incidence and duration under Langendorff perfusion and fibrotic changes in the atrium. In SAC-induced pressure overload in mice, MC deficiency in W/Wv mice reduced myocardium MC chymase upregulation and perivascular fibrosis and prevented cardiac function decompensation at 15 weeks after pressure overload (Hara et al., 2002).

MC Molecular and Cellular Mechanisms

Mast cells modulate cardiomyocyte hypertrophy and cardiac fibrosis by secreting inflammatory mediators. MC-derived bFGF and TGF-β1 regulate cardiomyocyte growth and death. MC mediators also regulate cardiac fibrosis progression or regression. For example, MCs release pro-inflammatory IL1, IL6, and interferon (IFN)-γ; anti-inflammatory IL10 and IL13; and pro-fibrotic TGF-β, vascular endothelial growth factor (VEGF),

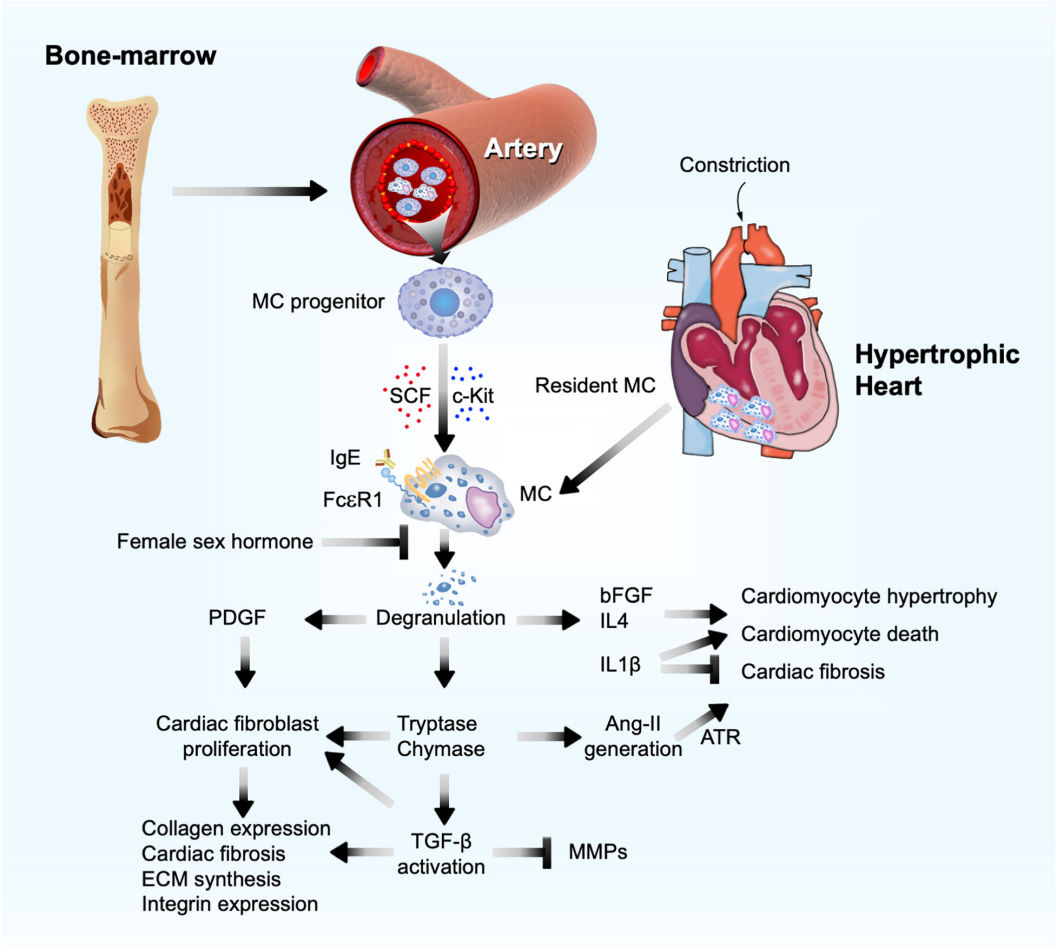

FIGURE 2 | Mast cell function in pressure overload-induced cardiac hypertrophy and fibrosis. Bone marrow MC progenitor-derived and heart-resident MCs get activated and release PDGF, proteases (chymase and tryptase), and cytokines to affect cardiomyocyte hypertrophy, cardiac cell death, and cardiac fibroblast ECM and fibrotic protein syntheses, as a mechanism to promote cardiac hypertrophy and fibrosis.

platelet-derived growth factor (PDGF), anti-fibrotic IL33, and prostaglandin D2 (PGD2) (Lefrançais et al., 2014; Overed-Sayer et al., 2014a,b; Janicki et al., 2015; Mukai et al., 2018). MC-derived tryptase and chymase are proteases that convert TGF-β from a latent form to an active form, an essential fibrotic growth factor during the development of cardiac fibrosis by stimulating myofibroblast trans-differentiation (Desmoulière et al., 1993), promoting ECM protein synthesis, increasing integrin expression (Kong et al., 2018), and acting as an inhibitor of ECM degradation by matrix metalloproteinases (MMP) (Baricos et al., 1999; **Figure 2**). MC tryptase can directly induce fibroblast differentiation independent of TGF-β (Abe et al., 1998; Akers et al., 2000; **Figure 2**). In TAC-induced cardiac hypertrophy in 5-week old Sprague Dawley rats, tryptase inhibition with nafamostat mesilate (5 mg/kg/day) reduced the ratio of LV weight to tibia length (TL) and plasma chymase levels. Yet, there was no significant difference in collagen volume fraction and hemodynamic indexes between TAC-treated rats and those that also received nafamostat mesilate (Li et al., 2016). Chymase is an angiotensin-converting enzyme (ACE) that generates Ang-II (Caughey et al., 2000; Li et al., 2004; Takai et al., 2004; Miyazaki et al., 2006; Bradding and Pejler, 2018). Ang-II, a well-recognized clinical determinant in reversing maladaptive cardiac hypertrophy, induces cardiomyocyte enlargement and accelerates fibroblast differentiation through its surface angiotensin receptor (ATR) (Lijnen et al., 2001; Ainscough et al., 2009) (**Figure 2**). In dogs with tachycardia-induced HF, chymase inhibitor SUNC8257 (10 mg/kg, orally twice a day) significantly decreased MC density, cardiac Ang-II expression, and collagen-type I, III, and TGF-β mRNA levels (Matsumoto et al., 2003). Several studies showed that Ang-II production from MC chymase played a negligible role in blood pressure. In spontaneous hypertensive rats, only ACE inhibitor and ATR blocker, but not chymase inhibitor, displayed anti-hypotensive effect (Kirimura et al., 2005). Both systolic and diastolic blood pressures did not differ between WT and W/Wv mice (Li et al., 2004).

Platelet-derived growth factor-α receptor signaling is required for cardiac fibroblast maintenance and activation. Deficiency of PDGF-α receptor expression or inhibition of PDGF-α receptor signaling led to cardiac fibroblast loss in mouse heart and cardiac fibroblast apoptosis in culture (Ivey et al., 2019). In co-cultures of neonatal rat cardiomyocytes or fibroblasts with mouse MCs, cardiomyocytes and cardiac fibroblasts induced MC expression of PDGF-A. In turn, MC-derived PDGF-A promoted cardiac fibroblast activation and collagen expression (Liao et al., 2010). Antibody-mediated neutralization of PDGF-α receptor alleviated the AF inducibility and fibrosis in TAC-induced hypertrophic mice (Liao et al., 2010). MC granules contain bFGF and IL1β that may also promote cardiomyocyte enlargement and remodeling after MC activation by IgE *in vivo* or *in vitro* (**Figure 2**). MCs are the major source of cardiac bFGF (Shiota et al., 2003). While the 18-kDa bFGF acts in adaptive trophic response, the 34-kDa high-molecular-weight bFGF exacerbates hypertrophy and contributes to cardiac cell death, thereby driving the myocardium towards a maladaptive phenotype (Kardami et al., 2004). In contrast, IL1β can be pleiotropic in hypertrophic heart. IL1β induced cardiomyocyte growth and hypertrophy, but reduced the growth of cultured cardiac fibroblasts (Palmer et al., 1995). Therefore, in pressure overload-induced hypertrophic mice, IL1β deficiency reduced heart weight (HW), cardiomyocyte size, and LV ejection fraction (EF), but greatly increased interstitial fibrosis. Mechanistic studies showed that pressure overload or mechanical stretch induced cardiac fibroblast release of IL1β to induce insulin-like growth factor-1 (IGF-1) production *via* the JAK/STAT signaling pathway. IL1β deficiency enhanced cardiomyocyte apoptosis with concurrent increase of c-Jun N-terminal kinase (JNK) activation and caspase-3 activities. IGF-1 replacement or JNK inhibitor blocked these adverse activities of IL1β deficiency (Honsho et al., 2009). Patients with longstanding pulmonary arterial hypertension (PAH) experienced pressure overload in the RV. Therefore, serum IL1β levels were elevated in these patients (Soon et al., 2010). PAH patients receiving 100 mg subcutaneous anakinra, a recombinant IL1 receptor antagonist, showed reduced plasma C-reactive protein and IL6 and significant improvement of HF symptoms (Trankle et al., 2019). In obese patients, both short-term (2 days) and long-term (4 weeks) treatment of anakinra reduced systolic blood pressure by 4–5 mmHg with decreased stroke systemic vascular resistance index and peripheral vascular resistance (Urwyler et al., 2020).

Therapeutic Potential of Targeting MCs

Tryptase and chymase inhibitors as well as MC stabilizers may become important regimens in alleviating pressure overload-induced cardiac hypertrophy and fibrosis. MC membrane stabilizers prevent MC degranulation and intracellular granule release, which decreases their interactions with cardiomyocytes, fibroblasts, or other cardiac inflammatory infiltrates following cardiac injury. From 8-week-old rats with spontaneous hypertension, treatment of MC stabilizer nedocromil (30 mg/kg/day) for 12 weeks reduced macrophage infiltration, normalized myocardium MC tryptase level, and prevented LV fibrosis, independent of hypertrophy and blood pressure, although myocardium MC content remained high. Spontaneous hypertension also increased myocardial TNF-α, IFN-γ, and pro-fibrotic IL4, but decreased myocardial IL6 and IL10. Treatment with nedocromil significantly reversed these cytokine profiles. In cultured cardiac fibroblasts from hypertensive rats, tryptase induced fibroblast proliferation and collagen synthesis (Levick et al., 2009). In pressure overload-induced cardiac fibrosis mice, MCs are an essential source of IL4 (**Figure 2**). MC stabilization with cromolyn reduced MC degranulation, IL4 expression, cardiac fibrosis, and infiltration of interstitial fibroblasts and macrophages in the fibrosis regions (Kanellakis et al., 2012). Similarly, administration of a MC stabilizer tranilast prevented the evolution from compensated hypertrophy to HF by diminishing MC degranulation in mice after SAC-induced pressure overload (Hara et al., 2002). Together, these preclinical studies suggest that MC stabilizers are potential therapeutic agents for pressure overload-induced hypertrophy and HF, although clinical studies are warranted to validate their efficacies.

MONOCYTES AND MACROPHAGES

Monocytes contain heterogeneous subsets that can be divided by their surface expression of Ly6C and chemokine C-C motif receptor-2 (CCR2), including classical $Ly6C^{high}CCR2^{high}$ monocytes and non-classical $Ly6C^{low}CCR2^{low}$ monocytes (Geissmann et al., 2003). $Ly6C^{high}$ monocytes are derived from $Ly6C^{+}$ progenitors in the bone marrow. Relying on the expression of CCR2, $Ly6C^{high}$ monocytes are released into the blood (Serbina and Pamer, 2006). $Ly6C^{high}$ monocytes give rise to $Ly6C^{low}$ monocytes through a nuclear receptor subfamily-4-dependent (NR4A1) transcriptional program (Hanna et al., 2011). It is commonly thought that macrophages merely arise from circulating blood monocytes. With the advent of fate mapping, parabiosis, and adoptive transfer techniques, studies demonstrated that tissue-resident macrophages replenish themselves mainly by local proliferation in steady-state heart (Ginhoux et al., 2010; Schulz et al., 2012; Hashimoto et al., 2013; Yona et al., 2013). These resident macrophages originate from embryonic yolk-sac progenitors independent of bone-marrow-derived monocytes (Epelman et al., 2014) (**Figure 3**). In contrast, during the perturbed state caused by hemodynamic stress, such as pressure overload and even ischemic injuries, the majority of macrophages are recruited and differentiated from blood monocytes (Molawi et al., 2014). Reacting to the marked upregulation of chemokines, mainly CCL2, CCL7, CCL12, and monocyte-chemoattractant protein (MCP-1) (Dewald et al., 2005; Hashimoto et al., 2013; Hilgendorf et al., 2014; Patel et al., 2018) and chemokine receptors CCR1, CCR2, CCR5, and C-X3-C motif chemokine receptor-1 (CX3CR1) (Weisheit et al., 2014, 2021; Nemska et al., 2016), $Ly6C^{high}CCR2^{high}$ and $Ly6C^{low}CX3CR1^{high}$ monocytes and macrophages infiltrate into hypertrophic hearts using CCR2 and CX3CR1 within the first week

after pressure overload injury (Weisheit et al., 2014, 2021; Nemska et al., 2016; Patel et al., 2017, 2018; Liao et al., 2018; **Figure 3**).

Monocyte and Macrophage Functions in Pressure Overload-Induced Cardiac Hypertrophy and Fibrosis

Cardiac monocytes and macrophages exert significant effects in response to pressure overload-induced adverse cardiac hypertrophy and fibrosis. A series of studies illustrated that SAC surgery in rats induced myocardium macrophage infiltration and fibroblast activation at the early phase of hypertrophy (Kuwahara et al., 2003, 2004). TAC-induced cardiac hypertrophy exhibited expansion of circulating $Ly6C^{high}$ and $Ly6C^{low}$ monocytes and pro-inflammatory $CD206^{-}$ cardiac macrophages at 1 week after surgery, prior to significant cardiac hypertrophy and dysfunction (Weisheit et al., 2014, 2021; Nemska et al., 2016; Patel et al., 2017, 2018; Liao et al., 2018; **Figure 1B**). Recent studies showed that peripheral monocytes from hypertension patients with or without LV hypertrophy also underwent phenotypic alterations. Patients with hypertension but without LV hypertrophy showed reduced monocyte surface CD163 expression and plasma IL10 levels, but increased plasma TNF-α. LV hypertrophy further reduced monocyte surface expression of CD163 and CD206 and increased plasma TNF-α. Treatment with antihypertensive drug irbesartan increased monocyte CD163 and CD206 expression in LV hypertrophic patients (Zhang et al., 2021; **Figure 3**), although it remains untested whether the similar alterations occurred in monocytes within the hypertrophic heart.

In TAC-induced hypertrophic mice, while neutrophils peaked at 3 days after injury, $Ly6C^{low}$ and $Ly6C^{high}$ macrophages peaked at 6 days after TAC (**Figure 1A**, bottom panel, and **Figure 1B**, upper and bottom panels). These macrophages expressed high levels of surface CD11b and CX3CR1. At this time point, myocardium expressed high levels of adhesion molecule intercellular adhesion molecule 1 (ICAM-1) on cardiac endothelial cells. Use of fluorescence microscopy detected $Ly6C^{low}$ macrophage attachment on the intra- and extravascular vessel wall (Weisheit et al., 2014). These observations may explain the $Ly6C^{low}$ macrophage accumulation in cardiac tissue after TAC. A recent study further tested the role of macrophages in the late phase of cardiac hypertrophy and fibrosis. Pressure overload-induced hypertrophy generated a two-phase response of cardiac macrophages. During the early compensated phase (1 week), there was an outburst of local infiltration and proliferation of macrophages. During the late decompensated phase (4 weeks), the infiltration of $Ly6C^{high}CX3CR1^{+}CCR2^{+}$ classic monocytes increased. Macrophages displayed a second phase of proliferation (**Figure 1B**, bottom panel). Macrophages expressed Kruppel-like factor 4 (KLF4), a key transcription factor that regulates macrophage proliferation and angiogenesis (Liao et al., 2018; **Figure 3**). Resident macrophages are involved in adaptive response to pressure overload. Deficiency of KLF4 reduced resident macrophage proliferation and increased cardiac tissue fibrosis, cell death, mitochondria damage, and cardiomyocyte hypertrophy (Liao et al., 2018). Clodronate (CL) liposomes have been used to deplete cardiac macrophages. CL binds to the intracellular ATP and inhibits ATP function, leading to macrophage apoptosis (Frith et al., 1997). Liposomes selectively deliver CL into macrophages *via* their phagocytic activity. Repeated administration of CL may also deplete macrophages and monocytes from the bone marrow and in peripheral blood (Robbins et al., 2013). In HF-prone hypertensive Ren-2 rats that carry two copies of the mouse renin-2 gene and exhibit moderate hypertension, myocardial hypertrophy, and excessive fibrosis likely due to Ang-II overproduction, intravenous administration of liposomal CL selectively depleted blood monocytes and myocardium macrophages. Macrophage depletion increased cardiac cell apoptosis and myocardial $CD4^{+}$ T-cell accumulation (**Figure 3**), thereby worsening the rat cardiac function with reduced EF, fractional shortening (FS), and heart weight/bodyweight (HW/BW) ratio, and increased end diastolic volume at 6 weeks after macrophage depletion. Therefore, macrophage depletion associated with myocardial dysfunction in hypertensive rats (Zandbergen et al., 2009; **Figure 3**). Yet, opposite observations were also made. In salt-sensitive Sabra rats with high-salt diet-induced cardiac hypertrophic mice, macrophage depletion with CL liposomes for 4 weeks blocked the elevation of systolic blood pressure, reduced cardiac fibrosis and hypertrophy, and protected cardiac function (Kain et al., 2016). Similar observations were made from the same rats that underwent TAC-induced cardiac hypertrophy. At 3 weeks after surgery with and without macrophage depletion, CL treatment also protected mice from LV hypertrophy with significantly reduced cardiac fibrosis and expression of hypertrophic genes, including TGF-β, collagen type IIIα-1, and atrial natriuretic factor (ANF) (Kain et al., 2016). These conflicting results remain unexplained. It is probably due to the differences in rat strains. Under the same treatments of high-salt diet or TAC-induced cardiac hypertrophy, CL-mediated macrophage depletion in Sprague Dawley rats did not affect myocardial T-cell accumulation, cardiac cell death, or cardiac function, although these results were not explained (Zandbergen et al., 2009).

Molecular and Cellular Mechanisms of Monocyte and Macrophage Actions

Monocytes and macrophages regulate cardiac fibrosis by clearing dead cells and debris, secreting growth factors and cytokines, controlling fibroblast activation, and producing proteases for ECM degradation (Kagitani et al., 2004; Wynn and Barron, 2010; Ren et al., 2011). Macrophages and monocytes are rich sources for pro-inflammatory cytokines IL1β and TNF-α; anti-inflammatory cytokines and growth factors IL10, PDGF, and TGF-β; and proteases MMP2 and many other MMPs (Fadok et al., 1998; Huynh et al., 2002). These macrophage- and monocyte-derived cytokines, growth factors, and proteases are released during the process of cardiomyocyte hypertrophy and fibroblast activation to promote cardiac cell death and initiate the ingestion of apoptotic cardiomyocytes and necrotic debris.

Cardiac macrophages contain steady-state $CCR2^{-}CD11c^{low}Ly6C^{-}$ resident macrophages that proliferate *in situ* under physiological conditions (Liao et al., 2018)

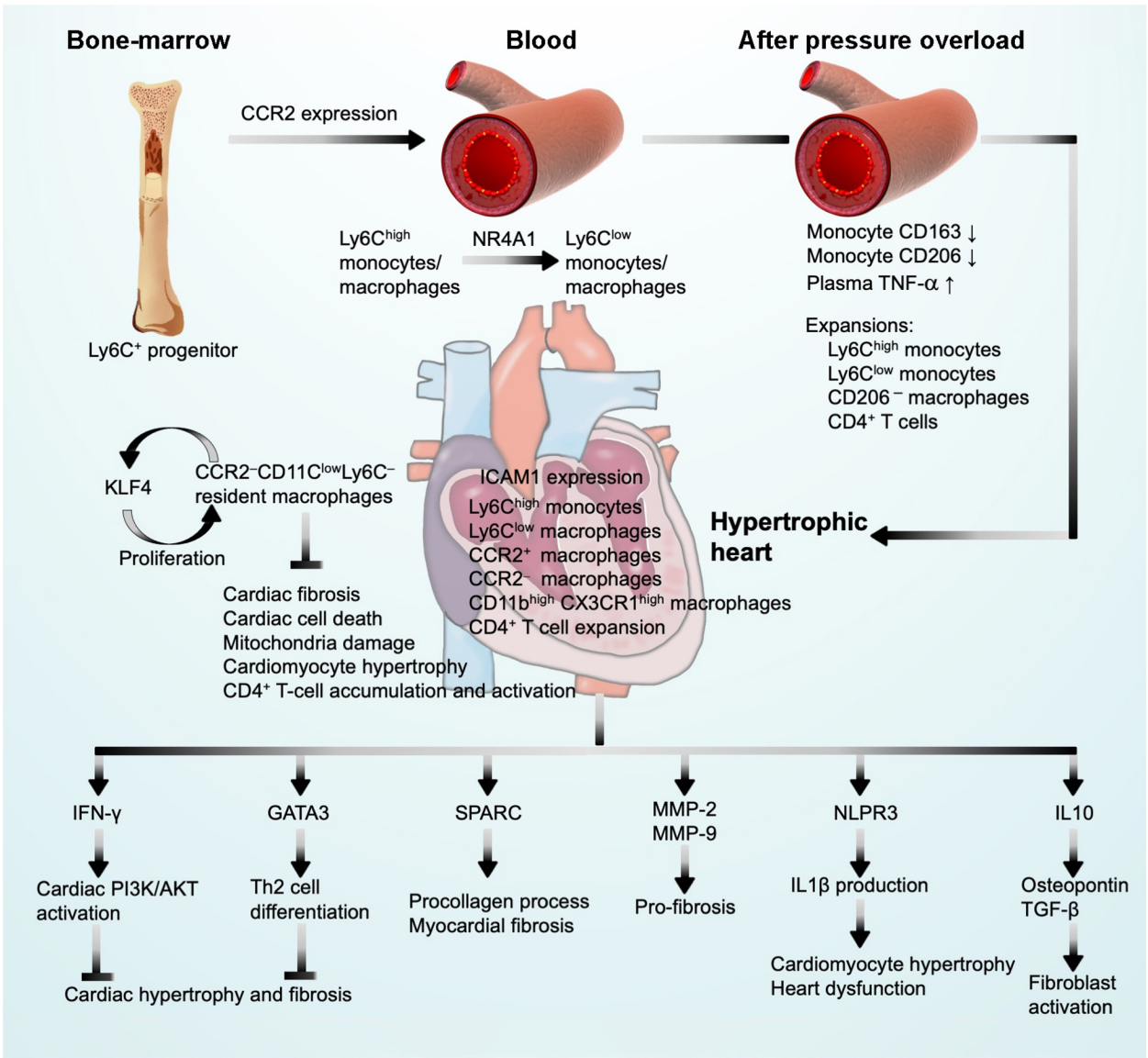

FIGURE 3 | Monocyte and macrophage function in pressure overload-induced cardiac hypertrophy and fibrosis. CCR2 expression drives Ly6C$^+$ monocyte progenitor trafficking to peripheral blood where monocyte differentiation may occur. After pressure overload injury, blood monocytes undergo phenotypic alterations and monocyte/macrophage expansion. These cells infiltrate into the heart where they produce IFN-γ and GATA3 to block cardiac hypertrophy and fibrosis, produce SPARC, MMP-2, MMP-9, IL1β, and IL10 to promote cardiac hypertrophy and cardiac fibrosis, leading to cardiac dysfunction, and express KLF4 to promote macrophage self-proliferation.

(**Figure 1B**, bottom panel, and **Figure 3**). Under inflammatory conditions, Ly6C^{high} monocytes infiltrate into the myocardium and differentiate into CCR2$^+$ and CCR2$^-$ mature macrophages that account for the majority of cardiac macrophages to coordinate cardiac inflammation (Epelman et al., 2014; **Figure 3**). Several studies have reported that the secretory molecules from macrophages contributed to the development of cardiac hypertrophy and fibrosis. It is the CCR2$^+$ macrophages that produce IL1β *via* the NLPR3 inflammasome mechanism under cardiac stress as a mechanism to promote cardiomyocyte hypertrophy and contractile dysfunction (Palmer et al., 1995; Harada et al., 1999; **Figure 3**). Therefore, blocking monocyte cardiac influx and consequent CCR2$^+$ macrophage expansion was cardioprotective, whereas complete depletion of macrophages that also target resident CCR2$^-$ macrophages abolished macrophage cardioprotective function (Kaikita et al., 2004; van Amerongen et al., 2007). Macrophages are the main source of MMPs, including MMP-1, -7, -8, -9, -12, and -13, among which MMP-2 might be the most relevant pro-fibrotic MMP (Heymans et al., 2005; Lim et al., 2006; Murray and Wynn, 2011; Matsusaka et al., 2016). Deficiency of MMP-2 reduced TAC-induced anterior and posterior wall thickness, LV mass,

LV systolic and diastolic blood pressures, LV weight/BW ratio, cardiomyocyte dilation, and cardiac fibrosis (Matsusaka et al., 2016). Under a similar condition, MMP-9 deficiency showed moderate effect on TAC-induced hypertrophy in mice (Heymans et al., 2005; **Figure 3**). Macrophages can also resolve fibrosis in the process of reparative phase by expressing high levels of TIMPs and MMP-13 (D'Angelo et al., 2001). Salty drinking water unilateral nephrectomy aldosterone (SAUNA) infusion-induced hypertension or natural aging for 18 or 30 months increased heart macrophage and Ly6C^{high} monocyte accumulation. CCR2 deficiency significantly blunted such accumulations. These cardiac macrophages express IL10. Selective depletion of IL10 in cardiac macrophages in *Cx3cr1 Il10*$^{-/-}$mice improved SAUNA-induced cardiac fibroblast activation, collagen deposition, and LV diastolic dysfunction. A mechanistic study suggested that IL10 controls cardiac macrophage expression of osteopontin and TGF-β, thereby inducing cardiac fibroblast expression of fibrotic proteins collagen and fibronectin (Hulsmans et al., 2018; **Figure 3**). Macrophage-derived SPARC (secreted protein acidic and rich in cysteine) is an ECM-associated protein that affects cardiac collagen disposition and cardiac stiffness (**Figure 3**). Macrophages represent a source of increased myocardium SPARC in a model of pressure overload-induced cardiac fibrosis. SPARC production in the myocardium followed a time course after pressure overload induction. SPARC production was not significantly changed at the beginning of pressure overload induction (3 days), but increased at 1 and 4 weeks following pressure overload. This expression pattern coincided with myocardium accumulation F4/80-positive macrophages as detected by immunohistochemistry and flow cytometry (McDonald et al., 2018; **Figure 1B**, upper panel).

In contrast to aforementioned pro-hypertrophic molecules, IFN-γ is a common pro-inflammatory but anti-hypertrophic cytokine expressed in CD68$^+$ macrophages. IFN-γ-deficient mice subjected to TAC resulted in a remarkable maladaptation of hypertrophy and fibrosis. Mechanistic studies showed that the cardiac activation of the PI3K/Akt signaling pathways is a key signaling pathway in IFN-γ-controlled compensatory hypertrophy (Kimura et al., 2018; **Figure 3**). GATA3 acts as a zinc-finger transcription factor and mediates Th2 cell differentiation (**Figure 3**). In T cells, GATA3 is specifically induced by IL4 through activation of its proximal promoter (Scheinman and Avni, 2009). Recent studies showed that GATA3 also played important roles in monocyte and macrophage pathobiology during cardiac remodeling (Yang et al., 2018). In myeloid-specific GATA3-deficient mice that were generated by crossing GATA3 floxed (*GATA3*$^{fl/fl}$) mice with LysM^{Cre} mice, TAC-induced cardiac dysfunction and adverse LV remodeling were much improved compared with those in the *LysM*^{Cre} control mice. A large number of pro-inflammatory Ly6C^{high} monocytes and macrophages and fewer reparative Ly6C^{low} macrophages are located in the myocardium of *LysM*^{Cre} control mice (Yang et al., 2018).

In pressure overload-induced hypertrophic mice, recruitment of Ly6C^{high}CCR2$^+$ monocytes caused significant expansion of cardiac CD3$^+$CD8$^+$ and CD3$^+$CD4$^+$ T cells. Anti-CCR2 antibody treatment did not affect such expansion in the myocardium, although this antibody blocked the expansion of these T cells in the heart draining lymph nodes (Patel et al., 2018), suggesting that cardiac T-cell expansion does not involve CCR2. Earlier studies showed that pressure overload activated cardiac T cells. The kinetics of cardiac T-cell infiltration associated with systolic dysfunction (Nevers et al., 2015). Using lymphocyte deficient RAG2-deficeint mice, T-cell-deficient *TCR*α$^{-/-}$ mice, CD4$^+$ T-cell-selective depleted mice, CD8$^+$ T-cell-selective depleted mice, and T-cell co-stimulation blocker abatacept, studies showed that cardiac CD4$^+$ T cells contribute to cardiac hypertrophy by promoting cardiac tissue fibrosis and inflammation (Laroumanie et al., 2014; Nevers et al., 2015; Kallikourdis et al., 2017). These results present additional mechanisms of cardiac monocyte infiltrates in pressure overload-induced hypertrophy (**Figure 3**).

Therapies by Targeting Monocytes and Macrophages

Therapeutic interventions targeting monocytes and macrophages by selectively depleting cardiac monocytes and macrophages or blocking the infiltration of circulating monocytes and macrophages might be promising approaches to alleviate pressure overload-induced cardiac hypertrophy and fibrosis. Targeting macrophage adhesion molecules or chemokine receptors that mediate macrophage adhesion and migration tested these possibilities. ICAM-1 is implicated in macrophage recruitment. In SAC-induced pressure overload and cardiac hypertrophy in rats, ICAM-1 was expressed in the intramyocardial coronary arteries at 1 day after surgery and peaked in 3 days. Immunohistochemistry indicated that CD68$^+$ macrophages were clustered next to these arteries. Antibody-mediated neutralization of ICAM-1 blocked myocardial macrophage accumulation and reduced fibroblast proliferation, TGF-β1 expression, and myocardial fibrosis, although arterial pressure and LV or cardiomyocyte hypertrophy did not differ from those treated with control IgG (Kuwahara et al., 2003).

Targeting monocyte/macrophage infiltration has also been proven effective to mitigate cardiac damage after pressure overload-induced hypertrophy. In chemokine Fraktalkine receptor CX3CR1-deficient *Cx3cr1*$^{GFP/GFP}$ mice, TAC-induced reductions in EF and cardiac output were fully recovered, along with reduced HW/BW, cardiac damage marker aldolase, cardiac hypertrophy and its marker B-type naturetic peptide (BNP), and cardiac fibrosis (Weisheit et al., 2021). Deficiency of CCR2 blocked cardiac tissue macrophage infiltration, increased myocardium capillary density, and improved cardiac function, although it did not affect cardiac tissue fibrosis and cardiomyocyte hypertrophy (Liao et al., 2018). These observations support a detrimental role of Ly6C^{high}CX3CR1$^+$CCR2$^+$ classic monocytes and macrophage in exacerbating TAC-induced cardiac hypertrophy. Interestingly, global ablation of macrophages together with DCs with AP20187 starting at 2 weeks after TAC surgery showed moderate effect in cardiac function and fibrosis (Patel et al., 2017). These negative results suggest that cardiac macrophages play a different role at different time courses after cardiac injury. Cardiac

macrophage depletion before macrophages peak at 1 week after TAC surgery may yield different results. It is also possible that different types of macrophages act differently in pressure overload-induced hypertrophy. In TAC-treated mice, immediate depletion of cardiac macrophages with CL reduced anterior wall thickness, LV volume and mass, cardiomyocyte thickness, blood wall thickness, and LV fibrosis (Kain et al., 2016). In the same model, intraperitoneal injection of CCR2 antagonist RS504393 starting at day 3 after TAC surgery for 4 days blocked cardiac macrophage accumulation, reduced cardiac vascular cell adhesion protein 1 (VCAM-1) expression, reduced HW/TL and cardiac fibrosis, and improved cardiac hypertrophy and cardiac function. Similar observations were made when the mice were treated with anti-CCR2 antibody (Patel et al., 2018). Together, results from these studies suggest that it is only effective to minimize pressure overload-induced cardiac injury by targeting monocyte/macrophage chemotaxis before or immediately after the pressure overload injury.

NEUTROPHILS

Neutrophils are the first leukocytes that appear in the myocardium following pressure overload-induced hypertrophy, within 3 days after the injury (Weisheit et al., 2014, 2021) (**Figure 1A**, bottom panel). In patients with concentric or eccentric LV hypertrophy, blood neutrophil-to-lymphocyte ratio (NLR) was elevated and correlated strongly with the LV mass index ($r = 0.508$, $p < 0.001$) (Afşin et al., 2019). Neutrophil transmigration is dependent on endothelial cell activation and subsequent expression of adhesion molecules (Woodfin et al., 2009; Filippi, 2019), a process that is enhanced by inflammatory stimuli, such as TNF-α, IL1β, and even MC-derived histamine (Mackay et al., 1993; Asako et al., 1994; Sahni et al., 2005). In an autocrine fashion, neutrophil activation stimulates cardiac fibroblast release of IL6 to upregulate endothelial cell ICAM-1 expression as a mechanism to attract further neutrophils and macrophages (Hofbauer et al., 2019).

Neutrophil Function in Pressure Overload-Induced Cardiac Hypertrophy and Fibrosis

In response to pressure overload, alterations in myocardium neutrophil contents associate with cardiac hypertrophy and fibrosis. In a mouse inter-renal aortic banding-induced LV hypertrophy model, histopathological and immunohistochemical examinations revealed that macrophage and neutrophil infiltration in LV and RV appeared next to the coronary arteries, containing abundant ICAM-1 immunostaining signals in the first 3 days after injury, long before vascular wall thickening, perivascular fibrosis (10 days), and cardiomyocyte hypertrophy (28 days). Cardiac neutrophils remained high until 42 days after aortic banding (Higashiyama et al., 2007). Similar observations were made in mice after TAC-induced cardiac hypertrophy. Cardiac neutrophils peaked in 3 days after TAC surgery, followed by macrophages in 6 days as determined by flow cytometry and fluorescence microscopy. Like those in inter-renal aortic banding-induced LV hypertrophic mice, cardiac neutrophil contents remained high from 3 to 21 days after TAC surgery, and possibly much longer (Weisheit et al., 2014; **Figure 1A**, bottom panel).

Myocardium neutrophils in hypertrophic heart play detrimental roles. In TAC-injured hypertrophic mice, neutrophil depletion with injection QOD of anti-mouse Ly6G antibody starting from 2 days before surgery for 2 weeks significantly reduced HW/TL ratio, posterior wall thickness, LV systolic and diastolic diameters, and cardiomyocyte hypertrophy, and increased EF. In 2 days after TAC, FACS analysis showed that neutrophil depletion blocked cardiac monocyte and macrophage accumulation (Wang et al., 2019b). Wnt signaling regulates cell proliferation, differentiation, polarity, adhesion, and motility (van Amerongen and Nusse, 2009; Wend et al., 2010). Wnt5a is a noncanonical Wnt that stimulates neutrophil chemotactic migration (Jung et al., 2013). Depletion of Wnt5a in myeloid cells in $Wnt5a^{f/f}LysM^{Cre/+}$ mice significantly blocked cardiac inflammatory cell (neutrophils, $Ly6C^{hi}$ monocytes, and macrophages) infiltration and myocardium pro-inflammatory cytokine and chemokine (IL1β, IL6, CXCL1, CXCL2, CXCL5, and CCL2) expression, and repaired TAC-induced cardiac dysfunction with reduced cardiomyocyte hypertrophy and cardiac fibrosis at 1, 4, and 8 weeks after TAC injury. In contrast, LysM-Cre-mediated myeloid cell overexpression of Wnt5a enhanced TAC-induced myocardium neutrophil accumulation and pro-inflammatory cytokine and chemokine expression and worsened TAC-induced cardiac dysfunction, cardiac cell hypertrophy, and fibrosis (Wang et al., 2019b). Yet, the limitation of this study is that the use of $LysM^{Cre/+}$ mice is not selective to neutrophils, but rather all myeloid cells. A better model is required.

The modern technique allowed detailed analysis of myocardium inflammatory infiltrates after pressure overload-induced cardiac hypertrophy. Single-cell RNA sequencing analysis of cardiac $CD45^{+}$ cells revealed 20 clusters of immune cells using the two-dimensional t-distributed stochastic neighbor embedding visualization. This technique demonstrated the presence of two distinct neutrophil clusters in the myocardium from sham-operated or TAC-treated mice. Although their functional differences in hypertrophic heart were not compared, both clusters of neutrophils showed different gene expression profiles. Both clusters expressed the neutrophil marker Csf3r and got expanded at 4 weeks after TAC injury. One cluster of neutrophils expressed high levels of chemokine receptor Ccr2 but not Ccr1 and Cxcr2. These cells also expressed the cell activation marker CD69. Unsupervised gene signature analysis revealed significant correlation of this cluster of neutrophils with transcription activity and antigen presentation signatures. In contrast, the other cluster of neutrophils expressed high levels of Ccr1 and Cxcr2 but low levels of Ccr2. These cells did not express CD69, but anti-fibrotic MMP-9 and arginase-2, essential for IL10-mediated anti-inflammatory responses (Dowling et al., 2021). Therefore, these two populations of neutrophils represent pro-inflammatory and anti-inflammatory activities in hypertrophic hearts and expand parallelly after pressure

overload injury (Martini et al., 2019; **Figure 4**), similar to the Ly6C^{high} and Ly6C^{low} pairs of monocytes/macrophages. Such unique expression profile of cell surface chemokine receptors on these two neutrophil populations suggests that these neutrophils use different sets of chemokines for their migration and cardiac accumulation. CCR2$^+$ pro-inflammatory neutrophils may predominantly use CCL (e.g., CCL2 and CCL3) as their chemokines, whereas CCR1$^+$CXCR2$^+$ anti-inflammatory neutrophils may use both CCL (e.g., CCL2 and CCL3) and CXCL (e.g., CXCL1, CXCL2, and CXCL8) chemokines to mediate their chemotactic migration (Capucetti et al., 2020; **Figure 4**).

Pressure overload-induced hypertrophy and consequent debanding (pressure unload) mimic human aortic stenosis and later aortic valve replacement. Different from those of only pressure overload-induced cardiac hypertrophy, neutrophils played a cardioprotective role in pressure unloaded hypertrophic mice when mice were treated with granulocyte colony-stimulating factor (G-CSF). G-CSF is a hematopoietic cytokine that regulates the proliferation, differentiation, and survival of myeloid progenitor cells and plays an eminent role in the regulation and production of neutrophil granulocytes. G-CSF treatment significantly reversed pressure overload-induced cardiac dysfunction and remodeling accompanied by a selective release of IL1β. Regression of cardiac hypertrophy by G-CSF generated a considerable myocardium neutrophil infiltration. A mechanistic study suggested that G-CSF-induced neutrophil infiltration increased myocardium IL1β expression that induced cardiac fibroblast expression of collagenases MMP-2 and MMP-9 or other ECM-degrading proteases, thereby assisting the regression of cardiac fibrosis (Szardien et al., 2012; **Figure 4**).

Mechanisms of Neutrophil Action

In response to the acute inflammation, neutrophils are recruited to eliminate dead cells and matrix debris under normal reparative conditions (Bratton and Henson, 2011; Sreejit et al., 2020). However, excessive accumulation of neutrophils or delayed clearance of debris accelerates cardiomyocyte injury, which leads to further fibrotic process (Bratton and Henson, 2011). Similar to the two clusters of neutrophils described in mouse hypertrophic hearts (Martini et al., 2019), earlier studies reported pro-inflammatory N1 neutrophils and anti-inflammatory N2 neutrophils from mouse infarcted hearts (Ma et al., 2016). While N1 neutrophils express pro-inflammatory CCL3, CCL5, IL1β, IL6, IL12, and TNF-α at the early phase of heart infarction, N2 express anti-inflammatory CD206, IL10, TGF-β, arginase-1, and Ym1 at the late phase of heart infarction. FACS, immunofluorescent double staining, and RT-PCR confirmed that N1 neutrophils were Ly6G$^+$CD206$^-$ that can be induced by LPS together with IFN-γ. N2 neutrophils were Ly6G$^+$CD206$^+$ that can be induced by IL4 (Ma et al., 2016), similar to M1 and M2 macrophages that we reported previously (Zhou et al., 2015). Therefore, the roles of N1 and N2 neutrophils in hypertrophic hearts may mimic those of M1 and M2 macrophages or Ly6C^{high} and Ly6C^{low} monocytes, although limited information is available to support this comparison.

N1 neutrophils degranulate and release MMPs, elastase, proteoglycans, and cathepsin G that mediate collagenous and non-collagenous connective tissue catabolism (Ma et al., 2013). In response to pressure overload injury, neutrophilic nicotinamide adenine dinucleotide phosphate (NADPH) oxidase gets activated (Li et al., 2002), leading to neutrophil degranulation and release of pro-fibrotic proteases and reactive oxygen species (ROS) (Ciz et al., 2012). Necrotic cell death after pressure overload (Nadal-Ginard et al., 2003) release adenosine triphosphate to activate NLRP3 inflammasomes as a mechanism to develop an inflammatory microenvironment for neutrophils to adhere and infiltrate (McDonald et al., 2010; **Figure 4**). In contrast, apoptotic cells can also release lactoferrin, a pleiotropic glycoprotein with anti-inflammatory properties and annexin A1 to block neutrophil adhesion and migration, thereby minimizing cardiac damage from pressure overload (Bournazou et al., 2009; Qin et al., 2019). Similarly, apoptotic neutrophils or tissue macrophages also release anti-inflammatory lipid mediators (lipoxins and resolvins) to increase apoptotic neutrophil CCR5 expression to remove neutrophil chemokine CCL3 and CCL5 as a mechanism to block consequent neutrophil migration and recruitment (Soehnlein and Lindbom, 2010; **Figure 4**).

The time course of cardiac neutrophil infiltration may impact cardiac function and remodeling differently after hypertrophic injury. Although there is currently no direct evidence, this hypothesis has been tested in other cardiac injury models. During the acute phase of eccentric hypertrophy in rats induced by aortocaval fistula (ACF), anti-rat neutrophil antibody-induced neutrophil depletion in LV myocardium 2 days before the surgery prevented myocardium MMP activation, collagen loss, and cardiomyocyte apoptosis at the first 24 h after the surgery and attenuated the development of eccentric hypertrophy at 2 and 3 weeks. These observations suggest that neutrophils enhance the progress of ACF-induced rat cardiac hypertrophy. In contrast, sustained neutrophil depletion over 4 weeks resulted in adverse cardiac remodeling with further increases in cardiac dilatation and macrophage infiltration (Kolpakov et al., 2009). In mouse infarcted hearts, pro-inflammatory Ly6G$^+$ N1 neutrophils accumulated at day 1 after myocardial infarction (MI) and then sharply reduced to the baseline at 7 days after infarction. In contrast, anti-inflammatory Ly6G$^+$CD206$^+$ N2 neutrophils started accumulating at 5 days after infarction and peaked at 7 days after infarction (Ma et al., 2016). The neutrophil populations at the early and late phases of cardiac hypertrophy may act differently. Chronic anti-neutrophil therapy against cardiac remodeling might not achieve the expected benefits.

Similar complications occurred at the molecular levels. Neutrophils produce S100a8/a9 that acts as an initial pro-inflammatory factor to trigger cardiac inflammation and fibrosis after pressure overload injury. Immunofluorescent staining revealed S100a8/a9 expression primarily from infiltrated neutrophils in mouse heart at 1 day after Ang-II infusion. Mouse cardiomyocytes and cardiac fibroblasts all express the S100a8/a9 receptors, including RAGE product and TLR4, independent of Ang-II stimulation (Wu et al., 2014). Therefore, neutrophil-derived S100a8/a9 may act on both major cardiac cells. To cardiac fibroblasts, S100a8/a9 induced the expression of a panel of cytokines and chemokines by activating the inflammatory nuclear factor-κB (NF-κB) pathway. In mice,

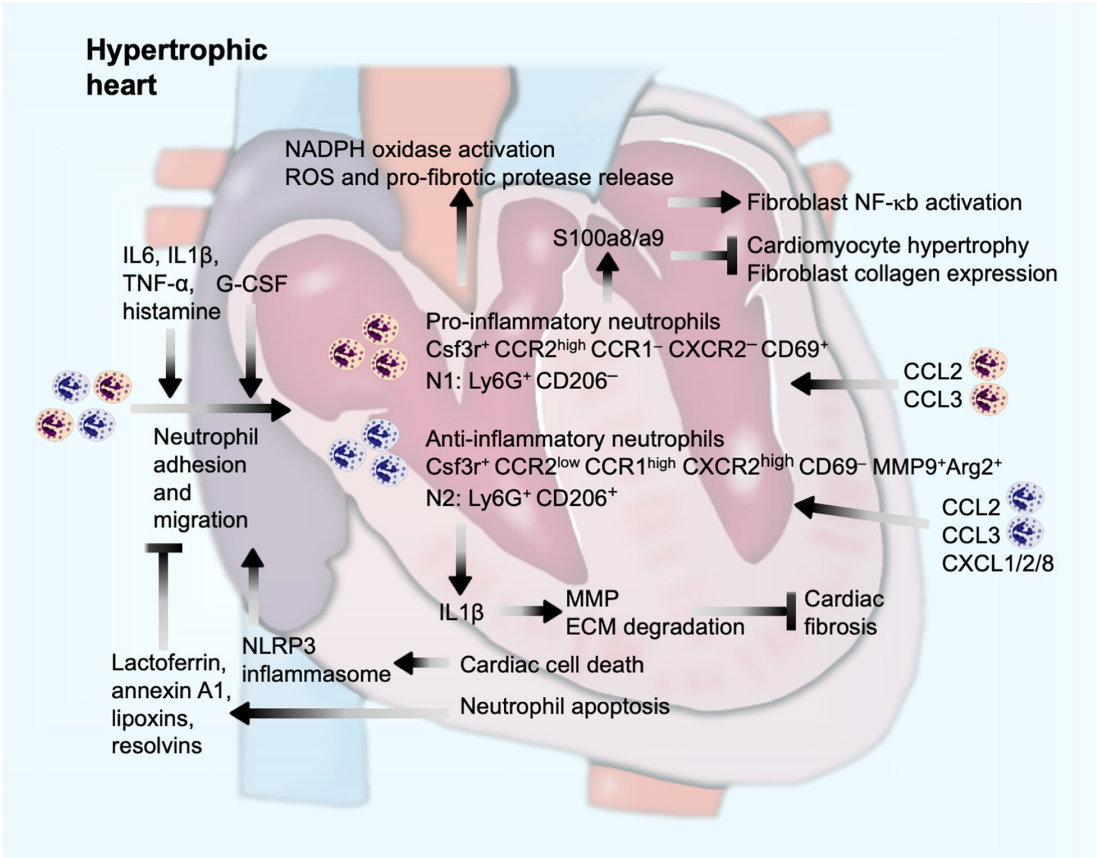

FIGURE 4 | Neutrophil function in pressure overload-induced cardiac hypertrophy and fibrosis. Cardiac injury and inflammatory molecules promote neutrophil adhesion and migration into the heart, a process that can be enhanced by G-CSF and neutrophil-derived Wnt5a, but blocked by lactoferrin and anti-inflammatory lipid-mediators from apoptotic cardiac cells or neutrophils. Inside the heart, neutrophils produce IL1β to promote ECM proteolysis and reduce cardiac fibrosis, induce activation of NADPH oxidase and release of ROS and pro-fibrotic proteases, or produce S100a8/a9 to induce fibroblast inflammatory activation or to block cardiomyocyte hypertrophy or fibroblast procollagen expression.

S100a8/a9 neutralization with its antibody blocked Ang-II infusion-induced NF-κB activation, inflammatory cell ($CD45^+$, $CD11b^+$, $CD45^+CD11b^+$, and $Gr1^+$ cells) infiltration, and cytokine (IL1β and TNF-α) and chemokine (CCL2, CCL3, CCL5, and CCL7) production, in addition to reduced cardiac interstitial fibrosis and cardiac cell hypertrophy (Wu et al., 2014; **Figure 4**). In contrast, S100a8/a9 plays a protective role against rat cardiomyocyte hypertrophy and cardiac fibroblast collagen expression. To cultured rat neonatal ventricular cardiomyocytes, norepinephrine induced cardiomyocyte hypertrophy, including elevated expression of atrial natriuretic peptide (ANP) and β-myosin heavy chain. Use of S100a8/a9 significantly blocked these activities of norepinephrine. S100a8/a9 RNA silencing exacerbated norepinephrine-induced rat neonatal cardiomyocyte hypertrophy (Wei et al., 2015; **Figure 4**). The same study also showed cardioprotective activity of S100a8/a9 against rat cardiac fibroblasts. Use of S100a8, S100a9, or S100a8/a9 significantly blocked the expression of pro-collagen I and III from cultured rat cardiac fibroblasts (Wei et al., 2015). It remains unclear why this study yielded opposite conclusion from those of Wu et al. (2014) or those from most other studies (Volz et al., 2012) besides the fact that this study used rat cells. Together, the role of neutrophils in cardiac hypertrophy remains elusive.

DENDRITIC CELLS

Dendritic cells are professional antigen-presenting cells that are capable of sensing chemoattracting inflammatory signals to mobilize and migrate to the regions of tissue injury, where DCs phagocytose dead cells and matrix debris as macrophages do in addition to their professional function to activate T cells (Banchereau et al., 2000). Common DC progenitors are heterogeneous, including those IFN-α-producing pDCs and cDCs (often called myeloid DCs) (Manh et al., 2013). CCR1 and CCL3 mediate the homing of immature DCs, while CCR7 and CXC-chemokine receptor type 4 (CXCR4) regulate mature DC homing to regional lymph nodes (Sallusto et al., 1999; Randolph et al., 2008; Delgado-Martín et al., 2011). Mature DCs travel to secondary lymphoid tissue to deliver antigenic peptides to T cells. T cells are stimulated by antigenic peptides bound to the major histocompatibility complex (MHC) molecules on DCs and

then release IL12, IL23, and IL27 after activation (Curtsinger and Mescher, 2010; Kimura et al., 2016; Li et al., 2019). T-cell activation results in T-cell proliferation and differentiation into their subtypes, such as regulatory T cells (Tregs), T helper cells (Th), and killer T cells.

DCs in Pressure Overload-Induced Cardiac Hypertrophy and Fibrosis

In response to pressure overload, bone-marrow-derived $CD11c^+$ DCs promote cardiac hypertrophy and fibrosis. In TAC-induced cardiac hypertrophic mice, the number of $CD11c^+$ cells and the percentage of $CD11c^+MHC\text{-}II^+$ (major histocompatibility complex class II molecule positive) DCs were increased in the LV myocardium, spleen, and peripheral blood. Diphtheria toxin (DT)-induced depletion of $CD11c^+$ DCs in irradiated WT recipient mice that received bone marrow transfer from CD11c-DTR/GFP transgenic donor mice significantly blocked TAC-induced cardiac dysfunction along with reduced cardiomyocyte hypertrophy, cardiac fibrosis, LV remodeling, and LV myocardium $CD45^+$ cells, $CD11b^+$ cells, $CD8^+$ T cells, or activated effector $CD44^+CD8^+$ T cells at 24 weeks after TAC injury. LV tissue homogenate from hypertrophic mice promoted DC activities in activating $CD4^+$ and $CD8^+$ T cells. These observations suggest that bone-marrow-derived $CD11c^+$ DCs play a maladaptive role in hemodynamic overload-induced cardiac inflammation, hypertrophy, and fibrosis through the presentation of cardiac self-antigens to T cells (Wang et al., 2017).

Time course study tested DC expansion in different organs after TAC-induced hypertrophy in mice. $CD11c^+MHC\text{-}II^+$ cDCs accumulated in the heart tissue in a biphasic manner, with peaks at both early (1 week) and late (8 weeks) phases. In contrast, $CD11c^{low}MHC\text{-}II^+B220^+$ pDCs peaked at 1 week after TAC surgery (**Figure 1A**, bottom panel). Although studies did not test whether cDCs and pDCs acted differently in pressure overload-induced hypertrophy, global ablation of DCs together with macrophages with AP20187 at 2 weeks after TAC injury did not affect hypertrophy. AP20187 dimerizes the cytoplasmic Fas fragments to induce Fas-induced mononuclear phagocyte apoptosis (Burnett et al., 2004). Yet, results from this study did not specify the role of cDCs or pDCs and were confounded by non-selective ablation of macrophages and monocytes. Furthermore, DC ablation was performed after the heart DCs passed the first week peak time after TAC surgery (Patel et al., 2017).

In $CD11c^+$DOG mice, DT-induced depletion of DCs reduced aldosterone and high-salt diet-induced cardiac hypertrophy, perivascular fibrosis, expression of cardiac collagen, connective tissue growth factor, lipocalin, and hypertrophic marker BNP (Araos et al., 2019). $CD11c^+$DOG mice are transgenic mice in which the DT receptor gene is expressed under the control of the CD11c promoter (Hochweller et al., 2008). In humans, blood cDC and pDC contents increased in HF patients with NYHA (New York Heart Association) class II with coronary artery disease (CAD) and further increased in patients with NYHA class III–IV, although such increases did not reach statistical significance. Blood cDC, pDC, and total DC counts were highest in NYHA III–IV patients with non-ischemic dilated cardiomyopathy. Yet, blood cDC and pDC counts did not associate with LV EF or systolic or diastolic functions (Athanassopoulos et al., 2009). Together, studies from pressure overload-induced hypertrophy models and human studies support a pathogenic role for DCs in this cardiac disease.

Mechanisms of DC Function

While the pleiotropic myelopoietic growth factor granulocyte-macrophage colony-stimulating factor (GM-CSF) (Zhan et al., 2019) induces immature DC differentiation into myeloid DCs (also called conventional DC1) (Greter et al., 2012; Becher et al., 2016), G-CSF induces conventional DC2 differentiation (Arpinati et al., 2000; Shaughnessy et al., 2006). TNF-α-activated DC1 stimulate Th1 cell activation and release of IFN-γ, whereas TNF-α-treated DC2 activate Th2 cells to release IL4 and IL10 (Arpinati et al., 2000; **Figure 5A**). DCs release different cytokines and express different co-stimulatory molecules to activate different T-cell subsets. For example, DCs release IL12 and IL18 to facilitate Th1 differentiation (Bellinghausen et al., 2003) but release IL13 and TSLP (thymic stromal lymphopoietin) to promote Th2 cell priming and expansion (Bellinghausen et al., 2003; Perrigoue et al., 2009; Okoye and Wilson, 2011). DCs also release IL1β, IL6, IL23, and TGF-β to control Th17 cell differentiation (Terhune et al., 2013) and release IL27 to expand and activate $CD8^+$ T cells, NKT cells, and Th1 cells, but suppress DCs and Th17 cells (Mascanfroni et al., 2013; Wei et al., 2013; Iwasaki et al., 2015; Huang et al., 2019; **Figure 5B**). DC expression of membrane-bound co-stimulatory molecule OX40 ligand (OX40L) provides a critical signal for Th2 survival, proliferation, activation, and cytokine expression (Jenkins et al., 2007; Okoye and Wilson, 2011). DCs also express co-stimulatory molecules Jagged and Delta-like ligands (DLL) that bind to the Notch receptors on T cells to control the differentiation of T-cell subtypes including Th1, Th2, Th9, Th17, and Treg cells (Tindemans et al., 2017; Sun et al., 2018; **Figure 5C**). Therefore, DC differentiation directly controls the differentiation of various T-cell subtypes as an indirect mechanism to contribute cardiac remodeling after pressure overload injury. For example, Th1 cells promote cardiac fibroblast fibrosis (Nevers et al., 2017) whereas Th2 cells regulate B cell-mediated humoral responses against extracellular pathogens in addition to secrete Th2 cytokines IL4, IL5, IL10, and IL13. We recently showed that IL4 protected mouse cardiomyocytes from H_2O_2-induced apoptosis (Liu et al., 2020). As discussed, induced DC depletion in $CD11c^+$DOG mice decreased the expression of profibrotic molecules collagen and connective tissue growth factor in hypertrophic heart (Araos et al., 2019), supporting a role for DCs in cardiac fibrosis. Besides the role of DCs in promoting T-cell activation as a mechanism to activate fibroblasts (Nevers et al., 2017), DCs also promote myofibroblast proliferation, differentiation, and activation (Chia et al., 2012), providing additional mechanisms of DC activity in profibrotic protein expression.

As an essential growth factor that drives DC differentiation (Rossetti et al., 2010), G-CSF improves cardiac function in mice

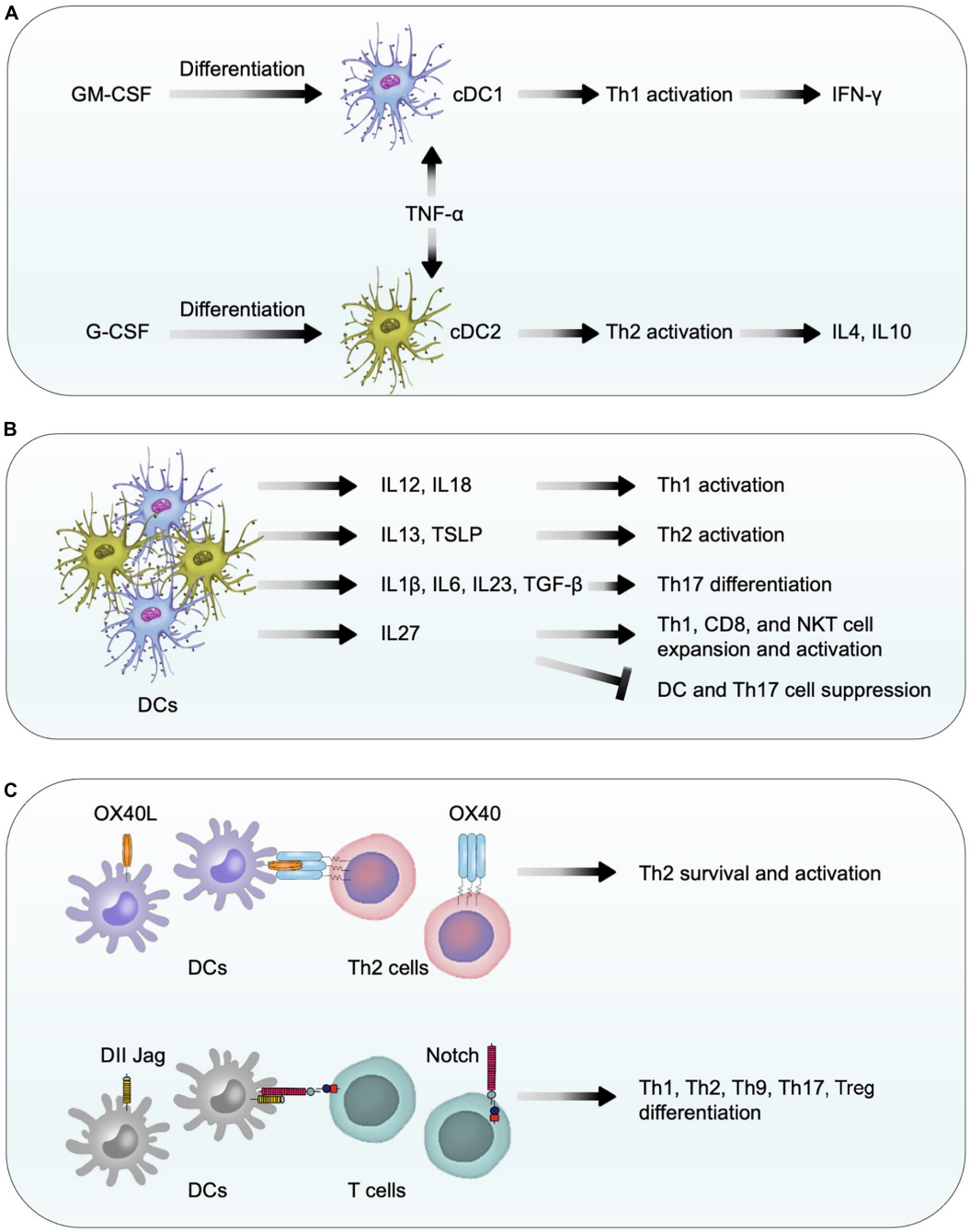

FIGURE 5 | Dendritic cell function in pressure overload-induced cardiac hypertrophy and fibrosis. **(A)** In response to GM-CSF and G-CSF, bone-marrow-derived CD11c^{+} DCs differentiate into conventional DC1 and DC2 cells. TNF-α activates conventional DC1 and DC2 to release Th1 and Th2 cytokines to affect cardiac fibroblast activation, fibrosis, and cell death. **(B)** DCs release different types of cytokines to control T-cell differentiation, expansion, and activation. **(C)** Using co-stimulatory molecules OX40L, Delta-like ligands, and Jagged, DCs promote the survival, differentiation, and activation of different T-cell subtypes.

after pressure overload-induced cardiac hypertrophy. G-CSF-treated mice showed increased cell adhesion molecule VCAM-1 and stem cell factor, reduced cardiac fibrosis and cardiac cell apoptosis, reduced LV posterior wall thickness, and increased cardiac cell post-surgery survival (Huber et al., 2015). A similar study was carried out by giving G-CSF to TAC-treated mice at different times: first 5 days after TAC injury or days 15 to 19. Mice were characterized at 28 days after TAC. Either treatment increased LV mass-to-BW ratio and LV anterolateral wall thickness, but reduced cardiac fibrosis and repaired cardiac function and remodeling at the 28-day time point (Li et al., 2012). Yet, these studies may not test a specific role for DCs in

hypertrophic heart because the pleiotropic growth factor G-CSF also acts on other hematopoietic cells (Bendall and Bradstock, 2014). Therefore, prior studies did not test whether G-CSF activity in DC differentiation played any role in mice or humans receiving G-CSF treatment (Li et al., 2012; Huber et al., 2015; Farhadfar et al., 2020).

EOSINOPHILS

Eosinophils are a subset of circulating innate immune cells that contribute to cardiac cell death and myocardial fibrosis through their abundant mediators, such as TGF-β, EOS cationic protein (ECP), EOS-derived neurotoxin (EDN), major basic protein (MBP), EOS peroxidase (EPO), lysosomal hydrolytic enzymes, EOS peroxidase, and type 2 cytokines (Jacobsen et al., 2012; Rosenberg et al., 2013; Liu et al., 2020; Toor et al., 2020). Blood EOS counts serve as a risk factor for human cardiac diseases such as MI (Kirkeby and Paudal, 1960; Hällgren et al., 1979). EOS were found in autopsy specimens of patients with cardiac rupture post-MI (Atkinson et al., 1985) and in atherectomy specimens from patients with in-stent stenosis (Rittersma et al., 2006). Interestingly, low blood EOS count independently predicts cardiovascular death and correlates negatively with death rates (Cikrikcioglu et al., 2012).

Although a direct evidence of EOS participation in cardiac hypertrophy is not publicly available, two independent studies demonstrated EOS functions in cardiac repair after MI injury. In patients with chest pain, blood EOS counts reduced within the first 12 h. In mice with experimental MI, blood and infarct region EOS counts increased over time. EOS genetic deficiency or antibody-mediated EOS depletion worsened the cardiac functions post-MI along with increased infarct size and myocardium fibrosis, reduced myocardium Th2 cytokines (IL4, IL10, and IL13), and increased myocardium chemokine C-X-C motif ligands (CXCL1 and CXCL2) and inflammatory cells (neutrophils and macrophages) at 4 days post-MI. Intraperitoneal administration of mouse recombinant IL4–anti-IL4 antibody complex did not improve heart function in WT mice, but significantly improved heart function in EOS-deficient Δ*dblGATA* mice (Toor et al., 2020). We reported similar but much more in-depth analyses of EOS function in cardiac remodeling post-MI. Mouse and human EOS protected H_2O_2-induced mouse cardiomyocyte death, blocked TGF-β-induced mouse cardiac fibroblast Smad2 and Smad3 activation, and reduced TNF-α-induced neutrophil adhesion on endothelial monolayer. Mechanistic studies showed that exacerbated cardiac dysfunction post-MI in EOS-deficient Δ*dblGATA* mice can be fully recovered by giving mice EOS cationic protein mEar1 (mouse EOS-associated-ribonuclease-1) or adoptive transfer of EOS from WT mice, but not those from IL4-deficient ($Il4^{-/-}$) mice, suggesting a role for EOS-derived mEar1 and IL4 in repairing cardiac injury. In cultured mouse cardiomyocytes, $Il4^{-/-}$ EOS or EOS pretreated with mEar1 antibody failed to block H_2O_2-induced cell death. Although recombinant IL4 did not affect TGF-β-induced Smad2 and Smad3 signaling, EOS from WT, $Il10^{-/-}$, and $Il13^{-/-}$ mice but not EOS from $Il4^{-/-}$ mice effectively blocked TGF-β-induced Smad2 and Smad3 activations in mouse cardiac fibroblasts. Human EOS acted, similarly. Human EOS isolated from human blood dose-dependently blocked hypoxia-induced apoptosis of primary cultured human cardiomyocytes and TGF-β-induced Smad2 and Smad3 signaling in primary human cardiac fibroblasts (Liu et al., 2020; **Figure 6A**). Although a direct test of EOS activity in pressure overload-induced cardiac hypertrophy remains unavailable, studies from mouse MI models (Liu et al., 2020; Toor et al., 2020) suggest that EOS also use IL4 and cationic proteins to block cardiomyocyte death and to control cardiac fibroblast activation.

INVARIANT NATURAL KILLER T CELLS

iNKT cells, a subset of T lymphocytes, are an innate-like T lymphocyte population that recognizes the glycolipid ligands presented from antigen-presenting cells by CD1d, a non-polymorphic MHC-class I-like molecule (Crosby and Kronenberg, 2018). In TAC-induced mouse cardiac hypertrophy, myocardium iNKT cells increased by three- to fourfold. Deficiency of iNKT cells in $J\alpha18^{-/-}$ mice increased LV end systolic and diastolic diameters, reduced LV FS, and increased LV mass. Histological and immunoblot analyses demonstrated that iNKT cell deficiency increased myocardium cardiomyocyte hypertrophy, cardiac fibrosis, and myocardium ERK signaling. iNKT cell deficiency also led to an imbalance of myocardium Th1 and Th2 cytokines with significantly reduced IL10, IFN-γ, and TNF-α (Takahashi et al., 2020; **Figure 6B**).

Use of CD1d-deficient mice indirectly proved a role for iNKT cell in cardiac hypertrophy (Wang et al., 2019a). Mice receiving Ang-II infusion showed cardiac dysfunction (significantly increased EF and FS), increased HW and cardiomyocyte size and expression of hypertrophic molecules ANP and BNP, increased cardiac fibrosis and collagen I and III expression, elevated TGF-β expression and Smad2 and Smad3 activation, and enhanced myocardium macrophage accumulation, NF-κB activation, and inflammatory cytokine expression (IL1β and TNF-α). All these pathological changes became worse in CD1d-deficient mice, but significantly improved when iNKT cells in WT mice were activated by treating mice with α-galactosylceramide (αGC) (**Figure 6B**). WT mice receiving bone marrow transplant (BMT) from CD1d-deficient mice displayed the same phenotypes as the CD1d-deficient mice in Ang-II infusion-induced cardiac dysfunction, hypertrophy, and remodeling. In Ang-II infusion-induced cardiac hypertrophy, administration of recombinant IL10 to CD1d-deficient mice fully reversed the adverse phenotypes of these recipient mice (Wang et al., 2019a). Therefore, like EOS, iNKT cells are another cardioprotective

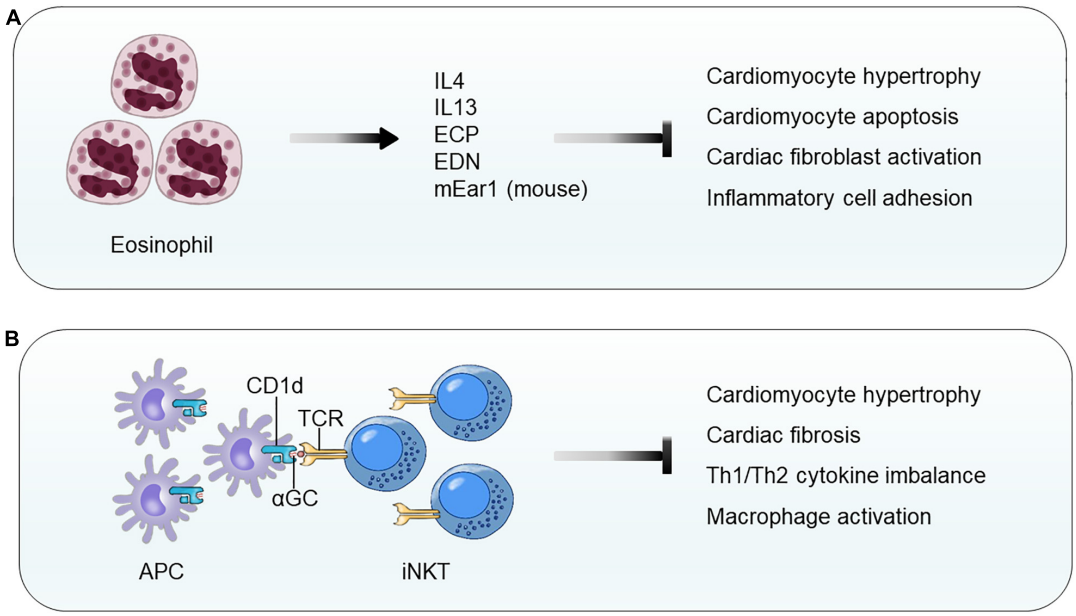

FIGURE 6 | Eosinophil and invariant natural killer T-cell function in pressure overload-induced cardiac hypertrophy and fibrosis. **(A)** EOS release cytokines (IL4 and IL13) and cationic proteins (e.g., human ECP, human EDN, and mouse mEar1) to block cardiomyocyte hypertrophy and apoptosis, cardiac fibroblast activation, and inflammatory cell adhesion and migration. **(B)** CD1d-αGC-mediated activation of iNKT cells blocks cardiomyocyte hypertrophy and apoptosis, Th1/Th2 cytokine imbalance, and macrophage activation.

cell type that prevents or mitigates cardiac hypertrophy, cardiac remodeling, and HF.

CONCLUSION AND FUTURE PROSPECTS

In conclusion, innate immune cells play essential roles in the initiation and progression of cardiac hypertrophy and fibrosis. A great number of studies have focused on various innate immune cell types and their molecules and regulators that are associated with cardiomyocyte hypertrophy and cardiac fibrotic remodeling after the onset of pressure overload. The accumulation of these cells in the atrium or ventricles occurs immediately after the initiation of injury until late phases. Yet, their cardioprotective or cardiodestructive activities can differ depending on the cell types, subtypes, secretory molecules, and time courses of myocardium infiltration. In general, EOS and iNKT cells display cardioprotective activities, but MCs, neutrophils, and DCs exert detrimental functions on cardiomyocytes and cardiac fibroblasts. Macrophages and monocytes possess two sides of influences, promoting the pathological development or negatively regulating cardiac hypertrophy and remodeling, depending on their expression of Ly6C and CD206 in addition to their different surface chemokine receptors. Pressure overload stimulates the secretion of cytokines, metabolites, or growth factors from innate immune cells and resident cardiomyocytes, which together mediate innate immune cell infiltration into the heart. In turn, these cells affect cardiomyocyte pro-hypertrophic pathways and cardiac fibroblast activation.

At the cellular levels, we can use different approaches to add, remove, or regulate the population or activities of each discussed cell type. Yet, the mechanisms by which each innate immune cell participates in pressure overload-induced cardiac hypertrophy and fibrosis have not been fully understood. The hypertrophic or pro-fibrogenic signaling modulated by innate immune cells or their granules and secretories remains unknown. The heterogeneity of different innate immune cell types and subsets provides an explanation for the functional complexities in the process of this cardiac disease. For instance, macrophage and monocyte heterogeneity alone exerts opposite functions depending on the cellular subtypes (**Figure 3**). Neutrophil expression of MMP and S100a8/a9 may reduce ECM accumulation and block cardiomyocyte hypertrophy and cardiac fibroblast pro-collagen expression, although these cells were proven cardiodestructive (**Figure 4**). Similarly, cDCs and pDCs may play opposite roles in cardiac fibrosis and cardiac cell death, although there is currently no study to test their functional differences (**Figure 5**). To date, EOS and iNKT behaved differently from MC, neutrophils, and DCs in hypertrophic heart or other relevant cardiac diseases such as MI. Indirect evidence supports a cardioprotective role for EOS and iNKT in cardiac hypertrophy and fibrosis (**Figures 6A,B**). Yet, it is always possible that future studies may find that some molecules from these cells might exert a cardiodestructive activity. Therefore, new techniques such as lineage-specific genetic tools might be helpful to analyze their specific clusters and precise roles. Furthermore, single-cell sequencing has emerged as a rapidly developing

frontier technology for cellular research. This technology might make it possible to identify innate immune cell heterogeneities and reveal their different cellular kinetics at the single-cell level.

Studies of pressure overload-induced hypertrophy and fibrosis were mostly performed in experimental animals with single genetic background or sex. The genetic background complexities of humans are much more sophisticated than experimental animals. Recent clinical studies support an essential role of inflammation in human cardiovascular diseases. Antibodies against IL1β and IL6 successfully reduced the systemic inflammation and cardiovascular events (Ridker et al., 2017; Ridker et al., 2021). Studies of innate immune cells in experimental models of pressure overload may benefit patient experiencing chronic pressure overload, such as those with HFpEF or hypertension (Mishra and Kass, 2021). Because of the complexities of macrophages, monocytes, and DC subsets, and functional differences of neutrophils at different stages after pressure overload, direct and nonselective targeting of these cells may not benefit patients. Yet, indirect evidence or preliminary studies of MCs, EOS, and iNKT cells in experimental models of pressure overload, HF, or heart infarction suggest the possibility to benefit patients by blocking MC degranulation, targeting MC proteases, using EOS-specific mediators such as EOS cationic protein, and activating iNKT cells with αGC. Therefore, with a better understanding of innate immune cells and their mechanisms regarding pressure overload-induced cardiac remodeling, development of therapeutic strategies to target innate immune cells as novel approaches to attenuate hypertensive cardiac hypertrophy and dysfunction in patients under chronic pressure overload may become possible.

AUTHOR CONTRIBUTIONS

XL wrote the draft and made the figures. G-PS edited the manuscript and designed the figures. JG helped edit the manuscript and the figures. All authors contributed to the article and approved the submitted version.

FUNDING

This study is supported by grants from the Finance Science and Technology Projects of Hainan Province (ZDYF2020214 to JG), the National Natural Science Foundation of China (91939107 and 81770487 to JG), the CAMS Innovation Fund for Medical Sciences (2019-I2M-5-023 to JG), the Open program for Key Laboratory of Emergency and Trauma of Ministry of Education (Hainan Medical University) (Grant KLET-201917 to JG), the National Heart, Lung, and Blood Institute (HL151627 to G-PS), and the National Institute of Neurological Disorders and Stroke (AG063839 to G-PS).

REFERENCES

Abe, M., Kurosawa, M., Ishikawa, O., Miyachi, Y., and Kido, H. (1998). Mast cell tryptase stimulates both human dermal fibroblast proliferation and type I collagen production. *Clin. Exp. Allergy* 28, 1509–1517. doi: 10.1046/j.1365-2222.1998.00360.x

Afşin, A., Asoğlu, R., Kurtoğlu, E., and Kaya, H. (2019). Neutrophil to lymphocyte ratio as a predictor of left ventricular hypertrophy in patients with newly diagnosed hypertension. *J. Hypertens. Manag.* 5:042. doi: 10.23937/2474-3690/1510042

Ainscough, J. F., Drinkhill, M. J., Sedo, A., Turner, N. A., Brooke, D. A., Balmforth, A. J., et al. (2009). Angiotensin II type-1 receptor activation in the adult heart causes blood pressure-independent hypertrophy and cardiac dysfunction. *Cardiovasc. Res.* 81, 592–600. doi: 10.1093/cvr/cvn230

Akers, I. A., Parsons, M., Hill, M. R., Hollenberg, M. D., Sanjar, S., Laurent, G. J., et al. (2000). Mast cell tryptase stimulates human lung fibroblast proliferation via protease-activated receptor-2. *Am. J. Physiol. Lung. Cell. Mol. Physiol.* 278, L193–L201. doi: 10.1152/ajplung.2000.278.1.L193

Alex, L., and Frangogiannis, N. G. (2018). The cellular origin of activated fibroblasts in the infarcted and remodeling myocardium. *Circ. Res.* 122, 540–542. doi: 10.1161/CIRCRESAHA.118.312654

Araos, P., Prado, C., Lozano, M., Figueroa, S., Espinoza, A., Berger, T., et al. (2019). Dendritic cells are crucial for cardiovascular remodeling and modulate neutrophil gelatinase-associated lipocalin expression upon mineralocorticoid receptor activation. *J. Hypertens.* 37, 1482–1492. doi: 10.1097/HJH.0000000000002067

Arpinati, M., Green, C. L., Heimfeld, S., Heuser, J. E., and Anasetti, C. (2000). Granulocyte-colony stimulating factor mobilizes T helper 2-inducing dendritic cells. *Blood* 95, 2484–2490.

Asako, H., Kurose, I., Wolf, R., DeFrees, S., Zheng, Z. L., Phillips, M. L., et al. (1994). Role of H1 receptors and P-selectin in histamine-induced leukocyte rolling and adhesion in postcapillary venules. *J. Clin. Invest.* 93, 1508–1515. doi: 10.1172/JCI117129

Athanassopoulos, P., Balk, A. H., Vaessen, L. M., Caliskan, K., Takkenberg, J. J., Weimar, W., et al. (2009). Blood dendritic cell levels and phenotypic characteristics in relation to etiology of end-stage heart failure: implications for dilated cardiomyopathy. *Int. J. Cardiol.* 131, 246–256. doi: 10.1016/j.ijcard.2007.10.031

Atkinson, J. B., Robinowitz, M., McAllister, H. A., and Virmani, R. (1985). Association of eosinophils with cardiac rupture. *Hum. Pathol.* 16, 562–568. doi: 10.1016/s0046-8177(85)80105-2

Banchereau, J., Briere, F., Caux, C., Davoust, J., Lebecque, S., Liu, Y. J., et al. (2000). Immunobiology of dendritic cells. *Annu. Rev. Immunol.* 18, 767–811. doi: 10.1146/annurev.immunol.18.1.767

Baricos, W. H., Cortez, S. L., Deboisblanc, M., and Xin, S. (1999). Transforming growth factor-beta is a potent inhibitor of extracellular matrix degradation by cultured human mesangial cells. *J. Am. Soc. Nephrol.* 10, 790–795.

Batlle, M., Roig, E., Perez-Villa, F., Lario, S., Cejudo-Martin, P., Garcia-Pras, E., et al. (2006). Increased expression of the renin-angiotensin system and mast cell density but not of angiotensin-converting enzyme II in late stages of human heart failure. *J. Heart. Lung. Transplant.* 25, 1117–1125. doi: 10.1016/j.healun.2006.04.012

Becher, B., Tugues, S., and Greter, M. (2016). GM-CSF: from growth factor to central mediator of tissue inflammation. *Immunity* 45, 963–973. doi: 10.1016/j.immuni.2016.10.026

Bellinghausen, I., Brand, P., Bottcher, I., Klostermann, B., Knop, J., and Saloga, J. (2003). Production of interleukin-13 by human dendritic cells after stimulation with protein allergens is a key factor for induction of T helper 2 cytokines and is associated with activation of signal transducer and activator of transcription-6. *Immunology* 108, 167–176. doi: 10.1046/j.1365-2567.2003.01576.x

Bendall, L. J., and Bradstock, K. F. (2014). G-CSF: from granulopoietic stimulant to bone marrow stem cell mobilizing agent. *Cytokine. Growth. Factor. Rev.* 25, 355–367. doi: 10.1016/j.cytogfr.2014.07.011

Berk, B. C., Fujiwara, K., and Lehoux, S. (2007). ECM remodeling in hypertensive heart disease. *J. Clin. Invest.* 117, 568–575. doi: 10.1172/JCI31044

Bournazou, I., Pound, J. D., Duffin, R., Bournazos, S., Melville, L. A., Brown, S. B., et al. (2009). Apoptotic human cells inhibit migration of granulocytes via release of lactoferrin. *J. Clin. Invest.* 119, 20–32. doi: 10.1172/JCI36226

Bradding, P., and Pejler, G. (2018). The controversial role of mast cells in fibrosis. *Immunol. Rev.* 282, 198–231. doi: 10.1111/imr.12626

Bratton, D. L., and Henson, P. M. (2011). Neutrophil clearance: when the party is over, clean-up begins. *Trends. Immunol.* 32, 350–357. doi: 10.1016/j.it.2011.04.009

Braun, M. U., Szalai, P., Strasser, R. H., and Borst, M. M. (2003). Right ventricular hypertrophy and apoptosis after pulmonary artery banding: regulation of PKC isozymes. *Cardiovasc. Res.* 59, 658–667. doi: 10.1016/s0008-6363(03)00470-x

Burnett, S. H., Kershen, E. J., Zhang, J., Zeng, L., Straley, S. C., Kaplan, A. M., et al. (2004). Conditional macrophage ablation in transgenic mice expressing a Fas-based suicide gene. *J. Leukoc. Biol.* 75, 612–623. doi: 10.1189/jlb.0903442

Capucetti, A., Albano, F., and Bonecchi, R. (2020). Multiple roles for chemokines in neutrophil biology. *Front. Immunol.* 11:1259. doi: 10.3389/fimmu.2020.01259

Caughey, G. H., Raymond, W. W., and Wolters, P. J. (2000). Angiotensin II generation by mast cell alpha- and beta-chymases. *Biochim. Biophys. Acta.* 1480, 245–257. doi: 10.1016/s0167-4838(00)00076-5

Chen, F., Chen, D., Zhang, Y., Jin, L., Zhang, H., Wan, M., et al. (2017). Interleukin-6 deficiency attenuates angiotensin II-induced cardiac pathogenesis with increased myocyte hypertrophy. *Biochem. Biophys. Res. Commun.* 494, 534–541. doi: 10.1016/j.bbrc.2017.10.119

Chia, J. J., Tian, S., and Lu, T. T. (2012). "CD11c+ cells are necessary for myofibroblast maintenance in bleomycin-induced cutaneous fibrosis," in *Proceedings of the ACR/ARHP Annual Meeting Abstract Number 2308*, (Washington, DC).

Chirinos, J. A., Orlenko, A., Zhao, L., Basso, M. D., Cvijic, M. E., Li, Z., et al. (2020). Multiple plasma biomarkers for risk stratification in patients with heart failure and preserved ejection fraction. *J. Am. Coll. Cardiol.* 75, 1281–1295.

Cikrikcioglu, M. A., Soysal, P., Dikerdem, D., Cakirca, M., Kazancioglu, R., Yolbas, S., et al. (2012). Absolute blood eosinophil count and 1-year mortality risk following hospitalization with acute heart failure. *Eur. J. Emerg. Med.* 19, 257–263. doi: 10.1097/MEJ.0b013e32834c67eb

Ciz, M., Denev, P., Kratchanova, M., Vasicek, O., Ambrozova, G., and Lojek, A. (2012). Flavonoids inhibit the respiratory burst of neutrophils in mammals. *Oxid. Med. Cell. Longev.* 2021:181295. doi: 10.1155/2012/181295

Crosby, C. M., and Kronenberg, M. (2018). Tissue-specific functions of invariant natural killer T cells. *Nat. Rev. Immunol.* 18, 559–574. doi: 10.1038/s41577-018-0034-2

Curtsinger, J. M., and Mescher, M. F. (2010). Inflammatory cytokines as a third signal for T cell activation. *Curr. Opin. Immunol.* 22, 333–340. doi: 10.1016/j.coi.2010.02.013

D'Angelo, M., Billings, P. C., Pacifici, M., Leboy, P. S., and Kirsch, T. (2001). Authentic matrix vesicles contain active metalloproteases (MMP). a role for matrix vesicle-associated MMP-13 in activation of transforming growth factor-beta. *J. Biol. Chem.* 276, 11347–11353. doi: 10.1074/jbc.M009725200

Delgado-Martín, C., Escribano, C., Pablos, J. L., Riol-Blanco, L., and Rodríguez-Fernández, J. L. (2011). Chemokine CXCL12 uses CXCR4 and a signaling core formed by bifunctional Akt, extracellular signal-regulated kinase (ERK)1/2, and mammalian target of rapamycin complex 1 (mTORC1) proteins to control chemotaxis and survival simultaneously in mature dendritic cells. *J. Biol. Chem.* 286, 37222–37236. doi: 10.1074/jbc.M111.294116

Desmoulière, A., Geinoz, A., Gabbiani, F., and Gabbiani, G. (1993). Transforming growth factor-beta 1 induces alpha-smooth muscle actin expression in granulation tissue myofibroblasts and in quiescent and growing cultured fibroblasts. *J. Cell. Biol.* 122, 103–111. doi: 10.1083/jcb.122.1.103

Dewald, O., Zymek, P., Winkelmann, K., Koerting, A., Ren, G., Abou-Khamis, T., et al. (2005). CCL2/Monocyte chemoattractant protein-1 regulates inflammatory responses critical to healing myocardial infarcts. *Circ. Res.* 96, 881–889. doi: 10.1161/01.RES.0000163017.13772.3a

Di, Paolo, N. C., and Shayakhmetov, D. M. (2016). Interleukin 1alpha and the inflammatory process. *Nat. Immunol.* 17, 906–913. doi: 10.1038/ni.3503

Dostal, D., Glaser, S., and Baudino, T. A. (2015). Cardiac fibroblast physiology and pathology. *Compr. Physiol.* 5, 887–909. doi: 10.1002/cphy.c140053

Dowling, J. K., Afzal, R., Gearing, L. J., Cervantes-Silva, M. P., Annett, S., Davis, G. M., et al. (2021). Mitochondrial arginase-2 is essential for IL-10 metabolic reprogramming of inflammatory macrophages. *Nat. Commun.* 12:1460. doi: 10.1038/s41467-021-21617-21612

Epelman, S., Lavine, K. J., Beaudin, A. E., Sojka, D. K., Carrero, J. A., Calderon, B., et al. (2014). Embryonic and adult-derived resident cardiac macrophages are maintained through distinct mechanisms at steady state and during inflammation. *Immunity* 40, 91–104. doi: 10.1016/j.immuni.2013.11.019

Fadok, V. A., Bratton, D. L., Konowal, A., Freed, P. W., Westcott, J. Y., and Henson, P. M. (1998). Macrophages that have ingested apoptotic cells in vitro inhibit proinflammatory cytokine production through autocrine/paracrine mechanisms involving TGF-beta. PGE2, and PAF. *J. Clin. Invest.* 101, 890–898. doi: 10.1172/JCI1112

Farhadfar, N., Hsu, J. W., Logan, B. R., Sees, J. A., Chitphakdithai, P., Sugrue, M. W., et al. (2020). Weighty choices: selecting optimal G-CSF doses for stem cell mobilization to optimize yield. *Blood Adv.* 4, 706–716. doi: 10.1182/bloodadvances.2019000923

Fernex, M., and Sternby, N. H. (1964). Mast cells and coronary heart disease. relationship between number of mast cells in the myocardium, severity of coronary atherosclerosis and myocardial infarction in an autopsy series of 672 cases. *Acta Pathol. Microbiol. Scand.* 62, 525–538. doi: 10.1111/apm.1964.62.4.525

Filippi, M. D. (2019). Neutrophil transendothelial migration: updates and new perspectives. *Blood* 133, 2149–2158. doi: 10.1182/blood-2018-12-844605

Frangogiannis, N. G. (2014). The inflammatory response in myocardial injury, repair, and remodelling. *Nat. Rev. Cardiol.* 11, 255–265. doi: 10.1038/nrcardio.2014.28

Frieler, R. A., and Mortensen, R. M. (2015). Immune cell and other noncardiomyocyte regulation of cardiac hypertrophy and remodeling. *Circulation* 131, 1019–1030. doi: 10.1161/CIRCULATIONAHA.114.008788

Frith, J. C., Mönkkönen, J., Blackburn, G. M., Russell, R. G., and Rogers, M. J. (1997). Clodronate and liposome-encapsulated clodronate are metabolized to a toxic ATP analog, adenosine 5'-(beta, gamma-dichloromethylene) triphosphate, by mammalian cells in vitro. *J. Bone. Miner. Res.* 12, 1358–1367. doi: 10.1359/jbmr.1997.12.9.1358

Fureder, W., Agis, H., Willheim, M., Bankl, H. C., Maier, U., Kishi, K., et al. (1995). Differential expression of complement receptors on human basophils and mast cells. Evidence for mast cell heterogeneity and CD88/C5aR expression on skin mast cells. *J. Immunol.* 155, 3152–3160.

Geissmann, F., Jung, S., and Littman, D. R. (2003). Blood monocytes consist of two principal subsets with distinct migratory properties. *Immunity* 19, 71–82. doi: 10.1016/s1074-7613(03)00174-2

Ginhoux, F., Greter, M., Leboeuf, M., Nandi, S., See, P., Gokhan, S., et al. (2010). Fate mapping analysis reveals that adult microglia derive from primitive macrophages. *Science* 330, 841–845. doi: 10.1126/science.1194637

Greter, M., Helft, J., Chow, A., Hashimoto, D., Mortha, A., Agudo-Cantero, J., et al. (2012). GM-CSF controls nonlymphoid tissue dendritic cell homeostasis but is dispensable for the differentiation of inflammatory dendritic cells. *Immunity* 36, 1031–1046. doi: 10.1016/j.immuni.2012.03.027

Grohe, C., Kahlert, S., Lobbert, K., Stimpel, M., Karas, R. H., Vetter, H., et al. (1997). Cardiac myocytes and fibroblasts contain functional estrogen receptors. *FEBS. Lett.* 416, 107–112.

Hahn, V. S., Yanek, L. R., Vaishnav, J., Ying, W., Vaidya, D., Lee, Y. Z. J., et al. (2020). Endomyocardial biopsy characterization of heart failure with preserved ejection fraction and prevalence of cardiac amyloidosis. *JACC. Heart. Fail.* 8, 712–724. doi: 10.1016/j.jchf.2020.04.007

Hällgren, R., Venge, P., Cullhed, I., and Olsson, I. (1979). Blood eosinophils and eosinophil cationic protein after acute myocardial infarction or corticosteroid administration. *Br. J. Haematol.* 42, 147–154. doi: 10.1111/j.1365-2141.1979.tb03707.x

Hanna, R. N., Carlin, L. M., Hubbeling, H. G., Nackiewicz, D., Green, A. M., Punt, J. A., et al. (2011). The transcription factor NR4A1 (Nur77) controls bone marrow differentiation and the survival of Ly6C- monocytes. *Nat. Immunol.* 12, 778–785. doi: 10.1038/ni.2063

Hara, M., Ono, K., Hwang, M. W., Iwasaki, A., Okada, M., Nakatani, K., et al. (2002). Evidence for a role of mast cells in the evolution to congestive heart failure. *J. Exp. Med.* 195, 375–381. doi: 10.1084/jem.20002036

Harada, E., Nakagawa, O., Yoshimura, M., Harada, M., Nakagawa, M., Mizuno, Y., et al. (1999). Effect of interleukin-1 beta on cardiac hypertrophy and production of natriuretic peptides in rat cardiocyte culture. *J. Mol. Cell. Cardiol.* 31, 1997–2006. doi: 10.1006/jmcc.1999.1030

Hashimoto, D., Chow, A., Noizat, C., Teo, P., Beasley, M. B., Leboeuf, M., et al. (2013). Tissue-resident macrophages self-maintain locally throughout adult life with minimal contribution from circulating monocytes. *Immunity* 38, 792–804. doi: 10.1016/j.immuni.2013.04.004

Helske, S., Syväranta, S., Kupari, M., Lappalainen, J., Laine, M., Lommi, J., et al. (2006). Possible role for mast cell-derived cathepsin G in the adverse remodelling of stenotic aortic valves. *Eur. Heart. J.* 27, 1495–1504. doi: 10.1093/eurheartj/ehi706

Heymans, S., Lupu, F., Terclavers, S., Vanwetswinkel, B., Herbert, J. M., Baker, A., et al. (2005). Loss or inhibition of uPA or MMP-9 attenuates LV remodeling and dysfunction after acute pressure overload in mice. *Am. J. Pathol.* 166, 15–25.

Higashiyama, H., Sugai, M., Inoue, H., Mizuyachi, K., Kushida, H., Asano, S., et al. (2007). Histopathological study of time course changes in inter-renal aortic banding-induced left ventricular hypertrophy of mice. *Int. J. Exp. Pathol.* 88, 31–38. doi: 10.1111/j.1365-2613.2006.00514.x

Hilgendorf, I., Gerhardt, L. M., Tan, T. C., Winter, C., Holderried, T. A., Chousterman, B. G., et al. (2014). Ly-6Chigh monocytes depend on Nr4a1 to balance both inflammatory and reparative phases in the infarcted myocardium. *Circ. Res.* 114, 1611–1622.

Hochweller, K., Striegler, J., Hammerling, G. J., and Garbi, N. (2008). A novel CD11c.DTR transgenic mouse for depletion of dendritic cells reveals their requirement for homeostatic proliferation of natural killer cells. *Eur. J. Immunol.* 38, 2776–2783.

Hofbauer, T. M., Mangold, A., Scherz, T., Seidl, V., Panzenböck, A., Ondracek, A. S., et al. (2019). Neutrophil extracellular traps and fibrocytes in ST-segment elevation myocardial infarction. *Basic. Res. Cardiol.* 114:33. doi: 10.1007/s00395-019-0740-3

Honsho, S., Nishikawa, S., Amano, K., Zen, K., Adachi, Y., Kishita, E., et al. (2009). Pressure-mediated hypertrophy and mechanical stretch induces IL-1 release and subsequent IGF-1 generation to maintain compensative hypertrophy by affecting Akt and JNK pathways. *Circ. Res.* 105, 1149–1158. doi: 10.1161/CIRCRESAHA.109.208199

Huang, Z., Zak, J., Pratumchai, I., Shaabani, N., Vartabedian, V. F., Nguyen, N., et al. (2019). IL-27 promotes the expansion of self-renewing CD8(+) T cells in persistent viral infection. *J. Exp. Med.* 216, 1791–1808. doi: 10.1084/jem.20190173

Huber, B. C., Beetz, N. L., Laskowski, A., Ziegler, T., Grabmaier, U., Kupatt, C., et al. (2015). Attenuation of cardiac hypertrophy by G-CSF is associated with enhanced migration of bone marrow-derived cells. *J. Cell. Mol. Med.* 19, 1033–1041. doi: 10.1111/jcmm.12494

Hulsmans, M., Sager, H. B., Roh, J. D., Valero-Munoz, M., Houstis, N. E., Iwamoto, Y., et al. (2018). Cardiac macrophages promote diastolic dysfunction. *J. Exp. Med.* 215, 423–440. doi: 10.1084/jem.20171274

Huynh, M. L., Fadok, V. A., and Henson, P. M. (2002). Phosphatidylserine-dependent ingestion of apoptotic cells promotes TGF-beta1 secretion and the resolution of inflammation. *J. Clin. Invest.* 109, 41–50. doi: 10.1172/JCI11638

Ito, B. R., Engler, R. L., and del Balzo, U. (1993). Role of cardiac mast cells in complement C5a-induced myocardial ischemia. *Am. J. Physiol.* 264, H1346–H1354. doi: 10.1152/ajpheart.1993.264.5.H1346

Ivey, M. J., Kuwabara, J. T., Riggsbee, K. L., and Tallquist, M. D. (2019). Platelet-derived growth factor receptor-alpha is essential for cardiac fibroblast survival. *Am. J. Physiol. Heart. Circ. Physiol.* 317, H330–H344. doi: 10.1152/ajpheart.00054.2019

Iwasaki, Y., Fujio, K., Okamura, T., and Yamamoto, K. (2015). Interleukin-27 in T cell immunity. *Int. J. Mol. Sci.* 16, 2851–2863. doi: 10.3390/ijms16022851

Jacobsen, E. A., Helmers, R. A., Lee, J. J., and Lee, N. A. (2012). The expanding role(s) of eosinophils in health and disease. *Blood* 120, 3882–3890. doi: 10.1182/blood-2012-06-330845

Janicki, J. S., Brower, G. L., and Levick, S. P. (2015). The emerging prominence of the cardiac mast cell as a potent mediator of adverse myocardial remodeling. *Methods Mol. Biol.* 1220, 121–139. doi: 10.1007/978-1-4939-1568-2_8

Jenkins, S. J., Perona-Wright, G., Worsley, A. G., Ishii, N., and MacDonald, A. S. (2007). Dendritic cell expression of OX40 ligand acts as a costimulatory, not polarizing, signal for optimal Th2 priming and memory induction in vivo. *J. Immunol.* 179, 3515–3523. doi: 10.4049/jimmunol.179.6.3515

Jung, Y. S., Lee, H. Y., Kim, S. D., Park, J. S., Kim, J. K., Suh, P. G., et al. (2013). Wnt5a stimulates chemotactic migration and chemokine production in human neutrophils. *Exp. Mol. Med.* 45:e27. doi: 10.1038/emm.2013.48

Kagitani, S., Ueno, H., Hirade, S., Takahashi, T., Takata, M., and Inoue, H. (2004). Tranilast attenuates myocardial fibrosis in association with suppression of monocyte/macrophage infiltration in DOCA/salt hypertensive rats. *J. Hypertens.* 22, 1007–1015. doi: 10.1097/00004872-200405000-00024

Kaikita, K., Hayasaki, T., Okuma, T., Kuziel, W. A., Ogawa, H., and Takeya, M. (2004). Targeted deletion of CC chemokine receptor 2 attenuates left ventricular remodeling after experimental myocardial infarction. *Am. J. Pathol.* 165, 439–447. doi: 10.1016/S0002-9440(10)63309-3

Kain, D., Amit, U., Yagil, C., Landa, N., Naftali-Shani, N., Molotski, N., et al. (2016). Macrophages dictate the progression and manifestation of hypertensive heart disease. *Int. J. Cardiol.* 203, 381–395. doi: 10.1016/j.ijcard.2015.10.126

Kallikourdis, M., Martini, E., Carullo, P., Sardi, C., Roselli, G., Greco, C. M., et al. (2017). T cell costimulation blockade blunts pressure overload-induced heart failure. *Nat. Commun.* 8:14680. doi: 10.1038/ncomms14680

Kandere-Grzybowska, K., Letourneau, R., Kempuraj, D., Donelan, J., Poplawski, S., Boucher, W., et al. (2003). IL-1 induces vesicular secretion of IL-6 without degranulation from human mast cells. *J. Immunol.* 171, 4830–4836. doi: 10.4049/jimmunol.171.9.4830

Kanellakis, P., Ditiatkovski, M., Kostolias, G., and Bobik, A. (2012). A pro-fibrotic role for interleukin-4 in cardiac pressure overload. *Cardiovasc. Res.* 95, 77–85. doi: 10.1093/cvr/cvs142

Kardami, E., Jiang, Z. S., Jimenez, S. K., Hirst, C. J., Sheikh, F., Zahradka, P., et al. (2004). Fibroblast growth factor 2 isoforms and cardiac hypertrophy. *Cardiovasc. Res.* 63, 458–466. doi: 10.1016/j.cardiores.2004.04.024

Kimura, A., Ishida, Y., Furuta, M., Nosaka, M., Kuninaka, Y., Taruya, A., et al. (2018). Protective roles of Interferon-γ in cardiac hypertrophy induced by sustained pressure overload. *J. Am. Heart. Assoc.* 7:e008145. doi: 10.1161/JAHA.117.008145

Kimura, D., Miyakoda, M., Kimura, K., Honma, K., Hara, H., Yoshida, H., et al. (2016). Interleukin-27-Producing CD4(+) T cells regulate protective immunity during malaria parasite infection. *Immunity* 44, 672–682. doi: 10.1016/j.immuni.2016.02.011

Kirimura, K., Takai, S., Jin, D., Muramatsu, M., Kishi, K., Yoshikawa, K., et al. (2005). Role of chymase-dependent angiotensin II formation in regulating blood pressure in spontaneously hypertensive rats. *Hypertens. Res.* 28, 457–464. doi: 10.1291/hypres.28.457

Kirkeby, K., and Paudal, B. (1960). The eosinophil count in the diagnosis and prognosis of myocardial infarction. *Acta Med. Scand.* 168, 21–24. doi: 10.1111/j.0954-6820.1960.tb06635.x

Kolpakov, M. A., Seqqat, R., Rafiq, K., Xi, H., Margulies, K. B., Libonati, J. R., et al. (2009). Pleiotropic effects of neutrophils on myocyte apoptosis and left ventricular remodeling during early volume overload. *J. Mol. Cell. Cardiol.* 47, 634–645. doi: 10.1016/j.yjmcc.2009.08.016

Kong, P., Shinde, A. V., Su, Y., Russo, I., Chen, B., Saxena, A., et al. (2018). Opposing actions of fibroblast and cardiomyocyte smad3 signaling in the infarcted myocardium. *Circulation* 137, 707–724. doi: 10.1161/CIRCULATIONAHA.117.029622

Kuwahara, F., Kai, H., Tokuda, K., Niiyama, H., Tahara, N., Kusaba, K., et al. (2003). Roles of intercellular adhesion molecule-1 in hypertensive cardiac remodeling. *Hypertension* 41(3 Pt 2), 819–823. doi: 10.1161/01.HYP.0000056108.73219.0A

Kuwahara, F., Kai, H., Tokuda, K., Takeya, M., Takeshita, A., Egashira, K., et al. (2004). Hypertensive myocardial fibrosis and diastolic dysfunction: another model of inflammation? *Hypertension* 43, 739–745. doi: 10.1161/01.HYP.0000118584.33350.7d

Laroumanie, F., Douin-Echinard, V., Pozzo, J., Lairez, O., Tortosa, F., Vinel, C., et al. (2014). CD4+ T cells promote the transition from hypertrophy to heart failure during chronic pressure overload. *Circulation* 129, 2111–2124. doi: 10.1161/CIRCULATIONAHA.113.007101

Leclerc, E., Fritz, G., Vetter, S. W., and Heizmann, C. W. (2009). Binding of S100 proteins to RAGE: an update. *Biochim. Biophys. Acta* 1793, 993–1007. doi: 10.1016/j.bbamcr.2008.11.016

Lefrançais, E., Duval, A., Mirey, E., Roga, S., Espinosa, E., Cayrol, C., et al. (2014). Central domain of IL-33 is cleaved by mast cell proteases for potent activation of group-2 innate lymphoid cells. *Proc. Natl. Acad. Sci. U S A.* 111, 15502–15507. doi: 10.1073/pnas.1410700111

Levick, S. P., McLarty, J. L., Murray, D. B., Freeman, R. M., Carver, W. E., and Brower, G. L. (2009). Cardiac mast cells mediate left ventricular fibrosis in the hypertensive rat heart. *Hypertension* 53, 1041–1047. doi: 10.1161/HYPERTENSIONAHA.108.123158

Li, J., Jubair, S., and Janicki, J. S. (2015). Estrogen inhibits mast cell chymase release to prevent pressure overload-induced adverse cardiac remodeling. *Hypertension* 65, 328–334. doi: 10.1161/HYPERTENSIONAHA.114.04238

Li, J., Jubair, S., Levick, S. P., and Janicki, J. S. (2016). The autocrine role of tryptase in pressure overload-induced mast cell activation, chymase release and cardiac fibrosis. *IJC. Metab. Endocr.* 10, 16–23. doi: 10.1016/j.ijcme.2015.11.003

Li, J. M., Gall, N. P., Grieve, D. J., Chen, M., and Shah, A. M. (2002). Activation of NADPH oxidase during progression of cardiac hypertrophy to failure. *Hypertension* 40, 477–484. doi: 10.1161/01.hyp.0000032031.30374.32

Li, J. M., Yao, Z. F., Zou, Y. Z., Ge, J. B., Guan, A. L., Wu, J., et al. (2012). The therapeutic potential of G-CSF in pressure overload induced ventricular reconstruction and heart failure in mice. *Mol. Biol. Rep.* 39, 5–12. doi: 10.1007/s11033-011-0703-708

Li, M., Liu, K., Michalicek, J., Angus, J. A., Hunt, J. E., Dell'Italia, L. J., et al. (2004). Involvement of chymase-mediated angiotensin II generation in blood pressure regulation. *J. Clin. Invest.* 114, 112–120. doi: 10.1172/JCI20805

Li, M., Naqvi, N., Yahiro, E., Liu, K., Powell, P. C., Bradley, W. E., et al. (2008). c-kit is required for cardiomyocyte terminal differentiation. *Circ. Res.* 102, 677–685. doi: 10.1161/CIRCRESAHA.107.161737

Li, Y., Yu, X., Ma, Y., and Hua, S. (2019). IL-23 and dendritic cells: what are the roles of their mutual attachment in immune response and immunotherapy? *Cytokine* 120, 78–84. doi: 10.1016/j.cyto.2019.02.018

Liao, C. H., Akazawa, H., Tamagawa, M., Ito, K., Yasuda, N., Kudo, Y., et al. (2010). Cardiac mast cells cause atrial fibrillation through PDGF-A-mediated fibrosis in pressure-overloaded mouse hearts. *J. Clin. Invest.* 120, 242–253. doi: 10.1172/JCI39942

Liao, X., Shen, Y., Zhang, R., Sugi, K., Vasudevan, N. T., Alaiti, M. A., et al. (2018). Distinct roles of resident and nonresident macrophages in nonischemic cardiomyopathy. *Proc. Natl. Acad. Sci. U S A.* 115, E4661–E4669. doi: 10.1073/pnas.1720065115

Lijnen, P. J., Petrov, V. V., and Fagard, R. H. (2001). Angiotensin II-induced stimulation of collagen secretion and production in cardiac fibroblasts is mediated via angiotensin II subtype 1 receptors. *J. Renin. Angiotensin. Aldosterone. Syst.* 2, 117–122.

Lim, D. H., Cho, J. Y., Miller, M., McElwain, K., McElwain, S., and Broide, D. H. (2006). Reduced peribronchial fibrosis in allergen-challenged MMP-9-deficient mice. *Am. J. Physiol. Lung. Cell. Mol. Physiol.* 291, L265–L271. doi: 10.1152/ajplung.00305.2005

Liu, J., Yang, C., Liu, T., Deng, Z., Fang, W., Zhang, X., et al. (2020). Eosinophils improve cardiac function after myocardial infarction. *Nat. Commun.* 11:6396. doi: 10.1038/s41467-020-19297-5

Lovelock, J. D., Monasky, M. M., Jeong, E. M., Lardin, H. A., Liu, H., Patel, B. G., et al. (2012). Ranolazine improves cardiac diastolic dysfunction through modulation of myofilament calcium sensitivity. *Circ. Res.* 110, 841–850. doi: 10.1161/CIRCRESAHA.111.258251

Luitel, H., Sydykov, A., Schymura, Y., Mamazhakypov, A., Janssen, W., Pradhan, K., et al. (2017). Pressure overload leads to an increased accumulation and activity of mast cells in the right ventricle. *Physiol. Rep.* 5:e13146. doi: 10.14814/phy2.13146

Ma, Y., Yabluchanskiy, A., Iyer, R. P., Cannon, P. L., Flynn, E. R., Jung, M., et al. (2016). Temporal neutrophil polarization following myocardial infarction. *Cardiovasc. Res.* 110, 51–61. doi: 10.1093/cvr/cvw024

Ma, Y., Yabluchanskiy, A., and Lindsey, M. L. (2013). Neutrophil roles in left ventricular remodeling following myocardial infarction. *Fibrogenesis. Tissue. Repair.* 6:11. doi: 10.1186/1755-1536-6-11

Mackay, F., Loetscher, H., Stueber, D., Gehr, G., and Lesslauer, W. (1993). Tumor necrosis factor alpha (TNF-alpha)-induced cell adhesion to human endothelial cells is under dominant control of one TNF receptor type, TNF-R55. *J. Exp. Med.* 177, 1277–1286. doi: 10.1084/jem.177.5.1277

Manh, T. P., Alexandre, Y., Baranek, T., Crozat, K., and Dalod, M. (2013). Plasmacytoid, conventional, and monocyte-derived dendritic cells undergo a profound and convergent genetic reprogramming during their maturation. *Eur. J. Immunol.* 43, 1706–1715. doi: 10.1002/eji.201243106

Martini, E., Kunderfranco, P., Peano, C., Carullo, P., Cremonesi, M., Schorn, T., et al. (2019). Single-Cell sequencing of mouse heart immune infiltrate in pressure overload-driven heart failure reveals extent of immune activation. *Circulation* 140, 2089–2107. doi: 10.1161/CIRCULATIONAHA.119.041694

Mascanfroni, I. D., Yeste, A., Vieira, S. M., Burns, E. J., Patel, B., Sloma, I., et al. (2013). IL-27 acts on DCs to suppress the T cell response and autoimmunity by inducing expression of the immunoregulatory molecule CD39. *Nat. Immunol.* 14, 1054–1063. doi: 10.1038/ni.2695

Matsumoto, T., Wada, A., Tsutamoto, T., Ohnishi, M., Isono, T., and Kinoshita, M. (2003). Chymase inhibition prevents cardiac fibrosis and improves diastolic dysfunction in the progression of heart failure. *Circulation* 107, 2555–2558. doi: 10.1161/01.CIR.0000074041.81728.79

Matsusaka, H., Ide, T., Matsushima, S., Ikeuchi, M., Kubota, T., Sunagawa, K., et al. (2016). Targeted deletion of matrix metalloproteinase 2 ameliorates myocardial remodeling in mice with chronic pressure overload. *Hypertension* 47, 711–717. doi: 10.1161/01.HYP.0000208840.30778.00

McDonald, B., Pittman, K., Menezes, G. B., Hirota, S. A., Slaba, I., Waterhouse, C. C., et al. (2010). Intravascular danger signals guide neutrophils to sites of sterile inflammation. *Science* 330, 362–366. doi: 10.1126/science.1195491

McDonald, L. T., Zile, M. R., Zhang, Y., Van Laer, A. O., Baicu, C. F., Stroud, R. E., et al. (2018). Increased macrophage-derived SPARC precedes collagen deposition in myocardial fibrosis. *Am. J. Physiol. Heart. Circ. Physiol.* 315, H92–H100. doi: 10.1016/j.immuni.2013.04.004

Mishra, S., and Kass, D. A. (2021). Cellular and molecular pathobiology of heart failure with preserved ejection fraction. *Nat. Rev. Cardiol.* 18, 400–423. doi: 10.1038/s41569-020-00480-486

Miyazaki, M., Takai, S., Jin, D., and Muramatsu, M. (2006). Pathological roles of angiotensin II produced by mast cell chymase and the effects of chymase inhibition in animal models. *Pharmacol. Ther.* 112, 668–676. doi: 10.1016/j.pharmthera.2006.05.008

Molawi, K., Wolf, Y., Kandalla, P. K., Favret, J., Hagemeyer, N., Frenzel, K., et al. (2014). Progressive replacement of embryo-derived cardiac macrophages with age. *J. Exp. Med.* 211, 2151–2158. doi: 10.1084/jem.20140639

Mukai, K., Tsai, M., Saito, H., and Galli, S. J. (2018). Mast cells as sources of cytokines, chemokines, and growth factors. *Immunol. Rev.* 282, 121–150. doi: 10.1111/imr.12634

Murray, P. J., and Wynn, T. A. (2011). Protective and pathogenic functions of macrophage subsets. *Nat. Rev. Immunol.* 11, 723–737. doi: 10.1038/nri3073

Nadal-Ginard, B., Kajstura, J., Leri, A., and Anversa, P. (2003). Myocyte death, growth, and regeneration in cardiac hypertrophy and failure. *Circ. Res.* 92, 139–150. doi: 10.1161/01.res.0000053618.86362.df

Nemska, S., Monassier, L., Gassmann, M., Frossard, N., and Tavakoli, R. (2016). Kinetic mRNA profiling in a rat model of left-ventricular hypertrophy reveals early expression of chemokines and their receptors. *PLoS One* 11:e0161273. doi: 10.1371/journal.pone.0161273

Nevers, T., Salvador, A. M., Grodecki-Pena, A., Knapp, A., Velazquez, F., Aronovitz, M., et al. (2015). Left ventricular T-Cell recruitment contributes to the pathogenesis of heart failure. *Circ. Heart. Fail.* 8, 776–787. doi: 10.1161/CIRCHEARTFAILURE.115.002225

Nevers, T., Salvador, A. M., Velazquez, F., Ngwenyama, N., Carrillo-Salinas, F. J., Aronovitz, M., et al. (2017). Th1 effector T cells selectively orchestrate cardiac fibrosis in nonischemic heart failure. *J. Exp. Med.* 214, 3311–3329. doi: 10.1084/jem.20161791

Okoye, I. S., and Wilson, M. S. (2011). CD4+ T helper 2 cells–microbial triggers, differentiation requirements and effector functions. *Immunology* 134, 368–377. doi: 10.1111/j.1365-2567.2011.03497.x

Olivetti, G., Lagrasta, C., Ricci, R., Sonnenblick, E. H., Capasso, J. M., and Anversa, P. (1989). Long-term pressure-induced cardiac hypertrophy: capillary and mast cell proliferation. *Am. J. Physiol.* 257(6 Pt 2), H1766–H1772. doi: 10.1152/ajpheart.1989.257.6.H1766

Overed-Sayer, C., Rapley, L., Mustelin, T., and Clarke, D. L. (2014a). Are mast cells instrumental for fibrotic diseases? *Front. Pharmacol.* 4:174. doi: 10.3389/fphar.2013.00174

Overed-Sayer, C., Rapley, L., Mustelin, T., and Clarke, D. L. (2014b). Interleukin-1 beta induces cardiac myocyte growth but inhibits cardiac fibroblast proliferation in culture. *J. Clin. Invest.* 95, 2555–2564. doi: 10.3389/fphar.2013.00174

Palmer, J. N., Hartogensis, W. E., Patten, M., Fortuin, F. D., and Long, C. S. (1995). Interleukin-1 beta induces cardiac myocyte growth but inhibits cardiac fibroblast proliferation in culture. *J. Clin. Invest.* 95, 2555–2564. doi: 10.1172/JCI117956

Panizo, A., Mindán, F. J., Galindo, M. F., Cenarruzabeitia, E., Hernández, M., and Díez, J. (1995). Are mast cells involved in hypertensive heart disease? *J. Hypertens.* 13, 1201–1208. doi: 10.1097/00004872-199510000-00015

Patel, B., Bansal, S. S., Ismahil, M. A., Hamid, T., Rokosh, G., Mack, M., et al. (2018). CCR2(+) monocyte-derived infiltrating macrophages are required for

adverse cardiac remodeling during pressure overload. *JACC. Basic. Transl. Sci.* 3, 230–244. doi: 10.1016/j.jacbts.2017.12.006

Patel, B., Ismahil, M. A., Hamid, T., Bansal, S. S., and Prabhu, S. D. (2017). Mononuclear phagocytes are dispensable for cardiac remodeling in established pressure-overload heart failure. *PLoS One* 12:e0170781. doi: 10.1371/journal.pone.0170781

Patella, V., Marinò, I., Lampärter, B., Arbustini, E., Adt, M., and Marone, G. (1995). Human heart mast cells. isolation, purification, ultrastructure, and immunologic characterization. *J. Immunol.* 154, 2855–2865.

Paul, M., Poyan Mehr, A., and Kreutz, R. (2006). Physiology of local renin-angiotensin systems. *Physiol. Rev.* 86, 747–803. doi: 10.1152/physrev.00036.2005

Perrigoue, J. G., Saenz, S. A., Siracusa, M. C., Allenspach, E. J., Taylor, B. C., Giacomin, P. R., et al. (2009). MHC class II-dependent basophil-CD4+ T cell interactions promote T(H)2 cytokine-dependent immunity. *Nat. Immunol.* 10, 697–705. doi: 10.1038/ni.1740

Qin, C. X., Rosli, S., Deo, M., Cao, N., Walsh, J., Tate, M., et al. (2019). Cardioprotective actions of the Annexin-A1 N-Terminal peptide, Ac2-26, against myocardial infarction. *Front. Pharmacol.* 10:269. doi: 10.3389/fphar.2019.00269

Randolph, G. J., Ochando, J., and Partida-Sánchez, S. (2008). Migration of dendritic cell subsets and their precursors. *Annu. Rev. Immunol.* 26, 293–316. doi: 10.1146/annurev.immunol.26.021607.090254

Ren, J., Yang, M., Qi, G., Zheng, J., Jia, L., Cheng, J., et al. (2011). Proinflammatory protein CARD9 is essential for infiltration of monocytic fibroblast precursors and cardiac fibrosis caused by Angiotensin II infusion. *Am. J. Hypertens.* 24, 701–707. doi: 10.1038/ajh.2011.42

Ridker, P. M., Everett, B. M., Thuren, T., MacFadyen, J. G., Chang, W. H., Ballantyne, C., et al. (2017). Antiinflammatory therapy with canakinumab for atherosclerotic disease. *N. Engl. J. Med.* 377, 1119–1131. doi: 10.1056/NEJMoa1707914

Ridker, P. M., Devalaraja, M., Baeres, F. M. M., Engelmann, M. D. M., Hovingh, G. K., Ivkovic, M., et al. (2021). IL-6 inhibition with ziltivekimab in patients at high atherosclerotic risk (RESCUE): a double-blind, randomised, placebo-controlled, phase 2 trial. *Lancet*. 397, 2060–2069. doi: 10.1016/S0140-6736(21)00520-521

Rittersma, S. Z., Meuwissen, M., van der Loos, C. M., Koch, K. T., de Winter, R. J., Piek, J. J., et al. (2006). Eosinophilic infiltration in restenotic tissue following coronary stent implantation. *Atherosclerosis* 184, 157–162. doi: 10.1016/j.atherosclerosis.2005.03.049

Robbins, C. S., Hilgendorf, I., Weber, G. F., Theurl, I., Iwamoto, Y., Figueiredo, J. L., et al. (2013). Local proliferation dominates lesional macrophage accumulation in atherosclerosis. *Nat. Med.* 19, 1166–1172. doi: 10.1038/nm.3258

Rockman, H. A., Ross, R. S., Harris, A. N., Knowlton, K. U., Steinhelper, M. E., Field, L. J., et al. (1991). Segregation of atrial-specific and inducible expression of an atrial natriuretic factor transgene in an in vivo murine model of cardiac hypertrophy. *Proc. Natl. Acad. Sci. U S A.* 88, 8277–8281. doi: 10.1073/pnas.88.18.8277

Rosenberg, H. F., Dyer, K. D., and Foster, P. S. (2013). Eosinophils: changing perspectives in health and disease. *Nat. Rev. Immunol.* 13, 9–22. doi: 10.1038/nri3341

Rossetti, M., Gregori, S., and Roncarolo, M. G. (2010). Granulocyte-colony stimulating factor drives the in vitro differentiation of human dendritic cells that induce anergy in naive T cells. *Eur. J. Immunol.* 40, 3097–3106. doi: 10.1002/eji.201040659

Sahni, A., Sahni, S. K., and Francis, C. W. (2005). Endothelial cell activation by IL1beta in the presence of fibrinogen requires alphavbeta3. *Arterioscler. Thromb. Vasc. Biol.* 25, 2222–2227. doi: 10.1161/01.ATV.0000183605.27125.6f

Sallusto, F., Palermo, B., Lenig, D., Miettinen, M., Matikainen, S., Julkunen, I., et al. (1999). Distinct patterns and kinetics of chemokine production regulate dendritic cell function. *Eur. J. Immunol.* 29, 1617–1625.

Scheinman, E. J., and Avni, O. (2009). Transcriptional regulation of GATA3 in T helper cells by the integrated activities of transcription factors downstream of the interleukin-4 receptor and T cell receptor. *J. Biol. Chem.* 284, 3037–3048. doi: 10.1074/jbc.M807302200

Schiattarella, G. G., and Hill, J. A. (2015). Inhibition of hypertrophy is a good therapeutic strategy in ventricular pressure overload. *Circulation* 131, 1435–1447. doi: 10.1161/CIRCULATIONAHA.115.013894

Schulz, C., Gomez Perdiguero, E., Chorro, L., Szabo-Rogers, H., Cagnard, N., Kierdorf, K., et al. (2012). A lineage of myeloid cells independent of Myb and hematopoietic stem cells. *Science* 336, 86–90. doi: 10.1126/science.1219179

Seong, S. Y., and Matzinger, P. (2004). Hydrophobicity: an ancient damage-associated molecular pattern that initiates innate immune responses. *Nat. Rev. Immunol.* 4, 469–478. doi: 10.1038/nri1372

Serbina, N. V., and Pamer, E. G. (2006). Monocyte emigration from bone marrow during bacterial infection requires signals mediated by chemokine receptor CCR2. *Nat. Immunol.* 7, 311–317. doi: 10.1038/ni1309

Shaughnessy, P. J., Bachier, C., Lemaistre, C. F., Akay, C., Pollock, B. H., and Gazitt, Y. (2006). Granulocyte colony-stimulating factor mobilizes more dendritic cell subsets than granulocyte-macrophage colony-stimulating factor with no polarization of dendritic cell subsets in normal donors. *Stem. Cells* 24, 1789–1797. doi: 10.1634/stemcells.2005-0492

Shimizu, I., and Minamino, T. (2016). Physiological and pathological cardiac hypertrophy. *J. Mol. Cell. Cardiol.* 97, 245–262. doi: 10.1016/j.yjmcc.2016.06.001

Shinde, A. V., and Frangogiannis, N. G. (2014). Fibroblasts in myocardial infarction: a role in inflammation and repair. *J. Mol. Cell. Cardiol.* 70, 74–82. doi: 10.1016/j.yjmcc.2013.11.015

Shiota, N., Rysä, J., Kovanen, P. T., Ruskoaho, H., Kokkonen, J. O., and Lindstedt, K. A. (2003). A role for cardiac mast cells in the pathogenesis of hypertensive heart disease. *J. Hypertens.* 21, 1935–1944. doi: 10.1097/00004872-200310000-00022

Silberman, G. A., Fan, T. H., Liu, H., Jiao, Z., Xiao, H. D., Lovelock, J. D., et al. (2010). Uncoupled cardiac nitric oxide synthase mediates diastolic dysfunction. *Circulation* 121, 519–528. doi: 10.1161/CIRCULATIONAHA.109.883777

Soehnlein, O., and Lindbom, L. (2010). Phagocyte partnership during the onset and resolution of inflammation. *Nat. Rev. Immunol.* 10, 427–439. doi: 10.1038/nri2779

Soon, E., Holmes, A. M., Treacy, C. M., Doughty, N. J., Southgate, L., Machado, R. D., et al. (2010). Elevated levels of inflammatory cytokines predict survival in idiopathic and familial pulmonary arterial hypertension. *Circulation* 122, 920–927. doi: 10.1161/CIRCULATIONAHA.109.933762

Sreejit, G., Abdel-Latif, A., Athmanathan, B., Annabathula, R., Dhyani, A., Noothi, S. K., et al. (2020). Neutrophil-Derived S100A8/A9 amplify granulopoiesis after myocardial infarction. *Circulation* 141, 1080–1094. doi: 10.1161/CIRCULATIONAHA.119.043833

Stillman, B. N., Hsu, D. K., Pang, M., Brewer, C. F., Johnson, P., Liu, F. T., et al. (2006). Galectin-3 and galectin-1 bind distinct cell surface glycoprotein receptors to induce T cell death. *J. Immunol.* 176, 778–789. doi: 10.4049/jimmunol.176.2.778

Streicher, J. M. (2019). The role of heat shock proteins in regulating receptor signal transduction. *Mol. Pharmacol.* 95, 468–474. doi: 10.1124/mol.118.114652

Sun, J., Krawczyk, C. J., and Pearce, E. J. (2018). Suppression of Th2 cell development by Notch ligands Delta1 and Delta4. *J. Immunol.* 180, 1655–1661. doi: 10.4049/jimmunol.180.3.1655

Sun, M., Chen, M., Dawood, F., Zurawska, U., Li, J. Y., Parker, T., et al. (2007). Tumor necrosis factor-alpha mediates cardiac remodeling and ventricular dysfunction after pressure overload state. *Circulation* 115, 1398–1407. doi: 10.1161/CIRCULATIONAHA.106.643585

Szardien, S., Nef, H. M., Voss, S., Troidl, C., Liebetrau, C., Hoffmann, J., et al. (2012). Regression of cardiac hypertrophy by granulocyte colony-stimulating factor-stimulated interleukin-1beta synthesis. *Eur. Heart. J.* 33, 595–605. doi: 10.1093/eurheartj/ehr434

Takahashi, M., Kinugawa, S., Takada, S., Kakutani, N., Furihata, T., Sobirin, M. A., et al. (2020). The disruption of invariant natural killer T cells exacerbates cardiac hypertrophy and failure caused by pressure overload in mice. *Exp. Physiol.* 105, 489–501. doi: 10.1113/EP087652

Takai, S., Jin, D., Sakaguchi, M., and Miyazaki, M. (2004). A single treatment with a specific chymase inhibitor, TY-51184, prevents vascular proliferation in canine grafted veins. *J. Pharmacol. Sci.* 94, 443–448. doi: 10.1254/jphs.94.443

Takeuchi, O., and Akira, S. (2010). Pattern recognition receptors and inflammation. *Cell* 140, 805–820. doi: 10.1016/j.cell.2010.01.022

Terhune, J., Berk, E., and Czerniecki, B. J. (2013). Dendritic cell-induced Th1 and Th17 cell differentiation for cancer therapy. *Vaccines (Basel)* 1, 527–549. doi: 10.3390/vaccines1040527

Tindemans, I., Peeters, M. J. W., and Hendriks, R. W. (2017). Notch signaling in T helper cell subsets: instructor or unbiased amplifier? *Front. Immunol.* 8:419. doi: 10.3389/fimmu.2017.00419

Toor, I. S., Rückerl, D., Mair, I., Ainsworth, R., Meloni, M., Spiroski, A. M., et al. (2020). Eosinophil deficiency promotes aberrant repair and adverse remodeling following acute myocardial infarction. *JACC. Basic. Transl. Sci.* 5, 665–681. doi: 10.1016/j.jacbts.2020.05.005

Trankle, C. R., Canada, J. M., Kadariya, D., Markley, R., De Chazal, H. M., Pinson, J., et al. (2019). IL-1 blockade reduces inflammation in pulmonary arterial hypertension and right ventricular failure: a single-arm, open-label, phase IB/II Pilot study. *Am. J. Respir. Crit. Care. Med.* 199, 381–384. doi: 10.1164/rccm.201809-1631LE

Urwyler, S. A., Ebrahimi, F., Burkard, T., Schuetz, P., Poglitsch, M., Mueller, B., et al. (2020). IL (Interleukin)-1 receptor antagonist increases ang (Angiotensin [1-7]) and decreases blood pressure in obese individuals. *Hypertension* 75, 1455–1463. doi: 10.1161/HYPERTENSIONAHA.119.13982

van, Amerongen, M. J., Harmsen, M. C., van Rooijen, N., Petersen, A. H., and van Luyn, M. J. (2007). Macrophage depletion impairs wound healing and increases left ventricular remodeling after myocardial injury in mice. *Am. J. Pathol.* 170, 818–829. doi: 10.2353/ajpath.2007.060547

van Amerongen, R., and Nusse, R. (2009). Towards an integrated view of Wnt signaling in development. *Development* 136, 3205–3214. doi: 10.1242/dev.033910

Volz, H. C., Laohachewin, D., Seidel, C., Lasitschka, F., Keilbach, K., Wienbrandt, A. R., et al. (2012). S100A8/A9 aggravates post-ischemic heart failure through activation of RAGE-dependent NF-kappaB signaling. *Basic. Res. Cardiol.* 107:250. doi: 10.1007/s00395-012-0250-z

Wagner, H. R., Crutcher, K. A., and Davis, J. N. (1979). Chronic estrogen treatment decreases beta-adrenergic responses in rat cerebral cortex. *Brain Res.* 171, 147–151. doi: 10.1016/0006-8993(79)90741-90748

Wang, H., Kwak, D., Fassett, J., Liu, X., Yao, W., Weng, X., et al. (2017). Role of bone marrow-derived CD11c(+) dendritic cells in systolic overload-induced left ventricular inflammation, fibrosis and hypertrophy. *Basic. Res. Cardiol.* 112:25. doi: 10.1007/s00395-017-0615-4

Wang, H. X., Li, W. J., Hou, C. L., Lai, S., Zhang, Y. L., Tian, C., et al. (2019a). CD1d-dependent natural killer T cells attenuate angiotensin II-induced cardiac remodelling via IL10 signalling in mice. *Cardiovasc. Res.* 115, 83–93. doi: 10.1093/cvr/cvy164

Wang, Y., Sano, S., Oshima, K., Sano, M., Watanabe, Y., Katanasaka, Y., et al. (2019b). Wnt5a-Mediated neutrophil recruitment has an obligatory role in pressure overload-induced cardiac dysfunction. *Circulation* 140, 487–499. doi: 10.1161/CIRCULATIONAHA.118.038820

Wei, J., Xia, S., Sun, H., Zhang, S., Wang, J., Zhao, H., et al. (2013). Critical role of dendritic cell-derived IL-27 in antitumor immunity through regulating the recruitment and activation of NK and NKT cells. *J. Immunol.* 191, 500–508. doi: 10.4049/jimmunol.1300328

Wei, X., Wu, B., Zhao, J., Zeng, Z., Xuan, W., Cao, S., et al. (2015). Myocardial hypertrophic preconditioning attenuates cardiomyocyte hypertrophy and slows progression to heart failure through upregulation of S100A8/A9. *Circulation* 131, 1506–1517. doi: 10.1161/CIRCULATIONAHA.114.013789

Weisheit, C., Zhang, Y., Faron, A., Köpke, O., Weisheit, G., Steinsträsser, A., et al. (2014). Ly6C(low) and not Ly6C(high) macrophages accumulate first in the heart in a model of murine pressure-overload. *PLoS One* 9:e112710. doi: 10.1371/journal.pone.0112710

Weisheit, C. K., Kleiner, J. L., Rodrigo, M. B., Niepmann, S. T., Zimmer, S., Duerr, G. D., et al. (2021). CX3CR1 is a prerequisite for the development of cardiac hypertrophy and left ventricular dysfunction in mice upon transverse aortic constriction. *PLoS One* 16:e0243788. doi: 10.1371/journal.pone.0243788

Wend, P., Holland, J. D., Ziebold, U., and Birchmeier, W. (2010). Wnt signaling in stem and cancer stem cells. *Semin. Cell Dev. Biol.* 21, 855–863. doi: 10.1016/j.semcdb.2010.09.004

Wernersson, S., and Pejler, G. (2014). Mast cell secretory granules: armed for battle. *Nat. Rev. Immunol.* 14, 478–494. doi: 10.1038/nri3690

Westermann, D., Lindner, D., Kasner, M., Zietsch, C., Savvatis, K., Escher, F., et al. (2011). Cardiac inflammation contributes to changes in the extracellular matrix in patients with heart failure and normal ejection fraction. *Circ. Heart. Fail.* 4, 44–52. doi: 10.1161/CIRCHEARTFAILURE.109.931451

Woodfin, A., Voisin, M. B., Imhof, B. A., Dejana, E., Engelhardt, B., and Nourshargh, S. (2009). Endothelial cell activation leads to neutrophil transmigration as supported by the sequential roles of ICAM-2, JAM-A, and PECAM-1. *Blood* 113, 6246–6257.

Wu, Y., Li, Y., Zhang, C. A. X., Wang, Y., Cui, W., Li, H., et al. (2014). S100a8/a9 released by CD11b+Gr1+ neutrophils activates cardiac fibroblasts to initiate angiotensin II-Induced cardiac inflammation and injury. *Hypertension* 63, 1241–1250. doi: 10.1161/HYPERTENSIONAHA.113.02843

Wynn, T. A., and Barron, L. (2010). Macrophages: master regulators of inflammation and fibrosis. *Semin. Liver. Dis.* 30, 245–257. doi: 10.1055/s-0030-1255354

Yang, H., Wang, H., and Andersson, U. (2020). Targeting inflammation driven by HMGB1. *Front. Immunol.* 11:484. doi: 10.3389/fimmu.2020.00484

Yang, M., Song, L., Wang, L., Yukht, A., Ruther, H., Li, F., et al. (2018). Deficiency of GATA3-Positive macrophages improves cardiac function following myocardial infarction or pressure overload hypertrophy. *J. Am. Coll. Cardiol.* 72, 885–904. doi: 10.1016/j.jacc.2018.05.061

Yona, S., Kim, K. W., Wolf, Y., Mildner, A., Varol, D., Breker, M., et al. (2013). Fate mapping reveals origins and dynamics of monocytes and tissue macrophages under homeostasis. *Immunity* 38, 79–91. doi: 10.1016/j.immuni.2012.12.001

You, J., Wu, J., Zhang, Q., Ye, Y., Wang, S., Huang, J., et al. (2018). Differential cardiac hypertrophy and signaling pathways in pressure versus volume overload. *Am. J. Physiol. Heart. Circ. Physiol.* 314, H552–H562. doi: 10.1152/ajpheart.00212.2017

Zandbergen, H. R., Sharma, U. C., Gupta, S., Verjans, J. W., van den Borne, S., Pokharel, S., et al. (2009). Macrophage depletion in hypertensive rats accelerates development of cardiomyopathy. *J. Cardiovasc. Pharmacol. Ther.* 14, 68–75. doi: 10.1177/1074248408329860

Zhan, Y., Lew, A. M., and Chopin, M. (2019). The pleiotropic effects of the GM-CSF rheostat on myeloid cell differentiation and function: more than a numbers game. *Front. Immunol.* 10:2679. doi: 10.3389/fimmu.2019.02679

Zhang, B., Weng, Z., Sismanopoulos, N., Asadi, S., Therianou, A., Alysandratos, K. D., et al. (2012). Mitochondria distinguish granule-stored from de novo synthesized tumor necrosis factor secretion in human mast cells. *Int. Arch. Allergy. Immunol.* 159, 23–32. doi: 10.1159/000335178

Zhang, J., Yang, L., and Ding, Y. (2021). Effects of irbesartan on phenotypic alterations in monocytes and the inflammatory status of hypertensive patients with left ventricular hypertrophy. *BMC. Cardiovasc. Disord.* 21:194. doi: 10.1186/s12872-021-02004-2007

Zhou, Y., Yu, X., Chen, H., Sjoberg, S., Roux, J., Zhang, L., et al. (2015). Leptin deficiency shifts mast cells toward anti-inflammatory actions and protects mice from obesity and diabetes by polarizing M2 macrophages. *Cell Metab.* 22, 1045–1058. doi: 10.1016/j.cmet.2015.09.013

Zierau, O., Zenclussen, A. C., and Jensen, F. (2012). Role of female sex hormones, estradiol and progesterone, in mast cell behavior. *Front. Immunol.* 3:169. doi: 10.3389/fimmu.2012.00169

Conflict of Interest: The authors declare that the research was conducted in the absence of any commercial or financial relationships that could be construed as a potential conflict of interest.

Publisher's Note: All claims expressed in this article are solely those of the authors and do not necessarily represent those of their affiliated organizations, or those of the publisher, the editors and the reviewers. Any product that may be evaluated in this article, or claim that may be made by its manufacturer, is not guaranteed or endorsed by the publisher.

frontiers in Cell and Developmental Biology

ORIGINAL RESEARCH
published: 17 September 2021
doi: 10.3389/fcell.2021.668032

CRISPR-Based Activation of Endogenous Expression of *TPM1* Inhibits Inflammatory Response of Primary Human Coronary Artery Endothelial and Smooth Muscle Cells Induced by Recombinant Human Tumor Necrosis Factor α

Maciej Gagat[1], Wioletta Zielińska[1†], Klaudia Mikołajczyk[1†], Jan Zabrzyński[2,3], Adrian Krajewski[1], Anna Klimaszewska-Wiśniewska[2], Dariusz Grzanka[2‡] and Alina Grzanka[1‡]*

[1] Department of Histology and Embryology, Faculty of Medicine, Nicolaus Copernicus University in Toruń, Collegium Medicum in Bydgoszcz, Bydgoszcz, Poland, [2] Department of Clinical Pathomorphology, Faculty of Medicine, Nicolaus Copernicus University in Toruń, Collegium Medicum in Bydgoszcz, Bydgoszcz, Poland, [3] Department of General Orthopaedics, Musculoskeletal Oncology and Trauma Surgery, University of Medical Sciences, Poznań, Poland

OPEN ACCESS

Edited by:
Guo-Ping Shi,
Brigham and Women's Hospital and Harvard Medical School, United States

Reviewed by:
Peter William Gunning,
University of New South Wales, Australia
Zhaojie Meng,
Brigham and Women's Hospital and Harvard Medical School, United States

***Correspondence:**
Maciej Gagat
mgagat@cm.umk.pl

[†] These authors have contributed equally to this work

[‡] These authors share senior authorship

Specialty section:
This article was submitted to Signaling, a section of the journal Frontiers in Cell and Developmental Biology

Received: 15 February 2021
Accepted: 25 August 2021
Published: 17 September 2021

Citation:
Gagat M, Zielińska W, Mikołajczyk K, Zabrzyński J, Krajewski A, Klimaszewska-Wiśniewska A, Grzanka D and Grzanka A (2021) CRISPR-Based Activation of Endogenous Expression of TPM1 Inhibits Inflammatory Response of Primary Human Coronary Artery Endothelial and Smooth Muscle Cells Induced by Recombinant Human Tumor Necrosis Factor α. Front. Cell Dev. Biol. 9:668032. doi: 10.3389/fcell.2021.668032

Tumor necrosis factor α (TNFα) is one of the most important proinflammatory cytokines, which affects many processes associated with the growth and characteristics of endothelial, smooth muscle, and immune system cells. However, there is no correlation between most *in vivo* and *in vitro* studies on its role in endothelial cell proliferation and migration. In this study, we examined the effect of recombinant human (rh) TNFα produced in HEK293 cells on primary human coronary artery endothelial cells (pHCAECs) in the context of F-actin organization and such processes as migration and adhesion. Furthermore, we evaluated the possibility of the inhibition of the endothelial inflammatory response by the CRISPR-based regulation of *TPM1* gene expression. We showed that TNFα-induced activation of pHCAECs was related to the reorganization of the actin cytoskeleton into parallel-arranged stress fibers running along the longer axis of pHCAECs. It allowed for the directed and parallel motion of the cells during coordinated migration. This change in F-actin organization promoted strong but discontinuous cell–cell contacts involved in signalization between migrating cells. Moreover, this form of intercellular connections together with locally increased adhesion was related to the formation of migrasomes and further migracytosis. Stabilization of the actin cytoskeleton through the CRISPR-based activation of endogenous expression of *TPM1* resulted in the inhibition of the inflammatory response of pHCAECs following treatment with rh TNFα and stabilization of cell–cell junctions through reduced cleavage of vascular endothelial cadherin (VE-cadherin) and maintenance of the stable levels of

α- and β-catenins. We also showed that CRISPR-based activation of *TPM1* reduced inflammatory activation, proliferation, and migration of primary human coronary artery smooth muscle cells. Therefore, products of the *TPM1* gene may be a potential therapeutic target for the treatment of proinflammatory vascular disorders.

Keywords: TNFα, endothelial cells, angiogenesis, F-actin, cell–cell junctions, cell adhesion, migrasomes, inflammation

INTRODUCTION

The endothelial barrier plays a pivotal role in the regulation of the functioning of the entire circulatory system (Godo and Shimokawa, 2017). For this reason, any disturbances in the endothelial structure are associated with unfavorable health effects. Endothelial dysfunction manifests into abnormalities in the anticoagulant and anti-inflammatory properties of cells as well as alterations in vascular growth and vascular remodeling. It is associated with phenomena like hypertension and atherosclerosis (Chistiakov et al., 2015; Gimbrone and García-Cardeña, 2016). Endothelium produces nitric oxide, which is responsible for the relaxation of the underlying vascular smooth muscle. Reduced activity of endothelial nitric oxide synthase is observed in diabetes and hypertension. It also promotes vasoconstriction, thrombosis, and infiltration of the immune system cells (Matsushita et al., 2001). In turn, it is associated with the increased production of proinflammatory factors that induce the excessive proliferation of vascular smooth muscle cells. Proinflammatory cytokines also cause further accumulation of immune cells at the site of endothelial layer disruption. The increased production of endothelium-derived contracting factors leads to even greater deregulation of vessel wall functioning (Virdis et al., 2010).

Disbalance between the vasodilators and vasoconstrictors is not the only phenomenon leading to disruption of the endothelial barrier. From a biological perspective, endothelial dysfunction begins much earlier and manifests by intense changes in the structure, level, and function of membrane and intracellular proteins (Gimbrone and García-Cardeña, 2016). They are associated particularly with abnormalities at the level of junctional proteins, which can be observed as alterations in the pattern of intercellular connections. The types of cell contacts that guarantee the continuity of the endothelial layer are adherens junctions (AJs) and tight junctions (TJs). The main proteins involved in those types of connections in vascular endothelium are vascular endothelial cadherin (VE-cadherin) and claudin-5. However, proinflammatory conditions lead to a loosening of the junctional network, which manifests in the discontinuity at the cell–cell border and the appearance of spaces between cells (Cerutti and Ridley, 2017). These spaces allow, for example, massive infiltration of monocytes to the vessel wall, observed during the development and exacerbation of atherosclerosis. Other effects of proinflammatory conditions are enhanced cell adhesion and increased migration (Kaczmarek et al., 2005; Perna et al., 2013). In our work, we suggest that increased intracellular tensions result in the mechanistic disruption of intercellular junctions, which leads to the loss of the endothelial barrier continuity.

Endothelial injury, as well as angiogenesis, propels the migration of endothelial cells, which aims to restore the continuity of the endothelial monolayer or formation of new vessels (Michaelis, 2014). The cells can migrate both individually and in a coordinated manner depending on the intercellular signals and environmental factors. Collective migration is defined as the migration of cells that remain functionally and physically connected through stable intercellular connections. At the same time, such cells are characterized by multicellular polarity and the organization of the cytoskeleton that allows them to generate traction forces. In this type of migration, cell movement is coordinated locally and as a result, tightly connected cells move in the same direction (Canver et al., 2016).

All these changes, however, would not be possible without alterations at the actin cytoskeleton level. Changes in the organization of F-actin are involved in such processes as migration, proliferation, and cell adhesion. Moreover, the interaction of the actin cytoskeleton with junctional proteins allows the transfer of tensions from the relatively weak intercellular junctions to the more resistant cytoskeleton (van Geemen et al., 2014). In the case of non-activated endothelium, F-actin is organized into characteristic star-like structures that guarantee an appropriate distribution of intracellular tensions and enable a quick response to external factors, for example, through the ability of multidirectional migration. However, cell activation in response to proinflammatory cytokines involves the remodeling of the actin network into thick bundles of highly polymerized and parallel stress fibers. The changes in the organization of the actin cytoskeleton are possible only due to the activity of actin-binding proteins, which include tropomyosins (Gunning et al., 2015).

We have shown that tropomyosin-1 inhibits both polymerization and depolymerization of the actin filaments induced by L-homocysteine and cigarette smoke extract and impacts the integrity of EA.hy926 endothelial cells (Gagat et al., 2013, 2014). However, whether and how the expression of tropomyosin-1 and stabilization of actin cytoskeleton affect the inflammatory response of endothelial cells remain unknown. Therefore, the main goal of this study is to show that CRISPR-based activation of *TPM1* expression can maintain the proper organization of coronary artery endothelial cell monolayer and inhibit proliferation of smooth muscle cells in inflammatory conditions mimicked by the use of human recombinant (rh) tumor necrosis factor α (TNFα). In the present study, we characterized the effect of rh TNFα on primary human coronary artery endothelial cells (pHCAECs) in the context of F-actin organization and modulation of F-actin-dependent processes, including cell migration, adhesion, and migracytosis. The obtained results are important not

only from the mechanistic point of view but also have the potential to be translated into clinical research and adapted during the design and development of new coronary stent devices.

MATERIALS AND METHODS

Cell Culture and Treatment

Primary human coronary artery endothelial cells and primary human coronary artery smooth muscle cells (pHCASMCs) were obtained from a healthy 23-year-old white male or 53-year-old white male, respectively (cause of death: head trauma secondary to blunt injury). The cells were provided by the American Type Culture Collection (ATCC) and maintained according to supplier recommendations. Briefly, the endothelial cells were cultured in a vascular cell basal medium (ATCC) supplemented with an endothelial cell growth kit (ATCC) containing 5 ng/ml recombinant human (rh) VEGF, 5 ng/ml rh EGF, 5 ng/ml rh FGF basic, 15 ng/ml rh IGF-1, 10 mM L-glutamine, 0.75 units/ml heparin sulfate, 1 μg/ml hydrocortisone hemisuccinate, 2% fetal bovine serum (FBS), 50 μg/ml ascorbic acid, and antibiotics (10 units/ml penicillin, 10 μg/ml streptomycin, and 25 μg/ml amphotericin B). The smooth muscle cells were cultured in a vascular cell basal medium (ATCC) supplemented with a vascular smooth muscle cell growth kit (ATCC) containing 5 ng/ml rh FGF-basic, 5 μg/ml rh insulin, 50 μg/ml ascorbic acid, 10 mM L-glutamine, 5 ng/ml rh EGF, 5% fetal bovine serum, and antibiotics (10 units/ml penicillin, 10 μg/ml streptomycin, and 25 μg/ml amphotericin B). The cells were initially seeded at a density of 5,000 viable cells/cm^2 and cultured in T-25 cm^2 flasks (Corning) at 37°C in a humidified atmosphere of 5% CO_2 and 95% air. After reaching confluence, the cells were treated with complete vascular growth medium containing rh TNFα (Sigma-Aldrich), expressed in HEK293 cells, at a concentration of 100 ng/ml for 24 h (or 36 h for time-dependent analysis of migration directiveness). The control cells were grown under the same condition without rh TNFα treatment. Only cells within three to four passages were used for all the experiments.

Detection of Functional Expression of Adhesion Molecules

The detection of functional expression of E-selectin and VCAM-1 was performed using antibody-coated magnetic beads. The immobilization of Dynabeads M-280 Sheep Anti-Mouse IgG (Thermo Fisher Scientific) was done according to manufacturer instructions. Briefly, 2 μg of mouse anti-E-selectin (clone: CL2/6) or mouse anti-VCAM-1 (clone: 1.G11B1) monoclonal antibodies (both from Thermo Fisher Scientific) was added to 50 μl of pre-washed beads and resuspended in 1 ml of Ca^{2+}- and Mg^{2+}-free phosphate-buffered saline (PBS, pH 7.4), supplemented with 0.1% bovine serum albumin (BSA, Sigma-Aldrich) and 2 mM EDTA (Sigma-Aldrich), and incubated with gentle tilting and rotation for 18 h at 4°C. The beads were then washed four times using a washing buffer and resuspended in 1 ml of complete and pre-warmed vascular growth medium. Five hundred microliters of resuspended beads was added to 100 ng/ml TNFα-treated or control pHCAECs grown in 24-well glass-bottom cell imaging plates (Eppendorf) and incubated in standard cell culture conditions for 30 min. After washing with Dulbecco's PBS (DPBS, ATCC), the cells were fixed in 4% paraformaldehyde in PBS for 20 min (Sigma-Aldrich) and stained for F-actin using Alexa Fluor 594 phalloidin (Thermo Fisher Scientific) for 20 min. The cells were then counterstained with 4′,6-diamidino-2-phenylindole (DAPI, Sigma-Aldrich) for 10 min. All steps were performed at room temperature (RT). Images were acquired on an Axio Observer Z1 inverted motorized microscope (Zeiss), using an EC Plan-Neofluar × 10/0.30 Ph1 air objective, Axiocam 503 mono camera, and ZEN 2 software (all from Zeiss). Parallel bright-field and fluorescence images were recorded at the same location.

Co-culture of Primary Human Coronary Artery Endothelial Cells With Jurkat T Cells

Jurkat T cells (clone E6-1, ATCC) were maintained according to supplier recommendations. Briefly, the cells were initially seeded at a density of 1×10^5 viable cells/ml and maintained in RPMI-1640 medium supplemented with 10% FBS and 50 μg/ml gentamycin (all from Lonza) in T-25 cm^2 flasks (Corning) at 37°C in a humidified atmosphere of 5% CO_2 and 95% air. After the desired density is reached, the cells were stimulated with 100 ng/ml rh TNFα for 2 h. The nuclei of cells were stained using the NucBlue Live Cell Stain ReadyProbes Reagent (Hoechst 33342 dye, Thermo Fisher Scientific) for 30 min. Around 2×10^5 counterstained Jurkat T cells were then washed with DPBS, resuspended in 500 μl of complete and pre-warmed vascular growth medium and added to TNFα-activated or control pHCAECs grown in 12-well plates (Corning). Jurkat T cells were co-cultured with pHCAECs in standard cell culture conditions for 30 min in the presence or absence of rh TNFα. Before co-culture, pHCAECs were cultured in the presence or absence of rh TNFα for 24 h. Time-lapse images were acquired, at 3.33-s intervals over 2 min, in standard cell culture conditions on an Axio Observer Z1 inverted motorized microscope (Zeiss) equipped with an incubation system for live-cell imaging (PeCon), using an EC Plan-Neofluar × 10/0.30 Ph1 air objective, Axiocam 503 mono camera, and ZEN 2 software (all from Zeiss). Parallel contrast phase and fluorescence images were recorded at the same location. The number of adherent Jurkat T cells was counted after washing cells three times with DPBS in three randomly chosen microscopic fields using ImageJ (NIH).

Confluent Cell Migration

Confluent cell migration assay was performed using six-well plates (Corning). After confluence is reached, the cells were cultured in complete vascular growth medium supplemented or not with 100 ng/ml rh TNFα. Time-lapse images were acquired, at 10-min intervals over 36 h in standard cell culture conditions on an Axio Observer Z1 inverted motorized microscope (Zeiss) equipped with an incubation system for live-cell imaging (PeCon), using an EC Plan-Neofluar × 10/0.30 Ph1 air objective, Axiocam 503 mono camera, and ZEN 2 software (all from

Zeiss). Phase contrast images were recorded at a location of the migration gap and sites of open-field migration. Cell movement was analyzed using the Manual Tracking plugin for ImageJ (NIH). To quantify the dynamics of cell migration, such as velocity or Euclidean distance and accumulated distance, the migration trajectories were then assessed with Chemotaxis and Migration Tool 2.0 (Ibidi).

Wound Healing and Open-Field Migration

Wound healing and open-field migration assays were performed using a two-well culture insert (Ibidi). pHCAECs were resuspended in 70 μl of complete vascular growth medium and plated at a density of 1,100 cells per well into each reservoir of a culture insert (Ibidi) that adhered to the bottom of a six-well plate (Corning) and grown in standard cell culture conditions. After confluence is reached, the insert was removed using forceps, and the plate was rinsed with DPBS to remove cell debris. Migrating cells were cultured in complete vascular growth medium supplemented or not with 100 ng/ml rh TNFα. Time-lapse images were acquired, at 10-min intervals over 24 h, in standard cell culture conditions on an Axio Observer Z1 inverted motorized microscope (Zeiss) equipped with an incubation system for live-cell imaging (PeCon), using an EC Plan-Neofluar × 10/0.30 Ph1 air objective, Axiocam 503 mono camera, and ZEN 2 software (all from Zeiss). Phase contrast images were recorded at a location of the migration gap and sites of open-field migration. Cell movement was analyzed using the Manual Tracking plugin for ImageJ (NIH). To quantify the dynamics of cell migration, such as velocity or Euclidean distance and accumulated distance, the migration trajectories were then assessed with Chemotaxis and Migration Tool 2.0 (Ibidi).

Modified Boyden Chamber Assay

Modified Boyden chamber assay was done using uncoated Transwell inserts with microporous polyethylene terephthalate (PET) membranes (3-μm pore size) placed in 24-well plates (both from Corning). pHCAECs were resuspended at a density of 1,650 cells per well in complete vascular growth medium and plated in the upper chamber of the Transwell inserts. The lower chamber of the wells contained 600 μl of complete vascular growth medium. After confluence is reached, the media in the upper Transwell chamber were replaced with complete vascular growth medium supplemented or not with 100 ng/ml rh TNFα. The media in the wells of the 24-well plate were the same and additionally supplemented with 20% FBS. After 24 h, the Transwell inserts were fixed with 4% formaldehyde for 15 min (Sigma-Aldrich) and washed three times with PBS, and the cells were stained with toluidine blue. All steps were performed at RT. The cells on the upper side of the membrane were removed with cotton swabs, and the inserts were left to air-dry. Bright-field images of the lower side of the membranes were captured by an Eclipse E800 microscope (Nikon) using a Plan Fluor × 10/0.30 air objective, DS-5Mc-U1 camera, and NIS-Elements 3.30 (all from Nikon). The number of migrated cells was counted in randomly chosen microscopic fields using ImageJ (NIH).

In vitro Tube Formation Assay

Endothelial tube formation assay was performed in μ-Slide Angiogenesis (Ibidi) according to the manufacturer's guidelines. Briefly, inner wells were filled with 10 μl of ice-cold, growth factor-reduced, and phenol-red-free Matrigel Basement Membrane Matrix (Corning) and set at 37°C. pHCAECs were resuspended in 50 μl of complete vascular growth medium supplemented or not with 100 ng/ml rh TNFα and plated at a density of 10,000 cells per well into the upper well and cultured in standard conditions. Time-lapse images were acquired, at 10-min intervals over 24 h, in standard cell culture conditions on an Axio Observer Z1 inverted motorized microscope (Zeiss) equipped with an incubation system for live-cell imaging (PeCon), using a Zeiss EC Plan-Neofluar × 10/0.30 Ph1 air objective, Axiocam 503 mono camera, and ZEN 2 software (all from Zeiss). Contrast phase images were recorded at the same location. Additionally, tube formation was monitored using a bright-field microscope at 3, 6, 12, and 24 h after seeding. The cells were fixed with 4% formaldehyde for 15 min (Sigma-Aldrich), washed three times with PBS, and stained with crystal violet. All steps were performed at RT. Bright-field images were captured by an Eclipse E800 microscope (Nikon) using a Plan UW × 2/0.06 air objective, DS-5Mc-U1 camera, and NIS-Elements 3.30 (all from Nikon). The number of tubes was counted using ImageJ (NIH).

Wash Assay

Wash assay was performed using six-well plates (Corning). The cells were initially seeded at a density of 5,000 viable cells/cm^2 in complete vascular growth medium supplemented or not with 100 ng/ml rh TNFα and cultured in a humidified atmosphere of 5% CO_2 and 95% air. At 0, 0.5, 2, and 4 h after seeding, the cells were washed three times with complete vascular growth to remove non-adherent cells. Contrast phase images were captured in standard cell culture conditions on an Axio Observer Z1 inverted motorized microscope (Zeiss) equipped with an incubation system for live-cell imaging (PeCon), using a Zeiss EC Plan-Neofluar × 10/0.30 Ph1 air objective, Axiocam 503 mono camera, and ZEN 2 software (all from Zeiss). The number of adherent cells was counted using ImageJ (NIH).

Temporal Analysis of Actin Cytoskeleton and Focal Adhesion Sites

For temporal analysis of TNFα-induced changes in the organization of actin cytoskeleton and actin-mediated focal adhesion, pHCAECs were transiently transduced using a baculovirus system to express the green fluorescent protein (GFP)-fused human actin and the red fluorescent protein (RFP) fused to the c-terminus of human talin. The cells were transiently transduced with CellLight Reagents BacMam 2.0 (Thermo Fisher Scientific) according to the manufacturer's recommendations. Briefly, pHCAECs were grown in 24-well cell imaging plates (Eppendorf) and cultured in standard conditions. After 70% confluence is reached, the cells were infected with CellLight actin-GFP and CellLight Talin-RFP BacMam 2.0 baculoviruses at a multiplicity of infection (MOI) of 30. After 16 h, the medium containing the baculoviruses was replaced with complete vascular

growth medium supplemented or not with 100 ng/ml rh TNFα, and the cells were cultured in standard conditions. Time-lapse images were acquired, at 10-min intervals over 24 h, in standard cell culture conditions on an Axio Observer Z1 inverted motorized microscope (Zeiss) equipped with an incubation system for live-cell imaging (PeCon), using a Zeiss EC Plan-Neofluar × 10/0.30 Ph1 air objective, Axiocam 503 mono camera, and ZEN 2 software (all from Zeiss). Fluorescence images were recorded at the same location. Furthermore, correlation between 3D morphology and localization of actin-GFP and talin-RFP in rh TNF-activated pHCAECs was imaged using an HT-2 correlative holotomographic and fluorescence microscope (Tomocube). For live-cell correlative holotomographic and fluorescence imaging, the cells were grown in 50-mm imaging dishes with 1.5H glass coverslip bottom (TomoDish, Tomocube) and covered before imaging with a square coverslip glass. For prevention against contamination and drying of the medium, the side of the dish was sealed by mineral oil (Sigma). Additionally, expression of actin-GFP and talin-RFP was examined by confocal microscopy. The cells were fixed with 4% formaldehyde for 15 min (Sigma-Aldrich), washed three times with PBS, and counterstained with DAPI (Sigma-Aldrich) for 10 min. All steps were performed at RT. Images were captured by a C1 laser scanning confocal microscope (Nikon) using a Plan VC Apo × 60/1.4 oil objective and Nikon EZ-C1 3.80 software (both from Nikon). The lasers used for DAPI, GFP, and RFP excitations were diode 408 nm with emission filter 450/35, diode 488 nm with emission filter 515/30, and He–Ne 543 nm with emission filter 650LP, respectively. All confocal images of triple-labeled cells were acquired and displayed with identical settings, including laser power, pixel dwell speed, and gain.

Coating With Extracellular Matrix Proteins

For the analysis of the possible effect of extracellular matrix (ECM) on different rearrangements of F-actin in TNFα-activated pHCAECs, the sterile glass coverslips (? 18 mm, Thermo Fisher Scientific) were covered by 5 g/cm^2 fibronectin (source: human plasma), laminin (source: Engelbreth-Holm-Swarm mouse tumor), collagen I (source: rat tail tendon), and collagen IV (source: Engelbreth-Holm-Swarm mouse tumor; all from Corning) according the manufacturer's instruction. The cells were grown on the coated glass coverslips in 12-well plates (Corning) and cultured in standard conditions. After confluence is reached, the cells were cultured for an additional period of 24 h in complete vascular growth medium supplemented or not with 100 ng/ml rh TNFα. The cells were then fixed with 4% formaldehyde for 15 min (Sigma-Aldrich), permeabilized for 10 min with 0.25% Triton X-100 (Serva), blocked with 3% BSA for 45 min (Sigma-Aldrich), and stained for F-actin using phalloidin–Alexa Fluor 488 (1:40) and phalloidin–Alexa Fluor 594 (1:40; both from Thermo Fisher Scientific). The cells were then counterstained with DAPI (Sigma-Aldrich) for 10 min. All of the fluorescence reaction steps were performed at RT. The slides were mounted in Aqua−Poly/Mount (Polysciences) and examined by confocal microscopy. Images were captured by a C1 laser scanning confocal microscope (Nikon) using a Plan VC Apo × 60/1.4 oil objective and Nikon EZ-C1 3.80 software (both from Nikon).

Transfection by Nucleofection

Endogenous expression of *TPM1* gene was regulated using CRISPR *TPM1* activation or knockout systems (both from Santa Cruz). The CRISPR activation system is a synergistic activation mediator transcription activation system designed to specifically upregulate *TPM1* and consists of three plasmids at a 1:1:1 mass ratio: a plasmid encoding the deactivated Cas9 nuclease (D10A and N863A) fused to the transactivation domain VP64, a plasmid encoding the MS2-p65-HSF1 fusion protein, and a plasmid encoding a *TPM1*-specific 20-nt guide RNA. The CRISPR *TPM1*-knockout system consists of a pool of three plasmids each encoding the Cas9 nuclease and a *TPM1*-specific 20-nt guide RNA. As a CRISPR control, we used the CRISPR control plasmid encoding the Cas9 nuclease and a non-specific 20-nt guide RNA. Components of the above-mentioned CRISPR systems were delivered into the cells by nucleofection technology according to the manufacturer's instruction using the P5 Primary Cell 4D-Nucleofector X Kit L and 4D-Nucleofector X unit (both from Lonza). Briefly, 4×10^5 cells were resuspended in 100 Nucleofector nucleofection solution and 2 μg of each CRISPR system was electroporated using the DY138 program at RT. The cells were then immediately transferred into pre-warmed complete vascular growth medium and cultured until confluency is reached for further procedures.

Fluorescence Localization of Proteins

For the fluorescence localization of proteins, the pHCAECs were grown on sterile glass coverslips (? 18 mm, Thermo Fisher Scientific) in 12-well plates (Corning) and cultured in standard conditions. After confluence is reached, the cells were cultured for an additional period of 24 h in complete vascular growth medium supplemented or not with 100 ng/ml rh TNFα. The cells were then fixed with 4% formaldehyde for 15 min (Sigma-Aldrich), permeabilized for 10 min with 0.25% Triton X-100 (Serva), and blocked with 3% BSA for 45 min (Sigma-Aldrich). Next, the cells were double stained using antibodies and phalloidin conjugates in the following arrangement: (i) mouse anti-talin (clone: 8D4) monoclonal antibody (1:500, Sigma-Aldrich), goat anti-mouse–Alexa Fluor 488 secondary antibody (1:200, Thermo Fisher Scientific), and phalloidin–Alexa Fluor 594 (1:40, Thermo Fisher Scientific); (ii) rabbit anti-VE-cadherin polyclonal antibody (1:200), donkey anti-rabbit–Alexa Fluor 594 secondary antibody (1:200), and phalloidin–Alexa Fluor 488 (1:40; all from Thermo Fisher Scientific); (iii) mouse anti-α-catenin (clone: 7A4) monoclonal antibody (1:250), goat anti-mouse–Alexa Fluor 488 secondary antibody (1:200), and phalloidin–Alexa Fluor 594 (1:40; all from Thermo Fisher Scientific); (iv) mouse anti-β-catenin (clone: 5H10) monoclonal antibody (1:250), goat anti-mouse–Alexa Fluor 488 secondary antibody (1:200), and phalloidin–Alexa Fluor 594 (1:40; all from Thermo Fisher Scientific); (v) mouse anti-ZO-1 (clone: 1A12) monoclonal antibody (1:200), goat anti-mouse–Alexa Fluor 488 secondary antibody (1:200), and phalloidin–Alexa Fluor 594

(1:40; all from Thermo Fisher Scientific); (vi) mouse anti-claudin-5 (clone: 4C3C2) monoclonal antibody (1:300), goat anti-mouse–Alexa Fluor 488 secondary antibody (1:200), and phalloidin–Alexa Fluor 594 (1:40; all from Thermo Fisher Scientific); (vii) rabbit anti-non-muscle myosin IIa (MYH9) polyclonal antibody (1:100), donkey anti-rabbit–Alexa Fluor 594 secondary antibody (1:200), and phalloidin–Alexa Fluor 488 (1:40; all from Thermo Fisher Scientific); (viii) rabbit anti-non-muscle myosin IIb (MYH10) polyclonal antibody (1:100), donkey anti-rabbit–Alexa Fluor 594 secondary antibody (1:200), and phalloidin–Alexa Fluor 488 (1:40; all from Thermo Fisher Scientific); (ix) rabbit anti-Arp 2/3 subunit 1B (ARPC1B) polyclonal antibody (1:100, Abcam), donkey anti-rabbit-Alexa Fluor 594 secondary antibody (1:200, Thermo Fisher Scientific), and phalloidin–Alexa Fluor 488 (1:40, Thermo Fisher Scientific); (x) rabbit anti-ROCK-1 polyclonal antibody (1:100), donkey anti-rabbit–Alexa Fluor 594 secondary antibody (1:200), and phalloidin–Alexa Fluor 488 (1:40; all from Thermo Fisher Scientific); (xi) rabbit anti-ROCK-2 polyclonal antibody (1:100), donkey anti-rabbit–Alexa Fluor 594 secondary antibody (1:200), and phalloidin–Alexa Fluor 488 (1:40; all from Thermo Fisher Scientific); (xii) mouse anti-E-selectin (clone: CL2/6) monoclonal antibody (1:100), goat anti-mouse–Alexa Fluor 488 secondary antibody (1:200), and phalloidin–Alexa Fluor 594 (1:40; all from Thermo Fisher Scientific); and (xiii) mouse anti-VCAM-1 (clone: 1.G11B1) monoclonal antibody (1:200), goat anti-mouse–Alexa Fluor 488 secondary antibody (1:200), and phalloidin–Alexa Fluor 594 (1:40; all from Thermo Fisher Scientific). The pHCASMCs were grown in similar conditions and stained using (i) mouse anti-ICAM-1 (clone: 1A29) monoclonal antibody (1:250) and goat anti-mouse–Alexa Fluor 594 secondary antibody (1:200; both from Thermo Fisher Scientific); (ii) mouse anti-VCAM-1 (clone: 1.G11B1) monoclonal antibody (1:200) and goat anti-mouse–Alexa Fluor 488 secondary antibody (1:200; both from Thermo Fisher Scientific); (iii) rabbit anti-CDKN2A/p16INK4a (clone: EPR1473) monoclonal antibody (1:100, Abcam) and donkey anti-rabbit–Alexa Fluor 594 secondary antibody (1:200, Thermo Fisher Scientific); (iv) rabbit anti-NFκB p65 polyclonal antibody (1:200) and donkey anti-rabbit–Alexa Fluor 594 secondary antibody (1:200; both from Thermo Fisher Scientific); and (v) rabbit CCN4/WISP1 polyclonal antibody (1:500) and donkey anti-rabbit–Alexa Fluor 594 secondary antibody (1:200; both from Thermo Fisher Scientific). All incubations with antibodies and/or phalloidin conjugates were carried out, respectively, for 1 h or 20 min, followed by three washes in PBS. The cells were then counterstained with DAPI (Sigma-Aldrich) for 10 min. All steps were performed at RT. The slides were mounted in Aqua−Poly/Mount (Polysciences) and examined by confocal microscopy. Images were captured by a C1 laser scanning confocal microscope (Nikon) using a Plan VC Apo × 60/1.4 oil objective and Nikon EZ-C1 3.80 software (both from Nikon). The lasers used for DAPI, Alexa Fluor 488, and Alexa Fluor 596 excitations were diode 408 nm with emission filter 450/35, diode 488 nm with emission filter 515/30, and He–Ne 543 nm with emission filter 650LP, respectively. All confocal images of triple-labeled cells were acquired and displayed with identical settings, including laser power, pixel dwell speed, and gain. The gain was set up for optimal visibility of specific proteins. In the case of the lack of possibility to show triple-labeled cells, the gain of the channel for F-actin was downregulated. The fluorescence intensity of selected proteins was quantified using ImageJ (NIH) and EZ-C1 (Nikon).

Immunoblot

Control pHCAECs and those treated with 100 ng/ml TNFα were lysed with RIPA buffer (Sigma-Aldrich) supplemented with Halt protease inhibitor cocktail (Thermo Fisher Scientific). After clarification of lysates (8,000 × *g* for 10 min at 4°C) and normalization of protein concentration by a BCA protein assay kit, 10 μg of total protein per lane was separated by SDS-PAGE at 225 V with Novex WedgeWell 10%–20% Tris-glycine gel and Mini Gel Tank (all from Thermo Fisher Scientific). The transfer onto a nitrocellulose membrane was performed by iBlot Dry Western Blotting System (Life Technologies). The membrane was then blocked for 10 min in a SuperSignal Western Blot Enhancer (Thermo Fisher Scientific) and incubated for 2.5 h or overnight in an iBind Flex Solution (Thermo Fisher Scientific) with (i) mouse anti-claudin-5 (clone: 4C3C2) monoclonal antibody (1:500) and goat anti-mouse–horseradish peroxidase secondary antibody (HRP, 1:2,000; both from Thermo Fisher Scientific); (ii) mouse anti-GAPDH (clone: ZG003) monoclonal antibody (1:500) and goat anti-mouse–HRP secondary antibody (1:2,000; both from Thermo Fisher Scientific); (iii) mouse anti-α-tropomyosin (clone: F-6) monoclonal antibody (1:100, Santa Cruz) and goat anti-mouse-HRP secondary antibody (1:2,000, Thermo Fisher Scientific); (iv) mouse anti-E-selectin (clone: CL2/6) monoclonal antibody (1:100) and goat anti-mouse–HRP secondary antibody (1:2,000; both from Thermo Fisher Scientific); (v) mouse anti-talin (clone: 8D4) monoclonal antibody (1:100, Sigma-Aldrich) and goat anti-mouse–HRP secondary antibody (1:2,000, Thermo Fisher Scientific); (vi) mouse anti-vinculin (clone: J144) monoclonal antibody (1:1,000) and goat anti-mouse-HRP secondary antibody (1:2,000; both from Thermo Fisher Scientific); (vii) mouse anti-α-catenin (clone: 7A4) monoclonal antibody (1:250) and goat anti-mouse–HRP secondary antibody (1:2,000; both from Thermo Fisher Scientific); (viii) mouse anti-β-catenin (clone: 5H10) monoclonal antibody (1:250) and goat anti-mouse–HRP secondary antibody (1:2,000; both from Thermo Fisher Scientific); (iv) rabbit anti-VE-cadherin polyclonal antibody (1:500) and goat anti-mouse–HRP secondary antibody (1:2,000; both from Thermo Fisher Scientific) using the iBind Flex Western System (Thermo Fisher Scientific). Protein bands were visualized using the 1-Step Ultra TMB-Blotting Solution (Thermo Fisher Scientific). All steps were performed at RT. All western blot assays were performed at least three times. Images were captured by the ChemiDoc MP Imaging System (Bio-Rad). Intensity of bands was quantified using ImageJ (NIH).

Statistical Analysis

The significant differences between two groups were calculated using an unpaired *t*-test or one-way ANOVA and Kruskal–Wallis test with Dunn's correction for multiple comparisons. Relations between cell migration parameters were assessed using

Pearson's correlation coefficient analysis. Statistical analyses were performed by using Prism 7 software (GraphPad). The Rayleigh test was used to determine cell movement homogeneity using Chemotaxis and Migration Tool 2.0 (Ibidi). A p-value < 0.05 was considered to be statistically significant and labeled on figures as * or \$, $p < 0.05$; ** or \$\$, $p < 0.01$; *** or \$\$\$, $p < 0.001$; **** or \$\$\$\$, $p < 0.0001$; and NS, non-significant. Results were expressed as means ± SD.

RESULTS

Tumor Necrosis Factor α Induces Inflammatory Activation of Primary Human Coronary Artery Endothelial Cells

Given that the use of *Escherichia coli* as an expression platform for recombinant proteins has several drawbacks (Rosano and Ceccarelli, 2014), we first examined whether rh TNFα expressed in HEK293 cells was able to activate coronary artery endothelial cells. To this end, pHCAECs were cultured to 100% confluence and then treated for 24 h with 100 ng/ml rh TNFα. We showed rh TNFα-induced surface and intracellular expressions of functional E-selectin (**Figure 1A** and **Supplementary Figure S1**) and VCAM-1 (**Supplementary Figures S2A,B**). We then examined the interactions between rh TNFα-activated pHCAECs and Jurkat T cells (**Figure 1B** and **Supplementary Video S1**). We observed a statistically significant increase in the number of Jurkat T cells adherent to pHCAECs (from 128.6 ± 47.00 per view in the control to 645 ± 81.01 in TNFα-activated cells, $p < 0.0001$) after 30 min of their co-culture (**Figure 1C** and **Supplementary Figure S2C**). Furthermore, we showed a statistically significant increase in the velocity of motile Jurkat T cells on pHCAECs (from 0.1641 ± 0.04247 to 0.4120 ± 0.07306 μm/min, $p < 0.0001$, respectively, for control and TNFα-activated pHCAECs; **Figure 1D**).

In summary, these data suggest that rh TNFα effectively activates pHCAECs and augments flattening, firm adhesion, and further migration of T cells on the endothelial monolayer.

Tumor Necrosis Factor α Augments the Invasive Potential of Primary Human Coronary Artery Endothelial Cells

Evidence from *in vitro* and *in vivo* data has demonstrated a dual role of TNFα in the angiogenic response of endothelial cells. It has been shown that TNFα generally exerts a proangiogenic effect *in vivo* and antiangiogenic *in vitro* (Fràter-Schröder et al., 1987; Sainson et al., 2008). However, it seems to function as a stimulatory or inhibitory agent dependent on the model used and experimental condition. As depicted in **Supplementary Figures S1, S2B**, the exposure of pHCAECs to 100 ng/ml rh TNFα resulted in remarkable changes in the cell morphology, whereby cells appeared enlarged and elongated. We next examined whether these morphological changes were accompanied by enhanced migration capacity of pHCAECs and ability to form tubules on the Matrigel. We first investigated the migration pattern of pHCAECs cultured in the confluence. As shown on rose plots in **Figure 2A**, during 24 h of incubation with 100 ng/ml rh TNFα, pHCAECs moved in a more persistent manner, with decreased changes in direction, whereas control cells exhibited a more random migration pattern, suggesting that TNFα promoted directional migration of pHCAECs. This finding was further supported by a high significance of the Rayleigh test (from $p = 2.74694 \times 10^{-3}$ to $p = 4.90393 \times 10^{-5}$, respectively, for control and TNFα-activated cells). As cultured in 100% confluence for 24 h, there was no effect of rh TNFα on Euclidean distance of migrating cells (**Figure 2B**). However, the accumulated distance traveled by rh TNFα-activated pHCAECs was significantly shorter compared to the control cells (from 808.8 ± 146.2 to 573.5 ± 124.0 μm, $p < 0.0001$; **Figure 2C**). Furthermore, we showed a statistically significant decrease in the velocity of these cells (from 0.5656 ± 0.1023 to 0.4035 ± 0.09019 μm/min, $p < 0.0001$, respectively, for control and TNFα-activated cells; **Figure 2D**). The extended tracking time of migrating cells for up to 36 h allowed us to demonstrate that longer rh TNFα treatment also promoted the migration of pHCAECs in a more directional manner (Rayleigh test: $p = 2.96697 \times 10^{-2}$ *vs.* $p = 4.24461 \times 10^{-5}$; **Supplementary Figure S3A**) without the effect on Euclidean distance (**Supplementary Figure S3B**). Longer exposition of pHCAECs to rh TNFα also revealed shorter accumulated distance of migrating cells (1215.0 ± 194.4 *vs.* 816.7 ± 194.6, $p < 0.0001$; **Supplementary Figure S3C**) related with their decreased velocity (0.5626 ± 0.09002 *vs.* 0.3781 ± 0.09008 μm/min, $p < 0.0001$; **Supplementary Figure S3D**), when compared to untreated pHCAECs. Furthermore, there was a negative correlation between time of treatment and Euclidean distance ($r = -0.5166$, $p = 0.0013$), accumulated distance ($r = -0.4916$, $p = 0.0023$), and velocity ($r = -0.4837$, $p = 0.0028$; **Supplementary Figures S3E–G**). Additional analysis revealed that Euclidean distance ($r = 0.6206$, $p < 0.0001$), accumulated distance ($r = 0.3723$, $p = 0.0253$), and velocity ($r = 0.3790$, $p = 0.0226$), but not time of treatment, were correlated with the directness of rh TNFα-activated pHCAECs (**Supplementary Figure S3I**), giving further support for the conclusion that pHCAECs undergo directed migration upon rh TNFα treatment. In control cells, we only observed the correlation between directness of cells and Euclidean distance ($r = 0.7929$, $p < 0.0001$; **Supplementary Figure S3H**).

Differently, wound healing (**Figure 2E** and **Supplementary Video S2**) and open-field migration (**Figure 2F** and **Supplementary Video S3**) assays showed faster migration of rh TNFα-activated pHCAECs as compared to the control, especially from the third hour of wound healing experiment or the 12th hour of open migration test.

We further analyzed the protrusion tips during rh TNFα-activated cell migration. As shown in **Supplementary Figures S3J,K** as well as in **Supplementary Videos S2, S3**, examination of the leading edge of migrating cells revealed rh TNFα-dependent formation of spindle-shaped leader cells with an aggressive phenotype oriented toward the direction of the movement. Analysis of trajectories of leader cells during the migration of TNFα-activated pHCAECs into the open field showed a statistically significant increase in Euclidean distance (from 374.4 ± 89.41 to 477.1 ± 120.4 μm, $p = 0.0004$,

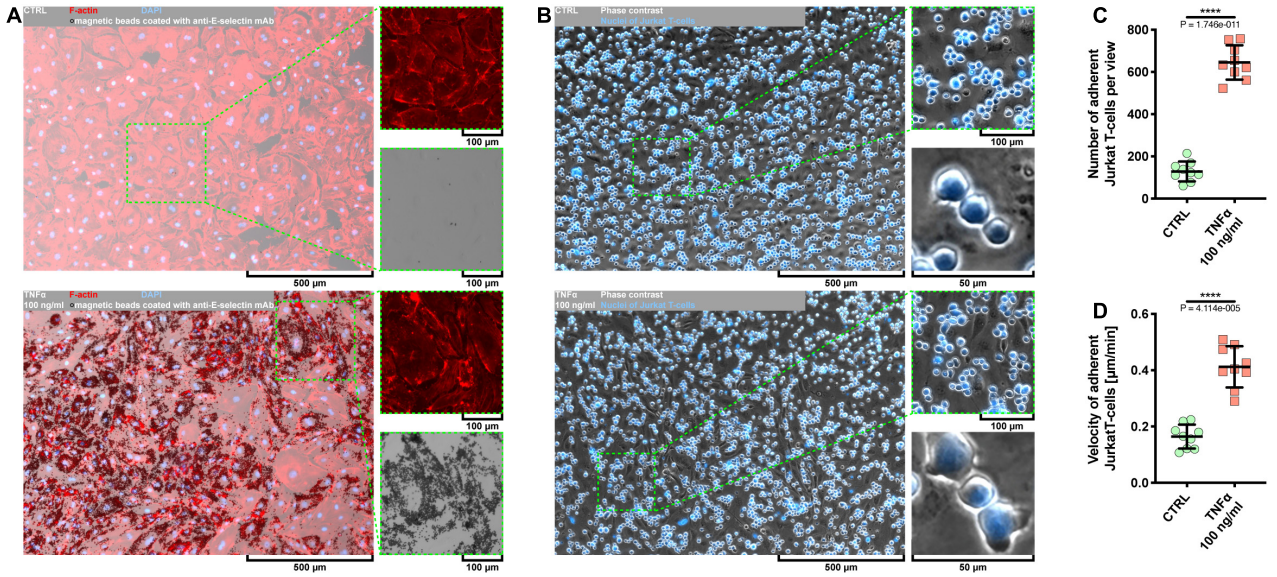

FIGURE 1 | Effect of TNFα on activation of pHCAECs. **(A)** Representative micrographs of intravital detection of E-selectin using magnetic beads coated with anti-E-selectin monoclonal antibodies (bright field). F-actin (red) and nuclei (blue) were stained fluorescently after fixation. CTRL refers to the control (top panel), TNFα 100 ng/ml to cells treated with rh TNFα (bottom panel), mAb to monoclonal antibodies. **(B)** Representative micrographs of intravital co-culture of pHCAECs (contrast phase) with Jurkat T cells (contrast phase and fluorescence). Nuclei of Jurkat T cells (blue) were stained with Hoechst 33342. CTRL refers to the control (top panel), TNFα 100 ng/ml to cells treated with rh TNFα (bottom panel). **(C)** Number of adherent Jurkat T cells to pHCAECs per microscopic field from the control and TNFα-activated pHCAECs after 30 min of their co-culture. CTRL refers to the control (top panel), TNFα 100 ng/ml to cells treated with rh TNFα, **** to $p < 0.0001$, as determined by unpaired *t*-test. **(D)** Velocity of motile Jurkat T cells on pHCAECs during 30 min of their co-culture. CTRL refers to the control (top panel), TNFα 100 ng/ml to cells treated with rh TNFα. ****$p < 0.0001$, as determined by unpaired *t*-test.

respectively, for control and TNFα-activated cells; **Figure 2G**), accumulated distances (from 554.1 ± 94.78 to 785.1 ± 138.2 µm, $p < 0.0001$, respectively, for control and TNFα-activated cells; **Figure 2H**), and velocity (from 0.3946 ± 0.07763 to 0.5703 ± 0.07103 µm/min, $p < 0.0001$, respectively, for control and TNFα-activated cells; **Figure 2I**), as compared to the control. TNFα-induced increase in the migratory potential of pHCAECs was also confirmed by their migration toward the chemo-attractant environment through 3-µm pores (**Figure 2J**). As shown in **Supplementary Figure S3L**, we observed a three-times-higher number of migrating pHCAECs after treatment with 100 ng/ml rh TNFα, when compared to the control (6.667 ± 3.240 *vs.* 22.89 ± 5.183, $p < 0.0001$). We further investigated if rh TNFα had any effect on pHCAEC formation of tube-like structures on Matrigel (**Figure 2K** and **Supplementary Video S4**). We observed a statistically significant increase in the number of tubules formed by rh TNFα-treated pHCAECs during the experiment (from 97.78 ± 10.33 to 141.3 ± 14.75 after 3 h, $p < 0.0001$; from 86.56 ± 5.833 to 100.2 ± 5.403 after 6 h, $p < 0.0001$; and from 45.22 ± 2.386 to 54.22 ± 1.856 after 6 h, $p < 0.0001$, respectively, for control and TNFα-activated cells; **Supplementary Figure S3M**).

In summary, these data suggest that in contrast to cooperative migration of control pHCAECs, rh TNFα activates the potential of pHCAECs to collective and coordinated invasion into a new environment through the acquisition of an aggressive phenotype characterized by spindle-like morphology oriented toward the direction of the movement. This ability was remarkably reduced due to contact inhibition between cells when pHCAECs were cultured at a high density in the closed system. The way of migration pattern of control pHCAECs was cooperative.

Tumor Necrosis Factor α Induces Reorganization of the F-Actin Pattern in Primary Human Coronary Artery Endothelial Cells, Leading to the Formation of Aggressive Phenotypes and Reorganization of Cell–Cell Junctions

Due to remarkable changes in the morphology of rh TNFα-activated pHCAECs and different patterns of their movement, we analyzed the organization of F-actin, distribution of focal adhesion sites, and cell–cell junction proteins. As shown in confocal micrographs in **Figures 3A–G**, exposition of pHCAECs to 100 ng/ml rh TNFα induced changes in the organizational pattern of F-actin. We observed the transformation of F-actin from the star-like configuration in control pHCAECs into linear stress fibers in rh TNF-activated cells, as well as changes in the organization of focal adhesion sites (**Figures 3A,B** and **Supplementary Video S5**). Analyses of the localization of actin-GFP and talin-RFP, as well as fluorescently labeled F-actin and talin, revealed that developed prominent stress fibers in rh TNFα-activated pHCAECs were preceded by the formation of tension forces between star-like arranged F-actin bundles within individual cells, which seems to determine the

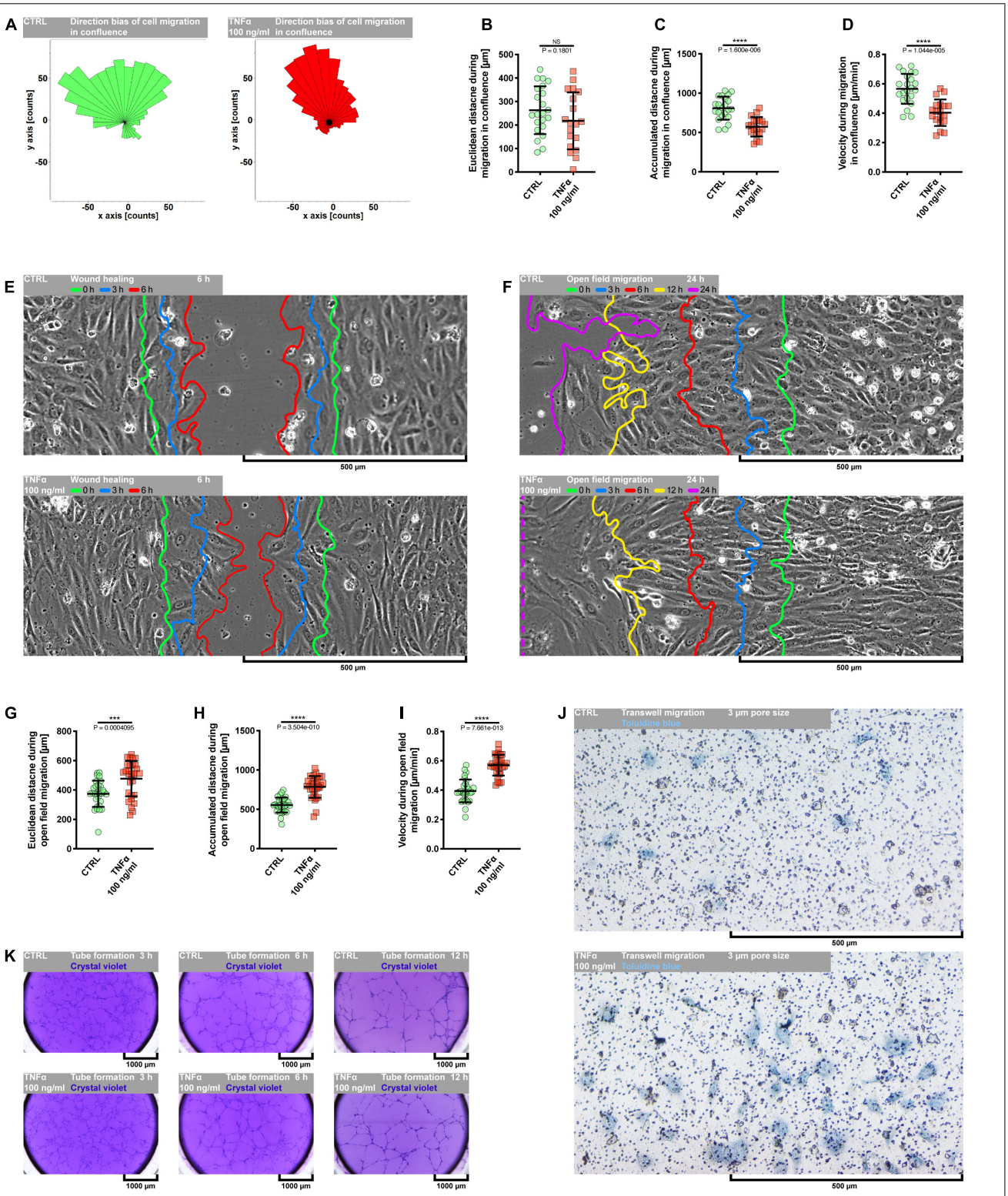

FIGURE 2 | Effect of TNFα on migration of pHCAECs. **(A)** Rose plot presenting direction bias of pHCAEC migration in confluence within 24 h. CTRL refers to the control (left panel), TNFα 100 ng/ml to cells treated with rh TNFα (right panel), ** to $p < 0.01$, **** to $p < 0.0001$, as determined by Rayleigh test. **(B)** Euclidean distance of pHCAECs during 24-h migration in 100% confluence. CTRL refers to the control, TNFα 100 ng/ml to cells treated with rh TNFα, NS to non-significant to the control, as determined by unpaired *t*-test. **(C)** Accumulated distance of pHCAECs during 24-h migration in 100% confluence.

(Continued)

FIGURE 2 | (Continued)
CTRL refers to the control, TNFα 100 ng/ml to cells treated with rh TNFα, **** to $p < 0.0001$, as determined by unpaired *t*-test. **(D)** Velocity of pHCAECs during 24-h migration in 100% confluence. CTRL refers to the control, TNFα 100 ng/ml to cells treated with rh TNFα, **** to $p < 0.0001$, as determined by unpaired *t*-test. **(E)** Representative contrast phase micrographs presenting pHCAEC migration to the wound site. Curves indicate area without cells in 0 h (green), 3 h (blue), and 6 h (red) of the wound healing assay. CTRL refers to the control (upper panel), TNFα 100 ng/ml to cells treated with rh TNFα (lower panel). **(F)** Representative contrast phase micrographs presenting pHCAEC migration to the open field. Curves indicate area without cells in 0 h (green), 3 h (blue), 6 h (red), 12 h (yellow), and 24 h (purple) of the open-field migration assay. CTRL refers to the control (upper panel), TNFα 100 ng/ml to cells treated with rh TNFα (lower panel). **(G)** Euclidean distance of pHCAECs during 24-h open-field migration. CTRL refers to the control, TNFα 100 ng/ml to cells treated with rh TNFα, *** to $p < 0.001$, as determined by unpaired *t*-test. **(H)** Accumulated distance of pHCAECs during 24-h open-field migration. CTRL refers to the control, TNFα 100 ng/ml to cells treated with rh TNFα, **** to $p < 0.0001$, as determined by unpaired *t*-test. **(I)** Velocity of pHCAECs during 24-h open-field migration. CTRL refers to the control, TNFα 100 ng/ml to cells treated with rh TNFα, **** to $p < 0.0001$, as determined by unpaired *t*-test. **(J)** Representative bright-field micrographs presenting migration of pHCAECs through 3-μm pores. The cells were stained with toluidine blue. CTRL refers to the control (upper panel), TNFα 100 ng/ml to cells treated with rh TNFα (lower panel). **(K)** Representative bright-field micrographs presenting tube formation by pHCAECs cultured on Matrigel. The tubular structures were stained with crystal violet after 3 h (left panel), 6 h (middle panel), and 12 h (right panel) from seeding. CTRL refers to the control (upper panels), TNFα 100 ng/ml to cells treated with rh TNFα (lower panels).

aggressive phenotype of pHCAECs. As shown in **Figures 3A,B** and **Supplementary Video S5**, this was related with increased cell–ECM adhesion, whereby adhesion sites were localized along newly formed and parallel-organized F-actin stress fibers (**Figures 3A,B**). The increased adhesion of rh TNFα-activated pHCAECs was confirmed in a wash assay (**Supplementary Figures S4A,B**). We found a statistically significant increase in the relative number of adherent cells per view after 1 h (from 1.033 ± 0.2395 to 1.153 ± 0.2252, $p = 0.0052$, respectively, for control and TNFα-activated cells), 2 h (from 0.9978 ± 0.2185 to 1.134 ± 0.3150, $p = 0.0378$), and 4 h (from 1.033 ± 0.2504 to 1.163 ± 0.3138, $p = 0.0225$) after seeding in complete vascular growth medium supplemented with rh TNFα (**Supplementary Figures S4C–F**).

Furthermore, we sought to determine whether seeding pHCAECs on different ECM proteins could affect the alignment pattern of stress fibers in response to rh TNFα. Stress fiber organization did not differ depending on ECM protein coatings and was the same as in pHCAECs cultured with rh TNFα on an uncoated surface. Indeed, actin stress fibers were parallel to each other, running along the longer axis of rh TNFα-activated pHCAECs regardless of whether they were cultured on fibronectin (**Supplementary Figures S5A,B**), laminin (**Supplementary Figures S5C,D**), collagen I (**Supplementary Figures S5E,F**), and collagen IV (**Supplementary Figures S5G,H**). It was also noticed that the formation of F-actin stress fibers was associated with increased membrane ruffling (**Supplementary Video S5**) and formation of punctae cell–cell junctions (**Figures 3C–G**). Furthermore, the discontinuous cell–cell contact areas in rh TNFα-activated pHCAECs were characterized by bright fluorescence of AJ proteins, such as VE-cadherin, α-catenin, and β-catenin (**Figures 3C–E**), and TJ proteins, namely, zonula occludens-1 (ZO-1) and claudin-5 (**Figures 3F,G**). Although we noticed posttranslational downregulation of claudin-5 after exposition of cells to rh TNFα, we also showed a strong 95-kDa reactive band, suggesting the oligomerization of claudin-5 (**Figure 3H**) and its different tethering of scaffold protein and F-actin due to different mechanical coupling of adjacent cells and their coordinated movement. Direct participation of AJ and TJ proteins in signalization between rh TNFα-activated cells is presented in the form of surface plots in **Figure 3I**.

Due to a fundamental role of non-muscle (NM) myosin II, actin-related protein (ARP) 2/3, and rho-associated coiled-coil containing protein kinases 1 and 2 (ROCK-1 and ROCK-2) in processes that require cellular reshaping and movement (Bhadriraju et al., 2007; Vicente-Manzanares et al., 2009; Smith et al., 2013) and our observations of the effect of rh TNFα on F-actin rearrangement, we analyzed the localization of these proteins in both star-like-shaped F-actin bundles and rh TNFα-induced cortical F-actin stress fibers or sites of punctae cell–cell junctions. As shown in the left panel of **Figures 4A–E**, NM myosin IIb, ARP 2/3 1B, and ROCK-1 were localized in star-like-shaped F-actin structures, indicating their role in the cooperative transmission of tensions between adjacent cells. Interestingly, TNFα-activated cells expressed NM myosin IIa, ARP 2/3 1B, and ROCK-1 in the regions of punctae cell–cell junctions (right panel in **Figures 4A–E**). These observations were confirmed by the analysis of the colocalization with F-actin (**Figure 4F**) and determined the tensional character of discontinuous junctions between rh TNFα-activated pHCAECs.

In summary, these data, at least partially, explain the change in the migration pattern of pHCAECs in response to rh TNFα (from cooperative in the control into coordinated in rh TNFα-activated cells). We suggest that the star-like-shaped organization of F-actin bundles determines the propensity of pHCAECs to cooperative migration, important in effective contribution of 'seal the gaps' function, whereas rh TNFα-induced formation of prominent, parallel stress fibers and subsequent organization of punctae, but strong cell–cell junctions, allows for the directed and parallel motion of the cells during coordinated migration.

Tumor Necrosis Factor α Induces Formation of Migrasomes Involved in Cell–Cell Signalization Between Migrating Primary Human Coronary Artery Endothelial Cells

Directional cell migration requires the series of changes in the structure and function of the cell at its different regions. These cover the formation of membrane-bounded cellular extensions at the leading edge and consequent retraction of the rear edge of the cell. It is widely accepted that tail retraction precedes and induces changes in migration direction and serves to maintain

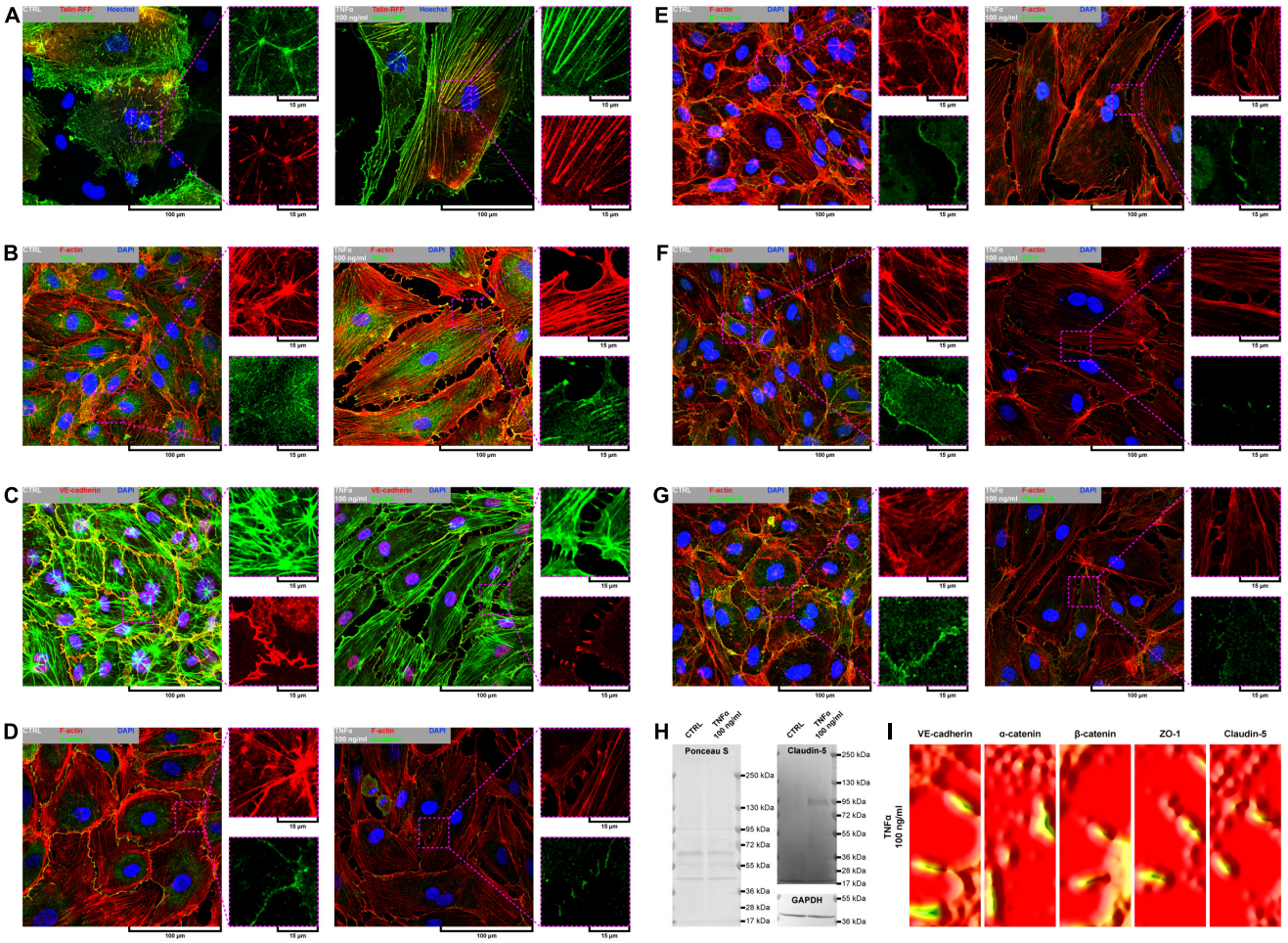

FIGURE 3 | Effect of TNFα on organizational pattern of F-actin, distribution of adhesion sites, and organization of cell–cell junctions in pHCAECs. **(A)** Representative confocal micrograph of intravital organization of F-actin and focal adhesion sites. Actin-GFP (red) and talin-RFP (green) were expressed using baculoviruses. Nuclei (blue) were stained with Hoechst 33342. CTRL refers to the control (left panel), TNFα 100 ng/ml to cells treated with rh TNFα (right panel). **(B)** Representative confocal micrograph of fluorescently stained F-actin and talin. Triple fluorescent staining for talin (green), F-actin (red), and DNA (blue) was performed after fixation. CTRL refers to the control (left panel), TNFα 100 ng/ml to cells treated with rh TNFα (right panel). **(C)** Representative confocal micrograph of fluorescently stained F-actin and VE-cadherin. Triple fluorescent staining for VE-cadherin (red), F-actin (green), and DNA (blue) was performed after fixation. CTRL refers to the control (left panel), TNFα 100 ng/ml to cells treated with rh TNFα (right panel). **(D)** Representative confocal micrograph of fluorescently stained F-actin and α-catenin. Triple fluorescent staining for α-catenin (green), F-actin (red), and DNA (blue) was performed after fixation. CTRL refers to the control (left panel), TNFα 100 ng/ml to cells treated with rh TNFα (right panel). **(E)** Representative confocal micrograph of fluorescently stained F-actin and β-catenin. Triple fluorescent staining for β-catenin (green), F-actin (red), and DNA (blue) was performed after fixation. CTRL refers to the control (left panel), TNFα 100 ng/ml to cells treated with rh TNFα (right panel). **(F)** Representative confocal micrograph of fluorescently stained F-actin and ZO-1. Triple fluorescent staining for ZO-1 (green), F-actin (red), and DNA (blue) was performed after fixation. CTRL refers to the control (left panel), TNFα 100 ng/ml to cells treated with rh TNFα (right panel), ZO-1 to zonula occludens-1. **(G)** Representative confocal micrograph of fluorescently stained F-actin and claudin-5. Triple fluorescent staining for claudin-5 (green), F-actin (red), and DNA (blue) was performed after fixation. CTRL refers to the control (left panel), TNFα 100 ng/ml to cells treated with rh TNFα (right panel). **(H)** Representative western blots for claudin-5 (upper right panel) and GAPDH (lower right panel) in lysates form pHCAECs. Protein transfer efficiency was assessed by Ponceau S staining (left panel). CTRL refers to the control (left lines), TNFα 100 ng/ml to cells treated with rh TNFα (right lines). **(I)** Representative surface plots of fluorescence intensity of VE-cadherin, α-catenin, β-catenin, ZO-1, and claudin-5 from regions of cell–cell interactions between rh TNFα pHCAECs. TNFα 100 ng/ml refers to cells treated with rh TNFα, ZO-1 to zonula occludens-1.

directionality of the force-generating leading edge of the cell (Xue et al., 2010; Theisen et al., 2012). During rh TNFα-induced coordinated migration of pHCAECs, we observed intensified formation of retraction fibers behind cells (**Figures 5A–D**). As shown **Figures 5A–E** and **Supplementary Video S5**, these long and tubular structures were rich in F-actin, and their formation resulted in increased adhesion and interactions between cells at the rear of migrating cells. We demonstrated that the tips of retraction fibers were continuously or discontinuously connected to the neighboring cells and were characterized by augmented adhesion, suggesting their role in transmission of F-actin-based mechanical forces for proper polarization of adjacent cells and coordination of their migration. These forces were generated by rapid contraction of retraction fibers toward the direction

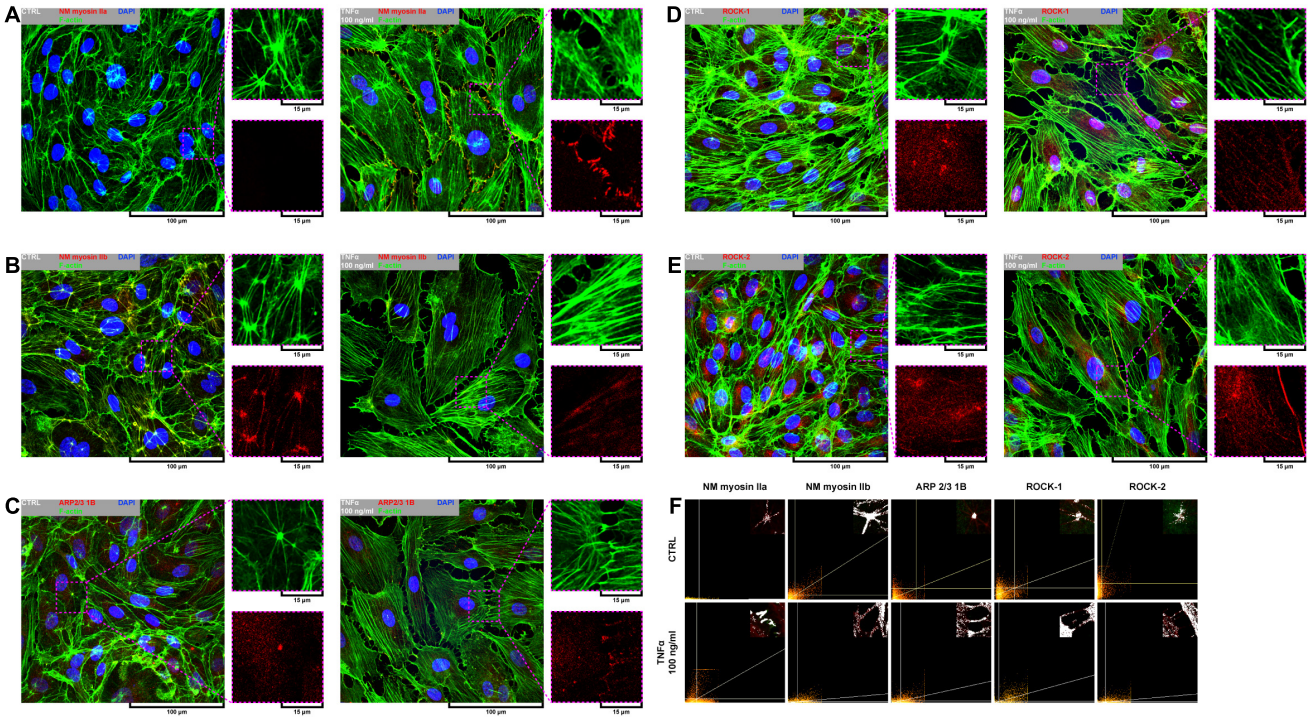

FIGURE 4 | Effect of TNFα on organizational pattern of F-actin and distribution of proteins regulating actin assembly and mechanics in pHCAECs. **(A)** Representative confocal micrograph of fluorescently stained F-actin and NM myosin IIa. Triple fluorescent staining for NM myosin IIa (red), F-actin (green), and DNA (blue) was performed after fixation. CTRL refers to the control (left panel), TNFα 100 ng/ml to cells treated with rh TNFα (right panel), NM to non-muscle. **(B)** Representative confocal micrograph of fluorescently stained F-actin and NM myosin IIb. Triple fluorescent staining for NM myosin IIb (red), F-actin (green), and DNA (blue) was performed after fixation. CTRL refers to the control (left panel), TNFα 100 ng/ml to cells treated with rh TNFα (right panel), NM to non-muscle. **(C)** Representative confocal micrograph of fluorescently stained F-actin and ARP2/3. Triple fluorescent staining for subunit 1B of ARP2/3 (red), F-actin (green), and DNA (blue) was performed after fixation. CTRL refers to the control (left panel), TNFα 100 ng/ml to cells treated with rh TNFα (right panel). **(D)** Representative confocal micrograph of fluorescently stained F-actin and ROCK-1. Triple fluorescent staining for ROCK-1 (red), F-actin (green), and DNA (blue) was performed after fixation. CTRL refers to the control (left panel), TNFα 100 ng/ml to cells treated with rh TNFα (right panel). **(E)** Representative confocal micrograph of fluorescently stained F-actin and ROCK-2. Triple fluorescent staining for ROCK-2 (red), F-actin (green), and DNA (blue) was performed after fixation. CTRL refers to the control (left panel), TNFα 100 ng/ml to cells treated with rh TNFα (right panel). **(F)** Representative co-localization maps of NM myosin IIa, NM myosin IIb, subunit 1B of ARP2/3, ROCK-1, and ROCK-2 with star-like-shaped F-actin (upper panels) or F-actin of cell–cell interactions (lower panels). CTRL refers to the control (upper panels), TNFα 100 ng/ml to cells treated with rh TNFα (lower panel).

of cell movement (**Figure 5F** and **Supplementary Video S5**). We also frequently observed formation of migrasomes at tips or the course of retraction fibers and their release by breaking the retraction fibers (**Supplementary Video S5**). Moreover, as shown in **Figures 5G–J**, the released migrasomes tended to occur at points of cell–cell and cell–ECM contact. We also noticed that during retraction fiber breakage, some migrasomes may be released to the cell culture medium, where they seem to play a role in intercellular signalization promoting directed cell migration (**Supplementary Video S6**).

In summary, these data show possible ways of signalization between TNFα-activated pHCAECs during their migration. The first concerns the generation of mechanical forces during contraction of retraction fibers, and the other one is related to migracytosis. We suggest here that the formation and release of migrasomes are highly related to increased adhesion and strength of punctae or continuous intercellular junctions at the tips of retraction fibers. Moreover, our observations allow us to assume that migrasomes released by TNFα-activated pHCAECs are involved in signalization between migrating pHCAECs.

Activation of Endogenous Expression of *TPM1* Inhibits Tumor Necrosis Factor α-Induced Inflammatory Response of Primary Human Coronary Artery Endothelial Cells and Force-Dependent Opening of Their Cell–Cell Junctions

It was shown by Tremblay et al. (2006) and in **Figure 1** or **Supplementary Figure S1** that E-selectin is the trigger of transendothelial migration but also accumulates quickly at punctae cell–cell junctions of activated endothelial cells, where it co-localizes with F-actin (Tremblay et al., 2006). We have previously shown that stabilization of F-actin by overexpression of α-tropomyosin protects endothelial integrity against L-homocysteine and cigarette smoke extract in EA.hy926 (Gagat et al., 2013, 2014). Similarly, our further studies revealed that

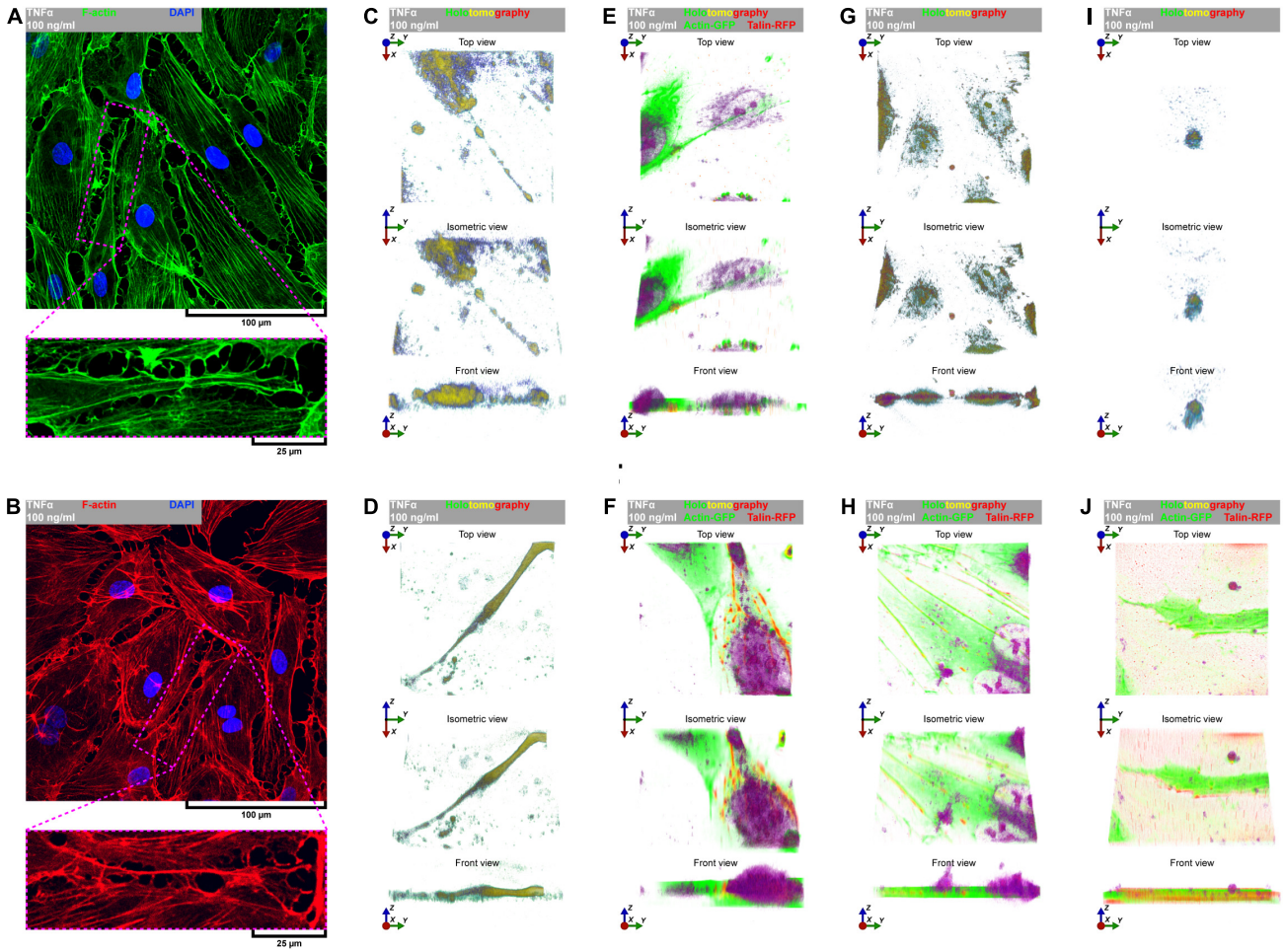

FIGURE 5 | TNFα-induced formation of migrasomes and migracytosis. **(A)** Representative confocal micrograph of fluorescently stained F-actin. Double fluorescent staining for F-actin (green) and DNA (blue) was performed after fixation. TNFα 100 ng/ml to cells treated with rh TNFα. **(B)** Representative confocal micrograph of fluorescently stained F-actin. Double fluorescent staining for F-actin (red) and DNA (blue) was performed after fixation. TNFα 100 ng/ml to cells treated with rh TNFα. **(C,D,G,I)** Representative intravital holotomography micrographs of pHCAECs forming and releasing migrasomes. TNFα 100 ng/ml to cells treated with rh TNFα. **(E,F,H,J)** Representative intravital correlative holotomographic and fluorescence micrographs of pHCAECs forming and releasing migrasomes. Actin-GFP (red) and talin-RFP (green) were expressed using baculoviruses. TNFα 100 ng/ml to cells treated with rh TNFα.

overexpression of α-tropomyosin preserves transformed alveolar epithelial cell–cell junctions against disintegration induced by cigarette smoke extract (Gagat et al., 2016). Here, we investigated the effect of CRISPR-based regulation of endogenous *TPM1* expression on the activation and posttranslational expression of cell–cell and cell–ECM adhesion proteins. First, we activated or deactivated endogenous expression of *TPM1* using CRISPR *TPM1* activation or knockout systems introduced to the cells by the nucleofection technique (**Figures 6A,B**). As shown in **Figure 6C**, the CRISPR systems worked effectively on modulating α-tropomyosin expression in pHCAECs (from 0.888 ± 0.0578 to 1.093 ± 0.0781, $p = 0.0044$ and to 0.305 ± 0.0122, $p < 0.0001$, respectively, for CRISPR *TPM1* activation and knockout systems). Furthermore, we showed that activation of endogenous expression of *TPM1* itself downregulated posttranslational expression of E-selectin (from 0.308 ± 0.0515, $p = 0.0112$, and 0.584 ± 0.0753, $p = 0.0002$, to 0.138 ± 0.0409, respectively, as compared to the cells transfected with CRISPR control and knockout systems and inhibited rh TNFα-induced activation of pHCAECs (**Figure 6D**). Next, we investigated the effect of endogenous expression of *TPM1* on posttranslational expression of talin. Due to its essential role in mediating cell adhesion, most of the studies regarding talin have focused mainly on talin-1. However, talin-2 is required for the generation of traction force and formation of invadopodia (Qi et al., 2016). We observed that activation of endogenous *TPM1* expression itself downregulated posttranslational expression of talin-2 (from 0.840 ± 0.0421 to 0.274 ± 0.0066, $p < 0.0001$), whereas *TPM1* knockdown led to a downregulation of both talin-1 (from 1.169 ± 0.0417 to 0.146 ± 0.0082, $p < 0.0001$) and talin-2 (0.840 ± 0.0421 to 0.516 ± 0.0293, $p < 0.0001$). After rh TNFα treatment, we also noticed decreased expression of talin-2 (from 0.274 ± 0.0066 to 0.188 ± 0.0239, $p = 0.0037$) in *TPM1* upregulated cells and its increase in *TPM1*-knockdown

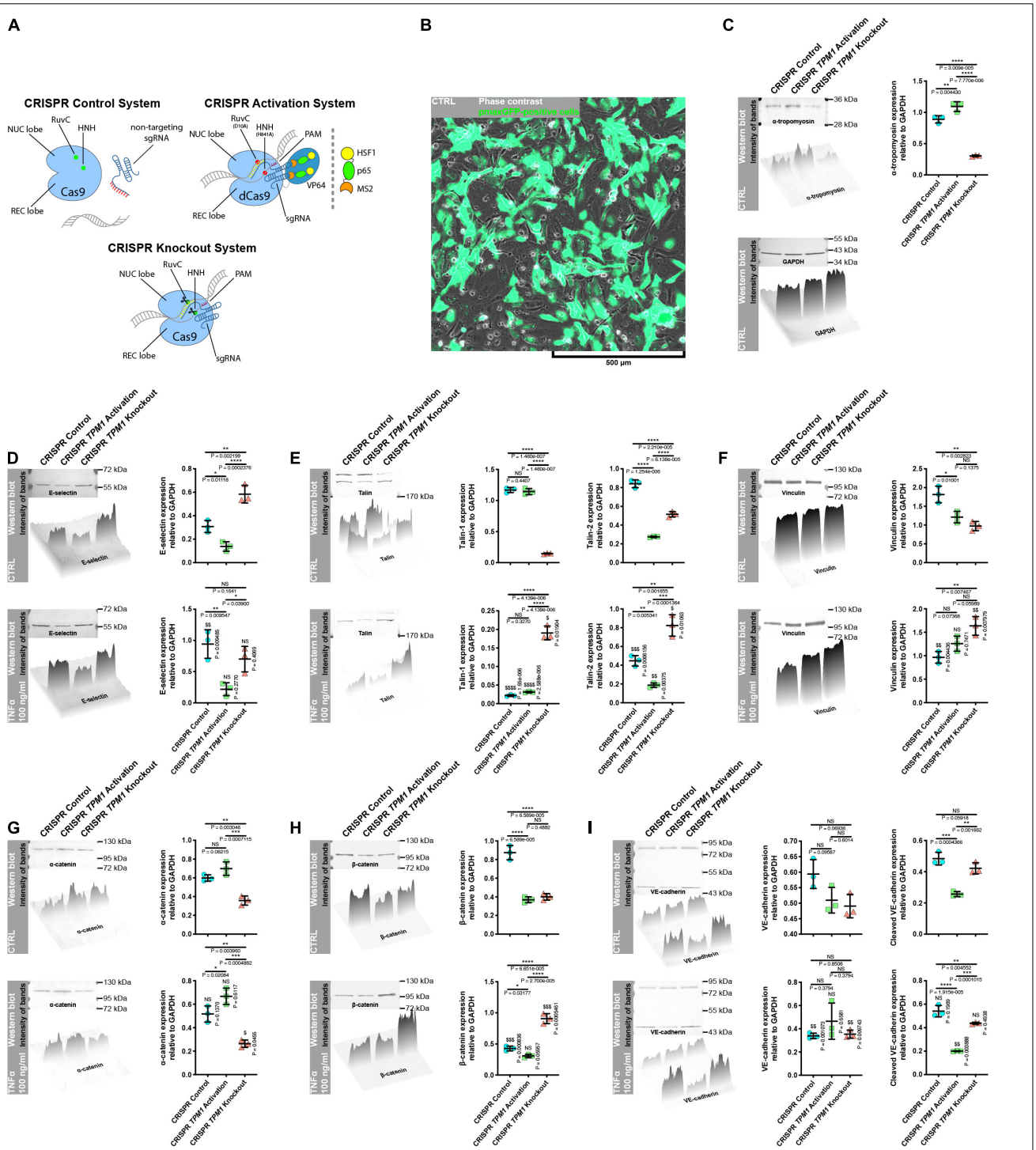

FIGURE 6 | Effect of TNFα on posttranslational expression of cell–cell and cell–ECM junctional proteins in pHCAECs with CRISPR-based modulated expression of *TPM1*. **(A)** Schematic overview of CRISPR systems used in regulation of *TPM1* expression in pHCAECs. The cells were nucleofected with a CRISPR control plasmid encoding the Cas9 nuclease and a non-specific guide RNA (upper left panel), CRISPR *TPM1* activation system encoding the nuclease-deficient dCas9 fused to the transactivation domain VP64, a plasmid encoding the MS2-p65-HSF1 fusion protein, and a guide RNA targeting sequences upstream of the *TPM1* transcriptional start site (upper left panel) or CRISPR *TPM1*-knockout system encoding the Cas9 nuclease and a *TPM1*-specific 20-nt guide RNA (lower panel). **(B)** Representative micrograph of intravital detection of pmaxGFP plasmid product (green fluorescence) in nucleofected pHCAECs (contrast phase). **(C)** Representative western blots, surface plot, and densitometric analysis for α-tropomyosin (upper panel) and GAPDH (lower panel). CTRL refers to the control, ** to $p < 0.01$, **** to $p < 0.0001$. **(D)** Representative western blots, surface plot, and densitometric analysis for E-selectin. CTRL refers to the control (upper panel), TNFα 100 ng/ml to cells treated with rh TNFα (lower panel), NS to non-significant, * to $p < 0.05$, ** to $p < 0.01$, **** $p < 0.0001$, as determined by the Kruskal–Wallis test, $$ to $p < 0.01$, as

(Continued)

FIGURE 6 | (Continued)
determined by unpaired *t*-test. **(E)** Representative western blots, surface plot, and densitometric analysis for talin. CTRL refers to the control (upper panel), TNFα 100 ng/ml to cells treated with rh TNFα (lower panel), NS to non-significant, ** to $p < 0.01$, *** to $p < 0.001$, **** to $p < 0.0001$, as determined by the Kruskal–Wallis test, $$ to $p < 0.01$, $$$ to $p < 0.001$, $$$$ $p < 0.0001$, as determined by unpaired *t*-test. **(F)** Representative western blots, surface plot, and densitometric analysis for vinculin. CTRL refers to the control (upper panel), TNFα 100 ng/ml to cells treated with rh TNFα (lower panel), NS to non-significant, * to $p < 0.05$, ** to $p < 0.01$, as determined by the Kruskal–Wallis test, $$ to $p < 0.01$, as determined by unpaired *t*-test. **(G)** Representative western blots, surface plot, and densitometric analysis for α-catenin. CTRL refers to the control (upper panel), TNFα 100 ng/ml to cells treated with rh TNFα (lower panel), NS to non-significant, * to $p < 0.05$, ** to $p < 0.01$, *** to $p < 0.001$, as determined by the Kruskal–Wallis test, $ to $p < 0.05$, as determined by unpaired *t*-test. **(H)** Representative western blots, surface plot, and densitometric analysis for β-catenin. CTRL refers to the control (upper panel), TNFα 100 ng/ml to cells treated with rh TNFα (lower panel), NS to non-significant, * to $p < 0.05$, **** to $p < 0.0001$, as determined by the Kruskal–Wallis test, $$$ to $p < 0.001$, as determined by unpaired *t*-test. **(I)** Representative western blots, surface plot, and densitometric analysis for VE-cadherin. CTRL refers to the control (upper panel), TNFα 100 ng/ml to cells treated with rh TNFα (lower panel), NS to non-significant, ** to $p < 0.01$, *** to $p < 0.001$, **** to $p < 0.0001$, as determined by the Kruskal–Wallis test, $$ to $p < 0.01$, as determined by unpaired *t*-test.

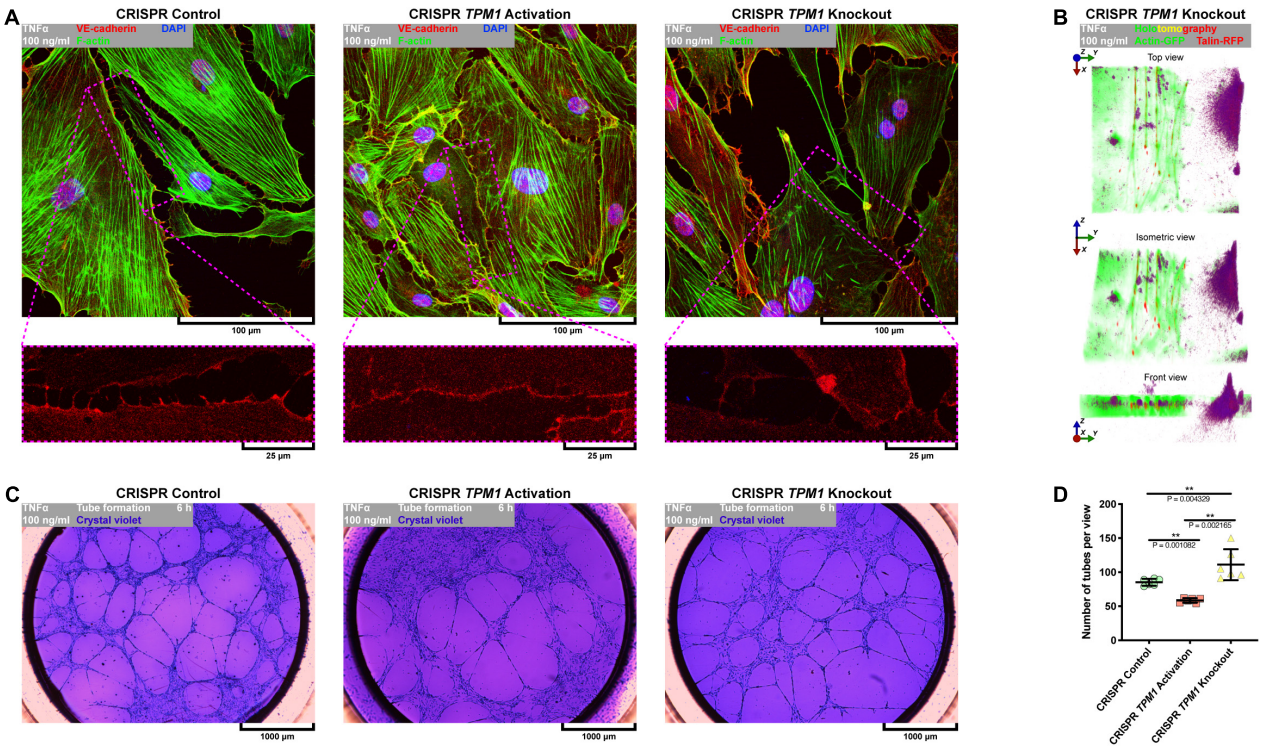

FIGURE 7 | Effect of CRISPR-based regulated expression of *TPM1* on F-actin organization, continuity of cell–cell junctions, and proangiogenic prosperities of TNFα-activated pHCAECs. **(A)** Representative confocal micrographs of fluorescently stained F-actin and VE-cadherin. Triple fluorescent staining for VE-cadherin (red), F-actin (green), and DNA (blue) was performed after fixation of pHCAECs nucleofected with CRISPR control (left panel), CRISPR *TPM1* activation (middle panel), or CRISPR *TPM1*-knockout systems (right panel). TNFα 100 ng/ml refers to cells treated with rh TNFα (right panel). **(B)** Representative intravital correlative holotomographic and fluorescence micrographs of pHCAECs nucleofected with the CRISPR *TPM1*-knockout system. Actin-GFP (red) and talin-RFP (green) were expressed using baculoviruses. TNFα 100 ng/ml to cells treated with rh TNFα. **(C)** Representative bright-field micrographs presenting tube formation by pHCAECs nucleofected with CRISPR control (left panel), CRISPR *TPM1* activation (middle panel), and CRISPR *TPM1*-knockout systems cultured on Matrigel. The tubular structures were stained with crystal violet after 6 h from seeding. TNFα 100 ng/ml refers to cells treated with rh TNFα. **(D)** Number of tubes per microscopic field formed by TNFα-activated pHCAECs with CRISPR-based regulated expression of *TPM1*. ** refers to $p < 0.01$, as determined by the Kruskal–Wallis test.

pHCAECs (from 0.516 ± 0.0293 to 0.824 ± 0.1143, $p = 0.0106$. We did not observe expression of talin-1 in rh TNFα-activated pHCAECs transfected with CRISPR control and *TPM1* activation systems (**Figure 6E**). Talin-2 has been shown to be able to recruit vinculin in the absence of mechanical force (Austen et al., 2015). It has also been suggested that vinculin coordinates polarized cell motility and plays a central role in the regulation of endothelial barrier function via dynamic balance between centripetal forces generated by contraction of stress fibers attached to focal adhesion sites and tethering forces applied by intracellular complexes (Birukova et al., 2016). Interestingly, here, we showed similar, and independent of rh TNFα treatment, posttranslational levels of vinculin in pHCAECs with activated *TPM1* expression. Differently, we noticed rh TNFα-induced upregulation of vinculin in cells transfected with the CRISPR *TPM1*-knockout system (from 0.973 ± 0.1228 to 1.637 ± 0.1992, $p = 0.0080$; **Figure 6F**). Both α-catenin and vinculin cooperatively support the strength of intercellular adhesion via a mechanoresponsive

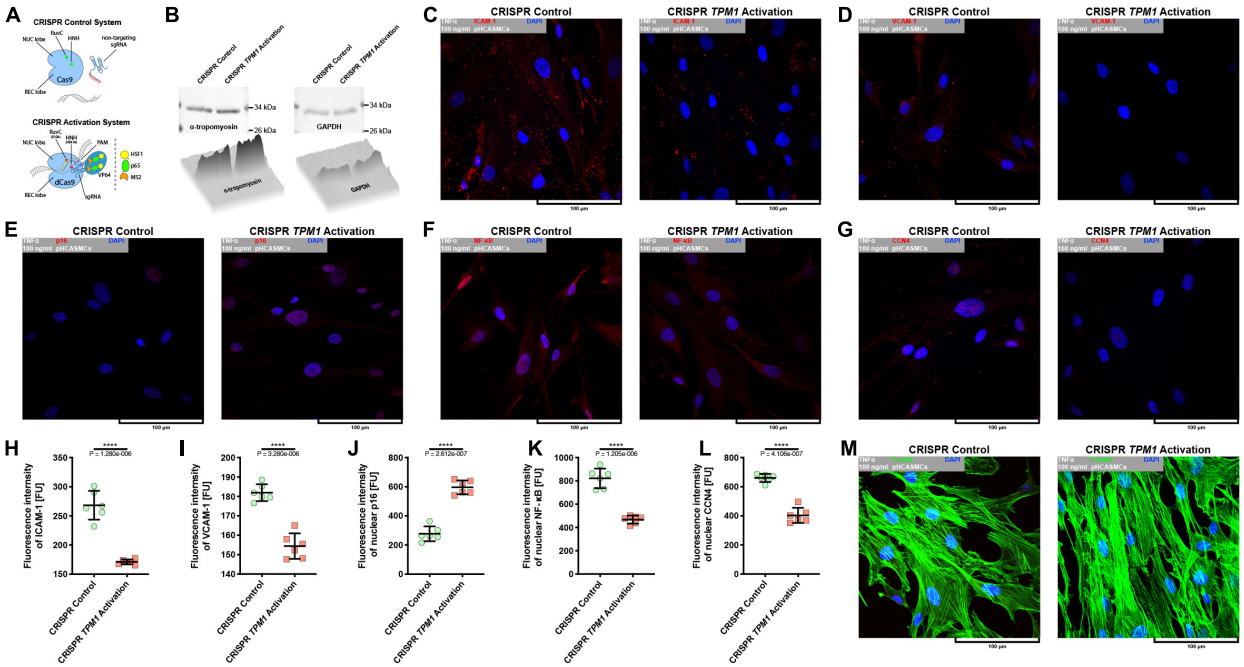

FIGURE 8 | Effect of CRISPR-based activation of endogenous *TPM1* expression on expression of molecular markers of TNFα-stimulated pHCASMC migration and proliferation. **(A)** Schematic overview of CRISPR systems used in regulation of *TPM1* expression in pHCASMCs. The cells were nucleofected with CRISPR control plasmid encoding the Cas9 nuclease and a non-specific guide RNA (upper panel) or CRISPR *TPM1* activation system encoding the nuclease-deficient dCas9 fused to the transactivation domain VP64, a plasmid encoding the MS2-p65-HSF1 fusion protein, and a guide RNA targeting sequences upstream of *TPM1* transcriptional start site (lower panel). **(B)** Representative western blots and surface plots for α-tropomyosin (left panel) and GAPDH (right panel) in lysates form pHCAECs. **(C)** Representative confocal micrographs of fluorescently stained ICAM-1. Double fluorescent staining for ICAM-1 (red) and DNA (blue) was performed after fixation of TNFα-stimulated pHCASMCs nucleofected with CRISPR control (left panel) or CRISPR *TPM1* activation systems (right panel). TNFα 100 ng/ml to cells treated with rh TNFα. **(D)** Representative confocal micrographs of fluorescently stained VCAM-1. Double fluorescent staining for VCAM-1 (red) and DNA (blue) was performed after fixation of TNFα-stimulated pHCASMCs nucleofected with CRISPR control (left panel) or CRISPR *TPM1* activation systems (right panel). TNFα 100 ng/ml refers to cells treated with rh TNFα. **(E)** Representative confocal micrographs of fluorescently stained p16. Double fluorescent staining for p16 (red) and DNA (blue) was performed after fixation of TNFα-stimulated pHCASMCs nucleofected with CRISPR control (left panel) or CRISPR *TPM1* activation systems (right panel). TNFα 100 ng/ml refers to cells treated with rh TNFα. **(F)** Representative confocal micrographs of fluorescently stained NFκB. Double fluorescent staining for NFκB (red) and DNA (blue) was performed after fixation of TNFα-stimulated pHCASMCs nucleofected with CRISPR control (left panel) or CRISPR *TPM1* activation systems (right panel). TNFα 100 ng/ml refers to cells treated with rh TNFα. **(G)** Representative confocal micrographs of fluorescently stained CCN4. Double fluorescent staining for CCN4 (red) and DNA (blue) was performed after fixation of TNFα-stimulated pHCASMCs nucleofected with CRISPR control (left panel) or CRISPR *TPM1* activation systems (right panel). TNFα 100 ng/ml refers to cells treated with rh TNFα. **(H)** Fluorescence intensity of ICAM-1 measured in TNFα-stimulated pHCASMCs nucleofected with CRISPR control or CRISPR *TPM1* activation systems. **** refers to $p < 0.0001$ as determined by unpaired *t*-test. **(I)** Fluorescence intensity of VCAM-1 measured in TNFα-stimulated pHCASMCs nucleofected with CRISPR control or CRISPR *TPM1* activation systems. **** refers to $p < 0.0001$ as determined by unpaired *t*-test. **(J)** Fluorescence intensity of p16 measured in nuclei of TNFα-stimulated pHCASMCs nucleofected with CRISPR control or CRISPR *TPM1* activation systems. **** refers to $p < 0.0001$ as determined by unpaired *t*-test. **(K)** Fluorescence intensity of NFκB measured in nuclei of TNFα-stimulated pHCASMCs nucleofected with CRISPR control or CRISPR *TPM1* activation systems. **** refers to $p < 0.0001$ as determined by unpaired *t*-test. **(L)** Fluorescence intensity of CCN4 measured in nuclei of TNFα-stimulated pHCASMCs nucleofected with CRISPR control or CRISPR *TPM1* activation systems. **** refers to $p < 0.0001$ as determined by unpaired *t*-test. **(M)** Representative confocal micrographs of fluorescently stained F-actin. Double fluorescent staining for F-actin (green) and DNA (blue) was performed after fixation of TNFα-stimulated pHCASMCs nucleofected with CRISPR control (left panel) or CRISPR *TPM1* activation systems (right panel). TNFα 100 ng/ml refers to cells treated with rh TNFα.

link between the cadherin-β–catenin complexes and F-actin (Thomas et al., 2013). Vinculin also protects VE-cadherin-containing AJs from opening during their force-induced remodeling (Huveneers et al., 2012). The rh TNFα-independent and stable levels of vinculin in pHCAECs with activated *TPM1* expression were supported by the lack of rh TNFα-induced changes in α-catenin and β-catenin levels (**Figures 6G,H**). Furthermore, this was related with the rh TNFα-independent expression of VE-cadherin and decreased level of cleaved VE-cadherin (from 0.257 ± 0.0163 to 0.200 ± 0.0031, $p = 0.0039$) (**Figure 6I**), suggesting that activation of endogenous expression of *TPM1* leads to stabilization of AJs. Our further experiments showed that pHCAECs with activated transcription of *TPM1* were able to form continuous AJs in the presence of 100 ng/ml rh TNFα. In contrast, rh TNFα induced punctae appearance of AJs between the cells transfected with both CRISPR control and *TPM1*-knockout systems (**Figure 7A**). We also observed massive migracytosis after inflammatory activation of *TPM1*-knockdown pHCAECs with 100 ng/ml rh TNFα (**Figures 7A,B**). As shown in **Figure 7C**, force-dependent disorganization of cell–cell junctions was accompanied by the ability to form tubules on Matrigel. We observed a statistically significant

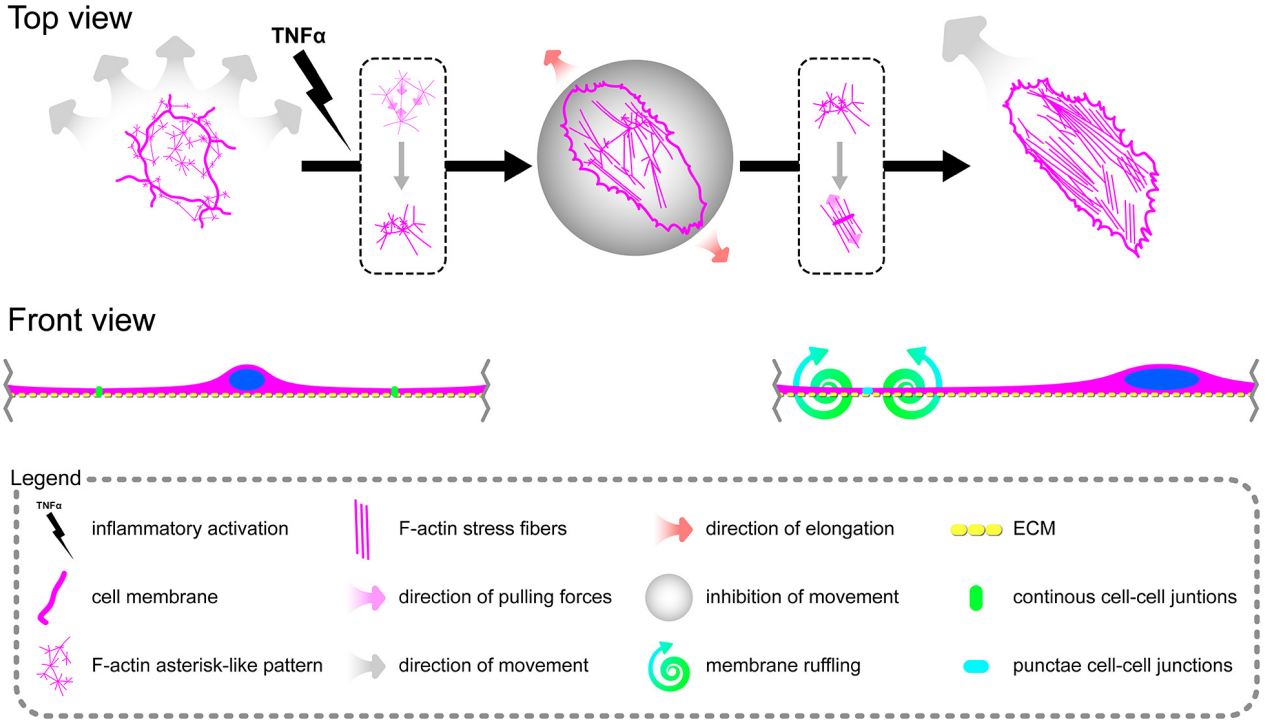

FIGURE 9 | Schematic overview of TNFα-induced reorganization of F-actin and its effect on migration of pHCAECs.

increase in the number of tubules formed by rh TNFα-activated pHCAECs with normal and downregulated expressions of *TPM1*, as compared to the cells with activated expression of *TPM1* (from 58.50 ± 3.391 to 85.17 ± 5.076, $p = 0.0011$, and 111.0 ± 22.70, $p = 0.0022$, respectively, for the cells transfected with CRISPR *TPM1* activation, control, and *TPM1*-knockdown systems; **Figure 7D**).

In summary, these data suggest that activation of endogenous expression of *TPM1* inhibits inflammatory response of pHCAECs and downstream leads to the stabilization of cell–cell junctions through reducing the cleavage of VE-cadherin and maintaining stable levels of α- and β-catenins. Differently, CRISPR-based knockout of *TPM1* leads to increased migracytosis in rh TNFα-activated pHCAECs, which was confirmed by the increased angiogenic capacity of these cells in parallel with the formation of aggressive phenotypes. The migrative potential was also confirmed by the TNFα-dependent increase in posttranslational expression of talin-2, vinculin, and β-catenin.

Activation of Endogenous Expression of *TPM1* Inhibits Tumor Necrosis Factor α-Induced Activation, Proliferation, and Migration of Primary Human Coronary Artery Smooth Muscle Cells

Because CRISPR-based activation of *TPM1* expression resulted in the stabilization of interactions between pHCAECs treated with 100 ng/ml rh TNFα, we decided to evaluate whether the elevated level of α-tropomyosin was able to affect pHCASMC response to rh TNFα. As shown in **Figures 8A,B**, transfection of pHCASMCs with CRISPR *TPM1* activation system effectively upregulated expression of α-tropomyosin in these cells. It has been shown that expression of both ICAM-1 and VCAM-1 on intimal and medial SMCs is prominent in fibrous plaques and advanced atherosclerotic lesions and that expression of VCAM-1 correlates with intimal neovessels and mononuclear cell infiltration (Kasper et al., 1996; O'Brien et al., 1996). Here, we observed that CRISPR-based activation of *TPM1* inhibited the inflammatory response of pHCASMCs to 100 ng/ml rh TNFα, as evidenced by reduced fluorescence of ICAM-1 and VCAM-1 (both $p < 0.0001$; **Figures 8C,D,H,I**). Furthermore, we investigated the effect of rh TNFα on functional nuclear markers of proliferation and migration of SMCs. We observed increased levels of nuclear fluorescence for p16 ($p < 0.0001$; **Figures 8E,J**) and reduced fluorescence for nuclear NFκB and CCN4 (both $p < 0.0001$) in TNFα-activated pHCASMCs with upregulated expression of α-tropomyosin, as compared to TNFα-activated cells transfected with the CRISPR control system (**Figures 8F,G,K,L**). These observations were confirmed by the analysis of F-actin organization. As shown in **Figure 8M**, TNFα promoted migrative distribution of the F-actin pattern in cells with normal expression of *TPM1*, whereas in pHCASMCs with CRISPR-based activation, expression of *TPM1* supported a typical smooth muscle 'hill and valley' morphology.

In summary, these data suggest that activation of the endogenous expression of *TPM1* inhibits inflammatory response of pHCASMCs and leads to the inhibition of their proliferation and migration.

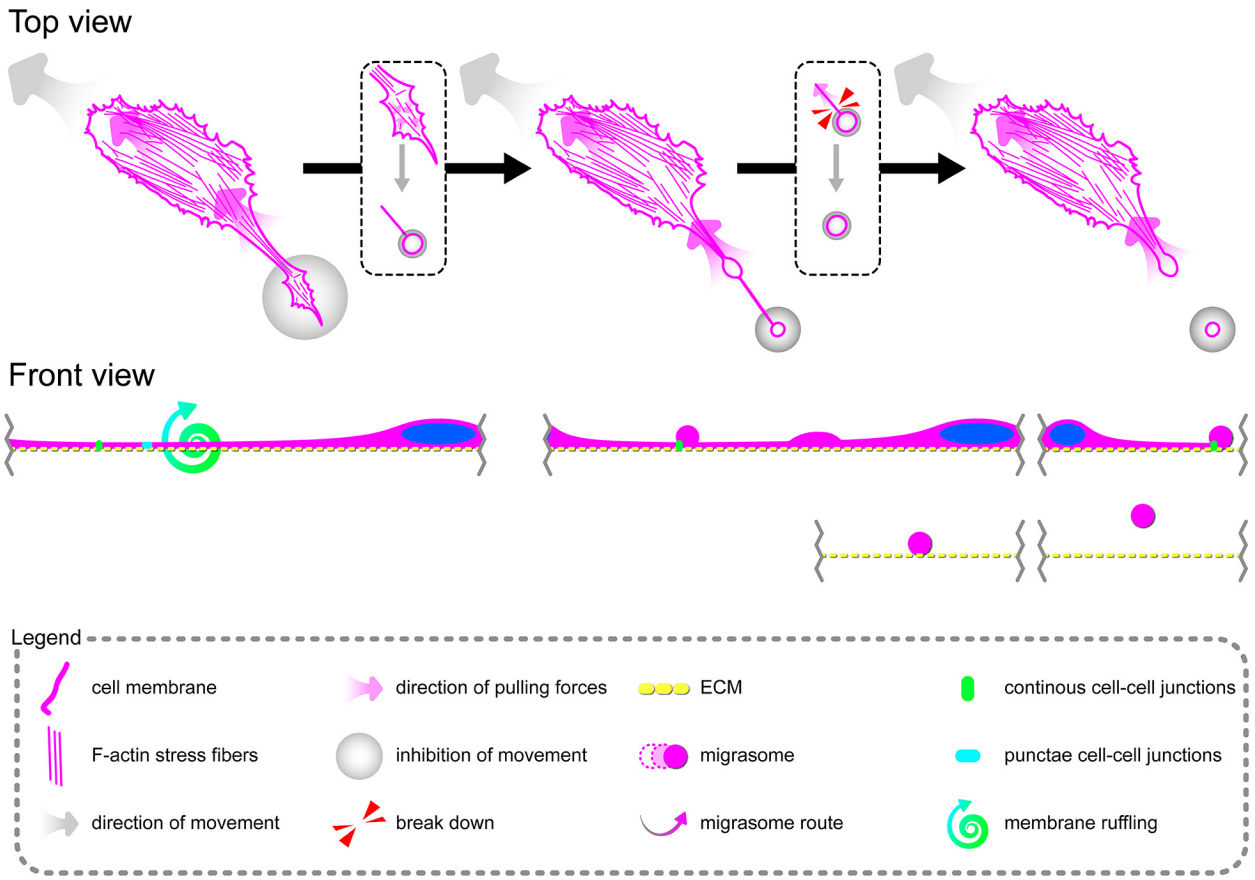

FIGURE 10 | Schematic overview of TNFα-induced formation of migrasomes and migracytosis in pHCAECs.

DISCUSSION

The basis of inflammation is the changes in blood vessels allowing the recruitment of leukocytes to the site of damage. It results in vessel dilatation and an increase in their permeability (Libby, 2002). Inflammation is also an essential factor accompanying both the angiogenic and atherogenic pathways (Silvestre et al., 2008). The entire inflammatory process is mediated through cytokines. TNFα is one of the representatives of proinflammatory cytokines produced mainly by monocytes or monocyte-derived macrophages and affects many processes associated with the growth and characteristics of endothelial, smooth muscle, or immune system cells (Heller and Krönke, 1994; Peppel et al., 2005). A dual role of TNFα has been shown in the angiogenic response of endothelial cells: a proangiogenic effect *in vivo* and an antiangiogenic *in vitro* (Fràter-Schröder et al., 1987; Sainson et al., 2008). It has been also suggested that TNFα inhibits endothelial cell proliferation *in vitro* (Fràter-Schröder et al., 1987). The TNFα apoptotic response of human umbilical vein and aortic and coronary artery endothelial cells when cultured *in vitro* was also shown (Fràter-Schröder et al., 1987; Chen et al., 2004; Rastogi et al., 2012; Jiang et al., 2016). The reason for that can be a host organism used for the production of recombinant TNFα. *Escherichia coli* is one of the organisms of choice for the production of recombinant proteins, such as TNFα, commonly used in vascular biology studies. However, protein expression in this system leads to many problems such as inclusion body formation related to incorrect disulfide bond formation, improper folding, or reduction in biological activity due to incomplete folding or mutations in cDNA (Rosano and Ceccarelli, 2014; Tavallaei et al., 2015). In the present study, we used rh TNFα produced in HEK293 cells, which effectively activated functional expression of E-selectin and VCAM-1 in pHCAECs. Although classical endothelial cell activation is defined by a shift in the expression of E-selectin, VCAM-1, and ICAM-1 (Gimbrone et al., 1997), we observed only a weak induction of functional expression of ICAM-1 (data not shown). Wu et al. (2004) indicated the heterogeneity of pHCAECs' response to TNFα stimulation, e.g., due to pathologic conditions of human coronary artery donors (Wu et al., 2004). However, it has been shown that soluble markers of endothelial injury are not uniformly increased in patients with documented coronary artery disease and that the plasma level of ICAM-1 did not allow identification of endothelial injury in such patients (Semaan et al., 2000). It was also suggested that the deficiency of ICAM-1 either alone or in combination with the deficiency of VCAM-1 did not alter nascent lesion formation, indicating the importance of VCAM-1 in the initiation of atherosclerosis

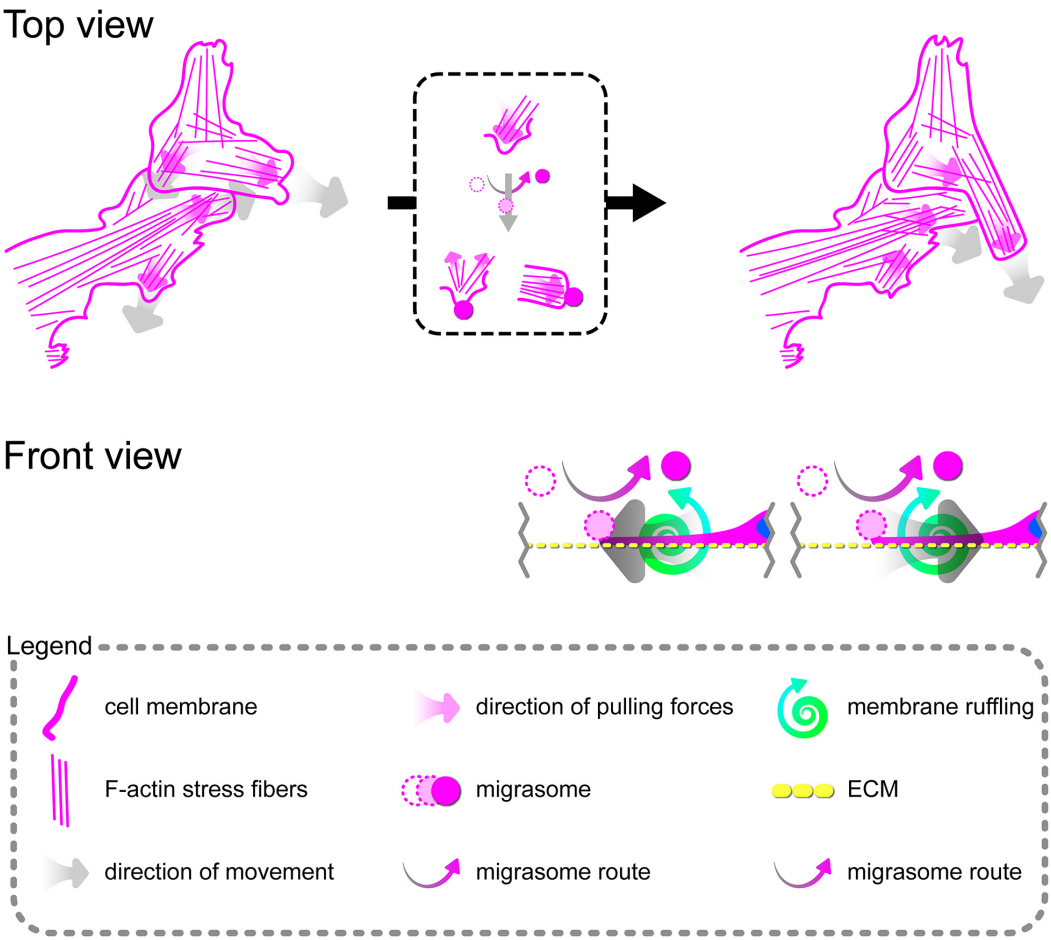

FIGURE 11 | Schematic overview of the mechanism of pHCAEC response to their interaction with migrasomes.

(Cybulsky et al., 2001). As the activation of endothelium is associated with enhanced interactions with leukocytes (Woodfin et al., 2009), we confirmed the flattening, firm adhesion, and further migration of Jurkat T cells on the surface of the rh TNFα-activated pHCAECs. These data are consistent with the results received by Jaczewska et al. (2014) who demonstrated increased interactions between Jurkat T cells and HUVECs following treatment with INF-γ or TNFα. In the course of the inflammatory process, the capture of leukocytes on the surface of the endothelium is possible due to the interaction of very late antigen-4 integrin on the leukocyte with selectins and VCAM-1 in endothelial cell walls (Abdala-Valencia et al., 2011). Similarly, the observed phenomenon of stronger adhesion of lymphocytes to endothelial monolayer was associated with increased expression of E-selectin and VCAM-1 cell adhesion molecules, which was also confirmed by Lu et al. (2016) and Munro et al. (1989). It was also suggested that the activation of endothelium includes not only changes in levels of adhesion molecules expression but also their redistribution from cell junctions to non-junctional membranes (JAM-A, JAM-C, and PECAM-1) or internalization from the plasma membrane (VE-cadherin) (Reglero-Real et al., 2016). Additionally, the effect of TNFα on TEM seems to depend on stimulation time. Within shorter stimulation times, leukocytes bind preferentially to the junctional regions of endothelial cells, whereas within longer periods, receptors in the junctional region are no longer easily available and TEM is intensified by cytoskeletal rearrangement and increased endothelial permeability (Jaczewska et al., 2014). Our observations seem to confirm this assumption since cytoskeletal rearrangement leading to the formation of discontinuous cell–cell junctions and intercellular gaps was finished at about 12–16 h from rh TNFα treatment.

Activation of pHCAECs following rh TNFα treatment led to morphological changes. One of the most obvious was a transformation of the shape of the cells into a spindle-like one and oriented toward the direction of cell migration. Similar to that found in our study, TNFα-induced spindle-shaped, narrowed, and elongated morphology was observed in HUVECs and hCMEC/D3 cells and correlated with the increased paracellular permeability (Miyazaki et al., 2017; Ni et al., 2017). Here, we showed that rh TNFα-induced change of the pHCAEC shape was related to the coordinated rearrangement of actin cytoskeleton from the star-like-shaped F-actin bundles into prominent, parallel-organized stress fibers. This perfectly

explains the transition of polygonal cobblestone-like pHCAECs to a uniformly spindle-shaped and aligned monolayer. Aster- or star-like-shaped structures were described by Fritzsche et al. (2017) as self-organized F-actin patterns, achieved by polarity sorting of actin filaments. In the *in silico* analysis, they showed two main nucleation pathways of this actin patterning. In the first scenario, Arp2/3 complexes bind to preexisting F-actin and nucleate new filaments from their pointed ends (−), leaving the barbed ends (+) pointing outward. In the second one, myosin II crosslinks with F-actin at their barbed ends (+) at the pattern centers, resulting in the point ends (−) pointing outward (Fritzsche et al., 2017). In our study, the core of star-like-shaped F-actin structures co-localized with ARP2/3, whereas radiating bundles co-localized with NM myosin IIb and ROCK-1. Furthermore, the analysis of the trajectories of cells showed that the star-like-shaped organization of F-actin bundles determines the propensity of pHCAECs to cooperative migration in any direction, important in the effective contribution of barrier function. Differently, parallel-organized stress fibers in activated pHCAECs promoted directed and parallel motion during the coordinated migration (**Figure 9**). These results suggest that rh TNFα induces the formation of the aggressive angiogenic phenotype of pHCAECs, which was confirmed in various migratory experiments.

The transformation of the F-actin pattern induced by rh TNFα was closely related to abnormalities in junctional regions and the distribution of focal adhesion sites. We proved that rh TNFα promotes discontinuous cell–cell contact, preceded by membrane ruffling during polarization of pHCAECs to achieve a spindle-like shape promoting their migration. Interestingly, TNFα-activated cells expressed NM myosin IIa, ARP 2/3 1B, and ROCK-1 in the regions of punctae cell–cell junctions. It was shown that NM myosin IIa controls cadherin clustering at AJs in a Rho-dependent manner, allowing proper adhesion of epithelial cells (de Beco et al., 2012). Smutny et al. (2010) showed that NM myosin IIa promotes the accumulation of E-cadherin in the AJs while NM myosin IIB stabilizes the associated perijunctional actin ring, increasing cell–cell adhesion and preventing them from disruptive forces. However, Efimova and Svitkina (2018) showed an association of NM myosin IIa with contractile actin bundle running parallel to linear AJs in endothelial cells. In our study, the NM myosin IIa correlated with a bright fluorescence of AJ and TJ proteins in the regions of punctae cell–cell junctions. Furthermore, we showed oligomerization of claudin-5 in activated pHCAECs. Claudin-5 preferentially forms hexamers, which make cell contacts much stronger than in the case of the monomeric form (Krause et al., 2008). Considering the above, this suggests that rh TNFα-induced punctae intercellular junctions are strong and play an important role in directed cell migration of pHCAECs, allowing follower cells to trail the leaders (Ozawa et al., 2020).

Ma et al. (2015) identified and described extracellular membrane-bounded vesicular structures that are characteristically generated along retraction fibers in migrating cells. They named these pomegranate-like structures as migrasomes and showed their formation in various cell lines, including MEF (mouse embryonic fibroblast), NIH3T3 (mouse embryonic fibroblast), HaCaT (human keratinocyte), MDA-MB-231 (human breast cancer), HCT116 (human colon cancer), SW480 (human adenocarcinoma), MGC803 (human gastric carcinoma), SKOV-3 (human ovarian adenocarcinoma), and B16 (mouse melanoma), and organs, such as the eye, lung, and intestine. These structures have been also observed in the lumen of blood vessels or pulmonary alveoli (Ma et al., 2015). However, the mechanism of their formation and biological or clinical importance is still unknown. Huang et al. (2019) proposed the mechanism of migrasome growing as an assembly of tetraspanin- and cholesterol-enriched membrane microdomains into micron-scale macrodomains. It has been also shown that tetraspanins are localized at digitation junctions, which reflect the transition processes before the establishment or after the disassembly of stable cell–cell junctions (Huang et al., 2018). Here, we showed intensified formation of migrasomes in TNFα-stimulated pHCAECs and that their formation is highly dependent on cell–cell and cell–ECM interaction, suggesting their role in the transmission of F-actin-based mechanical forces for proper polarization of adjacent cells and coordination of the cell migration direction. Furthermore, we frequently observed their release by breaking the retraction fibers, which resulted in their stay at points of cell–cell and/or cell–ECM contact as well as their release to the cell culture medium (**Figure 10**). Finally, we showed that floating migrasomes exert local cytoskeletal rearrangement and motility response (**Figure 11**), suggesting their involvement in intercellular signalization promoting directed migration of activated pHCAECs.

The data presented here showed that rh TNFα induces F-actin reorganization resulting in mechanical disruption of cell–cell junction continuity through the promotion of directed migration of pHCAECs. In this case, methods for regulation of the actin cytoskeleton structure might be clinically potent. One of such targets may be α-tropomyosin, which belongs to a family of actin-binding proteins. Tropomyosins are coiled-coil parallel dimers that form a head-to-tail polymer along the length of actin filaments regulating their access of other actin-binding proteins (Gunning et al., 2015). In mammals, over 40 tropomyosin isoforms are produced by alternative promoter selection, alternative splicing and/or 3′ end processing of four different genes: *TPM1*, *TPM2*, *TPM3*, and *TPM4* (Denz et al., 2004). Tropomyosin variants are classified into two major groups: high molecular weight (HMW; ∼284 amino acids and molecular weight between 33 and 40 kDa) and low molecular weight (LMW; ∼247 amino acids and molecular weight between 28 and 34 kDa) (Schevzov et al., 2011). In muscle cells, all actin filaments are saturated with tropomyosins and regulate muscle contraction in a calcium-dependent manner, while in non-muscle cells, saturation of actin vary from 30% to 90%, depending on the cell type and tropomyosins stabilize the actin cytoskeleton and participate in many cellular processes, including motility, cell–cell adhesion, and cell–extracellular interactions (Perry, 2001; Humayun-Zakaria et al., 2019; Janco et al., 2019). Our previous studies have shown that increased expression of α-tropomyosin protects endothelial integrity against L-homocysteine and cigarette smoke extract in EA.hy926 (Gagat et al., 2013, 2014) and preserves transformed alveolar epithelial

cell–cell junctions against disintegration induced by cigarette smoke extract (Gagat et al., 2016). α-Tropomyosin was also indicated to function as a tumor suppressor primarily by inhibiting cell proliferation, angiogenesis, and metastasis in renal cell carcinoma (Wang et al., 2019). Here, we showed that CRISPR-based activation of the endogenous expression of *TPM1* inhibits the inflammatory response of pHCAECs to TNFα and leads to the stabilization of cell–cell junctions through reduced cleavage of VE-cadherin and the maintenance of the stable levels of α- and β-catenins. We also showed that CRISPR-based knockout of *TPM1* leads to an increased angiogenic capacity of rh TNFα-activated pHCAECs and augments the formation of migrasomes and migracytosis in these cells. These findings pushed us to question how pHCASMCs with the activated expression of *TPM1* will respond to rh TNFα. Wang et al. (2011) showed that *TPM1* is a validated target of microRNA-21, which negatively regulates its posttranslational expression and leads to arteriosclerosis obliterans. They also showed that overexpression of *TPM1* decreased proliferation and migration of hASMCs, whereas its silencing significantly attenuated the antiproliferative and anti-migratory roles of the miR-21 inhibitor (Wang et al., 2011). Our results indicate that CRISPR-based activation of *TPM1* expression results in inhibition of the inflammatory response of pHCASMCs and exerts antiproliferative and anti-migratory activity.

Our study has several limitations. First of all, the study was performed in static conditions. However, the effect of rh TNFα is similar to that in *in vivo* studies, showing the proangiogenic action of TNFα. Also, due to the study design, we did not perform migratory tests on different ECM proteins, but we showed a lack of differences in the organization of F-actin in rh TNFα-activated pHCAECs when cultured on fibronectin, laminin, collagen I, and collagen IV coatings. Proliferation and migration of TNFα-activated pHCASMCs were also assessed based on the nuclear localization and fluorescence intensity of p16, NFκB, and CCN4. Furthermore, our study is based on morphological and semiquantitative analyses, but it allows for fast and easy translation of the findings into applied clinical studies. Finally, we used commercially available pHCAECs and pHCASMCs. Although we know the cause of the death of cell donors, we cannot unequivocally exclude that there was no generalized shock reaction of unknown duration that could affect the studied cells. In order to exclude this possible and reversible effect, only cells within three to four passages were used for all the experiments. It is also worth remembering that *TPM1* gene products occur in at least 29 isoforms (Cooley and Bergtrom, 2001). Unfortunately, in our study, we were unable to identify the isoform targeted by the applied CRISPR systems. Identification of the specific isoform, the expression of which determines the observed effect, is extremely important in the context of subsequent studies and their clinical application. However, in our study, tropomyosin was detected using the F-6 antibody (Santa Cruz) specific for an epitope mapping between amino acids 123 and 161. Furthermore, the molecular weight of the detected isoform of tropomyosin was in the range 33–35 kDa in pHCAECs and 33–34 kDa in pHCASMCs.

In conclusion, the present investigations demonstrated that rh TNFα-induced activation of pHCAECs results in actin cytoskeleton reorganization, promoting their directed and coordinated migration. We also proposed that the formation and release of migrasomes are highly related to increased adhesion and junctional strength of tips of retraction fibers with adjacent cells and that they play a role in intercellular signalization promoting directed cell migration. Furthermore, we showed that stabilization of F-actin through the activation of endogenous expression of *TPM1* inhibits inflammatory response of pHCAECs, allowing formation of continuous cell–cell junctions, and exerts antiproliferative and anti-migratory effects in pHCASMCs. Additional *in vivo* studies are needed to gain a better understanding of the role of α-tropomyosin in atherosclerosis and angiogenesis, as well as to examine the potential of *TPM1* as a candidate therapy target for proinflammatory vascular disorders. However, our findings may be adapted during the design and development of new coronary stent devices.

DATA AVAILABILITY STATEMENT

The original contributions presented in the study are included in the article/**Supplementary Material**, further inquiries can be directed to the corresponding author.

AUTHOR CONTRIBUTIONS

MG and AG conceptualized the project and designed the experiments. MG, WZ, KM, and AK performed the experiments. MG and DG interpreted the results. MG, KM, and WZ performed image analysis. MG and WZ performed statistical analysis. MG and WZ drafted the manuscript. KM and DG edited the manuscript. AK-W and JZ critically reviewed the manuscript. MG gained funding for the study. AG provided supervision. All authors contributed to the article and approved the submitted version.

FUNDING

This study was supported by grant no. 2015/17/D/NZ7/00809 to MG from National Science Centre, Poland.

ACKNOWLEDGMENTS

The authors are grateful to Magdalena Izdebska and Marta Hałas-Wiśniewska for sharing technical expertise.

SUPPLEMENTARY MATERIAL

The Supplementary Material for this article can be found online at: https://www.frontiersin.org/articles/10.3389/fcell.2021.668032/full#supplementary-material

Supplementary Figure S1 | TNFα-induced expression of E-selectin in pHCAECs. Triple fluorescent staining for E-selectin (green), F-actin (red), and DNA (blue) was performed after fixation. CTRL refers to the control (top panel), TNFα 100 ng/ml to cells treated with rh TNFα.

Supplementary Figure S2 | TNFα-induced expression of VCAM-1 in pHCAECs. **(A)** Representative micrographs of intravital detection of VCAM-1 using magnetic beads coated with anti-VCAM-1 monoclonal antibodies (bright field). F-actin (red) and nuclei (blue) were stained fluorescently after fixation. TNFα 100 ng/ml refers to cells treated with rh TNFα, mAb to monoclonal antibodies. **(B)** Representative confocal micrograph of fluorescently stained VCAM-1. Triple fluorescent staining for VCAM-1 (green), F-actin (red), and DNA (blue) was performed after fixation. TNFα 100 ng/ml refers to cells treated with rh TNFα. **(C)** Representative micrographs of adherent Jurkat T cells (contrast phase and fluorescence) after 30 min of their co-culture with pHCAECs (contrast phase). Nuclei of Jurkat cells (blue) were stained with Hoechst 33342. CTRL refers to the control (top panel), TNFα 100 ng/ml to cells treated with rh TNFα (bottom panel).

Supplementary Figure S3 | Effect of TNFα on migration of pHCAECs. **(A)** Rose plot presenting direction bias of pHCAEC migration in confluence within 36 h. CTRL refers to the control (left panel), TNFα 100 ng/ml to cells treated with rh TNFα (right panel), ** to $p < 0.01$, **** to $p < 0.0001$, as determined by Rayleigh test. **(B)** Euclidean distance of pHCAECs during 36-h migration in 100% confluence. CTRL refers to the control, TNFα 100 ng/ml to cells treated with rh TNFα, NS to non-significant to the control, as determined by unpaired *t*-test. **(C)** Accumulated distance of pHCAECs during 36-h migration in 100% confluence. CTRL refers to the control, TNFα 100 ng/ml to cells treated with rh TNFα, **** to $p < 0.0001$, as determined by unpaired *t*-test. **(D)** Velocity of pHCAECs during 36-h migration in 100% confluence. CTRL refers to the control, TNFα 100 ng/ml to cells treated with rh TNFα, **** to $p < 0.0001$, as determined by unpaired *t*-test. **(E)** Correlation between Euclidean distance of pHCAECs and time during 36-h migration in 100% confluence. CTRL refers to the control, TNFα 100 ng/ml to cells treated with rh TNFα, NS to non-significant, ** to $p < 0.01$, as determined by Pearson's correlation coefficient analysis. **(F)** Correlation between accumulated distance of pHCAECs and time during 36-h migration in 100% confluence. CTRL refers to the control, TNFα 100 ng/ml to cells treated with rh TNFα, NS to non-significant, ** to $p < 0.01$, as determined by Pearson's correlation coefficient analysis. **(G)** Correlation between velocity of pHCAECs and time during 36-h migration in 100% confluence. CTRL refers to the control, TNFα 100 ng/ml to cells treated with rh TNFα, NS to non-significant, ** to $p < 0.01$, as determined by Pearson's correlation coefficient analysis. **(H)** Correlation between time, accumulated distance, Euclidean distance or velocity, and directness of control pHCAECs during 36-h migration in 100% confluence. CTRL refers to the control, NS to non-significant, **** to $p < 0.0001$. **(I)** Correlation between time, accumulated distance, Euclidean distance or velocity, and directness of TNFα pHCAECs during 36-h migration in 100% confluence. TNFα 100 ng/ml refers to cells treated with rh TNFα, NS to non-significant, * to $p < 0.05$, **** to $p < 0.0001$. **(J)** Representative contrast phase micrograph presenting pHCAEC migration to the wound site. Curves indicate leading edge of migrating cells, arrows the direction of the movement. CTRL refers to the control (left panel), TNFα 100 ng/ml to cells treated with rh TNFα (right panel). **(K)** Representative contrast phase micrograph presenting pHCAEC migration to the open field. Curves indicate leading edge of migrating cells, arrows the direction of the movement. CTRL refers to the control (left panel), TNFα 100 ng/ml to cells treated with rh TNFα (right panel). **(L)** Number of pHCAECs migrated through 3-μm pores per microscopic field. CTRL refers to the control, TNFα 100 ng/ml to cells treated with rh TNFα, **** to $p < 0.0001$, as determined by unpaired *t*-test. **(M)** Number of tubes per microscopic field formed by pHCAECs on Matrigel after 3, 6, and 12 h after seeding. CTRL refers to the control, TNFα 100 ng/ml to cells treated with rh TNFα, * to $p < 0.05$, **** to $p < 0.0001$, as determined by Kruskal–Wallis test, $$$$ to $p < 0.0001$, as determined by unpaired *t*-test.

Supplementary Figure S4 | Effect of rh TNFα on adhesion of pHCAECs during initial 4 h from the seeding. **(A)** Number of adherent pHCAECs per microscopic field from the control and TNFα-activated pHCAECs. **(B)** Representative micrographs of adherent pHCAECs (contrast phase) within 4 h after seeding. CTRL refers to the control (top panel), TNFα 100 ng/ml to cells treated with rh TNFα (bottom panel). **(C)** Relative number of adherent pHCAECs per microscopic field from the control and TNFα-activated pHCAECs after 0.5 h from seeding. NS refers to non-significant to the control, as determined by unpaired *t*-test. **(D)** Relative number of adherent pHCAECs per microscopic field from the control and TNFα-activated pHCAECs after 1 h from seeding. ** refers to $p < 0.01$, as determined by unpaired *t*-test. **(E)** Relative number of adherent pHCAECs per microscopic field from the control and TNFα-activated pHCAECs after 2 h from seeding. * refers to $p < 0.05$, as determined by unpaired *t*-test. **(F)** Relative number of adherent pHCAECs per microscopic field from the control and TNFα-activated pHCAECs after 2 h from seeding. * refers to $p < 0.05$, as determined by unpaired *t*-test.

Supplementary Figure S5 | Effect of rh TNFα on organizational pattern of F-actin in pHCAECs cultured on different ECM coatings. **(A)** Representative confocal micrograph of fluorescently stained F-actin in pHCAECs cultured on fibronectin. Double fluorescent staining for F-actin (green) and DNA (blue) was performed after fixation. CTRL refers to the control (left panel), TNFα 100 ng/ml to cells treated with rh TNFα (right panel). **(B)** Representative confocal micrograph of fluorescently stained F-actin in pHCAECs cultured on fibronectin. Double fluorescent staining for F-actin (red) and DNA (blue) was performed after fixation. CTRL refers to the control (left panel), TNFα 100 ng/ml to cells treated with rh TNFα (right panel). **(C)** Representative confocal micrograph of fluorescently stained F-actin in pHCAECs cultured on laminin. Double fluorescent staining for F-actin (green) and DNA (blue) was performed after fixation. CTRL refers to the control (left panel), TNFα 100 ng/ml to cells treated with rh TNFα (right panel), EHS to Engelbreth-Holm-Swarm. **(D)** Representative confocal micrograph of fluorescently stained F-actin in pHCAECs cultured on laminin. Double fluorescent staining for F-actin (red) and DNA (blue) was performed after fixation. CTRL refers to the control (left panel), TNFα 100 ng/ml to cells treated with rh TNFα (right panel), EHS to Engelbreth-Holm-Swarm. **(E)** Representative confocal micrograph of fluorescently stained F-actin in pHCAECs cultured on collagen I. Double fluorescent staining for F-actin (green) and DNA (blue) was performed after fixation. CTRL refers to the control (left panel), TNFα 100 ng/ml to cells treated with rh TNFα (right panel). **(F)** Representative confocal micrograph of fluorescently stained F-actin in pHCAECs cultured on collagen I. Double fluorescent staining for F-actin (red) and DNA (blue) was performed after fixation. CTRL refers to the control (left panel), TNFα 100 ng/ml to cells treated with rh TNFα (right panel). **(G)** Representative confocal micrograph of fluorescently stained F-actin in pHCAECs cultured on collagen IV. Double fluorescent staining for F-actin (green) and DNA (blue) was performed after fixation. CTRL refers to the control (left panel), TNFα 100 ng/ml to cells treated with rh TNFα (right panel), EHS to Engelbreth-Holm-Swarm. **(H)** Representative confocal micrograph of fluorescently stained F-actin in pHCAECs cultured on collagen IV. Double fluorescent staining for F-actin (red) and DNA (blue) was performed after fixation. CTRL refers to the control (left panel), TNFα 100 ng/ml to cells treated with rh TNFα (right panel), EHS to Engelbreth-Holm-Swarm.

Supplementary Video S1 | Migration of Jurkat T cells on the surface of pHCAECs. CTRL refers to the control (upper panel), TNFα 100 ng/ml to cells treated with rh TNFα (lower panel). Nuclei of Jurkat cells were stained with Hoechst 33342. Time-lapse images were acquired for 2 min at 3.33-s intervals after 30 min from co-culture of pHCAECs (contrast phase) with counterstained Jurkat cells (contrast phase and fluorescence). Frame rate, 10 frames/s.

Supplementary Video S2 | TNFα-induced changes in migration of pHCAECs to the wound site. CTRL refers to the control (upper panel), TNFα 100 ng/ml to cells treated with TNFα (lower panel). Time-lapse images were acquired for 24 h at 10-min intervals. Frame rate, 20 frames/s.

Supplementary Video S3 | TNFα-induced changes in migration of pHCAECs to the open field. CTRL refers to the control (upper panel), TNFα 100 ng/ml to cells treated with TNFα (lower panel). Time-lapse images were acquired for 24 h at 10-min intervals. Frame rate, 20 frames/s.

Supplementary Video S4 | TNFα-induced changes in the ability of pHCAECs to form tubes on Matrigel. CTRL refers to the control (left panel), TNFα 100 ng/ml to cells treated with rh TNFα (right panel). Time-lapse images were acquired for 24 h at 10-min intervals. Frame rate, 20 frames/s.

Supplementary Video S5 | TNFα-induced changes in organization pattern of F-actin and distribution of focal adhesion sites. Actin-GFP (red) and talin-RFP (green) were expressed using baculoviruses. TNFα 100 ng/ml refers to cells treated with rh TNFα. Time-lapse images were acquired for 18 h at 10-min intervals after 2 h from treatment. Frame rate, 20 frames/s.

Supplementary Video S6 | TNFα-induced formation of migrasomes and migracytosis. Actin-GFP (red) and talin-RFP (green) were expressed using baculoviruses. TNFα 100 ng/ml refers to cells treated with rh TNFα. Time-lapse images were acquired for 6.5 h at 10-min intervals after 15 h from treatment. Frame rate, 3 frames/s.

Supplementary Video S7 | Interactions of pHCAECs with migrasome released to cell culture medium. Actin-GFP (green) and talin-RFP (red) were expressed using baculovirus system. TNFα 100 ng/ml refers to cells treated with rh TNFα. Time-lapse images were acquired for 1.25 h at 5-min intervals after 18 h from treatment. Frame rate, 3 frames/s.

REFERENCES

Abdala-Valencia, H., Berdnikovs, S., and Cook-Mills, J. M. (2011). Mechanisms for vascular cell adhesion molecule-1 activation of ERK1/2 during leukocyte transendothelial migration. *PLoS One* 6:e26706. doi: 10.1371/journal.pone.0026706

Austen, K., Ringer, P., Mehlich, A., Chrostek-Grashoff, A., Kluger, C., Klingner, C., et al. (2015). Extracellular rigidity sensing by talin isoform-specific mechanical linkages. *Nat. Cell Biol.* 17, 1597–1606. doi: 10.1038/ncb3268

Bhadriraju, K., Yang, M., Alom Ruiz, S., Pirone, D., Tan, J., and Chen, C. S. (2007). Activation of ROCK by RhoA is regulated by cell adhesion, shape, and cytoskeletal tension. *Exp. Cell Res.* 313, 3616–3623. doi: 10.1016/j.yexcr.2007.07.002

Birukova, A. A., Shah, A. S., Tian, Y., Moldobaeva, N., and Birukov, K. G. (2016). Dual role of vinculin in barrier-disruptive and barrier-enhancing endothelial cell responses. *Cell Signal.* 28, 541–551. doi: 10.1016/j.cellsig.2016.02.015

Canver, A. C., Ngo, O., Lownes Urbano, R., and Morss Clynedoi, A. (2016). Endothelial directed collective migration depends on substrate stiffness via localized myosin contractility and cell-matrix interactions. *J. Biomech.* 49, 1369–1380. doi: 10.1016/j.jbiomech.2015.12.037

Cerutti, C., and Ridley, A. J. (2017). Endothelial cell-cell adhesion and signaling. *Exp. Cell Res.* 358, 31–38. doi: 10.1016/j.yexcr.2017.06.003

Chen, J., Li, D., Zhang, X., and Mehta, J. L. (2004). Tumor necrosis factor-alpha-induced apoptosis of human coronary artery endothelial cells: modulation by the peroxisome proliferator-activated receptor-gamma ligand pioglitazone. *J. Cardiovasc. Pharmacol. Ther.* 9, 35–41. doi: 10.1177/107424840400900i106

Chistiakov, D. A., Orekhov, A. N., and Bobryshev, Y. V. (2015). Endothelial barrier and its abnormalities in cardiovascular disease. *Front Physiol.* 6:365. doi: 10.3389/fphys.2015.00365

Cooley, B. C., and Bergtrom, G. (2001). Multiple combinations of alternatively spliced exons in rat tropomyosin-alpha gene mRNA: evidence for 20 new isoforms in adult tissues and cultured cells. *Arch. Biochem. Biophys.* 390, 71–77. doi: 10.1006/abbi.2001.2347

Cybulsky, M. I., Iiyama, K., Li, H., Zhu, S., Chen, M., Iiyama, M., et al. (2001). A major role for VCAM-1, but not ICAM-1, in early atherosclerosis. *J. Clin. Invest.* 107, 1255–1262. doi: 10.1172/JCI11871

de Beco, S., Amblard, F., and Coscoy, S. (2012). New insights into the regulation of E-cadherin distribution by endocytosis. *Int. Rev. Cell Mol. Biol.* 295, 63–108. doi: 10.1016/B978-0-12-394306-4.00008-3

Denz, C. R., Narshi, A., Zajdel, R. W., and Dube, D. K. (2004). Expression of a novel cardiac-specific tropomyosin isoform in humans. *Biochem. Biophys. Res. Commun.* 320, 1291–1297. doi: 10.1016/j.bbrc.2004.06.084

Efimova, N., and Svitkina, T. M. (2018). Branched actin networks push against each other at adherens junctions to maintain cell-cell adhesion. *J. Cell Biol.* 217, 1827–1845. doi: 10.1083/jcb.201708103

Fràter-Schröder, M., Risau, W., Hallmann, R., Gautschi, P., and Böhlen, P. (1987). Tumor necrosis factor type alpha, a potent inhibitor of endothelial cell growth in vitro, is angiogenic in vivo. *Proc. Natl. Acad. Sci. U.S.A.* 84, 5277–5281. doi: 10.1073/pnas.84.15.5277

Fritzsche, M., Li, D., Colin-York, H., Chang, V. T., Moeendarbary, E., Felce, J. H., et al. (2017). Self-organizing actin patterns shape membrane architecture but not cell mechanics. *Nat. Commun.* 8:14347. doi: 10.1038/ncomms14347

Gagat, M., Grzanka, D., Izdebska, M., and Grzanka, A. (2013). Effect of L-homocysteine on endothelial cell-cell junctions following F-actin stabilization through tropomyosin-1 overexpression. *Int. J. Mol. Med.* 32, 115–129. doi: 10.3892/ijmm.2013.1357

Gagat, M., Grzanka, D., Izdebska, M., Sroka, W. D., Hałas-Wiśniewska, M., and Grzanka, A. (2016). Tropomyosin-1 protects transformed alveolar epithelial cells against cigaret smoke extract through the stabilization of F-actin-dependent cell-cell junctions. *Acta Histochem.* 118, 225–235. doi: 10.1016/j.acthis.2016.01.003

Gagat, M., Grzanka, D., Izdebska, M., Sroka, W. D., Marszałł, M. P., and Grzanka, A. (2014). Tropomyosin-1 protects endothelial cell-cell junctions against cigarette smoke extract through F-actin stabilization in EA.hy926 cell line. *Acta Histochem.* 116, 606–618. doi: 10.1016/j.acthis.2013.11.013

Gimbrone, M. A. Jr., and García-Cardeña, G. (2016). Endothelial cell dysfunction and the pathobiology of atherosclerosis. *Circ. Res.* 118, 620–636. doi: 10.1161/CIRCRESAHA.115.306301

Gimbrone, M. A. Jr., Resnick, N., Nagel, T., Khachigian, L. M., Collins, T., and Topper, J. N. (1997). Hemodynamics, endothelial gene expression, and atherogenesis. *Ann. N. Y. Acad. Sci.* 811, 1–10. doi: 10.1111/j.1749-6632.1997.tb51983.x

Godo, S., and Shimokawa, H. (2017). Endothelial functions. *Arterioscler. Thromb. Vasc. Biol.* 37, e108–e114. doi: 10.1161/ATVBAHA.117.309813

Gunning, P. W., Hardeman, E. C., Lappalainen, P., and Mulvihill, D. P. (2015). Tropomyosin – master regulator of actin filament function in the cytoskeleton. *J. Cell. Sci.* 128, 2965–2974. doi: 10.1242/jcs.172502

Heller, R. A., and Krönke, M. (1994). Tumor necrosis factor receptor-mediated signaling pathways. *J. Cell Biol.* 126, 5–9. doi: 10.1083/jcb.126.1.5

Huang, C., Fu, C., Wren, J. D., Wang, X., Zhang, F., Zhang, Y. H., et al. (2018). Tetraspanin-enriched microdomains regulate digitation junctions. *Cell. Mol. Life Sci.* 75, 3423–3439. doi: 10.1007/s00018-018-2803-2

Huang, Y., Zucker, B., Zhang, S., Elias, S., Zhu, Y., and Chen, H. (2019). Migrasome formation is mediated by assembly of micron-scale tetraspanin macrodomains. *Nat. Cell Biol.* 21, 991–1002. doi: 10.1038/s41556-019-0367-5

Humayun-Zakaria, N., Arnold, R., Goel, A., Ward, D., Savill, S., and Bryan, R. T. (2019). Tropomyosins: potential biomarkers for urothelial bladder cancer. *Int. J. Mol. Sci.* 20:1102. doi: 10.3390/ijms20051102

Huveneers, S., Oldenburg, J., Spanjaard, E., van der Krogt, G., Grigoriev, I., Akhmanova, A., et al. (2012). Vinculin associates with endothelial VE-cadherin junctions to control force-dependent remodeling. *J. Cell Biol.* 196, 641–652. doi: 10.1083/jcb.201108120

Jaczewska, J., Abdulreda, M. H., Yau, C. Y., Schmitt, M. M., Schubert, I., Berggren, P. O., et al. (2014). TNF-α and IFN-γ promote lymphocyte adhesion to endothelial junctional regions facilitating transendothelial migration. *J. Leukoc. Biol.* 95, 265–274. doi: 10.1189/jlb.0412205

Janco, M., Rynkiewicz, M. J., Li, L., Hook, J., Eiffe, E., Ghosh, A., et al. (2019). Molecular integration of the anti-tropomyosin compound ATM-3507 into the coiled coil overlap region of the cancer-associated Tpm3.1. *Sci. Rep.* 9:11262. doi: 10.1038/s41598-019-47592-9

Jiang, C., Fang, X., Jiang, Y., Shen, F., Hu, Z., Li, X., et al. (2016). TNF-α induces vascular endothelial cells apoptosis through overexpressing pregnancy induced noncoding RNA in Kawasaki disease model. *Int. J. Biochem. Cell Biol.* 72, 118–124. doi: 10.1016/j.biocel.2016.01.011

Kaczmarek, E., Erb, L., Koziak, K., Jarzyna, R., Wink, M. R., Guckelberger, O., et al. (2005). Modulation of endothelial cell migration by extracellular nucleotides: involvement of focal adhesion kinase and phosphatidylinositol 3-kinase-mediated pathways. *Thromb. Haemost.* 93, 735–742. doi: 10.1160/TH04-09-0576

Kasper, H. U., Schmidt, A., and Roessner, A. (1996). Expression of the adhesion molecules ICAM, VCAM, and ELAM in the arteriosclerotic plaque. *Gen. Diagn. Pathol.* 141, 289–294.

Krause, G., Winkler, L., Mueller, S. L., Haseloff, R. F., Piontek, J., and Blasig, I. E. (2008). Structure and function of claudins. *Biochim. Biophys. Acta* 1778, 631–645. doi: 10.1016/j.bbamem.2007

Libby, P. (2002). Inflammation in atherosclerosis. *Nature* 420, 868–874. doi: 10.1038/nature01323

Lu, Z. Y., Chen, W. C., Li, Y. H., Li, L., Zhang, H., Pang, Y., et al. (2016). TNF-α enhances vascular cell adhesion molecule-1 expression in human bone marrow mesenchymal stem cells via the NF-κB, ERK and JNK signaling pathways. *Mol. Med. Rep.* 14, 643–648. doi: 10.3892/mmr.2016.5314

Ma, L., Li, Y., Peng, J., Wu, D., Zhao, X., Cui, Y., et al. (2015). Discovery of the migrasome, an organelle mediating release of cytoplasmic contents during cell migration. *Cell Res.* 25, 24–38. doi: 10.1038/cr.2014.135

Matsushita, H., Chang, E., Glassford, A. J., Cooke, J. P., Chiu, C. P., and Tsao, P. S. (2001). eNOS activity is reduced in senescent human endothelial cells: preservation by hTERT immortalization. *Circ. Res.* 89, 793–798. doi: 10.1161/hh2101.098443

Michaelis, U. R. (2014). Mechanisms of endothelial cell migration. *Cell. Mol. Life. Sci.* 71, 4131–4148. doi: 10.1007/s00018-014-1678

Miyazaki, K., Hashimoto, K., Sato, M., Watanabe, M., Tomikawa, N., Kanno, S., et al. (2017). Establishment of a method for evaluating endothelial cell injury by TNF-α in vitro for clarifying the pathophysiology of virus-associated acute encephalopathy. *Pediatr. Res.* 81, 942–947. doi: 10.1038/pr.2017.28

Munro, J. M., Pober, J. S., and Cotran, R. S. (1989). Tumor necrosis factor and interferon-gamma induce distinct patterns of endothelial activation and associated leukocyte accumulation in skin of *Papio anubis*. *Am. J. Pathol.* 135, 121–133.

Ni, Y., Teng, T., Li, R., Simonyi, A., Sun, G. Y., and Lee, J. C. (2017). TNFα alters occludin and cerebral endothelial permeability: role of p38MAPK. *PLoS One* 12:e0170346. doi: 10.1371/journal.pone.0170346

O'Brien, K. D., McDonald, T. O., Chait, A., Allen, M. D., and Alpers, C. E. (1996). Neovascular expression of E-selectin, intercellular adhesion molecule-1, and vascular cell adhesion molecule-1 in human atherosclerosis and their relation to intimal leukocyte content. *Circulation* 93, 672–682. doi: 10.1161/01.cir.93.4.672

Ozawa, M., Hiver, S., Yamamoto, T., Shibata, T., Upadhyayula, S., Mimori-Kiyosue, Y., et al. (2020). Adherens junction regulates cryptic lamellipodia formation for epithelial cell migration. *J. Cell Biol.* 219:e202006196. doi: 10.1083/jcb.202006196

Peppel, K., Zhang, L., Orman, E. S., Hagen, P. O., Amalfitano, A., Brian, L., et al. (2005). Activation of vascular smooth muscle cells by TNF and PDGF: overlapping and complementary signal transduction mechanisms. *Cardiovasc. Res.* 65, 674–682. doi: 10.1016/j.cardiores.2004

Perna, A. F., Sepe, I., Lanza, D., Capasso, R., Zappavigna, S., Capasso, G., et al. (2013). Hydrogen sulfide reduces cell adhesion and relevant inflammatory triggering by preventing ADAM17-dependent TNF-α activation. *J. Cell Biochem.* 114, 1536–1548. doi: 10.1002/jcb.24495

Perry, S. V. (2001). Vertebrate tropomyosin: distribution, properties and function. *J. Muscle Res. Cell. Motil.* 22, 5–49. doi: 10.1023/a:1010303732441

Qi, L., Jafari, N., Li, X., Chen, Z., Li, L., Hytönen, V. P., et al. (2016). Talin2-mediated traction force drives matrix degradation and cell invasion. *J. Cell Sci.* 129, 3661–3674. doi: 10.1242/jcs.185959

Rastogi, S., Rizwani, W., Joshi, B., Kunigal, S., and Chellappan, S. P. (2012). TNF-α response of vascular endothelial and vascular smooth muscle cells involve differential utilization of ASK1 kinase and p73. *Cell Death Differ.* 19, 274–283. doi: 10.1038/cdd.2011.93

Reglero-Real, N., Colom, B., Bodkin, J. V., and Nourshargh, S. (2016). Endothelial cell junctional adhesion molecules: role and regulation of expression in inflammation. *Arterioscler. Thromb. Vasc. Biol.* 36, 2048–2057. doi: 10.1161/ATVBAHA.116.307610

Rosano, G. L., and Ceccarelli, E. A. (2014). Recombinant protein expression in *Escherichia coli*: advances and challenges. *Front. Microbiol.* 5:172. doi: 10.3389/fmicb.2014.00172

Sainson, R. C., Johnston, D. A., Chu, H. C., Holderfield, M. T., Nakatsu, M. N., Crampton, S. P., et al. (2008). TNF primes endothelial cells for angiogenic sprouting by inducing a tip cell phenotype. *Blood* 111, 4997–5007. doi: 10.1182/blood-2007-08-108597

Schevzov, G., Whittaker, S. P., Fath, T., Lin, J. J., and Gunning, P. W. (2011). Tropomyosin isoforms and reagents. *Bioarchitecture* 1, 135–164.

Semaan, H. B., Gurbel, P. A., Anderson, J. L., Muhlestein, J. B., Carlquist, J. F., Horne, B. D., et al. (2000). Soluble VCAM-1 and E-selectin, but not ICAM-1 discriminate endothelial injury in patients with documented coronary artery disease. *Cardiology* 93, 7–10. doi: 10.1159/000006995

Silvestre, J. S., Mallat, Z., Tedgui, A., and Lévy, B. I (2008). Post-ischaemic neovascularization and inflammation. *Cardiovasc. Res.* 78, 242–249. doi: 10.1093/cvr/cvn027

Smith, B. A., Daugherty-Clarke, K., Goode, B. L., and Gelles, J. (2013). Pathway of actin filament branch formation by Arp2/3 complex revealed by single-molecule imaging. *Proc. Natl. Acad. Sci. U.S.A.* 110, 1285–1290. doi: 10.1073/pnas.1211164110

Smutny, M., Cox, H. L., Leerberg, J. M., Kovacs, E. M., Conti, M. A., Ferguson, C., et al. (2010). Myosin II isoforms identify distinct functional modules that support integrity of the epithelial zonula adherens. *Nat. Cell Biol.* 12, 696–702. doi: 10.1038/ncb2072

Tavallaei, O., Bandehpour, M., Nafissi-Varcheh, N., and Kazemi, B. (2015). Periplasmic expression of TNF related apoptosis inducing ligand (TRAIL) in E.coli. *Iran. J. Pharm. Res.* 14, 617–626.

Theisen, U., Straube, E., and Straube, A. (2012). Directional persistence of migrating cells requires Kif1C-mediated stabilization of trailing adhesions. *Dev. Cell* 23, 1153–1166. doi: 10.1016/j.devcel.2012.11.005

Thomas, W. A., Boscher, C., Chu, Y. S., Cuvelier, D., Martinez-Rico, C., Seddiki, R., et al. (2013). α-Catenin and vinculin cooperate to promote high E-cadherin-based adhesion strength. *J. Biol. Chem.* 288, 4957–4969. doi: 10.1074/jbc.M112.403774

Tremblay, P. L., Auger, F. A., and Huot, J. (2006). Regulation of transendothelial migration of colon cancer cells by E-selectin-mediated activation of p38 and ERK MAP kinases. *Oncogene* 25, 6563–6573. doi: 10.1038/sj.onc.1209664

van Geemen, D., Smeets, M., van Stalborch, A.-M., Woerdeman, L., Daemen, M., Hordijk, P., et al. (2014). F-actin–anchored focal adhesions distinguish endothelial phenotypes of human arteries and veins. *Arterioscler. Thromb. Vasc. Biol.* 34, 2059–2067. doi: 10.1161/ATVBAHA.114.304180

Vicente-Manzanares, M., Ma, X., Adelstein, R. S., and Horwitz, A. R. (2009). Non-muscle myosin II takes centre stage in cell adhesion and migration. *Nat. Rev. Mol. Cell Biol.* 10, 778–790. doi: 10.1038/nrm2786

Virdis, A., Ghiadoni, L., and Taddei, S. (2010). Human endothelial dysfunction: EDCFs. *Pflugers Arch.* 459, 1015–1023. doi: 10.1007/s00424-009-0783-7

Wang, J., Tang, C., Yang, C., Zheng, Q., and Hou, Y. (2019). Tropomyosin-1 functions as a tumor suppressor with respect to cell proliferation, angiogenesis and metastasis in renal cell carcinoma. *J. Cancer* 10, 2220–2228. doi: 10.7150/jca.28261

Wang, M., Li, W., Chang, G. Q., Ye, C. S., Ou, J. S., Li, X. X., et al. (2011). MicroRNA-21 regulates vascular smooth muscle cell function via targeting tropomyosin 1 in arteriosclerosis obliterans of lower extremities. *Arterioscler. Thromb. Vasc. Biol.* 31, 2044–2053. doi: 10.1161/ATVBAHA.111.229559

Woodfin, A., Voisin, M. B., Imhof, B. A., Dejana, E., Engelhardt, B., and Nourshargh, S. (2009). Endothelial cell activation leads to neutrophil transmigration as supported by the sequential roles of ICAM-2, JAM-A, and PECAM-1. *Blood* 113, 6246–6257. doi: 10.1182/blood-2008-11-188375

Wu, H., Yao, Q., Lumsden, A., and Chen, C. (2004). Characterization of two populations of human coronary artery endothelial cells. *J. Surg. Res.* 118, 38–44. doi: 10.1016/j.jss.2004.01.009

Xue, F., Janzen, D. M., and Knecht, D. A. (2010). Contribution of filopodia to cell migration: a mechanical link between protrusion and contraction. *Int. J. Cell Biol.* 2010:507821. doi: 10.1155/2010/507821

Conflict of Interest: MG, DG, and AG are the authors on a patent disclosing the intravascular stent, especially for coronary vessels which inner covering comprises monoclonal anti-VE-cadherin antibodies and a system of induction of tropomyosin-1 expression.

The remaining authors declare that the research was conducted in the absence of any commercial or financial relationships that could be construed as a potential conflict of interest.

Publisher's Note: All claims expressed in this article are solely those of the authors and do not necessarily represent those of their affiliated organizations, or those of the publisher, the editors and the reviewers. Any product that may be evaluated in this article, or claim that may be made by its manufacturer, is not guaranteed or endorsed by the publisher.

frontiers in Cell and Developmental Biology

ORIGINAL RESEARCH
published: 01 November 2021
doi: 10.3389/fcell.2021.673993

Role of Outer Membrane Vesicles From *Helicobacter pylori* in Atherosclerosis

Na Wang[1,2†], Faying Zhou[3†], Caiyu Chen[1,2], Hao Luo[1,2], Jingwen Guo[1,2], Wei Wang[1,2], Jian Yang[4] and Liangpeng Li[1,2*]*

[1] Department of Cardiology, Daping Hospital, The Third Military Medical University, Chongqing, China, [2] Chongqing Key Laboratory of Hypertension Research, Chongqing Institute of Cardiology, Chongqing, China, [3] Department of Neurology and Centre for Clinical Neuroscience, Daping Hospital, The Third Military Medical University, Chongqing, China, [4] Department of Clinical Nutrition, The Third Affiliated Hospital of Chongqing Medical University, Chongqing, China

Infection is thought to be involved in the pathogenesis of atherosclerosis. Studies have shown the association between *helicobacter pylori* (*H. pylori*) and coronary artery disease. It is interesting to find *H. pylori* DNA and cytotoxin-associated gene A (CagA) protein in atherosclerotic plaque. Outer membrane vesicles (OMVs), secreted by *H. pylori*, exert effects in the distant organ or tissue. However, whether or not OMVs from *H. pylori* are involved in the pathogenesis of atherosclerosis remains unknown. Our present study found that treatment with OMVs from CagA-positive *H. pylori* accelerated atherosclerosis plaque formation in ApoE$^{-/-}$ mice. *H. pylori*-derived OMVs inhibited proliferation and promoted apoptosis of human umbilical vein endothelial cells (HUVECs), which was also reflected in *in vivo* studies. These effects were normalized to some degree after treatment with lipopolysaccharide (LPS)-depleted CagA-positive OMVs or CagA-negative OMVs. Treatment with *H. pylori*-derived OMVs increased reactive oxygen species (ROS) levels and enhanced the activation of nuclear factor-κB (NF-κB) in HUVECs, which were reversed to some degree in the presence of a superoxide dismutase mimetic TEMPOL and a NF-κB inhibitor BAY11-7082. Expressions of interleukin-6 (IL-6) and tumor necrosis factor alpha (TNF-α), two inflammatory factors, were augmented after treatment with OMVs from *H. pylori.* These suggest that *H. pylori*-derived OMVs accelerate atherosclerosis plaque formation via endothelium injury. CagA and LPS from *H. pylori*-OMVs, at least in part, participate in these processes, which may be involved with the activation of ROS/NF-κB signaling pathway. These may provide a novel strategy to reduce the incidence and development of atherosclerosis.

Keywords: *H. pylori*, outer membrane vesicles, atherosclerosis, endothelial cells, CagA, lipopolysaccharide, inflammatory factor

OPEN ACCESS

Edited by:
Xiang Cheng,
Huazhong University of Science and Technology, China

Reviewed by:
Hua Zhu,
The Ohio State University, United States
Traci Testerman,
University of South Carolina, United States

****Correspondence:***
Jian Yang
jianyang@hospital.cqmu.edu.cn
Liangpeng Li
liangpeng.li@hotmail.com

† These authors have contributed equally to this work

Specialty section:
This article was submitted to Signaling, a section of the journal Frontiers in Cell and Developmental Biology

Received: *28 February 2021*
Accepted: *02 September 2021*
Published: *01 November 2021*

Citation:
Wang N, Zhou F, Chen C, Luo H, Guo J, Wang W, Yang J and Li L (2021) Role of Outer Membrane Vesicles From Helicobacter pylori in Atherosclerosis. Front. Cell Dev. Biol. 9:673993. doi: 10.3389/fcell.2021.673993

INTRODUCTION

Cardiovascular disease is a major cause of death worldwide (Myers and Mendis, 2014). Atherosclerosis, a chronic metabolic or inflammatory disease, is characterized by accumulation of cholesterol and recruitment of macrophages in the arterial wall. The intact endothelial layer is important to keep the proliferation, migration and apoptosis of vascular smooth muscle cells (VSMCs) in the normal range. Therefore, endothelial injury is thought to be involved in the development of atherosclerosis (Ali et al., 2013).

Nowadays, the relationship between infection and coronary heart disease (CAD) has attracted more and more attention. Infection of bacteria from the oral cavity, and perhaps even the gut, correlates with atherosclerosis (Koren et al., 2011). *Helicobacter pylori* (*H. pylori*) infection is the most common infection in the world, particularly in the developing countries. Previous studies have shown the positive relationship between *H. pylori* and CAD (Rožanković et al., 2011). However, how *H. pylori* are involved in the pathogenesis of CAD is still unknown. It is interesting to find the *H. pylori* DNA and cytotoxin-associated gene A (CagA) protein in atherosclerotic plaque (Kowalski, 2001). As one kind of bacteria in the stomach, how *H. pylori* escapes from the defensive system in blood and goes to atherosclerotic plaque remains unknown.

H. pylori, gram-negative bacteria, exhibits tropism toward the gastric epithelium (Cover and Peek, 2013). The mechanisms underlying *H. pylori* infection-induced tissue injury are not clearly established. Several studies showed that *H. pyloric* release outer membrane vesicles (OMVs) *in vitro* and *in vivo* (Chmiela et al., 2018; Jarzab et al., 2020). These OMVs, contained proteins, lipopolysaccharide (LPS), and lipoproteins, could be transferred to the cytosol and nucleus in the recipient cells even at a distance (Keenan et al., 2008; Parker et al., 2010). A growing body of evidence indicates that OMVs have important physiological functions, including signal transduction, immune regulation, cell adhesion, blood coagulation, and induction of inflammation (Hodges and Hecht, 2012; Davies et al., 2019). However, whether or not OMVs from *H. pylori* are involved in the pathogenesis of atherosclerosis is still unknown. In the present study, we test the hypothesis that OMVs from *H. pylori* accelerate atherosclerosis plaque formation via endothelium injury. Furthermore, we found that CagA and LPS from *H. pylori*-derived OMVs, at least in part, participate in OMVs-induced proliferation inhibition and apoptosis in human umbilical vein endothelial cells (HUVECs). These may provide a novel strategy to reduce the incidence and development of atherosclerosis.

MATERIALS AND METHODS

Bacterial and Cell Culture

The well-characterized *H. pylori* clinical isolates were used in this study. *H. pylori* 26695 (CagA-positive) and *H. pylori* NCTC11637 (CagA-negative), kindly offered by Prof. Qinghua Xie (Department of Microbiology and Biochemical Pharmacy, College of Pharmacy and Laboratory Medicine, The Third Military Medical University), were grown on blood agar plates (10% rabbit blood, 5% glucose, 10 μg/mL norvancomycin hydrochloride, 2 μg/mL amphotericin B, 5 μg/mL trimethoprim, 0.38 μg/mL polymyxin B). For liquid cultures, bacterial growth from one plate was harvested and inoculated into a 100 mL volume of Skirrow's medium supplemented with 10% newborn calf serum, 5% glucose, 10 μg/mL norvancomycin hydrochloride, 2 μg/mL amphotericin B, 5 μg/mL trimethoprim, 0.38 μg/mL polymyxin B. Cultures were incubated at 37°C in a microaerobic environment (5% O_2, 10% CO_2, and 85% N_2) with constant rotation (120 rpm) (Yamaoka et al., 1997).

HUVECs, purchased from American Type Culture Collection, were cultured with Dulbecco's modified eagle medium with 10% fetal bovine serum, penicillin (100 IU/mL), and streptomycin (100 μg/mL) at 37°C in a humidified atmosphere of 5% CO_2 and 95% air. HUVECs were incubated with control (vehicle), OMVs (10 μg/mL) with or without a superoxide dismutase mimetic TEMPOL (4-hydroxy-2,2,6,6-tetramethylpiperidinyl-1-oxyl) or a nuclear factor-κB (NF-κB) inhibitor BAY11-7082 for 24 h.

Harvesting and Identifying of Outer Membrane Vesicles From *H. pylori*

After 72 h incubation, bacteria were removed from the broth cultures by two centrifugations (10,000 g, 15 min, 4°C). The culture supernatants were then ultracentrifuged (100,000 g, 2 h, 4°C) to recover OMVs. Resultant OMV pellets were washed twice in sterile phosphate-buffered saline (PBS), and followed with being assayed for protein content using a modification of the Lowry procedure. Samples were stored at −20°C until required (Chitcholtan et al., 2008). Then, OMVs with indicating concentrations from *H. pylori* were co-cultured with HUVECs for 24 h. The OMV concentration was indicated by its protein concentration. The content of LPS was measured according to the instruction of a commercial test kit (Wuhao Biotechnology Co., Ltd., Shanghai, China). For LPS depletion, 200 ng/mL polymyxin B, a well-known inhibitor of activation properties of LPS (Pérez-Pérez et al., 1995), was pre-treated with OMVs for 1 h at 37°C before the co-culture of OMVs and HUVECs.

Animals and Outer Membrane Vesicles Treatment

Seven- to eight-week-old $ApoE^{-/-}$ male mice were provided by the Experimental Animal Center of Daping Hospital (Chongqing, China). All procedures were approved by the Daping Hospital Animal Use and Care Committee. All experiments conformed to the guidelines of the ethical use of animals, and all efforts were made to minimize animal suffering and reduce the number of animals used.

All mice were housed in cages with free access to feed and water at 25°C, 60 ± 10% humidity, and a 12 h light/dark photoperiod. The mice were assigned to control or OMVs group when they started the high-fat and high-cholesterol diet containing 21% fat and 0.15% cholesterol. $ApoE^{-/-}$ mice were intragastrically administered with vehicle or OMVs from *H. pylori* 200 μL/day for 4 weeks. At the end of 12-week-old, the mice were anesthetized and sacrificed by cervical dislocation.

Measurement of Atherosclerotic Lesions in the Aorta

To measure the extent of atherosclerosis in the aorta, the entire aorta was removed, and then placed in 4% paraformaldehyde. The fixed aorta was stained with Oil Red O to delineate the atherosclerotic lesions, and images were obtained with a light microscope. The Oil Red O-positive area and total aortic surface area were measured using Image J software. Atherosclerotic lesions of the aorta were defined as the percentage of Oil Red

O-positive area to total aortic surface area, which was presented as fold changes compared to the control group in each set.

Proliferation Assay

Cell proliferation was analyzed using a Cell Counting Kit (CCK-8) (Dojindo, Kuma-moto, Japan) according to the manufacturer's instructions. Briefly, 1×10^4 cells were inoculated into 96-well plates. After 60% confluence, HUVECs were induced quiescent in serum-free medium for 24 h. Then, 90 μL of medium and 10 μL of the CCK-8 solution were added to each well and the plate was maintained at 37°C for 1 h. Optical density (OD) values were determined at 450 nm with Varioskan Flash microplate reader (Thermo Scientific). Data are given as a percent of the control value. All experiments were repeated for six times.

[^{3}H] thymidine (1 μCi/mL) was added to the growth medium of each well 6 h before the measurements. In brief, after the medium was removed, cells were treated with 0.25 mL 0.05% trypsin-0.53 mM EDTA for 5 min and diluted to 10 mL with a balanced electrolyte solution. Cells were then treated with 10% trichloroacetic acid (TCA) to precipitate acid-insoluble materials from which DNA was extracted with 0.1 mol/L NaOH. DNA was collected on a Whatman GF/B filter and washed twice with 5 mL ice-cold PBS. The filter was then cut and shaken in 3.5 mL scintillation fluid for 24 h before counting in a liquid scintillation counter (Beckman LS6500, Beckman). [^{3}H]-thymidine incorporation was determined using a liquid scintillation counter.

Determination of Apoptotic Cells

HUVECs grown on slides were fixed for 15 min in 4% paraformaldehyde. Samples were exposed to the enzymatic reaction mixture containing terminal deoxynucleotidyl transferase and fluorescein-dUTP for 2 h at 37°C and 4′,6-diamidino-2-phenylindole (DAPI) staining for about 10 s. After washing with PBS, the percentage of the terminal deoxynucleotidyl transferase-mediated dUTP nick end labeling (TUNEL)-positive cells relative to total cells was calculated by counting all cells in five random microscopic fields at a magnification of 20×.

Immunoblotting

Cells were washed with PBS, followed by the addition of 100 μL of cell lysis buffer. Supernatants were harvested by centrifugation (15,000 g, 20 min, 4°C), and the concentrations were determined using the bicinchoninic acid method. The cytoplasmic and nuclear protein were harvested with the protein extraction kit (Beyotime, Jiangsu, China) and then subjected to immunoblotting.

Equal amount of proteins (50 μg) were subjected to SDS-PAGE with 10% polyacrylamide gel, which was followed by electrotransfer into polyvinylidene fluoride membranes and blocked with Tris-buffered saline (TBS), containing 5% non-fat dry milk for 1 h. The membranes were incubated overnight with the primary antibodies against NF-κB p65 (1:300; BD Transduction Laboratory, Minneapolis, MN, United States), IkBa (1:500; Santa Cruz Biotechnology, Santa Cruz, CA), caspase-3 (1:500; Santa Cruz Biotechnology, Santa Cruz, CA), cleaved caspase- 3 (1:500; Santa Cruz Biotechnology, Santa Cruz, CA), GAPDH (1:500, Santa Cruz Biotechnology), gp91^{phox} (1:300; BD Transduction Laboratory, Minneapolis, MN, United States), superoxide dismutase 2 (SOD2, 1:300; Santa Cruz Biotechnology, Santa Cruz, CA), and CagA (1:300; Santa Cruz Biotechnology, Santa Cruz, CA) at 4°C, and then incubated with the secondary antibodies at room temperature for 1 h. The Odyssey Infrared Imaging System (Li-COR Biosciences) was used to visualize the bands, and Quantity One image analysis software was used to analyze the relative intensities. GAPDH or caspase-3 was used to normalize the densitometric intensity for proteins.

Dihydroethidium Staining

After treatment with *H. pylori*-derived-OMVs, HUVECs were loaded with 1 μM dihydroethidium (DHE) (Abcam, United States) and maintained for 15 min at 37°C. The intracellular levels of ROS were determined using a fluorescent microscope. The fluorescence intensity values from five different fields were quantified using ImageJ software.

ELISA Assay

One milliliter blood were drawn from ApoE$^{-/-}$ mice and centrifuged at 4°C and 3,000 r/min for 15 min. The supernatant was used to test inflammatory factors, including tumor necrosis factor alpha (TNF-α) and interleukin-6 (IL-6), according to the instruction of an enzyme-linked immunosorbent assay (ELISA) kit (Abcam, Cambridge, MA, United States).

Hematoxylin-Eosin Staining

Artery segments were immersed in ice-cold 4% paraformaldehyde for 30 min. Samples were transferred to 30% sucrose–PBS solution at 4°C for 24 h, embedded in optimum cutting temperature (OCT) compound. For the microscopic quantification of the lesion area, the aorta was processed through routine steps of desiccation followed by clearing, dipping and embedding in wax, and serial sectioning (5 μm). Sections were stained with HE using the standard protocol. Then, light microscopy was used to observe the tissues.

Statistical Analysis

The data are presented as mean ± standard deviation (SD). Comparisons within the groups were performed using ANOVA for repeated measures (or paired *t*-test when only 2 groups were compared), and comparison among groups (or *t*-test when only two groups were compared) was performed using factorial ANOVA with Holm-Sidak as the *ad hoc* test. A value of $P < 0.05$ was considered significant.

RESULTS

Isolation and Identification of Outer Membrane Vesicles From *H. pylori*

OMVs from *H. pylori* culture supernatants were isolated through a series of ultracentrifugation steps as previously described. To further identify the OMVs from *H. pylori*, electron

microscopic, immunoblotting and ELISA analyses were used. As shown in **Figure 1A**, the electron micrograph showed that OMVs from *H. pylori* were round, with size about 20–300 nm. Immunoblotting showed the high CagA levels in OMVs from CagA-positive *H. pylori* (**Figure 1B**). Results of ELISA measurement also showed the substantially higher levels of LPS in *H. pylori*-derived OMVs, compared to vehicle (**Figure 1C**). These results identified that OMVs from *H. pylori* were correct. It should be noted that the OMVs used in our present study referred to the OMVs from CagA-positive *H. pylori.*

H. pylori-Derived Outer Membrane Vesicles Accelerate Atherosclerosis Plaque Formation

To determine the role of *H. pylori*-derived OMVs in the pathogenesis of atherosclerosis, we intragastrically administered OMVs from *H. pylori* into ApoE$^{-/-}$ mice for 4 weeks. After examination, the aortas were cut longitudinally and respectively stained with Oil Red O and HE. Results with Oil Red O staining revealed that compared with controls, OMVs-treated ApoE$^{-/-}$ mice had more atherosclerotic plaque (**Figure 2A**). This is similar with the results with HE staining, in which ApoE$^{-/-}$ mice treated with *H. pylori*-derived OMVs had more serious atherosclerosis than control mice (**Figure 2B**). These indicate that *H. pylori*-derived OMVs accelerate atherosclerosis plaque formation. In addition, the serum lipid profiles were also determined. Our results showed that *H. pylori*-derived OMVs increased cholesterol levels in ApoE$^{-/-}$ mice (**Figure 2C**), while the levels of serum low density lipoprotein (LDL) and high density lipoprotein (HDL) had no significant difference with control (**Figures 2D,E**).

Moreover, the TUNEL staining was used to check the apoptosis in arteries. Results showed that TUNEL-positive nuclei in the arterial lumen were evidently higher in arteries from OMVs-treated ApoE$^{-/-}$ mice than that from control mice (**Figure 2F**). However, there was no difference in the arterial media. These suggested that the injured arterial lumen may, at least in part, participate in the *H. pylori*-derived OMVs-mediated atherosclerosis plaque formation.

H. pylori-Derived Outer Membrane Vesicles Inhibit Proliferation and Promote Apoptosis of Human Umbilical Vein Endothelial Cells

To investigate the possible effects of *H. pylori*-derived OMVs in the arterial lumen, the proliferation of HUVECs was examined. Via cell proliferation analysis, we found that *H. pylori*-derived OMVs suppressed the proliferation of HUVECs in a concentration-dependent manner (**Figure 3A**). Results from [^{3}H]-thymidine incorporation also showed that *H. pylori*-derived OMVs with different concentrations exerted the inhibitory effects in HUVECs (**Figure 3B**). These indicated that *H. pylori*-derived OMVs inhibit HUVECs proliferation.

Next, the apoptosis of HUVECs were also determined. Results showed that incubation of HUVECs with *H. pylori*-derived OMVs (10 μg/mL) for 24 h increased the ratio of cleaved-caspase-3 to total caspase-3 expression, a common apoptosis marker (**Figure 3C**). We also found that compared with control, TUNEL-positive nuclei in HUVECs treated with *H. pylori*-derived OMVs were markedly increased (**Figure 3D**). These

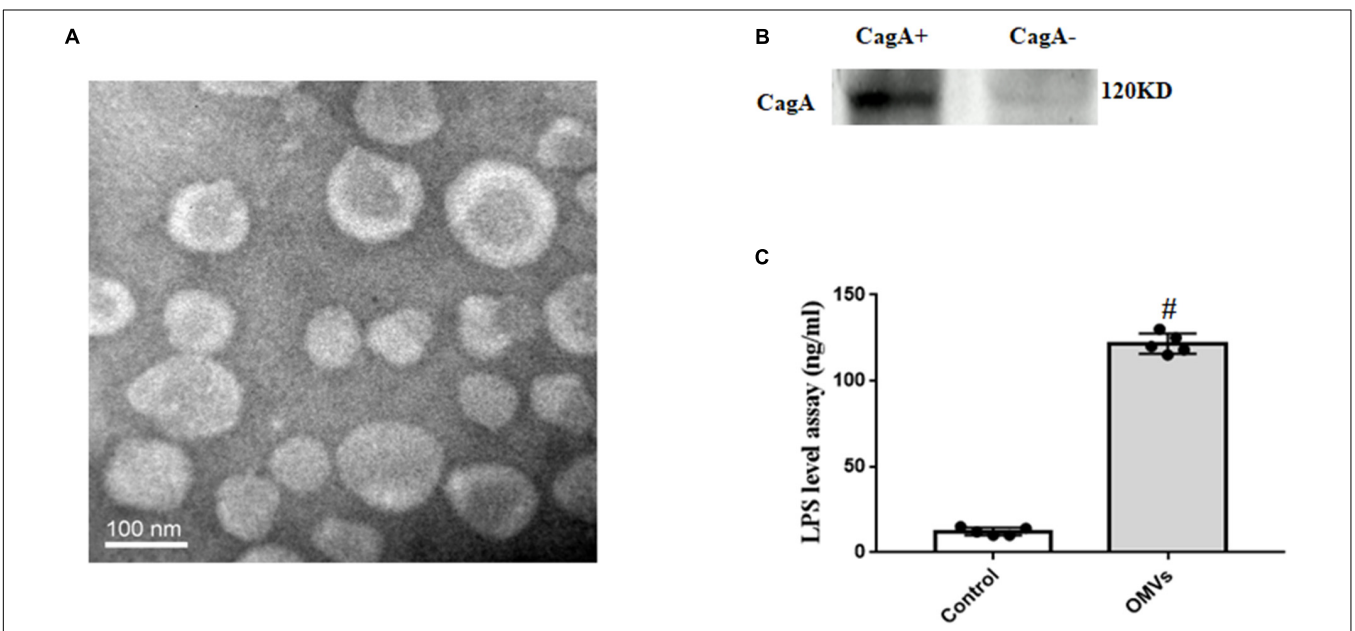

FIGURE 1 | Identification and characterization of OMVs from *H. pylori*. **(A)** Electron micrographs of OMVs from *H. pylori*. Isolated OMVs from *H. pylori* were fixed with negative staining with Na-phosphotungstate, and observed by transmission electron microscope. **(B)** CagA expression in *H. pylori*-derived OMVs (CagA$^+$: OMVs from CagA-positive *H. pylori*; CagA$^-$: OMVs from CagA-negative *H. pylori*). **(C)** LPS levels in *H. pylori*-derived OMVs and vehicle were determined by ELISA ($n = 5$, $^{\#}P < 0.01$ vs. control).

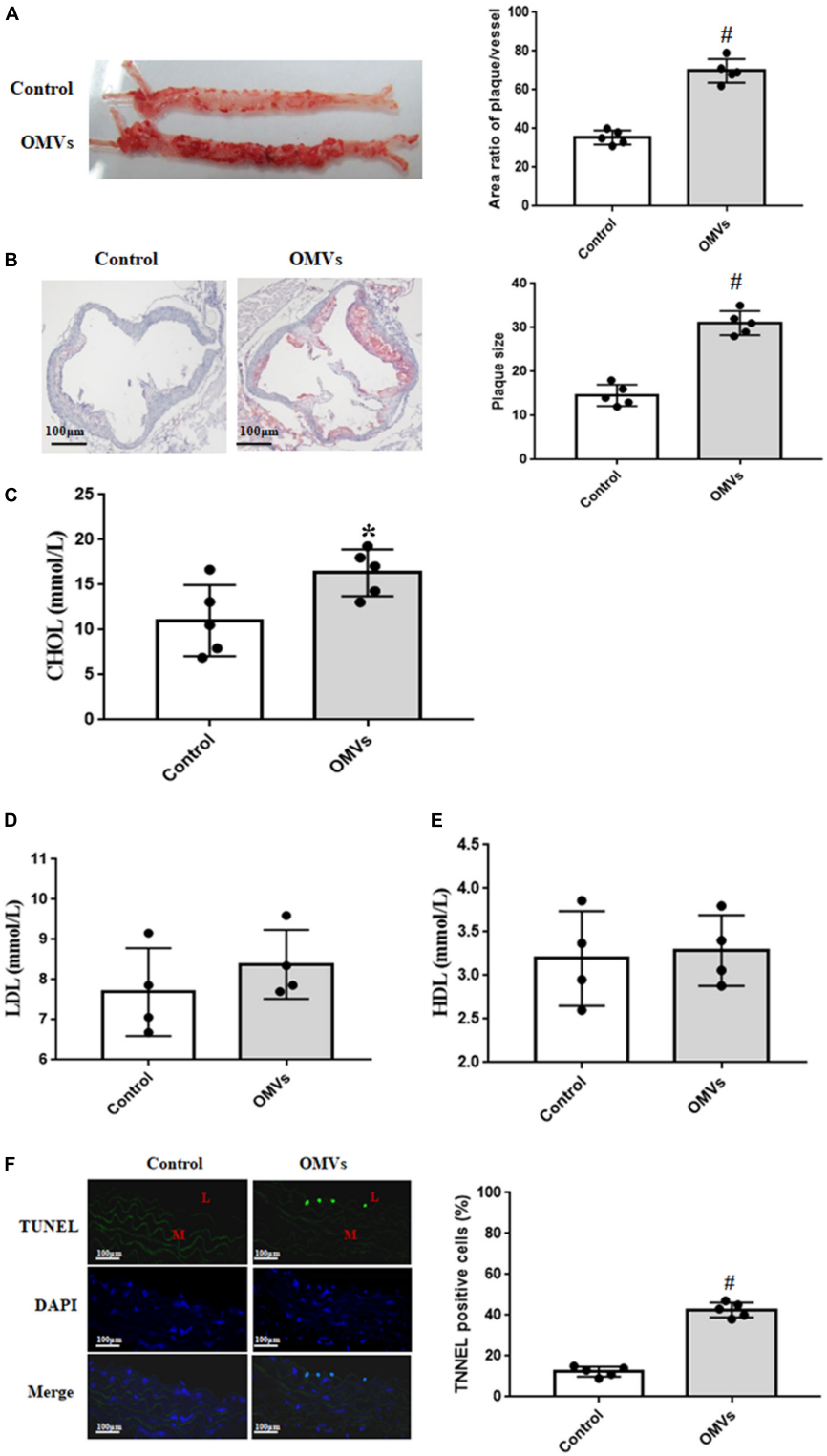

FIGURE 2 | *H. pylori*-derived OMVs accelerate atherosclerosis plaque formation in ApoE$^{-/-}$ mice. **(A)** Continuous atherosclerosis plaques were measured by Oil Red O staining in ApoE$^{-/-}$ mice treated with *H. pylori*-derived OMVs ($n = 5$, $^{\#}P < 0.01$ vs. control). **(B)** Cross-section histological analysis were determined by HE staining in ApoE$^{-/-}$ mice treated with *H. pylori*-derived OMVs ($n = 5$, $^{\#}P < 0.01$ vs. control). **(C–E)** The levels of serum lipids, including cholesterol (**C**, CHOL), low density lipoprotein cholesterol (**D**, LDL), high density lipoprotein cholesterol (**E**, HDL), were determined by ELISA in ApoE$^{-/-}$ mice treated with *H. pylori*-derived OMVs ($n = 4$ or 5, $^{*}P < 0.05$ vs. control). **(F)** Apoptosis were measured by TUNEL staining in arteries from ApoE$^{-/-}$ and control mice. Magnification is × 20; blue, cell nuclei (DAPI staining); green, TUNEL staining; L, lumen; M, media ($n = 5$, $^{\#}P < 0.01$ vs. control).

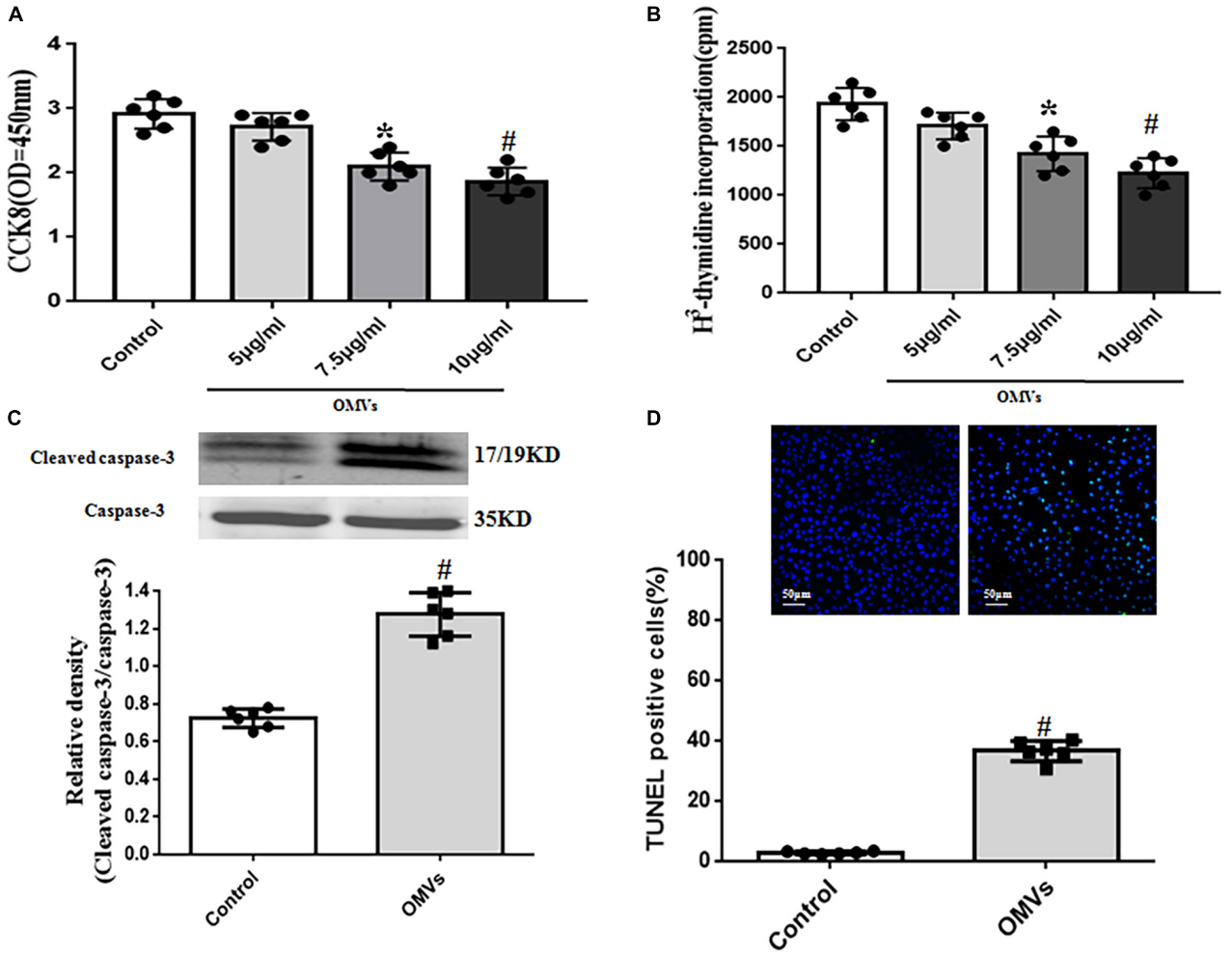

FIGURE 3 | Role of *H. pylori*-derived OMVs on proliferation and apoptosis of HUVECs. **(A,B)** Proliferation of HUVECs treated with *H. pylori*-derived OMVs (5, 7.5, 10 μg/ml) were assayed by cell counting kit-8 (CCK8) **(A)** and [^{3}H] thymidine incorporation **(B)**. Absorbance was detected at 450 nm ($n = 6$, $^*P < 0.05$ or $^\#P < 0.01$ vs. control. **(C)** Cleaved caspase-3 and total caspase-3 levels in HUVECs were determined by immunoblotting. Data were expressed as the ratio of cleaved caspase-3 to total caspase-3 expression ($n = 6$, $^\#P < 0.01$ vs. control). **(D)** Apoptosis of HUVECs was determined by TUNEL staining. Data were expressed as the ratio of apoptotic cells to total cells ($n = 6$, $^\#P < 0.01$ vs. control).

showed the direct evidence that *H. pylori*-derived OMVs promote apoptosis of HUVECs.

Role of Lipopolysaccharide and Cytotoxin-Associated Gene A in the *H. pylori*-Derived Outer Membrane Vesicles -Induced Proliferation Inhibition and Apoptosis in Human Umbilical Vein Endothelial Cells

OMVs, varying in their abundance, size and composition, contain materials such as functional transmembrane proteins, RNAs, and DNA (Parker and Keenan, 2012). To make clear which components of OMVs affect HUVECs proliferation and apoptosis, *H. pylori*-derived OMVs were treated with Triton X-100 and then incubated with RNase to remove RNAs. Results showed that after co-treatment with RNase, the proliferation inhibition and apoptosis induced by *H. pylori*-derived-OMVs were not changed (**Figures 4A,B**), suggesting that proteins, other than RNAs, might participate in *H. pylori*-derived OMVs-mediated effects in HUVECs. To further confirm the role of proteins in the effects, *H. pylori*-derived OMVs were denatured after heated in 95°C for 30 min. Our results found that the proliferation inhibition and apoptosis induced by *H. pylori*-derived-OMVs were lost in HUVECs treated with the denatured OMVs (**Figures 4A,B**), indicating that proteins in the OMVs may participate in the effects induced by *H. pylori*-derived-OMVs in HUVECs.

It is known that the components of OMVs are complex. Among them, LPS and CagA have been reported to regulate cell proliferation and apoptosis (Valenzuela et al., 2013). To explore whether or not LPS and CagA contribute to the OMVs-mediated proliferation inhibition and apoptosis in HUVECs,

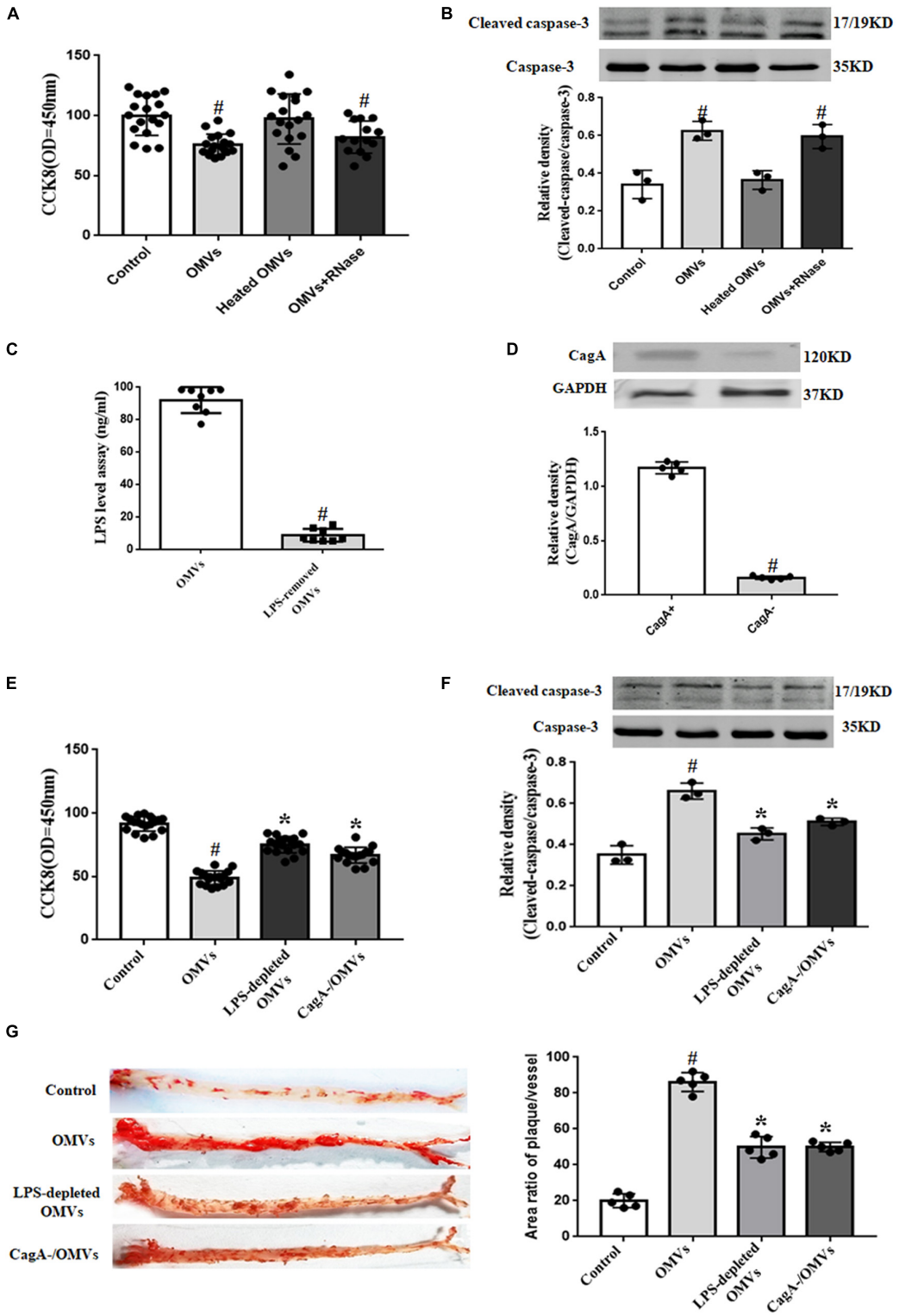

FIGURE 4 | Role of LPS and CagA in *H. pylori*-derived OMVs-mediated proliferation inhibition and apoptosis in HUVECs. **(A,B)** HUVECs were administrated with control (vehicle), OMVs (10 μg/mL), heated OMVs or RNase-treated OMVs for 24 h. Proliferation of HUVECs were determined by CCK8 **(A)** ($n = 18$, $^{\#}P < 0.01$ vs. control); apoptosis of HUVECs were determined by the ratio of cleaved-caspase-3 to caspase-3 expression **(B)** ($n = 3$, $^{\#}P < 0.01$ vs. control). **(C)** LPS levels were determined by ELISA after treatment with polymyxin B for 1 h at 37°C ($n = 8$, $^{\#}P < 0.01$ vs. OMVs). **(D)** CagA levels in CagA-positive or -negative OMVs were determined by immunoblotting ($n = 5$, $^{\#}P < 0.01$ vs. CagA^{+}). **(E,F)** HUVECs were administrated with control (vehicle), OMVs (10 μg/mL), LPS-depleted OMVs or

(Continued)

FIGURE 4 | (Continued)
CagA-negative OMVs for 24 h. Proliferation of HUVECs were determined by CCK8 **(E)** ($n = 13$, $^{*}P < 0.05$ vs. OMVs or $^{\#}P < 0.01$ vs. control); apoptosis of HUVECs were determined by the ratio of cleaved-caspase-3 to total caspase-3 expression **(F)** ($n = 3$, $^{*}P < 0.05$ vs. OMVs or $^{\#}P < 0.01$ vs. control). **(G)** Continuous atherosclerosis plaques were measured by Oil Red O staining in ApoE$^{-/-}$ mice treated with control (vehicle), OMVs, LPS-depleted OMVs or CagA^{-} OMVs after 4 weeks ($n = 5$, $^{*}P < 0.05$ vs. OMVs or $^{\#}P < 0.01$ vs. control).

LPS was depleted by treatment with polymyxin B, an inhibitor of activation properties of LPS (**Figure 4C**), and CagA-negative OMVs was also used (**Figure 4D**). Results showed that both OMVs-induced proliferation inhibition and apoptosis in HUVECs were normalized to some degree after treatment with LPS-depleted OMVs or CagA-negative OMVs (**Figures 4E,F**). The results in *in vitro* experiments were also reflected in *in vivo* studies. We found that compared with the ApoE$^{-/-}$ mice treated with *H. pylori*-derived-OMVs, there were less atherosclerosis plaque formation in ApoE$^{-/-}$ mice treated with LPS-depleted OMVs or OMVs originated from CagA-negative bacterial strain (**Figure 4G**). These results indicated that both LPS and CagA, at least in part, participate in the effects induced by *H. pylori*-derived-OMVs in HUVECs.

Role of Reactive Oxygen Species /NF-κB Signaling Pathway in the *H. pylori*-Derived Outer Membrane Vesicles -Induced Proliferation Inhibition and Apoptosis in Human Umbilical Vein Endothelial Cells

It is well known that reactive oxygen species (ROS) play a vital role in the regulation of cell proliferation and apoptosis (Brown and Griendling, 2015). In our present study, treatment with *H. pylori*-derived-OMVs (10 μg/ml, 24 h) increased ROS levels in HUVECs (**Figure 5A**). We also found that *H. pylori*-derived-OMVs up-regulated the expression of the NADPH oxidase protein gp91^{phox}, but down-regulated the expression of the antioxidant protein SOD2, which were both normalized to some degree after treatment with polymyxin B or CagA-negative OMVs (**Figure 5B**). Studies have shown that increased ROS lead to the activation of NF-κB, which causes the proliferation inhibition and apoptosis of HUVECs (Jang et al., 2017; Safi et al., 2018). Thus, the NF-κB activity in HUVECs was investigated. We found that *H. pylori*-derived-OMVs increased the protein expression of NF-κB p65 subunit, but decreased the protein levels of IκBα, an inhibitor of NF-κBα, which were normalized to some degree after administration with LPS-depleted OMVs or CagA-negative OMVs (**Figures 5C,D**).

To further define the role of ROS and NF-κB in the effects of *H. pylori*-derived-OMVs, a superoxide dismutase mimetic TEMPOL and a NF-κB inhibitor BAY11-7082 were used. We found that *H. pylori*-derived-OMVs increased the ratio of cleaved-caspase-3 to caspase-3 expression and decreased the proliferation of HUVECs, which were normalized to some degree in the presence of TEMPOL or BAY11-7082 (**Figures 5E,F**). In addition, the levels of inflammatory factors, downstream targets of NF-κB, were also determined. Results showed that compared with the control, the expressions of IL-6 and TNF-α were significantly augmented after treatment with *H. pylori*-derived-OMVs (**Figures 5G,H**). These results indicated that activation of ROS/NF-κB signaling pathway may be involved in the proliferation inhibition and apoptosis induced by *H. pylori*-derived-OMVs in HUVECs.

DISCUSSION

Atherosclerosis is a complex disease process with multiple risk factors (von Scheidt et al., 2021). Up to now, the exact mechanism of processes leading to initiation of atherosclerotic lesions has remained unclear. Clinical and experimental studies have shown that specific pathogens, including chlamydia pneumoniae, mycobacterium tuberculosis, human immunodeficiency virus, may promote to the development of atherosclerosis and the occurrence of clinical events (Tumurkhuu et al., 2018; Zhao et al., 2019). Therefore, the possible proatherogenic roles of common infectious pathogens are worthy of further exploration.

H. pylori, one of the most common bacterial pathogens in human beings, colonizes the gastric mucosa. In recent years, many studies have demonstrated the associations between *H. pylori* infection and cardiovascular diseases such as atherosclerosis. Epidemiological studies have suggested an association between *H. pylori* infection and atherosclerosis as a common clinical feature of atherosclerosis (Matsuo et al., 2017). *H. pylori*-specific DNA had been detected in atheromatous plaque (Kowalski, 2001). Patients with *H. pylori* infection are about three times more at risk of CAD (Fang et al., 2019). However, how *H. pylori* escapes from the defensive system and goes to atherosclerotic plaque is still unknown.

Extracellular vesicles (EVs), membrane-enclosed structures released from prokaryotic and eukaryotic cells, play a vital role to promote intercellular communication (Yang et al., 2020). EVs contain different materials such as RNAs, proteins, DNA, microRNA, and lipids, which can be delivered from the cell of origin to a recipient cell, which is in the vicinity or distant from the cell of origin (Jansen et al., 2017). *H. pylori* release parts of its outer membrane in the form of vesicles. These OMVs released by several gram-negative bacteria contain numerous bacterial antigens and virulence factors (Jarzab et al., 2020). *H. pylori*-derived OMVs are small, circular structures with intact outer membranes that are shed from the surface (Fiocca et al., 1999). Studies have reported that OMVs derived from bacteria play an important role in the pathogenesis of cardiovascular diseases such as atherosclerosis and thromboembolism (Anderson et al., 2010). For example, oral bacteria *Porphyromonas gingivalis*-derived OMVs promote calcification of VSMCs and induce the inflammatory responses in HUVECs (Ho et al., 2016; Yang et al., 2016). In our present study, *H. pylori*-derived

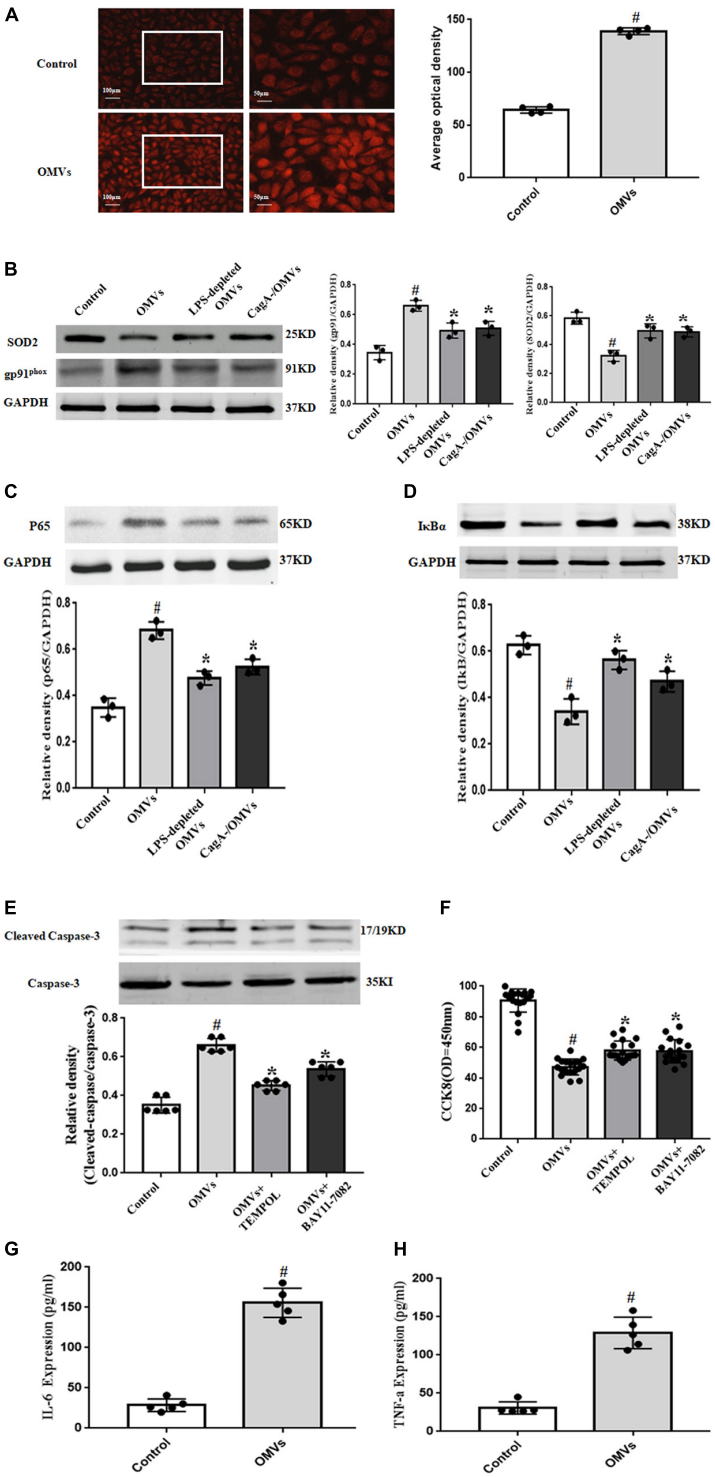

FIGURE 5 | Role of ROS/NF-κB signaling pathway in *H. pylori*-derived OMVs-mediated effects in HUVECs. **(A)** ROS were determined by dihydroethidium staining in HUVECs treated with *H. pylori*-derived OMVs (10 μg/mL) for 24 h ($n = 4$, $^{\#}P < 0.01$ vs. control). **(B–D)** HUVECs were administrated with control (vehicle), OMVs (10 μg/mL), LPS-depleted OMVs or CagA-negative OMVs for 24 h. The expressions of SOD2 and gp91^{phox} **(B)**, p65 **(C)**, IκBα **(D)** were determined by immunoblotting ($n = 3$, $^{*}P < 0.05$ vs. OMVs or $^{\#}P < 0.01$ vs. control). **(E)** HUVECs were treated with control (vehicle), OMVs (10 μg/mL), OMVs + TEMPOL, and OMVs + BAY11-7082 for 24 h. The expression of cleaved-caspase-3 and total caspase-3 were determined by immunoblotting ($n = 6$, $^{*}P < 0.05$ vs. OMVs or $^{\#}P < 0.01$ vs. control). **(F)** Proliferation of HUVECs were assayed by CCK8 after treatment with vehicle, OMVs (10 μg/mL), OMVs + TEMPOL, and OMVs + BAY11-7082 for 24 h ($n = 17$, $^{*}P < 0.05$ vs. OMVs or $^{\#}P < 0.01$ vs. control). **(G,H)** ApoE$^{-/-}$ mice or control mice were intragastrically administered with vehicle or *H. pylori*-derived OMVs for 4 weeks. Levels of IL-6 **(G)** and TNF-α **(H)** were determined by ELISA ($n = 5$, $^{\#}P < 0.05$ vs. control).

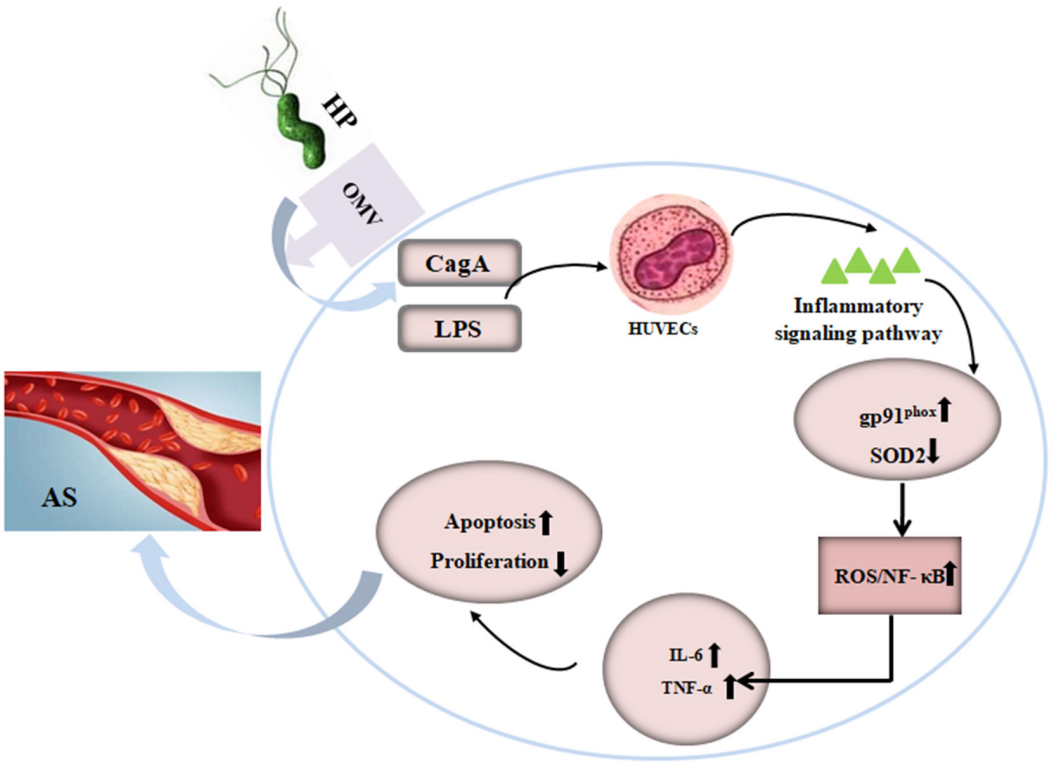

FIGURE 6 | Schematic representation of the effect of OMVs from *H. pylori* on atherosclerosis plaque formation in ApoE$^{-/-}$ mice. AS, atherosclerosis; CagA, cytotoxin-associated gene A; HP, *Helicobacter pylori*; HUVECs, human umbilical vein endothelial cells; IL-6, interleukin-6; LPS, lipopolysaccharide; NK-κB, nuclear factor-κB; OMVs, outer membrane vesicles; SOD2, superoxide dismutase 2; TNF-α, tumor necrosis factor-α.

OMVs were isolated and identified by different methods. Both Oil Red O and HE staining showed that ApoE$^{-/-}$ mice intragastrically administered with *H. pylori*-derived OMVs had more serious atherosclerosis, indicating that *H. pylori*-derived OMVs accelerate atherosclerosis plaque formation. We also found that injured arterial lumen may participate in the *H. pylori*-derived OMVs-mediated atherosclerosis plaque formation, which was verified by further *in vitro* studies, in which *H. pylori*-derived OMVs inhibited proliferation and promoted apoptosis of HUVECs.

H. pylori-derived OMVs contain some materials including CagA and LPS, which are associated with cardiovascular diseases such as atherosclerosis. CagA-positive *H. pylori* infection impairs endothelial function in patients and mice through exosome-mediated mechanisms (Xia et al., 2020), promotes coronary atherosclerosis via increasing serum oxidized LDL and high-sensitivity C-reactive protein in patients with CAD (Huang et al., 2011). Chronic infection by CagA-positive *H. pylori* correlates with high circulating levels of B-type natriuretic peptide and IL-6 in patients with acute CAD (Figura et al., 2014). Studies have also shown that CagA *per se* exerts functions in the progression of atherosclerosis. For example, exosomal CagA derived from *H. pylori*-infected gastric epithelial cells induces macrophage foam cell formation and promotes atherosclerosis (Yang et al., 2019). On the other hand, it is well accepted that LPS aggravates atherosclerosis via evoking a systemic inflammation (Ostos et al., 2002; Gitlin and Loftin, 2009). In our present study, OMVs-induced proliferation inhibition and apoptosis in HUVECs were reversed after treatment with LPS-depleted OMVs or CagA-negative OMVs. These were reflected in *in vivo* studies, which showed that there was less atherosclerosis plaque formation in ApoE$^{-/-}$ mice treated with LPS-depleted OMVs or CagA-negative OMVs. These indicated that CagA and LPS participate in the proliferation inhibition and apoptosis in HUVECs induced by *H. pylori*-derived-OMVs.

ROS/NF-κB signaling pathway is involved in the development of atherosclerosis (Ellulu et al., 2016; Zhang et al., 2016). OMVs exert physiological functions via regulating ROS levels. For example, *Porphyromonas gingivalis*-derived OMVs induce a shift in macrophage metabolism from oxidative phosphorylation to glycolysis, increase mitochondrial ROS production, causing pyroptotic cell death in macrophages (Fleetwood et al., 2017). *Borrelia burgdorferi* originated-OMVs serve to directly counter superoxide production via SOD2 expression in human neuroblastoma cells (Wawrzeniak et al., 2020). OMVs from *Proteus mirabilis* regulate the function of boar sperm via increasing ROS levels and inducing sperm membrane reconstruction (Gao et al., 2018). Studies have also shown the regulation of OMVs on the activation of NF-κB. *H. pylori*-derived OMVs stimulate IL-8 secretion through NF-κB activation in two

human gastric epithelial cell lines and a human monocytic cell line (Choi et al., 2020). OMVs from non-pathogenic *Escherichia (E.) coli* or pathogenic *E. coli* trigger NF-κB translocation to the nucleus, resulting in up-regulation of adhesion molecules and cytokines, and then initiating the inflammatory cascade in endothelial cells (Soult et al., 2013). In our present study, we found that *H. pylori*-derived OMVs increased ROS levels and activated NF-κB in HUVECs, which were, respectively, normalized to some degree after administration with LPS-depleted OMVs or CagA-negative OMVs. The roles of ROS and NF-κB were further verified by treatment with a superoxide dismutase mimetic TEMPOL and a NF-κB inhibitor BAY11-7082. In addition, we found that *H. pylori*-derived OMVs increased the levels of inflammatory factors IL-6 and TNF-α, two downstream targets of NF-κB, in HUVECs. These suggested that ROS/NF-κB signaling pathway is involved in the *H. pylori*-derived OMVs-mediated effects in HUVECs.

It should be noted that some effects of *H. pylori* on atherosclerotic plaques are, at least in part, direct (Testerman et al., 2019). However, this does not mean that OMVs play no role in the *H. pylori*-accelerated atherosclerosis. OMVs could be transferred to the cytosol and nucleus in the recipient cells even at a distance (Keenan et al., 2008; Parker et al., 2010), indicating that OMVs generated in the stomach could be transported to the plaque, promoting atherosclerosis. It is similar with the distant effects of exosomes derived from *H. pylori*-infected gastric epithelial cells. *H. pylori* infection impairs endothelial function, induces macrophage foam cell formation and promotes atherosclerosis through exosome-mediated mechanisms (Yang et al., 2019; Xia et al., 2020). But it is also possible that OMVs are generated in the plaque and act locally although it hasn't been reported yet. We cannot define which one could have an even greater chance of causing local damage. Moreover, OMVs were either able to cross the mucosa and enter the bloodstream or were acting at a distance, perhaps via cytokine induction. This question could be answered by determining whether CagA is present within plaques or the endothelium, which needs to be studied in the future. In addition, Testerman et al. (2019) reported that of the *H. pylori*-positive animals, 64% had evidence of *H. pylori* infection in both the stomach and arteries. Further studies showed that live *H. pylori* are frequently present in coronary arteries of *H. pylori*-infected monkeys and the density of bacteria found in plaques is strongly related to colonization density in the stomach. These indicate that the effect of OMVs-accelerated atherosclerosis may, at least in part, be associated with the amount of gastric *H. pylori* (Testerman et al., 2019).

In conclusion, we present evidence that *H. pylori*-derived OMVs accelerate atherosclerosis plaque formation via endothelium injury (**Figure 6**). CagA and LPS from *H. pylori*-derived OMVs, at least in part, participate in these processes. Activation of ROS/NF-κB signaling pathway may be involved in the *H. pylori*-derived OMVs-mediated effects in endothelial cells. These afford a novel mechanism between *H. pylori* infection and atherosclerosis, and suggest that preventing and eradicating the *H. pylori* infection may be a new strategy to reduce the incidence and development of atherosclerosis.

DATA AVAILABILITY STATEMENT

The original contributions presented in the study are included in the article/supplementary material, further inquiries can be directed to the corresponding author/s.

ETHICS STATEMENT

The animal study was reviewed and approved by the Daping Hospital Animal Use and Care Committee.

AUTHOR CONTRIBUTIONS

NW, FZ, and CC contributed to conception and design of the study. HL organized the database. WW performed the statistical analysis. JG wrote the first draft of the manuscript. JY wrote sections of the manuscript. LL contributed to the interpretation of the data and the revision the manuscript. All authors contributed to manuscript revision, read, and approved the submitted version.

FUNDING

This study was supported in part by the National Natural Science Foundation of China (82070296 and 81770425).

ACKNOWLEDGMENTS

We would like to acknowledge the help of Prof. Qinghua Xie (Department of Microbiology and Biochemical Pharmacy, College of Pharmacy and Laboratory Medicine, The Third Military Medical University) for the kind gift of *H. pylori*.

REFERENCES

Ali, Z. A., Rinze, R., Douglas, G., Hu, Y., Xiao, Q., Qi, W., et al. (2013). Tetrahydrobiopterin determines vascular remodeling through enhanced endothelial cell survival and regeneration. *Circulation* 11, S50–S58. doi: 10.1161/CIRCULATIONAHA.112.000249

Anderson, H. C., Mulhall, D., and Garimella, R. (2010). Role of extracellular membrane vesicles in the pathogenesis of various diseases, including cancer, renal diseases, atherosclerosis, and arthritis. *Lab. Invest.* 90, 1549–1557. doi: 10.1038/labinvest.2010.152

Brown, D. I., and Griendling, K. K. (2015). Regulation of signal transduction by reactive oxygen species in the cardiovascular system. *Circ. Res.* 116, 531–549. doi: 10.1161/CIRCRESAHA.116.303584

Chitcholtan, K., Hampton, M. B., and Keenan, J. I. (2008). Outer membrane vesicles enhance the carcinogenic potential of *Helicobacter pylori*. *Carcinogenesis* 29, 2400–2405. doi: 10.1093/carcin/bgn218

Chmiela, M., Walczak, N., and Rudnicka, K. (2018). *Helicobacter pylori* outer membrane vesicles involvement in the infection development and *Helicobacter pylori*-related diseases. *J. Biomed. Sci.* 25:78. doi: 10.1186/s12929-018-0480-y

Choi, M. S., Ze, E. Y., Park, J. Y., Shin, T. S., and Kim, J. G. (2020). *Helicobacter pylori*-derived outer membrane vesicles stimulate interleukin 8 secretion through nuclear factor kappa B activation. *Korean J. Intern. Med.* 36, 854–867. doi: 10.3904/kjim.2019.432

Cover, T. L., and Peek, R. M. Jr. (2013). Diet, microbial virulence, and *Helicobacter pylori*-induced gastric cancer. *Gut Microbes* 4, 482–493. doi: 10.4161/gmic.26262

Davies, C., Taylor, A. J., Elmi, A., Winter, J., Liaw, J., Grabowska, A. D., et al. (2019). Sodium taurocholate stimulates campylobacter jejuni outer membrane vesicle production via down-regulation of the maintenance of lipid asymmetry pathway. *Front. Cell. Infect. Microbiol.* 29:177. doi: 10.3389/fcimb.2019.00177

Ellulu, M. S., Patimah, I., Khaza'ai, H., Rahmat, A., Abed, Y., and Ali, F. (2016). Atherosclerotic cardiovascular disease: a review of initiators and protective factors. *Inflammopharmacology* 24, 1–10. doi: 10.1007/s10787-015-0255-y

Fang, Y., Fan, C., and Xie, H. (2019). Effect of *Helicobacter pylori* infection on the risk of acute coronary syndrome: a systematic review and meta-analysis. *Medicine* 98:e18348. doi: 10.1097/MD.0000000000018348

Figura, N., Palazzuoli, A., Vaira, D., Campagna, M., Moretti, E., Iacoponi, F., et al. (2014). Cross-sectional study: CagA-positive *Helicobacter pylori* infection, acute coronary artery disease and systemic levels of B-type natriuretic peptide. *J. Clin. Pathol.* 67, 251–257. doi: 10.1136/jclinpath-2013-201743

Fiocca, R., Necchi, V., Sommi, P., Ricci, V., Telford, J., Cover, T. L., et al. (1999). Release of *Helicobacter pylori* vacuolating cytotoxin by both a specific secretion pathway and budding of outer membrane vesicles. Uptake of released toxin and vesicles by gastric epithelium. *J. Pathol.* 188, 220–226. doi: 10.1002/(sici)1096-9896(199906)188:2<220::aid-path307>3.0.co;2-c

Fleetwood, A. J., Lee, M. K. S., Singleton, W., Achuthan, A., Lee, M. C., O'Brien-Simpson, N. M., et al. (2017). Metabolic remodeling, inflammasome activation, and pyroptosis in macrophages stimulated by *Porphyromonas gingivalis* and its outer membrane vesicles. *Front. Cell. Infect. Microbiol.* 7:351. doi: 10.3389/fcimb.2017.00351

Gao, H., Gao, Y., Yang, C., Dong, D., Yang, J., Peng, G., et al. (2018). Influence of outer membrane vesicles of *Proteus mirabilis* isolated from boar semen on sperm function. *Vet. Microbiol.* 224, 34–42. doi: 10.1016/j.vetmic.2018.08.017

Gitlin, J. M., and Loftin, C. D. (2009). Cyclooxygenase-2 inhibition increases lipopolysaccharide-induced atherosclerosis in mice. *Cardiovasc. Res.* 81, 400–407. doi: 10.1093/cvr/cvn286

Ho, M. H., Guo, Z. M., Chunga, J., Goodwin, J. S., and Xie, H. (2016). Characterization of innate immune responses of human endothelial cells induced by *Porphyromonas gingivalis* and their derived outer membrane vesicles. *Front. Cell. Infect. Microbiol.* 6:139. doi: 10.3389/fcimb.2016.00139

Hodges, K., and Hecht, G. (2012). Interspecies communication in the gut, from bacterial delivery to host-cell response. *J. Physiol.* 590, 433–440. doi: 10.1113/jphysiol.2011.220822

Huang, B., Chen, Y., Xie, Q., Lin, G., Wu, Y., Feng, Y., et al. (2011). CagA-positive *Helicobacter pylori* strains enhanced coronary atherosclerosis by increasing serum OxLDL and HsCRP in patients with coronary heart disease. *Dig. Dis. Sci.* 56, 109–114. doi: 10.1007/s10620-010-1274-6

Jang, J. H., Kim, E. A., Park, H. J., Sung, E. G., Song, I. H., Kim, J. Y., et al. (2017). Methylglyoxal-induced apoptosis is dependent on the suppression of c-FLIPL expression via down-regulation of p65 in endothelial cells. *J. Cell. Mol. Med.* 21, 2720–2731. doi: 10.1111/jcmm.13188

Jansen, F., Xiang, X., and Werner, N. (2017). Role and function of extracellular vesicles in calcific aortic valve disease. *Eur. Heart J.* 38, 2714–2716. doi: 10.1093/eurheartj/ehx477

Jarzab, M., Posselt, G., Meisner-Kober, N., and Wessler, S. (2020). *Helicobacter pylori*-derived outer membrane vesicles (OMVs): role in bacterial pathogenesis? *Microorganisms* 8:1328. doi: 10.3390/microorganisms8091328

Keenan, J. I., Davis, K. A., Beaugie, C. R., McGovern, J. J., and Moran, A. P. (2008). Alterations in *Helicobacter pylori* outer membrane and outer membrane vesicle-associated lipopolysaccharides under iron-limiting growth conditions. *Innate Immun.* 14, 279–290. doi: 10.1177/1753425908096857

Koren, O., Spor, A., Felin, J., Fåk, F., Stombaugh, J., Tremaroli, V., et al. (2011). Human oral, gut, and plaque microbiota in patients with atherosclerosis. *Proc. Natl. Acad. Sci. U.S.A.* 108, 4592–4598. doi: 10.1073/pnas.1011383107

Kowalski, M. (2001). *Helicobacter pylori* (*H. pylori*) infection in coronary artery disease: influence of *H. pylori* eradication on coronary artery lumen after percutaneous transluminal coronary angioplasty. The detection of *H. pylori* specific DNA in human coronary atherosclerotic plaque. *J. Physiol. Pharmacol.* 52, 3–31.

Matsuo, Y., Kido, Y., and Yamaoka, Y. (2017). *Helicobacter pylori* outer membrane potein-related pathogenesis. *Toxins* 9:101. doi: 10.3390/toxins9030101

Myers, L., and Mendis, S. (2014). Cardiovascular disease research output in WHO priority areas between 2002 and 2011. *J. Epidemiol. Glob. Health* 4, 23–28. doi: 10.1016/j.jegh.2013.09.007

Ostos, M. A., Recalde, D., Zakin, M. M., and Scott-Algara, D. (2002). Implication of natural killer T cells in atherosclerosis development during a LPS-induced chronic inflammation. *FEBS Lett.* 519, 23–29. doi: 10.1016/s0014-5793(02)02692-3

Parker, H., Chitcholtan, K., Hampton, M. B., and Keenan, J. I. (2010). Uptake of *Helicobacter pylori* outer membrane vesicles by gastric epithelial cells. *Infect. Immun.* 78, 5054–5061. doi: 10.1128/IAI.00299-10

Parker, H., and Keenan, J. I. (2012). Composition and function of *Helicobacter pylori* outer membrane vesicles. *Microbes. Infect.* 14, 9–16. doi: 10.1016/j.micinf.2011.08.007

Pérez-Pérez, G. I., Shepherd, V. L., Morrow, J. D., and Blaser, M. J. (1995). Activation of human THP-1 cells and rat bone marrow-derived macrophages by *Helicobacter pylori* lipopolysaccharide. *Infect. Immun.* 63, 1183–1187. doi: 10.1128/IAI.63.4.1183-1187.1995

Rožanković, P. B., Huzjan, A. L., Cupić, H., Benčić, I. J., Bašić, S., and Demarin, V. (2011). Influence of CagA-positive *Helicobacter pylori* strains on atherosclerotic carotid disease. *J. Neurol.* 258, 753–761. doi: 10.1007/s00415-010-5824-9

Safi, S. Z., Shah, H., Qvist, R., Bindal, P., Mansor, M., Yan, G. O. S., et al. (2018). Beta adrenergic receptors stimulation attenuates phosphorylation of NF-κB and IκBα in hyperglycemic endothelial clls. *Cell. Physiol. Biochem.* 51, 1429–1436. doi: 10.1159/000495591

Soult, M. C., Lonergan, N. E., Shah, B., Kim, W. K., Britt, L. D., and Sullivan, C. J. (2013). Outer membrane vesicles from pathogenic bacteria initiate an inflammatory response in human endothelial cells. *J. Surg. Res.* 184, 458–466. doi: 10.1016/j.jss.2013.05.035

Testerman, T. L., Semino-Mora, C., Cann, J. A., Qiang, B., Peña, E. A., Liu, H., et al. (2019). Both diet and *Helicobacter pylori* infection contribute to atherosclerosis in pre- and postmenopausal cynomolgus monkeys. *PLoS One* 14:e0222001. doi: 10.1371/journal.pone.0222001

Tumurkhuu, G., Dagvadorj, J., Porritt, R. A., Crother, T. R., Shimada, K., Tarling, E. J., et al. (2018). Chlamydia pneumoniae hijacks a host autoregulatory IL-1β loop to drive foam cell formation and accelerate atherosclerosis. *Cell Metab.* 28, 432.e4–448.e4. doi: 10.1016/j.cmet.2018.05.027

Valenzuela, M., Bravo, D., Canales, J., Sanhueza, C., Díaz, N., Almarza, O., et al. (2013). *Helicobacter pylori*-induced loss of survivin and gastric cell viability is attributable to secreted bacterial gamma-glutamyl transpeptidase activity. *J. Infect. Dis.* 208, 1131–1141. doi: 10.1093/infdis/jit286

von Scheidt, M., Zhao, Y., de Aguiar Vallim, T. Q., Che, N., Wierer, M., Seldin, M. M., et al. (2021). The transcription factor MAFF regulates an atherosclerosis relevant network connecting inflammation and cholesterol metabolism. *Circulation* doi: 10.1161/CIRCULATIONAHA.120.050186 [Epub ahead of print].

Wawrzeniak, K., Gaur, G., Sapi, E., and Senejani, A. G. (2020). Effect of *Borrelia burgdorferi* outer membrane vesicles on host oxidative stress response. *Antibiotics* 9:275. doi: 10.3390/antibiotics9050275

Xia, X., Zhang, L., Chi, J., Li, H., Liu, X., Hu, T., et al. (2020). *Helicobacter pylori* infection impairs endothelial function through an exosome-mediated mechanism. *J. Am. Heart Assoc.* 9, e014120. doi: 10.1161/JAHA.119.014120

Yamaoka, Y., Kita, M., Kodama, T., Sawai, N., Kashima, K., and Imanishi, J. (1997). Induction of various cytokines and development of severe mucosal inflammation by cagA gene positive *Helicobacter pylori* strains. *Gut* 41, 442–451. doi: 10.1136/gut.41.4.442

Yang, L., Han, B., Zhang, Z., Wang, S., Bai, Y., Zhang, Y., et al. (2020). Extracellular vesicle-mediated delivery of circular RNA SCMH1 promotes functional recovery in rodent and nonhuman primate ischemic stroke models. *Circulation* 142, 556–574. doi: 10.1161/CIRCULATIONAHA.120.045765

Yang, S., Xia, Y. P., Luo, X. Y., Chen, S. L., Li, B. W., Ye, Z. M., et al. (2019). Exosomal CagA derived from *Helicobacter pylori*-infected gastric epithelial cells induces macrophage foam cell formation and promotes atherosclerosis. *J. Mol. Cell. Cardiol.* 135, 40–51. doi: 10.1016/j.yjmcc.2019.07.011

Yang, W. W., Guo, B., Jia, W. Y., and Jia, Y. (2016). *Porphyromonas gingivalis*-derived outer membrane vesicles promote calcification of vascular smooth muscle cells through ERK1/2-RUNX2. *FEBS Open Biol.* 6, 1310–1319. doi: 10.1002/2211-5463.12151

Zhang, J., Wang, X., Vikash, V., Ye, Q., Wu, D., Liu, Y., et al. (2016). ROS and ROS-mediated cellular signaling. *Oxid. Med. Cell. Longev.* 2016:4350965. doi: 10.1155/2016/4350965

Zhao, W., Wang, X., Deik, A. A., Hanna, D. B., Wang, T., Haberlen, S. A., et al. (2019). Elevated plasma ceramides are associated with antiretroviral therapy use and progression of carotid artery atherosclerosis in HIV Infection. *Circulation* 139, 2003–2011. doi: 10.1161/CIRCULATIONAHA.118.037487

Conflict of Interest: The authors declare that the research was conducted in the absence of any commercial or financial relationships that could be construed as a potential conflict of interest.

Publisher's Note: All claims expressed in this article are solely those of the authors and do not necessarily represent those of their affiliated organizations, or those of the publisher, the editors and the reviewers. Any product that may be evaluated in this article, or claim that may be made by its manufacturer, is not guaranteed or endorsed by the publisher.

Advantages of publishing in Frontiers

OPEN ACCESS
Articles are free to read for greatest visibility and readership

FAST PUBLICATION
Around 90 days from submission to decision

HIGH QUALITY PEER-REVIEW
Rigorous, collaborative, and constructive peer-review

TRANSPARENT PEER-REVIEW
Editors and reviewers acknowledged by name on published articles

Frontiers
Avenue du Tribunal-Fédéral 34
1005 Lausanne | Switzerland

Visit us: www.frontiersin.org
Contact us: frontiersin.org/about/contact

REPRODUCIBILITY OF RESEARCH
Support open data and methods to enhance research reproducibility

DIGITAL PUBLISHING
Articles designed for optimal readership across devices

FOLLOW US
@frontiersin

IMPACT METRICS
Advanced article metrics track visibility across digital media

EXTENSIVE PROMOTION
Marketing and promotion of impactful research

LOOP RESEARCH NETWORK
Our network increases your article's readership